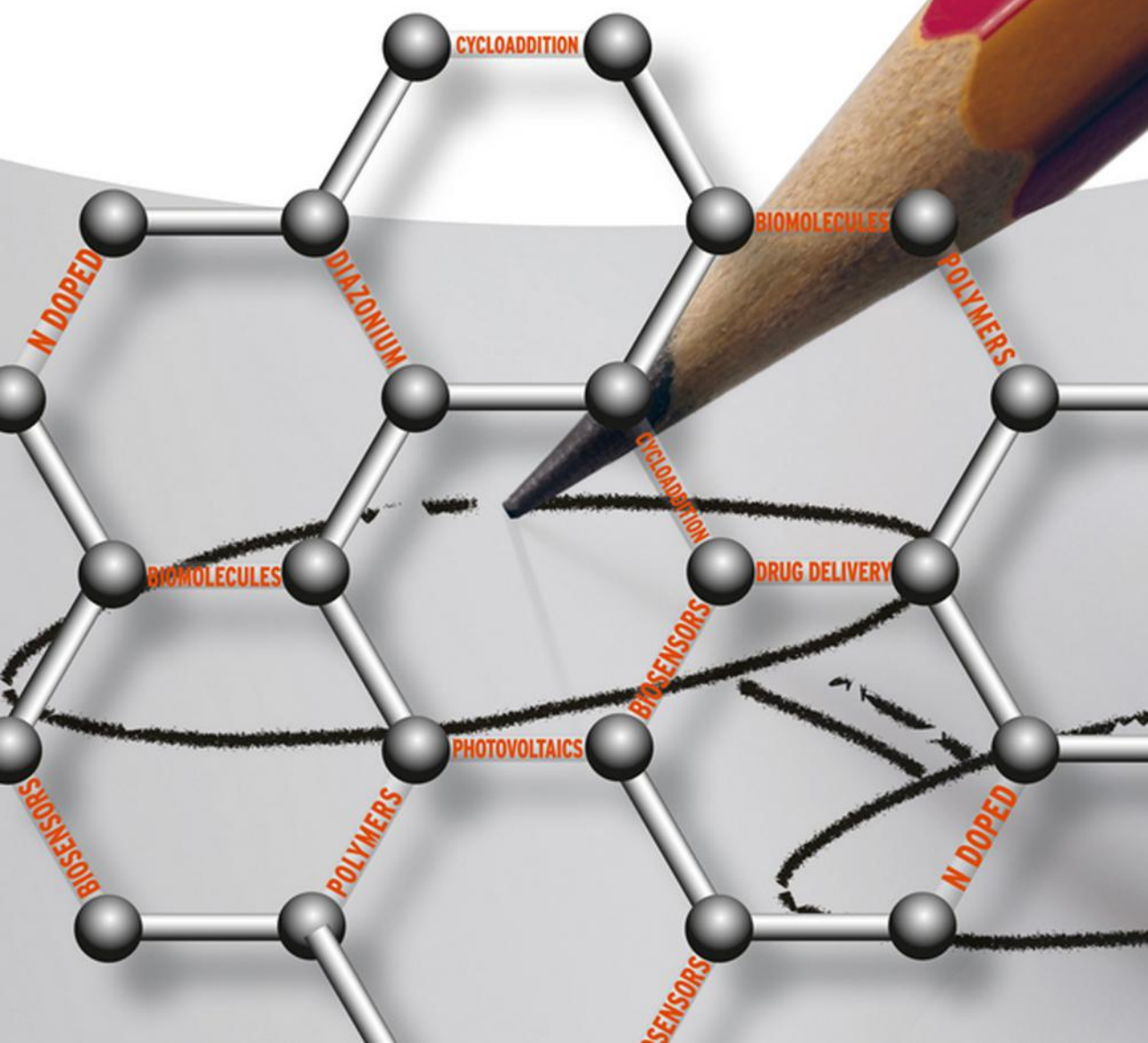


Edited by
Vasilios Georgakilas

Functionalization of Graphene



Edited by
Vasilios Georgakilas

Functionalization of Graphene

Related Titles

Yusoff, A.b. (ed.)

Graphene Optoelectronics Synthesis, Characterization, Properties, and Applications

2014
Print ISBN: 978-3-527-33634-0, also available in
digital formats

Jiang, D., Chen, Z. (eds.)

Graphene Chemistry Theoretical Perspectives

2014
Print ISBN: 978-1-119-94212-2, also available in
digital formats

Rao, C.N., Sood, A.K. (eds.)

Graphene Synthesis, Properties, and Phenomena

2013
Print ISBN: 978-3-527-33258-8, also available in
digital formats

Fujita, S., Suzuki, A.

Electrical Conduction in Graphene and Nanotubes

2013
Print ISBN: 978-3-527-41151-1, also available in
digital formats

Jiang, D., Chen, Z.

Graphene Chemistry Theoretical Perspectives

2013
Print ISBN: 978-1-119-94212-2, also available in
digital formats

Malic, E., Knorr, A.

Graphene and Carbon Nanotubes Ultrafast Relaxation Dynamics and Optics

2013
Print-ISBN: 978-3-527-41161-0, also available
in digital formats

Jorio, A., Dresselhaus, M.S., Saito, R.,
Dresselhaus, G.

Raman Spectroscopy in Graphene Related Systems

2011
Print ISBN: 978-3-527-40811-5, also available in
digital formats

Akasaka, T.T. (ed.)

Chemistry of Nanocarbons

2010
Print ISBN: 978-0-470-72195-7, also available in
digital formats

Kruger, A.

Carbon Materials and Nanotechnology

2010
Print ISBN: 978-3-527-31803-2, also available in
digital formats

Guldi, D.M., Martín, N. (eds.)

Carbon Nanotubes and Related Structures Synthesis, Characterization, Functionalization, and Applications

2010
Print ISBN: 978-3-527-32406-4, also available in
digital formats

Edited by Vasilios Georgakilas

Functionalization of Graphene

WILEY-VCH
Verlag GmbH & Co. KGaA

The Editor

Dr. Vasilios Georgakilas

University of Patras
Department of Material Science
26504 Rio
Greece

All books published by **Wiley-VCH** are carefully produced. Nevertheless, authors, editors, and publisher do not warrant the information contained in these books, including this book, to be free of errors. Readers are advised to keep in mind that statements, data, illustrations, procedural details or other items may inadvertently be inaccurate.

Library of Congress Card No.: applied for

British Library Cataloguing-in-Publication Data

A catalogue record for this book is available from the British Library.

Bibliographic information published by the Deutsche Nationalbibliothek

The Deutsche Nationalbibliothek lists this publication in the Deutsche Nationalbibliografie; detailed bibliographic data are available on the Internet at <<http://dnb.d-nb.de>>.

© 2014 Wiley-VCH Verlag GmbH & Co. KGaA, Boschstr. 12, 69469 Weinheim, Germany

All rights reserved (including those of translation into other languages). No part of this book may be reproduced in any form – by photoprinting, microfilm, or any other means – nor transmitted or translated into a machine language without written permission from the publishers. Registered names, trademarks, etc. used in this book, even when not specifically marked as such, are not to be considered unprotected by law.

Print ISBN: 978-3-527-33551-0

ePDF ISBN: 978-3-527-67278-3

ePub ISBN: 978-3-527-67277-6

Mobi ISBN: 978-3-527-67276-9

oBook ISBN: 978-3-527-67279-0

Cover-Design Bluesea Design, McLeese Lake, Canada

Typesetting Laserwords Private Limited, Chennai, India

Printing and Binding Markono Print Media Pte Ltd., Singapore

Printed on acid-free paper

Contents

Preface XIII

List of Contributors XV

- 1 An Introduction to Graphene** 1
Konstantinos Spyrou and Petra Rudolf
- 1.1 Brief History of Graphite 1
- 1.2 Graphene and Graphene Oxide 2
- 1.2.1 Preparation of Graphene from Graphene Oxide 3
- 1.2.2 Isolation of Pristine Graphene Monolayers 5
- 1.2.3 Large Scale Production of GO by Langmuir-Blodgett Methods 6
- 1.2.4 Other Methods of Graphene Production 6
- 1.3 Characterization of Graphene 9
- 1.3.1 Microscopic Observation 9
- 1.3.2 Raman Spectroscopy 11
- 1.3.3 Thermogravimetric Analysis 12
- 1.3.4 Optical Properties of Graphene 13
- 1.3.5 X-Ray Diffraction Pattern 17
- References 18
- 2 Covalent Attachment of Organic Functional Groups on Pristine Graphene** 21
Vasilios Georgakilas
- 2.1 Introduction 21
- 2.2 Cycloaddition Reactions 22
- 2.2.1 1,3-Dipolar Cycloaddition of Azomethine Ylide 22
- 2.2.1.1 Through a Substituted Aldehyde Pathway 24
- 2.2.1.2 Through Substituted α Amino Acid Pathway 27
- 2.2.2 Cycloaddition by Zwitterionic Intermediate 28
- 2.2.3 Diels–Alder Cycloaddition 29
- 2.2.4 Nitrene Addition 30
- 2.2.5 Carbene Addition 35
- 2.2.6 Aryne Addition 36
- 2.2.7 Bingel Type Cycloaddition 37

2.3	Addition of Free Radicals	39
2.3.1	Diazonium Salt Reaction	39
2.3.2	Other Radical Additions	42
2.4	Nucleophilic Addition	46
2.5	Electrophilic Addition on Graphene	46
2.6	Organometallic Chemistry of Graphene	48
2.7	Post Functionalization Reactions	50
2.8	Conclusion	55
	References	56
3	Addition of Organic Groups through Reactions with Oxygen Species of Graphene Oxide	59
	<i>Vasilios Georgakilas</i>	
3.1	Introduction	59
3.1.1	Graphene/Polymer Nanocomposites	60
3.2	The Role of Carboxylic Acids of GO	61
3.2.1	Organic Functionalization through Amide Bond Formation	61
3.2.1.1	Lipophilic Derivatives	61
3.2.1.2	Hydrophilic – Biocompatible Derivatives	62
3.2.1.3	Addition of Chromophores	64
3.2.1.4	Polymer Graphene Composite	69
3.2.2	Esterification of GO	71
3.2.3	Functionalization of GO through Heterocyclic Ring Formation	75
3.3	The Role of Hydroxyl Groups of GO	77
3.4	Miscellaneous Additions	78
3.4.1	Reaction of Carboxylic Acid and Hydroxyl Groups with Isocyanate Derivatives	78
3.4.2	Reaction of Epoxides with Carboxylic Acids or Hydroxyl Groups	78
3.4.3	Interaction of Ammonia with Carboxylic Acids and Epoxides of GO	80
3.4.4	Enrichment of GO in Carboxylic Acids	81
3.4.5	Addition of Gallium-Phthalocyanine (Ga-Pc) to GO through Ga–O Covalent Bond	82
3.5	The Role of Epoxide Groups of GO	83
3.5.1	Nucleophilic Addition of Amine to Epoxides	83
3.5.2	Addition of Chromophores	85
3.5.3	Addition of Polymers	86
3.6	Post Functionalization of GO	87
3.6.1	Post Functionalization of Organically Modified GO via Click Chemistry	87
3.6.2	Counter Anion Exchange	89
3.7	Conclusions	90
	References	92

4	Chemical Functionalization of Graphene for Biomedical Applications	95
	<i>Cinzia Spinato, Cécilia Ménard-Moyon, and Alberto Bianco</i>	
4.1	Introduction	95
4.2	Covalent Functionalization of Graphene Nanomaterials	97
4.2.1	Synthesis of GO and rGO	99
4.2.1.1	Synthesis of Graphene Oxide	99
4.2.1.2	Reduction of Graphene Oxide	99
4.2.2	Functionalization of Graphene Oxide with Polymers	100
4.2.2.1	PEGylated-GO Conjugates	100
4.2.2.2	Covalent Linkage of Biopolymers	103
4.2.3	Tethering of Antibodies	105
4.2.4	Attachment of Nucleic Acids	106
4.2.5	Grafting of Peptides and Enzymes	108
4.2.6	Attachment of Other Organic Molecules and Biomolecules	108
4.3	Non-covalent Functionalization of Graphene	110
4.3.1	Adsorption via π -Stacking	110
4.3.1.1	Adsorption of Drugs	111
4.3.1.2	Adsorption of Pyrene Derivatives	111
4.3.1.3	Non-covalent Interactions with Nucleic Acids and Aptamers	113
4.3.1.4	Immobilization of Enzymes, Proteins, and Other Macromolecules	116
4.3.2	Electrostatic and Hydrophobic Interactions	116
4.3.2.1	Coating with Polymers and Biopolymers	116
4.3.2.2	Deposition of Nanoparticles	119
4.3.2.3	Adsorption of Quantum Dots	121
4.4	Graphene-Based Conjugates Prepared by a Combination of Covalent and Non-covalent Functionalization	121
4.4.1	Polymer- and Biopolymer-Grafted Graphene Nanomaterials Used as Nanocarriers	121
4.4.1.1	Polymer-Functionalized GO for Drug Delivery	122
4.4.1.2	Polymer-Functionalized GO for Gene Delivery	123
4.4.1.3	Chitosan-Functionalized GO	125
4.4.2	GO Functionalized with Targeting Ligands and Antibodies	125
4.4.2.1	Folic Acid-Conjugated GO	125
4.4.2.2	Antibody-Functionalized GO for Radioimaging and Biosensing	127
4.5	Conclusions	129
	Acknowledgments	130
	References	130
5	Immobilization of Enzymes and other Biomolecules on Graphene	139
	<i>Ioannis V. Pavlidis, Michaela Patila, Angeliki C. Polydera, Dimitrios Gournis, and Haralampos Stamatis</i>	
5.1	Introduction	139

5.2	Immobilization Approaches	141
5.3	Applications of Immobilized Biomolecules	145
5.3.1	Biosensors	145
5.3.1.1	Glucose Oxidase-Based Biosensors	146
5.3.1.2	Horseradish Peroxidase-Based Biosensors	150
5.3.1.3	Tyrosinase-Based Biosensors	151
5.3.1.4	Cytochrome <i>c</i> -Based Biosensors	152
5.3.1.5	Other Protein/Enzyme Biosensors	152
5.3.1.6	DNA Sensors	152
5.3.1.7	Immunosensors and Aptasensors	154
5.3.2	Biocatalysis	155
5.3.3	Biofuel Cells	159
5.3.4	Drug and Gene Delivery	161
5.4	Interactions between Enzymes and Nanomaterials	162
5.5	Conclusions	165
	Abbreviations	165
	References	166
6	Halogenated Graphenes: Emerging Family of Two-Dimensional Materials	173
	<i>Kasibhatta Kumara Ramanatha Datta and Radek Zbořil</i>	
6.1	Introduction	173
6.2	Synthesis of Halogenated Graphenes	174
6.2.1	Fluorographene	175
6.2.1.1	Mechanical or Chemical Exfoliation – from Graphite Fluoride to Fluorographene	175
6.2.1.2	Fluorination of Graphene – from Graphene to Fluorographene	175
6.2.2	Nonstoichiometric Fluorinated Graphene and Fluorinated Graphene Oxide	175
6.2.3	Other Halogenated Graphenes	178
6.3	Characterization of Halogenated Graphenes	179
6.3.1	Fluorographene	179
6.3.2	Partially Fluorinated and Halogenated Graphenes	183
6.4	Chemistry, Properties, and Applications of Fluorographene and Fluorinated Graphenes	184
6.5	Chemistry and Properties of Chlorinated and Brominated Graphenes	190
6.6	Other Interesting Properties of Halogenated Graphenes and Their Applications	190
6.7	Halogenated Graphene–Graphene Heterostructures – Patterned Halogenation	193
6.8	Conclusion and Future Prospects	195
	References	195

7	Noncovalent Functionalization of Graphene	199
	<i>Kingsley Christian Kemp, Yeonchoo Cho, Vimlesh Chandra, and Kwang Soo Kim</i>	
7.1	Noncovalent Functionalization of Graphene – Theoretical Background	199
7.1.1	Insight into the π -Interaction of Benzene	200
7.1.2	Adsorption on Graphene	201
7.2	Graphene–Ligand Noncovalent Interactions – Experiment	202
7.2.1	Polycyclic Molecules	202
7.2.2	Biomolecules	205
7.2.3	Polymers	207
7.2.4	Other Molecules	210
7.3	Conclusions	213
	References	213
8	Immobilization of Metal and Metal Oxide Nanoparticles on Graphene	219
	<i>Germán Y. Vélez, Armando Encinas, and Mildred Quintana</i>	
8.1	Introduction	219
8.2	Graphene Production	219
8.2.1	Graphene Oxide (GO)	220
8.2.2	Functionalized Graphene (<i>f</i> -Graphene)	220
8.2.3	Graphene Growth on Metal Surfaces	220
8.2.4	Micromechanical Cleavage of Graphite	221
8.3	Graphene Functionalized with Metal Nanoparticles (M-NPs)	221
8.3.1	GO-Reducing Approach	221
8.3.1.1	Reduction Assisted by Sonication	222
8.3.2	Anchoring NPs on <i>f</i> -Graphene	223
8.3.2.1	Controlling Size of NPs	226
8.3.3	Applications of M-NPs/Graphene Nanohybrids	227
8.3.3.1	Optoelectronic Devices	227
8.3.3.2	Applications in Catalysis	229
8.3.3.3	Applications in Biology	232
8.4	Graphene Functionalized with Metal Oxide Nanoparticles	233
8.4.1	Lithium Batteries	233
8.4.2	Optical Properties	236
8.4.2.1	Water Splitting	237
8.4.2.2	<i>f</i> -Graphene-POM	238
8.4.3	Photocatalytic Reduction of GO	238
8.5	Graphene Functionalized with Magnetic NPs	242
8.5.1	Magnetic Properties	243
8.5.2	Applications of GO-Mag NPs	246
8.5.2.1	Magnetic Separation of Metals and Pollutants with GO-Mag NPs	247
8.5.2.2	Biomedical Applications of GO-Mag NPs	248

8.6	Conclusions	252
	References	252
9	Functionalization of Graphene by other Carbon Nanostructures	255
	<i>Vasilios Georgakilas</i>	
9.1	Introduction	255
9.2	Graphene–C ₆₀ Nanocomposites	255
9.2.1	Covalent Bonding of C ₆₀ on GO	256
9.2.2	Deposition of C ₆₀ on Graphene	256
9.3	Graphene–CNT Hybrid Nanostructures	262
9.3.1	Graphene–CNT Composites by Simple Mixing	264
9.3.2	Graphene–CNTs Hybrid Nanostructures by Direct Development of CNTs on Graphene Surface	272
9.4	Graphene–Carbon Nanospheres	274
9.5	Graphene–Carbon Nitride Dots Hybrid Nanocomposite	277
9.6	Conclusions	279
	References	280
10	Doping of Graphene by Nitrogen, Boron, and Other Elements	283
	<i>Achutharao Govindaraj and C.N.R. Rao</i>	
10.1	Introduction	283
10.2	Nitrogen-Doped Graphene	284
10.2.1	DC Arcing	284
10.2.2	Heating with Ammonia, Hydrazine, and Other Reagents	287
10.2.3	Chemical Functionalization Route	288
10.2.4	Solvothermal Synthesis	289
10.2.5	Chemical Vapor Deposition and Pyrolysis	293
10.2.6	Pyrolysis Methods	300
10.2.7	Other Methods	306
10.3	Boron Doping	320
10.3.1	Mechanical Exfoliation	321
10.3.2	Thermal Annealing	321
10.3.3	Chemical Vapor Deposition	323
10.3.4	Other Methods	326
10.4	BN Doping in Graphene	329
10.5	Doping with Other Elements	334
10.6	Properties and Applications	339
	References	352
11	Layer-by-Layer Assembly of Graphene-Based Hybrid Materials	359
	<i>Antonios Kouloumpis, Panagiota Zygouri, Konstantinos Dimos, and Dimitrios Gournis</i>	
11.1	Introduction	359
11.2	LbL Graphene-Based Hybrid Films	360

11.2.1	Hybrid Thin Films for Electronics	360
11.2.2	Hybrid Thin Films as Sensors	375
11.2.3	Hybrid Films for Other Applications	383
11.3	Graphene-Based Hybrids through the Langmuir–Blodgett Approach	385
11.3.1	Monolayers of Graphene Oxide	385
11.3.2	Nanocomposite Films	389
11.3.3	Applications and Properties of LB Thin Films	390
11.4	Conclusions	397
	References	397

Index	401
--------------	------------

Preface

Graphene is one of the most attractive carbon nanostructures of the past decade with unique mechanical, electrical, and optical properties that have been attracted tremendous interest in academics and industry. It is expected to play an important role in nanotechnology in the near future.

Although graphene is under certain conditions a relatively chemically inert material, it interacts with various organic and inorganic reactants affording a great variety of derivatives. Following the isolation of graphene and mainly the establishment of several procedures for its production in sufficient quantities, several researchers – inspired from analogous successful chemical modification of fullerene and carbon nanotubes – have performed a great number of chemical functionalization of graphene with analogous success.

Chemical functionalization is an important tool for enriching graphene with physicochemical and other properties particular to their potential use in various applications. The aim of this book is to present a comprehensive description of the several functionalization procedures applied on graphene. In the first chapter, a brief description of graphene is presented. The second and third chapters present a detailed compilation of the covalent organic functionalizations of graphene. The reactions are separated in two chapters according to whether or not oxygen groups of graphene are involved. The fourth and fifth chapters are focused on the functionalized graphene derivatives that are planned to be involved in bio applications. The sixth chapter is focused on the very interesting hydrogen and halogen derivatives of graphene as well as its properties. The seventh chapter describes noncovalent interactions of graphene with organic molecules and other reactive species. The eighth chapter presents a great variety of graphene derivatives with metallic nanoparticles and their potential applications especially in catalytic processes. The ninth chapter presents interesting all the carbon hybrid nanostructures that are formed by the combination of graphene with other carbon nanostructures such as carbon nanotubes, fullerenes, and carbon nanoparticles.

The tenth chapter describes the formation of doped graphene with heteroatoms such as nitrogen or boron as well as its interesting properties. Finally, the last chapter presents the layer-by-layer assemblies of hybrid nanostructures that have graphene monolayers as a major component.

I would like to thank Wiley – VCH for the kind acceptance to publish this book. I dedicate this book to my wife for her continuous encouragement.

November 2013

Vasilios Georgakilas

List of Contributors

Alberto Bianco

CNRS, Institut de Biologie
Moléculaire et Cellulaire
Laboratoire d'Immunopathologie
et Chimie Thérapeutique
15 Rue René Descartes
67084 Strasbourg cedex
France

Vimlesh Chandra

Pohang University of Science and
Technology
Department of Chemistry
Center for Superfunctional
Materials
San 31, Hyojadong, Namgu
Pohang, 790-784
Republic of Korea

and

Ulsan National Institute of
Science and Technology
School of Nano-Bioscience and
Chemical Engineering
UNIST-gil 50
Ulsan 689-798
Republic of Korea

Yeonchoo Cho

Pohang University of Science and
Technology
Department of Chemistry
Center for Superfunctional
Materials
San 31, Hyojadong, Namgu
Pohang, 790-784
Republic of Korea

and

Ulsan National Institute of
Science and Technology
School of Nano-Bioscience and
Chemical Engineering
UNIST-gil 50
Ulsan 689-798
Republic of Korea

Kingsley Christian Kemp

Pohang University of Science and
Technology
Department of Chemistry
Center for Superfunctional
Materials
San 31, Hyojadong, Namgu
Pohang, 790-784
Republic of Korea

and

Ulsan National Institute of
Science and Technology
School of Nano-Bioscience and
Chemical Engineering
UNIST-gil 50
Ulsan 689-798
Republic of Korea

**Kasibhatta Kumara Ramanatha
Datta**

Palacky University in Olomouc
Department of Physical
Chemistry
Faculty of Science
Regional Centre of Advanced
Technologies and Materials
tř. 17. listopadu 12
Olomouc, 771 46
Czech Republic

Konstantinos Dimos

University of Ioannina
Department of Materials Science
and Engineering
University Campus
45110 Ioannina
Greece

Armando Encinas

Universidad Autónoma de San
Luis Potosí
Instituto de Física
Manuel Nava 6
Zona Universitaria
78290 San Luis Potosí
México

Vasilios Georgakilas

University of Patras
Department of Material Science
University Campus
26504 Rio
Greece

Dimitrios Gournis

University of Ioannina
Department of Materials Science
and Engineering
University Campus
45110 Ioannina
Greece

Achutharao Govindaraj

CSIR Centre of Excellence in
Chemistry
and International Centre for
Materials Science
New Chemistry Unit
Jawaharlal Nehru Centre for
Advanced Scientific Research
Jakkur P.O. Bangalore-560064
India

and

Solid State and Structural
Chemistry Unit
Indian Institute of Science
Malleswaram
Bangalore 560 012
India

Kwang Soo Kim

Pohang University of Science and
Technology
Department of Chemistry
Center for Superfunctional
Materials
San 31, Hyojadong, Namgu
Pohang, 790-784
Republic of Korea

and

Ulsan National Institute of
Science and Technology
School of Nano-Bioscience and
Chemical Engineering
UNIST-gil 50
Ulsan 689-798
Republic of Korea

Antonios Kouloumpis

University of Ioannina
Department of Materials Science
and Engineering
University Campus
45110 Ioannina
Greece

Cécilia Ménard-Moyon

CNRS, Institut de Biologie
Moléculaire et Cellulaire
Laboratoire d'Immunopathologie
et Chimie Thérapeutique
15 Rue René Descartes
67084 Strasbourg cedex
France

Ioannis V. Pavlidis

University of Ioannina
Laboratory of Biotechnology
Department of Biological
Applications and Technologies
University Campus
45110 Ioannina
Greece

Michaela Patila

University of Ioannina
Laboratory of Biotechnology
Department of Biological
Applications and Technologies
University Campus
45110 Ioannina
Greece

Angeliki C. Polydera

University of Ioannina
Laboratory of Biotechnology
Department of Biological
Applications and Technologies
University Campus
45110 Ioannina
Greece

Mildred Quintana

Universidad Autónoma de San
Luis Potosí
Instituto de Física
Manuel Nava 6
Zona Universitaria
78290 San Luis Potosí
México

C.N.R. Rao

CSIR Centre of Excellence in
Chemistry
New Chemistry Unit
International Centre for Materials
Science
Jawaharlal Nehru Centre for
Advanced Scientific Research
Jakkur P.O. Bangalore 560 064
India

and

Solid State and Structural
Chemistry Unit
Indian Institute of Science
Malleswaram
Bangalore 560 012
India

Petra Rudolf

Faculty of Mathematics and
Natural Science
Surfaces and Thin Films Zernike
Institute for Advanced Materials
Nijenborgh 4
9747 AG Groningen
The Netherlands

Cinzia Spinato

CNRS, Institut de Biologie
Moléculaire et Cellulaire
Laboratoire d'Immunopathologie
et Chimie Thérapeutique
15 Rue René Descartes
67084 Strasbourg cedex
France

Konstantinos Spyrou

Faculty of Mathematics and
Natural Science
Surfaces and Thin Films Zernike
Institute for Advanced Materials
Nijenborgh 4
9747 AG Groningen
The Netherlands

Haralampos Stamatis

University of Ioannina
Laboratory of Biotechnology
Department of Biological
Applications and Technologies
University Campus
45110 Ioannina
Greece

Germán Y. Vélez

Universidad Autónoma de San
Luis Potosí
Instituto de Física
Manuel Nava 6
Zona Universitaria
78290 San Luis Potosí
México

Radek Zbořil

Palacky University in Olomouc
Department of Physical
Chemistry
Faculty of Science
Regional Centre of Advanced
Technologies and Materials
tř. 17. listopadu 12
Olomouc, 771 46
Czech Republic

Panagiota Zygouri

University of Ioannina
Department of Materials Science
and Engineering
University Campus
45110 Ioannina
Greece

1

An Introduction to Graphene

Konstantinos Spyrou and Petra Rudolf

1.1

Brief History of Graphite

Carbon takes its name from the latin word *carbo* meaning charcoal. This element is unique in that its unique electronic structure allows for hybridization to build up sp^3 , sp^2 , and sp networks and, hence, to form more known stable allotropes than any other element. The most common allotropic form of carbon is *graphite* which is an abundant natural mineral and together with diamond has been known since antiquity. Graphite consists of sp^2 hybridized carbon atomic layers which are stacked together by weak van der Waals forces. The single layers of carbon atoms tightly packed into a two-dimensional (2D) honeycomb crystal lattice is called *graphene*. This name was introduced by Boehm, Setton, and Stumpp in 1994 [1]. Graphite exhibits a remarkable anisotropic behavior with respect to thermal and electrical conductivity. It is highly conductive in the direction parallel to the graphene layers because of the in-plane metallic character, whereas it exhibits poor conductivity in the direction perpendicular to the layers because of the weak van der Waals interactions between them [2]. The carbon atoms in the graphene layer form three σ bonds with neighboring carbon atoms by overlapping of sp^2 orbitals while the remaining p_z orbitals overlap to form a band of filled π orbitals – the valence band – and a band of empty π^* orbitals – the conduction band – which are responsible for the high *in-plane* conductivity.

The interplanar spacing of graphite amounts to 0.34 nm and is not big enough to host organic molecules/ions or other inorganic species. However several intercalation strategies have been applied to enlarge the interlayer galleries of graphite from 0.34 nm to higher values, which can reach more than 1 nm in some cases, depending on the size of the guest species. Since the first intercalation of potassium in graphite, a plethora of chemical species have been tested to construct what are known as graphite intercalation compounds (GICs). The inserted species are stabilized between the graphene layers through ionic or polar interactions without influencing the graphene structure. Such compounds can be formed not only with lithium, potassium, sodium, and other alkali metals, but also with anions such as nitrate, bisulfate, or halogens.

In other cases the insertion of guest molecules may occur through covalent bonding via chemical grafting reactions within the interlayer space of graphite; this results in structural modifications of the graphene planes because the hybridization of the reacting carbon atoms changes from sp^2 to sp^3 . A characteristic example is the insertion of strong acids and oxidizing reagents that creates oxygen functional groups on the surfaces and at the edges of the graphene layers giving rise to graphite oxide. Schafheutl [3] first (1840) and Brodie [4] 19 years later (1859) were the pioneers in the production of graphite oxide. The former prepared graphite oxide with a mixture of sulfuric and nitric acid, while the latter treated natural graphite with potassium chlorate and fuming nitric acid. Staudenmaier [5] proposed a variation of the Brodie method where graphite is oxidized by addition of concentrated sulfuric and nitric acid with potassium chlorate. A century later (1958) Hummers and Offeman [6] reported the oxidation of graphite and the production of graphite oxide on immersing natural graphite in a mixture of H_2SO_4 , $NaNO_3$, and $KMnO_4$ as a result of the reaction of the anions intercalated between the graphitic layers with carbon atoms, which breaks the aromatic character. The strong oxidative action of these species leads to the formation of anionic groups on graphitic layers, mostly hydroxylates, carboxylates, and epoxy groups. The out of planar C–O covalent bonds increase the distance between the graphene layers from 0.35 nm in graphite to about 0.68 nm in graphite oxide [7]. This increased spacing and the anionic or polar character of the oxygen groups formed impart to graphene oxide (GO) a strongly hydrophilic behavior, which allows water molecules to penetrate between the graphene layers and thereby increase the interlayer distance even further. Thus graphite oxide becomes highly dispersible in water. The formation of sp^3 carbon atoms during oxidation disrupts the delocalized π system and consequently electrical conductivity in graphite oxide deteriorates reaching between 10^3 and $10^7 \Omega \text{ cm}$ depending on the amount of oxygen [2, 8].

1.2 Graphene and Graphene Oxide

For several decades the isolation of graphene monolayer seemed to be impossible on the basis of, among other things, theoretical studies on the thermodynamic stability of two-dimensional crystals [9]. An important step in this direction was made by a research group in Manchester guided by Geim and Novoselov in 2004 [10] who reported a method for the creation of single layer graphene on a silicon oxide substrate by peeling the graphite by micromechanical cleavage (scotch tape method). Graphene exhibited outstanding structural [11], electrical [12], and mechanical properties [13] and 6 years later Novoselov and Geim were honored with the Nobel Prize in Physics “*for groundbreaking experiments regarding the two-dimensional material graphene.*” During this time a number of methods for the production of graphene monolayers have been developed. These methods can be divided into different categories depending on the chemical or physical process

employed to obtain the single layer graphene. The next three sections describe the three types of chemical methods.

1.2.1

Preparation of Graphene from Graphene Oxide

Although the report on single sheets of GO [14, 15] obtained by procedures established by Staudenmaier and Hummers and Offeman [4–6] had been published, the scientific community largely continued to consider graphite oxide a layered graphitic material. It was not until after the isolation of pristine graphene by micromechanical cleavage that the question was reexamined and it was ascertained that the method developed by Hummers and Offeman produces exfoliated oxidized single graphene layers by the dispersion of graphite oxide in water. These chemically prepared monolayers of GO can be considered the precursors for the production of graphene by the removal of the oxygen groups. The precise structure of GO depends on the oxidation process and is still a subject of debate. The most accepted models are the Lerf–Klinowski and the Dékány models [16, 17]. Recently Ajayan *et al.* confirmed that for GO prepared with the protocol that resulted in the Lerf–Klinowski model, ring lactols are present at the edges of the GO sheets (Figure 1.1) [18].

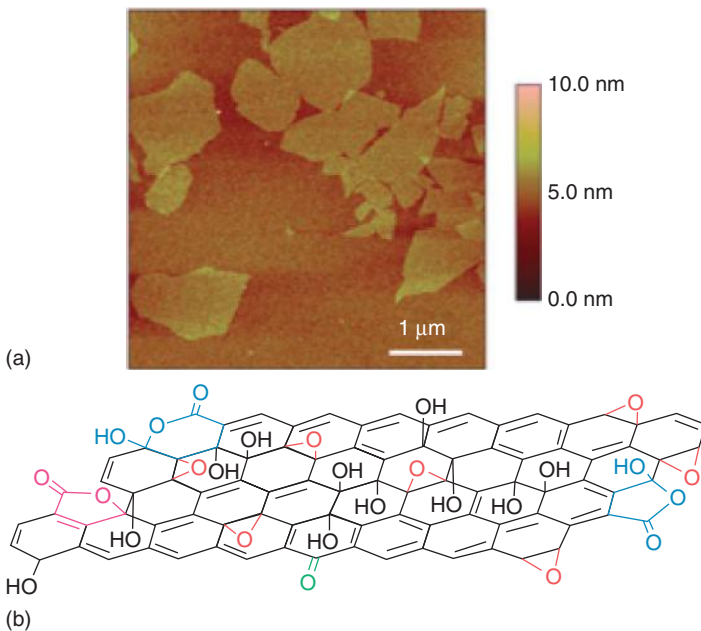


Figure 1.1 Atomic force microscopy (AFM) image and structural model of graphene oxide (GO) sheets. (a) An AFM image of GO sheets on a silicon substrate.

(b) A structural model of GO introduced by Ajayan *et al.* (Reproduced with permission from [18].)

Table 1.1 Summary of reduction agents for chemical reduction of graphene oxide [22].

Reduction agent	Temperature (°C) during reduction	Reduction time (h)	Electrical conductivity (S m ⁻¹) after reduction	References
Hydrazine	100	24	$\sim 2 \times 10^2$	[20]
Hydroquinone	25	20	—	[23]
Alkali	50–90	A few minutes	—	[24]
Sodium borohydride	25	2	$\sim 4.5 \times 10^1$	[25]
Ascorbic acid (vitamin C)	95	24	$\sim 7.7 \times 10^3$	[26]
Hydroiodic acid	100	1	$\sim 3 \times 10^4$	[27]
Hydroiodic acid (with acetic acid)	40	40	$\sim 3.0 \times 10^4$	[28]
Sulfur-containing compounds ^a	95	3	—	[29]
Pyrogallol	95	1	$\sim 4.9 \times 10^2$	[26]
Benzylamine	90	1.5	—	[30]
Hydroxyl amine	90	1	$\sim 1.1 \times 10^2$	[31]
Aluminum powder (with hydrochloric acid)	25	0.5	$\sim 2.1 \times 10^3$	[32]
Iron powder (with hydrochloric acid)	25	6	$\sim 2.3 \times 10^3$	[33]
Amino acid (L-cysteine)	25	12–72	—	[34]
Sodium hydrosulfite	60	0.25	$\sim 1.4 \times 10^3$	[35]
Alcohols	100	24	$\sim 2.2 \times 10^3$	[23]
Dimethylformamide	153	1	$\sim 1.4 \times 10^3$	[36]

^aSulfur-containing compounds include NaHSO₃, Na₂S, Na₂S₂O₃, SOCl₂, and SO₂.

The first dispersion of single graphene layers was presented in 2006 by Ruoff's group, which used hydrazine hydrate for the reduction of GO prepared by Hummers method [19, 20]. Although several reductive procedures have been applied by several research groups (see Table 1.1 and references therein) in the following years, none achieved full reduction of the GO monolayers into graphene. This agrees with the theoretical finding that a reduction of GO from 75% to 6.25% (C:O ratio 16:1) coverage is relatively easy but further reduction seems to be rather difficult [21]. For this reason the final isolated carbon monolayers derived from the reduction of GO are usually called partially reduced graphene oxide (*r*GO) or chemically converted graphene (CCG). The results of the various reductive procedures that have been developed are summarized in the following table.

Reduction of GO can be also be achieved via thermal annealing at temperatures >1000 °C [36], photochemical reduction [37], and electrochemical reduction [38, 39]. One of the biggest disadvantages of GO is the very low electrical conductivity. According to theory, GO becomes conducting when the functional groups

reach 25% [21]. After the removal of the oxygen groups, *r*GO can be further graphitized by annealing at elevated temperatures. In this process defects that remain after reduction are rearranged and the aromatic character of the monolayers increases. However, the presence of oxygen groups on the graphene surface is not always undesirable. In fact, by exploiting the well-established carbon chemistry the oxygen functional groups can be used for further functionalization of the layers for applications in catalysis, gas sensors, energy storage, and environmental remediation.

1.2.2

Isolation of Pristine Graphene Monolayers

Exfoliation of graphite into single graphene layers can also be achieved by ultrasonication in organic solvents. Acoustic cavitation provides unusual chemical conditions because extremely high temperatures and pressures are reached for short times in the liquid [40]. If the free energy of mixing is negative and the solvent is able to stabilize colloidal graphene because its surface energy matches that of graphene, the graphitic basal structure is broken and small graphite fragments intercalated by solvent molecules are produced [41, 42]. Dimethylformamide (DMF) [43], *N*-methyl pyrrolidone (NMP) [41], pyridine and other perfluorinated solvents [44], and *o*-dichlorobenzene [45] were the first solvents successfully used for this purpose (Figure 1.2).

Sonication methods usually provide a mixture of several derivatives where single graphene represents a percentage of 1–15% and the rest consists of few-layer graphene nanosheets, where the number of layers range from 2 to 10 [41, 44]. The final percentage of single graphene layers can be increased by selective centrifugation. The advantage in these methods is that the graphitic character of the exfoliated layers is less affected than in oxidation. However the implosion of cavitation bubbles causes violent collisions between particles at very high speed

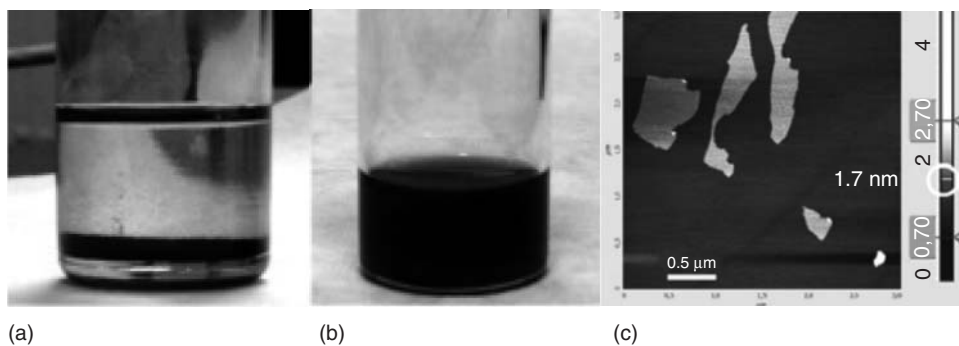


Figure 1.2 (a) Graphite precipitation in benzene after sonication; and (b) partial exfoliation of graphite in pyridine by sonication affords a dark colloidal dispersion with

concentration 0.3 mg ml^{-1} . (c) AFM image of several pyridine-etched single graphenes layers. (Reproduced with permission from [44].)

that, in air-saturated sonicated solutions, dissociate the solvent and form peroxy radicals [46]. The radical reactions are usually destructive and very effective in breaking C–C bonds [47]. Consequently prolonged sonication treatments result in a reduction of the sheet size and a higher number of defects [48] mostly consisting in oxidized carbon atoms at graphene edges in the form of epoxy, carbonyl, and carboxyl groups [49]. Such damage during exfoliation of graphite in DMF can be considerably reduced by the addition of *N*-2-mercapto-propionyl glycine (tiopronin), a molecule that inhibits reactions promoted by oxygen, peroxides, and radicals [50]. An alternative route to sonication, which also has the advantage of mitigating the development of defects, is the method developed by Ester Vazquez *et al.* who have used mechanochemical activation by ball-milling to exfoliate graphite through interactions with melamine (2,4,6-triamine-1,3,5-triazine) under solid conditions [51].

1.2.3

Large Scale Production of GO by Langmuir-Blodgett Methods

A simple protocol to deposit large GO flakes (5–20 μm) makes use of the Langmuir–Blodgett technique (LB) [52, 53] where a highly diluted and well dispersed water solution of GO is employed as a subphase for the LB deposition.

By applying external pressure through the movable barriers of a LB trough the packing of the GO layers floating at the air–water interface can be modified. Different from molecular and hard colloidal particle monolayers, the GO single layer flakes tend to fold and wrinkle to resist collapsing into multilayers. The first report of large-flake production of GO by using the LB method and controllable deposition was presented by Cote *et al.* [52]. As illustrated in Figure 1.3 by controlling the surface pressure, a high coverage of the GO sheets can be achieved and the method is suitable for large scale production. The injection of a long-chain molecule (e.g., octadecylamine) at the air–water interface causes the GO sheets to bind covalently and results in the formation of surfactant-GO layers [53]. This hybrid Langmuir film can be transferred to an arbitrary support (higher hydrophobicity of the substrate increases the transfer ratio and the quality of the deposited layer) by horizontally lowering the desired substrate to contact the surfactant-GO-water interface – this way of transferring is known as the *Langmuir–Schaefer method*.

1.2.4

Other Methods of Graphene Production

Alternative ways for the production of single graphene layers via physical and physicochemical routes are less relevant for the present monograph and are therefore only briefly mentioned in this section for completeness. Single graphene layers can be produced with very good results by thermal annealing of silicon carbide (SiC) [54] and chemical vapor deposition (CVD) [55–61]. Although several transition metals have been used as catalysts in graphene production, nickel

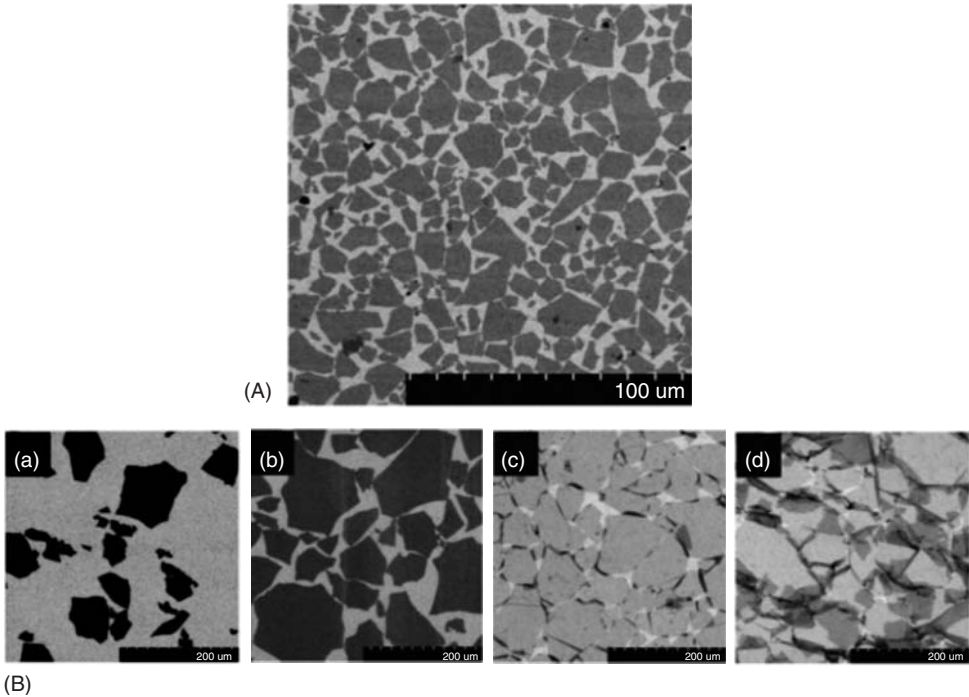


Figure 1.3 (A) SEM (scanning electron microscope) images of highly covered graphene oxide monolayers, scale bar of 100 μm . Langmuir–Blodgett assembly of graphene oxide layers. (B) (a–d) SEM images of graphene oxide layers on a silicon wafer for different surface pressures. The packing density gradually increased by

controlling the water interface pressure: (a) dilute monolayer of isolated flat sheets, (b) monolayer of close-packed GO, (c) over-packed monolayer with sheets folded at interconnected edges, and (d) over packed monolayer with folded and partially overlap sheets. (Reproduced with permission from [52].)

and copper are the most promising, taking into account their low cost also. On the other hand the thermal annealing of SiC at high temperatures that range between 1000 and 1600 $^{\circ}\text{C}$ results in the sublimation of silicon atoms and the graphitization of the remaining carbon atoms. Another interesting method for the preparation of graphene sheets with predetermined size, also called *graphene nanoribbons*, is the chemical unzipping of multiwalled carbon nanotubes [62]. More precisely, the carbon nanotubes are cut along their axis by plasma etching or strong oxidation. A scheme that presents several procedures for the preparation of graphene nanoribbons as well as an atomic force microscopy (AFM) image of these graphene structures are shown in Figure 1.4. Graphene nanoribbons have the length of the nanotube and their width is equal to the circumference of the nanotube. Their electronic properties are largely determined by the edge structure (armchair or zigzag) and, for certain edge structures, exhibit an energy gap which increases with decreasing width of the nanoribbon [63].

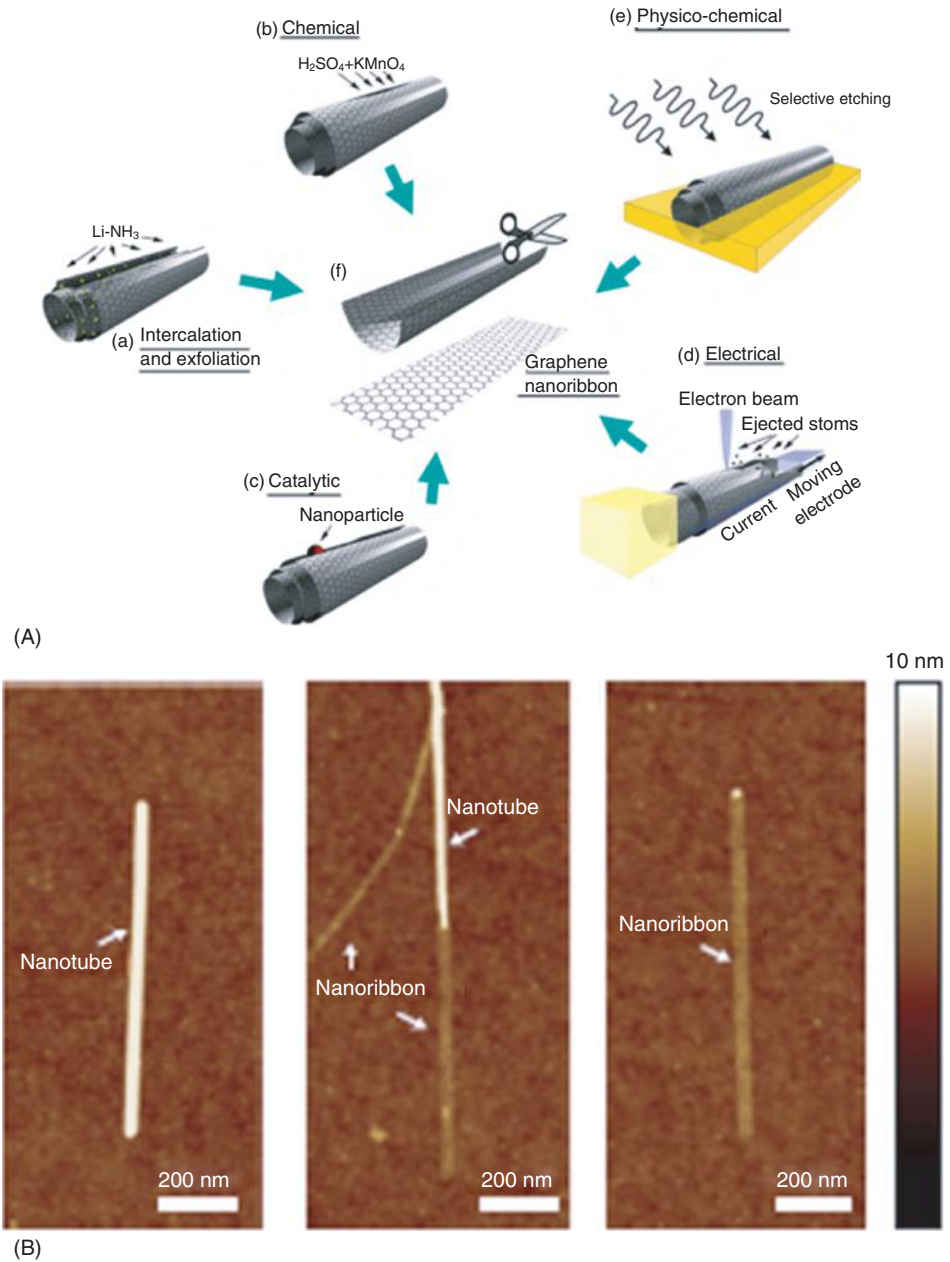


Figure 1.4 (A) Schematic representation of the several ways to unzip carbon nanotubes and produce graphene nanoribbons. (Reproduced with permission from [62].)

(B) Characteristic AFM images of graphene nanoribbons by unzipping carbon nanotubes. (Reproduced with permission from [64].)

1.3 Characterization of Graphene

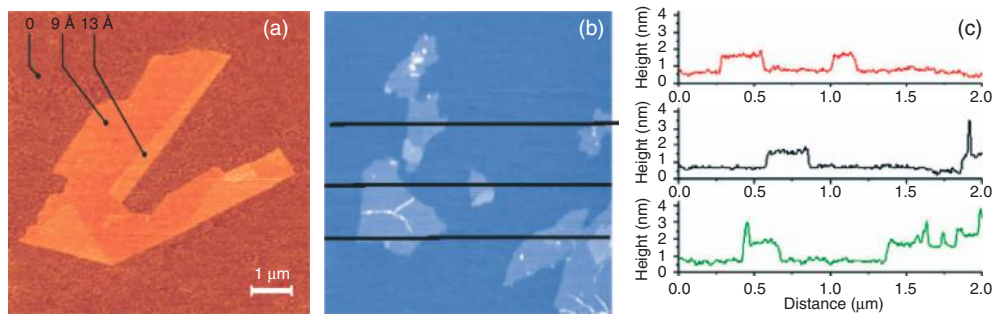
The isolation of single graphene sheets offers opportunities for its investigation by various spectroscopic and microscopic techniques; samples can be either in the form of dispersion or graphene sheets deposited on the proper substrates. In this section the most commonly used characterization tools are introduced. As for most nanomaterials electronic microscopies and AFM are powerful tools for the characterization of graphene and graphene derivatives. Raman spectroscopy and spectromicroscopy can distinguish single layer graphene from double layer and few-layer graphene and give clear indications on the number of defects present in the material. Thermogravimetric analysis (TGA) diagrams are useful to trace changes in the structure of graphitic materials before and after functionalization of graphene sheets. Optical microscopy can visualize a single graphene layer that is placed on the right substrate. X-ray diffraction (XRD) informs on the success of exfoliation or intercalation of graphite and is particularly useful to demonstrate functionalization.

1.3.1

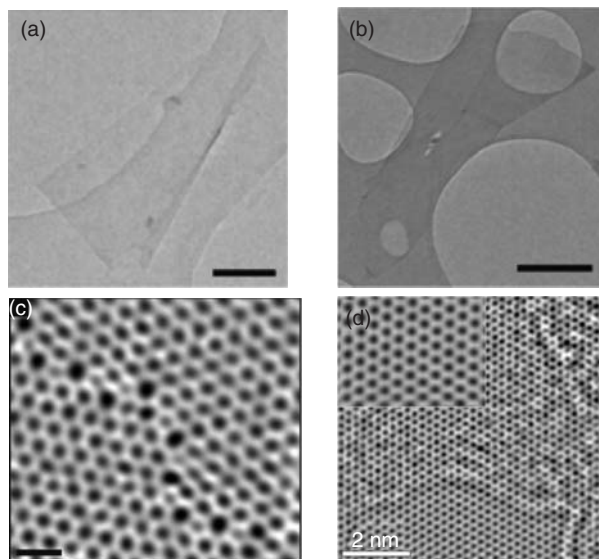
Microscopic Observation

The characterization of a graphene material by AFM is often performed by drop casting or spin coating a highly diluted graphene dispersion on a silicon wafer since such deposits are flat enough to allow for recording of height differences on the monoatomic level. Figure 1.5A shows representative AFM images of single graphene sheets. One can clearly observe the height differences between the flat and folded part of the graphene layer. The average height of annealed single layer graphene flakes is typically in the range of 0.8–1.2 nm when decorated with oxygen- and hydro-containing groups [65]. After graphitization treatments at high temperature, the average height of the flakes drops to 0.3–0.5 nm [55], showing the “fingerprint” of a single atomic sheet as similar to the mechanically exfoliated flakes [66].

Typical TEM (transmission electron microscope) images of single layer graphene are presented in Figure 1.5B-a,b; the film is almost transparent. When recorded with aberration-corrected instruments defect structures at grain boundaries can be imaged with atomic resolution as shown in Figure 1.5B-c. The atomic structure of graphene sheets is visualized by exit wave reconstruction, which is an advanced TEM technique in which 10–30 HR-TEM images are acquired at different defocus values and combined into the complex wave of electrons at the exit plane of the sample. An example of a phase image of such an exit wave of electrons leaving a graphene sheet is presented in Figure 1.5B-d [50]. In contrast to single high resolution TEM images, phase images allow for a quantitative interpretation of the contrast and permit to distinguish single and double graphene layers [69]. The inset of Figure 1.5B-d shows a defect-free graphene lattice, in which the positions of the



(A)



(B)

Figure 1.5 (A) (a) AFM image of pristine single graphene sheet. The height which corresponds to the thickness of a single layer is 0.9 nm while a folded sheet is measured at height of 1.3 nm. (Reproduced with permission from [67].) (b) AFM image and height profile of a single GO layer. (Reproduced with permission from [20].) (c) height profile collected along the lines marked in black on the AFM micrograph.

(B) TEM images of (a,b) pristine single graphene sheets. (Reproduced with permission from [41].) (c) Aberration-corrected TEM image: grain boundary in a single graphene sheet. (Reproduced with permission from [68].) (d) HR-TEM of a graphene monolayer produced by exfoliation of graphite in the presence of tiopronin as radical trap. (Reproduced with permission from [50].)

individual carbon atoms can be distinguished. This image clearly indicates a single graphene sheet, as the AB stacking of a double sheet would lead to the presence of additional atoms in the center of the hexagons. The overview image shown in Figure 1.5B-d also indicates that adsorbents are likely to be present at the surface of the graphene layer giving rise to the ripple-like contrast present in this image.

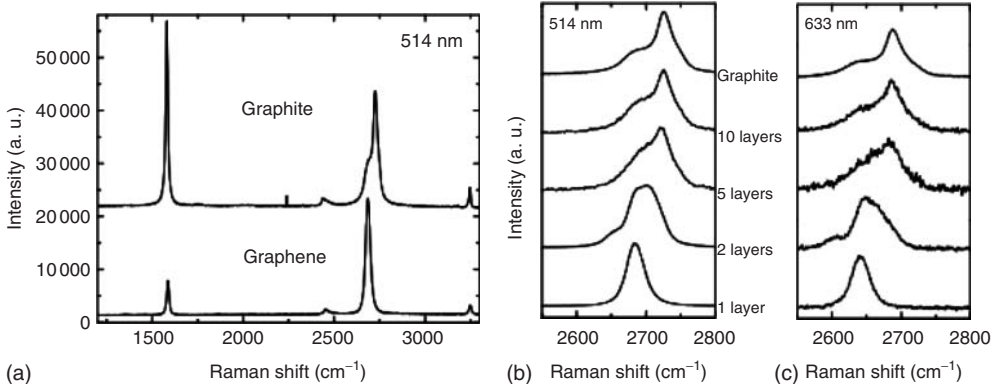


Figure 1.6 (a–c) The Raman spectra of pristine graphene in comparison with that of graphite and the G' band of several multilayered graphene nanosheets. (Reproduced with permission from [70].)

1.3.2

Raman Spectroscopy

Raman spectroscopy is a widely used tool for the characterization of carbon materials; it is particularly informative on the structure of graphene nanosheets regarding the number of graphene layers, as well as the existence of defects and the extent of functionalization. The pioneering study of the Raman spectrum of pristine single graphene was by Ferrari *et al.* [70] which, as shown in Figure 1.6, explained how for few-layer graphene consisting of – one to five layers, the precise number of layers can be extracted from the spectrum. The Raman spectrum of a pristine single graphene layer has two characteristic features at 1580 cm^{-1} , and at 2700 cm^{-1} called the G band and the G' band, respectively [71]. The G band is a result of the doubly degenerate zone center E_{2g} mode [72]. The G band also bears testimony to the number of layers. As the layer thickness increases, the band position shifts to lower wavenumbers conforming to the calculated positions for these band locations. The position of the G band is also sensitive to doping and strain leads to splitting of this band [73]. The G' band is the second order of zone boundary phonons and very often referred to as $2D$ band. The first order of the zone boundary phonons is only observed as a peak around 1350 cm^{-1} , called D band, when graphene has a sufficient number of defect sites. In the case of a pristine graphene monolayer produced by micromechanical cleavage such a band is not detected because of the lack of defects [73].

As seen in Figure 1.6c, the G' peak changes with the number of layers: The G' peak of a single layer of graphene is a sharp symmetrical peak below 2700 cm^{-1} . For bilayer graphene this peak is shifted to slightly higher wave numbers and becomes broader with a shoulder toward lower wavenumbers. As the number of the layers increases the peak shifts to higher wave numbers and finally in a five layer nanosheet it appears as a broad double peak where the two components have

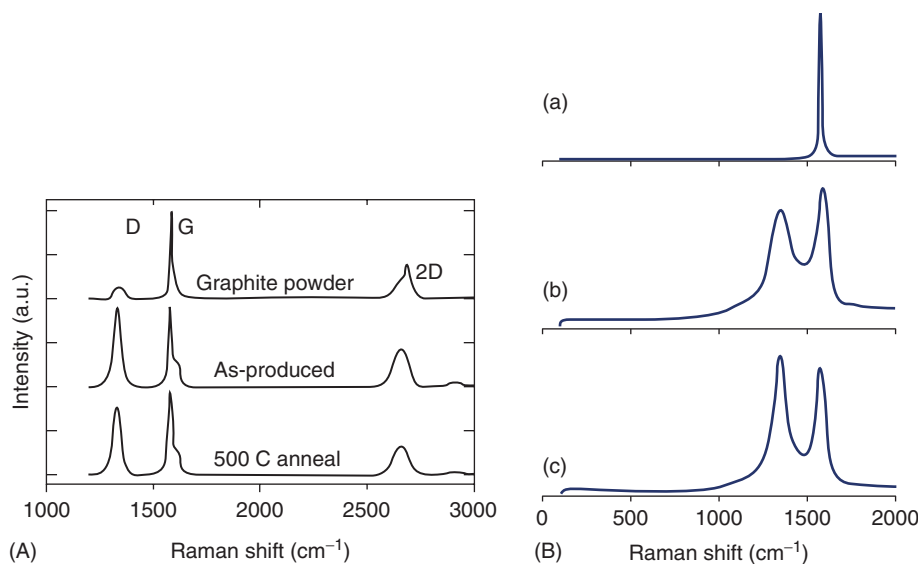


Figure 1.7 (A) Raman spectrum of graphene as produced and after annealing at 500 °C in comparison with that of the starting graphite. (Reproduced with

permission from [74].) (B) The Raman spectra of graphite (a), GO (b), and the reduced GO (c). (Reproduced with permission from [20].)

a $1/2$ ratio (see Figure 1.6c). For a nanosheet with more than five layers the G' band is similar to that of a sample with five layers.

Raman spectra without D band are rarely observed for large pristine single graphene sheets prepared by micromechanical cleaving without defects. In most cases pristine graphene sheets have a sufficient number of defects to result in some D band intensity. The height of the D band directly depends on the number of the sp^3 carbon atoms of graphene surface and thus, on the number of defects of the graphene nanosheets. As regards the quality of graphene, D band is an indication for the aromatic character and the “quality” of the graphene nanosheet and is related to the production method and the starting material. As an example, Figure 1.7A reports spectra relative to graphene sheets produced by the exfoliation of graphite in water and stabilized with a surfactant which show an intense D band that remains even after annealing at 500 °C [74]. A similarly intense D band is discerned in the Raman spectra of GO sheets. Here the D band is a common characteristic of the Raman spectra since the existence of sp^3 carbon atoms in the graphitic surface goes along with the formation of oxygen groups (see Figure 1.7B) [20].

1.3.3

Thermogravimetric Analysis

Articles related to the characterization of graphene nanosheets and its derivatives typically include TGA since the structural changes of graphitic materials before

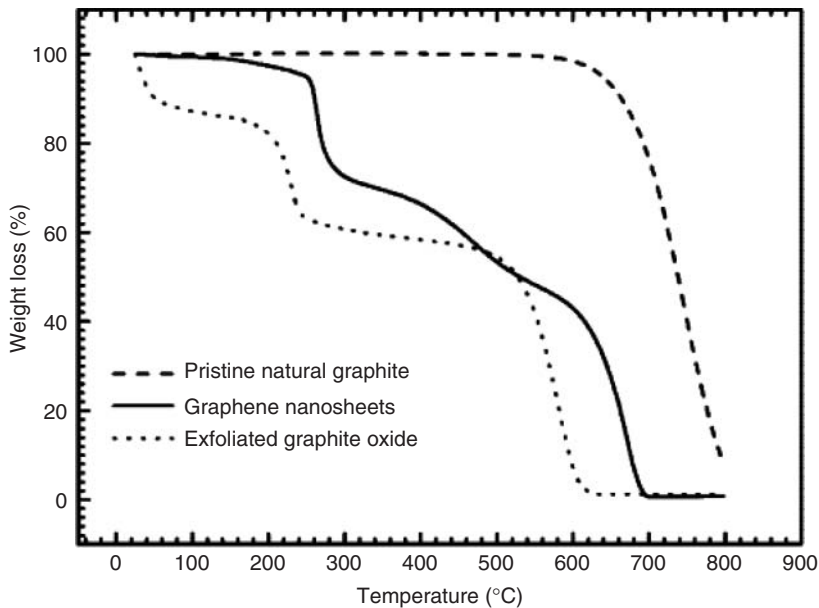


Figure 1.8 TGA curves of natural graphite, *r*GO (graphene nanosheets in the diagram) and exfoliated GO. (Reproduced with permission from [75].)

and after procedures such as the oxidation and exfoliation of graphite or the functionalization of graphene sheets give rise to marked differences in the mass loss as a function of increasing temperature (with constant heating rate). As an example, Figure 1.8 reports the TGA data for Graphite, GO, and *r*GO as presented by Wang *et al.* [75]. The combustion of graphite starts at 650 °C when the sample is heated in air, while GO loses 20% of its weight at 200 °C and is finally decomposed at 550 °C. The first weight loss of GO is attributed to the removal of the oxygen groups while the lower combustion temperature of GO in comparison with graphite demonstrates the lower thermal stability of GO because of the presence of defects created after elimination of oxygen functional moieties. An intermediate thermal behavior is recorded in *r*GO which mirrors the lower number of oxygen groups in this material. For both GO and *r*GO the lower combustion temperature is also influenced by the exfoliation which makes the sheets more easily accessible to air than when they are tightly packed in graphite.

1.3.4

Optical Properties of Graphene

Almost everyone has seen graphene nanosheets deposited on solid substrates. In fact the gray trace left by the movement of a pencil on a white paper is nothing else but overlaid graphene nanosheets. Likewise, if pristine graphene nanosheets are dispersed in organic solvents the liquid shows a gray color and becomes darker

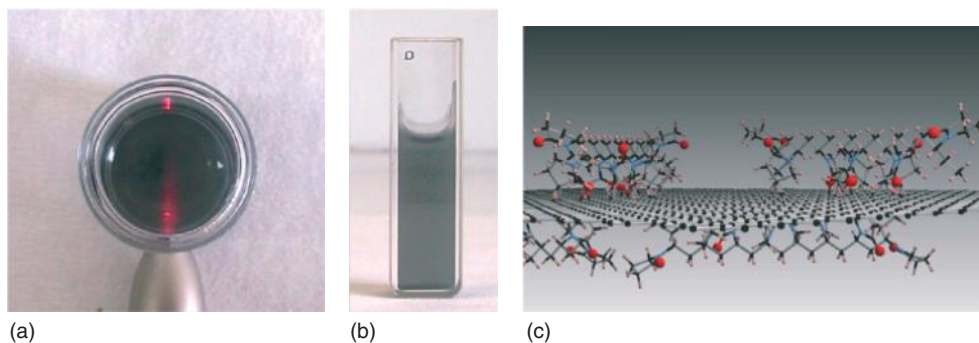


Figure 1.9 (a) A laser beam passing through a dispersion of graphene in water (0.1 mg ml⁻¹); and (c) schematic model of poly-vinyl pyrrolidone-coated graphene. (Reproduced with permission from [76].)

as the amount of graphene increases. A simple way to identify the presence of nanoparticles in dispersion is based on the Tyndall effect as illustrated in Figure 1.9. A laser beam becomes visible passing through the liquid because of the scattering of the light by the dispersed nanoparticles [76].

Graphene as an extended aromatic system has sufficient light absorption; even a single sheet of graphene is visible through an optical microscope if deposited on 300 nm of silicon oxide on top of silicon as a result of an interference effect [10]. After this work several other groups visualized graphene on several other substrates [43, 77, 78]. As shown in Figure 1.10 [79], graphene's optical absorbance of white light has been measured to amount to 2.3%, which means that a bilayer absorbs

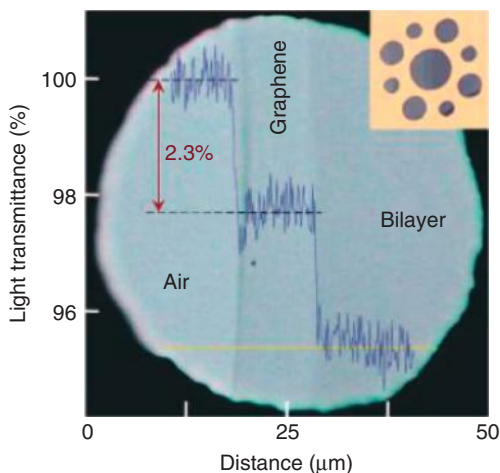


Figure 1.10 A single and a bilayer graphene on a porous membrane. (Reproduced with permission from [80].)

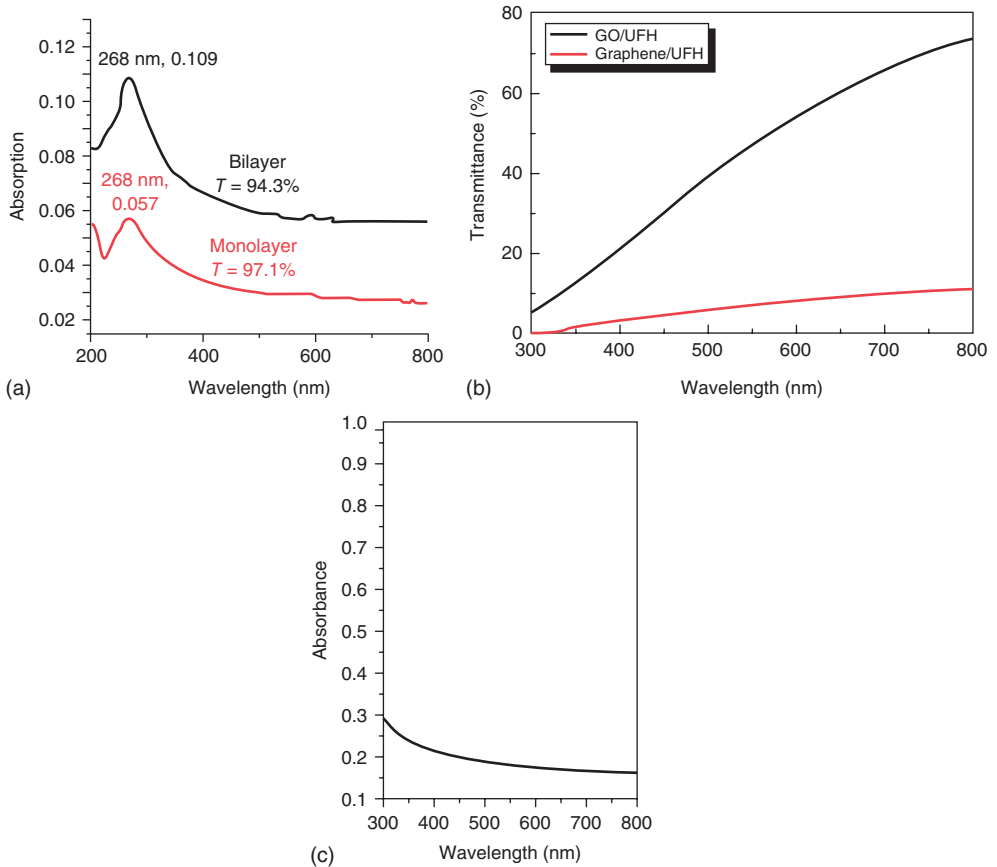


Figure 1.11 (a) The UV-vis absorption spectra of monolayer graphene and bilayer graphene; peaks are labeled with the wavelength of maximum absorption and the value of maximum absorption. The UV transmittance (T , %) is measured at 550 nm. (Reproduced with permission from [81].)

(b) UV-vis spectra of GO and graphene in water solution functionalized both with heparin (unfractionated heparin). (Reproduced with permission from [82].) (c): UV-vis spectrum of graphene nanosheets in DMF. (Reproduced with permission from [44].)

4.6% and a five-layer-thick flake near 11.5% [80]. The maximum of the absorption is at 268 nm (Figure 1.11a) [81]. UV-Vis spectrum of graphene/unfractionated heparin production after reduction exhibits remarkable lower transmittance compared to the initial graphite oxide/unfractionated heparin solution (Figure 1.11b). The UV-vis spectrum of graphene flakes dispersed in DMF looks very similar with a continuously rising curve from 700 to 300 nm (Figure 1.11c) [44].

Solid GO has a brownish color and dispersions of GO nanosheets also have a brownish tint. The color becomes darker and grayer as GO is reduced to rGO. Because of the different electronic structure, insulated GO has a much

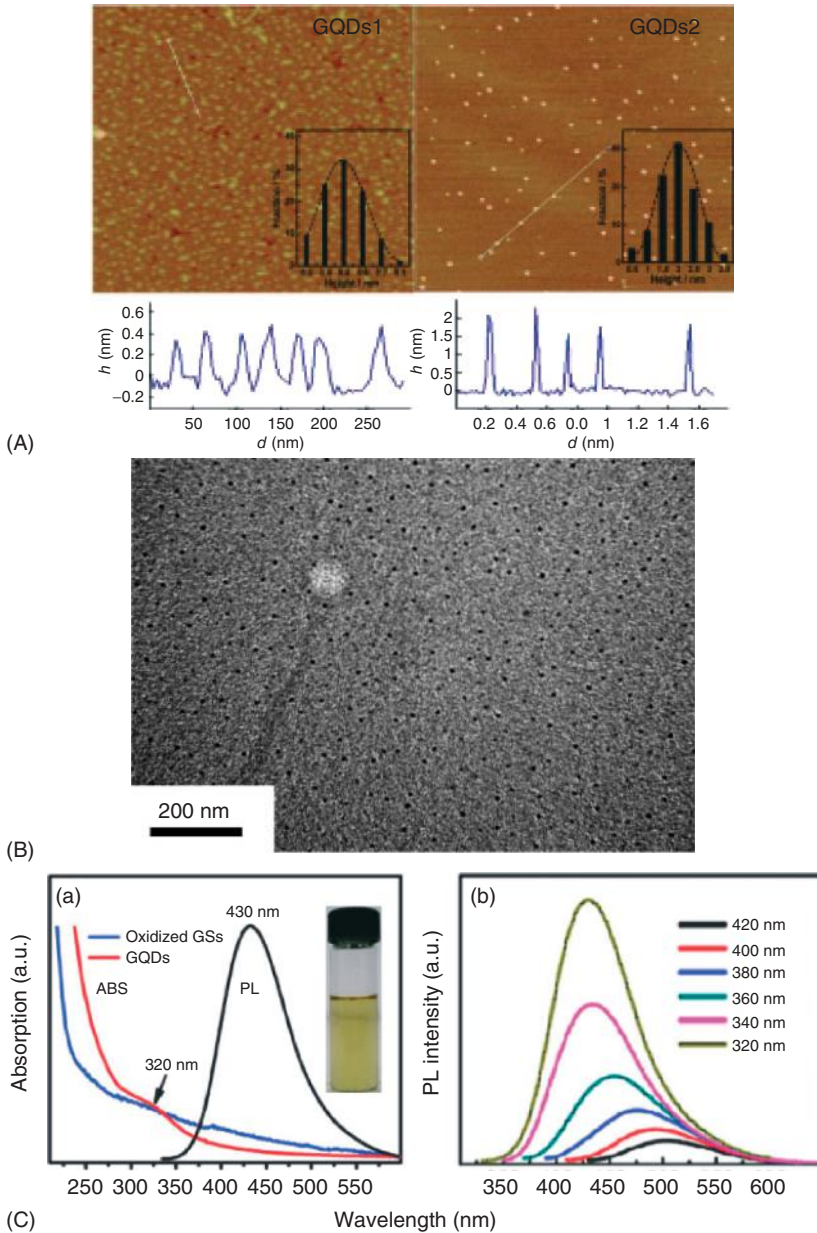


Figure 1.12 (A) and (B) AFM and TEM image of GQDs. (Reproduced with permission from [83, 84].) (C) (a) UV-vis absorption (red line) and photolithography (PL) (at 320 nm excitation) spectra of GQDs dispersed in water; UV-vis absorption (blue

line) spectrum of oxidized graphene. Inset: image of GQD aqueous solution. (b) PL spectra of the GQDs at different excitation wavelengths. (Reproduced with permission from [84].)

higher transmittance in comparison to pristine graphene or *r*GO as illustrated in Figure 1.13, upper right panel [82].

The electronic properties of graphene can also be changed by reducing the dimensions of the graphene layers. As illustrated in Figure 1.12, graphene quantum dots (GQDs) consisting of one or few graphene layers with size less than 100 nm show new optoelectronic properties, because of the quantum confinement and the effect of the large percentage of edge atoms. GQDs have a band gap and exhibit a strong photoluminescence, which can be tuned by controlling their size and other morphological factors (Figure 1.12C) [83–88]. Finally the optical transitions in graphene can also be changed by applying a gate voltage in a field-emitting transistor configuration [89]. This is also the way to tune the band gap in bilayer graphene [90].

1.3.5

X-Ray Diffraction Pattern

The different steps for the isolation of graphene from graphite are suitably monitored by collecting XRD patterns of the starting material, intermediates, and the final product. As shown in Figure 1.13, graphite exhibits a basal reflection (002) peak at $2\theta = 26.6^\circ$ which corresponds to a d spacing of 0.335 nm and represents the interlayer distance.

After the oxidation of graphite and before exfoliation the graphite oxide intermediate basal (002) reflection peak is shifted to 11.2° which corresponds to a d spacing of 0.79 nm. This increase in the interlayer space is attributed to the intercalation of

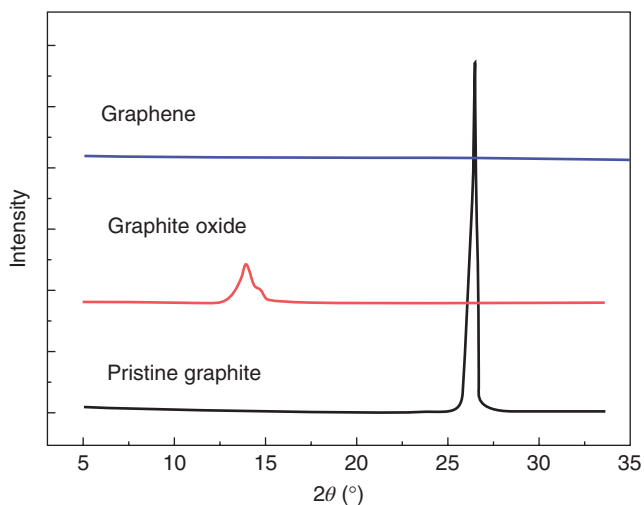


Figure 1.13 X-ray diffraction patterns of pristine graphite, graphite oxide, and graphene. (Reproduced with permission from [91].)

water molecules between the oxidized graphene layers. The width of the strongest diffraction peak can also be used to verify the degree of exfoliation as it is linked to the coherently diffracting domain size via the Debye–Scherrer equation. When graphite oxide is completely exfoliated this diffraction peak disappears [91].

References

- Boehm, H.P., Setton, R., and Stumpp, E. (1994) *Pure Appl. Chem.*, **66**, 1893.
- Chung, D.D.L. (2002) *J. Mater. Sci.*, **37**, 1475.
- Schafheutl, C. (1840) *Philos. Mag.*, **16**, 570.
- Brodie, B.C. (1859) *Philos. Trans. R. Soc. London*, **149**, 249.
- Staudenmaier, L. (1898) *Ber. Dtsch. Chem. Ges.*, **31**, 1481.
- Hummers, W.S. and Offeman, R.E. (1958) *J. Am. Chem. Soc.*, **80**, 1339.
- Bourlinos, A.B., Gournis, D., Petridis, D., Szabo, T., Szeri, A., and Dekany, I. (2003) *Langmuir*, **19**, 6050.
- Allen, M.J., Tung, V.C., and Kaner, R.B. (2010) *Chem. Rev.*, **110**, 132.
- Prezhdo, O.V. (2011) *Surf. Sci.*, **605**, 1607.
- Novoselov, K.S., Geim, A.K., Morozov, S.V., Jiang, D., Zhang, Y., Dubonos, S.V., Grigorieva, I.V., and Firsov, A.A. (2004) *Science*, **306**, 666.
- Meyer, J.C., Geim, A.K., Katsnelson, M.I., Novoselov, K.S., Booth, T.J., and Roth, S. (2007) *Nature*, **446**, 60–63.
- Castro, N., Guinea, F., Peres, N.M.R., Novoselov, K.S., and Geim, A.K. (2009) *Rev. Mod. Phys.*, **81**, 109.
- Frank, I.W., Tanenbaum, D.M., van der Zande, A.M., and McEuen, P.L.J. (2007) *Vac. Sci. Technol.*, **25**, 2558–2561.
- Boehm, H.P., Clauss, A., Fischer, G., and Hofmann, U. (1962) *Proceedings of the Fifth Conference on Carbon*, Pergamon Press, London, p. 73.
- Boehm, H.P., Clauss, A., Fischer, G.O., and Hofmann, U. (1962) *Z. Naturforsch.*, **17**, 150.
- Lerf, A., He, H., Forster, M., and Klinowski, J. (1998) *J. Phys. Chem. B*, **102**, 4477–4482.
- Szabo, T. *et al.* (2006) *Chem. Mater.*, **18**, 2740–2749.
- Gao, W., Alemany, L.B., Ci, L., and Ajayan, P.M. (2009) *Nat. Chem.*, **1**, 403.
- Stankovich, S., Dikin, D.A., Dommett, G.H.B., Kohlhaas, K.M., Zimney, E.J., Stach, E.A., Piner, R.D., Nguyen, S.T., and Ruoff, R.S. (2006) *Nature*, **442**, 282.
- Stankovich, S., Dikin, D.A., Piner, R.D., Kohlhaas, K.A., Kleinhammes, A., Jia, Y., Wu, Y., Nguyen, S.T., and Ruoff, R.S. (2007) *Carbon*, **45**, 1558.
- Boukhvalov, D.W. and Katsnelson, M.I. (2008) *J. Am. Chem. Soc.*, **130**, 10697–10701.
- Song, M. and Cai, D. (2012) in *Polymer–Graphene Nanocomposites*, RSC Nanoscience and Nanotechnology, vol. 26 (ed. V. Mittal), The Royal Society of Chemistry, pp. 1–52.
- Dreyer, D.R., Murali, S., Zhu, Y., Ruoff, R.S., and Bielawski, C.W. (2011) *J. Mater. Chem.*, **21**, 3443.
- Fan, X., Peng, W., Li, Y., Li, X., Wang, S., Zhang, G., and Zhang, F. (2008) *Adv. Mater.*, **20**, 4490.
- Shin, H.J., Kim, K.K., Benayad, A., Yoon, S.M., Park, H.K., Jung, I.S., Jin, M.H., Jeong, H.K., Kim, J.M., Choi, J.Y., and Lee, Y.H. (2009) *Adv. Funct. Mater.*, **19**, 1987.
- Fernandez-Merino, M.J., Guardia, L., Paredes, J.I., Villar-Rodil, S., Solçs-Fernandez, P., Martçnez-Alonso, A., and Tascon, J.M.D. (2010) *J. Phys. Chem. C*, **114**, 6426.
- Pei, S., Zhao, J., Du, J., Ren, W., and Cheng, H.M. (2010) *Carbon*, **48**, 4466.
- Moon, I.K., Lee, J., Ruoff, R.S., and Lee, H. (2010) *Nat. Commun.*, **1**, 73.
- Chen, W., Yan, L., and Bangal, P.R. (2010) *J. Phys. Chem. C*, **114**, 19885.
- Liu, S., Tian, J., Wang, L., and Sun, X. (2011) *Carbon*, **49**, 3158.
- Zhou, X., Zhang, J., Wu, H., Yang, H., Zhang, J., and Guo, S. (2011) *J. Phys. Chem. C*, **115**, 11957.

32. Fan, Z., Wang, K., Wei, T., Yan, J., Song, L., and Shao, B. (2010) *Carbon*, **48**, 1686.
33. Fan, Z., Kai, W., Yan, J., Wei, T., Zhi, L., Feng, J., Ren, Y., Song, L., and Wei, F. (2011) *ACS Nano*, **5**, 191.
34. Chen, D., Li, L., and Guo, L. (2011) *Nanotechnology*, **22**, 325601.
35. Zhou, T., Chen, F., Liu, K., Deng, H., Zhang, Q., Feng, J., and Fu, Q. (2011) *Nanotechnology*, **22**, 045704.
36. Schniepp, H.C., Li, J.L., Mc Allister, M.J., Sai, H., Herrera-Alonso, M., Adamson, D.H., Prud'homme, R.K., Car, R., Saville, D.A., and Aksay, I.A. (2006) *J. Phys. Chem. B*, **110**, 8535.
37. Cote, L.J., Cruz-Silva, R., and Huang, J. (2009) *J. Am. Chem. Soc.*, **131**, 11027.
38. Zhou, M., Wang, Y., Zhai, Y., Zhai, J., Ren, W., Wang, F., and Dong, S. (2009) *Chem. Eur. J.*, **15**, 6116.
39. An, S.J., Zhu, Y., Lee, S.H., Stoller, M.D., Emilsson, T., Park, S., Velamakanni, A., An, J., and Ruoff, R.S. (2010) *J. Phys. Chem. Lett.*, **1**, 1259.
40. Suslick, K.S. (1990) *Science*, **247**, 1439–1445.
41. Hernandez, Y., Nicolosi, V., Lotya, M., Blighe, F.M., Sun, Z.Y., De, S., McGovern, I.T., Holland, B., Byrne, M., Gun'ko, Y.K., Boland, J.J., Niraj, P., Duesberg, G., Krishnamurthy, S., Goodhue, R., Hutchison, J., Scardaci, V., Ferrari, A.C., and Coleman, J.N. (2008) *Nat. Nanotechnol.*, **3**, 563–568.
42. Coleman, J.N. (2013) *Acc. Chem. Res.*, **46**, 14–22.
43. Blake, P., Brimicombe, P.D., Nair, R.R., Booth, T.J., Jiang, D., Schedin, F., Ponomarenko, L.A., Morozov, S.V., Gleeson, H.F., Hill, E.W., Geim, A.K., and Novoselov, K.S. (2008) *Nano Lett.*, **8**, 1704–1708.
44. Bourlinos, A.B., Georgakilas, V., Zboril, R., Steriotis, T.A., and Stubos, A.K. (2009) *Small*, **5**, 1841–1845.
45. Hamilton, C.E., Lomeda, J.R., Sun, Z., Tour, J.M., and Barron, A.R. (2009) *Nano Lett.*, **9**, 3460.
46. Misik, V. and Riesz, P. (1996) *Free Radical Biol. Med.*, **20**, 129.
47. Guittonneau, F., Abdelouas, A., Grambow, B., and Huclier, S. (2010) *Ultrason. Sonochem.*, **17**, 391.
48. Khan, U., O'Neil, A., Loyta, M., De, S., and Coleman, J.N. (2010) *Small*, **6**, 864–871.
49. Dreyer, D.R., Park, S., Bielawski, C.W., and Ruoff, R.S. (2010) *Chem. Soc. Rev.*, **39**, 228–240.
50. Quintana, M., Grzelczak, M., Spyrou, K., Kooi, B., Bals, S., Van Tendeloo, G., Rudolf, P., and Prato, M. (2012) *Chem. Commun.*, **48**, 12159–12161.
51. León, V., Quintana, M., Herrero, M.A., Fierro, J.L.G., de la Hoz, A., Prato, M., and Vázquez, E. (2011) *Chem. Commun.*, **47**, 10936.
52. Cote, L.J., Kim, F., and Huang, J. (2009) *J. Am. Chem. Soc.*, **131**, 1043–1049.
53. Gengler, R.Y.N., Velingura, A., Enotiadis, A., Diamanti, E.K., Gournis, D., Józsa, C., Wees, B.J.V., and Rudolf, P. (2010) *Small*, **6**, 35.
54. Emtsev, K.V., Bostwick, A., Horn, K., Jobst, J., Kellogg, G.L., Ley, L., McChesney, J.L., Ohta, T., Reshanov, S.A., Rotenberg, E., Schmid, A.K., Waldmann, D., Weber, H.B., and Seyller, T. (2009) *Nat. Mater.*, **8**, 203.
55. Sutter, P.W., Flege, J.I., and Sutter, E.A. (2008) *Nat. Mater.*, **7**, 406.
56. Coraux, J., N'Diaye, A.T., Busse, C., and Michely, T. (2008) *Nano Lett.*, **8**, 565.
57. Kim, K.S., Zhao, Y., Jiang, H., Lee, S.Y., Kim, J.M., Kim, K.S., Ahn, J.H., Kim, P., Choi, J.Y., and Hong, B.H. (2009) *Nature*, **457**, 706.
58. Rina, A., Jia, X., Ho, J., Nezich, D., Son, H., Bulovic, V., Dresselhaus, M.S., and Kong, J. (2009) *Nano Lett.*, **9**, 30.
59. Li, X., Cai, W., An, J., Kim, S., Nah, J., Yang, D., Piner, R., Velamakanni, A., Jung, I., Tutuc, E.K., Banerjee, S.K., Colombo, L., and Ruoff, R.S. (2009) *Science*, **324**, 1312.
60. Batzill, M. (2012) *Surf. Sci. Rep.*, **67**, 83–115.
61. Mattevi, C., Kim, H., and Chhowalla, M. (2011) *J. Mater. Chem.*, **21**, 3324.
62. Terrones, M., Botello-Méndez, A.R., Delgado, J.C., López-Urtaas, F., Vega-Cantú, Y.I., Rodríguez-Macías, F.J., Elías, A.L., Muñoz-Sandoval, E., Cano-Márquez, A.G., Charlier, J.C., and Terrones, H. (2010) *Nano Today*, **5**, 351.

63. Han, M.Y., Özyilmaz, B., Zhang, Y., and Kim, P. (2007) *Phys. Rev. Lett.*, **98**, 206805.
64. Jiao, L., Wang, X., Diankov, G., Wang, H., and Dai, H. (2010) *Nat. Nanotechnol.*, **5**, 321.
65. Gomez-Navarro, C., Weitz, R.T., Bittner, A.M., Scolari, M., Mews, A., Burghard, M., and Kern, K. (2007) *Nano Lett.*, **7**, 3499.
66. Tombros, N., Jozsa, C., Popinciuc, M., Jonkman, H.T., and van Wees, B.J. (2007) *Nature*, **448**, 571.
67. Novoselov, K.S. *et al.* (2005) *Proc. Natl. Acad. Sci. U.S.A.*, **102**, 10451.
68. Huang, P.Y., Ruiz-Vargas, C.S., van der Zande, A.M., Whitney, W.S., Levendorf, M.P., Kevek, J.W., Garg, S., Alden, J.S., Hustedt, C.J., Zhu, Y., Park, J., McEuen, P.L., and Muller, D.A. (2011) *Nature*, **469**, 389.
69. Jinschek, J.R., Yucelen, E.H., Calderon, A., and Freitag, B. (2011) *Carbon*, **49**, 556–562.
70. Ferrari, A.C., Meyer, J.C., Scardaci, V., Casiraghi, C., Lazzeri, M., Mauri, F., Piscanec, S., Jiang, D., Novoselov, K.S., Roth, S., and Geim, A.K. (2006) *Phys. Rev. Lett.*, **97**, 187401.
71. Parka, J.S., Reina, A., Saito, R., Kong, J., Dresselhaus, G., and Dresselhaus, M.S. (2009) *Carbon*, **47**, 1303–1310.
72. Tuinstra, F. and Koenig, J. (1970) *J. Chem. Phys.*, **53**, 1126.
73. Mohiuddin, T., Lombardo, A., Nair, R., Bonetti, A., Savini, G., Jalil, R., Bonini, N., Basko, D., Galiotis, C., Marzari, N., Novoselov, K., Geim, A., and Ferrari, A. (2009) *Phys. Rev. B*, **79** (20), 205433.
74. De, S., King, P.J., Lotya, M., O'Neill, A., Doherty, E.M., Hernandez, Y., Duesberg, G.S., and Coleman, J.N. (2009) *Small*, **6**, 1–7.
75. Wang, G., Yang, J., Park, J., Gou, X., Wang, B., Liu, H., and Yao, J. (2008) *J. Phys. Chem. C*, **112**, 8192–8195.
76. Bourlinos, A.B., Georgakilas, V., Zboril, R., Steriotis, T.A., Stubos, A.K., and Trapalis, C. (2009) *Solid State Commun.*, **149**, 2172–2176.
77. Jung, I., Pelton, M., Piner, R., Dikin, D.A., Stankovich, S., Watcharotone, S., Hausner, M., and Ruoff, R.S. (2007) *Nano Lett.*, **7**, 3569.
78. Ni, Z.H., Chen, W., Fan, X.F., Kuo, J.L., Yu, T., Wee, A.T.S., and Shen, Z.X. (2008) *Phys. Rev. B*, **77**, 115416.
79. Blake, P., Hill, E.W., Neto, A.H.C., Novoselov, K.S., Jiang, D., Yang, R., Booth, T.J., and Geim, A.K. (2007) *Appl. Phys. Lett.*, **91**, 063124.
80. Nair, R.R., Blake, P., Grigorenko, A.N., Novoselov, K.S., Booth, T.J., Stauber, T., Peres, N.M.R., and Geim, A.K. (2008) *Science*, **320**, 1308.
81. Sun, Z., Yan, Z., Yao, J., Beitler, E., Zhu, Y., and Tour, J.M. (2010) *Nature*, **468**, 549–552.
82. Lee, D.Y., Khatun, Z., Lee, J.H., and Lee, Y.K. (2011) *Biomacromolecules*, **12**, 336–341.
83. Dong, Y., Chen, C., Zheng, X., Gao, L., Cui, Z., Yang, H., Guo, C., Chi, Y., and Li, C.M. (2012) *J. Mater. Chem.*, **22**, 8764.
84. Pan, D., Zhang, J., Li, Z., and Wu, M. (2010) *Adv. Mater.*, **22**, 734–738.
85. Shen, J., Zhu, Y., Yang, X., Zong, J., Zhang, J., and Li, C. (2012) *New J. Chem.*, **36**, 97–101.
86. Xie, M., Su, Y., Lu, X., Zhang, Y., Yang, Z., and Zang, Y. (2013) *Mater. Lett.*, **93**, 161–164.
87. Yang, F., Zhao, M., Zheng, B., Xiao, D., Wo, L., and Guo, Y. (2012) *J. Mater. Chem.*, **22**, 25471.
88. Zhang, M., Bai, L., Shang, W., Xie, W., Ma, H., Fu, Y., Fang, D., Sun, H., Fan, L., Han, M., Liu, C., and Yang, S. (2012) *J. Mater. Chem.*, **22**, 7461.
89. Wang, F., Zhang, Y., Tian, C., Girit, C., Zettl, A., Crommie, M., and Shen, Y.R. (2008) *Science*, **320**, 206.
90. Zhang, Y., Tang, T.T., Girit, C., Hao, Z., Martin, M.C., Zettl, A., Crommie, M.F., Shen, Y.R., and Wang, F. (2009) *Nature*, **459**, 820.
91. Zhang, H.B., Zheng, W.G., Yan, Q., Yang, Y., Wang, J.W., Lu, Z.H. *et al.* (2010) *Polymer*, **51**, 1191–1196.

2

Covalent Attachment of Organic Functional Groups on Pristine Graphene

Vasilios Georgakilas

2.1

Introduction

Graphene is a carbon nanostructure with high chemical stability in general, which is provided by the extended aromatic character of the graphitic lattice. In practice, this stability is usually associated with the influence of chemical substances like gases, acids, or bases under specific conditions determined by chemical processes such as catalytic procedures. On the other hand, several organic reactions have been applied on graphene up to now affording a large number of derivatives. In general the reactions with graphene are divided in two main categories. The first category includes the reactions of the carboxyl, hydroxyl, and epoxy groups that are spread on a graphene oxide (GO) layer as a consequence of their preparation procedure. The reactions of this category are described in the next chapter. The second category includes the covalent attachment of organic functional groups directly on sp^2 carbon atoms of pristine graphene or GO and they are described in this chapter.

The chemical reactivity of sp^2 carbon atoms of graphene originates from various sources that are described below. It is known that a number of carbon atoms at the defect sites and at the edges have sp^3 hybridization. The existence of these sp^3 carbon atoms decreases the aromatic character in the areas around the defects and near the edges and consequently increases the reactivity of the neighboring sp^2 carbon atoms or carbon-carbon double (C=C) bonds. In addition, because the direct covalent addition to graphitic carbon atoms changes their hybridization from sp^2 to sp^3 , as the reaction proceeds the number of sp^3 carbon atoms of the graphene layer is increased. As a consequence, during the reaction the aromatic character of graphene is decreased continuously and the chemical reactivity is increased. Furthermore, although theoretically graphene has a planar structure, the combination of the large 2D surface area with the minimal thickness creates a number of anomalous – out of planar – curved domain-like folds and wrinkles that induce local strain and hence chemical reactivity to the C=C bonds analogous to the induced reactivity of carbon nanotubes as a result of the curvature of the cylindrical shape.

The organic modification of graphene through covalent bonds with graphitic carbon atoms has advantages and disadvantages. The addition of organic groups on the graphene surface, which is followed by the transformation of the hybridized carbon atoms from sp^2 to sp^3 , disrupts the aromatic systems. This change has an important influence on the electronic and the mechanical properties of the organic graphene derivatives. Usually the extent of this influence depends on the percentage of the carbon atoms that have reacted and the type of reaction as well. The advantages of derivatization are related to the nature of the added organic functionalities, which can enrich graphene with various novel physicochemical properties. Thus graphene can be functionalized with organophilic or hydrophilic organic groups, chromophores, drugs, biomolecules, or polymers acquiring analogous properties and characteristics. Making the graphene nanoplatelets highly organophilic, its dispersion in organic solvents and subsequent dispersion or mixing with analogous polymers is facilitated. In addition the organic character that is gained after the modification increases the chemical affinity with polymers which is a crucial factor for the enhancement of the mechanical strength in polymer nanocomposites. In general carbon nanostructures – graphene, carbon nanotubes, nanohorns – dispersed in organic solvents can be purified, characterized, and handled much easier than in solid phase. In the case of graphene the absence of a stabilizer in the liquid phase very often leads to the reorganization of graphene monolayers into larger graphitic aggregates or in the absence of the liquid phase, into graphite.

The characterization of the functionalized graphene is usually based on microscopic techniques such as AFM (atomic force microscope), TEM (transmission electron microscope), HRTEM (high-resolution transmission electron microscope) for the identification of graphene and spectroscopic techniques such as UV–vis, FTIR (Fourier transform infrared), Raman, XPS (X-ray photoelectron spectroscopy), photoluminescence spectroscopy, and thermogravimetric analysis (TGA) for its morphology. Free radicals, dienophiles, and other reactive intermediates are the most frequently used organic species in the direct organic functionalization of graphene. The following sections include the description of the most widely used reactions of this category through the presentation of representative examples.

2.2

Cycloaddition Reactions

2.2.1

1,3-Dipolar Cycloaddition of Azomethine Ylide

1,3-Dipolar cycloaddition is the name given to the reaction between a 1,3-dipole and a double or triple carbon bond, which is a dipolarophile. The 1,3-dipole is usually a triatomic molecule or a part of a molecule that shares four π electrons. The result of the reaction is the formation of a five-membered ring. In 1,3-dipolar cycloaddition with graphene, the latter has the role of dipolarophile. One of the

Through substituted α amino acid pathway

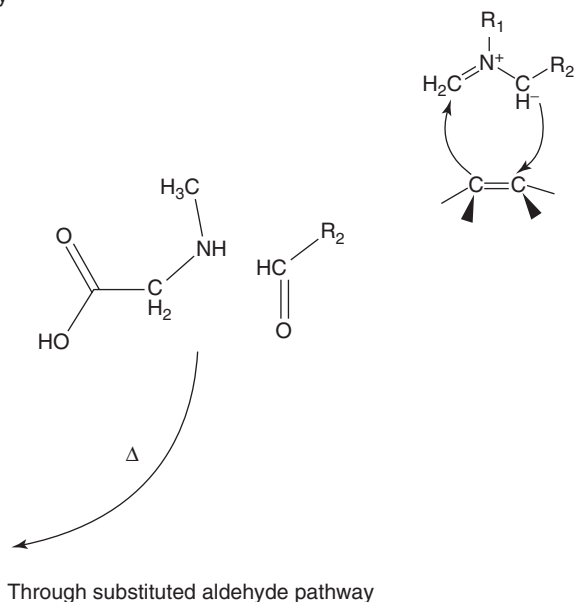
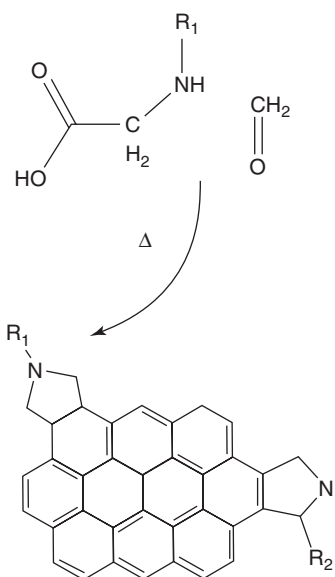


Figure 2.1 The reaction mechanism of 1,3-dipolar cycloaddition of azomethine ylide with graphene. One reaction pathway includes the combination of an R_1 substituted N -methyl glycine and

formaldehyde and an alternative pathway includes the combination of N -methyl glycine and R_2 substituted aldehyde. In the right part the dipolar reactive intermediate is presented.

most attractive 1,3-dipole is azomethine ylide; a very reactive intermediate that is formed by the condensation of an α glycine and an aldehyde under heating. The addition of azomethine ylide on C=C bonds of graphene leads to the formation of pyrrolidine rings perpendicular to the graphene surface. The mechanism of the reaction is described in Figure 2.1. This reaction can be applied on pristine graphene as well as on GO since the reactive sp^2 carbon atoms are present in abundance in both graphene nanostructures.

One of the most attractive advantages of this functionalization originates from the variety of the functional groups that can be part of N -methyl glycine or aldehyde reactants. Thus designing the functionalization of graphene with a specific organic group (R_1 or R_2 in the scheme of Figure 2.1), this could be added either as a part of the aldehyde ($-R_2$) or the α amino acid ($-R_1$). As a consequence, there are two different pathways that could be followed. In the first one, the reactive azomethine ylide is formed by the combination of a substituted aldehyde (with the group $-R_2$) with the simplest α amino acid, the N -methyl glycine (*through substituted aldehyde pathway*). In this case the organic functional group that is added on graphene ($-R_2$) is located in one of the carbon atoms of the pyrrolidine ring near nitrogen. In the second pathway the reaction is performed by the condensation of – the simplest aldehyde – paraformaldehyde and the functionalized α amino acid, which now

bears the specific functional group ($-R_1$) (through a substituted amino acid pathway). Now the added functional group is attached to the nitrogen atom of pyrrolidine ring. An obvious difference between the two pathways as regards the resulting graphene derivative is the final position of the added group relative to the graphitic surface. In the first pathway, the group is located close and more parallel to the graphitic surface whereas in the second pathway the added group is placed almost perpendicular to the graphene surface. Of course the reaction could be performed even with both reactants as substituted amino acid and aldehyde.

2.2.1.1 Through a Substituted Aldehyde Pathway

After a successful application of 1,3-dipolar cycloaddition with a plethora of azomethine ylides on fullerenes [1–3] and carbon nanotubes [4–10], the reaction has been applied successfully on graphene nanoplatelets. Starting from 1,4-dihydroxy benzaldehyde and *N*-methyl glycine, pristine graphene is decorated with pyrrolidine rings, which are substituted by dihydroxyphenyl groups (Figure 2.2A) [11]. The covering of graphene surface with hydroxylated phenyl groups increases substantially the dispersibility of the modified graphene nanoplatelets in polar solvents such as ethanol or dimethylformamide (DMF) (Figure 2.2B). In addition hydroxyl groups can be further functionalized leading to a plethora of graphene derivatives. Such post functionalization has been shown in pyrrolidine functionalized carbon nanotubes [5].

For every pyrrolidine ring that is formed perpendicular to the graphene surface two sp^2 carbon atoms from the graphene sheet change their hybridization to sp^3 . This change is clearly indicated in the Raman spectrum of the product by the ratio I_D/I_G between the two characteristic bands (G and D) of graphene (see Figure 2.2C).

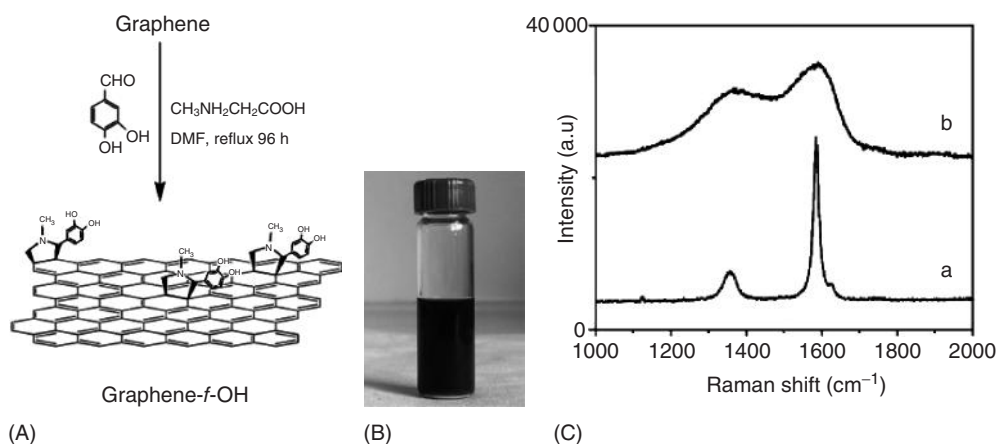


Figure 2.2 (A) 1,3-Dipolar cycloaddition of graphene nanoplatelets by azomethine ylide starting from a dihydroxy phenyl substituted aldehyde and *N*-methyl glycine and (B) image showing the dispersion of

pyrrolidine functionalized graphene in DMF. (C) Raman spectra of (a) pristine graphene and (b) pyrrolidine functionalized graphene. (Reprinted with permission from Ref. [11], Copyright 2010, Royal Society of Chemistry.)

In fact the above I_D/I_G ratio increases analogously with the degree of the covalent functionalization. This change is attributed to the indirect influence of the number of the sp^3 carbon atoms of graphene on the intensity of the D band. In the next figure a highly functionalized graphene derivative is presented where the D band is more than the half of G band in comparison with Raman spectrum of pristine graphene where the D band is far less.

In another application of this reaction pathway, the covalent attachment on graphene of a tetraphenylporphyrin (TPP) or a palladium tetraphenylporphyrin (Pd-TPP) chromophoric groups through a pyrrolidine ring is performed by the contribution to the reaction of an aldehyde substituted by (TPP) or (Pd-TPP) and *N*-methyl glycine (see Figure 2.3) [12]. The I_D/I_G ratio in the Raman spectrum increased from 0.22 before the functionalization to 0.4 in the porphyrin functionalized graphene because of the sp^2 to sp^3 transformation of the reacting carbon atoms of graphene.

TGA is a useful technique for the estimation of the total added groups on graphene after a functionalization reaction. This is because of the heat that is needed for the removal of the added organic groups on graphene is different from the heat that is needed for other processes such as evaporation of solvent, removal of physisorbed molecules, oxidation of graphene. In this example in the TGA diagram of the TPP and Pd-TPP functionalized graphenes, a 20% mass loss is recorded between 200 and 500 °C, which is not observed in the TGA diagram of the pristine graphene (see Figure 2.4). This mass loss is attributed to the removal of the added groups from graphene and as a consequence the percentage also indicates the number of the added groups in the final product.

Finally a conjugated polyfluorenyl polymer substituted by benzaldehyde groups as side chains has been also grafted on reduced GO using 1,3-dipolar cycloaddition. As described in the next figure (Figure 2.5) the grafting of the polymer is achieved

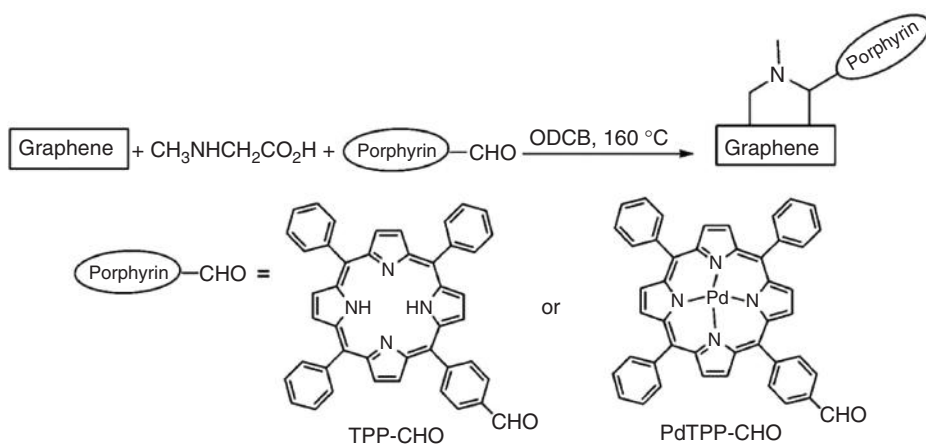


Figure 2.3 Immobilization of porphyrin on graphene through 1,3-dipolar cycloaddition. (Reprinted with permission from Ref. [12], Copyright 2011, Wiley-VCH Verlag GmbH & Co KGaA, Weinheim.)

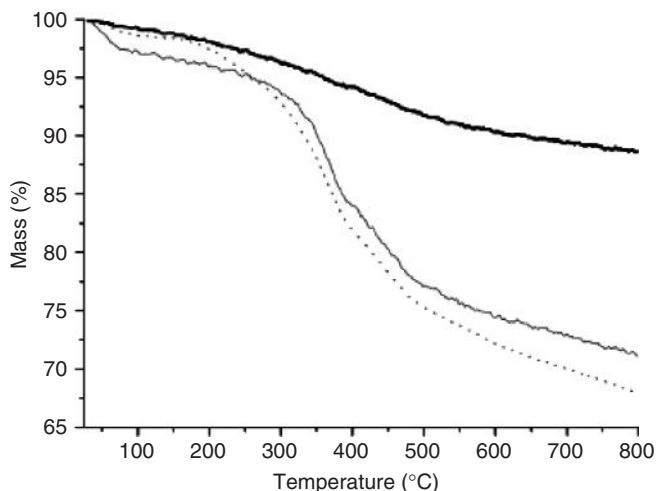


Figure 2.4 TGA curves of graphene (thick solid line), graphene-TPP (thin solid line), and graphene-PdTPP (dotted line). (Reprinted with permission from Ref. [12], Copyright 2011, Wiley-VCH Verlag GmbH & Co KGaA, Weinheim.)

by an azomethine ylide intermediate that is formed by the condensation of the benzaldehyde groups of the conjugated polymer with *N*-methyl glycine and C=C bonds on *r*GO [13, 14]. The basic structural difference between pristine graphene and GO, which is the presence of oxygen groups (epoxides, carboxyl, hydroxyl) on the surface of GO does not influence the 1,3-dipolar cycloaddition directly. However there are several factors that influence the final result of the functionalization and have to do with the nature of the graphitic nanostructure, for example, GO is better dispersible in organic solvents and it forms more stable and concentrated colloidal solutions than pristine graphene. The I_D/I_G ratio in the Raman spectrum of the initial *r*GO nanoplatelets was about 0.5 (the I_D/I_G ratio of GO before the reduction was about 1.83).

In the polymer functionalized graphene the I_D/I_G ratio increased from 0.5 in the *r*GO to 1.3 indicating a rather high degree of functionalization. The UV–vis spectrum of the conjugated polymer was composed of two characteristic overlapped absorption bands at 307 and 367 nm, which is attributable to a π, π^* transition of the polymer bone. After the grafting of the polymer on the *r*GO surface, which can be seen as an intramolecular donor–acceptor system, the intensity of the absorption band at 307 nm increased whereas that at 367 nm decreased and blueshifted at 357 nm as a consequence of the interaction with the graphitic surface. The conjugate polymer/*r*GO composite has been examined for nonvolatile rewritable memory application. For this study a device was fabricated with a structure consisting of three layers from indium tin oxide (ITO), polymer composite, and aluminum. The switch-on voltage of the device was around -1.2 V and the ON/OFF state current ratio exceeded 10^4 [14].

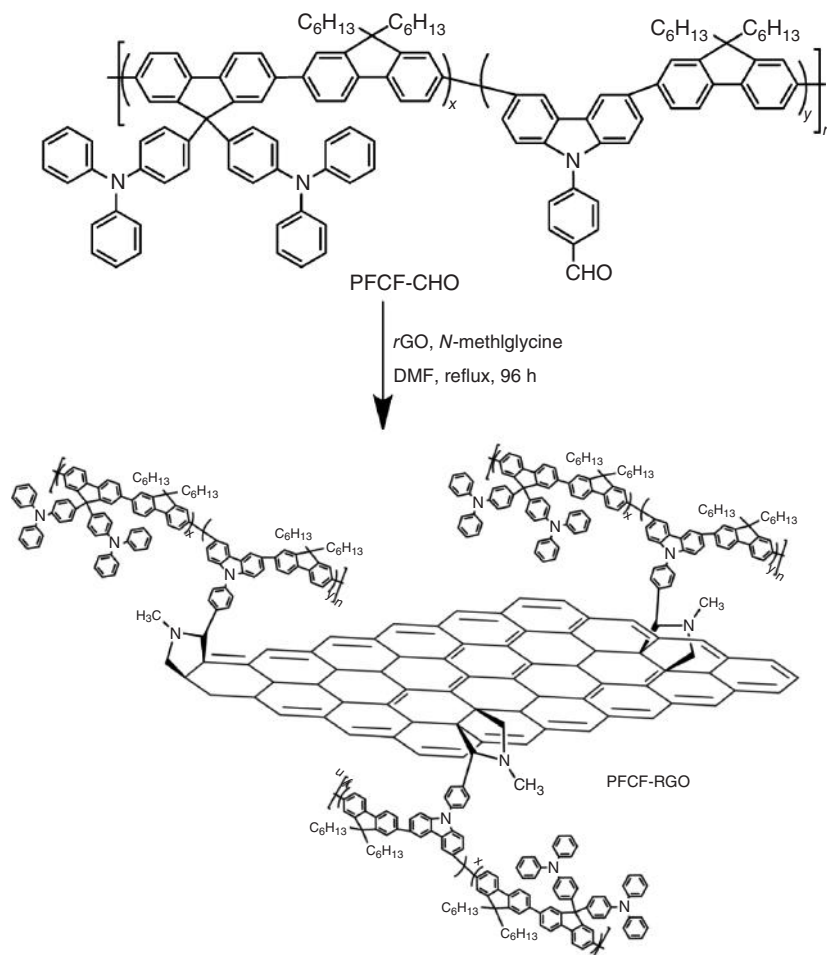


Figure 2.5 Covalent addition of a conjugated polymer on reduced GO through substituted aldehyde pathway. (Reprinted with permission from Ref. [14], Copyright 2011, Wiley-VCH Verlag GmbH & Co KGaA, Weinheim.)

2.2.1.2 Through Substituted α Amino Acid Pathway

Substituted α amino acid with an NH_2 terminated organic functional group combined with paraformaldehyde has been used by Prato *et al.* to form substituted pyrrolidine rings on graphene through substituted α amino acid pathway [15]. During this reaction, NH_2 is protected by the Boc (*tert*-butoxycarbonyl) group, which is removed easily by treatment of the product with hydrochloric acid. These NH_2 groups bind selectively to gold (Au) nanorods, which are used as markers revealing the positions of the pyrrolidine rings on the graphene surface [15]. As shown in a characteristic TEM image of the Au decorated graphenes, the Au nanorods, and consequently the pyrrolidine rings are spread over the total area of

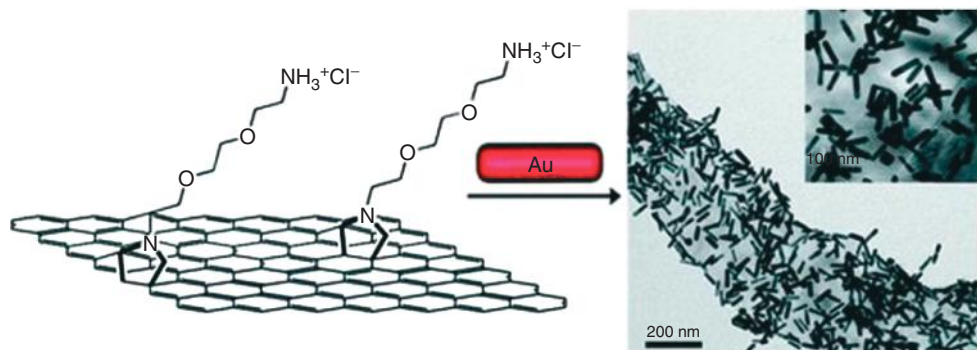


Figure 2.6 Amino terminated pyrrolidine rings on graphene surface. (Reprinted with permission from Ref. [15], Copyright 2010, American Chemical Society.)

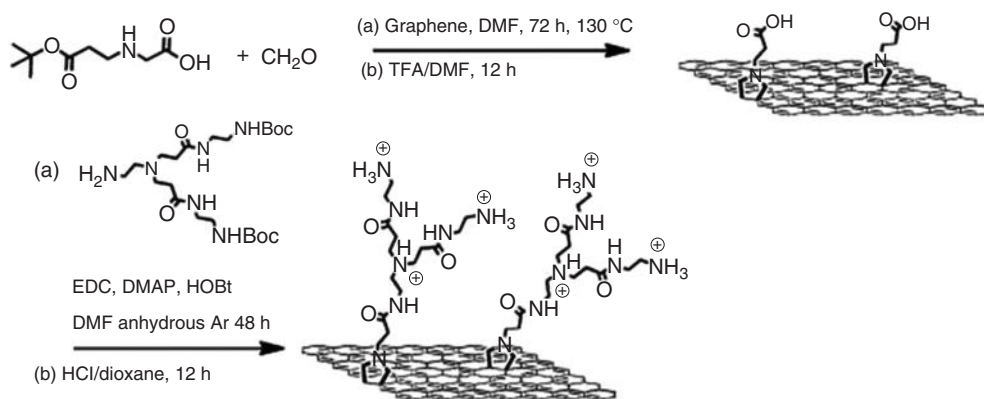


Figure 2.7 Carboxylate terminated pyrrolidine rings attached on graphene surface. (Reprinted with permission from Ref. [16], Copyright 2011, Royal Society of Chemistry.)

the graphene layer implying that 1,3-dipolar cycloaddition is not dependent on the position of the carbon atoms on the surface (see Figure 2.6).

In another characteristic example of 1,3-dipolar cycloaddition through the substituted α amino acid pathway, an ester terminated *N*-methyl glycine is used and finally after hydrolysis of the product, graphene is functionalized with pyrrolidine rings that bear carboxyl groups. At the last stage graphene is then easily post functionalized with alcohols, phenols, or amines as shown in the example in Figure 2.7 [16].

2.2.2

Cycloaddition by Zwitterionic Intermediate

A five-membered ring is also formed by the reaction of a zwitterionic intermediate that results by the condensation of 4-dimethylaminopyridine with an acetylene dicarboxylate as presented in Figure 2.8. The functionalized graphene nanoplatelets are dispersible in organic solvents such as DMF, CHCl_3 , or water depending on

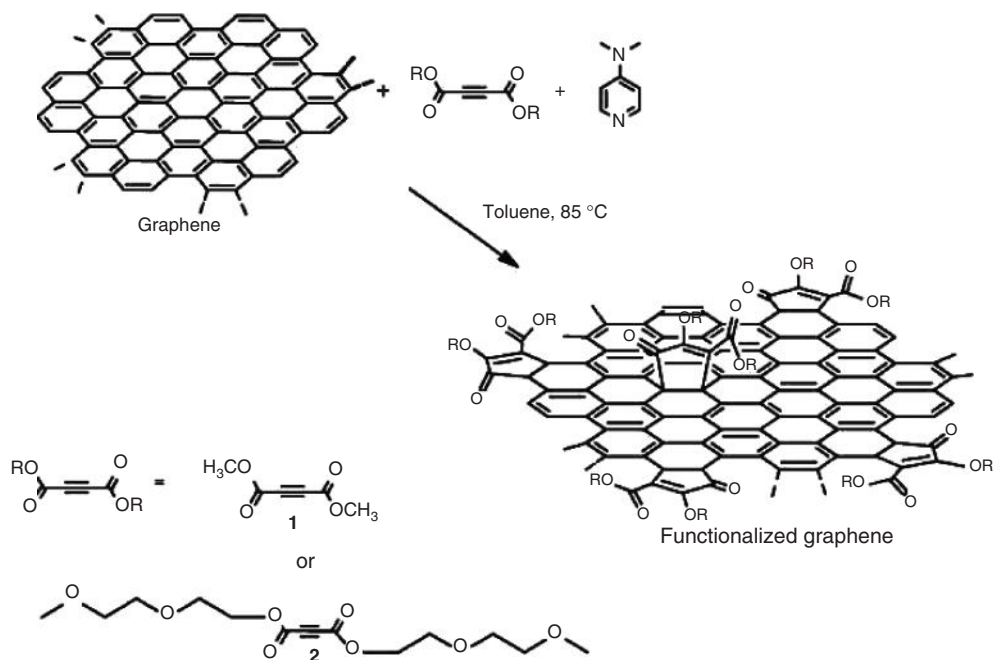


Figure 2.8 Functionalization of graphene by a zwitterionic intermediate. The functionalized graphenes are dispersible in DMF and CHCl_3 in case of reactant 1 and water in case of 2. (Reprinted with permission from Ref. [17], Copyright 2012, Royal Society of Chemistry.)

the substituted functional groups [17]. The I_D/I_G ratio of the Raman spectrum increased from 0.3 in pristine graphene to 0.4 and 0.54, respectively, for the two products that are described in Figure 2.8, indicating a medium degree of functionalization.

2.2.3

Diels–Alder Cycloaddition

Diels–Alder (DA) cycloaddition is a widely used organic reaction between conjugated dienes and dienophile alkenes and has been applied successfully in carbon nanostructures [18–22]. Graphene, due to its polyaromatic character, can act as diene or dienophile depending on the character of the added reactant. Haddon *et al.* has studied the reactivity of several forms of graphene nanosheets as regards DA cycloaddition [23]. In the reaction of tetracyanoethylene (TCNE) or maleic anhydride, graphene acts as diene whereas in case of a 2,3-dimethoxy-1,3-butadiene or 9-methyl anthracene addition, graphene behaves as dienophile. In both cases a six membered ring is formed lying perpendicular to the graphene surface (see Figure 2.9) [23]. The DA cycloaddition with TCNE, in general, is performed at room temperature on graphene nanosheets suspended in dichloromethane. The reaction has a reversible character, which means that under certain conditions graphene returns to the pristine form by removal of the added groups and recovery of the

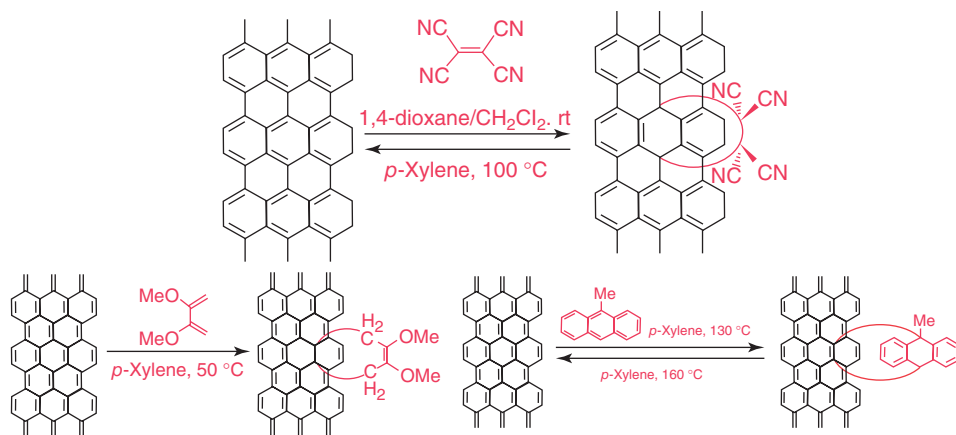


Figure 2.9 Diels–Alder cycloaddition reaction between graphene and dienophile or diene. (Reprinted with permission from Ref. [23], Copyright 2011, American Chemical Society.)

electronic properties. The reverse reaction of the TCNE functionalized graphene is performed in a *p*-xylene dispersion by heating at 100 °C. According to the I_D/I_G ratio recorded in the Raman spectra, before and after the cycloaddition with TCNE or maleic anhydride, single layer graphene is by far more reactive than the few-layer graphene and highly oriented pyrolytic graphite (HOPG), which have similar reactivity. In addition the maleic anhydride reaction is temperature sensitive. The reactivity of graphene as dienophile was examined by the DA cycloaddition of 2,3-dimethoxy-1,3-butadiene or 9-methyl anthracene. When the I_D/I_G ratio recorded in the Raman spectra of graphene before and after DA reaction exceed 1, the yield of these DA reactions could be very high after optimization of parameters such as the temperature, the solvent, the ratio of the reactants or the duration of the reaction.

A polyethylene glycol (PEG) monomethyl ether chain can be grafted on a chemically reduced graphene oxide (*r*GO) surface when it is terminated by a cyclopentadienyl group. The latter reacts as diene with a double bond of the graphene surface in a DA cycloaddition (Figure 2.10). The product of the reaction is *r*GO nanosheets functionalized with covalently grafted PEG chains [24]. The I_D/I_G ratio here is increased from 1.18 in *r*GO to 1.34–1.38 in the polymer functionalized *r*GO showing a rather low yielding reaction.

2.2.4

Nitrene Addition

Nitrenes are reactive intermediates that originate from organic azides after the thermal or photochemical removal of an N_2 molecule. They react easily with $C=C$ double bonds of graphene forming three-membered aziridine rings, which connect the graphene surface with the organic part of the azides. Depending on this organic part, graphene nanoplatelets are finally decorated by aromatic species [25, 26], polymers [27], or aliphatic chains which can be further substituted

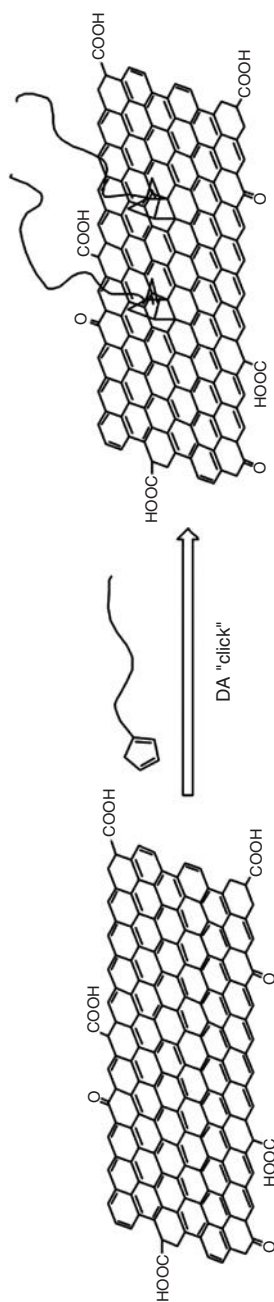


Figure 2.10 Diels–Alder cycloaddition of a cyclopentadienyl terminated PEG monomethyl ether. (Reprinted with permission from Ref. [24]. Copyright 2012, Royal Society of Chemistry.)

by functional groups such as carboxyl or hydroxyl groups, perfluoroalkyl chains [28–30]. These functional groups can contribute in a post functionalization of the modified graphene. As an example, gold nanoparticles dispersed in a suspension of carboxy-alkyl aziridine functionalized graphene are captured selectively by the carboxyl groups and thus immobilized on the surface of the functionalized graphene (Figure 2.11a). The positions of the gold nanoparticles as revealed by TEM images indicate the positions of the functional groups (Figure 2.11b). The organically modified graphene is easily dispersible in organic solvents. The formation of aziridine rings on the graphene surface is accompanied by analogous increase of the sp^3/sp^2 ratio of the carbon atoms of graphene which is then recorded as an increase of the I_D/I_G ratio between the D and G bands of the functionalized

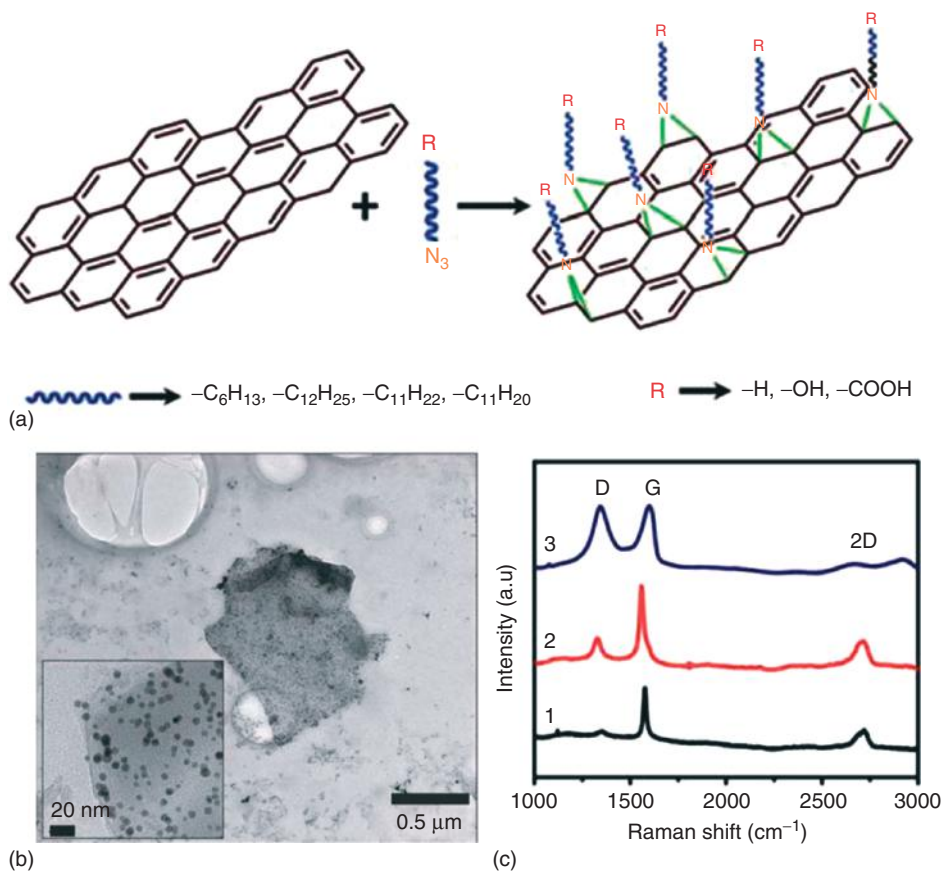


Figure 2.11 (a) Addition of alkyl azide on graphene surface and the formation of aziridine rings. (b) TEM image of gold nanoparticles dispersed on the surface of graphene functionalized by azido undecanoic acid and (c) Raman spectra of pristine graphene

sheets (1) and after functionalization by azido undecanoic acid in 1:1 ratio (2), and 1:10 ratio (3) where the excess is referred to the *azide*. (Reprinted with permission from Ref. [28]. Copyright 2011, Royal Society of Chemistry.)

graphene (Figure 2.11c, lines 1 and 2). A further increase of the I_D/I_G ratio is recorded when graphene reacts with a 1 : 10 excess of the alkyl azide (Figure 2.11c, line 3). This observation shows a direct relation between the ratio of the reactants and the extension of the functionalization of graphene. In other words, the degree of graphene functionalization could be controlled by the ratio of the reactants. A broad 2D band shifted below 2700 cm^{-1} indicates an increased percentage of graphene monolayers and few layers graphene in the final product [28].

The successful aziridine ring formation after the azide reaction with graphene is indicated by the FTIR spectrum of the product in comparison with that of the added azide. The absence of the corresponding peak at 2100 cm^{-1} that is assigned to the stretching vibration of the azido group of tetraphenyl ethylene (TPE) [30] in the FTIR spectrum of the TPE functionalized graphene, in combination with the appearance of other peaks assigned to the organic part of the added TPE indicates the efficient aziridine ring formation on graphene the surface (see Figure 2.12).

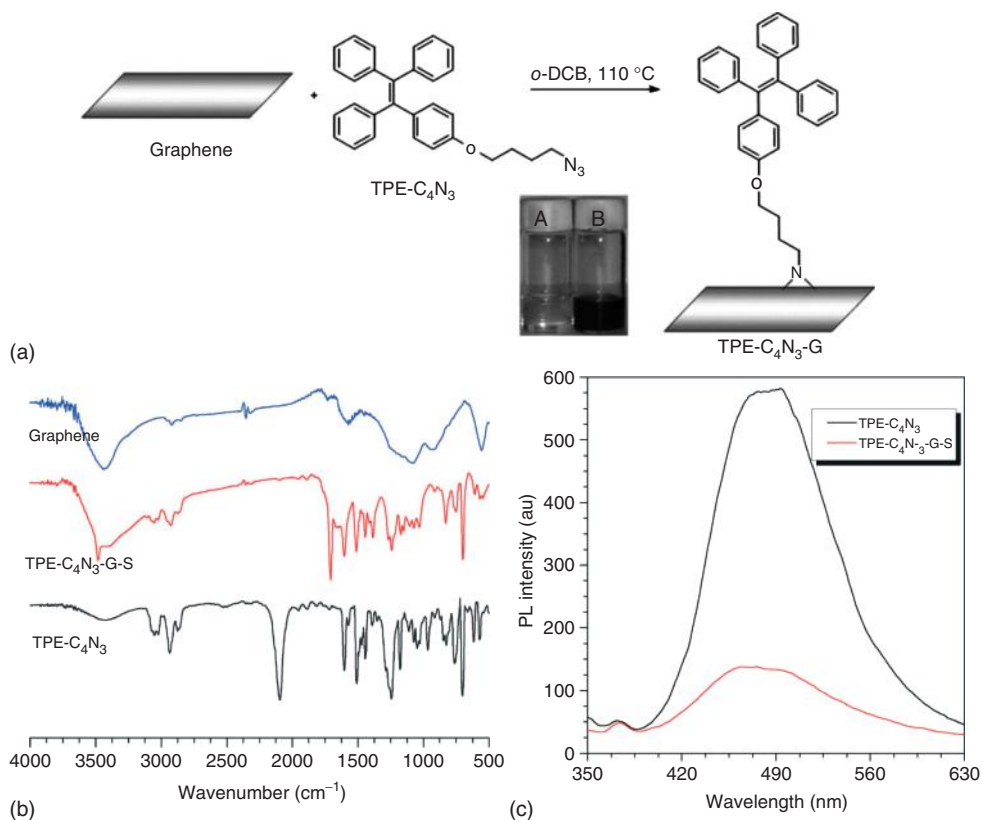


Figure 2.12 (a) Addition of tetraphenyl azide on graphene surface by the formation of aziridine rings. (b) FTIR spectra of the reactants, graphene and TPE azide, and the product TPE-Graphene and (c) fluorescence

emission spectra of TPE azide and TPE functionalized graphene. (Reprinted with permission from Ref. [30]. Copyright 2012, Royal Society of Chemistry.)

TPE azide is a member of the family of the aggregation-induced emission molecules. These molecules appeared to be emissive only in the solid state or when they are aggregated in clusters. For TPE azide this behavior is observed by recording its fluorescence emission spectra in a water/tetrahydrofuran (THF) solvent system. The fluorescence spectrum of TPE azide in THF has an emission band around 480 nm with maximum intensity. As the percentage of water was increased the number and the size of the aggregates decreased and the fluorescence emission band decreased until it disappeared. This behavior was not observed in the TPE functionalized graphene. The intensity of the fluorescence emission peak at 480 nm is significantly quenched by the covalent grafting on graphene because of the intramolecular electronic interaction between TPE and graphene.

Nitrene addition can be also used for the grafting of polymers onto graphene nanoplatelets [25]. These polymers should have azide groups in the polymer chain in abundance. Polyacetylene functionalized in its side chain with alkyne azide groups can be grafted covalently on a graphene surface through nitrene addition (Figure 2.13). The prepared polymer composite has enhanced dispersibility in common organic solvents as a result of the chemical affinity to the functionalized polyacetylene. The aziridine formation is indicated by the decreased

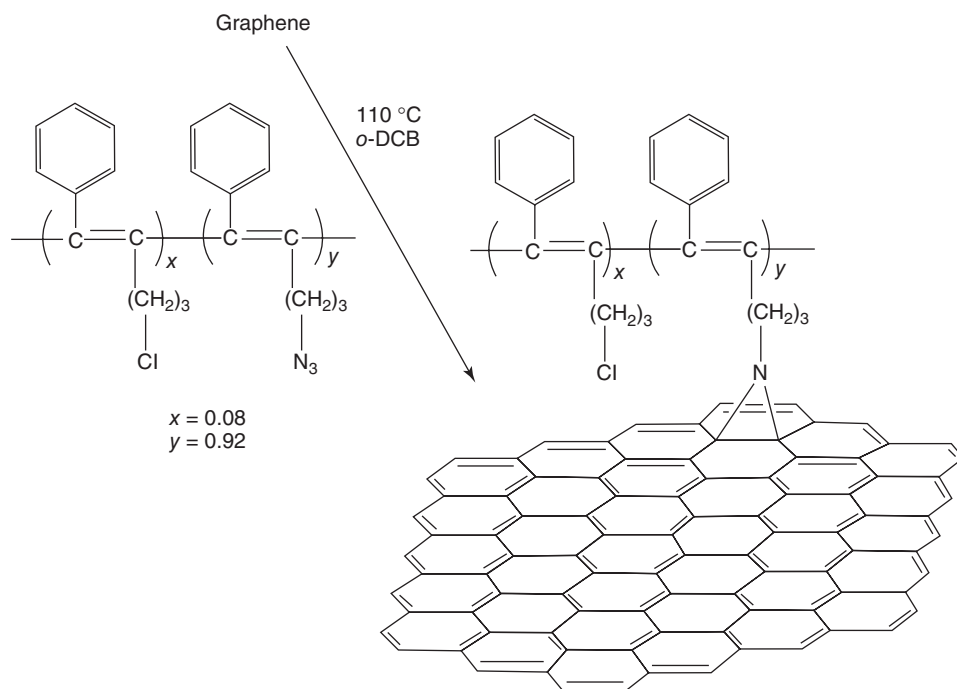


Figure 2.13 Formation of a polyacetylene/graphene composite through an aziridine ring linker [25].

band at 2097 cm^{-1} of azide in the final composite compared with the azide substituted polyacetylene [25]. The same reaction has also been used for the functionalization of graphene with phenylalanine. The reaction takes place between N-protected azidophenylalanine with exfoliated graphene sheets dispersed in *o*-dichlorobenzene [26].

2.2.5

Carbene Addition

Analogous to nitrenes, carbenes are electron deficient highly reactive organic intermediates that can attack sp^3 carbon atoms of C–H bonds replacing hydrogen or C=C bonds in a [1+2] cycloaddition reaction. As a consequence the interaction of graphene with carbenes leads to the functionalization of graphene through both possible reactions as graphene has plenty of C=C as well as C–H bonds at the edges or the defect sites. The reaction of carbene with graphene is not yet well exploited although there is enough experience by way of previews of functionalization of carbon nanotubes, diamond, and fullerenes with carbene derivatives [31–34]. Dichlorocarbene prepared from chloroform treated by sodium hydroxide is added on graphene nanoplatelets by [1+2] reaction forming three-membered rings.

A more sophisticated carbene functionalization of graphene has been presented by Ismaili *et al.* in their effort to immobilize gold nanoparticles on a graphene surface with organic linkers [35]. Carbene in this case is formed by the photochemical treatment of a 3-aryl-3-(trifluoromethyl)-diazirine derivative, which is equipped with a gold nanoparticle attached at the end of the molecule through a Au–S bond. Diazirines are three-membered heterocyclic rings where a sp^3 carbon atom is bonded with the two nitrogen atoms of an azo group. Carbenes are produced by the decomposition of diazirines and the removal of nitrogen atoms as N_2 , which can be done by heating or irradiating diazirine molecules. 3-Aryl-3-(trifluoromethyl)-diazirine derivatives are often used in carbene production because of the advantage of their not having possible intramolecular rearrangement pathways for the corresponding carbenes, that leads to by-products decreasing the yield of a carbene addition reaction. Here, gold nanoparticles covered by alkane thiol chains are also partly functionalized by 3-aryl-3-(trifluoromethyl)-diazirine molecules through a thiol-alkyloxy linker where thiol is binded on gold and oxygen on the aryl ring as presented in Figure 2.14A.

The final immobilization of gold nanoparticles on the graphene surface is revealed by the comparison of characteristic TEM images of graphene before and after the carbene addition (see Figure 2.14B). In a blank control experiment graphene was also treated with the gold functionalized diazirine by the same procedure without the irradiation step that is necessary for carbene production. As depicted in the corresponding TEM images gold nanoparticles are rarely immobilized on the graphene surface; in this case in contradiction to the samples of the normally irradiated graphenes, these were fully covered by gold nanoparticles. The control experiment supports the hypothesis that the carbene

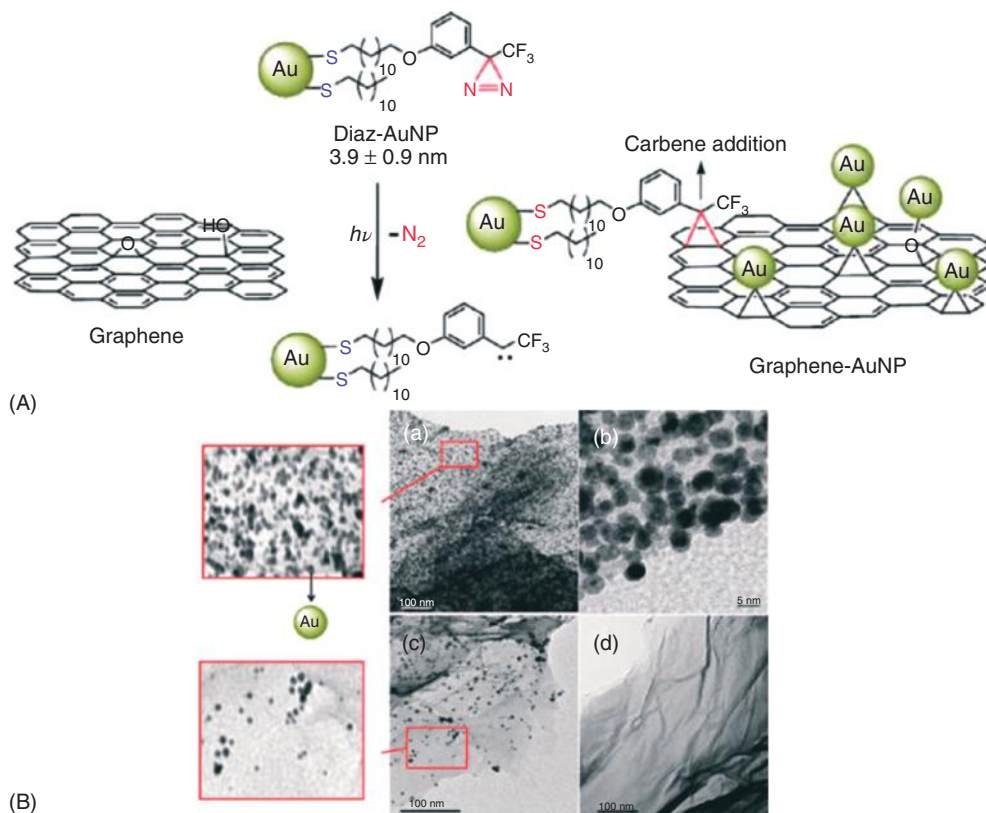


Figure 2.14 (A) Addition of a 3-aryl-3-(trifluoromethyl)-diazirine derivative on graphene surface through a [1+2] cycloaddition as a link for gold nanoparticles immobilization. (B) Characteristic TEM images of (a) and (b) with different resolution, graphene with gold nanoparticles that are

bound covalently through carbene addition after irradiation, (c) graphene with rarely dispersed gold nanoparticles that are deposited without the carbene reaction, and (d) the starting graphene material. (Reprinted with permission from Ref. [35], Copyright 2011, American Chemical Society.)

addition occurs mainly on C=C bond as well as on C–H or oxygen groups of graphene.

2.2.6

Aryne Addition

Arynes are highly reactive organic intermediates that are produced from phenyl derivatives by the removal of two ortho substituents. Because of their reactive character, arynes interact easily with C=C bonds or dienes in a [2+2] or a DA [4+2] cycloaddition, respectively. In the unique paradigm that graphene has been functionalized through aryne cycloaddition, Ma *et al.* used 2-(trimethylsilyl) aryl

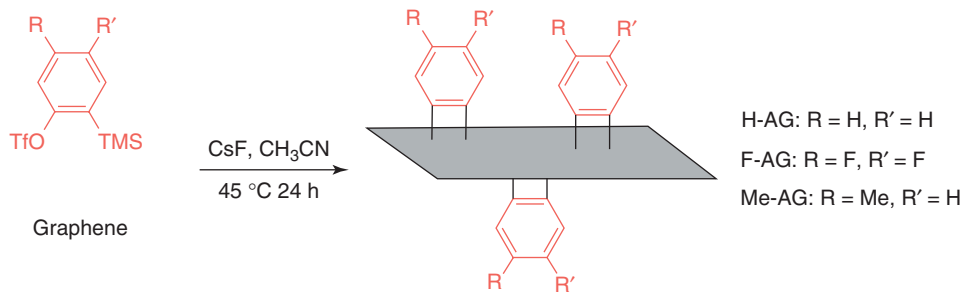


Figure 2.15 Aryne addition on graphene surface. (Reprinted with permission from Ref. [36], Copyright 2010, Royal Society of Chemistry.)

triate as starting material for the production of the aryne intermediate (see Figure 2.15). After the connection of the modified arene on graphene by a four membered ring, the dispersibility of the modified graphene increased remarkably in solvents such as DMF, *o*-DCB (1,2-dichlorobenzene), ethanol, chloroform, and water. Arene can be substituted by several different functional groups [36].

2.2.7

Bingel Type Cycloaddition

An interesting Bingel type functionalization of graphene with the assistance of microwave power has been described by Tagmatarchis *et al.* [37] Bingel reaction is a characteristic [2+1] cycloaddition that has been successfully applied before in the previously invented carbon nanostructures; in fullerenes, carbon nanotubes, and carbon nanohorns [38–40]. Usually diethyl dibromomalonate is used with diazabicyclo[5.4.0]undec-7-ene (DBU) as catalyst in the presence of the carbon nanostructure in suspension. The cycloaddition is performed at room temperature by simple stirring for 2 h. The use of microwave irradiation here decreases the reaction time remarkably and in general, reactions under microwaves have less by-products. Initially graphene nanoplatelets dispersed in benzyl amine were used as starting material for a Bingel type cycloaddition with diethyl malonate and tetrathiafulvalene (TTF) monosubstituted diethyl malonate (see Figure 2.16). The mixture of the two main reactants, DBU and carbon tetrabromide (CBr₄) was microwave irradiated for several minutes in one or two steps. The finally isolated product diethyl malonated graphene is dispersible in several organic solvents such as dichloromethane, toluene, DMF. Several conditions related to the ratio of the reactants, the power of the microwave as well as the duration, the concentration of the reactants, and their combination are described in this work. The efficient graphene functionalization was indicated by the FTIR spectra of the products with the appearance of peaks at 2920 and 2847 cm⁻¹ assigned to C–H stretching vibrations and at 1705 and 1727 cm⁻¹ assigned to the vibration of carbonyl groups both belonging to the malonate units. In the Raman spectra

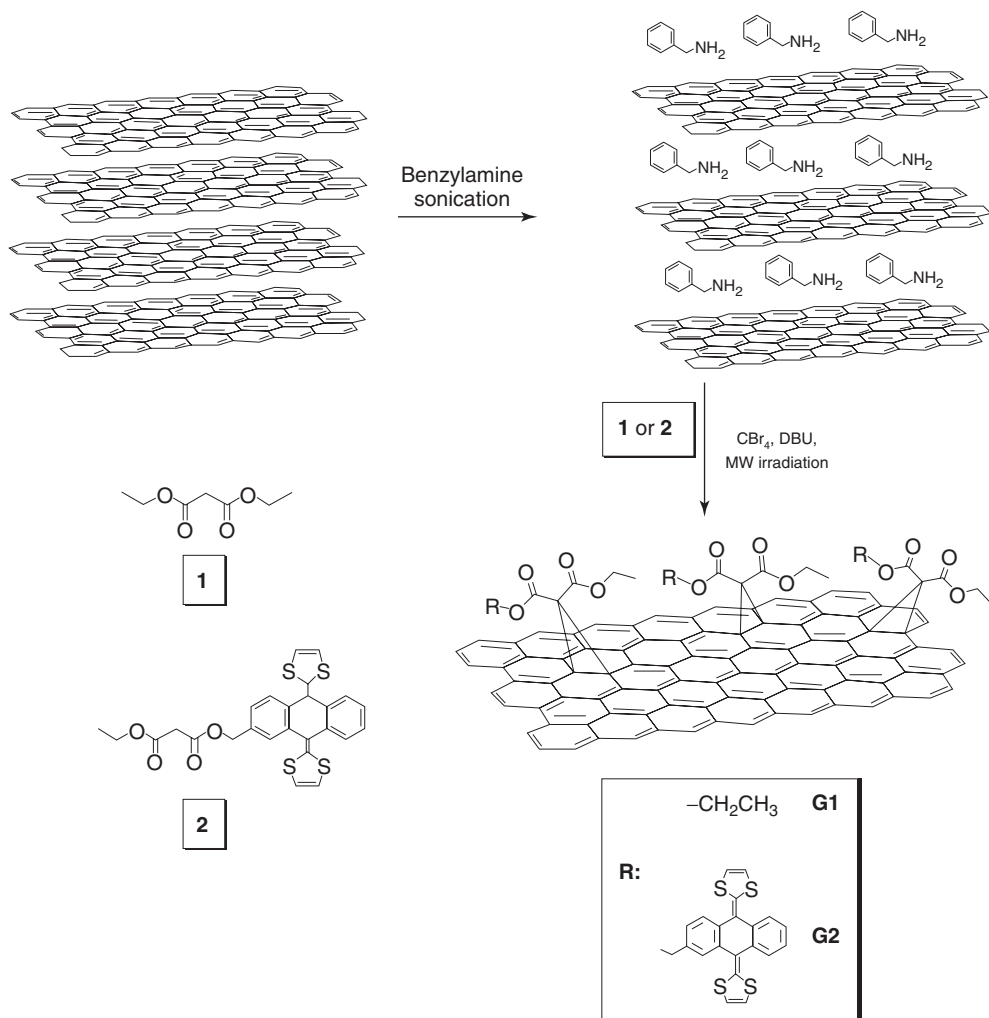


Figure 2.16 Bingel cyclopropanation on graphene nanoplatelets dispersed in benzyl amine using microwave irradiation. (Reprinted with permission from Ref. [37], Copyright 2010, American Chemical Society.)

the D band, which is almost not visible in the initial graphene became higher than the G band after the functionalization ($I_D/I_G > 1$) indicating a high degree of functionalization. From the TGA and the estimation of graphene/malonate mass ratio, the number of carbon atoms that correspond to one malonate unit was found to be 44 for 1-diethyl malonate and 128 for the TTF substituted malonate. Finally, the reaction is reversible by heating the malonate functionalized graphene in an inert atmosphere. The reversed graphene recovers most of its aromatic character and electronic properties.

2.3

Addition of Free Radicals

Free radicals are very reactive organic intermediates that attack sp^2 carbon atoms forming covalent bonds. Usually they are produced from organic molecules by the selective removal of an easily leaving group dissociating an σ covalent bond.

2.3.1

Diazonium Salt Reaction

A characteristic procedure for the preparation of free radical is by heating the diazonium salt of an organic molecule whereas the radical is produced by the removal of an N_2 molecule (see Figure 2.17). The addition of an organic radical to the graphene surface changes the hybridization of the reacted carbon atoms from sp^2 to sp^3 . This change results in the disruption of the aromatic system and consequently influences the electronic properties of graphene remarkably. As presented in a characteristic experiment by Tour *et al.* [41] the conductivity of graphene is decreased as a function of the duration of the radical addition reaction and can be easily controlled. On the other hand, functionalization of graphene introduces a band gap which can be predetermined, offering to graphene interesting semiconducting properties [42].

Aryl diazonium salts substituted in *para* position by several functional groups such as chlorine, bromo, iodine, nitro, methoxy, carboxy, cyano, have been also added by this method on graphene surfaces showing the versatile character of

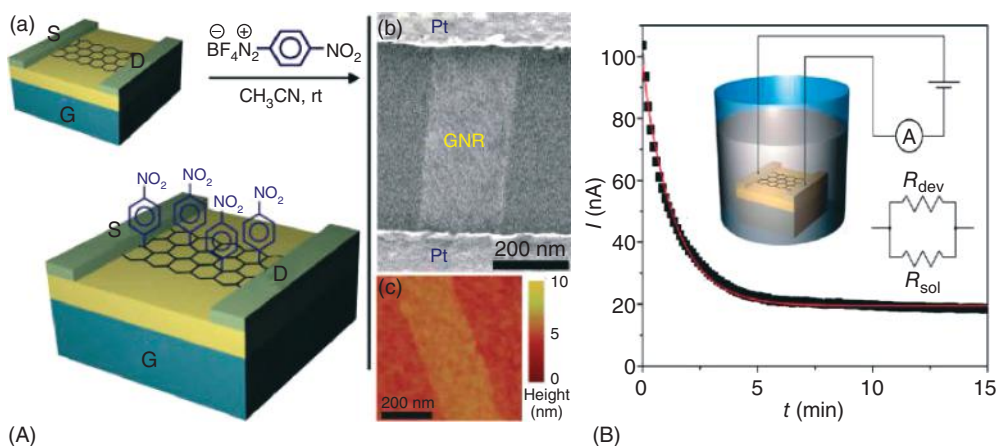


Figure 2.17 (A) (a) Addition of nitro phenyl radicals on graphene nanoribbons placed in a device to measure the conductivity of the functionalized graphene nanoribbons. (b) TEM and (c) AFM images of a graphene nanoribbon. (B) Time dependence

of I during the functionalization of graphene nanoribbons with nitrophenyl radicals. The inset represents the device of the experiment. (Reprinted with permission from Ref. [41], Copyright 2010, American Chemical Society.)

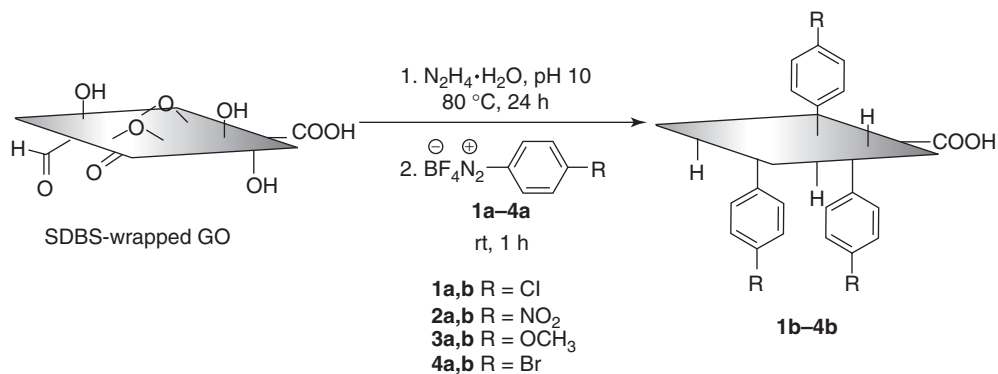


Figure 2.18 Addition of *para* substituted aryl groups on chemically converted graphene through diazonium salt reaction. (Reprinted with permission from Ref. [44], Copyright 2008, American Chemical Society.)

this method (see Figure 2.18). The initial carbon nanostructured materials here are chemically or thermally reduced graphenes, which are rendered in dispersion with the assistance of a surfactant [43]. The functionalized graphene products were dispersible in polar aprotic solvents [44]. The diazonium salt reactions have been applied in several type of graphenes such epitaxial graphene [45] and graphene from micromechanical cleavage [46].

The addition of organic free radical through the diazonium salt decomposition has the advantage that the organic addend can bear functional groups such as carboxylate, which is not easily done with other reactions. In a characteristic example carboxy phenyl groups are attached covalently on graphene and then post functionalized through an esterification reaction with perfluoro-1-octanol (see Figure 2.19). The functionalized graphene before esterification is dispersible in water whereas after the esterification, the hydrophobic perfluoroalkyl chains were dispersible in *o*-dichlorobenzene. Cyclic voltammetry measurements of the perfluoroalkyl derivatized graphene (F-graphene) showed a band gap suitable for an electron accepting function in organic photovoltaic systems. Actually the power conversion efficiency of an organic photovoltaic cell with poly(3-hexylthiophene) (P3HT) in combination with the F-graphene exceed 1% in the best P3HT/F-Gr ratio [47].

Chlorophenyl groups has also been added on graphene nanoplatelets with the diazonium salt reaction to investigate the antimicrobial activity of the prepared graphene product. The advantage of the chlorophenyl functionalized graphene is the broad biocide activity of chlorine [48]. The diazonium salt reaction has been used by Tour *et al.* in an effort to selectively functionalize graphene nanoplatelets in the edges leaving the graphitic surface unaffected. After the complete exfoliation of the graphene monolayers it is not possible to control the addition of the free radicals with regard to the reacted graphene area as the edges and the rest of the surface are both exposed almost equally to the reactive radicals. However this does not happen with the expanded graphite where the main graphene surface

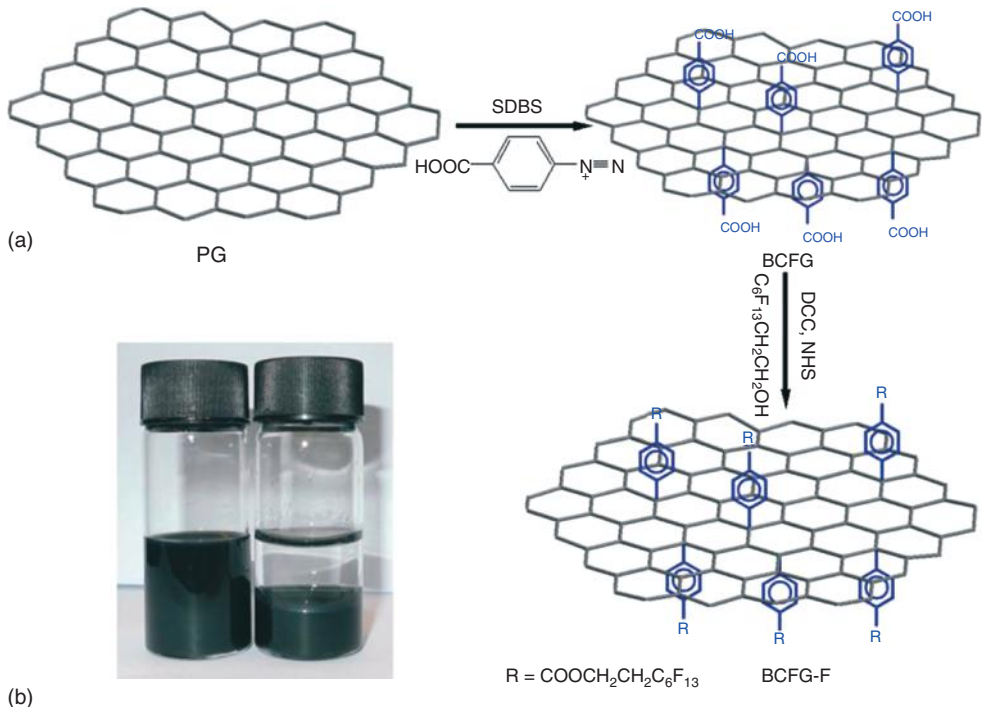


Figure 2.19 (a) Addition of carboxy phenyl groups on graphene surface through diazonium salt reaction and the post functionalization by esterification of carboxylate with a perfluoro-1-octanol. (b) The left bottle contains the functionalized graphene before

esterification dispersible in water, while the right bottle contains the product of the esterification in a biphasic system of water and *o*-dichlorobenzene. (Reprinted with permission from Ref. [47], Copyright 2012, Royal Society of Chemistry.)

is protected by the small distance between the graphene sheets from the bulky 4-bromophenyl radicals while the edges are still exposed. As a consequence the reaction of 4-bromophenyl diazonium salt with thermally expanded graphite lead to the functionalization of the graphene nanosheets by bromophenyl groups selectively at the edges. This observation was the result of elemental mapping of Br using energy filtered transmission electron spectroscopy. The edge-functionalized graphene nanoplatelets are easily dispersed in DMF after the reaction [49].

Apart from the band gap opening by nitro phenyl and antimicrobial activity of chlorophenyl functionalized graphene, hydroxyethyl phenyl groups have been added on graphene surface to act as linkers for the grafting of polystyrenic chains on the graphene surface. The polymerization of styrene monomer via atom transfer radical method (ATRP, atom transfer radical polymerization) in the presence of hydroxyethyl functionalized graphene nanoplatelets leads to the formation of a polystyrene/graphene nanocomposite where polystyrene chains are covalently attached on graphene nanoplatelets (see Figure 2.20) [50–52]. The density of the

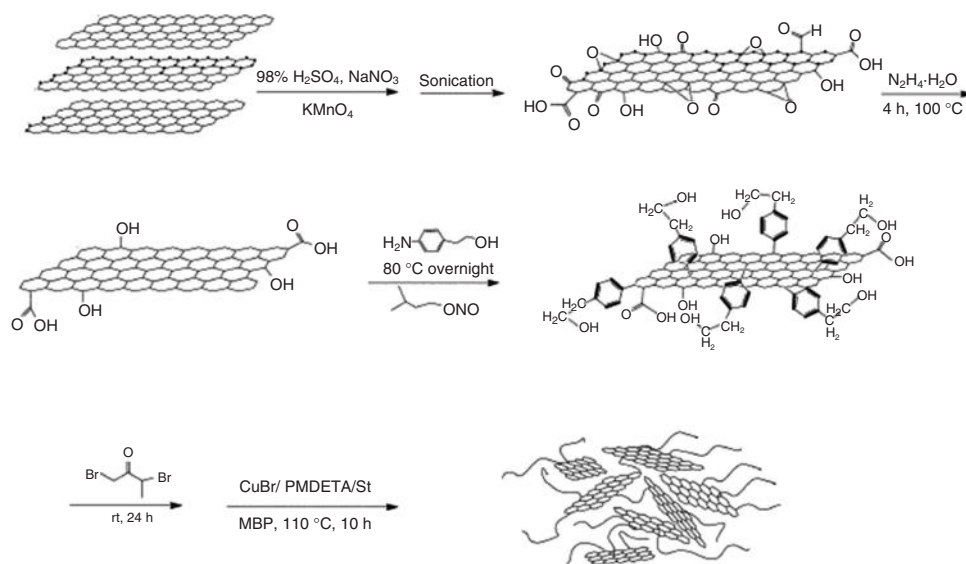


Figure 2.20 Polymerization of styrene in the presence of hydroxyethyl functionalized graphene through diazonium salt reaction. (Reprinted with permission from Ref. [50], Copyright 2009, Royal Society of Chemistry.)

grafted polymer chains as well as their length can be controlled by adjusting the concentration of the diazonium compound and styrenic monomer [51].

Aryl diazonium addition reaction has been used by Strano *et al.* in an effort to study the reactivity of pristine graphene monolayer in comparison with graphitic nanosheets with more than one layer. They also tried to find differences in the reactivity between the areas of graphene monolayers near the edges and in the core surface. The results of their study showed a remarkably higher reactivity as regards graphene monolayer compared to that of a multilayer or even a bilayer one. In addition the reactivity at the edges was at least two times higher than that of the core of the graphene monolayer [46]. In another important application thiol substituted aryl diazonium salt has been used as a π -conjugated molecular linker that can connect gold nanoparticles with *r*GO nanoplatelets in nonvolatile memory device applications. After the diazonium salt reaction 4-mercapto-phenyl rings are directly bonded on the *r*GO surface and simultaneously trap gold nanoparticles with the free thiol group (see Figure 2.21) [53].

2.3.2

Other Radical Additions

Organic free radicals are also produced by the photocatalytic dissociation of benzoylperoxide derivatives and can react with sp^2 carbon atoms of graphene. In a characteristic work, graphene monolayers mechanically isolated from Kish graphite were deposited on a silicon substrate and immersed in a benzoyl peroxide

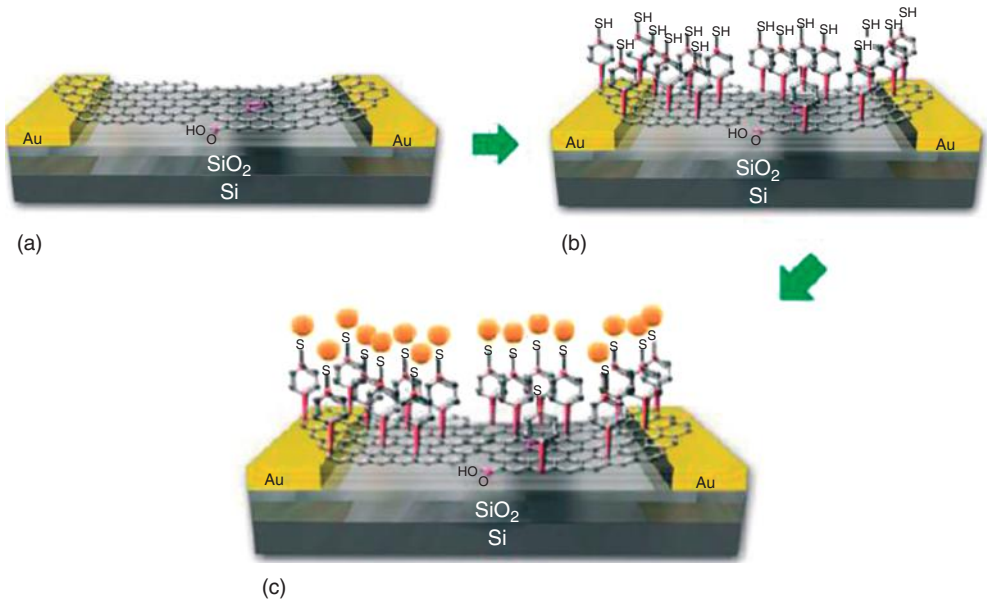


Figure 2.21 Schematic representation of the preparation of a nonvolatile memory device (a) deposition of graphene monolayer on a silicon dioxide substrate between two electrodes, (b) modification of graphene with

mercapto phenyl groups, and (c) deposition of gold nanoparticles. (Reprinted with permission from Ref. [53], Copyright 2011, American Chemical Society.)

solution in toluene. Benzoyl peroxide was dissociated photochemically producing the reactive phenyl radicals, by focusing with an Ar-ion laser beam in specific places of the graphene sheet. The addition of phenyl radicals on graphene was directly observed by the appearance of a D band in the Raman spectra of graphene after the reaction, which is because of the transformation of the reacting carbon atoms of the graphene surface from sp^2 to sp^3 hybridization (see Figure 2.22). According to the author, the expected decrease in the conductivity of graphene after the functionalization is accompanied by an increase in the hole doping, which is attributed to the contribution of the unreacted benzoyl peroxide, which is presented as physisorbed material on the graphene surface [54].

The involvement of free radicals addition is also present in polymer grafting on graphene methods. Several known free radical polymerization procedures as well as atom transfer radical polymerization (ATR) and reversible addition-fragmentation chain transfer (RAFT) have been used to prepare polymer composites with chains grafted on the graphene surface [50–52, 55]. Polystyrene–polyacrylamide copolymer was grafted on the graphene surface by an *in situ* free radical polymerization of the monomers in the presence of dispersed graphene nanoplatelets (see Figure 2.23). The graphene/copolymer composite has an amphiphilic character controllable by tuning the ratio of the monomers. Thus in general it is dispersible

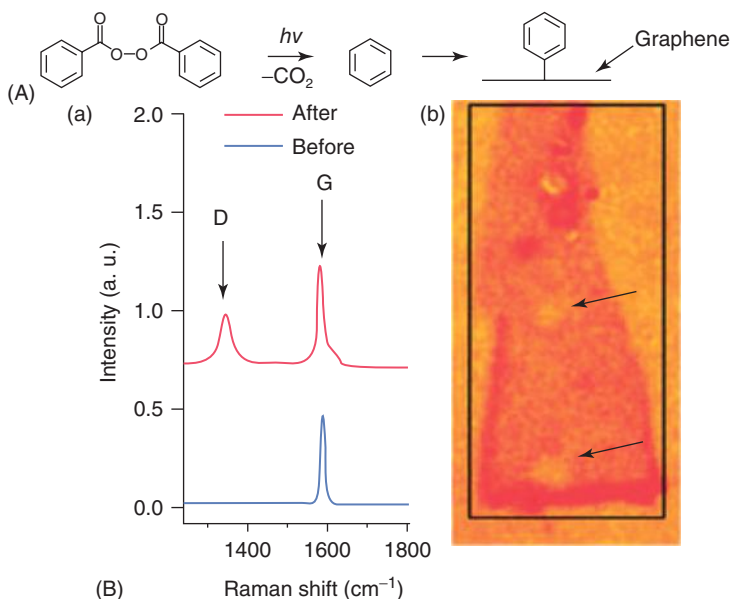


Figure 2.22 (A) Photochemical production of phenyl radicals and their addition on graphene. (B) (a) Raman spectra from graphene before and after phenyl addition and (b) optical image of graphene after the photochemical reaction with the arrows indicating holes created by prolonged laser exposure. (Reprinted with permission from Ref. [54], Copyright 2009, American Chemical Society.)

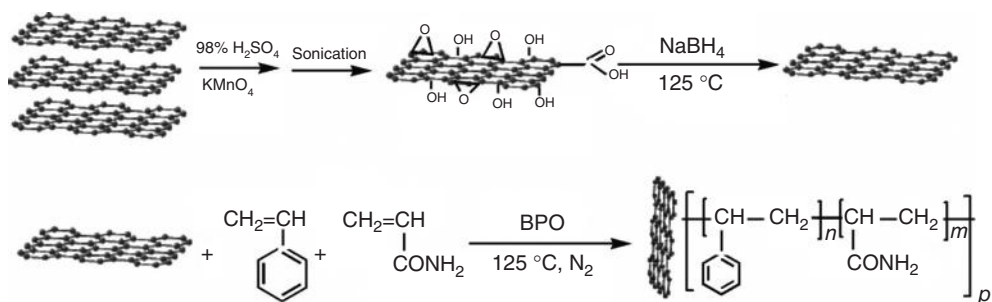


Figure 2.23 Preparation of graphene nanosheets and *in situ* free radical polymerization of styrene and acrylamide in the presence of graphene. (Reprinted with permission from Ref. [55], Copyright 2010, Wiley-VCH Verlag GmbH & Co KGaA, Weinheim.)

in water because of the hydrophilic character of the acrylamide monomer and in xylene because of the organophilic character of the styrene monomer [55].

An alternative approach for the preparation of polystyrene/graphene polymer composite includes the sonochemical polymerization of the styrene monomer in the presence of graphite. The ultrasonication of a suspension of graphite in styrene for 2 h under Argon with a Titanium horn resulted in the exfoliation

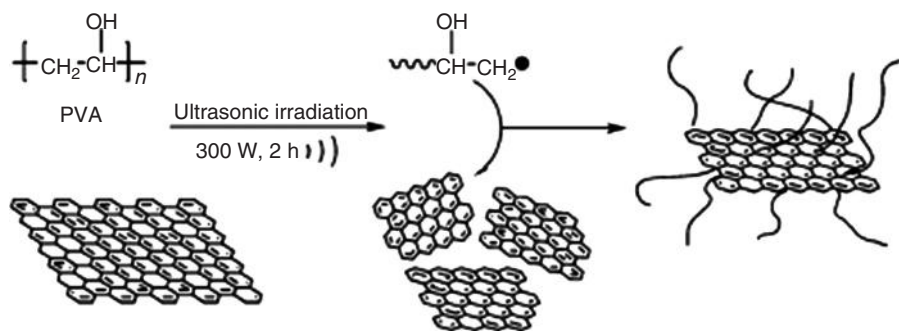


Figure 2.24 Ultrasonic preparation of a polymer composite by grafting PVA macroradicals on graphene oxide nanoplatelets. (Reprinted with permission from Ref. [57], Copyright 2012, Royal Society of Chemistry.)

of graphene flakes in the styrene and the polymerization of styrene entrapping the dispersed graphene nanoplatelets. The existence in the Raman spectra of the product, of a D band 4 cm^{-1} lower and a 2D band 8 cm^{-1} than that of graphite indicates that polymer composite contains single or few-layer graphenes [56].

The ultrasonication has been also used for the construction of polymer/GO nanocomposite starting from already prepared polymer in solution. The composite is formed by ultrasonication of a suspension of GO powder in a polyvinyl alcohol (PVA) solution in water when PVA microradicals that are formed by the ultrasonication procedure are grafted on GO nanoplatelets (see Figure 2.24). The mechanical properties of the PVA/GO composite after the grafting procedure appeared fairly increased compared to a PVA/GO composite that is prepared by the simple mixing of GO with the polymer. Actually the tensile strength was increased by 12.6% whereas Young's modulus was at 15.6% with 0.3 wt% GO [57].

Microwave power can be also used for the preparation of the polymer/graphene composite. The reduction of GO by sodium hydroxide applying a short time microwave irradiation leads to a dark brown colored partly reduced GO suspension. The last is functionalized by polyacrylamide chains which are formed via a free radical polymerization and grafted on the graphene surface by a second short time microwave treatment of a mixture of the acrylamide monomer, a radical initiator, and suspended *r*GO in water [58]. Finally the prepared polymer composite is treated further in a post-reduction step by a third microwave irradiation in hydrazine hydrate to restore to a greater extent the aromatic character of the graphitic layer. The UV-vis spectra of GO, *r*GO, and the finally post reduced product showed that both reduction steps were effective as a redshift of the main absorption band from 230 to 250 nm and then to 270 nm, which is observed in the spectra of the three nanomaterials, is attributed to the partial restoration of the aromatic character of graphene (see Figure 2.25).

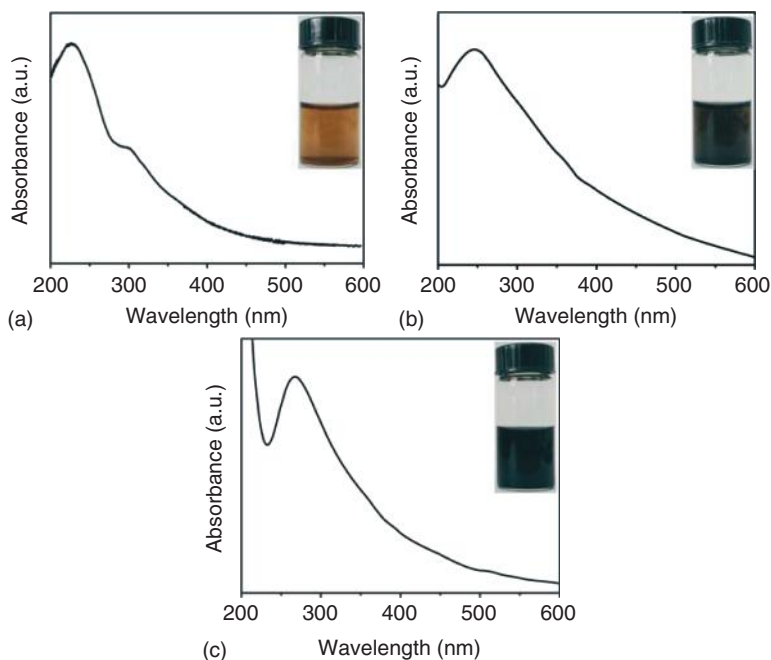


Figure 2.25 UV-vis spectra of (a) graphene oxide, (b) partly chemically reduced graphene, and (c) post reduced poly(acrylamide) (PAM)/graphene composite. Insets: Digital photos from the three nanostructures in suspension. (Reprinted with permission from Ref. [58], Copyright 2011, Royal Society of Chemistry.)

2.4 Nucleophilic Addition

The covalent grafting of a poly-9,9'-diheylfluorene carbazole on the graphene surface has been achieved by the nucleophilic addition of nitrogen anions of carbazole species. The nitrogen anions are produced by the reductive action of sodium hydride (see Figure 2.26) [59]. In a similar approach poly(*N*-vinylcarbazole) has been grafted on the graphene surface by the nucleophilic addition of a carbanion intermediate of the polymer to the graphene surface [60].

2.5 Electrophilic Addition on Graphene

Graphene nanoplatelets can undergo an electrophilic substitution by halogenated organic molecules with the assistance of *n*-butyl lithium (*n*-BuLi). By the addition of an excess of *n*-BuLi to a suspension of rGO, the latter is functionalized by Li atoms by a deprotonation and/or a carbometalation process (see Figure 2.27).

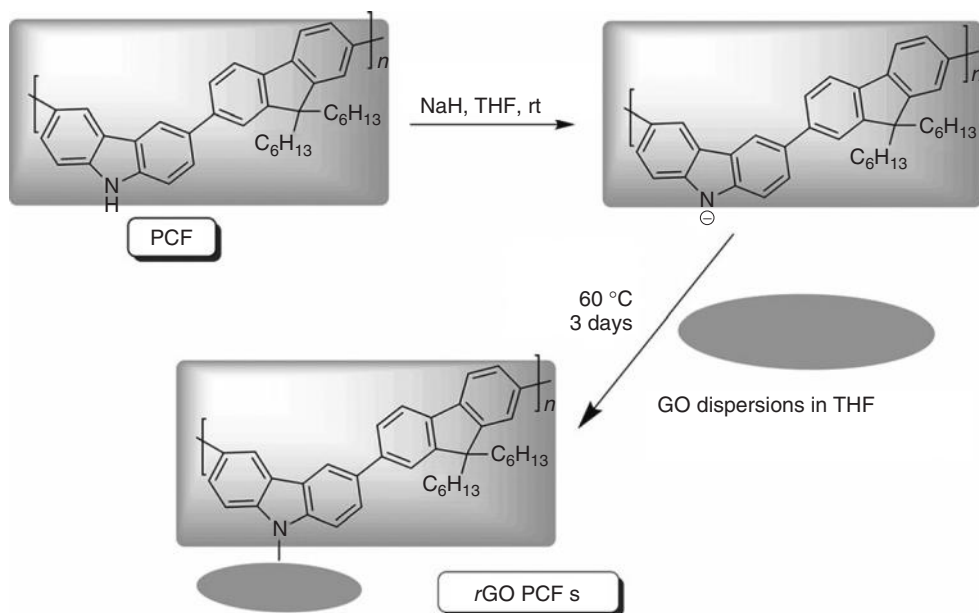


Figure 2.26 Addition of poly-9,9'-diheptylfluorene carbazole on graphene through a nucleophilic addition of a nitrogen anion intermediate. (Reprinted with permission from Ref. [59], Copyright 2012, Wiley-VCH Verlag GmbH & Co KGaA, Weinheim.)

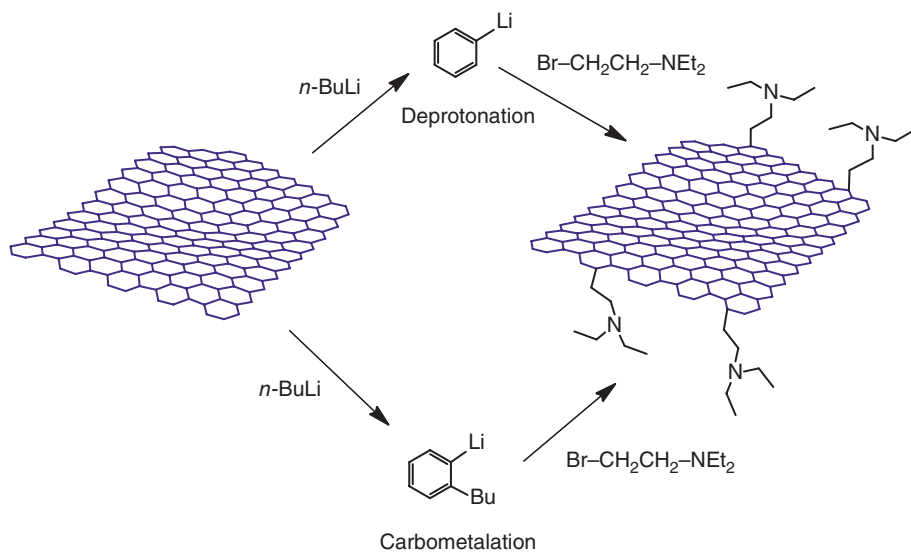


Figure 2.27 Covalent functionalization of graphene by aminoethyl functional groups by electrophilic substitution. (Reprinted with permission from Ref. [61], Copyright 2012, Royal Society of Chemistry.)

The presence of Li atoms on the surface of graphene favors the electrophilic attack of diethylamino-ethyl bromide producing amino-functionalized rGO. The amino-functionalized rGO nanoplatelets can be used as solid basic catalyst in heterogeneous catalytic systems [61].

2.6

Organometallic Chemistry of Graphene

Haddon *et al.* [62] has been used as chromium complexes in an effort to investigate and explore the organometallic chemistry of graphene, graphite, and carbon nanotubes. A zero-valent transition metal such as chromium (Cr) in the form of $\text{Cr}(\text{CO})_6$ or $(\eta^6\text{-benzene})\text{Cr}(\text{CO})_3$ reacts with an hexagonal aromatic ring of the graphene surface forming a covalent hexahapto (η^6)-arene-metal complex [62]. The covalent interaction between graphene and Cr metal is formed by an efficient overlap of empty d_π orbital of chromium with the occupied π -orbitals of the hexagonal ring of graphene. Chromium can form a complex with one graphene monolayer that substitutes the half carbon monoxide (CO) ligands ($\eta^6\text{-graphene-Cr}(\text{CO})_3$) or with two, which substitute for all CO ligands ($\eta^6\text{-graphene}_2\text{Cr}$). Using a selected competitive ligand, Cr complex can be removed from the graphene surface, which then appears to restore the original pristine character.

In contrast to the rest of the covalent functionalizations of graphene that are followed by change of the hybridization of the reacted carbon atoms from sp^2 to sp^3 , the hexahapto functionalization brings no serious changes in the aromatic character of the hexagonal ring or the sp^2 character of the involved carbon atoms. Regarding this observation, Haddon *et al.* [63] prepared hexahapto Cr complex with graphene nanoplatelets deposited on a SiO_2 substrate between two gold electrodes, in order to study the electronic properties of a single graphene monolayer functionalized covalently by metal transition atoms. The complexation was performed by three different combinations of Cr precursors, solvents, and reaction temperature as presented in Figure 2.28, without noticeable differences in the quality of the product or the yield of the complexation.

In general the device with the deposited SiO_2 on the graphene monolayer is immersed in a solution of a zero-valent Cr complex and heated for several hours. Another important observation is that single monolayer graphene is more reactive than few-layer graphene nanosheet. As regards the electronic properties, the Cr modified graphene showed a room-temperature field effect mobility in a range of $200\text{--}2000\text{ cm}^2\text{ (V s)}^{-1}$ and an on/off ratio of 5–13. The Cr groups are easily removed by exposing the functionalized graphene in an electron rich ligand such as anisole. In the Raman spectrum of functionalized graphene a very low D band appeared while the I_D/I_G is increased slightly from 0 to 0.13. After the decomplexation the I_D/I_G ratio decreased to 0.03 as D band almost disappeared like the pristine graphene monolayer (see Figure 2.29).

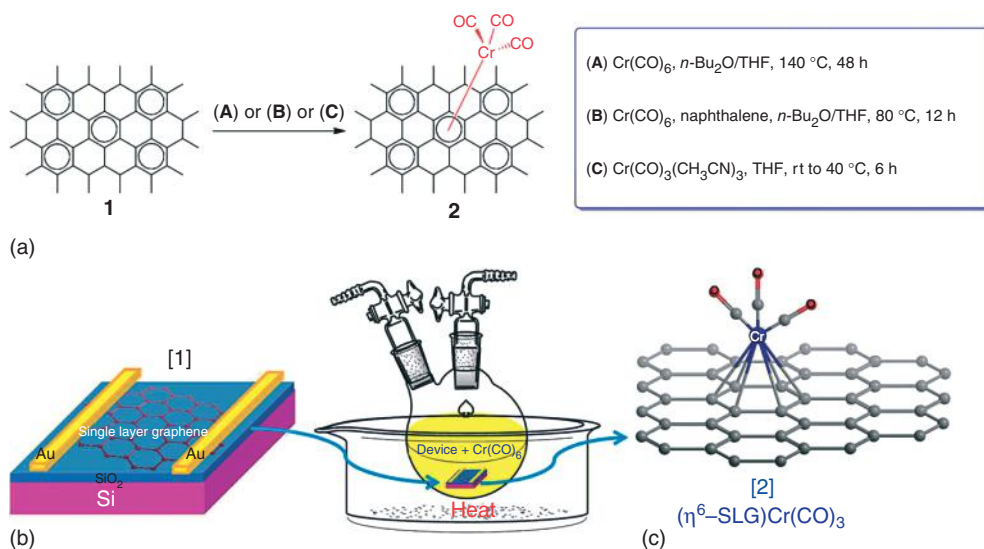


Figure 2.28 Schematic representation of Cr hexahapto covalent functionalization of single graphene layer deposited on SiO₂, with three different procedures. (Reprinted with permission from Ref. [63], Copyright 2013, Wiley-VCH Verlag GmbH & Co KGaA, Weinheim.)

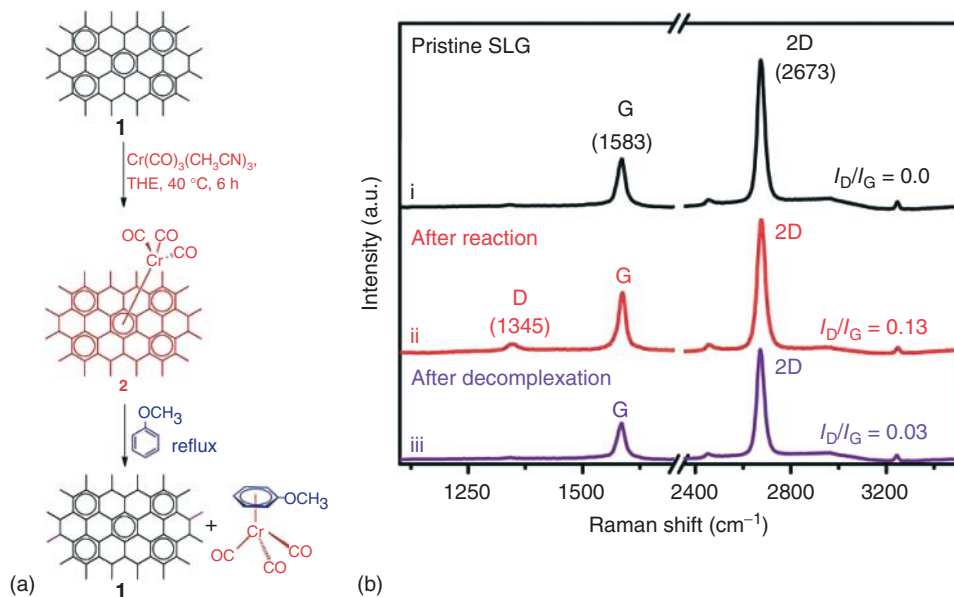


Figure 2.29 (a) A complexation–decomplexation reaction procedure of graphene and (b) Raman spectra of pristine single layer graphene (i), after complexation (ii), and

after de functionalization (iii). (Reprinted with permission from Ref. [63], Copyright 2013, Wiley-VCH Verlag GmbH & Co KGaA, Weinheim.)

2.7 Post Functionalization Reactions

The graphene nanoplatelets functionalized with organic species obtain among other things two important characteristics: (i) they are usually highly dispersible in a plethora of organic solvents depending on the nature of the added group and

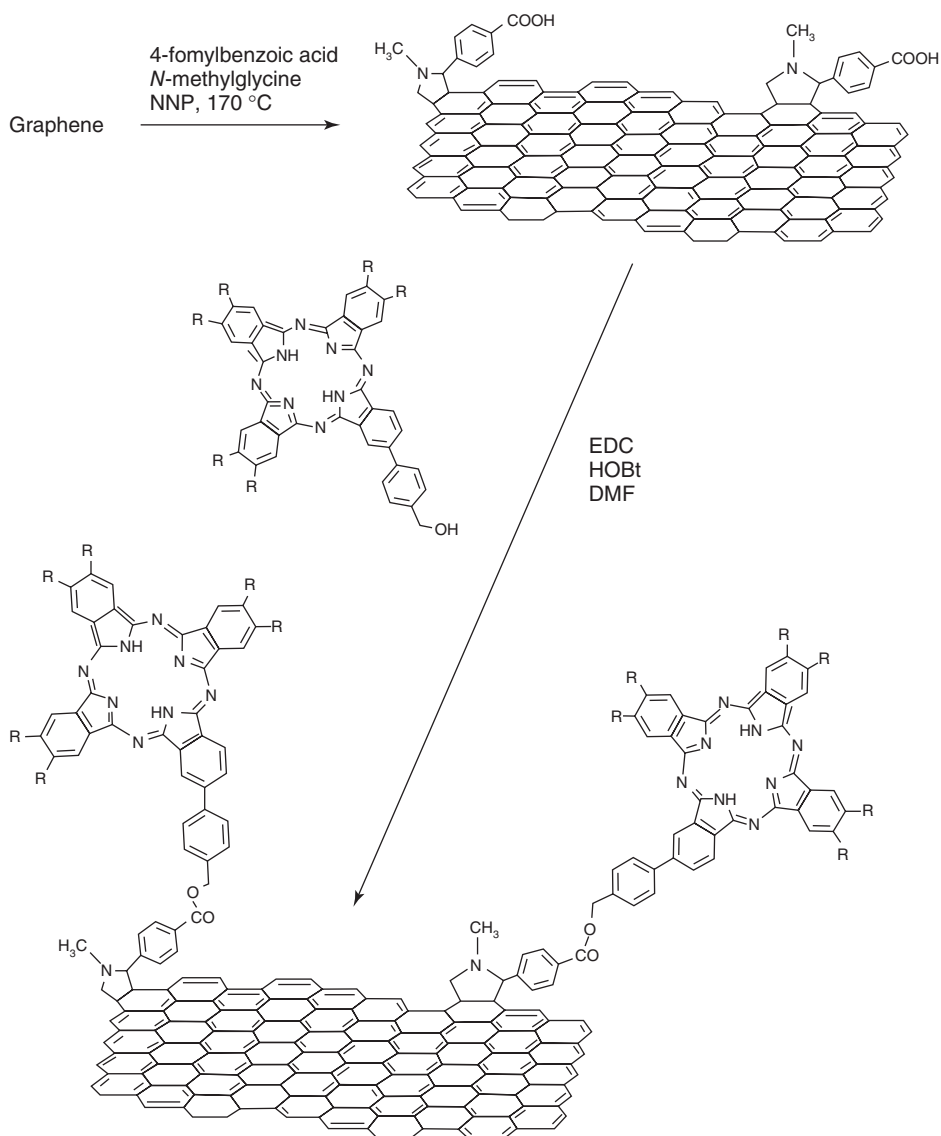


Figure 2.30 Post functionalization of pyrrolidine modified graphene through esterification [64].

(ii) these organic species that are added on graphene can bear functional groups that could be used for a post functionalization of graphene. In other words the functionalization of graphene makes them more organic, resembling a core-shell structure with graphene as a core and the organics as a shell. A characteristic example of a post functionalization reaction involves the covalent attachment of a phthalocyanine molecule on a pyrrolidine modified graphene with the assistance of a carboxyphenyl group that is placed on the pyrrolidine ring. First the graphene monolayer is functionalized by pyrrolidine rings by the reaction between *N*-methyl glycine and 4-formylbenzoic acid. Then a phthalocyanine molecule which bears a benzylic alcohol as active group is covalently bonded through esterification with the carboxyl group of pyrrolidine ring (see Figure 2.30) [64].

The graphene nanoplatelets functionalized with aryl by the diazonium salt reaction are also candidates for post functionalization reactions since the aryl can be substituted by several organic functional groups such as halides, carboxy, or hydroxylates. As an example a porphyrin boronic ester is covalently bonded on *para* iodo phenyl functionalized graphene by a Suzuki coupling reaction (see Figure 2.31) [65].

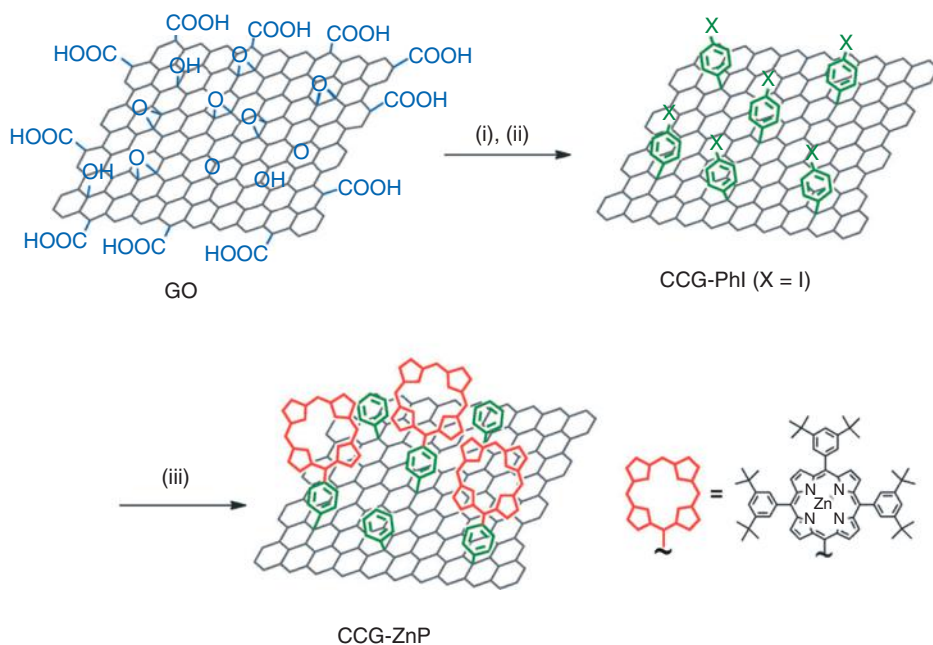


Figure 2.31 Post functionalization of chemically reduced graphene. (i) Partial reduction of graphene oxide with hydrazine, (ii) diazonium salt reaction with 4-iodobenzenediazonium tetrafluoroborate,

and (iii) Suzuki coupling between iodophenyl modified graphene and porphyrin boronic ester. (Reprinted with permission from Ref. [65], Copyright 2012, Wiley-VCH Verlag GmbH & Co KGaA, Weinheim.)

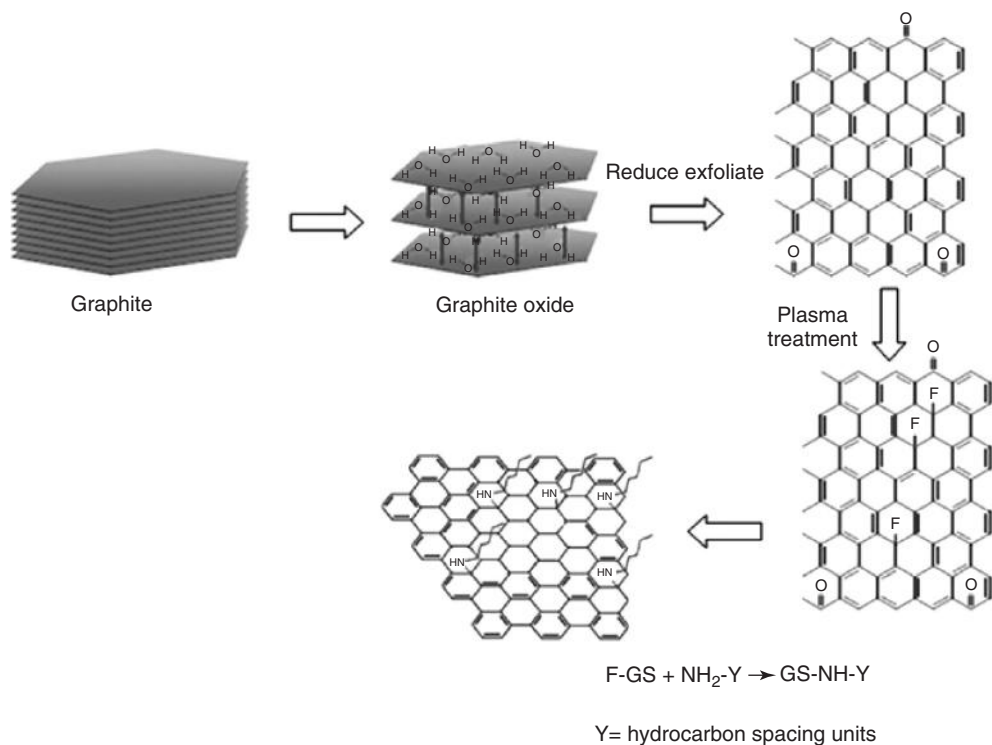


Figure 2.32 Fluorination of graphene by plasma treatment and post functionalization by nucleophilic substitution of butyl amine. (Reprinted with permission from Ref. [67], Copyright 2010, Royal Society of Chemistry.)

Post functionalization could also be characterized by the nucleophilic substitution of fluorine by alkyl amines or other functional groups. The fluorination of graphene nanoplatelets is performed by the plasma assisted decomposition of CF_4 . The fluorinated graphene sheets are then dispersed in the liquid *n*-butyl amine and post functionalized with the help of ultrasonication [66, 67] (Figure 2.32).

Diazonium salt reaction has been also used for the addition of *para* alkyne substituted phenyl species, which then act as dipolarophiles in a 1,3-dipolar cycloaddition of an azide functionalized polyfluorene. Briefly, *rGO* is functionalized by *para* alkyne substituted phenyl group. Then an alkyl azide substituted polyfluorene is grafted by a 1,3-dipolar cycloaddition between the azide and alkyne group forming a five-membered triazole ring. Actually the triazole ring is the link that connects the polyfluorene chains and the graphene nanoplatelets (see Figure 2.33) [68].

Para alkyne substituted aryl graphene – prepared by the diazonium salt reaction – has been also used for the 1,3-dipolar cycloaddition of azido phenyl substituted zinc-porphyrin and ruthenium-phenanthroline photoactive molecules. The procedure starts with the addition of the trimethylsilyl protected ethynyl-aryl diazonium salt on the graphene surface. In the post functionalization reaction

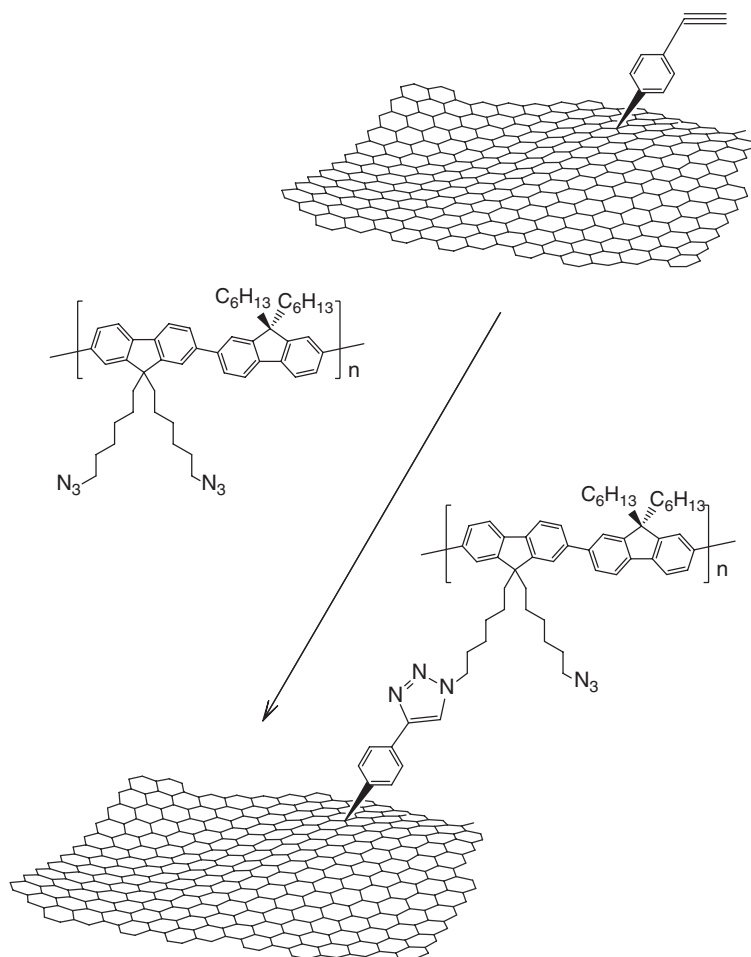
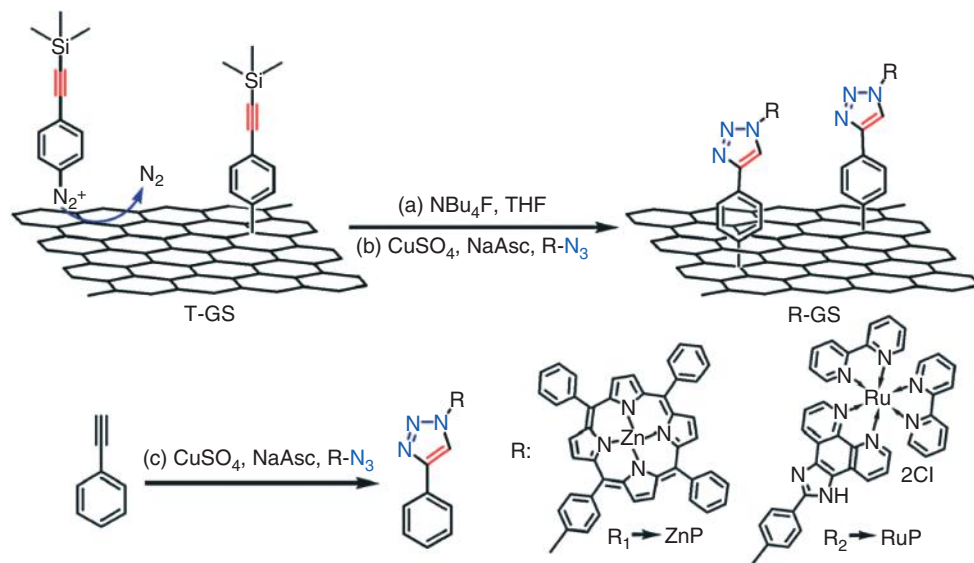


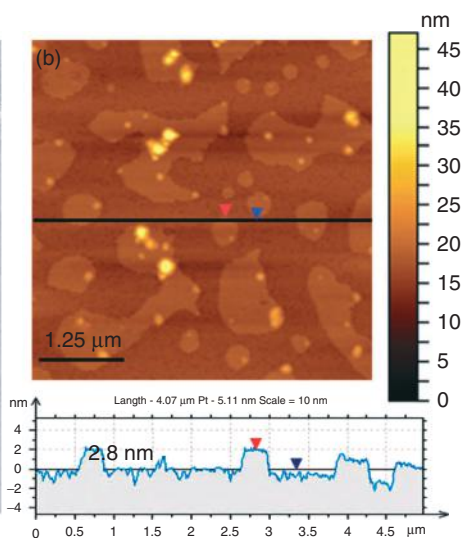
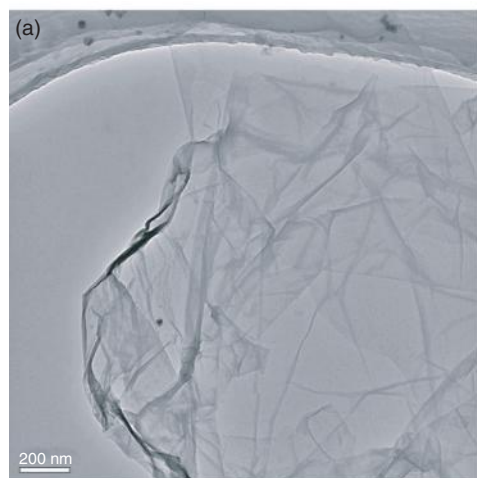
Figure 2.33 1,3-Dipolar cycloaddition of poly[(9,9-dihexylfluorene)-co-alt-(9,9-bis-(6-azidoethyl)fluorene)] (PFA) with alkyne-modified graphene [68].

the azide substituted chromophoric molecules are covalently bonded on graphene using the triazole ring that formed the 1,3-dipolar cycloaddition as a link (see Figure 2.34) [69].

The last example of a post functionalization reaction referred to is an *ionic interaction* between sulfonated phenyl substituted graphenes and oligomeric quaternary ammonium salts. In the first step of the procedure GO nanosheets are partially reduced and then reacted with sulfonated aryl diazonium salt. The produced graphene nanoplatelets are easily dispersed in water due to the repulsive interaction between the charged graphitic surfaces. Then a post functionalization of the ionically modified graphenes by an ammonium salt with an oligomeric



(A)



(B)

Figure 2.34 (A) 1,3-Dipolar cycloaddition of azide substituted chromophores on ethynyl aryl functionalized graphene. (B) (a) TEM and (b) AFM image of ethynyl aryl modified

graphene nanoplatelets. (Reprinted with permission from Ref. [69], Copyright 2011, Royal Society of Chemistry.)

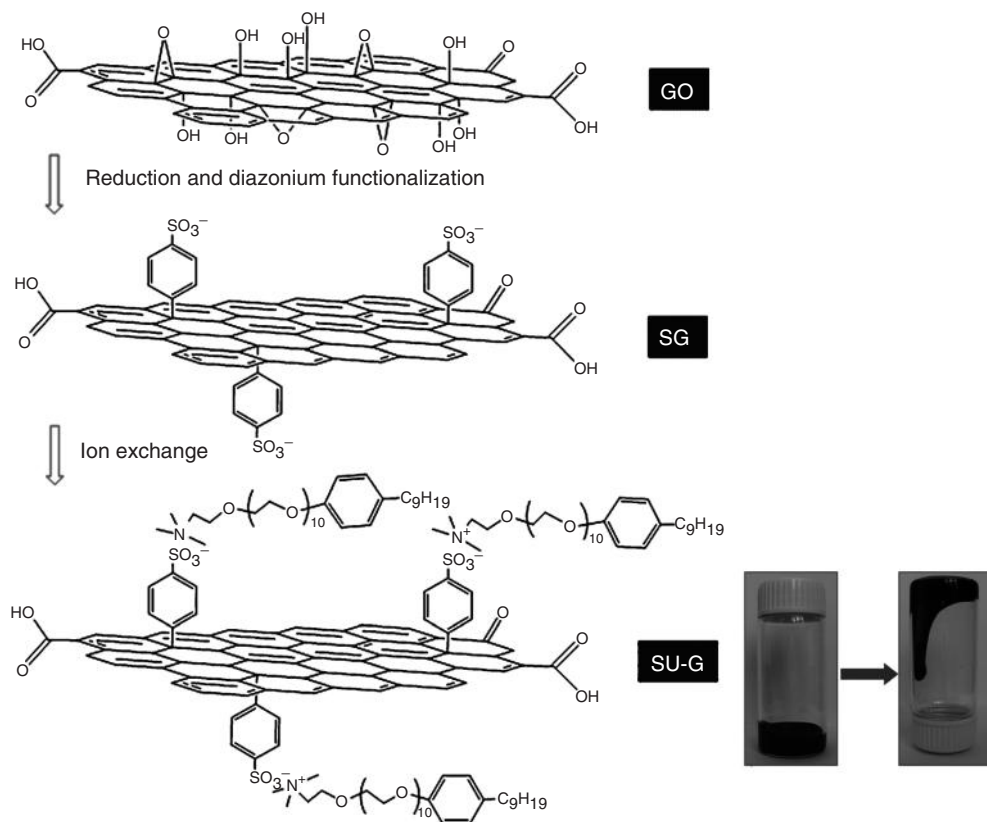


Figure 2.35 Post functionalization of ionically modified graphene nanoplatelets by oligomeric alkyl–ethoxy mixed chains. (Reprinted with permission from Ref. [70], Copyright 2012, Wiley-VCH Verlag GmbH & Co KGaA, Weinheim.)

chain follows (see Figure 2.35). The finally produced graphene nanoplatelets are rendered unfolded and the bulk product behaves as a viscous liquid when it is slightly heated [70].

2.8 Conclusion

The covalent functionalization of dienophiles, free radicals, and other reactive organic species is performed directly on sp^2 carbon atoms of pristine graphene or GO and has developed remarkably over the last year, offering a significant number of organic graphene derivatives, which cover a wide range of applications. Although the direct covalent addition increases the number of sp^3 carbon atoms of graphene with analogous impact on the physicochemical properties of graphene, the functionalized derivatives are among other things highly dispersible in several

solvents, mix homogenously with polymers or other matrices and finally add significant value to carbon nanomaterials.

References

- Kordatos, K., Da Ros, T., Bosi, S., Vazquez, E., Bergamin, M., Cusan, C., Pellarini, F., Tomberli, V., Baiti, B., Pantarotto, D., Georgakilas, V., Spalluto, G., and Prato, M. (2001) *J. Org. Chem.*, **66**, 4915.
- Maggini, M., Scorrano, G., and Prato, M. (1993) *J. Am. Chem. Soc.*, **115**, 9798.
- Prato, M. and Maggini, M. (1998) *Acc. Chem. Res.*, **31**, 519.
- Georgakilas, V., Kordatos, K., Prato, M., Guldi, D.M., Holzinger, M., and Hirsch, A. (2002) *J. Am. Chem. Soc.*, **124**, 761.
- Georgakilas, V., Bourlinos, A., Gournis, D., Tsooufis, T., Trapalis, C., Alonso, A.M., and Prato, M. (2008) *J. Am. Chem. Soc.*, **130**, 8733.
- Pastorin, G., Wu, W., Wieckowski, S., Briand, J.P., Kostarelos, K., Prato, M., and Bianco, A. (2006) *Chem. Commun.*, 1182–1184.
- Ballesteros, B., de la Torre, G., Ehli, C., Rahman, G.M.A., Rueda, F.A., Guldi, D.M., and Torres, T. (2007) *J. Am. Chem. Soc.*, **129**, 5061.
- Campidelli, S., Sooambar, C., Diz, E.L., Ehli, C., Guldi, D.M., and Prato, M. (2006) *J. Am. Chem. Soc.*, **128**, 12544–12552.
- Yao, Z., Braidy, N., Botton, G.A., and Adronov, A. (2003) *J. Am. Chem. Soc.*, **125**, 16015.
- Xu, G., Zhu, B., Han, Y., and Bo, Z. (2007) *Polymer*, **48**, 7510.
- Georgakilas, V., Bourlinos, A.B., Zboril, R., Steriotis, T.A., Dallas, P., Stubos, A.K., and Trapalis, C. (2010) *Chem. Commun.*, **46**, 1766.
- Zhang, X., Hou, L., Cnossen, A., Coleman, A.C., Ivashenko, O., Rudolf, P., van Wees, B.J., Browne, W.R., and Feringa, B.L. (2011) *Chem. Eur. J.*, **17**, 8957.
- Zhang, B., Chen, Y., Liu, G., Xu, L.Q., Chen, J., Zhu, C.X., Neoh, K.G., and Kang, E.T. (2012) *J. Polym. Sci., Part A: Polym. Chem.*, **50**, 378.
- Zhang, B., Liu, G., Chen, Y., Zeng, L.J., Zhu, C.X., Neoh, K.G., Wang, C., and Kang, E.T. (2011) *Chem. Eur. J.*, **17**, 13646.
- Quintana, M., Spyrou, K., Grzelczak, M., Browne, W.R., Rudolf, P., and Prato, M. (2010) *ACS Nano*, **4**, 3527.
- Quintana, M., Montellano, A., del Rio Castillo, A.E., Van Tendeloo, G., Bittencourt, C., and Prato, M. (2011) *Chem. Commun.*, **47**, 9330.
- Zhang, X., Browne, W.R., and Feringa, B.L. (2012) *RSC Adv.*, **2**, 12173.
- Chang, C.M. and Liu, Y.L. (2009) *Carbon*, **47**, 3041.
- Zydzia, N., Hübner, C., Bruns, M., and Barner-Kowollik, C. (2011) *Macromolecules*, **44**, 3374.
- Munirasu, S., Albuera, J., Boschetti-de-Fierro, A., and Abetz, V. (2010) *Macromol. Rapid Commun.*, **31**, 574.
- Wang, G.W., Chen, Z.X., Murata, Y., and Komatsu, K. (2005) *Tetrahedron*, **61**, 4851.
- Delgado, J.L., de la Cruz, P., Langa, F., Urbina, A., Casado, J., and López Navarrete, J.T. (2004) *Chem. Commun.*, 1734.
- Sarkar, S., Bekyarova, E., Niyogi, S., and Haddon, R.C. (2011) *J. Am. Chem. Soc.*, **133**, 3324.
- Yuan, J., Chen, G., Weng, W., and Xu, Y. (2012) *J. Mater. Chem.*, **22**, 7929.
- Xu, X., Luo, Q., Lv, W., Dong, Y., Lin, Y., Yang, Q., Shen, A., Pang, D., Hu, J., Qin, J., and Li, Z. (2011) *Macromol. Chem. Phys.*, **212**, 768.
- Strom, T.A., Dillon, E.P., Hamilton, C.E., and Barron, A.R. (2010) *Chem. Commun.*, **46**, 4097.
- He, H. and Gao, C. (2010) *Chem. Mater.*, **22**, 5054.

28. Vadukumpully, S., Gupta, J., Zhang, Y., Xu, G.Q., and Valiyaveetil, S. (2011) *Nanoscale*, **3**, 303.
29. Liu, L.H. and Yan, M. (2011) *J. Mater. Chem.*, **21**, 3273.
30. Xu, X., Lv, W., Huang, J., Li, J., Tang, R., Yan, J., Yang, Q., Qina, J., and Li, Z. (2012) *RSC Adv.*, **2**, 7042.
31. Lawrence, E.J., Wildgoose, G.G., Aldous, L., Wu, Y.A., Warner, J.H., Compton, R.G., and McNaughten, P.D. (2011) *Chem. Mater.*, **23**, 3740.
32. Ismaili, H., Lagugne-Labarthet, F., and Workentin, M.S. (2011) *Chem. Mater.*, **23**, 1519.
33. Ismaili, H. and Workentin, M.S. (2011) *Chem. Commun.*, **47**, 7788–7790.
34. Akasaka, T., Liu, M.T.H., Niino, Y., Maeda, Y., Wakahara, T., Okamura, M., Kobayashi, K., and Nagase, S. (2000) *J. Am. Chem. Soc.*, **122**, 7134–7135.
35. Ismaili, H., Geng, D., Sun, A.X., Kantzas, T.T., and Workentin, M.S. (2011) *Langmuir*, **27**, 13261.
36. Zhong, X., Jin, J., Li, S., Niu, Z., Hu, W., Li, R., and Ma, J. (2010) *Chem. Commun.*, **46**, 7340.
37. Economopoulos, S.P., Rotas, G., Miyata, Y., Shinohara, H., and Tagmatarchis, N. (2010) *ACS Nano*, **4**, 7499.
38. Diederich, F. and Thilgen, C. (1996) *Science*, **271**, 317.
39. Coleman, K.S., Bailey, S.R., Fogden, S., and Green, M.L.H. (2003) *J. Am. Chem. Soc.*, **125**, 8722.
40. Economopoulos, S.P., Pagona, G., Yudasaka, M., Iijima, S., and Tagmatarchis, N. (2009) *J. Mater. Chem.*, **19**, 7326.
41. Sinitskii, A., Dimiev, A., Corley, D.A., Fursina, A.A., Kosynkin, D.V., and Tour, J.M. (2010) *ACS Nano*, **4**, 1949.
42. Niyogi, S., Bekyarova, E., Itkis, M.E., Zhang, H., Shepperd, K., Hicks, J., Sprinkle, M., Berger, C., Ning Lau, C., de Heer, W.A., Conrad, E.H., and Haddon, R.C. (2010) *Nano Lett.*, **10**, 4061.
43. Jin, Z., Lomeda, J.R., Price, B.K., Lu, W., Zhu, Y., and Tour, J.M. (2009) *Chem. Mater.*, **21**, 3045.
44. Lomeda, J.R., Doyle, C.D., Kosynkin, D.V., Hwang, W.F., and Tour, J.M. (2008) *J. Am. Chem. Soc.*, **130**, 16201.
45. Bekyarova, E., Itkis, M.E., Ramesh, P., Berger, C., Sprinkle, M., de Heer, W.A., and Haddon, R.C. (2009) *J. Am. Chem. Soc.*, **131**, 1336.
46. Sharma, R., Baik, J.H., Perera, C.J., and Strano, M.S. (2010) *Nano Lett.*, **10**, 398.
47. Ye, L., Xiao, T., Zhao, N., Xu, H., Xiao, Y., Xu, J., Xiong, Y., and Xu, W. (2012) *J. Mater. Chem.*, **22**, 16723.
48. Mondal, T., Bhowmick, A.K., and Krishnamoorti, R. (2012) *J. Mater. Chem.*, **22**, 22481.
49. Sun, Z., Kohama, S., Zhang, Z., Lomeda, J.R., and Tour, J.M. (2010) *Nano Res.*, **3**, 117.
50. Fang, M., Wang, K., Lu, H., Yang, Y., and Nutt, S. (2009) *J. Mater. Chem.*, **19**, 7098.
51. Fang, M., Wang, K., Lu, H., Yang, Y., and Nutt, S. (2010) *J. Mater. Chem.*, **20**, 1982.
52. Zhang, P., Jiang, K., Ye, C., and Zhao, Y. (2011) *Chem. Commun.*, **47**, 9504.
53. Cui, P., Seo, S., Lee, J., Wang, L., Lee, E., Min, M., and Lee, H. (2011) *ACS Nano*, **5**, 6826.
54. Liu, H., Ryu, S., Chen, Z., Steigerwald, M.L., Nuckolls, C., and Brus, L.E. (2009) *J. Am. Chem. Soc.*, **131**, 17099.
55. Shen, J., Hu, Y., Li, C., Qin, C., and Ye, M. (2009) *Small*, **5**, 82.
56. Xu, H. and Suslick, K.S. (2011) *J. Am. Chem. Soc.*, **133**, 9148.
57. Shen, B., Zhai, W., Lu, D., Wang, J., and Zheng, W. (2012) *RSC Adv.*, **2**, 4713.
58. Long, J., Fang, M., and Chen, G. (2011) *J. Mater. Chem.*, **21**, 10421.
59. Xu, X., Chen, J., Luo, X., Lu, J., Zhou, H., Wu, W., Zhan, H., Dong, Y., Yan, S., Qin, J., and Li, Z. (2012) *Chem. Eur. J.*, **18**, 14384.
60. Li, P.P., Chen, Y., Zhu, J., Feng, M., Zhuang, X., Lin, Y., and Zhan, H. (2011) *Chem. Eur. J.*, **17**, 780.
61. Yuan, C., Chen, W., and Yan, L. (2012) *J. Mater. Chem.*, **22**, 7456.
62. Sarkar, S., Niyogi, S., Bekyarova, E., and Haddon, R.C. (2011) *Chem. Sci.*, **2**, 1326.

63. Sarkar, S., Zhang, H., Huang, J.W., Wang, F., Bekyarova, E., Lau, C.N., and Haddon, R.C. (2013) *Adv. Mater.*, **25**, 1131.
64. Ragoussi, M.E., Malig, J., Katsukis, G., Butz, B., Spiecker, E., de la Torre, G., Torres, T., and Guldi, D.M. (2012) *Angew. Chem. Int. Ed.*, **51**, 6421.
65. Umeyama, T., Mihara, J., Tezuka, N., Matano, Y., Stranius, K., Chukharev, V., Tkachenko, N.V., Lemmetyinen, H., Noda, K., Matsushige, K., Shishido, T., Liu, Z., Takai, K.H., Suenaga, K., and Imahori, H. (2012) *Chem. Eur. J.*, **18**, 4250.
66. Bon, S.B., Valentini, L., Verdejo, R., Fierro, J.L.G., Peponi, L., Lopez-Manchado, M.A., and Kenny, J.M. (2009) *Chem. Mater.*, **21**, 3433.
67. Valentini, L., Cardinali, M., Bon, S.B., Bagnis, D., Verdejo, R., Lopez-Manchado, M.A., and Kenny, J.M. (2010) *J. Mater. Chem.*, **20**, 995.
68. Castelaïn, M., Martínez, G., Merino, P., Martín-Gago, J.Á., Segura, J.L., Ellis, H.J., and Salavagione, G. (2012) *Chem. Eur. J.*, **18**, 4965.
69. Wang, H.X., Zhou, K.G., Xie, Y.L., Zeng, J., Chai, N.N., Li, J., and Zhang, H.L. (2011) *Chem. Commun.*, **47**, 5747.
70. Li, Q., Dong, L., Sun, F., Huang, J., Xie, H., and Xiong, C. (2012) *Chem. Eur. J.*, **18**, 705.

3

Addition of Organic Groups through Reactions with Oxygen Species of Graphene Oxide

Vasilios Georgakilas

3.1

Introduction

One of the first organic functionalizations on carbon nanostructures was the covalent attachment of an aliphatic amine through an amide bond that formed between the amine and acyl chloride groups that are created on a carbon nanotube surface by a strong oxidation process [1]. A great number of organic functionalizations followed later based on the rich organic chemistry mainly of carboxyl, as well as on hydroxyl and epoxy groups that normally exist on oxidized carbon nanotubes [2–4]. Inspired by the successful functionalization of carbon nanotubes, amidation, esterification, and other organic reactions that involve oxygen species such as carboxyl, hydroxyl, and epoxy groups have been successfully applied on graphene surfaces and are presented in this chapter.

As described in Chapter 1, the strong oxidative treatment of graphite leads to its exfoliation and the formation of the graphene oxide (GO) monolayers, which are highly dispersible in water. The oxygen groups that remain on the graphene surface after the oxidation process are carboxyl groups near the edges and hydroxyl and epoxy groups at the core surface of the graphene layer. These groups are the reactive centers of GO for the development of a number of organic derivatizations. GO can be partly reduced affording the so-called chemically converted graphene (ccG) or reduced graphene oxide (rGO) nanosheets. However, comparing the reactivity of GO and rGO, the organic functionalizations of graphitic nanosheets that involve oxygen groups perform better before the reduction as the number of the available reactive oxygen sites is much higher and therefore the reaction yield is higher. After the organic functionalization, the graphitic character of the modified graphene can be partly restored by a reductive process, which removes the excess of the oxygen groups, depending on the purpose of the functionalization. For example, if the challenge is the electrical conductivity or the mechanical properties of the final graphene derivative, the restoration of the graphitic character is necessary, whereas it is better to keep the oxygen groups if the hydrophilic character of graphene is needed.

The functionalized GO in general are characterized by TEM (transmission electron microscope) and AFM (atomic force microscope) spectroscopy, UV-vis, FT-IR (Fourier transform infrared spectroscopy), X-ray photoelectron spectroscopy (XPS), and thermogravimetric analysis (TGA). The microscopic techniques are usually used to verify the presence of monolayers or few-layer graphenes in the product, as the organic functional groups are not visible under microscopy. The UV-vis spectrum of a functionalized GO is different from that of GO as it consists of the absorption bands of the functional groups that are superimposed on the absorption band of GO and can be seen as an indication of the functionalization. In cases where a chromophore is the added group on GO, UV-vis, and photoluminescence (PL) are necessary tools for the characterization of the composite products. For example, fluorescence emission of an active group is usually quenched by the interaction of this group with the graphitic surface. The degree of this quenching indicates the character and quality of this interaction. FT-IR spectroscopy is a powerful tool for the characterization of the product since the involved groups (carboxyl, epoxy, hydroxy) and the formed covalent bonds (amide, ester, ether, siloxy bond, etc.) have characteristic absorption bands in the infrared spectra. Similarly XPS is often employed to evaluate the covalent bonds that are formed during functionalization. Finally the Raman spectra of functionalized graphene are less important when the functionalization does not include the sp^2/sp^3 transformation of the hybridization of carbon atoms of graphene such as in the reactions that involve oxygen groups. However, very often Raman spectroscopy is used to indicate the degree of the partial reduction of GO, which usually follows the functionalization through the I_D/I_G ratio.

In this chapter, the organic functionalizations are organized in categories based on the organic reaction involved. GO after functionalization by the oxygen groups is seen as functionalized graphene rather than functionalized GO. For example, the product that results by attaching alkyl groups on GO by an ether bond can be characterized as alkyloxy functionalized graphene or alkyl functionalized GO. However, a great number of oxygen groups remain unaffected after the functionalization influencing the character of the final functionalized product. Thus, in order to discriminate the reactions of this chapter from the direct reactions of pristine graphene, it is better to keep the GO symbol or *rGO* (for the partially *rGO*), extended with the symbol of the functional group.

3.1.1

Graphene/Polymer Nanocomposites

One of the most well studied issues regarding the role of carbon nanostructures in applications is the formation of nanocomposites from polymers and carbon nanostructures, mainly carbon nanotubes and graphene or graphitic nanosheets in general. The advantages of these carbon nanostructures in composite materials are based on the remarkable mechanical properties and their optical and electrical properties as well. Dispersion of graphene in a polymer matrix could increase the mechanical strength of the polymer composite and the electrical

conductivity. Usually thin films of graphene/polymer composites are also transparent which means that they can be used as transparent conductive film – electrodes in optoelectronic applications.

Graphene/polymer composite can be formed by a simple mixing of a polymer matrix with pristine or functionalized graphene or GO depending on the ability to disperse both components in common solvents. A well studied technique for the formation of polymer nanocomposites is the covalent grafting of the polymer chains on the graphene or GO surface. This covalent attachment usually ensures more homogeneous dispersion of the graphene nanoplatelets in the polymer matrix and better results as regards the mechanical or electronic interactions between the two components. As regards the procedures that have been established for this covalent attachment, usually they are divided in two general types. The first type is referred to as *grafted from* and includes the reactions where polymeric chains start and are developed from the surface of graphene, which means that the polymerizations are performed in the presence of graphene nanosheets. The second type is referred to as *grafted to* and includes the reactions where the polymer is pre-synthesized and is covalently bonded on the graphene surface with the aim of functional groups that are located at side chains or at the ends of the polymer chains. Since the graphene/polymer composites and their properties and application have been the subject of several reviews [5–7] and book chapters, the scope of this chapter is to include a number of characteristic polymer/graphene composites focusing on the chemical bond that is formed between the two components.

3.2

The Role of Carboxylic Acids of GO

GO is decorated by a large number of carboxylic acid groups that are usually located near the edges of the graphitic nanoplatelets. Carboxylic acids can react: (i) with amines or organic molecules and polymers that bear amine groups through the formation of amide bonds, (ii) alcohols, phenols, and epoxides forming ester bonds, and (iii) several other miscellaneous organic reactive compounds resulting in the organic functionalization of GO.

3.2.1

Organic Functionalization through Amide Bond Formation

3.2.1.1 Lipophilic Derivatives

One of the earliest examples of this reaction was introduced by Haddon *et al.* and includes the attachment of octadecylamine (ODA) on GO through the formation of amide bonds with its carboxylic groups [8]. GO was used as prepared from the oxidation of graphite without further reduction and thus a great number of oxygen species were available for covalent functionalization. The first step of the functionalization included the transformation of the carboxylic acid groups of GO to acyl chlorides by thionyl chloride and the second step the direct reaction between

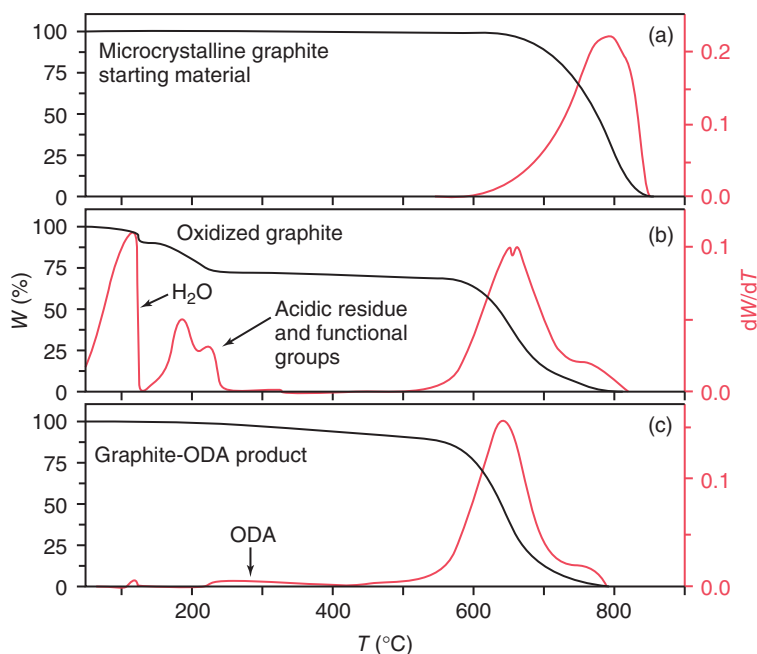


Figure 3.1 TGA curves of graphite starting material (a) GO (b) and GO-ODA (c) under air. (Reprinted with permission from Ref. [8], Copyright 2006, American Chemical Society.)

the alkylamine and the acyl chloride of GO and the formation of an amide bond. The octadecyl functionalized GO (GO-ODA) was dispersible in tetrachloromethane (CCl_4), 1,2 dichloroethane, and tetrahydrofuran (THF) (0.5 mg ml^{-1}). The TGA diagram of graphite showed that the latter is stable under heating and is burnt only over 700°C in air. In contrast GO and GO-ODA are totally burnt below 600°C (see Figure 3.1). A low mass loss between 200 and 400°C is attributed to the removal of ODA groups.

Similarly prepared *r*GO-ODA has been homogeneously dispersed in lipophilic polymers such as isotactic polypropylene by blending together in a common non-polar solvent such as xylene. The raw GO in this reaction is partially reduced by hydrazine and the amidation was performed by *r*GO, ODA, and *N,N'*-dicyclohexylcarbodiimide (DCC) in dimethylformamide (DMF). The composite showed enhanced thermal stability and strong adhesion of graphene nanosheets with the polymer matrix [9]. GO-ODA derivative has also shown stable dispersibility in hexadecane and enhanced lubricity [10]. Lipophilic behavior was also observed in graphene functionalized by 4,4'-diamino-diphenyl ether [11].

3.2.1.2 Hydrophilic – Biocompatible Derivatives

GO has been functionalized through amide bonds with several biocompatible polymers such as polyethyleneglycole, dextran, and chitosan, in order to be used in bioapplications. The biocompatible polyethylene glycol (PEG) is grafted on the

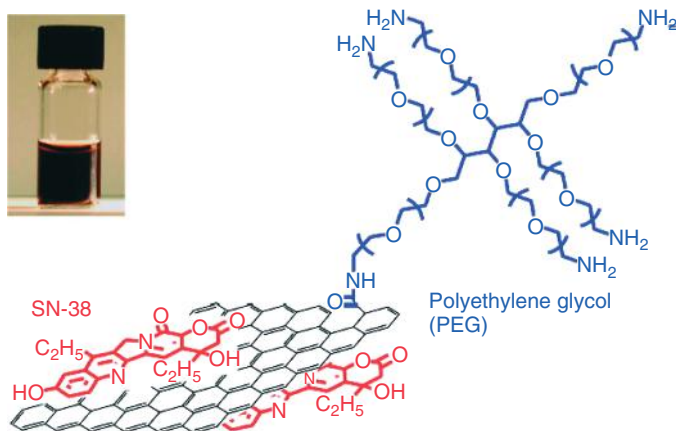


Figure 3.2 Schematic representation of GO-PEG-SN38 complex and a photo of the same complex in water solution (inset). (Reprinted with permission from Ref. [12], Copyright 2008, American Chemical Society.)

carboxylic groups of graphene through amide bonds using amine terminated PEG chains [12]. Owing to the highly hydrophilic character of PEG, the PEGylated graphene (GO-PEG) is highly dispersible in water as well as other biological solutions such as serum and can be used as carrier for the transportation of hydrophobic drugs in biological systems. For example, a highly hydrophobic compound, the camptothecin analog called SN38 which is a potent topoisomerase inhibitor was grafted on PEGylated graphene through π,π stacking (see Figure 3.2). The complex PEGylated GO/SN38 system (GO-PEG/SN38) that occurred was soluble in water at a concentration of up to 1 mg ml^{-1} . The SN38 is released from the complex slowly when the latter is dispersed in serum at 30% in 3 days whereas in phosphate buffer saline (PBS) the complex was rather stable. The close proximity of SN38 and GO-PEG in the complex is indicated by the strong fluorescence quenching of the GO-PEG-SN38 complex after excitation in comparison with the stable fluorescence band that was recorded after the excitation of SN38.

GO has been functionalized by dextran (Dex) polymer which is also biocompatible. Since dextran cannot react directly with carboxyl groups, it was primarily modified by amine terminated groups at several places of the polymer chain (see Figure 3.3). The as-prepared GO-Dex composite showed enhanced stability in physiological solutions and remarkably reduced cell toxicity. In addition, *in vivo* experiments in mice showed that GO-Dex intravenously inserted in an animal body is almost totally removed after one week without causing noticeable short term toxicity in the treated animals [13].

Chitosan can directly form amide bonds with carboxyl groups since its monomer contains six membered rings substituted among others by amine groups. The reaction is performed under microwave irradiation and the polymer modified GO can then be partially reduced by hydrazine producing chitosan modified rGO,

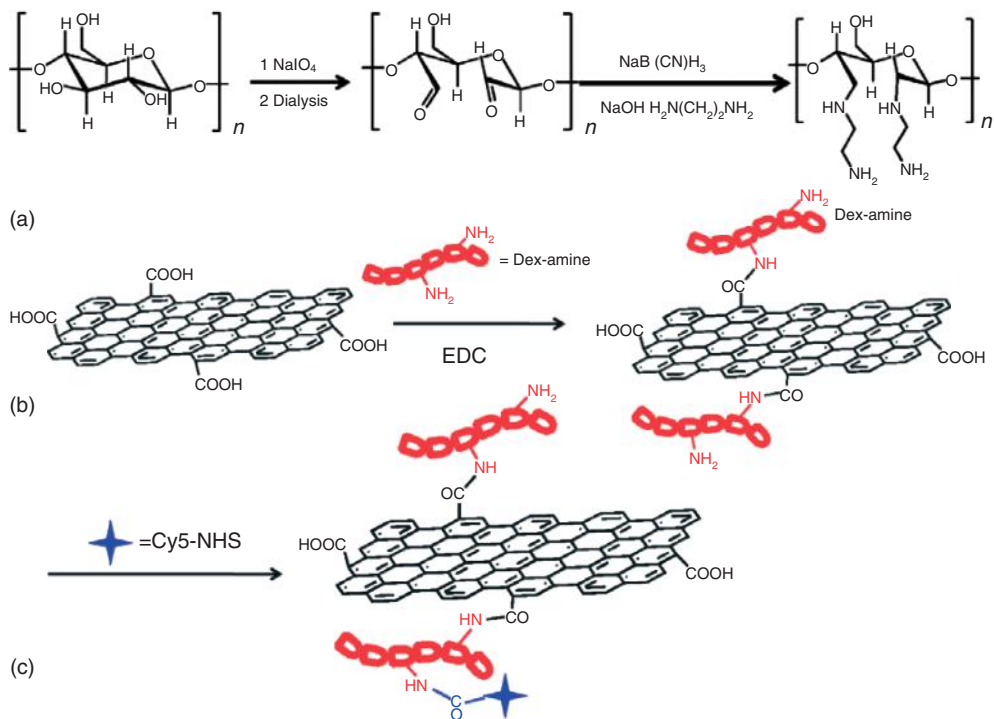


Figure 3.3 (a–c) The modification of dextran with amine terminated groups and the grafting on GO through amide bond formation. The Dex-GO is finally fluorescence labeled by Cy5-NHS (*N*-hydroxysuccinimide)

for the tracking of the composite during their insertion into the cells. (Reprinted with permission from Ref. [13], Copyright 2011, Elsevier B.V.)

which is highly soluble in water [14] (Figure 3.4). Water soluble derivatives are produced by the functionalization of GO by proteins such as bovine serum albumin [15], 4-aminobenzene sulfonic acid [11], and so on.

3.2.1.3 Addition of Chromophores

Porphyrins and phthalocyanines are attractive chromophoric organic compounds with extended π -conjugated structures that have been used as photoactive functional groups in solar energy conversion systems. In addition they exhibit excellent nonlinear optic (NLO) and optical limiting (OL) properties. The similar behavior that has also been observed for graphene has resulted in superior NLO properties and broadband OL performance that was exhibited by the combination of porphyrins and phthalocyanines with graphene nanosheets. Analogous results have been observed with C_{60} [16, 17] and oligothiophene [18] molecules in combination with graphene nanosheets. Such combinations are often performed by the covalent attachment of the chromophoric molecules on graphene surface. When at least one of the phenyl rings of porphyrin or phthalocyanine is substituted by an amine

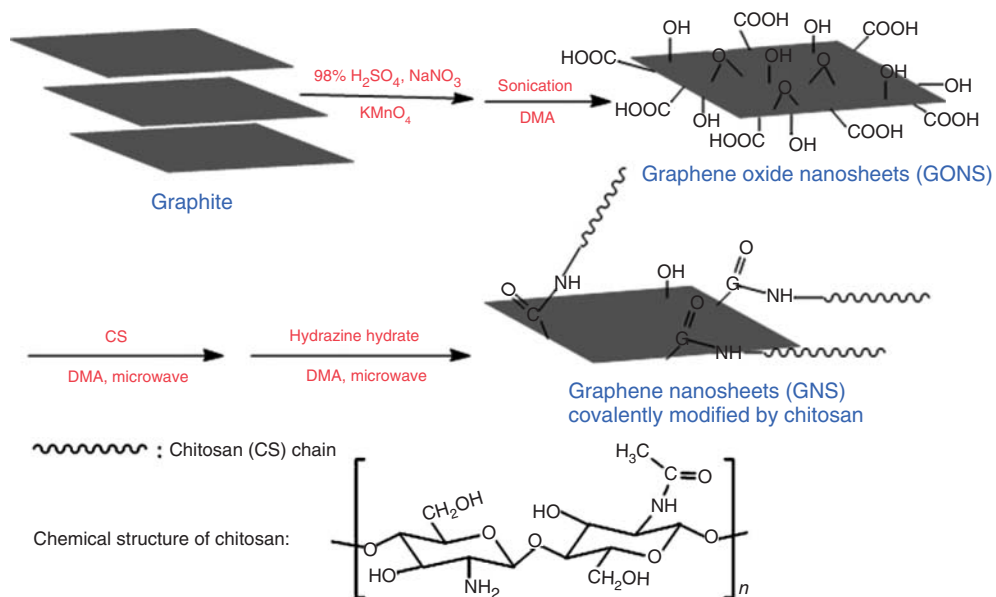


Figure 3.4 Functionalization of GO by chitosan. (Reprinted with permission from Ref. [14], Copyright 2011, Elsevier B.V.)

group the latter can be amide bonded on GO [16, 19, 20]. Pyrrolidine functionalized C₆₀ can be covalently bonded on graphene surface [16]. Oligothiophene should be also amine terminated in order to be attached by the same reaction on graphene surface [18].

GOs covalently functionalized by amine substituted tetraphenyl porphyrin (TPP) have been studied further for their interesting photophysical properties and use in energy conversion systems (see Figure 3.5). The porphyrin functionalized GO (GO-H₂P) is dispersible in DMF (about 1 mg ml⁻¹). The UV-vis spectrum of GO-H₂P shows a continuously increasing absorption band from 700 nm to the UV region, which is attributed to the absorption of GO superimposed by a band at 420 nm that is the characteristic Soret-band of porphyrins. The fluorescence emission band of GO-H₂P is remarkably reduced in comparison with pure porphyrin, indicating an efficient fluorescence quenching that takes place during the excitation of the GO-H₂P composite. This behavior is attributed to the successful electron transfer from the singlet excited state of H₂P to GO. A photoelectrochemical cells constructed based on GO-H₂P hybrid showed incident photoconversion efficiency (IPCE) near 1.3% [21].

Oligo(phenylenevinylene) (OPV) is also a chromophoric electron donor molecule that has been used in donor-acceptor systems designed for photovoltaic application. Amine substituted OPV have been covalently attached on GO through amide bonds [22]. GO nanosheets with five graphitic layers on average that are used as starting material, were prepared by thermal exfoliation. OPV-amine functionalized GO is

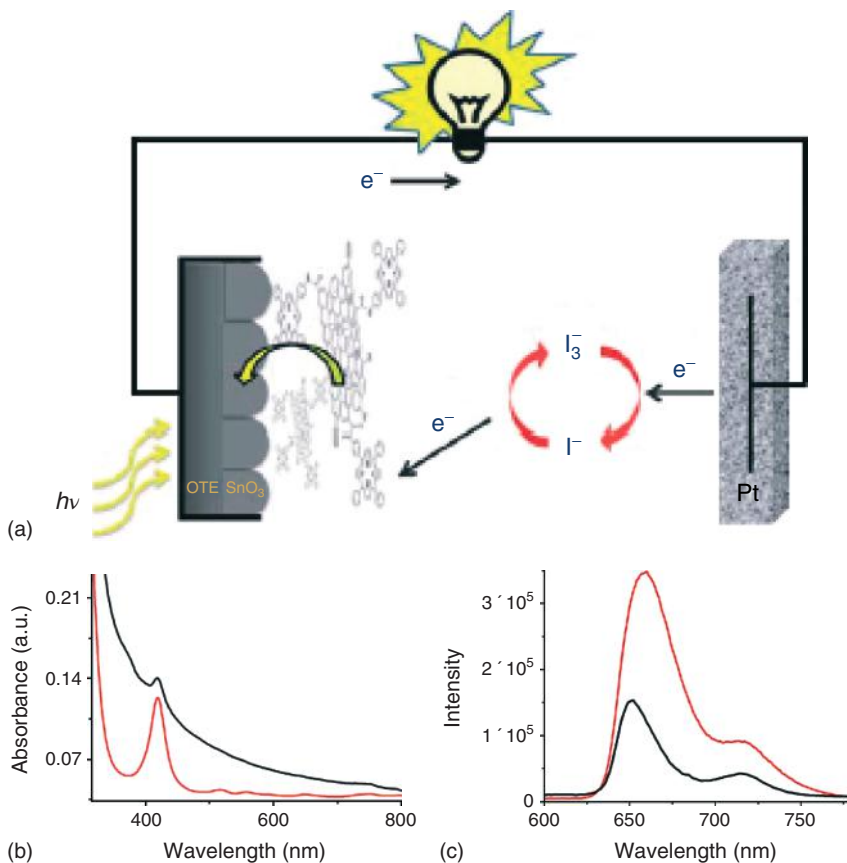


Figure 3.5 (a) Schematic representation of a photoelectrochemical cell with the aim of GO-P₂H hybrid. (b) UV-vis absorption bands of GO-H₂O the upper black line and H₂P the red line. (c) Fluorescence emission

spectra of H₂P the upper red line and GO-H₂P the black line. (Reprinted with permission from Ref. [21], Copyright 2011, Royal Society of Chemistry.)

highly dispersible in organic solvents because of the lipophilic character of OPV. The amide bonds are indicated by the characteristic amide I and II bands at 1572 and 1639 cm⁻¹ respectively, in the FT-IR spectrum of the OPV-GO product. As regards the Raman spectrum of the OPV-GO, a remarkable increase in the relative intensity of the 2G band as well as a shift of this band to lower wavelength is attributed to a significant decrease in the average number of layers of GO nanosheets owing to the better exfoliation that is achieved after the reaction. The efficiency of the combination of chromophores with carbon nanostructures in donor-acceptor systems is usually examined by PL studies. The UV-vis absorption spectrum of OPV-GO is the expected combination of the two independent spectra. The PL emission band of the corresponding spectrum of OPV-GO is significantly reduced in comparison with that of pure OPV molecule. This decrease in the

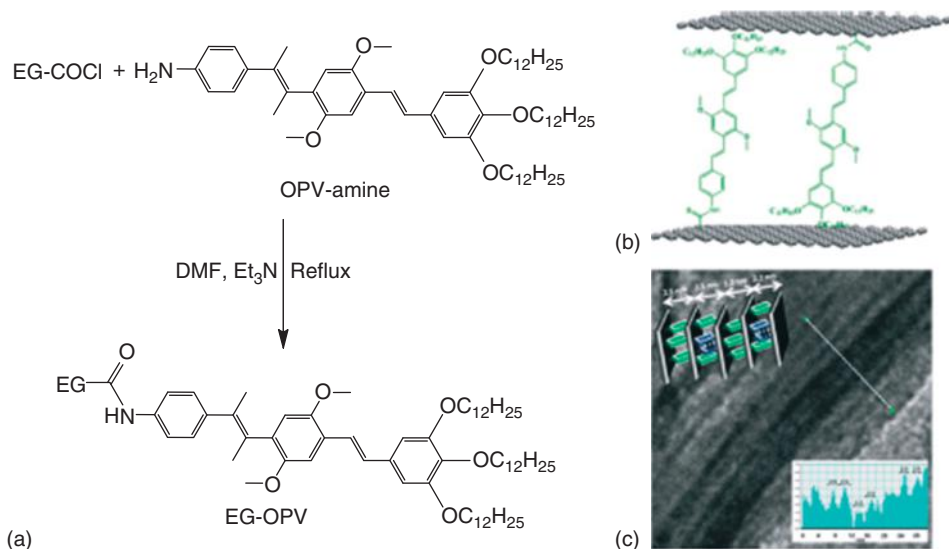


Figure 3.6 (a) Synthesis of OPV functionalized graphene. (b) Proposed structure of OPV-GO with OPV molecules perpendicular between two graphene layers as indicated by microscopic data and (c) TEM image of the layered graphene structure (insets shows the

interlayer distances across the white line and the graphic representation of the arrangement). (Reprinted with permission from Ref. [22], Copyright 2012, Royal Society of Chemistry.)

intensity of the emission band is attributed to a fluorescence quenching that is promoted by a strong interaction between the GO layer and the chromophore. Such interactions are observed in directly connected components. The TEM image of the product showed the presence of bilayer and multilayer nanosheets with an interlayer spacing that ranges between 2 and 2.4 nm. Such interlayer spacing fits to a perpendicular configuration of the functional groups as presented in Figure 3.6.

Azobenzene chromophore covalently functionalized on GO (Azo-GO) can be presented in the *cis* and *trans* isomers depending on the position of the aromatic rings (see Figure 3.7) [23]. The reaction produces the thermodynamically stable *trans* Azo-GO isomer although an equilibration with the *cis* isomer is established only after UV irradiation of the product. This change in the conformation of Azo-GO is followed by an increase in the conductivity of the composite because of the formation of the *cis* isomer.

Azo-GO is prepared by covalent attachment of an amino substituted azobenzene (see Figure 3.7) on GO through amide bond and presents high dispersibility in organic solvents such as DMF and acetone. An estimation of the degree of Azo functionalization based on XPS analysis is expressed as one Azo group per 87 carbon atoms of GO. The crystal structure of Azo-GO that occurs when the hybrid is passed to the solid phase removing the solvent is studied by XRD (X-ray diffraction) spectroscopy. An interesting feature that is observed comparing XRD patterns of Azo-GO and GO is the characteristic decrease in the interlayer

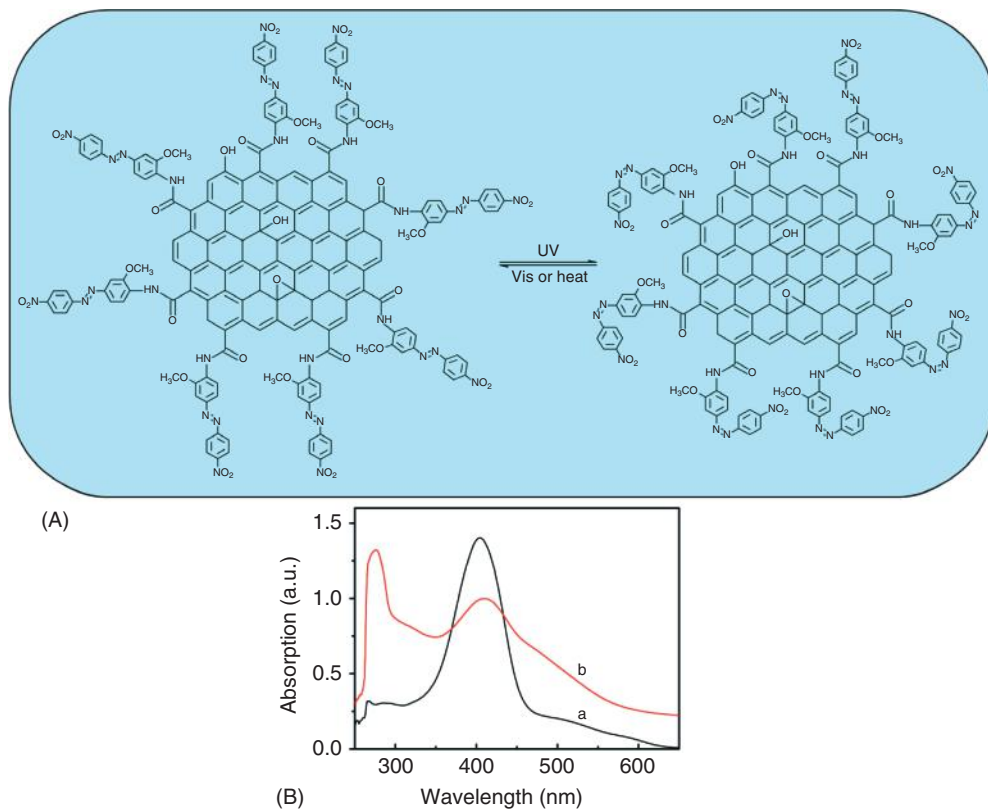


Figure 3.7 (A) Photoisomerization process of Azo-GO. (B) UV-vis spectra of (a) Azobenzene and (b) Azo-GO in DMF. (Reprinted with permission from Ref. [23], Copyright 2010, Elsevier B.V.)

distance between the graphitic layers after the Azo functionalization. Usually the intercalation of an organic molecule between graphitic layers results in the opposite phenomenon – increase of the interlayer distance – because of the larger size of the organic groups in comparison with the oxygen groups of GO. In this case, in the XRD pattern of GO, a peak at 12.1° is recorded corresponding to an interlayer distance of 0.73 nm, whereas in Azo-GO the XRD pattern consists of a peak at $2\theta = 25.3^\circ$, which corresponds to 0.35 nm interlayer spacing showing a graphite like structure. The interlayer spacing in GO is attributed to the appearance of oxygen groups at the graphitic surface; in the solid form of GO the oxygen groups are intercalated between the graphitic layers. The peak that corresponds to the Azo intercalated GO layers appears very weak and broad and thus is not informative. This means that the appearance of the Azo groups did not help the GO layers to stack easily whereas a percentage of the graphene nanosheets – possibly because of a reductive removal of the oxygen groups – are stacked in the form of graphite. The covalent attachment of the Azo group is showed by the appearance

of the characteristic peak of the amide bond in FT-IR spectrum as well as by the redshift of the absorption bands in the UV–vis spectra of Azo-GO in comparison with the relative absorption bands of the separated components (see Figure 3.7). The intense band of azobenzene has a maximum at 405 nm assigned to the π,π^* transition of the trans isomer. The same band in Azo-GO is red shifted at 410 nm. A further peak below 300 nm in the spectrum of Azo-GO is assigned to the π -plasmon transition of GO and is redshifted 9 nm owing to the interaction between GO and azobenzene groups. The intensity of the band at 410 nm is decreased during irradiation because of the trans \rightarrow cis transformation. The metastable cis isomer is transformed back to trans isomer in the dark, showing that photoisomerization is a reversible process. A simple device that constructed a thin layer of Azo-GO between two indium tin oxide (ITO) electrodes showed a gradual increase of the conductivity during UV irradiation that follows the trans \rightarrow cis transformation.

3.2.1.4 Polymer Graphene Composite

The amidation reaction has been further used for the grafting of several amine functionalized polymers on graphene surface. Aryl amine terminated triphenylamine-based polyazomethine (TPAPAM) conjugated polymer is grafted on GO through amide bonds (see Figure 3.8). Although the fluorescence emission bands of

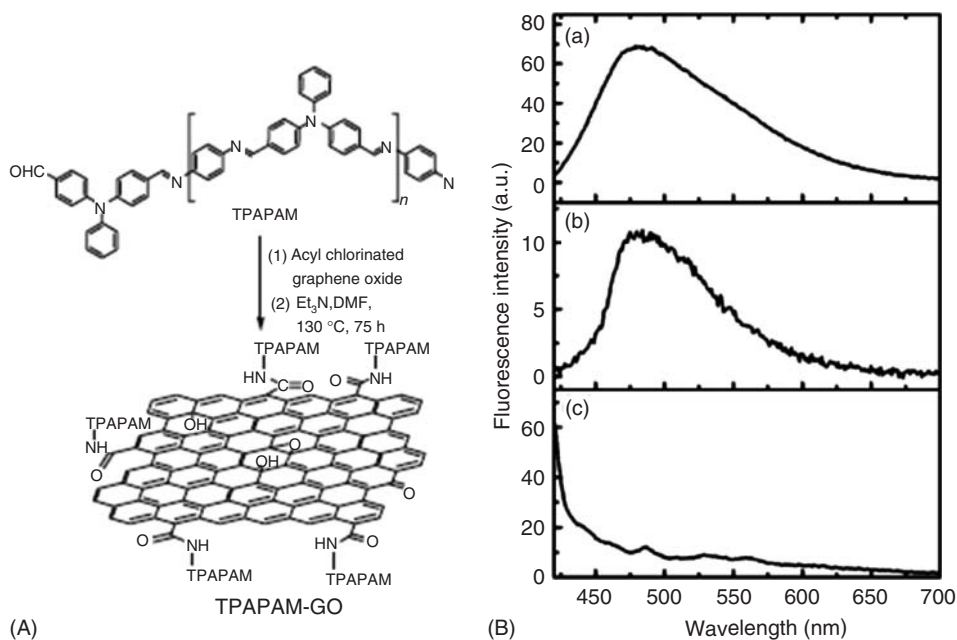


Figure 3.8 (A) TPAPAM functionalized GO. (B) Fluorescence spectra of (a) TPAPAM-GO, (b) TPAPAM, and (c) GO in THF (4 mg/l). The excitation wavelength is

410 nm. Reprinted with permission from Ref. [24], Copyright 2010, Wiley-VCH Verlag GmbH & Co KGaA, Weinheim.

chromophores that are connected to GO are usually partially quenched, here the attachment of TPAPAM on GO has the opposite results as regards PL behavior of the hybrid. In fact the PL intensity of TPAPAM-GO is highly increased in comparison with that of the pure polymer, showing that the connection of the two components improves remarkably the electronic interactions between them. The composite was used to fabricate a TPAPAM-GO based nonvolatile memory device using ITO and aluminum (Al) as electrodes according to the scheme: ITO/TPAPAM-GO/Al [24]. The device showed successful performance with a typical bistable electrical switching and nonvolatile rewritable memory effect, with a turn-on voltage at 1 V and ON/OFF current ratio of more than 10^3 .

An interesting composite nanomaterial, which combines carbon and silicon oxide, has been constructed by the covalent attachment – through amidation – of polyhedral oligomeric silsesquioxane (POSS) on GO (see Figure 3.9) [25]. As presented in the figure the covalent bonding occurred between amine terminated chain of POSS and the carboxylic acid groups of GO in the presence of DCC. The nucleophilic addition of amines to GO by epoxide ring opening is also a possible addition pathway here.

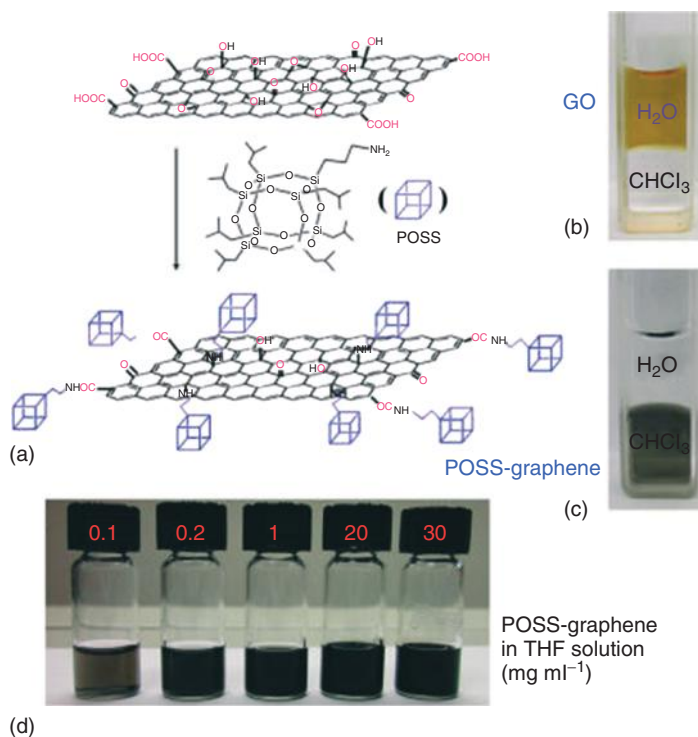


Figure 3.9 (a) The functionalization of GO by amine terminated POSS. Dispersion of GO (b) and rGO-POSS (c) in the biphasic water/chloroform system. (d) Dispersion of rGO-POSS in THF in several concentration in milligrams per milliliter. (Reprinted with permission from Ref. [25], Copyright 2012, American Chemical Society.)

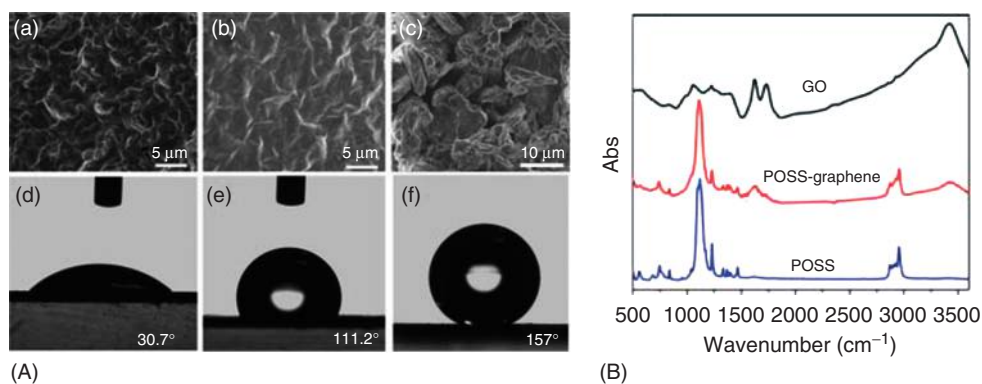


Figure 3.10 (A) SEM (secondary electron microscope) images of (a) GO film, *rGO*-POSS film with normal (b) and enhanced roughness (c). A water droplet and the air/water contact angle on a film of GO (d), and *rGO*-POSS with normal (e) and high roughness (f). (B) The FT-IR spectrum of *rGO*-POSS and starting materials. (Reprinted with permission from Ref. [25], Copyright 2012, American Chemical Society.)

In the FT-IR spectra of the POSS functionalized GO (*rGO*-POSS), a remarkable decrease of the intensity of the characteristic bands assigned to hydroxyl, (3400 cm^{-1}) carboxyl (1731 cm^{-1}), and epoxy (1228 cm^{-1}) groups indicated the successful functionalization of GO and its partial reduction as well. The presence of POSS is further characterized by a strong band at 1110 cm^{-1} assigned to the Si–O–Si stretching vibration and a weak band at $2700\text{--}3000\text{ cm}^{-1}$ assigned to the iso-butyl substituents of POSS (see Figure 3.10). The existence of POSS cages at the surface of GO prevents the nanoplatelets from aggregation when they are dispersed in a solvent; as a consequence *rGO*-POSS is highly dispersible in several organic solvents such as THF, hexane, chloroform, acetone, and toluene. *rGO*-POSS showed a hydrophobic character indicating that this property of butyl groups of POSS cover the hydrophilic character of GO surface. In addition an increase in the surface roughness can transform a *rGO*-POSS film superhydrophobic (see Figure 3.10). Finally 1% dispersion of *rGO*-POSS in poly-methyl-methacrylate (PMMA) resulted in a $10\text{ }^{\circ}\text{C}$ increase of the T_g of the polymer indicating analogous enhancement of the thermal stability of the polymer composite.

3.2.2

Esterification of GO

Alcohols or organic molecules and polymers that bear hydroxyl or phenolic groups can react with carboxylic acids in esterification reactions. Thus GO can be involved in esterification reactions by its carboxylic acid or hydroxyl groups with a variety of organic species such as cyclodextrin [26], hydroxyl substituted polymers [27–29], conjugated polymers [30], and carboxyl terminated fullerene [31].

Cyclodextrins are highly hydrophilic cyclic oligomers of glucose. Their structure forms a hydrophobic cavity that can host organic molecules, biomolecules, or

inorganic species with potential application in biosensors, drug delivery, electronics, and so on. Owing to the large number of hydroxyl groups, hydroxypropyl β -cyclodextrin (HPCD) can be grafted by esterification on GO forming a composite material (HPCD-GO), which disperses well in water and polar organic solvents [26]. The final HPCD-*r*GO product is produced after the partial reduction of HPCD-GO by sodium borohydride and it showed similar dispersibility. The high hydrophilicity of HPCD-*r*GO is attributed to the hydrophilic character of the external part of β -cyclodextrin which is covered by hydroxyl groups. On the other hand, the cavity of cyclodextrin is less hydrophilic and can host hydrophobic organic molecules, which fit in the size of the cavity, acting as a carrier for these molecules in a nonfriendly environment such as water. The guest molecules are held into the cavity by van der Waals interactions or hydrogen bonds. TPP is an excellent candidate as a guest molecule since it is a hydrophobic molecule that fits very well with the dimensions of circular dichroism (CD) cavity. In addition it is a photo induced electron donor that offers the opportunity for the study of the electron transfer between the donor TPP and the acceptor GO or *r*GO in the frame of this host–guest system.

The insertion of TPP in the cavity of the HPCD-*r*GO is performed by a simple addition of HPCD-*r*GO in a solution of TPP. The existence of the Soret absorption band at 417 nm in the UV–vis spectrum of TPP modified HPCD-*r*GO (TPP/HPCD-*r*GO) confirms the presence of the hydrophobic TPP in the cavity of cyclodextrin dispersed in water. A strong indication for the electron transfer from porphyrin to *r*GO comes from sufficient decrease of the fluorescence emission band of TPP/HPCD-*r*GO at 417 nm (see Figure 3.11). However the mixing of TPP with HPCD-GO (the HPCD functionalized GO before reduction) does not exhibit analogous fluorescence quenching. Because the host–guest interaction is also effective between TPP and HPCD-GO it is indicated that electron transfer is not available in this case because of the disability of GO to carry electrons.

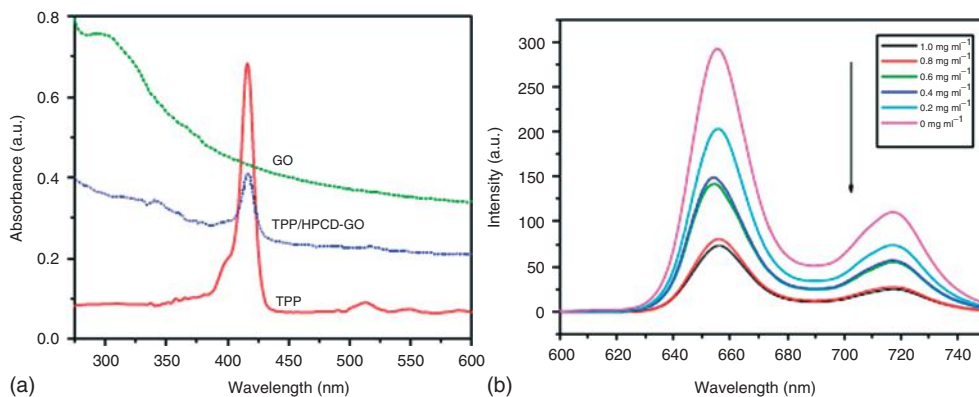


Figure 3.11 (a) UV-Vis spectra of GO, TPP, and TPP/HPCD-GO. (b) Fluorescence emission spectra of TPP before and after the addition of HPCD-GO in several concentrations. (Reprinted with permission from Ref. [26], Copyright 2010, Elsevier B.V.)

This indication is in agreement with the poor electrical conductivity of GO in comparison with its reduced form or pristine graphene. Finally the interaction of TPP/HPCD-*r*GO system with hemoglobin has been examined showing that such systems can be used as a biosensor of hemoglobin with promising results.

Polymers rich in hydroxyl groups are also easily grafted on GO by esterification. A characteristic paradigm is the reaction of polyvinyl alcohol (PVA) with GO. This esterification has been performed directly or through the formation of the reactive acyl chloride intermediate. The PVA functionalized GO (PVA-GO) is highly dispersible in water and dimethylsulfoxide. This dispersibility is retained even after the partial reduction of PVA-GO by hydrazine [27]. In addition, the product (PVA-*r*GO) showed significant changes in crystallinity after the reduction. TGA also indicated enhanced thermal stability of the nanocomposites (Figure 3.12).

In several cases polymers that are not hydroxyl functionalized can be modified properly in order to be available for esterification. For example, poly(vinyl chloride) is substituted by para-hydroxyl-phenylthio groups which then can act as reactive sites in esterification with carboxyl groups of GO [28]. Hydroxymethyl terminated of poly(3-hexylthiophene) (P3HT-CH₂OH) has also been grafted on graphene by esterification. PH3T and its derivatives are conjugated polymers that are used in photovoltaic systems as photoactivated electron donors in combination with electron acceptor molecules such as C₆₀ derivatives with the most well-known [6, 6]-phenyl-C61-butyric acid methyl ester (PCBM). The P3HT-CH₂O-GO composite product showed much higher power conversion efficiency (about 0.6%) in comparison with pure (P3HT) or a simple mixture of P3HT and GO (ranged between 0.18 and 0.20%) applied in a bilayer photovoltaic device [29, 30] (Figure 3.13).

Apart from these methods where a pre-synthesized polymer is covalently bonded on GO surface (“grafted to” procedure), a polymer/GO composite can be formed by the atom transfer radical polymerization method (ATRP) when the initiator is chemically bonded on the GO surface. In this “grafted from” method the polymerization starts from the graphene surface and the polymer chains that are developed are chemically bonded on GO at their ends. The ATRP method has been used for the preparation of composites with the covalent attachment between GO nanosheets and polymers such as polystyrene (PS), poly-butyl-acrylate, and PMMA [32]. A characteristic example is the formation of a PMMA/GO composite (see Figure 3.14) [33]. The first step of the procedure is the adaptation of an ethyleneglycol molecule to carboxylic acids, which then in the second step is substituted by the polymer initiator 2-bromo-2-methylpropionyl bromide. The third step is the polymerization that starts by the addition of methyl methacrylate monomer and the appropriate catalysts. The as-prepared GO-PMMA product was further dispersed as a filler in a PMMA polymer matrix leading to a mechanical reinforcement of the final PMMA composite. The higher concentration of GO-PMMA in the polymer without the appearance of aggregates cannot exceed 1% w/w.

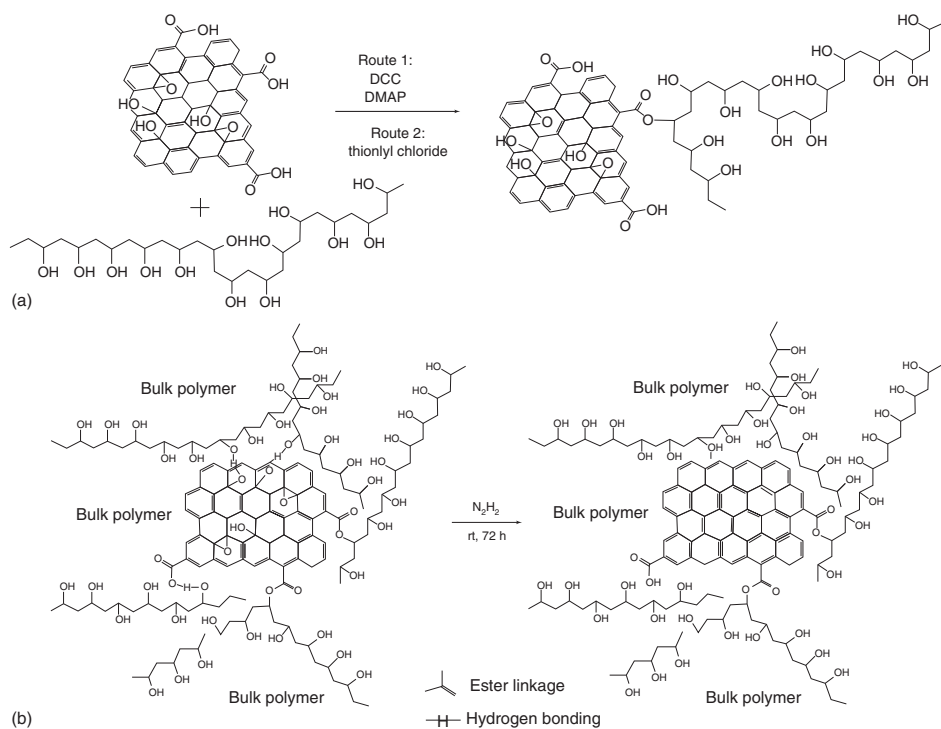


Figure 3.12 (a) Esterification of GO by PVA with two different procedures. (b) Partial reduction of PVA functionalized GO by hydrazine. (Reprinted with permission from Ref. [27], Copyright 2009, American Chemical Society.)

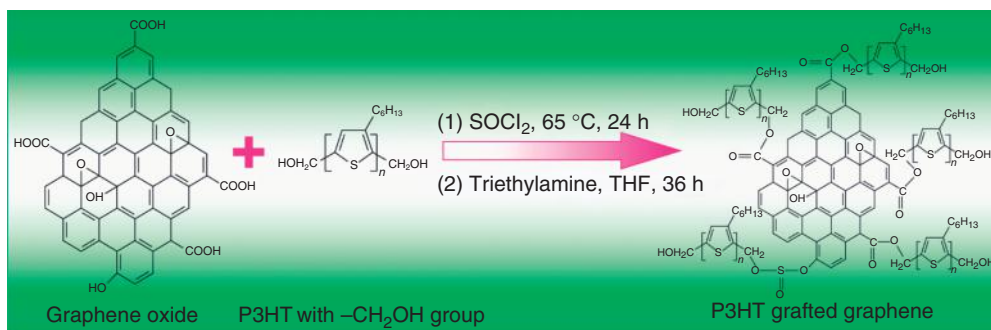


Figure 3.13 Esterification of GO with -CH₂OH terminated P3HT. (Reprinted with permission from Ref. [30], Copyright 2010, American Chemical Society.)

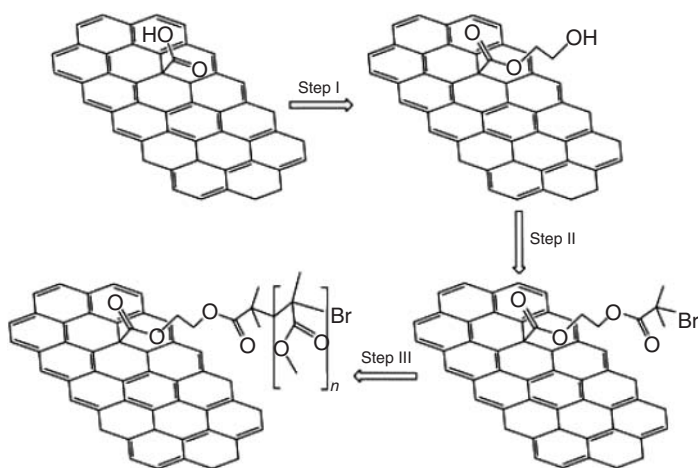


Figure 3.14 Atom transfer radical (ATR) polymerization of PMMA starting from the surface of GO. (Reprinted with permission from Ref. [33], Copyright 2010, Royal Society of Chemistry.)

3.2.3

Functionalization of GO through Heterocyclic Ring Formation

The presence of carboxyl group at the graphitic surface in GO offers the opportunity of performing miscellaneous organic reactions such as the formation of benzoxazole and benzimidazole heterocyclic rings by the condensation of carboxylic acids and an *o*-amino phenol or a *o*-phenyl diamine, respectively, in the presence of polyphosphoric acid as catalyst (see Figure 3.15) [34]. The functionalization is then followed by a reduction that removes the unreacted oxygen groups and restores the aromatic character of graphene. The final benzoxazole reduced graphene oxide and benzimidazole reduced graphene oxide derivatives (BO-*r*GO and BI-*r*GO, respectively) were characterized among others by XRD spectroscopy. The XRD pattern of

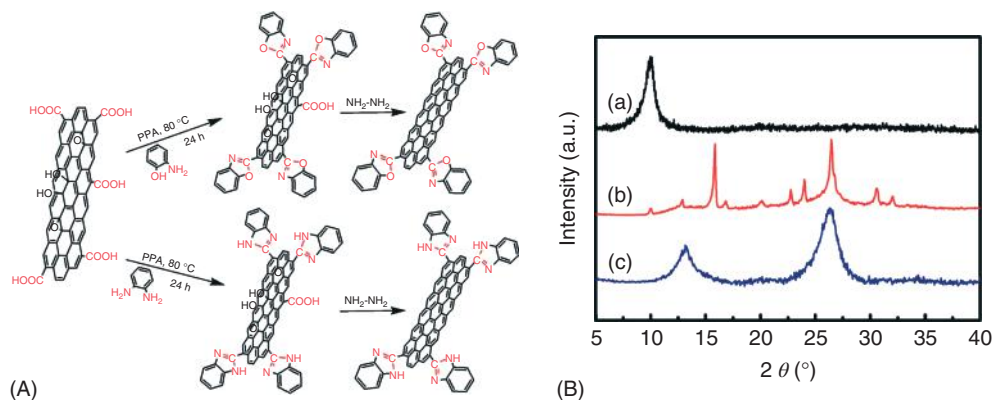


Figure 3.15 (A) The formation of heterocyclic rings by the condensation of C=O and *o*-aminophenol or *o*-diaminobenzene. (B) The XRD pattern of (a) GO, (b) BO-rGO, and (c) BI-rGO. (Reprinted with permission from Ref. [34], Copyright 2012, Royal Society of Chemistry.)

the row GO has a characteristic intense peak at 9.98° , which corresponds to an interlayer distance of 0.88 nm and it is attributed to the oxygen functionalities of GO. The XRD pattern of the functionalized BO-rGO and BI-rGO have a peak at $13\text{--}16^\circ$ which corresponds to higher d-spacing and it is attributed to the intercalation of the heterocyclic rings between the graphitic layers (see Figure 3.16). A second peak around 26.3° indicates the existence of unreacted but reduced GO nanosheets that

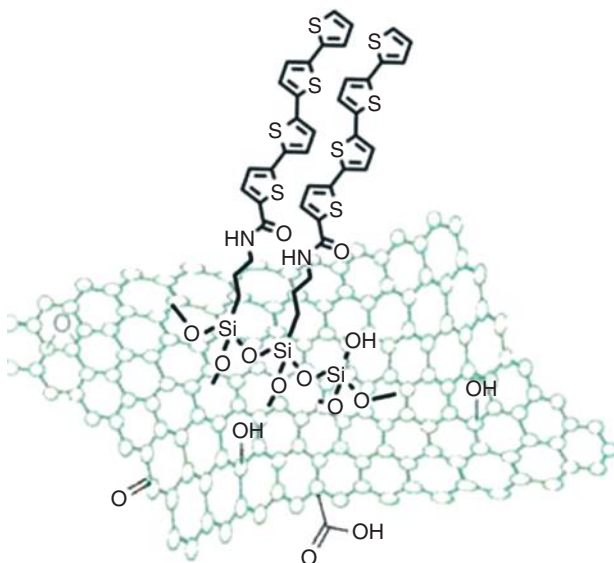


Figure 3.16 Oligothiophene functionalized GO by silanization of hydroxyl groups of GO. (Reprinted with permission from Ref. [35], Copyright 2010, Royal Society of Chemistry.)

have been restacked. Both products showed high specific capacitance (730 F g^{-1} for BO-rGO and 781 F g^{-1} for BI-rGO, respectively) and good stability when they are used as electrodes in supercapacitors.

3.3 The Role of Hydroxyl Groups of GO

Apart from amidation and esterification reactions that are related to the carboxylic groups of GO and nucleophilic addition to epoxide, other reactions originated by the chemical reactivity of hydroxyl groups have been also developed. These groups are spread mainly on the core surface of the graphitic layer [36]. A characteristic reaction of hydroxyl groups of GO is the silylation – the reaction between a hydroxyl group and an ethoxy substituted silane. For example, triethoxysilyl terminated quaterthiophene has been attached on GO by silylation [37]. The reaction was carried out with the assistance of microwave irradiation in order to achieve a better yield in a shorter time.

Octadecane aliphatic chain has been also attached on GO by etherification [38]. 1-Bromo-octadecane reacts with hydroxyl group of GO in the presence of pyridine under reflux. The resulting octadecyl functionalised GO (OD-rGO) is partially reduced possibly by the action of pyridine. The characterization of the product was based on its FT-IR spectrum with the presence of the doublet bands at 2854 and 2923 cm^{-1} , which are attributed to the antisymmetric and symmetric C–H stretching vibrations of $-\text{CH}_2-$ from OD groups and the band at 1200 cm^{-1} assigned to the C–O–C asymmetric stretch. The thickness of the functionalized nanosheets was increased to 1.7 nm relative to 0.6 nm , which is the thickness of GO. The last observation is in agreement with the presence of the alkyl chains between the GO layers when the latter is in solid phase (Figure 3.17).

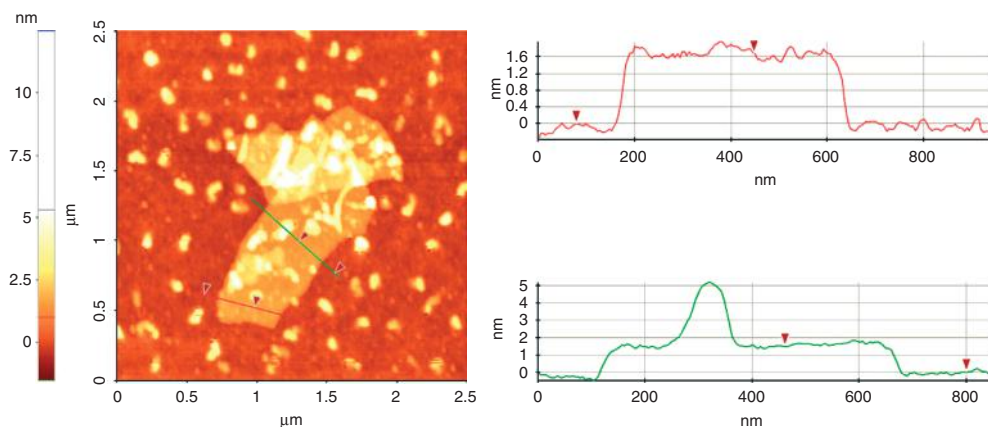


Figure 3.17 AFM image of OD-rGO, and the height profile of a separated nanosheet. (Reprinted with permission from Ref. [38], Copyright 2010, Elsevier B.V.)

3.4 Miscellaneous Additions

3.4.1

Reaction of Carboxylic Acid and Hydroxyl Groups with Isocyanate Derivatives

In several applications the hydrophobic character of a graphene derivative is favored. The homogeneous mixing of GO with a hydrophobic compound is not favored without an analogous modification of GO, which will induce in GO a similar hydrophobic character. For example, in order to improve the performance of photovoltaic systems, the blending of GO with the hydrophobic P3HT is much more efficient when the hydrophilic GO has been modified to a hydrophobic derivative. This transformation has been performed by the functionalization of GO with phenylisocyanate (PhCON-GO). In general organic isocyanate can react with both carboxyl and hydroxyl groups of GO forming amide or carbamate esteric bonds [37, 39]. The phenyl functionalized GO is then dispersible in dichlorobenzene and can be mixed with P3HT producing a homogeneous blend that has been used successfully in photovoltaic devices. Excitation of PhCON-GO at 422 nm resulted in the appearance of a fluorescence band centered near 580 nm which however is partly quenched in comparison with pure P3HT, indicating the electronic interaction between the two components. This interaction was then confirmed by the improvement of the performance of a photovoltaic device where P3HT had been replaced by PhCON-GO/P3HT composite [40].

The addition of isocyanate functionalized organic compounds has been used in several GO derivatives. 1,4-Diisocyanato benzene or 4,4'-diisocyanato-3,3'-dimethylbiphenyl are organic molecules that have a rigid core – phenyl or biphenyl – and two reactive isocyanate groups at opposite places. The reaction of these molecules with GO leads to a cross linking of the GO layers and the formation of a pillared lamellar hybrid porous material (see Figure 3.18) [41]. However, the BET (Brunauer–Emmett–Teller) surface area was not increased by the insertion of the organic spacer between the graphitic layers in comparison with that of GO, mainly because of the limited appearance of rigid spacers.

3.4.2

Reaction of Epoxides with Carboxylic Acids or Hydroxyl Groups

Epoxides can react with GO either by carboxyl groups forming α -hydroxyl esters or by hydroxyls forming α -hydroxyl ethers. Methyl oleate epoxide addition is a characteristic example of this procedure that produces oleate functionalized GO (oleo-GO) by a simple heating of a mixture of the two components without solvents or catalysts. The heating process helps further in the partial reduction of GO during the action of the epoxide. The oleo-rGO product showed an amphiphilic character as the functional groups consisted of long aliphatic chains and hydroxyl

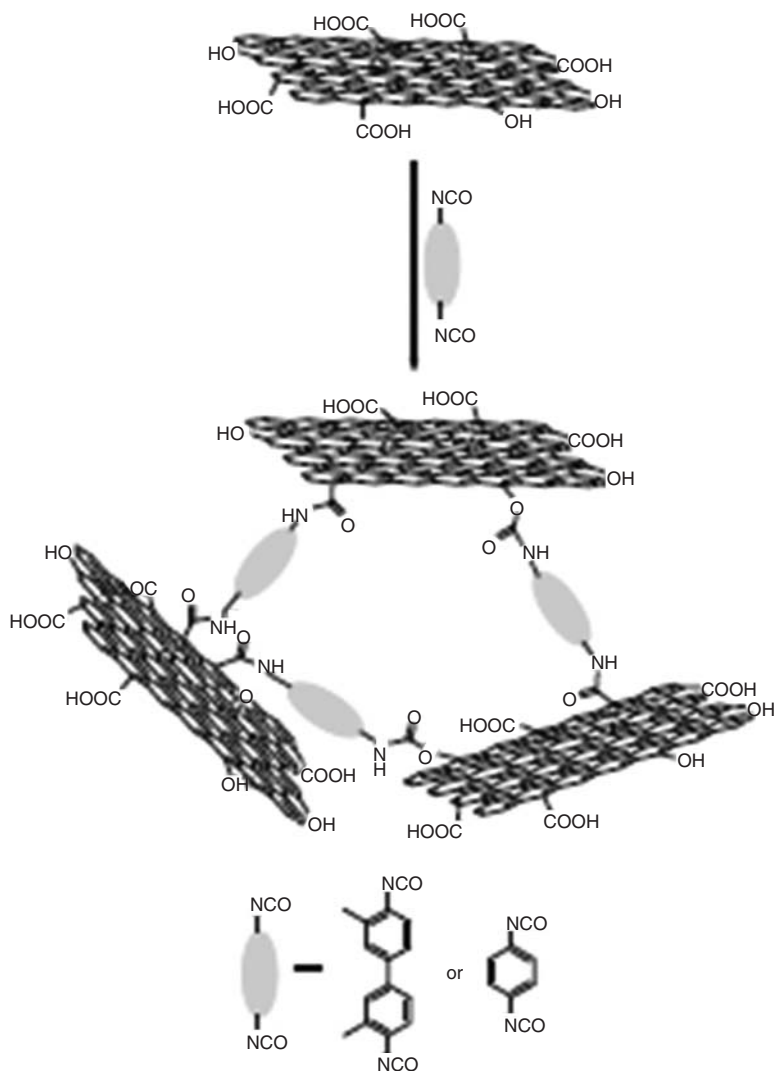


Figure 3.18 The cross linking reaction of diisocyanate organics with GO. (Reprinted with permission from Ref. [41], Copyright 2009, Elsevier B.V.)

groups as well, and it was homogeneously mixed with poly-lactic acid affording a polymer-graphene nanocomposite with improved mechanical properties [42] (Figure 3.19).

Carboxylic acids of GO can be covalently attached on ferrocene through acylation reaction [43]. In this reaction carboxylic acid groups of GO are involved in a Friedel Crafts selective monoacylation using activated acidic alumina and trifluoroacetic anhydride as catalyst (Figure 3.20).

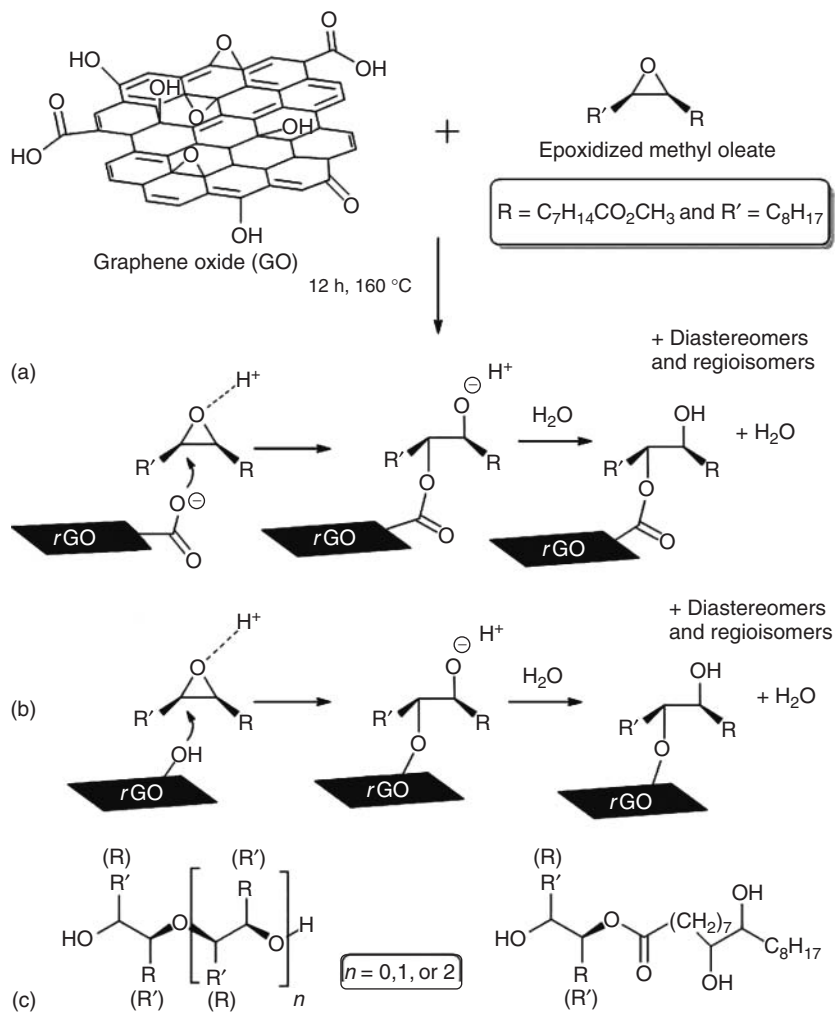


Figure 3.19 The reaction of GO with methyl oleate epoxides and the possible reaction paths. (a) esterification, (b) etherification, and (c) byproducts of ether or ester derivatives that occurs by the possible

condensation of epoxides. (Reprinted with permission from Ref. [42], Copyright 2012, Wiley-VCH Verlag GmbH & Co KGaA, Weinheim.)

3.4.3

Interaction of Ammonia with Carboxylic Acids and Epoxides of GO

The treatment of GO with ammonia water (aqueous solution of ammonia) at high temperature (180 °C, in a high boiling point solvent such as ethyleneglycol) resulted in both the partial reduction of GO and the functionalization of graphene with amide and amine groups [44]. The partial reduction of GO was directly observed

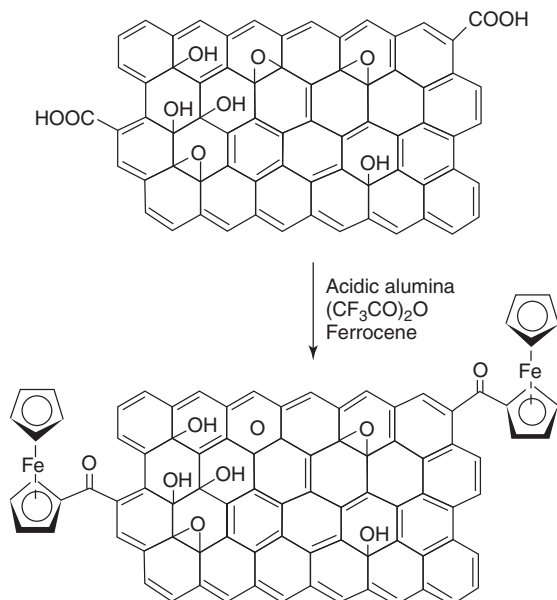


Figure 3.20 Functionalization of GO by ferrocene through a Friedel Crafts acylation. (Reprinted with permission from Ref. [43], Copyright 2010, Royal Society of Chemistry.)

by the characteristic change of color as the brownish GO dispersion changed to the dark gray color of *rGO*. The amide groups ($-\text{CONH}_2$) produced by the reaction of ammonia with carboxylic acids whereas the nucleophilic substitution of ammonia to epoxide resulted in the ring opening and the formation of an amine and hydroxyl group in place of an epoxide ring. The amine modified *rGO* (*rGO*- NH_2) showed improved dispersibility in water and polar organic solvents (DMF, THF) and enhanced BET surface area in the solid form in comparison with GO. The extent of the overall substitution of the oxygen of GO by nitrogen is indicated by XPS spectroscopy. The carbon to oxygen ratio was increased from ~ 1.7 in GO to ~ 10.6 in the final product *rGO*- NH_2 showing a successful reduction procedure. The subsequent carbon to nitrogen ratio depends on the amount of ammonia during the reaction and ranges between ~ 10 and ~ 52 (Figure 3.21).

3.4.4

Enrichment of GO in Carboxylic Acids

In order to achieve better dispersion of GO in polyaniline, GO can be enriched in carboxylic acid groups, which interact better than hydroxyl and epoxy groups with polyaniline chains [45]. A simple way to achieve this enrichment is based on the transformation of epoxy and hydroxyl groups to carboxyl terminated functional groups. First the epoxide rings are opened by the reductive action of HBr affording hydroxyls. Then the hydroxyls are functionalized by esterification with a

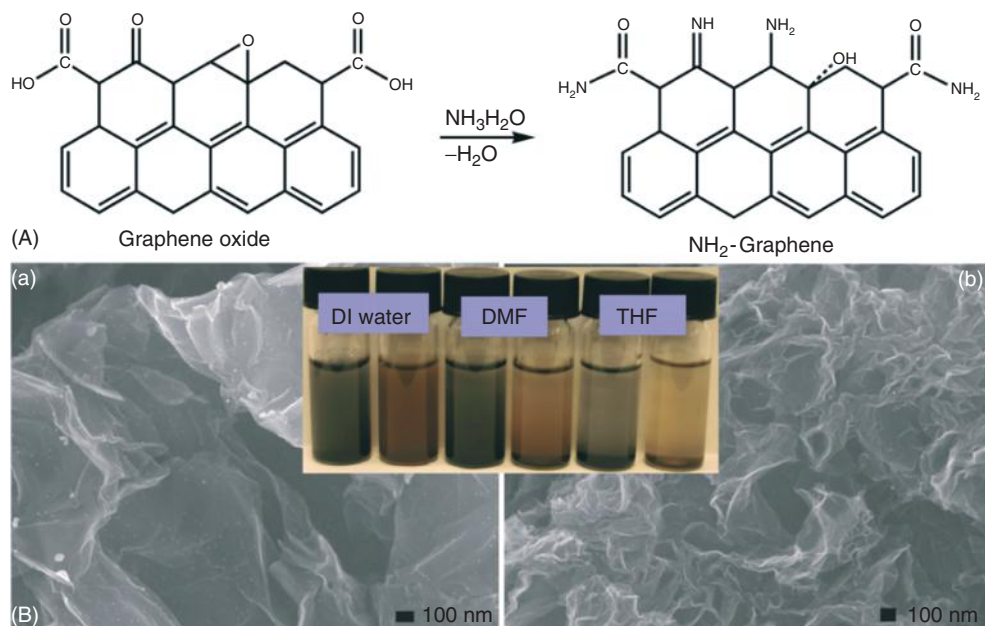


Figure 3.21 (A) Schematic representation of the interaction of ammonia water with GO. (B) SEM images of GO (a) and amine modified rGO (b) and in the inset:

the photographs of 0.3 mg ml^{-1} rGO-NH₂ and GO in deionized water, DMF, and THF, respectively. (Reprinted with permission from Ref. [44], Copyright 2011, Elsevier B.V.)

double carboxylic acid such as oxalic. By this procedure the overall GO surface is functionalized by free carboxylic acid groups (GO-COOH). The carboxyl enriched GO is easily dispersible in aniline without aggregate formation because of the strong repulsive forces of the carboxylic groups. As a consequence GO-COOH will be entrapped between the developed polymeric chains during the polymerization of aniline and thus well dispersed in the finally formed polyaniline/GO-COOH composite material where the graphitic layers and polymer chains are strongly held together by H bonding and electrostatic interactions.

3.4.5

Addition of Gallium-Phthalocyanine (Ga-Pc) to GO through Ga–O Covalent Bond

Gallium substituted porphyrin (Ga–O–Pc) has been attached axially on GO by a covalent Ga–O bond between the metal of the porphyrin and oxygen of hydroxyl groups of GO (see Figure 3.22) [46]. The aryl rings of porphyrin are substituted by *tert*-butyl groups. The formation of Ga–O covalent bond is confirmed by XPS spectroscopy where a characteristic peak at 20.8 eV assigned to Ga–Cl bond is shifted, after the reaction with GO, to 17.2 eV assigned to Ga–O. The UV–vis spectrum of Ga-porphyrin functionalized GO (Ga–O–Pc/GO) contains the characteristic bands of the components. On the other hand, the fluorescence spectrum of the composite

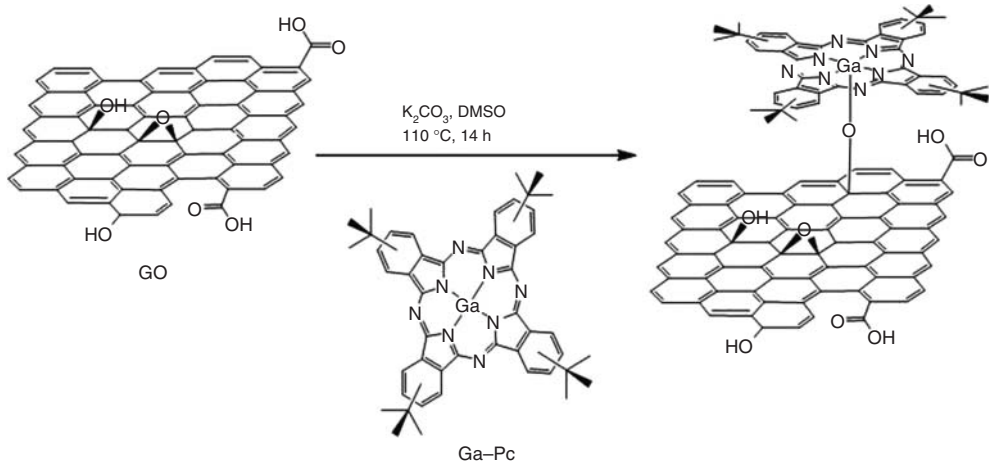


Figure 3.22 The functionalization of GO with Ga-Pc by an axial Ga-O covalent bond [46].

is highly influenced – the emission band at 700 nm is decreased – by a quenching process that indicates sufficient electron transfer between Pc and GO. Finally, the hybrid composite showed much better NLO response and OL performance than GO [46].

3.5

The Role of Epoxide Groups of GO

3.5.1

Nucleophilic Addition of Amine to Epoxides

Apart from the carboxylic acid groups that are located at the edges of GO layers, epoxides also exist and are located mainly at the core of GO layers. Amine substituted organic compounds, from simple alkylamines [47] and arylamines [48] to more specific organic molecules [49], chromophores [50] and polymers [51–53], react with these epoxides and simultaneously attach covalently with the ring opening of epoxy groups. 6-Amino-4-hydroxy-naphthalenesulfonic (ANS) acid is an organic molecule that is attached by its amine group to GO. ANS has sulfonic and hydroxyl groups that offer high hydrophilicity to this molecule as well as to the ANS functionalized GO. After the reaction of ANS with GO and the formation of the organically modified GO (ANS-GO), the latter was reduced by hydrazine in order to restore to the product its graphitic character. Although the removal of oxygen groups from functionalized graphene influences the hydrophilic character negatively, ANS-rGO is highly hydrophilic (3 mg ml^{-1}) owing to the presence of hydroxyl and sulfonic groups of ANS [48] (Figure 3.23).

GO has been functionalized by aminopropyl triethoxysilane (APTS) by the same reaction. The grafted silane groups were then slowly hydrolyzed in an excess of

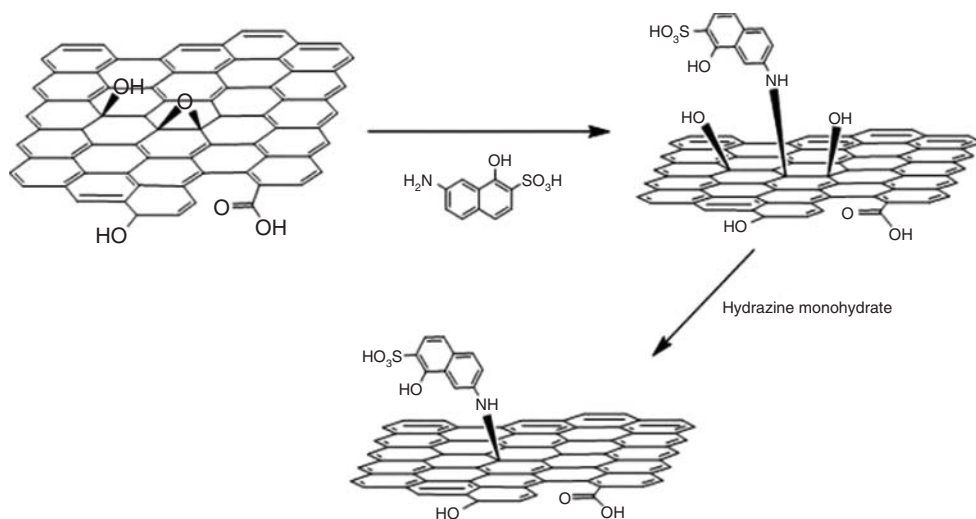


Figure 3.23 Functionalization of GO by ANS followed by reduction of GO by hydrazine [48].

APTS forming a GO incorporated silica monolith, with enhanced mechanical properties [54]. Apart from amidation reaction of ODA that presented in Section 3.1, the latter also react with epoxide groups of GO under certain conditions. Simultaneously with the nucleophilic addition to epoxides, ODA acts as a reductive agent for GO. As a consequence a simple reflux heating of GO in excess of ODA leads to the formation of partially reduced ODA functionalized GO (*r*GO-ODA). During the reaction, the XRD pattern of the layered *r*GO-ODA product showed a diffraction peak at 4.9° which corresponds to a spacing of 1.8 nm between the graphitic layers after 10 h of refluxing, which is further increased to 2.3 nm (2 h Bragg angle of 3.7°) after 20 h of refluxing. The increased distance between the layers is a further indication for the intercalation of the oleylamine chains. The presence of ODA in the final product is characterized by the appearance of the two peaks at 2919 and 2848 cm^{-1} in the FT-IR spectrum resulting from the $-\text{CH}_2$ stretching of the octadecyl chain together with the peak at 720 cm^{-1} . In the XPS spectrum of GO-ODA the peaks that correspond to C–O and C–O–C groups are weakened in comparison with GO, indicating the simultaneous reduction of GO during the alkylamine addition, while a new peak that corresponds to C–N bonds appears [55] (Figure 3.24).

The final product showed a highly lipophilic character and is homogeneously dispersible in PS owing to the presence of long aliphatic chains, and because of the partial reduction of GO its color turns to black in contrast to the brownish color of GO. The polymer composite that was produced (PS-GO-ODA) showed a sharp transition from insulative to conductive character with a low percolation threshold at 0.45 vol% and a final conductivity of $4.6 \times 10^{-1}\text{ S m}^{-1}$ in a concentration

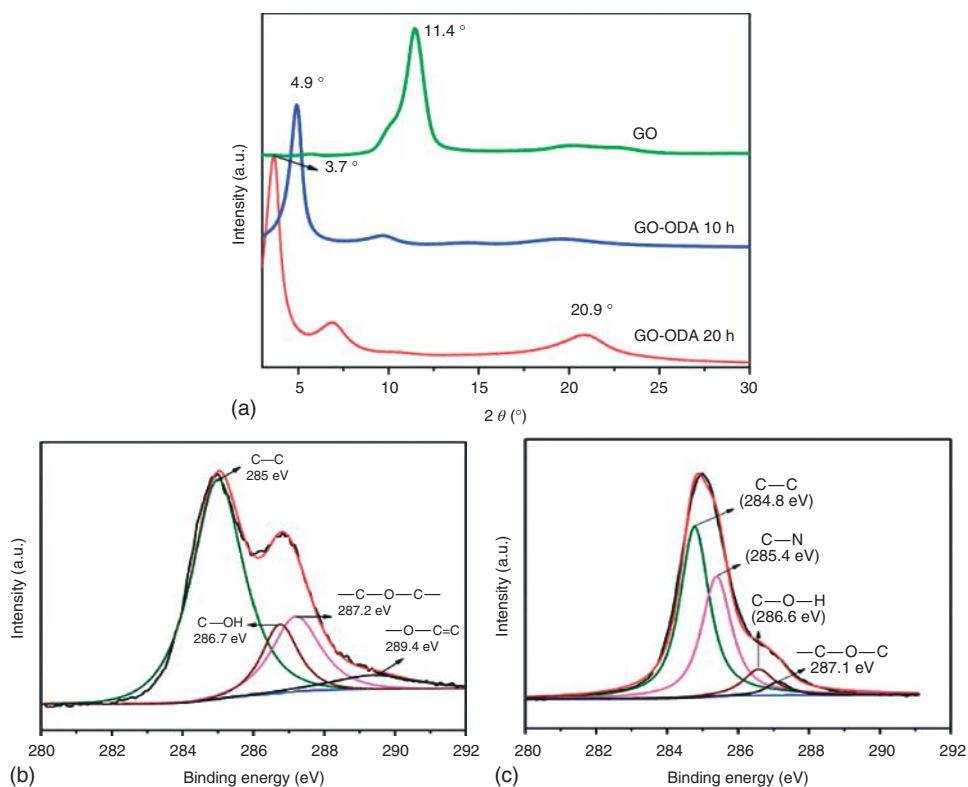


Figure 3.24 (a) XRD spectra of GO and GO-ODA (b) and FT-IR spectra of GO, ODA, and GO-ODA (c). XPS spectra of GO and GO-ODA. (Reprinted with permission from Ref. [55], Copyright 2011, Elsevier B.V.)

of 0.92 vol% [55] (Figure 3.25). A similar behavior as regards the additive and the reductive character has been presented by ethylamine and diethylamine [56].

The nucleophilic addition of amines to epoxides can be also used for the functionalization of GO by ionic liquids that offer to GO remarkable dispersibility because of their ionic character [57].

3.5.2

Addition of Chromophores

Amine terminated zinc phthalocyanine (Zn-PC) can be grafted on GO by reaction with epoxy groups under analogous conditions (see Figure 3.26) [50]. The electron-donor hybrid material showed a characteristic fluorescence quenching behavior that can be attributed to the strong interaction of the two covalently attached components. Further, a photoelectrochemical cell, which has been produced by the deposition of a thin film of ZnPc-GO onto a nanostructured SnO_2 and between two optical transparent electrodes, showed an ISPE value of 2.2% which is one order

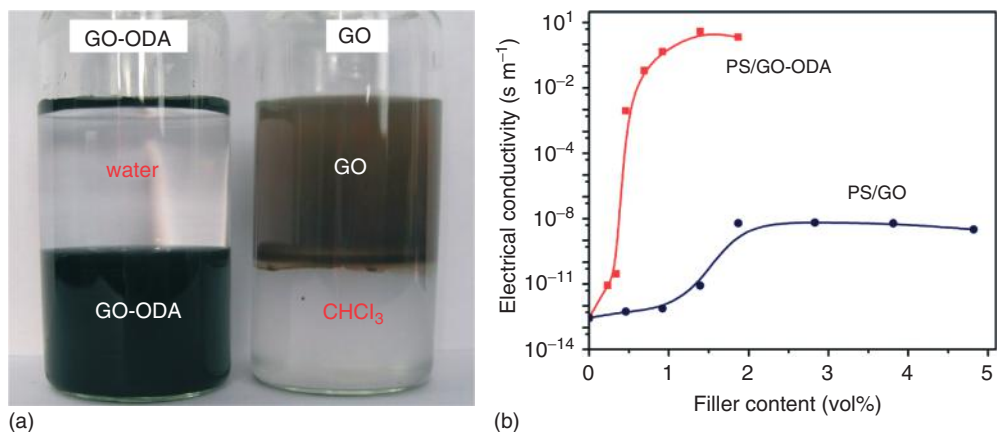


Figure 3.25 (a) Dispersion of GO and GO-ODA in a chloroform/water biphasic system. The color of GO-ODA is indicative for the partial reduction of GO. (b) The electrical conductivity of PS-GO-ODA and PS-GO as a function of the filler content. (Reprinted with permission from Ref. [55], Copyright 2011, Elsevier.)

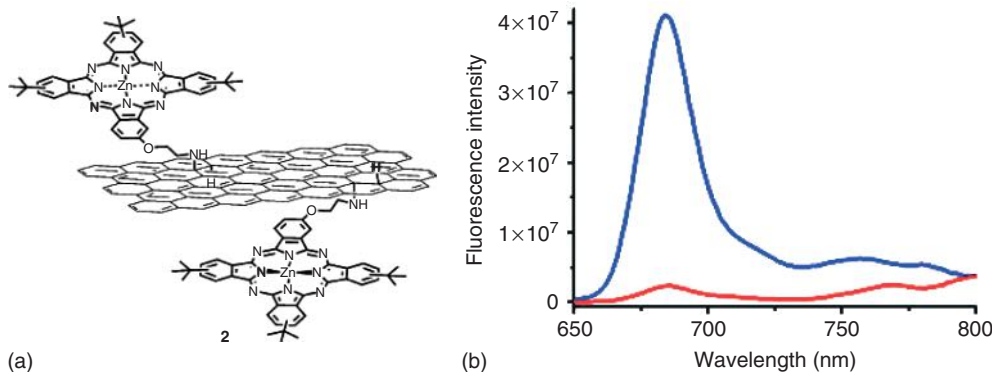


Figure 3.26 (a) Covalent bonded Zn-Pc on GO. (b) Fluorescence spectra of Zn-Pc (the blue line) and the quenched fluorescence band of Zn-Pc/GO (red line). (Reprinted with permission from Ref. [50], Copyright 2012, American Chemical Society.)

of magnitude larger than a similar cell prepared with pristine graphene instead of ZnPc-GO.

3.5.3

Addition of Polymers

Polymers with a large number of amine groups can be grafted on GO through the nucleophilic addition to epoxide groups. Polyallylamine (PAA) is a long aliphatic

alkyl chain functionalized by short reactive methylamine side chains [52]. Similarly poly-L-lysine (PLL) has been grafted covalently on GO offering high dispersibility in water and biocompatibility [53].

3.6

Post Functionalization of GO

In several applications a specific functionalization of GO is needed that is not always possible to produce from the organic chemistry of oxygen functional groups that are available on graphene surfaces. In these cases a post functionalization of the organically premodified graphene nanoplatelets is highly favorable. The importance of post functionalizations of GO is of great importance as it offers the opportunity to design the chemical procedure in order to achieve the best results.

3.6.1

Post Functionalization of Organically Modified GO via Click Chemistry

A variety of organic reactions that have common characteristics are in general described as “click chemistry.” Usually this term characterizes the covalent attachment of different organic parts in one compound with a simple, easy, and high yielding organic reaction. One of the most popular reactions of this category is the copper catalyzed 1,3 Huisgen cycloaddition between azides and alkynes (see Figure 3.27). The condensation of the two functionalities resulted in the formation of a 1,2,3-triazole heteroaromatic ring that serves as a link between the two components. The application of this reaction in azide functionalized GO can lead to the attachment of alkyne terminated polymers [58, 59] or organic compounds [58] on graphitic surface as shown in the Figure 3.28. The azide functionalization of GO has been performed by the amidation of carboxylic groups of GO with 3-azidopropyl-1-amine.

Another interesting application of a click reaction is used in the formation of a water dispersible poly(*N*-isopropylacrylamide) (PNIPAM) /GO composite [60]. The first step of the procedure is the attachment of propargylamine on GO through amidation which leads to alkynyl functionalized GO nanoplatelets. Azide substituted PNIPAM was then reacted with alkynyl-GO by 1,3 Huisgen cycloaddition that resulted in the connection of the polymer with GO nanoplatelets with the triazole ring linkers. The PNIPAM/GO composite can function as a potential carrier for the drug delivery of hydrophobic drugs such as camptothecin, as PNIPAM is a highly hydrophilic and biocompatible polymer (Figure 3.29).

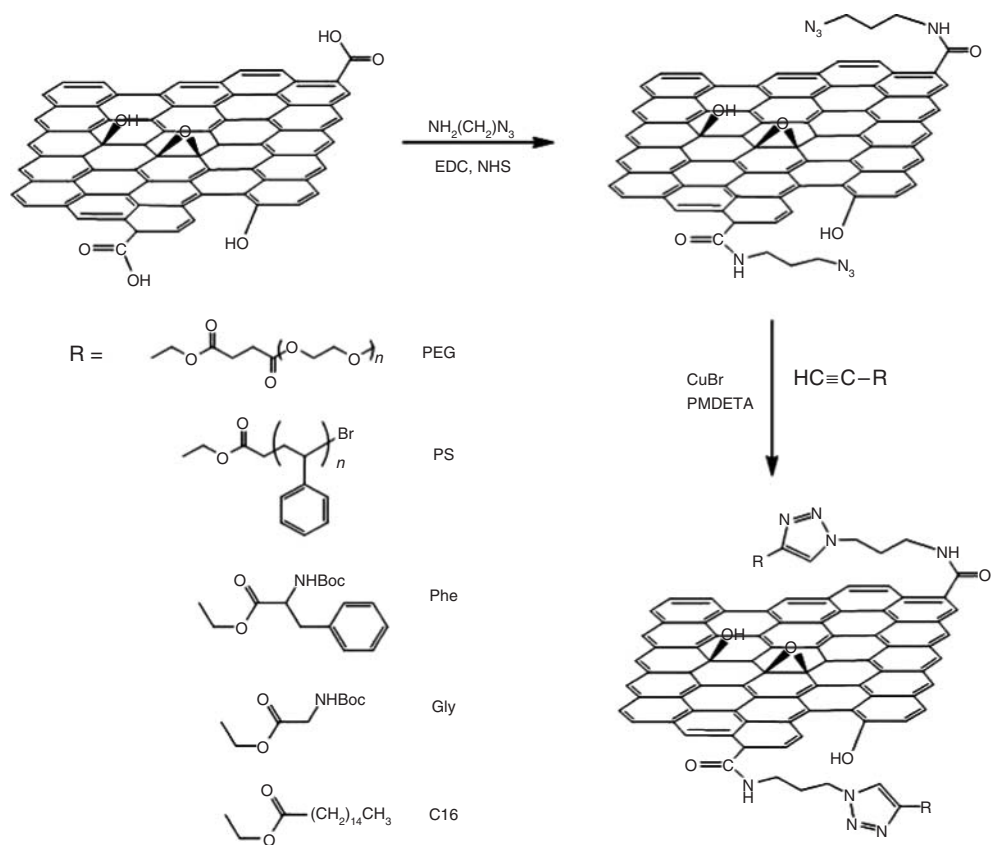


Figure 3.27 1,3 Huisgen cycloaddition of azide functionalized GO with several alkyne terminated polymers and small organic molecules [58].

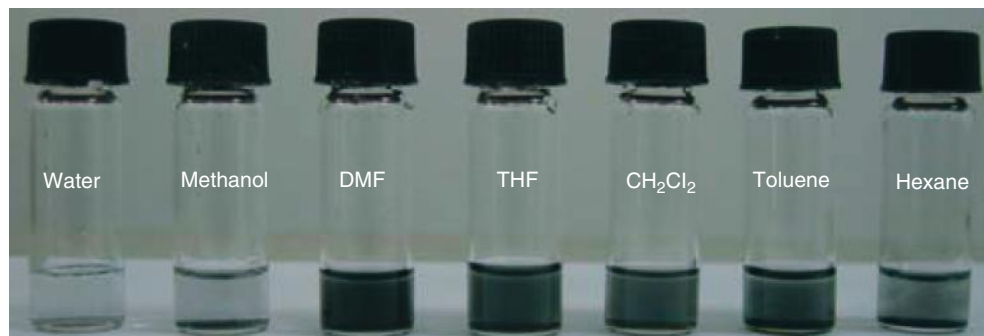


Figure 3.28 Dispersion of PS functionalized GO by azide-alkyne 1,3 cycloaddition. (Reprinted with permission from Ref. [59], Copyright 2010, Royal Society of Chemistry.)

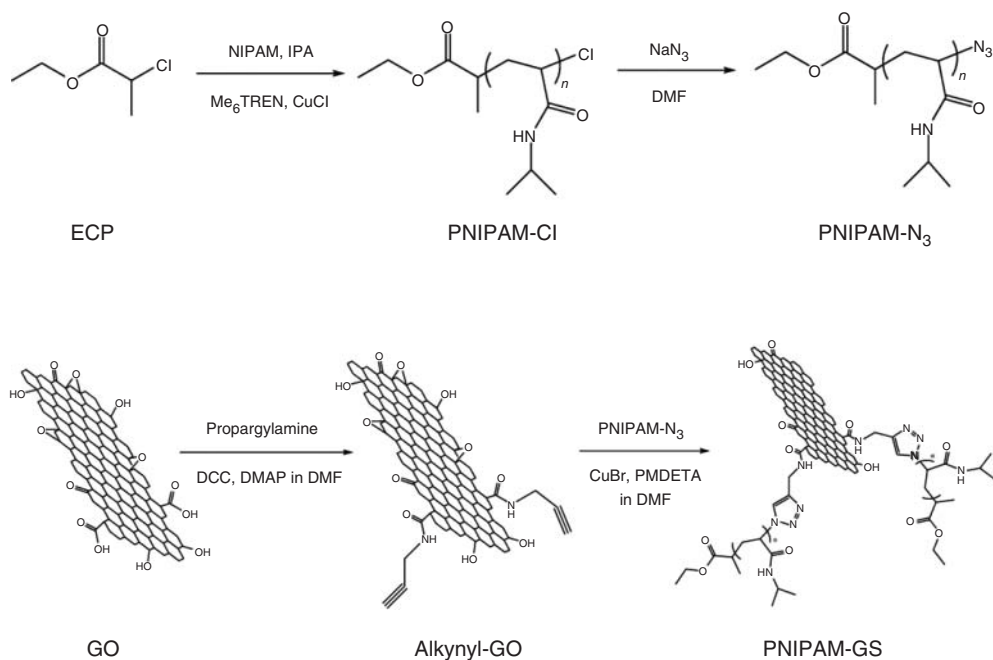


Figure 3.29 Click reaction between alkyne functionalized GO and azide substituted PNIPAM polymer. (Reprinted with permission from Ref. [60], Copyright 2011, Wiley-VCH Verlag GmbH & Co KGaA, Weinheim.)

3.6.2

Counter Anion Exchange

The attachment of organic functional groups as counter anions in GO that are pre-functionalized by an ionic compound can be seen also as a post functionalization reaction of GO. For example, the attachment of 1-(3-aminopropyl)imidazole on GO carboxylic acids by amidation followed by the addition of 1-bromobutane on the imidazole ring leads to an ionic imidazole derivative attached on GO, with bromide anion (Br^-) as counter ion. The hydrophilic $[\text{Br}^-]$ imidazolium GO can be transformed to the lipophilic hexafluorophosphate anion $[\text{PF}_6^-]$ analog by the counter anion exchange of $[\text{Br}^-]$ by $[\text{PF}_6^-]$ that followed the treatment of GO derivative with NaPF_6 . Porphyrin functionalized by carboxylates can also be exchanged $[\text{Br}^-]$ in a similar reaction [61] (Figure 3.30).

The post functionalization reaction has been also used for the addition of ferrocene on GO nanoplatelets (see Figure 3.31). Ferrocene aldehyde has been covalently attached on amine pre-functionalized GO by a $\text{C}=\text{N}$ bond (Schiff base type). The amine functionalization of GO was performed by the covalent addition of diethylamine on carboxylic acids of GO by amidation [62].

Finally carboxylic acids of GO can be functionalized by polyglycerol chains by the addition of glycidol (a hydroxymethyl-ethylene oxide) to GO and opening of

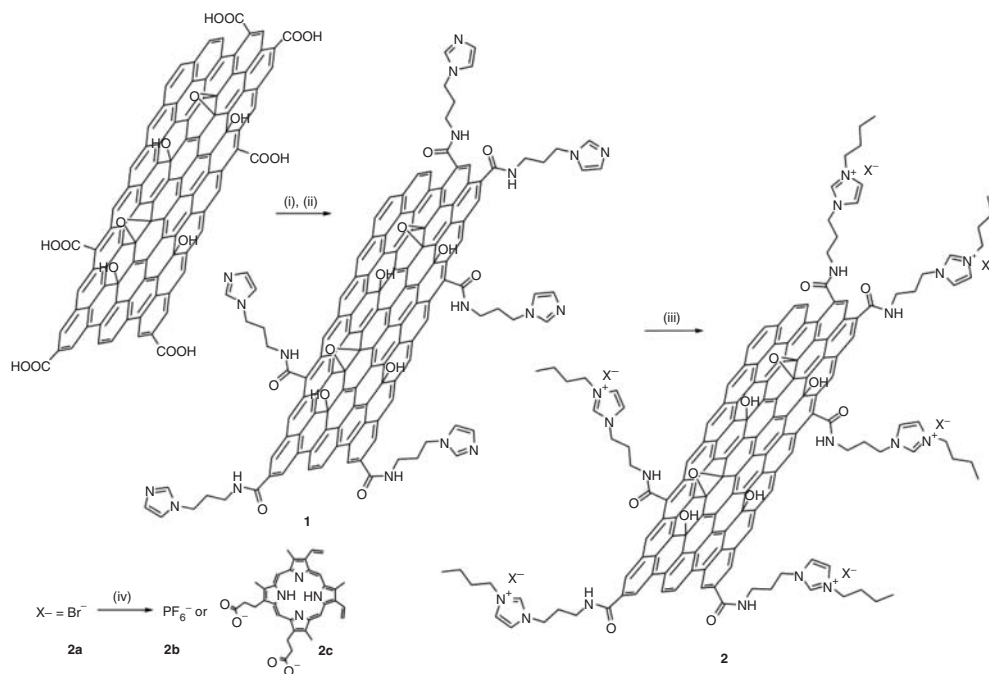


Figure 3.30 Preparation of imidazolium modified GO and counter anion exchange by $[\text{PF}_6^-]$ and a porphyrin anion derivative. (Reprinted with permission from Ref. [61], Copyright 2010, Elsevier V.B.)

the epoxide ring [63]. The highly hydroxylated GO is then used as a substrate for the immobilization of magnetic nanoparticles. The nanoparticles are made from metallic iron (Fe) nanoparticles covered by a gold (Au) layer that protects Fe from oxidation. Fe@Au nanoparticles are externally covered by 4-mercaptophenyl boronic acid through a Au–S bonds. The boronic acid functionalized Fe@Au are covalently bonded on the polyglycerol functionalized GO as presented in the next Figure 3.32.

3.7

Conclusions

The several oxygen functional groups of GO offer to graphene a wide variety of organic derivatives thanks to their rich organic chemistry. GO is used as graphene precursor, which is produced easily in high yield; it is functionalized without further decrease of its aromatic character and can finally be reduced restoring its aromatic character in part. The organically functionalized GO are easily dispersible in organic solvents or in water; a property that facilitates a further post functionalization of graphene derivatives.

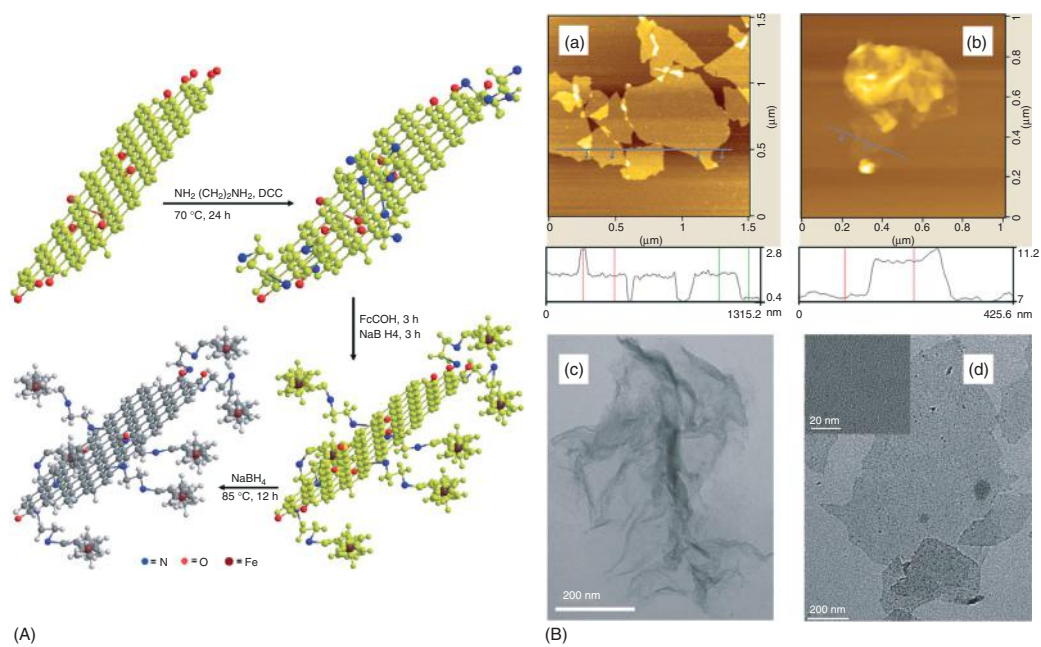


Figure 3.31 (A) Post functionalization of amine modified GO by ferrocene aldehyde. (B) AFM (upper) and TEM (down) images of GO (a,c) and ferrocene-GO (b,d). (Reprinted with permission from Ref. [62], Copyright 2012, Royal Society of Chemistry.)

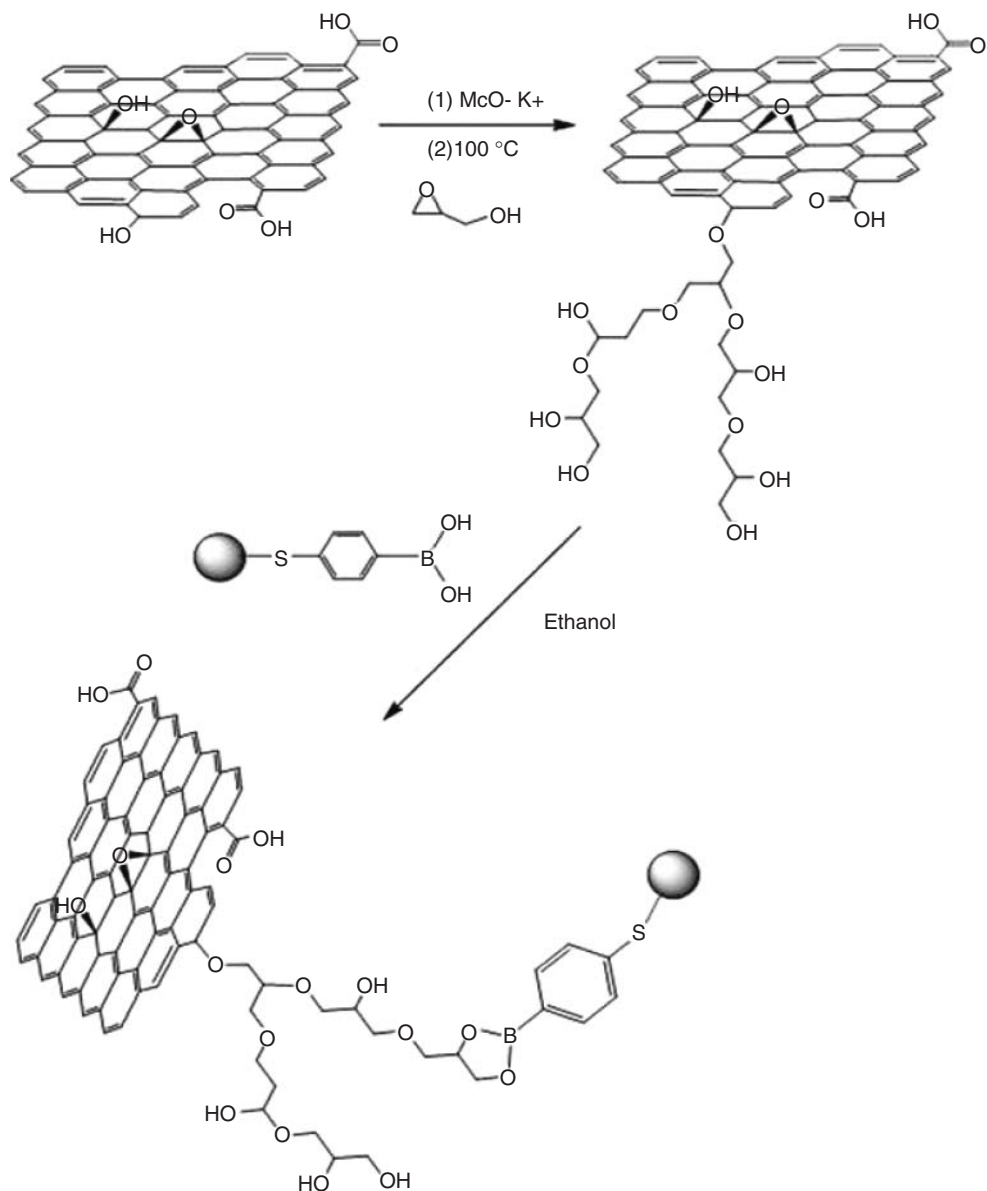


Figure 3.32 Immobilization of Fe@Au nanoparticles on polyglycerol functionalized GO [63].

References

1. Chen, J., Hamon, M.A., Hu, H., Chen, Y., Rao, A.M., Eklund, P.C., and Haddon, R.C. (1998) *Science*, 282, 95.
2. Hirsch, A. and Vostrowsky, O. (2005) *Top. Curr. Chem.*, 245, 193–237.
3. Niyogi, S., Hamon, M.A., Hu, H., Zhao, B., Bhowmik, P., Sen, R., Itkis, M.E.,

- and Haddon, R.C. (2002) *Acc. Chem. Res.*, **12**, 1105.
4. Balasubramanian, K. and Burghard, M. (2005) *Small*, **1** (2), 180–192.
 5. Kuilla, T., Bhadra, S., Yao, D., Kim, N.H., Bose, S., and Lee, J.H. (2010) *Prog. Polym. Sci.*, **35**, 1350.
 6. Kim, H., Abdala, A.A., and Macosko, C.W. (2010) *Macromolecules*, **43**, 6515–6530.
 7. Potts, J.R., Dreyer, D.R., Bielawski, C.W., and Ruoff, R.S. (2011) *Polymer*, **52**, 5–25.
 8. Niyogi, S., Bekyarova, E., Itkis, M.E., McWilliams, J.L., Hamon, M.A., and Haddon, R.C. (2006) *J. Am. Chem. Soc.*, **128**, 7720–7721.
 9. Cao, Y., Feng, J., and Wu, P. (2010) *Carbon*, **48**, 1670–1692.
 10. Choudhary, S., Mungse, H.P., and Khatri, O.P. (2012) *J. Mater. Chem.*, **22**, 21032.
 11. Shen, J., Shi, M., Ma, H., Yan, B., Li, N., Hu, Y., and Ye, M. (2010) *J. Colloid Interface Sci.*, **351**, 366.
 12. Liu, Z., Robinson, J.T., Sun, X., and Dai, H. (2008) *J. Am. Chem. Soc.*, **130**, 10876–10877.
 13. Zhang, S., Yang, K., Feng, L., and Liu, Z. (2011) *Carbon*, **49**, 4040–4049.
 14. Hu, H., Wang, X., Wang, J., Liu, F., Zhang, M., and Xu, C. (2011) *Appl. Surf. Sci.*, **257**, 2637–2642.
 15. Shen, J., Shi, M., Yan, B., Ma, H., Li, N., Hu, Y., and Ye, M. (2010) *Colloids Surf., B: Biointerfaces*, **81**, 434–438.
 16. Liu, Z.B., Xu, Y.F., Zhang, X.Y., Zhang, X.L., Chen, Y.S., and Tian, J.G. (2009) *J. Phys. Chem. B*, **113**, 9681–9686.
 17. Zhang, X., Huang, Y., Wang, Y., Ma, Y., Liu, Z., and Chen, Y. (2008) *Carbon*, **47**, 313–347.
 18. Liu, Y., Zhou, J., Zhang, X., Liu, Z., Wan, X., Tian, J., Wang, T., and Chen, Y. (2009) *Carbon*, **47**, 3113–3121.
 19. Xu, Y., Liu, Z., Zhang, X., Wang, Y., Tian, J., Huang, Y., Ma, Y., Zhang, X., and Chen, Y. (2009) *Adv. Mater.*, **21**, 1275–1279.
 20. Zhu, J., Li, Y., Chen, Y., Wang, J., Zhang, B., Zhang, J., and Blau, W.J. (2011) *Carbon*, **49**, 1900–1905.
 21. Karousis, N., Sandanayaka, A.S.D., Hasobe, T., Economopoulos, S.P., Sarantopoulou, E., and Tagmatarchis, N. (2011) *J. Mater. Chem.*, **21**, 109.
 22. Matte, H.S.S.R., Jain, A., and George, S.J. (2012) *RSC Adv.*, **2**, 6290–6294.
 23. Zhang, X., Feng, Y., Huang, D., Li, Y., and Feng, W. (2010) *Carbon*, **48**, 3236–3241.
 24. Zhuang, X.D., Chen, Y., Liu, G., Li, P.P., Zhu, C.X., Kang, E.T., Neoh, K.G., Zhang, B., Zhu, J.H., and Li, Y.X. (2010) *Adv. Mater.*, **22**, 1731–1735.
 25. Xue, Y., Liu, Y., Lu, F., Qu, J., Chen, H., and Dai, L. (2012) *J. Phys. Chem. Lett.*, **3**, 1607–1612.
 26. Xu, C., Wang, X., Wang, J., Hu, H., and Wan, L. (2010) *Chem. Phys. Lett.*, **498**, 162–167.
 27. Salavagione, H.J., Gomez, M.A., and Martinez, G. (2009) *Macromolecules*, **42**, 6331–6334.
 28. Salavagione, H.J. and Martínez, G. (2011) *Macromolecules*, **44**, 2685–2692.
 29. Dai, L. (2013) *Acc. Chem. Res.*, **46**, 31.
 30. Yu, D.S., Yang, Y., Durstock, M., Baek, J.B., and Dai, L.M. (2010) *ACS Nano*, **4**, 5633–5640.
 31. Zhang, Y., Ren, L., Wang, S., Marathe, A., Chaudhuri, J., and Li, G. (2011) *J. Mater. Chem.*, **21**, 5386.
 32. Lee, S.H., Dreyer, D.R., An, J., Velamakanni, A., Piner, R.D., Park, S., Zhu, Y., Kim, S.O., Bielawski, C.W., and Ruoff, R.S. (2010) *Macromol. Rapid Commun.*, **31**, 281.
 33. Goncalves, G., Marques, P.A.A.P., Timmons, A.B., Bdkin, I., Singh, M.K., Emami, N., and Gracio, J. (2010) *J. Mater. Chem.*, **20**, 9927–9934.
 34. Ai, W., Zhou, W., Du, Z., Du, Y., Zhang, H., Jia, X., Xie, L., Yi, M., Yu, T., and Huang, W. (2012) *J. Mater. Chem.*, **22**, 23439.
 35. Melucci, M., Treossi, E., Ortolani, L., Giambastiani, G., Morandi, V., Klar, P., Casiraghi, C., Samori, P., and Palermo, V. (2010) *J. Mater. Chem.*, **20**, 9052–9060.
 36. Ruoff, R. (2008) *Nat. Nanotechnol.*, **3**, 10–11.
 37. Stankovich, S., Piner, R.D., Nguyen, S.T., and Ruoff, R.S. (2006) *Carbon*, **44**, 3342–3347.
 38. Liu, J., Wang, Y., Xu, S., and Sun, D.D. (2010) *Mater. Lett.*, **64**, 2236–2239.

39. Wang, G., Wang, B., Park, J., Yang, J., Shen, X., and Yao, J. (2009) *Carbon*, **47**, 68–72.
40. Liu, Q., Liu, Z., Zhang, X., Yang, L., Zhang, N., Pan, G., Yin, S., Chen, Y., and Wei, J. (2009) *Adv. Funct. Mater.*, **19**, 894–904.
41. Zhang, D.D., Zu, S.Z., and Han, B.H. (2009) *Carbon*, **47**, 2993–3000.
42. Ahn, K., Sung, J., Li, Y., Kim, N., Ikenberry, M., Hohn, K., Mohanty, N., Nguyen, P., Sreepurasad, T.S., Kraft, S., Berry, V., and Sun, X.S. (2012) *Adv. Mater.*, **24**, 2123–2129.
43. Avinash, M.B., Subrahmanyam, K.S., Sundarayya, Y., and Govindaraju, T. (2010) *Nanoscale*, **2**, 1762–1766.
44. Lai, L., Chen, L., Zhan, D., Sun, L., Liu, J., Lim, S.H., Poh, C.K., Shen, Z., and Lin, J. (2011) *Carbon*, **49**, 3250–3257.
45. Liu, Y., Deng, R., Wang, Z., and Liu, H. (2012) *J. Mater. Chem.*, **22**, 13619.
46. Xi Li, Y., Zhu, J., Chen, Y., Zhang, J., Wang, J., Zhang, B., He, Y., and Blau, W.J. (2011) *Nanotechnology*, **22**, 205704.
47. Compton, O.C., Dikin, D.A., Putz, K.W., Brinson, L.C., and Nguyen, S.T. (2010) *Adv. Mater.*, **22**, 892–896.
48. Kuila, T., Khanra, P., Bose, S., Kim, N.H., Ku, B.C., Moon, B., and Lee, J.H. (2011) *Nanotechnology*, **22**, 305710.
49. Liu, J., Chen, G., and Jiang, M. (2010) *Macromolecules*, **43**, 8086.
50. Karousis, N., Ortiz, J., Ohkubo, K., Hasobe, T., Fukuzumi, S., Santos, Á.S., and Tagmatarchis, N. (2012) *J. Phys. Chem. C*, **116**, 20564–20573.
51. Hsiao, M.C., Liao, S.H., Yen, M.Y., Liu, P., Pu, N.W., Wang, C.A., and Ma, C.C.M. (2010) *ACS Appl. Mater. Interfaces*, **2**, 3092.
52. Park, S., Dikin, D.A., Nguyen, S.T., and Ruoff, R.S. (2009) *J. Phys. Chem. C*, **113**, 15801.
53. Shan, C., Yang, H., Han, D., Zhang, Q., Ivaska, A., and Niu, L. (2009) *Langmuir*, **25** (20), 12030–12033.
54. Yang, H., Li, F., Shan, C., Han, D., Zhang, Q., Niu, L., and Ivaska, A. (2009) *J. Mater. Chem.*, **19**, 4632–4638.
55. Li, W., Tang, X.Z., Zhang, H.B., Jiang, Z.G., Yu, Z.Z., Du, X.S., and Mai, Y.W. (2011) *Carbon*, **49**, 4724–4730.
56. Kim, N.H., Kuila, T., and Lee, J.H. (2013) *J. Mater. Chem. A*, **1**, 1349–1358.
57. Yang, H., Shan, C., Li, F., Han, D., Zhang, Q., and Niu, L. (2009) *Chem. Commun.*, 3880–3882.
58. Kou, L., He, H., and Gao, C. (2010) *Nano-Micro Lett.*, **2**, 177–183.
59. Sun, S., Cao, Y., Feng, J., and Wu, P. (2010) *J. Mater. Chem.*, **20**, 5605–5607.
60. Pan, Y., Bao, H., Sahoo, N.G., Wu, T., and Li, L. (2011) *Adv. Funct. Mater.*, **21**, 2754–2763.
61. Karousis, N., Economopoulos, S.P., Sarantopoulou, E., and Tagmatarchis, N. (2010) *Carbon*, **48**, 854–860.
62. Fan, L., Zhang, Q., Wang, K., Li, F., and Niu, L. (2012) *J. Mater. Chem.*, **22**, 6165.
63. Pham, T.A., Kumar, N.A., and Jeong, Y.T. (2010) *Synth. Met.*, **160**, 2028–2036.

4

Chemical Functionalization of Graphene for Biomedical Applications

Cinzia Spinato, Cécilia Ménard-Moyon, and Alberto Bianco

4.1

Introduction

The interest of the scientific community in graphene has been exponentially increasing since its discovery in 2004, thanks to its unique chemical and physical properties [1, 2]. Applications of graphene in the fields of nanoelectronics, photovoltaics, material science, and engineering have already been intensely explored and consolidated [3–7], whereas the great potential of graphene and its oxidized form, graphene oxide (GO), in the biological and biomedical fields has been revealed only in the past few years [8]. Despite this recent attention, graphene nanomaterials have already found numerous applications in biotechnology including biosensing [9–11], disease diagnostics [12], antibacterial [13–16] and antiviral materials [17], cancer targeting [18], photothermal therapy (PTT) [19–21], drug delivery [22–24], electrical stimulation of cells [25], and tissue engineering [26, 27]. The advantages that prompted the rapid diffusion of graphene are its high specific surface area because of the bidimensional flat shape of graphene sheets and the tunable surface modification leading to enhanced biocompatibility. This constitutes a great added value as molecules and functional groups can be attached or adsorbed on both sides of graphene surface, thus allowing a high density of functionalization and drug loading. All these properties make graphene nanomaterials even more promising than carbon nanotubes (CNTs).

Graphene is the most important member of a bigger family, namely the family of graphene nanomaterials, together with few-layer graphene (FLG), GO, reduced graphene oxide (rGO), and nano graphene oxide (NGO) (Figure 4.1). We normally name as graphene a monolayer graphene sheet, whereas FLG is constituted by 2–10 stacked graphene layers, originally obtained as a by-product of graphene production [1]. GO is the oxidized form of graphene. It consists of monolayer graphene presenting numerous oxygenated groups such as carboxyl, hydroxyl, and epoxide groups on its surface and edges. Reduction of GO by thermal and chemical treatment in reducing conditions produces rGO, which presents a reduced oxygen content. NGO designates GO having a lateral dimension lower than 100 nm and it is sometimes called graphene nanosheets (GNSs).

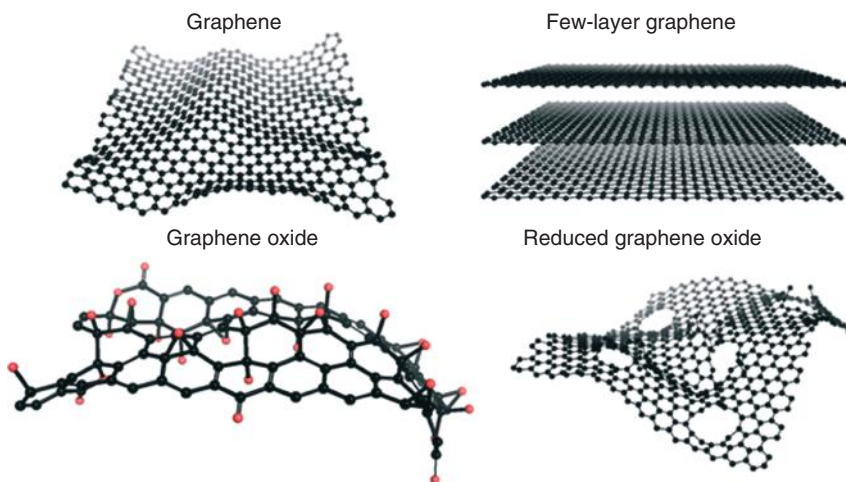


Figure 4.1 Structural models of members of the graphene nanomaterial family.

The family of graphene nanomaterials is characterized by substantially different properties such as surface area, number of layers, lateral dimension, surface chemistry, defect density, composition, and purity. Some of these parameters are clearly influential in the assessment of the biological potential of the graphenic material.

The lateral dimension of the graphene-family nanomaterials lies between a few nanometers to several microns.

The surface area is critical for the biological response to nanomaterials because of surface phenomena such as physical adsorption and catalytic chemical reaction. In monolayer graphene every carbon atom is exposed to the surrounding medium on two sides, thus graphene displays the highest surface area among sp^2 -hybridized carbon sheets ($2600 \text{ m}^2 \text{ g}^{-1}$), which is far above that of pristine single-walled CNTs ($1300 \text{ m}^2 \text{ g}^{-1}$). The surface area and the adsorption capacity for biological molecules, also depend on the number of layers and significantly decrease with higher layer numbers [28].

One other fundamental property to be taken into account for the employment of carbon nanomaterials in the biological field is their grade of purity, which depends to a large extent on the production method. Graphene can be isolated from graphite flakes by repeated mechanical exfoliation. Chemical vapor deposition (CVD) and reduction of GO are mostly employed for the production of scalable amounts of graphene [29–31]. However, exfoliation of GO and liquid phase exfoliation of graphite are the most suitable methods for biological applications because they easily provide large amounts of graphene with a high degree of purity. GO is produced as monolayer by oxidation of graphite through scalable and inexpensive methods [32–34].

The family of graphene nanomaterials shows high variability in terms of surface chemistry, which is the determinant for the type of biofunctionalization that can be

carried out, and in terms of stability in water or in typical biological media. Pristine graphene is very hydrophobic because of its extended aromatic surface, and it is more reactive at the edges and at the defects sites. Its high surface area and the delocalization of π -electrons can be exploited to solubilize and bind aromatic organic molecules, although the poor water dispersibility of nonfunctionalized graphene might require the use of surfactants to allow its employment in the biological medium. In contrast, GO is more hydrophilic than graphene and has a higher water dispersibility. The oxygenated groups on its surface offer the possibility to immobilize molecules through hydrogen bonding, electrostatic interactions, or by further functionalization [35]. As a consequence, GO is often preferred over graphene for biomedical investigations.

One drawback of graphene is the strong tendency of the exfoliated graphene sheets to irreversibly aggregate or even to restack forming once again multilayers similar to graphite, driven by strong π - π stacking interactions and van der Waals forces [36]. Therefore, functionalization has to be carried out to decrease graphene hydrophobicity, and to improve dispersibility and processability in organic and aqueous solutions [36–38]. Furthermore, biological moieties can be introduced on a graphene surface through chemical and/or physical functionalization, thus allowing to combine graphene's outstanding properties with biological activity [39, 40]. Both covalent and non-covalent functionalization have been used to modify graphene properties, and combinations of covalent and non-covalent modifications have also proved to be an interesting approach [35, 41–43]. Generally, covalent modifications involve chemical derivatives of GO or rGO obtained by conjugation of hydrophilic polymers or nucleic acids (NAs), amine coupling to carboxylic groups or sulfonylation. Non-covalent modifications exploit hydrophobic forces or π - π interactions on a graphene surface or rely on the stabilization effect of surfactants that adsorb on the surface producing colloidal suspensions of graphene sheets [12, 44, 45].

This chapter intends to give some examples of the chemical functionalization, which goes beyond investigations on graphene nanomaterials for their application in the biomedical and biotechnological fields. Rather than an exhaustive coverage of its use, the most interesting studies from a chemical and biological point of view will be presented and discussed. The chapter will be divided into three main sections based on the type of chemical functionalization involved. In Section 4.2 graphene conjugates obtained by covalent functionalization will be described, whereas Section 4.3 will deal with non-covalently functionalized graphene conjugates. Finally, Section 4.4 will report on the combination of covalent and non-covalent functionalization of graphene for biomedical applications.

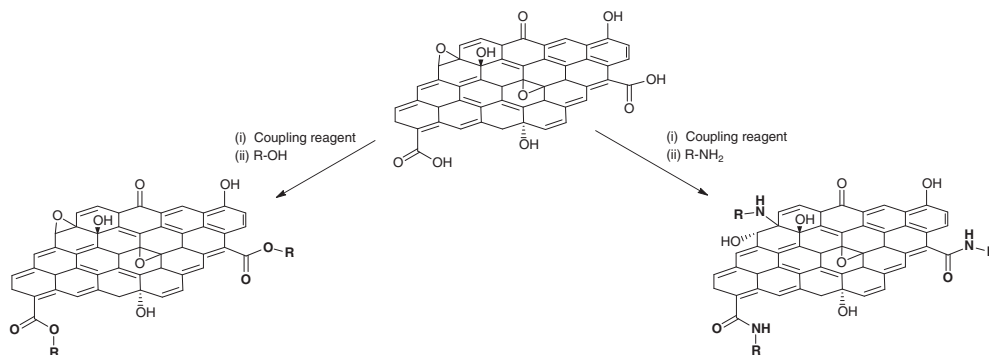
4.2

Covalent Functionalization of Graphene Nanomaterials

Numerous investigations have been pursued on covalent functionalization of graphene, with the main focus on imparting aqueous solubility, processability,

and biocompatibility to graphene [35, 41, 42]. Covalent addition of molecules to graphene is associated with rehybridization of sp^2 carbon atoms of the π -network into a sp^3 configuration, leading to a partial or total loss of π - π conjugation and modifications of the intrinsic physical and chemical properties of graphene. Functionalization of graphene can take place both at the edges or at the basal surface, although with different energy requirements. In fact the terminal dangling bonds undergo reaction with lower energy barriers as their rehybridization to the sp^3 tetrahedral geometry does not imply additional strain for the inner carbon atoms. There are essentially two main routes for the covalent functionalization of graphene: (i) the formation of covalent bonds between highly reactive species, including free radicals and dienophiles, and C=C bonds of pristine graphene and (ii) the formation of covalent bonds between organic functional groups and the oxygen groups of GO. The latter is the most exploited method for the connection of solubilizing and bioactive moieties to graphene. Indeed, the various reactive functional groups of GO (e.g., hydroxyl, epoxy, and carboxylic acid groups) provide higher dispersibility, biocompatibility, and possibility of further functionalization, which render GO a better candidate for biological applications, in comparison to pristine graphene.

Different techniques have been explored for the covalent derivatization of GO [35], but those related to the preparation of materials for biological purposes mainly involve esterification, amidation of the carboxyl groups with concomitant epoxy ring opening, or derivatization of hydroxyl groups. The reaction between the carboxylic acids of GO and hydroxyl or amine derivatives requires the use of coupling reagents such as *N*-hydroxysuccinimide (NHS), 1-hydroxybenzotriazole hydrate (HOBt), or 1-ethyl-3-(3-dimethylaminopropyl)-carbodiimide (EDC) to activate the GO carboxylic groups (Scheme 4.1). The coupling leads to the formation of ester and amide bonds, respectively, although epoxy ring opening can also occur during amidation, leading to amino-linked functionalities.



Scheme 4.1 Derivatization of GO by esterification (left) and amidation (right).

In the following part, a brief subsection is dedicated to the synthesis of GO and its reduced form (*r*GO), and then some relevant examples of covalent conjugates are presented, according to the type of functionality tethered on graphene.

4.2.1

Synthesis of GO and *r*GO

Graphene low solubility in organic solvents and water is a prime limitation because it hampers its manipulation and limits the full exploitation of its properties. However, these issues are overcome by oxidation of graphene to GO [46, 47]. The oxygenated groups of GO can be conjugated with various moieties such as polymers, biomolecules (targeting ligands), DNA, proteins, quantum dots (QDs), and nanoparticles to impart multiple functionalities to GO [8, 46, 48, 49].

4.2.1.1 Synthesis of Graphene Oxide

GO is generally synthesized by chemical oxidation of graphene through Hummers method [32] or modified Hummers method [50]. These processes consist in the treatment of graphite with potassium permanganate (KMnO₄) and sulfuric acid (H₂SO₄). The resulting oxidized graphite displays a homogeneous distribution of oxygen-containing species whose negative charge induces the exfoliation of graphene sheets to single-layer graphene by electrostatic repulsion. As-prepared GO displays a variety of oxygenated groups, such as hydroxyl functions, carboxylic acids, epoxides, carbonyl groups, phenols, and quinones on its surface and edges [51] (Figure 4.2). However, there is still some ambiguity regarding the presence or absence of carboxylic acids on the periphery of the basal plane [46, 47]. The chemical composition is strictly dependent on the synthetic conditions. The oxidizing treatment and subsequent exfoliation afford monolayer-GO with size range between ten and several hundreds of nanometers.

4.2.1.2 Reduction of Graphene Oxide

*r*GO is an attractive material, because the structure and properties of graphene can be partially restored upon reduction. GO reduction can be achieved by thermal or chemical methods, or by microwave irradiation [52, 53]. However the treatment of GO with strong reducing agents such as hydrazine or NaBH₄ under mild heating

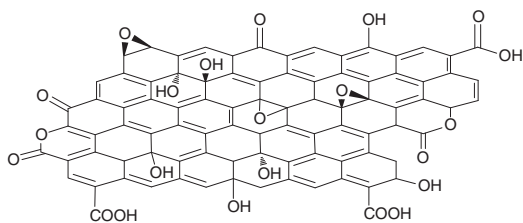


Figure 4.2 Structural model of graphene oxide. (Adapted from Ref. [47].)

is the most common approach. Recently, reduction of GO has been carried out through more green and biocompatible methods employing natural reductants such as glucose [20], bovine serum albumin (BSA) [54], vitamin C [55], and bacteria [56].

4.2.2

Functionalization of Graphene Oxide with Polymers

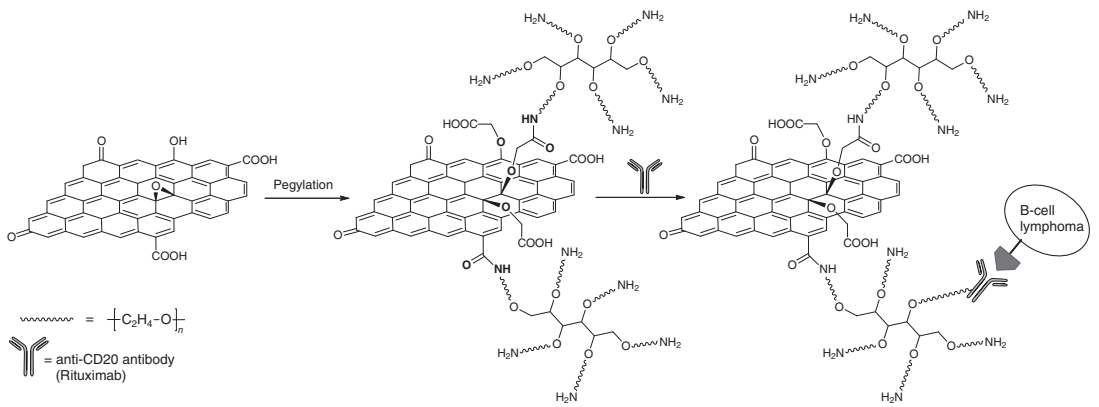
GO can be grafted to polymers bearing reactive species including hydroxyls and amines, like poly(ethylene glycol) (PEG), poly-L-lysine (PLL), chitosan, thus combining the peculiar properties of the functional moieties with those of graphene. The attachment of polymers to GO is a widely used approach to endow it with better dispersibility in specific solvents and enhanced biocompatibility. It is generally followed by further functionalization with targeting ligands, drugs, imaging probes, or other moieties. In many cases, GO is first treated under strong basic conditions, to open the epoxide and to hydrolyze possible ester groups, and then reacted with chloroacetic acid to convert hydroxyls into carboxylic acids [39]. This intermediate product called GO-COOH displays an increased amount of carboxylic groups available for derivatization.

4.2.2.1 PEGylated-GO Conjugates

PEG is so far the polymer that has been most employed for the preparation of graphenic materials for biological purposes, going from drug delivery [23, 39] to PTT [18] and imaging [39, 57]. PEG is a biocompatible and highly hydrophilic polymer of variable length and once grafted onto GO it increases its aqueous dispersibility and stability in several physiological solutions, such as serum and cell medium. In addition to imparting high dispersibility and stability, PEG also allows the blood circulation half-life of nanomaterials to increase by avoiding opsonization. Indeed, the PEG coating prevents the adsorption of opsonins present in the blood serum. Opsonization would result in the removal of the nanomaterials from the blood stream by macrophages before they reach the desired organ [58]. Thanks to these remarkable properties, PEGylated GO stood out as an important candidate for the delivery of drugs, both by a covalent approach and by non-covalent adsorption of the drug on PEG-GO, as is discussed later on.

Inspired by these investigations on CNTs [59, 60], Dai and coworkers [39] explored first the properties of PEGylated NGO for cell imaging. Amine-terminated PEG stars (6-armed branched PEG molecules) were grafted onto NGO sheets via carbodiimide activation chemistry by formation of amide bonds. The resulting functionalized NGO exhibited intrinsic photoluminescence in the near-infrared range (NIR), providing a NIR probe for cellular imaging. They further conjugated PEG-NGO to a B-cell specific antibody, Rituximab, to selectively recognize and bind B-cell lymphoma, proving selective targeting (Scheme 4.2).

Later on, Liu and coworkers [18] investigated the *in vivo* behavior of NGO by labeling PEG-NGO with Cy7, a commonly used NIR fluorescent probe, via



Scheme 4.2 PEGylation of NGO by PEG stars and further conjugation with anti-CD20 antibody; schematic illustration of the selective binding with B-cell lymphoma. (Adapted from Ref. [39].)

amide bond. *In vivo* fluorescence imaging revealed a remarkably high tumor uptake of NGO, and PEGylated NGO showed efficient tumor passive targeting and relatively low retention in the reticuloendothelial system (RES). Irradiation of tumor-bearing mice with a low-power NIR laser led to complete ablation of the tumor (Figure 4.3), showing the potential of graphene derivatives for *in vivo* PTT [18].

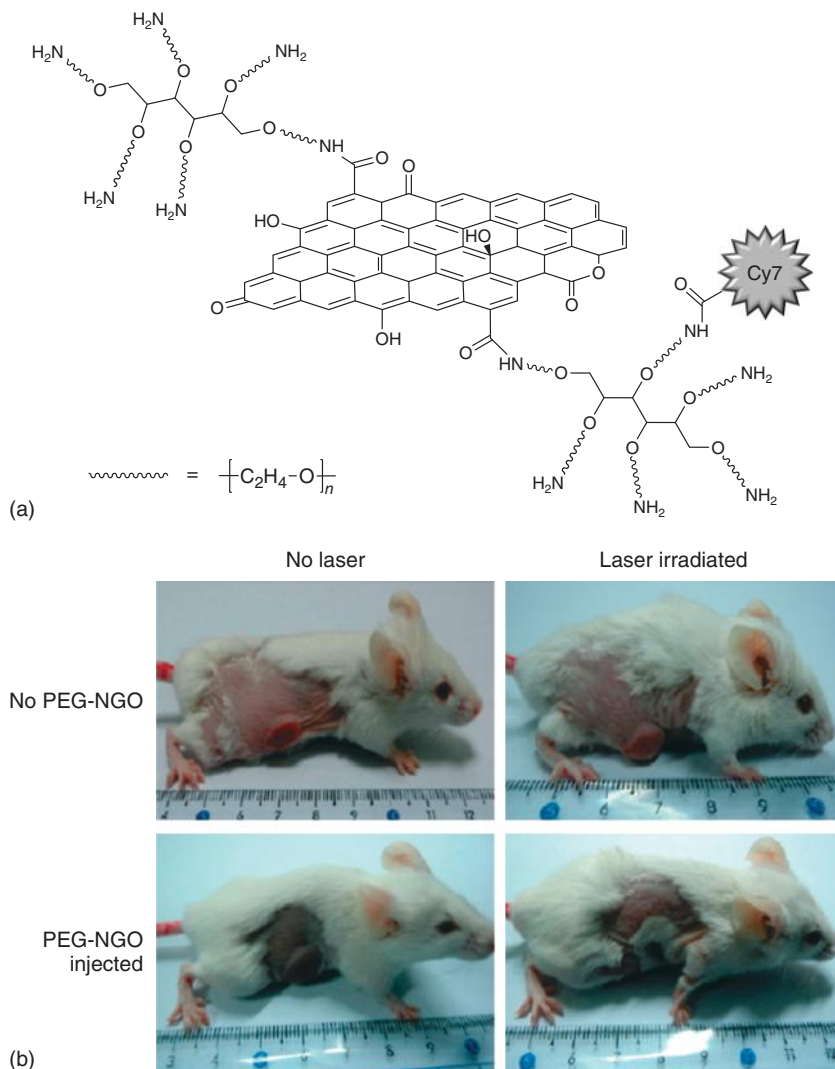


Figure 4.3 (a) Representation of PEG-NGO labeled with Cy7 (b) and photos of *in vivo* PTT study on mice after various treatments. (Adapted and reproduced with permission from Ref. [18]. Copyright 2010, American Chemical Society.)

In a recent report, PEGylated GO was also labeled with ^{125}I ($t_{1/2} = 60$ days) to assess its long-term biodistribution and potential toxicity in mice. Radiolabeled GO was found to accumulate mainly in RES and did not cause hematological or biochemical adverse effects [61].

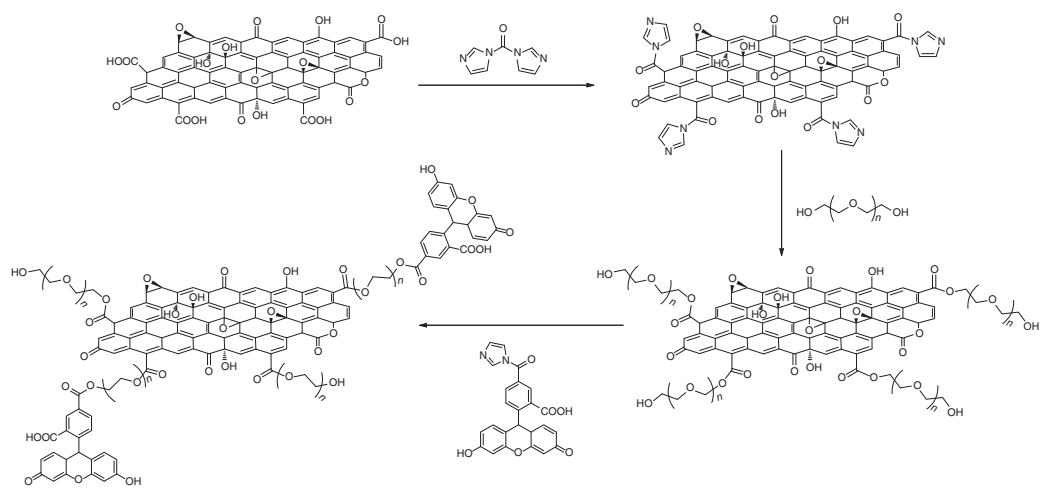
Another graphene-based fluorescent probe for intracellular imaging was prepared by covalently binding fluorescein to GO through a PEG spacer [57]. Instead of star PEG, a linear PEG polymer (PEG 2000) was used as a bridge to covalently tether the aromatic fluorophore and was essential to prevent physisorption and fluorescence quenching by GO. PEG 2000 was covalently grafted to GO by derivatization of carboxylic groups via activation with 1,1-carbonyldiimidazole (CDI). Fluorescein also activated by CDI was then chemically connected to PEG hydroxyl groups (Scheme 4.3). The as-prepared conjugate exhibited excellent pH-tunable fluorescence properties and showed efficient cellular uptake by HeLa cells, a human cervical cancer cell line.

PEG was used as a solubilizing moiety and also as a spacer in the preparation of a GO-streptavidin conjugate used to capture biotinylated protein complexes via streptavidin-biotin interaction [62]. An amine-terminated biotin (biotin-PEG₈-NH₂) was coupled to the carboxylic groups of GO, and streptavidin was then tethered to the system. The complex showed high streptavidin loading and excellent recognition capability toward biotinylated DNA, fluorophores, and Au nanoparticles.

Cai and coworkers reported the preparation of radiolabeled antibody-PEG-GO conjugate for *in vivo* targeting and positron emission tomography (PET) imaging of tumor-bearing mice [63, 64]. Glycoprotein CD105 is a vascular target in cancer and has a crucial marker role for tumor angiogenesis. NGO sheets functionalized with six-arm branched PEG, were covalently coupled with NOTA (1,4,7-triazacyclononane-1,4,7-triacetic acid), a very stable chelator for radiometals, and TRC105, an antibody with high affinity for both human and murine CD105. The covalent conjugate NOTA-GO-TRC105 was then labeled with three radioisotopes having different half-lives: ^{61}Cu ($t_{1/2} = 3.4$ h), ^{66}Ga ($t_{1/2} = 9.3$ h), and ^{64}Cu ($t_{1/2} = 12.7$ h) [63, 64]. *In vitro* experiments demonstrated that the covalent conjugation of TRC105 onto GO did not compromise the antigen-binding affinity and that the radiolabeled construct retained its stability in mouse serum. The conjugates rapidly accumulated in xenografted murine breast cancer cells and were able to specifically target CD105 in the tumor vasculature (Figure 4.4). Thanks to poor extravasation, targeting the GO-nanocarrier toward the tumor vasculature was achieved with high efficiency.

4.2.2.2 Covalent Linkage of Biopolymers

PLL has been attached to graphene sheets with the purpose of achieving a better water solubility [40]. It is a biocompatible polymer rich in amino groups, which has been used to promote cell adhesion, drug delivery, and biofouling. Grafting of PLL occurred by cross-linking between the epoxy groups on GO and the amine groups of PLL under basic conditions. In these conditions, GO was reduced to graphene. The PLL/rGO conjugate was further used as a biosensor for hydrogen peroxide detection showing amplified sensing ability.



Scheme 4.3 Synthesis of fluorescein-labeled PEG-GO. (Adapted from Ref. [57].)

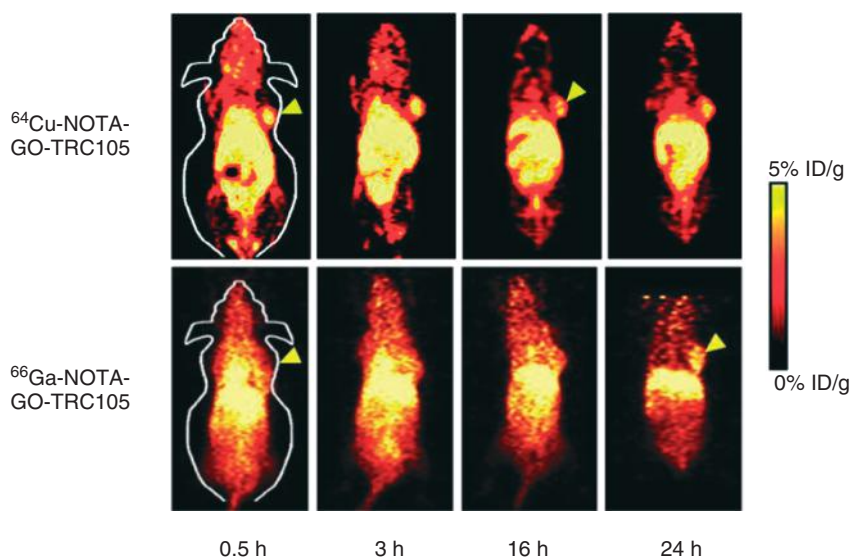


Figure 4.4 PET imaging of 4T1 tumor-bearing mice after intravenous injection of NOTA-GO-TRC105, labeled with two different isotopes: ^{66}Ga and ^{64}Cu . Arrowheads

indicate the tumors. (Reproduced with permission from Ref. [63, 64]. Copyright 2012, Elsevier and American Chemical Society.)

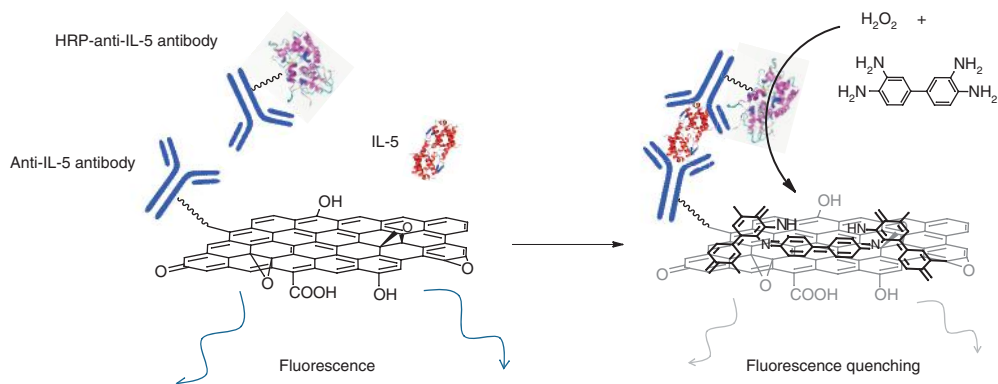
Chitosan is a biocompatible and biodegradable polycationic biopolymer which has been largely employed for tissue engineering. Gels of chitosan are known to be osteoconductive and to enhance bone formation [65]. The group of Misra reported the synthesis of GO-chitosan scaffolds and the biological responses of osteoblast cells to this conjugate [66]. The GO-chitosan scaffold was synthesized by covalent linkage of the carboxyl groups of GO with the amine groups of chitosan. This conjugate was found to facilitate cell attachment and proliferation, therefore constituting a promising platform for bone tissue regeneration.

4.2.3

Tethering of Antibodies

Recently, the group of Park reported an immunosensing system based on GO exploited for the detection of interleukin 5 (IL-5) through the quenching of intrinsic GO fluorescence [67]. IL-5 is a cytokine able to stimulate B cell growth and immunoglobulin secretion. GO was deposited on an amino-modified glass surface by electrostatic interactions and anti-IL-5-capture antibodies (Abs) were then covalently branched on GO-arrays by carbodiimide-assisted amidation reaction. Introduction of IL-5 and anti-IL-5 antibody-horseradish peroxidase (HRP) conjugate determined the formation of a sandwich immuno-complex on GO. Capturing of IL-5 by the antibody was detected by quenching of the intrinsic fluorescence GO,

induced by peroxidase-catalyzed polymerization of 3,3'-diaminobenzidine (DAB), in the presence of H_2O_2 (Scheme 4.4).



Scheme 4.4 Schematic representation of GO-based immunosensing platform for the detection of IL-5: the formation of a sandwich immune-complex between HRP-anti-IL-5 antibody, IL-5, and the antibodies on GO

induces DAB polymerization in the presence of H_2O_2 , resulting in the quenching of GO intrinsic fluorescence. (Adapted from Ref. [67].)

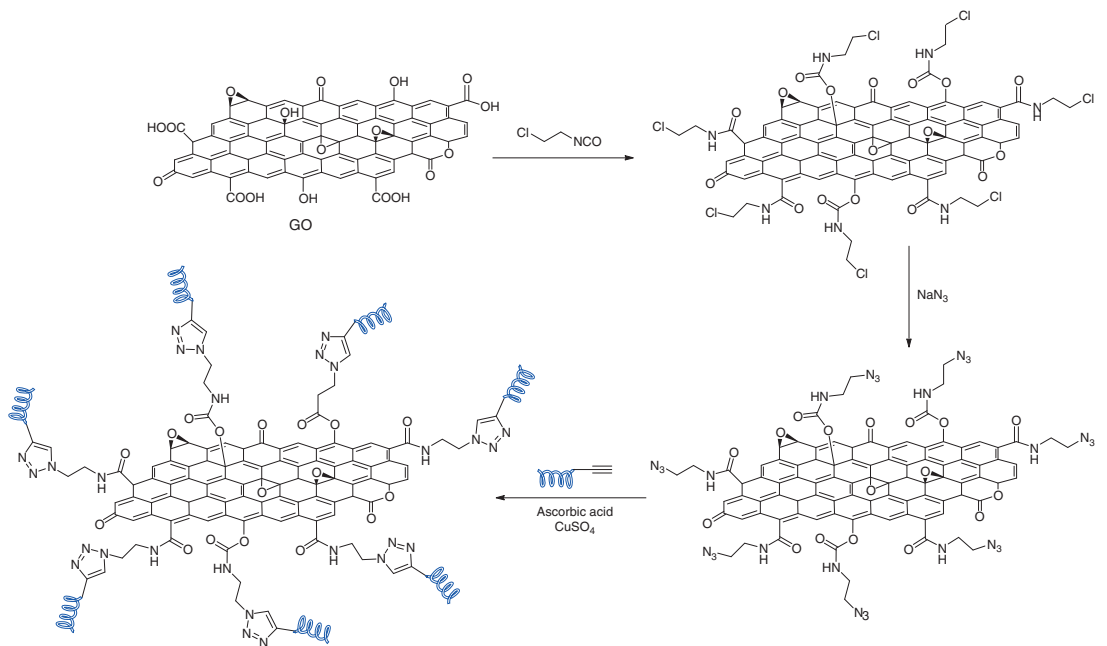
The same group also designed a different immunosensing platform based on chemiluminescence resonance energy transfer (CRET) between graphene and chemiluminescent donors [68]. They employed a luminol/hydrogen peroxide chemiluminescence reaction catalyzed by HRP for the biomolecular recognition of CRP (C-reactive protein), a protein marker for human inflammation and cardiovascular diseases. *rGO* was first functionalized with sulfonic acid groups through reaction with aryl diazonium salts in order to prevent aggregation and increase dispersibility [37]. An anti-CRP antibody was then coupled to *rGO* by using both EDC and NHS. This graphene-based CRET platform was applied to the immunoassay of CRP in human serum samples with successful results.

By changing the capture antibodies, the application of this type of immunoassay biosensors can be extended to the detection of other chemical or biological molecules. For example, another Ab-GO conjugate was reported to detect rotavirus with high sensitivity and selectivity [69].

4.2.4

Attachment of Nucleic Acids

Nowadays there is an increasing interest in DNA nanotechnologies because of the remarkable properties of DNA, such as self-assembly and biorecognition capability, which make it particularly suitable for the development of biosensors and functional nano-architectures.



Scheme 4.5 Representation of the synthetic route of DNA-graphene oxide. (Adapted from Ref. [71].)

The group of Pumera [70] demonstrated the possibility to functionalize graphene with single-stranded DNA (ssDNA) oligomers through carbodiimide chemistry. The resulting DNA-graphene hybrid displayed strong biorecognition ability and could be used for selective and sensitive detection of DNA. Simultaneously, Wang *et al.* described a novel approach to functionalize graphene with DNA by copper-catalyzed “click” chemistry [71]. The functional groups of GO were first derivatized with 2-chloroethyl isocyanate, followed by nucleophilic substitution with sodium azide (Scheme 4.5). The functionalized azide-graphene was coupled with alkyne-terminated DNA strands in the presence of a catalytic amount of copper, obtaining a stable polyvalent graphene hybrid with high DNA density. This hybrid was further assembled via hybridization with DNA tetrahedron-structured probes, a versatile scaffold used in biosensing, creating a nanocomplex with exceptional electrochemiluminescence properties, potentially useful in the fields of biosensors and DNA nanotechnology.

4.2.5

Grafting of Peptides and Enzymes

Wang *et al.* exploited GO affinity toward biomolecules and its quenching ability toward fluorophores to build a GO-peptide conjugate for the intracellular sensing of caspase-3, a protein-degrading enzyme directly involved in apoptosis phenomena [72]. The authors designed a peptide probe featuring a caspase-3 cleavable site constituted by a peptide fragment (DEVD), labeled with a fluorescein-amidite (FAM) on one side, and linked on the other side to a peptide spacer stable to protease. This peptide probe and a cell penetration TAT peptide were then grafted on GO by amidation with EDC/NHS coupling method, yielding a nanoconjugate with quenched fluorescence (Scheme 4.6).

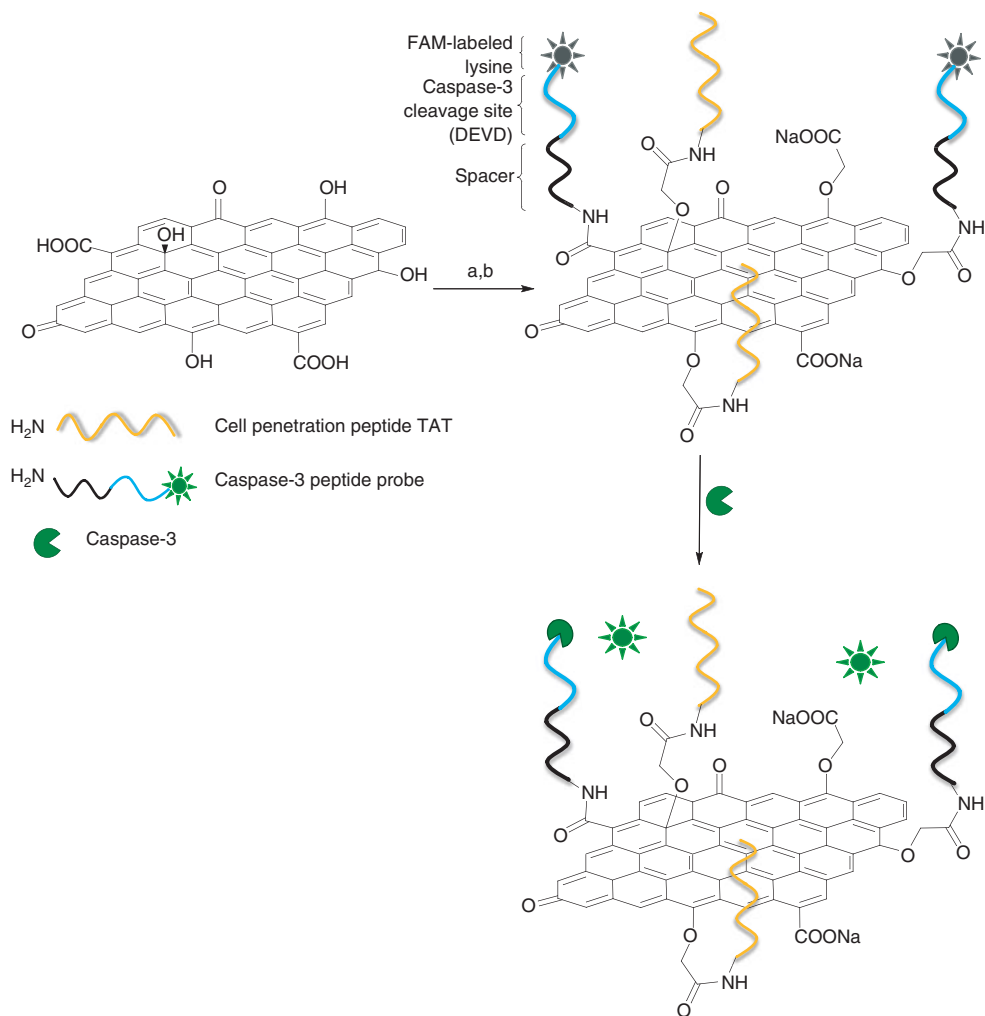
In vitro assays revealed that the GO-peptide conjugate was efficiently delivered into cells. The cleavage of the peptide by caspase-3 induced the release of the fluorescent label from the GO surface leading to recovery of fluorescence and the consequent detection of the DNA sequence. Therefore, GO-peptide conjugates represent a sensitive and selective sensor for contrast imaging of apoptotic signaling in live cells.

GO also proved to be an ideal substrate for the immobilization of enzymes. HRP and lysozyme were immobilized on GO by amidation between the carboxylic acid groups of GO and the amines of the enzyme [73]. In both cases, electrostatic forces and hydrogen bonding also contribute to the interactions.

4.2.6

Attachment of Other Organic Molecules and Biomolecules

Chemically and electrochemically reduced graphene and GO have been largely used in biosensing for the detection of biomolecules, for example, through the preparation of graphene-based electrodes.



Scheme 4.6 Synthesis of the GO-peptide conjugate and caspase-3 detection by peptide cleavage and fluorescence recovery. (a) $\text{ClCH}_2\text{COONa}$, NaOH and (b) EDC, sulfo-NHS, TAT peptide, caspase-3 peptide probe. (Adapted from Ref. [72].)

Poly(vinyl)pyrrolidone (PVP)-protected graphene was obtained by functionalization of GO with PVP followed by reduction with hydrazine and ammonia. Subsequently the conjugate was modified with polyethylenimine-functionalized (PEI) ionic liquid (IL). The graphene hybrid was dropped on a carbon electrode and then soaked in a glucose oxidase solution to afford a nanocomposite with high electrocatalytic activity toward the reduction of O_2 and H_2O_2 , thus with a good biosensing potential [74]. Shan *et al.* also used IL-functionalized graphene and chitosan to construct an electrochemical biosensor for the detection of NADH (β -nicotinamide adenine dinucleotide) and ethanol [75]. In this case,

an imidazolium IL was grafted onto graphene by epoxide ring-opening reaction between GO and 1-(3-aminopropyl)-3-methylimidazolium bromide in basic conditions, leading also to the reduction of GO.

Recently, a multifunctional graphene-platform with interesting fluorescence and magnetic properties was reported. GO was reduced by a microwave-assisted process and simultaneously magnetized by decomposition of ferrocene and formation of metallic iron nanoparticles on the graphene sheet. Water dispersibility and fluorescence were then imparted through covalent functionalization with polyacrylic acid and fluorescein *o*-methacrylate via radical reaction with the double bonds of rGO. It was demonstrated that this multifunctional graphene exhibited an excellent biocompatibility *in vitro* and resulted in a useful *in vitro* and *in vivo* probe for optical imaging in zebrafish [76].

4.3

Non-covalent Functionalization of Graphene

Non-covalent modification of graphene essentially involves π -stacking interactions, hydrophobic effects, van der Waals forces, and electrostatic interactions. Different from covalent functionalization, non-covalent modification does not involve rehybridization of the carbon atoms and introduction of surface defects. Thus, the π -system of graphene and its electronic properties are not altered. Adsorption of molecules can occur on both sides of the graphene surface, thus allowing very high loading, especially with aromatic molecules via π -stacking.

While the adsorption on bare graphene is mainly driven by π -stacking and hydrophobicity, the adsorption of molecules on the GO surface can also be assisted by H-bonding and electrostatic interactions. Nonetheless, the basal plane of GO displays sp^3 -hybridized regions interspersed with unmodified aromatic graphenic domains which are hydrophobic and available for π - π interactions [77, 78]. GO surface is therefore a useful platform for the adsorption and delivery of aromatic drugs insoluble in water. A large variety of graphene conjugates have been prepared relying on non-covalent interactions, and they have been applied in drug and gene delivery, imaging, tissue engineering, and biosensing, the last one representing a major application of non-covalent graphene complexes [10, 11]. This is because non-covalent functionalization of graphene offers the possibility to reversibly adsorb molecules onto the graphene surface without altering the electronic network.

In the following section non-covalent conjugates of graphene and GO will be presented, prepared via π -stacking, or based on other interactions.

4.3.1

Adsorption via π -Stacking

Aromatic compounds with extended π -systems such as pyrene and perylene are the most suitable candidates to interact with the graphene surface by π -stacking

and hydrophobic forces. Indeed, aromatic hydrocarbons have also been used as exfoliating agents to afford monolayer and FLG, as they can intercalate between the graphene sheets. Graphene conjugates based on π -stacking or on a combination of π - π interactions and other non-covalent forces have been prepared with a variety of compounds, such as pyrene derivatives, DNA, aptamers, aromatic drugs, dyes, and other biomolecules.

4.3.1.1 Adsorption of Drugs

Complexation of GO with hydrophobic drug molecules has the great advantage of increasing the solubility of the drugs, while preserving its structural integrity.

Inspired by the high loading capacity of CNTs, Yang *et al.* investigated the possibility of loading doxorubicin (DOX) on GO by mixing both components in an aqueous solution [79]. DOX strongly stacked onto GO by effect of π - π interactions between the aromatic domains of the graphene plane and the condensed quinoid rings of DOX (Figure 4.5). In addition, numerous H-bonding can be formed between the hydroxyl and carboxyl groups of GO and the hydroxyls and amino functions of DOX. Upon investigations of the pH-dependence of drug loading onto GO, it was observed that the highest loading capacity occurred at neutral pH (0.91 mg of drug per mg of GO), whereas the highest drug release took place at acid pH because of increased solubility of DOX.

A different GO-based carrier for DOX targeted delivery has been prepared by complexation with chitosan modified with folic acid (FA) [80]. GO loaded with DOX was then encapsulated with FA-chitosan by electrostatic interactions. FA was used as the targeting ligand as the folate receptors are over expressed on cancer cells. The release of DOX was pH-sensitive.

4.3.1.2 Adsorption of Pyrene Derivatives

Thanks to their extended aromaticity, pyrene derivatives strongly adsorb onto CNTs, fullerene, but also graphene and GO via both π -stacking and hydrophobic forces.

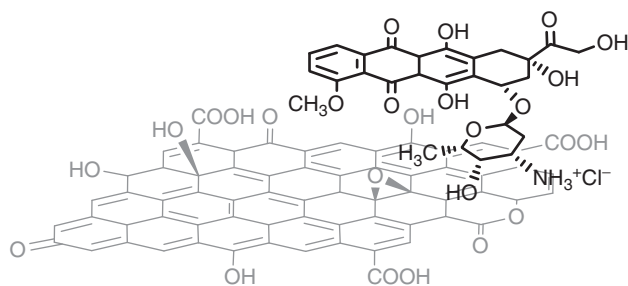


Figure 4.5 Representation of DOX adsorption on graphene oxide. (Adapted from Ref. [79].)

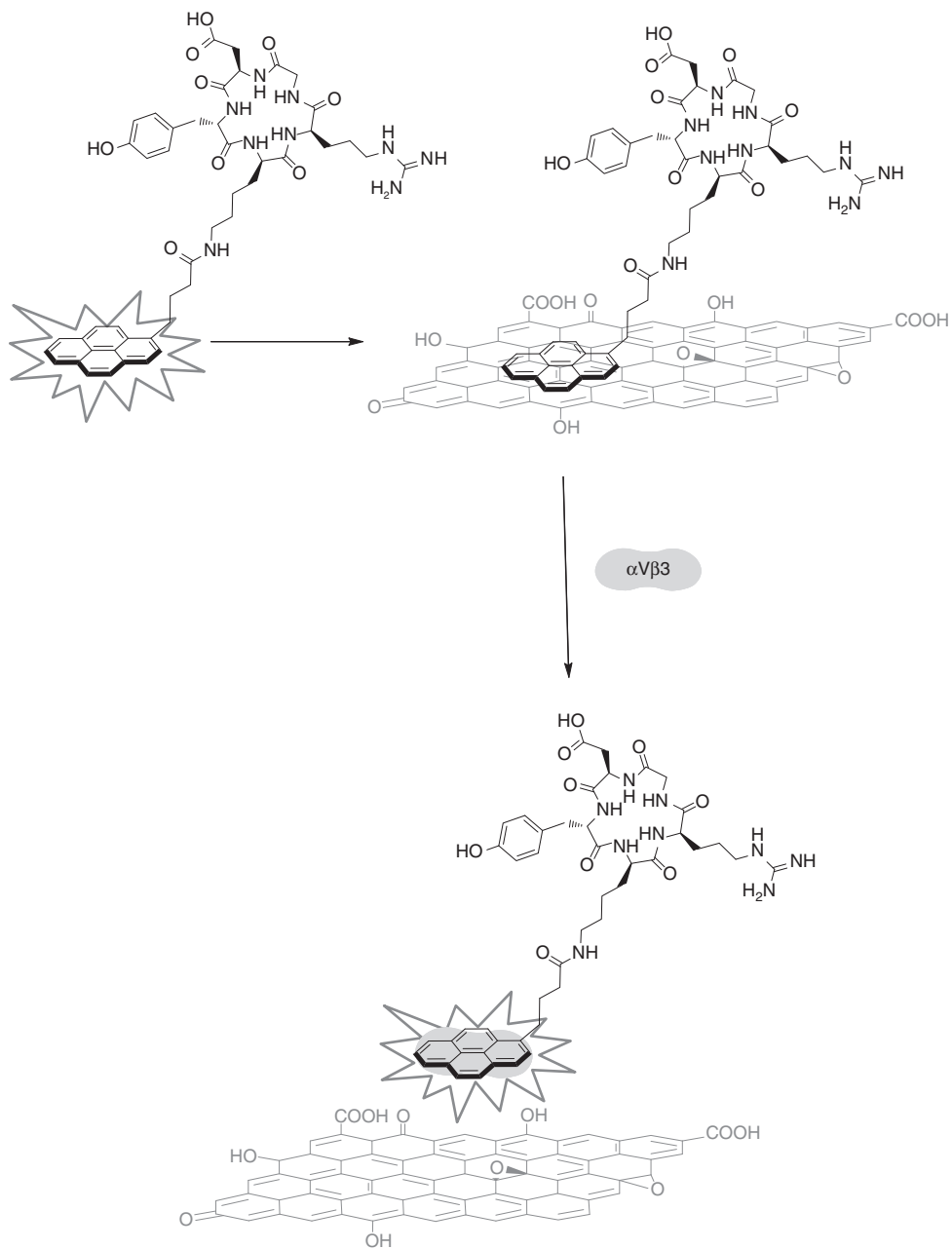


Figure 4.6 Schematic representation of the RGD-pyrene-GO biosensor: fluorescence quenching of RGD-pyrene by π - π stacking with GO and dissociation by integrin $\alpha V\beta 3$ introduction. (Adapted from Ref. [81].)

The pyrene fluorescence properties have been exploited by the group of Chen to prepare a GO-based biosensor for integrin, a surface marker of cancer cells [81]. Pyrene was derivatized with cyclic Arg-Gly-Asp (RGD) peptide, an integrin ligand, and adsorbed onto GO, resulting in the quenching of the fluorescence by energy transfer to GO. The competitive binding of RGD-pyrene with integrin caused its dissociation from the GO surface and restored the fluorescence again. *In vitro* assays on breast cancer cells showed that the RGD-pyrene-GO probe was able to work as a real-time and sensitive biomarker (Figure 4.6).

In another study, a tripodal pyrene structure bearing a terminal NHS ester was adsorbed onto graphene by π -stacking. An anti *Escherichia coli* antibody was then covalently conjugated to the NHS ester. A good recognition capacity toward bacterial cells was observed, whereas adsorption of the antibody directly on bare graphene caused the complete loss of its detection ability [82]. Multilayer enzyme electrodes prepared by assembly of multi-pyrene architectures or polymer-modified-pyrene molecules onto graphene were also exploited for the detection of glucose oxidase or maltose activity [83, 84].

Pyrene functionalized with ssDNA has been used to exfoliate graphene flakes into water-dispersible single- and bilayered graphene sheets. The immobilized DNA was further hybridized with complementary DNA labeled with gold nanoparticles, providing a nanocomposite for sensing bioapplication [85].

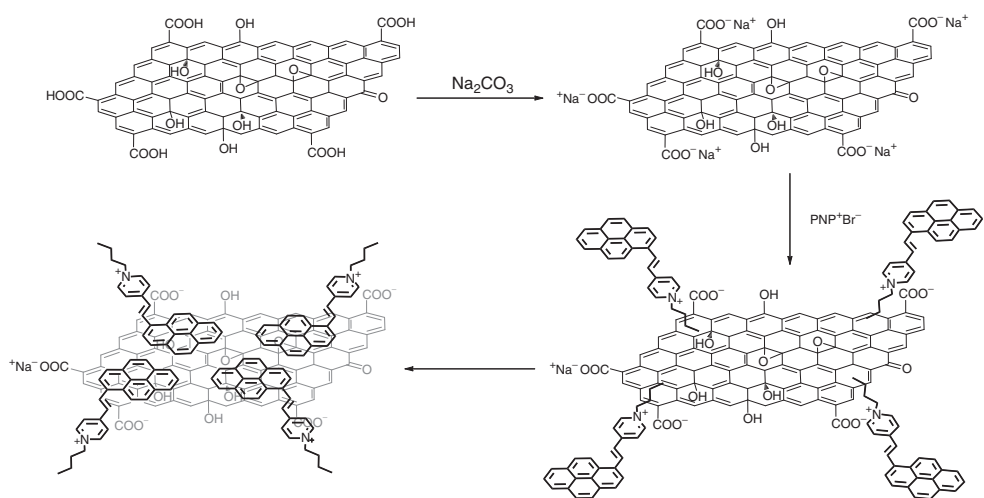
An alternative sensor for DNA has been prepared by exploiting the fluorescent properties of a positively charged pyrene derivative [86]. Pyrenyl-*N*-butylpyridinium bromide (PNP^+Br^-) was tethered on negatively charged GO by ion-exchange process combined with π - π interactions via the pyrene moiety, forming a fluorescence quenching complex (PNP^+GO^-) (Scheme 4.7).

Studies on specificity of this complex toward different biomolecules present in blood serum (DNA, RNA, proteins, etc.) revealed a high selectivity toward double-strand DNA (dsDNA). The strong ionic interactions between dsDNA and PNP^+GO^- induced the release of PNP (pyrenyl-*N*-butylpyridinium) from the GO surface and the recovery of fluorescence.

4.3.1.3 Non-covalent Interactions with Nucleic Acids and Aptamers

Both graphene and GO can strongly interact with NAs and aptamers through π -stacking. On the contrary, dsDNA cannot be stably adsorbed onto graphene because the internal position of the nucleobases prevents their interaction with the graphene surface [87, 88]. This principle, combined with the optoelectronic properties of graphene, greatly prompted the use of graphene for the development of fluorescence resonance energy transfer (FRET)-based biosensors (Figure 4.7) [10, 11, 89]. Aptamers are a novel class of functional ssDNA or RNA that can bind target molecules with high specificity and strong binding affinity.

They have been largely employed as a sensitive and selective platform for target protein detection. Lu *et al.* first gave evidence that GO could bind and quench dye-labeled ssDNA and then release the fluorescence upon unbinding of the probe



Scheme 4.7 Preparation of PNP⁺ GO⁻: representation of the ion-exchange process of GO with Na⁺ and with PNP⁺. (Adapted from Ref. [86].)

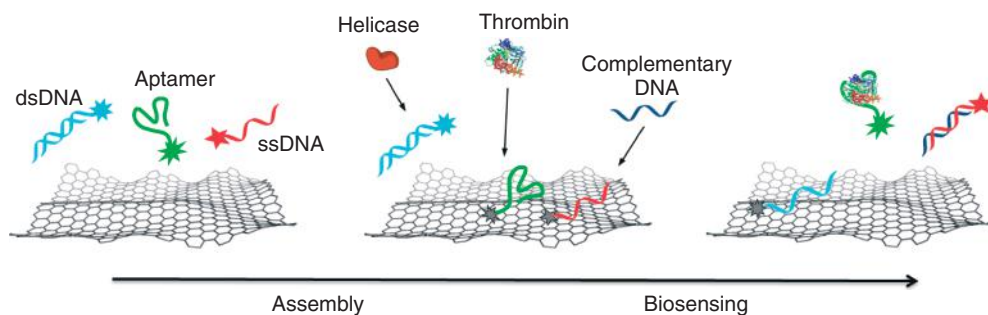


Figure 4.7 Principles of graphene-based FRET biosensors. Dye-labeled ssDNA and aptamers are adsorbed onto the surface of graphene or GO with consequent fluorescence quenching. In the presence of the corresponding analyte, the binding between the probe and its target (e.g., complementary ssDNA and thrombin), determines the

desorption from the surface and the fluorescence is recovered. Conversely, dsDNA remains fluorescent until an enzyme (e.g., helicase) is introduced; ssDNA is then released, and the fluorophore on the ssDNA is quenched by graphene. (Adapted from Ref. [89].)

induced by recombination with the complementary sequence [87]. GO complexed with different dye-labeled probes was able to differentiate sequence-specific DNA filaments, leading to a multicolor simultaneous sensor [90]. Moreover, DNA loaded onto GO was found to be protected against enzymatic degradation in an intracellular environment, thus furnishing an optimal platform for the delivery of genes inside cells [91].

In another example, a dye-labeled aptamer adsorbed onto graphene was used for the detection of thrombin, a protein fundamental in the regulation of tumor growth and metastasis. Recognition of thrombin by the aptamer caused the detachment of the conjugate from GO surface and turned on the fluorescence [92].

Min and coworkers [88] exploited the greater affinity of ssDNA toward GO to assess the unwinding activity of helicase, a class of enzymes able to unwind double-strand NAs into single-strands. Helicase is implicated in virus replication and cellular processes. Viral helicase inhibitors are powerful drug candidates in the treatment of hepatitis C and other viral infections. In this approach, introduction of helicase into a mixture of dye-labeled dsDNA and GO induced the unwinding of the two strands, and fluorescence quenching was observed because of the interaction of the fluorescently labeled ssDNA with GO (Figure 4.8).

More recently, the same group relied on the same method to develop a multiplexed helicase assay for the screening of inhibitors of hepatitis C virus helicase, discovering five highly selective inhibitor drugs [93].

GO-aptamer complexes have been used as sensors for proteins [92], hormones [87], ATP (adenosine triphosphate) [94, 95], and for harmful metal ions such as

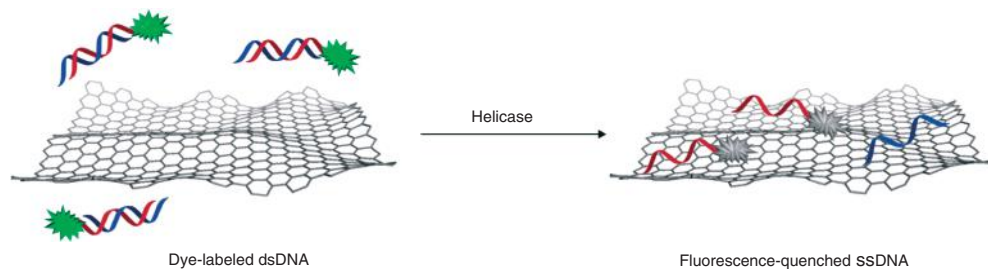


Figure 4.8 Representation of the GO-based probe for the assay of helicase unwinding activity. (Adapted from Ref. [88].)

Cu (II) [96], Ag (II) [97], and Pb (II) [98]. In addition, the combined adsorption of ssDNA and hemin, an iron protoporphyrin, onto rGO led to a universal biosensing platform for the colorimetric assay of a broad range of targets including metal ions, DNA, and small molecules [99, 100].

4.3.1.4 Immobilization of Enzymes, Proteins, and Other Macromolecules

Enzymes and proteins can also interact with graphene and GO basal plane. The aromatic residues can adsorb onto graphene by π -stacking, while charged or polar residues can electrostatically interact with the oxygen-containing groups of graphene. Platforms for sensing biomolecules based on FRET have been designed by adsorbing proteins or peptides as probes onto GO. In a representative study, the peptide hydrolysis induced by a protease induced the release of the dye-labeled peptide segment, turning on the fluorescence [101]. Immobilization of proteins onto graphene has also been achieved by linking a terminal lysine to pyrene butanoic acid derivatized with NHS adsorbed onto GO [102].

A ssDNA-protein-graphene composite has been prepared by first co-assembling ssDNA with graphene sheets and then tethering cytochrome *c* (a redox protein) by electrostatic interactions [103].

4.3.2

Electrostatic and Hydrophobic Interactions

Electrostatic and hydrophobic interactions have been exploited to non-covalently bind polymers, surfactants, metal ions, QDs, or (bio) macromolecules devoid of aromatic moieties. In many studies, coating of graphene or GO with polymer is associated with the loading of drugs, DNA, or QDs to impart multiple properties.

4.3.2.1 Coating with Polymers and Biopolymers

Several polymers and surfactants have been used to increase the dispersibility and biocompatibility of graphene and GO [104, 105]. Negatively charged GO has been

coated with polycationic polymers by electrostatic interactions [106, 107], and used for gene delivery, for example. Biologically compatible and biodegradable natural polymers such as lignin and cellulose derivatives have been used as dispersant to prepare stable aqueous suspensions of GNSs [108].

Reduced-nano graphene oxide (*r*NGO) (average diameter 27 nm) has been non-covalently functionalized with an amphiphilic polymer, PEG grafted poly(maleic anhydride-*alt*-1-octadecene) (C_{18} PMH-PEG₅₀₀₀), and the resulting hybrid was found to be a powerful agent for PTT in cancer therapy [19]. *r*NGO/ C_{18} PMH-PEG₅₀₀₀ was able to effectively target the tumor *in vivo* by the enhanced and permeability retention (EPR) effect and to efficiently ablate cancer cells under low laser power irradiation. Moreover, a comparative study of *r*NGO/ C_{18} PMH-PEG₅₀₀₀ with bigger size *r*GO/ C_{18} PMH-PEG₅₀₀₀ and covalent NGO-PEG pointed out that the conjugates featuring smaller size graphenes were more effective in terms of photothermal heating under NIR laser irradiation [19]. Dai's group conjugated a peptide containing the RGD motif or a fluorescent probe (Cy5) to PEG to target the integrin receptors over expressed on several cancer cell lines and to image the intracellular localization of the complexes, respectively. The so-formed *r*GO/RGD-Cy5 conjugate showed a selective cellular uptake in cancer cells and highly effective photo ablation of cells *in vitro* (Figure 4.9) [21].

PEI is a cationic polymer widely used in gene transfection due to its strong binding with NAs, good cellular uptake, and proton sponge effect that induces endosomal escape and release in the cytosol. PEI has been anchored onto negatively charged GO by electrostatic interactions, yielding a GO-PEI complex with enhanced stability in physiological conditions and reduced *in vitro* toxicity toward HeLa cells,

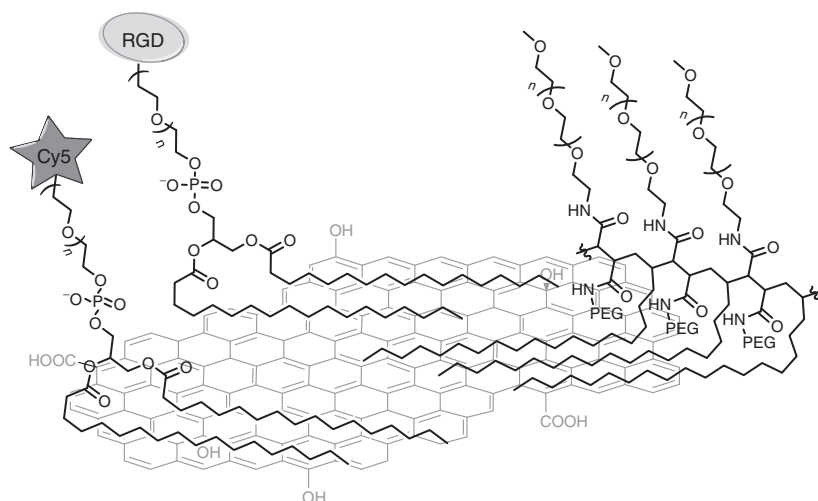
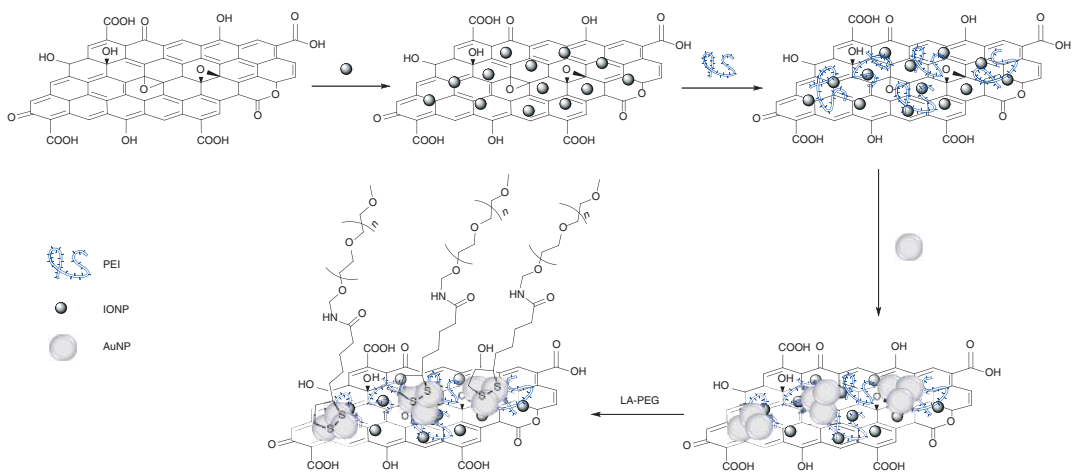


Figure 4.9 Schematic representation of *r*GO loaded with PEG-RGD, PEG-Cy5, and the surfactant C_{18} -PMH-PEG₅₀₀₀. (Adapted from Ref. [21].)



Scheme 4.8 Schematic representation of GO-IONP-Au-PEG synthesis. (Adapted from Ref. [107].)

compared to PEI alone. Plasmid DNA (pDNA) was then effectively loaded onto GO-PEI and showed a good intracellular gene transfection efficiency [106].

Very recently Liu and coworkers reported the preparation of a graphene oxide-iron oxide nanoparticle (GO-IONP) composite for applications in imaging and PTT [107]. The iron oxide NPs were deposited on GO by a hydrothermal reaction. The GO-IONP was then covered with PEI. Negatively charged gold nanoparticles were deposited on positive GO-IONP composite, followed by functionalization with lipoic acid-modified PEG (Scheme 4.8). The GO-IONP-Au-PEG hybrid displayed a physiological stability and a negligible *in vitro* cytotoxicity, together with intense NIR absorption and strong magnetic properties. *In vitro* and *in vivo* animal tests evidenced that this hybrid was a remarkable PTT agent for effective tumor ablation with magnetic and molecular targeting abilities.

GO has been also coated with PVP and used as photothermal agent for cancer therapy [109] and sensor for ochratoxin A, a potentially carcinogenic food mycotoxin [110]. In the latter example, coating of GO with PVP was essential to prevent the unspecific adsorption of ochratoxin A.

Liu *et al.* immobilized gelatin, a linear polypeptide, onto the GO surface through hydrophobic interactions, with concomitant reduction of GO [111]. DOX was then adsorbed onto the gelatin/*rGO* surface and the resulting construct was able to kill cancer cells.

Heparin is a natural glycosaminoglycan with anticoagulant properties, which has been largely employed in the coating of nanomaterials to improve their blood biocompatibility [112–114]. Following the positive results obtained by heparinization of CNTs [114], Lee *et al.* prepared a *rGO*/heparin conjugate assembled by hydrophobic interactions. Besides, the high negative charge density of the sulfonate groups of heparin rendered the *rGO*/heparin conjugate dispersible and stable in water. Assessment of the blood compatibility of the conjugate showed that long heparin chains adsorbed on *rGO* retained significantly their anticoagulant activity [115].

A non-covalent complex of GO with an enzyme-activable photosensitizer has been synthesized by physical adsorption of a hyaluronic acid-chlorin e6 conjugate (HA-Ce6) on the GO surface [116]. Ce6 is a second generation porphyrinic photosensitizer, whereas hyaluronic acid is a biocompatible poly-disaccharide, which can be degraded by enzymatic cleavage. The HA-Ce6-GO complex was efficient in killing *in vitro* cancer cells over expressing a lysosomal enzyme and is a promising tool for NIR fluorescence imaging of tumors.

4.3.2.2 Deposition of Nanoparticles

The deposition and adsorption of metal particles on graphene nanomaterials has already been thoroughly investigated and applied in the fields of optoelectronics and technologies [35, 117–121]. In addition, it is very attractive for applications in targeting, imaging, and biomedicine. Metal ions such as Mg(II), Cu(II), Re(V), Fe(II/III) can be adsorbed onto GO, NGO, and *rGO* by complexation

with oxygenated functional groups [122, 123]. GO and graphene-based magnetic nanoparticle hybrid materials have been successfully employed as anticancer drug carriers and for magnetic resonance imaging [111, 124–127].

Yang *et al.* have prepared a superparamagnetic GO-Fe₃O₄ hybrid by chemical deposition of iron ions. The composite was used for controlled targeted delivery of DOX [125]. Later on, the same group modified GO-Fe₃O₄ with 3-aminopropyl triethoxysilane linked to FA, thus obtaining multifunctionalized GO with dual targeting properties [126]. Loading of DOX afforded a nanocarrier with pH-sensitive drug release characteristics and high cytotoxicity toward HeLa cells. In another study, a rGO-iron oxide composite non-covalently functionalized with PEG was used as a theranostic probe for multimodal imaging and PTT. Accumulation of the composite in mice tumor was confirmed by optical, photoacoustic, and magnetic resonance imaging (Figure 4.10). Moreover, the PTT treatment led to a very efficient tumor ablation using a low laser power density [127].

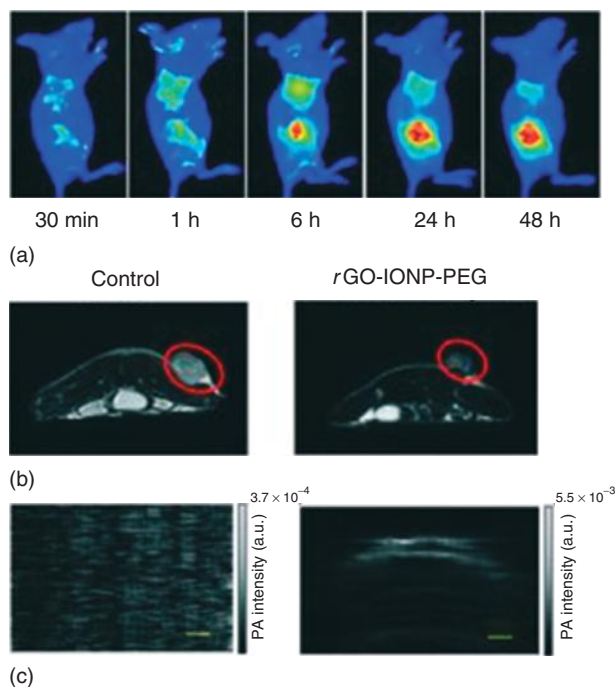


Figure 4.10 Multimodal imaging of tumor-bearing mice of rGO-IONP-PEG: (a) fluorescence imaging using Cy5 labeled rGO-IONP-PEG; (b) T2-weighted MR imaging and (c) photoacoustic imaging using rGO-IONP-PEG. All the images showed

that rGO-IONP-PEG could passively accumulate in the tumor after intravenous injection. (Adapted from Ref. [127] with permission. Copyright 2012, Wiley-VCH Verlag GmbH & Co. KGaA, Weinheim.)

In another report, a rhenium radiotracer was deposited on GO for biodistribution studies in mice [128]. The labeling procedure consisted in the reduction of Re(VII) to Re(V), which possesses empty electron orbitals that could be filled with electrons donated by carboxyl and hydroxyl groups of GO, yielding a stable labeling complex showing good compatibility with red blood cells. Radioactive measurements on the distribution of $^{188}\text{Re-GO}$ in mice evidenced high levels of accumulation in the lungs, liver, and spleen, which could be exploited for targeted drug delivery. Nevertheless long retention of $^{188}\text{Re-GO}$ in the tissues and pathological changes at high dosage were also reported [128].

4.3.2.3 Adsorption of Quantum Dots

QDs are nanostructures constituted by elements from period table groups III–V or II–VI with interesting optical and electronic properties that make them very attractive for applications in biological labeling, imaging, and biosensing. Indeed, QDs can be an alternative to the traditional organic fluorophores as they allow an increased signal-to-noise ratio with a higher photostability [129–132]. The direct labeling of graphene or GO with fluorophores or QDs generally leads to a complete quenching of the fluorescent signal by energy transfer with graphene or GO. Therefore, the preliminary coating of either graphene or QDs with polymers or biomolecules is essential to prevent this quenching effect. As an example, *rGO* was conjugated with QDs using BSA as a linker between the two nanomaterials for fluorescence imaging of live HeLa cells [133]. In another report, QDs protected by a monolayer organic shell have been deposited on the *rGO* surface for the imaging of different cancer cells [134]. To improve dispersibility, PLL has been adsorbed onto *rGO* and FA was covalently linked to PLL. After adsorption of PLL, coating of both QDs and *rGO* afforded a minimal fluorescence loss and mitigated the cytotoxicity of the nanocomposite. The strong fluorescence of the construct was used for *in vivo* imaging of internal tissues in small animals. The QD-*rGO* nanocomposite was found to be an optimal platform for tumor imaging, PTT, and *in situ* monitoring of the progress of treatment (Figure 4.11).

4.4

Graphene-Based Conjugates Prepared by a Combination of Covalent and Non-covalent Functionalization

4.4.1

Polymer- and Biopolymer-Grafted Graphene Nanomaterials Used as Nanocarriers

The preliminary surface modification of graphene and GO followed by adsorption of organic or biological molecules has been largely employed in the design of delivery systems. Grafting of polymers on GO is so far the most exploited way to achieve water-dispersible and biocompatible carriers for the delivery of drugs [22, 23, 39], NAs [135–138], or photosensitizers for photodynamic therapy (PDT) [139].

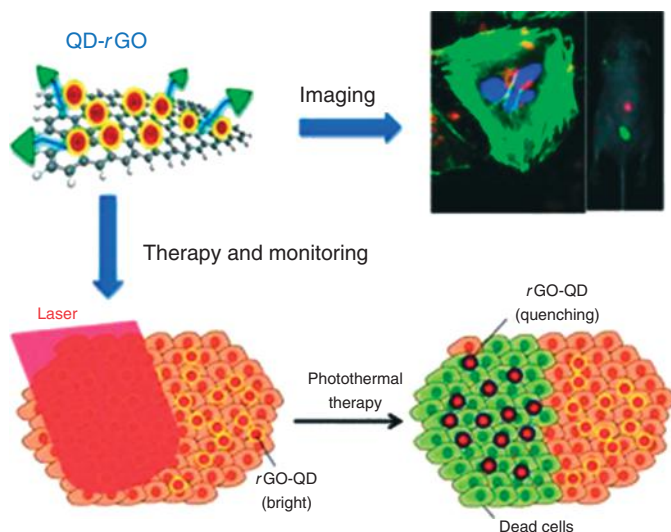


Figure 4.11 Quantum-dot-tagged *rGO* nanocomposites (left) internalized into targeted tumor cells display bright fluorescence (right). By the absorption of NIR radiation and its conversion into heat they also

cause simultaneous cell death and fluorescence reduction (bottom). (Reproduced with permission from Ref. [134]. Copyright 2012, Wiley-VCH Verlag GmbH & Co. KGaA, Weinheim.)

Among organic polymers, PEG and PEI have been mostly used as they can be easily anchored to GO through amidation or by adsorption.

4.4.1.1 Polymer-Functionalized GO for Drug Delivery

One of the first examples of drug loading on PEGylated GO was reported by Dai's group, who covalently used the aforementioned NGO-PEG-Rituximab conjugate for the targeted delivery of DOX into lymphoma cells [39]. The antibody Rituximab was covalently grafted to the PEG chains on NGO and DOX was then loaded on the conjugate. Acidic intracellular conditions induced the release of DOX from the GO surface, because of the higher solubility of DOX at acidic pH [39]. In another study, a similar NGO-PEG/DOX construct was used for combined chemotherapy and photothermal cancer treatment, with remarkable tumor ablation *in vivo* [22].

The same group has exploited the NGO-PEG nanocarrier for the delivery of other water-insoluble aromatic anticancer drugs, such as camptothecin (CPT) analogs and Iressa, which are potent inhibitors of the DNA topoisomerase and the epidermal growth factor receptor, respectively [23]. NGO conjugated with six-armed PEG was complexed with CPT SN-38 via π -stacking and hydrophobic interactions. The resulting material exhibited excellent aqueous dispersibility, while maintaining high cancer cell killing potency, similar to that of the free SN-38 molecules (Figure 4.12).

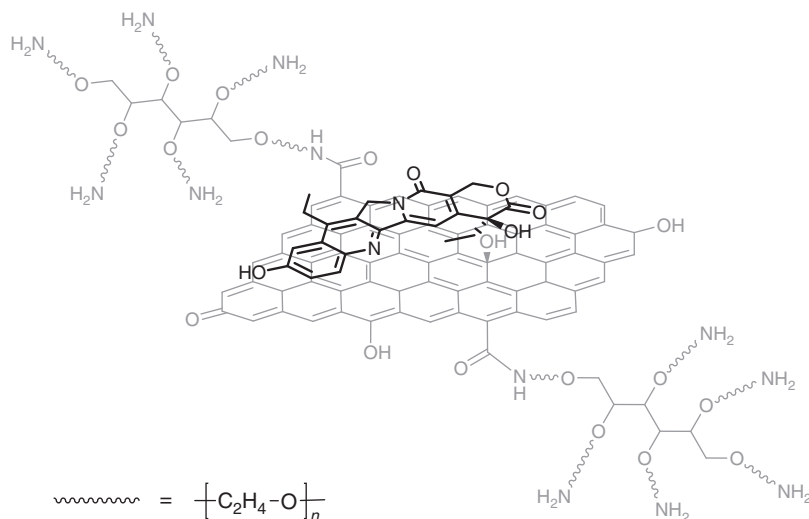


Figure 4.12 Schematic representation of NGO-PEG loaded with camptothecin SN-38. (Adapted from Ref. [23].)

4.4.1.2 Polymer-Functionalized GO for Gene Delivery

GO-based nanocarriers have been also explored for gene delivery [135–137]. For instance, Kim and coworkers [135] prepared a cationic gene carrier by covalently linking branched PEI to GO via EDC/NHS-mediated amidation. A pDNA was complexed by electrostatic interactions between negatively charged pDNA and positively charged PEI-GO (Figure 4.13). PEI-GO/pDNA showed a very efficient gene delivery and excellent photoluminescence activity.

An analog PEI-GO conjugate able to efficiently deliver pDNA into cells by migrating into the nucleus has been reported by Zhang's group [136]. In another report, they used PEI-GO conjugate to investigate the synergistic effect of delivering short interfering RNA (siRNA) and anticancer drugs to overcome the multiple drug resistance of cancer cells. Delivery of PEI-GO/siRNA followed by PEI-GO/DOX into HeLa cells led to a significantly enhanced chemotherapy efficacy, as the PEI-GO/siRNA dramatically enhanced the cytotoxicity of the PEI-GO/DOX [137].

Kong *et al.* [138] have prepared a PEG-NGO platform for the diagnosis of caspase-3, an enzyme directly involved in the activation of cell apoptosis. In this study, a caspase-3 cleavable site constituted by the peptide sequence DEVD was labeled with tetramethyl-6-carboxyrhodamine (TAMRA) and then coupled with a thiol-modified oligonucleotide partial sequence of *E. coli* RNAI. The TAMRA-DEVD-ssDNA was able to self-assemble onto PEG-NGO by π - π interactions, resulting in fluorescence quenching by FRET (Figure 4.14).

Caspase-3 activity in live cells allowed the recovery of the fluorescence by enzymatic cleavage at the level of DEVD sequence. *In vivo* experiments showed a remarkable potential of the PEG-NGO/TAMRA-DEVD-ssDNA construct for

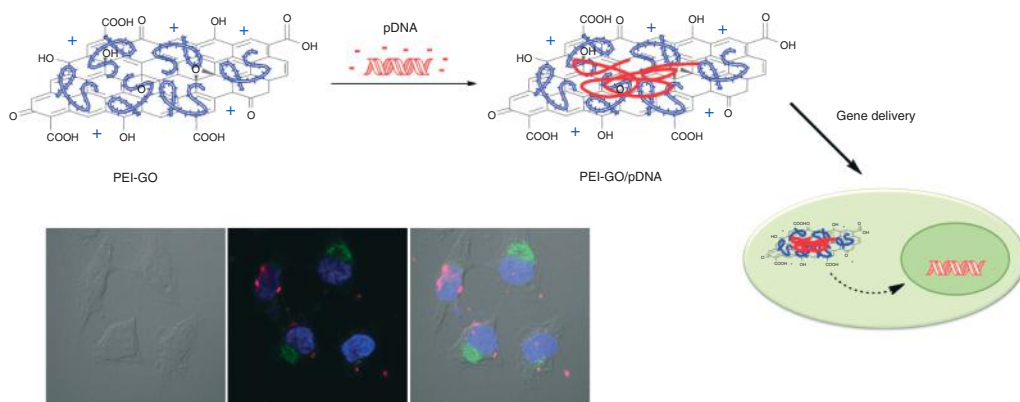


Figure 4.13 Schematic representation of the coating of PEI-GO with pDNA by electrostatic interactions and gene delivery mechanism inside the cell. Confocal fluorescence microscopic images of HeLa cell lines treated with PEI-GO/pDNA (bright field, dark field, merged), pDNA (red), nucleus (blue), PEI-GO (green) showing the efficient distribution of pDNA inside the cells. (Adapted and reproduced with permission from Ref. [135]. Copyright 2011, American Chemical Society.)

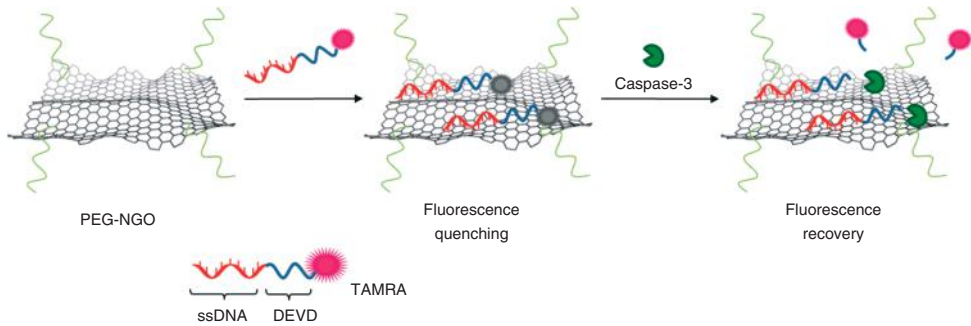


Figure 4.14 Preparation of PEG-NGO/TAMRA-DEVD-ssDNA probe and representation of caspase-3 detection by peptide cleavage and fluorescence recovery. (Adapted from Ref. [138].)

specific imaging and diagnosis of apoptosis-related diseases like hypoxic-ischemic encephalopathy and liver cirrhosis [138].

4.4.1.3 Chitosan-Functionalized GO

Chitosan is a natural polymer widely employed in tissue engineering, cell adhesion, and food delivery. It can be grafted onto GO through amidation (Scheme 4.9).

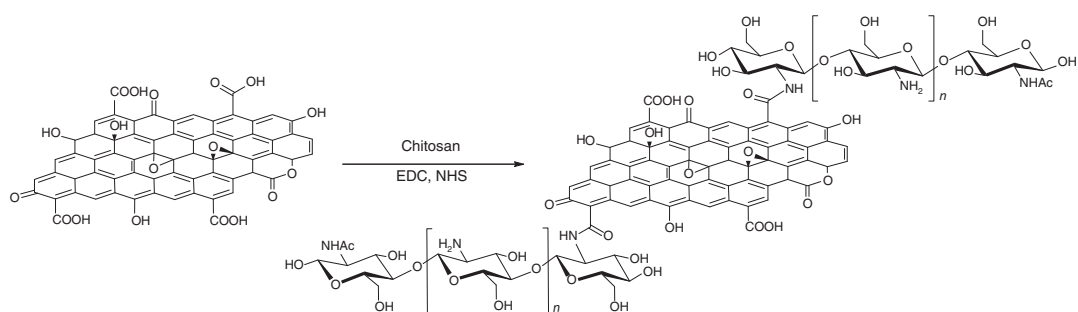
GO-chitosan can be loaded with pDNA or anticancer drugs via π - π and hydrophobic interactions for gene transfection and drug delivery, respectively [140, 141]. GO-chitosan loaded with CPT showed a significantly higher cytotoxicity toward cancer cells, compared to free CPT, at the same chemotherapeutic dose [140]. Adsorption and controlled release of small-size drugs, ibuprofen (IBU) and 5-fluorouracil (5-FU), has also been reported [141]. IBU is an anti-inflammatory drug with an aromatic system and it was adsorbed onto GO by π - π interactions assisted by H-bonding between the carboxylic groups of IBU and the glucopyranose rings of chitosan. 5-FU is a hydrophilic anticancer drug with a poor π -system, leading to a lower loading on GO-chitosan in comparison to IBU. Both GO-chitosan/IBU and GO-chitosan/5-FU hybrids displayed a pH-sensitive release behavior of the drugs, because of the polar interactions with GO-chitosan and to the drug protonation at low pH.

4.4.2

GO Functionalized with Targeting Ligands and Antibodies

4.4.2.1 Folic Acid-Conjugated GO

Zhang and coworkers [24] reported the functionalization of GO with FA and the loading of two drugs for targeted multiple drug delivery. As an alternative to the typical PEG approach, NGO was sulfonated to impart stability in physiological solutions [37]. For this purpose, hydroxyl, epoxides, and ester groups present on the NGO surface were first converted into carboxylic groups by initial epoxide opening followed by the reaction with chloroacetic acid [23]. Sulfonic acid groups



Scheme 4.9 Synthesis of GO-chitosan conjugate. (Adapted from Ref. [140].)

were subsequently attached to NGO by reaction with the diazonium salt of *p*-aminobenzenesulfonic acid. FA was then covalently conjugated to NGO-SO₃H by formation of an amide bond between the amine of FA and the COOH of GO. CPT and DOX were co-loaded onto FA-NGO by non-covalent interactions. Cellular uptake experiments revealed the efficient and targeted delivery of the anticancer drugs into cells overexpressing the folate receptor. Furthermore, the cytotoxic effect of FA-NGO/DOX/CPT was higher than that of FA-NGO loaded with only one drug [24].

Later, an FA-NGO construct was loaded with Ce6 for targeted PDT of tumor cells [142]. Photosensitizers are porphyrin-based molecules used in PDT to induce cell death through the generation of reactive oxygen species upon irradiation [143]. Significant reduction in cell viability was reported in a human stomach cancer cell line positive for FA receptors, when exposed to FA-GO/Ce6 following irradiation with the appropriate wavelength.

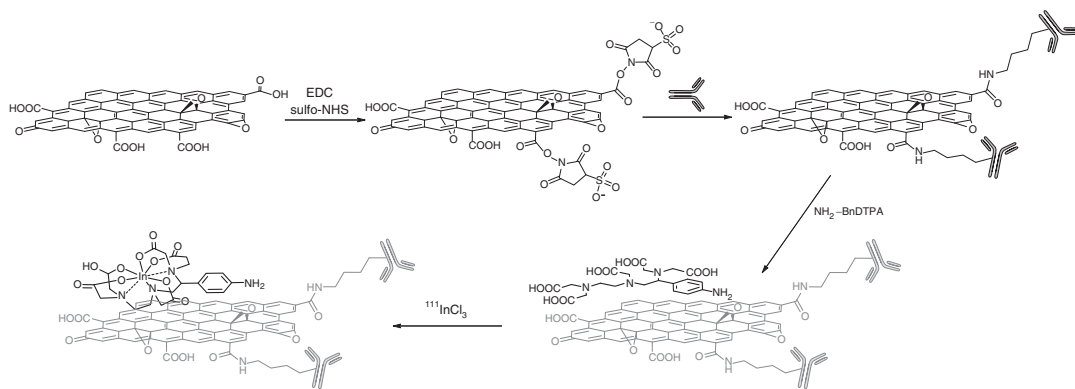
In another example, a FA-conjugated GO-hemin construct was prepared for selective and colorimetric detection of cancer cells based on peroxidase-like activity. GO was first modified with poly(allylamine hydrochloride) (PAH) by reaction between the amino groups of PAH and the epoxy groups on GO in basic conditions. FA was then conjugated to the terminal amines of PAH through amidation. Hemin was then introduced via adsorption onto GO, affording a platform able to quantitatively detect cancer cells with a peroxidase-like activity [144].

4.4.2.2 Antibody-Functionalized GO for Radioimaging and Biosensing

The versatile chemistry of GO has also been exploited for radiopharmaceutical investigations. Indeed, the possibility to covalently functionalize the GO surface with targeting moieties and loading of a radiolabel is interesting for imaging.

In this context, Cornelissen *et al.* have used a radiolabeled antibody-NGO conjugate for *in vivo* targeting and imaging of HER2-positive tumors with single-photon emission computed tomography (SPECT) [145]. HER2 is a receptor overexpressed by several breast cancers. The anti-HER2 antibody Trastuzumab was grafted onto NGO via the amino groups of the lysine side chains by amidation in the presence of EDC and sulfo-NHS. A metal ion chelator, 2-(4-aminobenzyl)-diethylene-triaminepentaacetic acid (*p*-NH₂-BnDTPA), was then adsorbed onto NGO via π -stacking, followed by chelation of indium-111 (Scheme 4.10). Interestingly, ¹¹¹In itself did not adsorb onto the GO surface. The as-prepared radiolabeled NGO-Trastuzumab conjugate allowed a clear tumor visualization *in vivo* by SPECT and showed specific tumor uptake with better pharmacokinetics compared to radiolabeled Trastuzumab.

In another work, an antibody-NGO conjugate has been used for the detection of α -fetoprotein (AFP), a potential diagnostic biomarker for hepatocellular carcinoma [146]. The capture antibody was covalently connected to sulfonyl-modified GO via EDC chemistry [37], whereas the reporter antibody was coupled to thioglycolic acid-capped CdTe QDs used as fluorescence donor. Trace amounts of AFP biomarker could be detected by fluorescence changes induced by the self-assembly of Ab-GO nanoconjugate with Ab/CdTe QD, where AFP acted as a “bridge” between the



Scheme 4.10 Synthesis of ^{111}In - p -NH₂-BnDTPA/NGO-Trastuzumab. (Adapted from Ref. [145].)

two. Interestingly, the fluorescence quenching efficiency is distance-independent, breaking the 100 Å distance limit of traditional biosensors.

4.5

Conclusions

Since the discovery of graphene a lot of effort has been devoted to its functionalization, with the aim of imparting desirable physical and chemical properties to graphene. Graphene functionalization is furthermore crucial to its employment in the biological field, because it is fundamental to improve graphene dispersibility and processability in organic and aqueous solutions. Within the family of graphene nanomaterials, GO is often preferred as starting material for the preparation of graphene derivatives because of the rich chemistry of the oxygen-containing groups, which can convey to GO multifunctionalities and multimodalities advantageous for diverse biological applications. Besides, the polar groups of GO render it more hydrophilic and dispersible than pristine graphene, giving easier access to further modifications.

As outlined in the chapter, functionalization of graphene-based materials can be accomplished through covalent or non-covalent approaches, or through the combination of covalent and non-covalent modifications.

Covalent derivatization of graphene for biological applications is generally achieved through esterification or amidation of the carboxyl groups of GO, assisted by coupling reagents. Different polymers were covalently grafted to GO to construct drug nanocarriers or agents for PTT and imaging, whereas several biosensing platforms have been developed by grafting antibodies, NAs, peptides, or organic molecules to graphene and GO.

The non-covalent modification of graphene occurs by adsorption of molecules on the surface of the graphenic material, driven by π - π interactions, hydrophobic effects, electrostatic interactions, or H-bonding in the case of GO. High payload can be reached as the adsorption can take place on both sides of the planar surface of graphene. π -Stacking and hydrophobic interactions are mainly involved in the adsorption of pyrene, ssDNA, aptamers, and aromatic drugs. The coating of graphene with molecules devoid of aromatic moieties such as QDs, nanoparticles, polymers, and biopolymers is driven by electrostatic and hydrophobic interactions. The applications of these graphene-based non-covalent conjugates span a wide range of applications such as drug and gene delivery, imaging, tissue engineering, and biosensing.

Covalent functionalization associated with non-covalent adsorption is an assessable way to impart good solubility and biocompatibility to graphene and it is mainly employed in the construction of delivery systems. In fact, this strategy responds well to the need to deliver insoluble therapeutics and to have a controlled release from the carrier. Covalent modification of graphene with polymer has been so far the most adopted approach. Graphene conjugates covalently and non-covalently

functionalized have been reported for drug and gene delivery, enzyme activity detection, radioimaging, and biosensing.

This chapter has highlighted the main chemical strategies underlying the preparation of graphene derivatives for biological and biomedical applications. The scientific interest aroused in the biological exploitation of graphene-based materials has already confirmed its great potential in these fields and definitely prompts for further investigations.

Acknowledgments

This work was supported by CNRS. The authors wish also to acknowledge support from the European Union FP7 RADDEL program (ITN Marie Curie Actions PEOPLE-2011-290023). A. Bianco wishes to acknowledge the CNRS financial support from PICS (Project for International Scientific Cooperation). C. Spinato is recipient of a fellowship from the European Union (ITN Marie Curie Actions PEOPLE-2011-290023). We wish also to thank the European Community program FP7-ICT-2013-FET-F (GRAPHENE, n. 604391).

References

1. Novoselov, K.S., Geim, A.K., Morozov, S.V., Jiang, D., Zhang, Y., Dubonos, S.V., Grigorieva, I.V., and Firsov, A.A. (2004) Electric field effect in atomically thin carbon films. *Science*, **306**, 666–669.
2. Geim, A.K. (2009) Graphene: status and prospects. *Science*, **324**, 1530–1534.
3. Huang, X., Yin, Z., Wu, S., Qi, X., He, Q., Zhang, Q., Yan, Q., Boey, F., and Zhang, H. (2011) Graphene-based materials: synthesis, characterization, properties, and applications. *Small*, **7**, 1876–1902.
4. Dai, L. (2013) Functionalization of graphene for efficient energy conversion and storage. *Acc. Chem. Res.*, **46**, 31–42.
5. Wang, X., Zhi, L., and Mullen, K. (2008) Transparent, conductive graphene electrodes for dye-sensitized solar cells. *Nano Lett.*, **8**, 323–327.
6. Stankovich, S., Dikin, D.A., Dommett, G.H.B., Kohlhaas, K.M., Zimney, E.J., Stach, E.A., Piner, R.D., Nguyen, S.T., and Ruoff, R.S. (2006) Graphene-based composite materials. *Nature*, **442**, 282–286.
7. Stoller, M.D., Park, S., Zhu, Y., An, J., and Ruoff, R.S. (2008) Graphene-based ultracapacitors. *Nano Lett.*, **8**, 3498–3502.
8. Mao, H.Y., Laurent, S., Chen, W., Akhavan, O., Imani, M., Ashkarran, A.A., and Mahmoudi, M. (2013) Graphene: promises, facts, opportunities, and challenges in nanomedicine. *Chem. Rev.*, **113**, 3407–3424.
9. Akhavan, O., Ghaderi, E., and Rahighi, R. (2012) Toward single-DNA electrochemical biosensing by graphene nanowalls. *ACS Nano*, **6**, 2904–2916.
10. Shao, Y., Wang, J., Wu, H., Liu, J., Aksay, I.A., and Lin, Y. (2010) Graphene based electrochemical sensors and biosensors: a review. *Electroanalysis*, **22**, 1027–1036.
11. Kuila, T., Bose, S., Khanra, P., Mishra, A.K., Kim, N.H., and Lee, J.H. (2011) Recent advances in graphene-based

- biosensors. *Biosens. Bioelectron.*, **26**, 4637–4648.
12. Mohanty, N. and Berry, V. (2008) Graphene-based single-bacterium resolution biodevice and DNA Transistor: interfacing graphene derivatives with nanoscale and microscale biocomponents. *Nano Lett.*, **8**, 4469–4476.
 13. Akhavan, O. and Ghaderi, E. (2009) Photocatalytic reduction of graphene oxide nanosheets on TiO₂ Thin film for photoinactivation of bacteria in solar light irradiation. *J. Phys. Chem. C*, **113**, 20214–20220.
 14. Akhavan, O. and Ghaderi, E. (2010) Toxicity of graphene and graphene oxide nanowalls against bacteria. *ACS Nano*, **4**, 5731–5736.
 15. Hu, W., Peng, C., Luo, W., Lv, M., Li, X., Li, D., Huang, Q., and Fan, C. (2010) Graphene-based antibacterial paper. *ACS Nano*, **4**, 4317–4323.
 16. Ma, J., Zhang, J., Xiong, Z., Yong, Y., and Zhao, X.S. (2011) Preparation, characterization and antibacterial properties of silver-modified graphene oxide. *J. Mater. Chem.*, **21**, 3350–3352.
 17. Akhavan, O., Choobtashani, M., and Ghaderi, E. (2012) Protein degradation and RNA efflux of viruses photocatalyzed by graphene–tungsten oxide composite under visible light irradiation. *J. Phys. Chem. C*, **116**, 9653–9659.
 18. Yang, K., Zhang, S., Zhang, G., Sun, X., Lee, S.-T., and Liu, Z. (2010) Graphene in mice: ultrahigh in vivo tumor uptake and efficient photothermal therapy. *Nano Lett.*, **10**, 3318–3323.
 19. Yang, K., Wan, J., Zhang, S., Tian, B., Zhang, Y., and Liu, Z. (2012) The influence of surface chemistry and size of nanoscale graphene oxide on photothermal therapy of cancer using ultra-low laser power. *Biomaterials*, **33**, 2206–2214.
 20. Akhavan, O., Ghaderi, E., Aghayee, S., Fereydooni, Y., and Talebi, A. (2012) The use of a glucose-reduced graphene oxide suspension for photothermal cancer therapy. *J. Mater. Chem.*, **22**, 13773–13781.
 21. Robinson, J.T., Tabakman, S.M., Liang, Y., Wang, H., Sanchez Casalongue, H., Vinh, D., and Dai, H. (2011) Ultrasmall reduced graphene oxide with high near-infrared absorbance for photothermal therapy. *J. Am. Chem. Soc.*, **133**, 6825–6831.
 22. Zhang, W., Guo, Z., Huang, D., Liu, Z., Guo, X., and Zhong, H. (2011) Synergistic effect of chemo-photothermal therapy using PEGylated graphene oxide. *Biomaterials*, **32**, 8555–8561.
 23. Liu, Z., Robinson, J.T., Sun, X., and Dai, H. (2008) PEGylated nanographene oxide for delivery of water-insoluble cancer drugs. *J. Am. Chem. Soc.*, **130**, 10876–10877.
 24. Zhang, L., Xia, J., Zhao, Q., Liu, L., and Zhang, Z. (2010) Functional graphene oxide as a nanocarrier for controlled loading and targeted delivery of mixed anticancer drugs. *Small*, **6**, 537–544.
 25. Heo, C., Yoo, J., Lee, S., Jo, A., Jung, S., Yoo, H., Lee, Y.H., and Suh, M. (2011) The control of neural cell-to-cell interactions through non-contact electrical field stimulation using graphene electrodes. *Biomaterials*, **32**, 19–27.
 26. Agarwal, S., Zhou, X., Ye, F., He, Q., Chen, G.C.K., Soo, J., Boey, F., Zhang, H., and Chen, P. (2010) Interfacing live cells with nanocarbon substrates. *Langmuir*, **26**, 2244–2247.
 27. Park, S., Mohanty, N., Suk, J.W., Nagaraja, A., An, J., Piner, R.D., Cai, W., Dreyer, D.R., Berry, V., and Ruoff, R.S. (2010) Biocompatible, robust free-standing paper composed of a TWEEN/graphene composite. *Adv. Mater.*, **22**, 1736–1740.
 28. Sanchez, V.C., Jachak, A., Hurt, R.H., and Kane, A.B. (2012) Biological interactions of graphene-family nanomaterials: an interdisciplinary review. *Chem. Res. Toxicol.*, **25**, 15–34.
 29. Wei, D. and Liu, Y. (2010) Controllable synthesis of graphene and its applications. *Adv. Mater.*, **22**, 3225–3241.
 30. Allen, M.J., Tung, V.C., and Kaner, R.B. (2010) Honeycomb carbon: a review of graphene. *Chem. Rev.*, **110**, 132–145.
 31. Park, S. and Ruoff, R.S. (2009) Chemical methods for the production of graphenes. *Nat. Nanotech.*, **4**, 217–224.

32. Hummers, W.S. and Offeman, R.E. (1958) Preparation of graphitic oxide. *J. Am. Chem. Soc.*, **80**, 1339–1339.
33. Staudenmaier, L. (1898) Verfahren zur Darstellung der Graphitsäure. *Ber. Dtsch. Chem. Ges.*, **31**, 1481–1487.
34. Shen, J., Hu, Y., Shi, M., Lu, X., Qin, C., Li, C., and Ye, M. (2009) Fast and facile preparation of graphene oxide and reduced graphene oxide nanoplatelets. *Chem. Mater.*, **21**, 3514–3520.
35. Georgakilas, V., Otyepka, M., Bourlinos, A.B., Chandra, V., Kim, N., Kemp, K.C., Hobza, P., Zboril, R., and Kim, K.S. (2012) Functionalization of graphene: covalent and non-covalent approaches, derivatives and applications. *Chem. Rev.*, **112**, 6156–6214.
36. Li, D., Müller, M.B., Gilje, S., Kaner, R.B., and Wallace, G.G. (2008) Processable aqueous dispersions of graphene nanosheets. *Nat. Nanotech.*, **3**, 101–105.
37. Si, Y. and Samulski, E.T. (2008) Synthesis of water soluble graphene. *Nano Lett.*, **8**, 1679–1682.
38. Niyogi, S., Bekyarova, E., Itkis, M.E., McWilliams, J.L., Hamon, M.A., and Haddon, R.C. (2006) Solution properties of graphite and graphene. *J. Am. Chem. Soc.*, **128**, 7720–7721.
39. Sun, X., Liu, Z., Welsher, K., Robinson, J.T., Goodwin, A., Zaric, S., and Dai, H. (2008) Nano-graphene oxide for cellular imaging and drug delivery. *Nano Res.*, **1**, 203–212.
40. Shan, C., Yang, H., Han, D., Zhang, Q., Ivaska, A., and Niu, L. (2009) Water-soluble graphene covalently functionalized by biocompatible poly-L-lysine. *Langmuir*, **25**, 12030–12033.
41. Chua, C.K. and Pumera, M. (2013) Covalent chemistry on graphene. *Chem. Soc. Rev.*, **42**, 3222–3233.
42. Park, J. and Yan, M. (2013) Covalent functionalization of graphene with reactive intermediates. *Acc. Chem. Res.*, **46**, 181–189.
43. Hsieh, C.-T. and Chen, W.-Y. (2011) Water/oil repellency and work of adhesion of liquid droplets on graphene oxide and graphene surfaces. *Surf. Coat. Technol.*, **205**, 4554–4561.
44. Zu, S.-Z. and Han, B.-H. (2009) Aqueous dispersion of graphene sheets stabilized by pluronic copolymers: formation of supramolecular hydrogel. *J. Phys. Chem.*, **C113**, 13651–13657.
45. Wang, G., Shen, X., Wang, B., Yao, J., and Park, J. (2009) Synthesis and characterisation of hydrophilic and organophilic graphene nanosheets. *Carbon*, **47**, 1359–1364.
46. Chen, D., Feng, H., and Li, J. (2012) Graphene oxide: preparation, functionalization, and electrochemical applications. *Chem. Rev.*, **112**, 6027–6053.
47. Dreyer, D.R., Park, S., Bielawski, C.W., and Ruoff, R.S. (2009) The chemistry of graphene oxide. *Chem. Soc. Rev.*, **39**, 228–240.
48. Shen, H. (2012) Biomedical applications of graphene. *Theranostics*, **2**, 283–294.
49. Chung, C., Kim, Y.-K., Shin, D., Ryoo, S.-R., Hong, B.H., and Min, D.-H. (2013) Biomedical applications of graphene and graphene oxide. *Acc. Chem. Res.*, **46** (10), 2211–2224.
50. Cote, L.J., Cruz-Silva, R., and Huang, J. (2009) Flash reduction and patterning of graphite oxide and its polymer composite. *J. Am. Chem. Soc.*, **131**, 11027–11032.
51. Gao, W., Alemany, L.B., Ci, L., and Ajayan, P.M. (2009) New insights into the structure and reduction of graphite oxide. *Nat. Chem.*, **1**, 403–408.
52. Pei, S. and Cheng, H.-M. (2012) The reduction of graphene oxide. *Carbon*, **50**, 3210–3228.
53. Chen, W., Yan, L., and Bangal, P.R. (2010) Preparation of graphene by the rapid and mild thermal reduction of graphene oxide induced by microwaves. *Carbon*, **48**, 1146–1152.
54. Liu, J., Fu, S., Yuan, B., Li, Y., and Deng, Z. (2010) Toward a universal «adhesive nanosheet» for the assembly of multiple nanoparticles based on a protein-induced reduction/decoration of graphene oxide. *J. Am. Chem. Soc.*, **132**, 7279–7281.
55. Gao, J., Liu, F., Liu, Y., Ma, N., Wang, Z., and Zhang, X. (2010) Environment-friendly method to produce graphene

- that employs Vitamin C and amino acid. *Chem. Mater.*, **22**, 2213–2218.
56. Salas, E.C., Sun, Z., Lüttge, A., and Tour, J.M. (2010) Reduction of graphene oxide via bacterial respiration. *ACS Nano*, **4**, 4852–4856.
 57. Peng, C., Hu, W., Zhou, Y., Fan, C., and Huang, Q. (2010) Intracellular imaging with a graphene-based fluorescent probe. *Small*, **6**, 1686–1692.
 58. Bottini, M., Rosato, N., and Bottini, N. (2011) PEG-modified carbon nanotubes in biomedicine: current status and challenges ahead. *Biomacromolecules*, **12**, 3381–3393.
 59. Dai, H. (2002) Carbon nanotubes: opportunities and challenges. *Surf. Sci.*, **500**, 218–241.
 60. Liu, Z., Tabakman, S., Welsher, K., and Dai, H. (2009) Carbon nanotubes in biology and medicine: In vitro and in vivo detection, imaging and drug delivery. *Nano Res.*, **2**, 85–120.
 61. Yang, K., Wan, J., Zhang, S., Zhang, Y., Lee, S.-T., and Liu, Z. (2011) In vivo pharmacokinetics, long-term biodistribution, and toxicology of PEGylated graphene in mice. *ACS Nano*, **5**, 516–522.
 62. Liu, Z., Jiang, L., Galli, F., Nederlof, I., Olsthoorn, R.C.L., Lamers, G.E.M., Oosterkamp, T.H., and Abrahams, J.P. (2010) A graphene oxide-streptavidin complex for biorecognition – towards affinity purification. *Adv. Funct. Mater.*, **20**, 2857–2865.
 63. Hong, H., Zhang, Y., Engle, J.W., Nayak, T.R., Theuer, C.P., Nickles, R.J., Barnhart, T.E., and Cai, W. (2012) In vivo targeting and positron emission tomography imaging of tumor vasculature with ⁶⁶Ga-labeled nano-graphene. *Biomaterials*, **33**, 4147–4156.
 64. Hong, H., Yang, K., Zhang, Y., Engle, J.W., Feng, L., Yang, Y., Nayak, T.R., Goel, S., Bean, J., Theuer, C.P., Barnhart, T.E., Liu, Z., and Cai, W. (2012) In vivo targeting and imaging of tumor vasculature with radiolabeled, antibody-conjugated nanographene. *ACS Nano*, **6**, 2361–2370.
 65. Di Martino, A., Sittinger, M., and Risbud, M.V. (2005) Chitosan: a versatile biopolymer for orthopaedic tissue-engineering. *Biomaterials*, **26**, 5983–5990.
 66. Depan, D., Girase, B., Shah, J.S., and Misra, R.D.K. (2011) Structure–process–property relationship of the polar graphene oxide-mediated cellular response and stimulated growth of osteoblasts on hybrid chitosan network structure nanocomposite scaffolds. *Acta Biomater.*, **7**, 3432–3445.
 67. Lim, S.Y., Ahn, J., Lee, J.S., Kim, M.-G., and Park, C.B. (2012) Graphene-oxide-based immunosensing through fluorescence quenching by peroxidase-catalyzed polymerization. *Small*, **8**, 1994–1999.
 68. Lee, J.S., Joung, H.-A., Kim, M.-G., and Park, C.B. (2012) Graphene-based chemiluminescence resonance energy transfer for homogeneous immunoassay. *ACS Nano*, **6**, 2978–2983.
 69. Jung, J.H., Cheon, D.S., Liu, F., Lee, K.B., and Seo, T.S. (2010) A graphene oxide based immuno-biosensor for pathogen detection. *Angew. Chem. Int. Ed.*, **49**, 5708–5711.
 70. Bonanni, A., Ambrosi, A., and Pumera, M. (2012) Nucleic acid functionalized graphene for biosensing. *Chem. Eur. J.*, **18**, 1668–1673.
 71. Wang, Z., Ge, Z., Zheng, X., Chen, N., Peng, C., Fan, C., and Huang, Q. (2012) Polyvalent DNA – graphene nanosheets «click» conjugates. *Nanoscale*, **4**, 394–399.
 72. Wang, H., Zhang, Q., Chu, X., Chen, T., Ge, J., and Yu, R. (2011) Graphene oxide–peptide conjugate as an intracellular protease sensor for caspase-3 activation imaging in live cells. *Angew. Chem. Int. Ed.*, **50**, 7065–7069.
 73. Zhang, J., Zhang, F., Yang, H., Huang, X., Liu, H., Zhang, J., and Guo, S. (2010) Graphene oxide as a matrix for enzyme immobilization. *Langmuir*, **26**, 6083–6085.
 74. Shan, C., Yang, H., Song, J., Han, D., Ivaska, A., and Niu, L. (2009) Direct electrochemistry of glucose oxidase and biosensing for glucose based on graphene. *Anal. Chem.*, **81**, 2378–2382.

75. Shan, C., Yang, H., Han, D., Zhang, Q., Ivaska, A., and Niu, L. (2010) Electrochemical determination of NADH and ethanol based on ionic liquid-functionalized graphene. *Biosens. Bioelectron.*, **25**, 1504–1508.
76. Gollavelli, G. and Ling, Y.-C. (2012) Multi-functional graphene as an in vitro and in vivo imaging probe. *Biomaterials*, **33**, 2532–2545.
77. Lerf, A., He, H., Forster, M., and Klinowski, J. (1998) Structure of graphite oxide revisited. *J. Phys. Chem.*, **B102**, 4477–4482.
78. Hontoria-Lucas, C., López-Peinado, A.J., López-González, J.d.D., Rojas-Cervantes, M.L., and Martín-Aranda, R.M. (1995) Study of oxygen-containing groups in a series of graphite oxides: Physical and chemical characterization. *Carbon*, **33**, 1585–1592.
79. Yang, X., Zhang, X., Liu, Z., Ma, Y., Huang, Y., and Chen, Y. (2008) High-efficiency loading and controlled release of doxorubicin hydrochloride on graphene oxide. *J. Phys. Chem. C*, **112**, 17554–17558.
80. Depan, D., Shah, J., and Misra, R.D.K. (2011) Controlled release of drug from folate-decorated and graphene mediated drug delivery system: synthesis, loading efficiency, and drug release response. *Mater. Sci. Eng. C*, **31**, 1305–1312.
81. Wang, Z., Huang, P., Bhirde, A., Jin, A., Ma, Y., Niu, G., Neamati, N., and Chen, X. (2012) A nanoscale graphene oxide-peptide biosensor for real-time specific biomarker detection on the cell surface. *Chem. Commun.*, **48**, 9768–9770.
82. Mann, J.A., Alava, T., Craighead, H.G., and Dichtel, W.R. (2013) Preservation of antibody selectivity on graphene by conjugation to a tripod monolayer. *Angew. Chem. Int. Ed.*, **52**, 3177–3180.
83. Liu, J., Kong, N., Li, A., Luo, X., Cui, L., Wang, R., and Feng, S. (2013) Graphene bridged enzyme electrodes for glucose biosensing application. *Analyst*, **138**, 2567–2575.
84. Zeng, G., Xing, Y., Gao, J., Wang, Z., and Zhang, X. (2010) Unconventional layer-by-layer assembly of graphene multilayer films for enzyme-based glucose and maltose biosensing. *Langmuir*, **26**, 15022–15026.
85. Liu, F., Choi, J.Y., and Seo, T.S. (2010) DNA mediated water-dispersible graphene fabrication and gold nanoparticle-graphene hybrid. *Chem. Commun.*, **46**, 2844–2846.
86. Balapanuru, J., Yang, J.-X., Xiao, S., Bao, Q., Jahan, M., Polavarapu, L., Wei, J., Xu, Q.-H., and Loh, K.P. (2010) A graphene oxide-organic dye ionic complex with DNA-sensing and optical-limiting properties. *Angew. Chem. Int. Ed.*, **49**, 6549–6553.
87. Lu, C.-H., Yang, H.-H., Zhu, C.-L., Chen, X., and Chen, G.-N. (2009) A graphene platform for sensing biomolecules. *Angew. Chem.*, **121**, 4879–4881.
88. Jang, H., Kim, Y.-K., Kwon, H.-M., Yeo, W.-S., Kim, D.-E., and Min, D.-H. (2010) A graphene-based platform for the assay of duplex-DNA unwinding by helicase. *Angew. Chem. Int. Ed.*, **49**, 5703–5707.
89. Wang, Y., Li, Z., Wang, J., Li, J., and Lin, Y. (2011) Graphene and graphene oxide: biofunctionalization and applications in biotechnology. *Trends Biotechnol.*, **29**, 205–212.
90. He, S., Song, B., Li, D., Zhu, C., Qi, W., Wen, Y., Wang, L., Song, S., Fang, H., and Fan, C. (2010) A graphene nanoprobe for rapid, sensitive, and multicolor fluorescent DNA analysis. *Adv. Funct. Mater.*, **20**, 453–459.
91. Lu, C.-H., Zhu, C.-L., Li, J., Liu, J.-J., Chen, X., and Yang, H.-H. (2010) Using graphene to protect DNA from cleavage during cellular delivery. *Chem. Commun.*, **46**, 3116–3118.
92. Chang, H., Tang, L., Wang, Y., Jiang, J., and Li, J. (2010) Graphene fluorescence resonance energy transfer aptasensor for the thrombin detection. *Anal. Chem.*, **82**, 2341–2346.
93. Jang, H., Ryoo, S.-R., Kim, Y.-K., Yoon, S., Kim, H., Han, S.W., Choi, B.-S., Kim, D.-E., and Min, D.-H. (2013) Discovery of hepatitis C virus NS3 helicase inhibitors by a multiplexed, high-throughput helicase activity assay

- based on graphene oxide. *Angew. Chem. Int. Ed.*, **52**, 2340–2344.
94. Wang, Y., Li, Z., Hu, D., Lin, C.-T., Li, J., and Lin, Y. (2010) Aptamer/graphene oxide nanocomplex for in situ molecular probing in living cells. *J. Am. Chem. Soc.*, **132**, 9274–9276.
 95. He, Y., Wang, Z.-G., Tang, H.-W., and Pang, D.-W. (2011) Low background signal platform for the detection of ATP: when a molecular aptamer beacon meets graphene oxide. *Biosens. Bioelectron.*, **29**, 76–81.
 96. Liu, M., Zhao, H., Chen, S., Yu, H., Zhang, Y., and Quan, X. (2011) Label-free fluorescent detection of Cu(II) ions based on DNA cleavage-dependent graphene-quenched DNazymes. *Chem. Commun.*, **47**, 7749–7751.
 97. Wen, Y., Xing, F., He, S., Song, S., Wang, L., Long, Y., Li, D., and Fan, C. (2010) A graphene-based fluorescent nanoprobe for silver(I) ions detection by using graphene oxide and a silver-specific oligonucleotide. *Chem. Commun.*, **46**, 2596–2598.
 98. Zhao, X.-H., Kong, R.-M., Zhang, X.-B., Meng, H.-M., Liu, W.-N., Tan, W., Shen, G.-L., and Yu, R.-Q. (2011) Graphene–DNAzyme based biosensor for amplified fluorescence «turn-on» detection of Pb²⁺ with a high selectivity. *Anal. Chem.*, **83**, 5062–5066.
 99. Tao, Y., Lin, Y., Ren, J., and Qu, X. (2013) Self-assembled, functionalized graphene and DNA as a universal platform for colorimetric assays. *Biomaterials*, **34**, 4810–4817.
 100. Guo, Y., Deng, L., Li, J., Guo, S., Wang, E., and Dong, S. (2011) Hemin–graphene hybrid nanosheets with intrinsic peroxidase-like activity for label-free colorimetric detection of single-nucleotide polymorphism. *ACS Nano*, **5**, 1282–1290.
 101. Zhang, M., Yin, B.-C., Wang, X.-F., and Ye, B.-C. (2011) Interaction of peptides with graphene oxide and its application for real-time monitoring of protease activity. *Chem. Commun.*, **47**, 2399–2401.
 102. Kodali, V.K., Scrimgeour, J., Kim, S., Hankinson, J.H., Carroll, K.M., de Heer, W.A., Berger, C., and Curtis, J.E. (2011) Nonperturbative chemical modification of graphene for protein micropatterning. *Langmuir*, **27**, 863–865.
 103. Patil, A.J., Vickery, J.L., Scott, T.B., and Mann, S. (2009) Aqueous stabilization and self-assembly of graphene sheets into layered bio-nanocomposites using DNA. *Adv. Mater.*, **21**, 3159–3164.
 104. Kuilla, T., Bhadra, S., Yao, D., Kim, N.H., Bose, S., and Lee, J.H. (2010) Recent advances in graphene based polymer composites. *Prog. Polym. Sci.*, **35**, 1350–1375.
 105. Park, Y.-J., Park, S.Y., and In, I. (2011) Preparation of water soluble graphene using polyethylene glycol: comparison of covalent approach and noncovalent approach. *J. Ind. Eng. Chem.*, **17**, 298–303.
 106. Feng, L., Zhang, S., and Liu, Z. (2011) Graphene based gene transfection. *Nanoscale*, **3**, 1252–1257.
 107. Shi, X., Gong, H., Li, Y., Wang, C., Cheng, L., and Liu, Z. (2013) Graphene-based magnetic plasmonic nanocomposite for dual bioimaging and photothermal therapy. *Biomaterials*, **34**, 4786–4793.
 108. Yang, Q., Pan, X., Huang, F., and Li, K. (2010) Fabrication of high-concentration and stable aqueous suspensions of graphene nanosheets by noncovalent functionalization with lignin and cellulose derivatives. *J. Phys. Chem. C*, **114**, 3811–3816.
 109. Markovic, Z.M., Harhaji-Trajkovic, L.M., Todorovic-Markovic, B.M., Kepić, D.P., Arsikin, K.M., Jovanović, S.P., Pantovic, A.C., Dramićanin, M.D., and Trajkovic, V.S. (2011) In vitro comparison of the photothermal anticancer activity of graphene nanoparticles and carbon nanotubes. *Biomaterials*, **32**, 1121–1129.
 110. Sheng, L., Ren, J., Miao, Y., Wang, J., and Wang, E. (2011) PVP-coated graphene oxide for selective determination of ochratoxin A via quenching fluorescence of free aptamer. *Biosens. Bioelectron.*, **26**, 3494–3499.
 111. Liu, K., Zhang, J.-J., Cheng, F.-F., Zheng, T.-T., Wang, C., and Zhu,

- J.-J. (2011) Green and facile synthesis of highly biocompatible graphene nanosheets and its application for cellular imaging and drug delivery. *J. Mater. Chem.*, **21**, 12034–12040.
112. Luppi, E., Cesaretti, M., and Volpi, N. (2005) Purification and characterization of heparin from the italian clam *Callista chione*. *Biomacromolecules*, **6**, 1672–1678.
 113. Kidane, A.G., Salacinski, H., Tiwari, A., Bruckdorfer, K.R., and Seifalian, A.M. (2004) Anticoagulant and antiplatelet agents: their clinical and device application(s) together with usages to engineer surfaces. *Biomacromolecules*, **5**, 798–813.
 114. Murugesan, S., Park, T.-J., Yang, H., Mousa, S., and Linhardt, R.J. (2006) Blood compatible carbon nanotubes–nano-based neoproteoglycans. *Langmuir*, **22**, 3461–3463.
 115. Lee, D.Y., Khatun, Z., Lee, J.-H., Lee, Y., and In, I. (2011) Blood compatible graphene/heparin conjugate through noncovalent chemistry. *Biomacromolecules*, **12**, 336–341.
 116. Cho, Y., Kim, H., and Choi, Y. (2013) A graphene oxide–photosensitizer complex as an enzyme-activatable theranostic agent. *Chem. Commun.*, **49**, 1202–1204.
 117. Jin, Z., Nackashi, D., Lu, W., Kittrell, C., and Tour, J.M. (2010) Decoration, migration, and aggregation of palladium nanoparticles on graphene sheets. *Chem. Mater.*, **22**, 5695–5699.
 118. Wu, Z.-S., Ren, W., Wen, L., Gao, L., Zhao, J., Chen, Z., Zhou, G., Li, F., and Cheng, H.-M. (2010) Graphene anchored with Co_3O_4 nanoparticles as anode of lithium ion batteries with enhanced reversible capacity and cyclic performance. *ACS Nano*, **4**, 3187–3194.
 119. Zhang, L.-S., Jiang, L.-Y., Yan, H.-J., Wang, W.D., Wang, W., Song, W.-G., Guo, Y.-G., and Wan, L.-J. (2010) Mono dispersed SnO_2 nanoparticles on both sides of single layer graphene sheets as anode materials in Li-ion batteries. *J. Mater. Chem.*, **20**, 5462–5467.
 120. Myung, S., Park, J., Lee, H., Kim, K.S., and Hong, S. (2010) Ambipolar memory devices based on reduced graphene oxide and nanoparticles. *Adv. Mater.*, **22**, 2045–2049.
 121. Yang, S., Feng, X., Ivanovici, S., and Müllen, K. (2010) Fabrication of graphene-encapsulated oxide nanoparticles: towards high-performance anode materials for lithium storage. *Angew. Chem. Int. Ed.*, **49**, 8408–8411.
 122. Ren, H., Wang, C., Zhang, J., Zhou, X., Xu, D., Zheng, J., Guo, S., and Zhang, J. (2010) DNA cleavage system of nanosized graphene oxide sheets and copper ions. *ACS Nano*, **4**, 7169–7174.
 123. Yang, S.-T., Chang, Y., Wang, H., Liu, G., Chen, S., Wang, Y., Liu, Y., and Cao, A. (2010) Folding/aggregation of graphene oxide and its application in Cu^{2+} removal. *J. Colloid Interface Sci.*, **351**, 122–127.
 124. Cong, H.-P., He, J.-J., Lu, Y., and Yu, S.-H. (2010) Water-soluble magnetic-functionalized reduced graphene oxide sheets: in situ synthesis and magnetic resonance imaging applications. *Small*, **6**, 169–173.
 125. Yang, X., Zhang, X., Ma, Y., Huang, Y., Wang, Y., and Chen, Y. (2009) Superparamagnetic graphene oxide– Fe_3O_4 nanoparticles hybrid for controlled targeted drug carriers. *J. Mater. Chem.*, **19**, 2710–2714.
 126. Yang, X., Wang, Y., Huang, X., Ma, Y., Huang, Y., Yang, R., Duan, H., and Chen, Y. (2011) Multi-functionalized graphene oxide based anticancer drug-carrier with dual-targeting function and pH-sensitivity. *J. Mater. Chem.*, **21**, 3448–3454.
 127. Yang, K., Hu, L., Ma, X., Ye, S., Cheng, L., Shi, X., Li, C., Li, Y., and Liu, Z. (2012) Multimodal imaging guided photothermal therapy using functionalized graphene nanosheets anchored with magnetic nanoparticles. *Adv. Mater.*, **24**, 1868–1872.
 128. Zhang, X., Yin, J., Peng, C., Hu, W., Zhu, Z., Li, W., Fan, C., and Huang, Q. (2011) Distribution and biocompatibility studies of graphene oxide in mice after intravenous administration. *Carbon*, **49**, 986–995.
 129. Dubertret, B., Calame, M., and Libchaber, A.J. (2001) Single-mismatch

- detection using gold-quenched fluorescent oligonucleotides. *Nat. Biotechnol.*, **19**, 365–370.
130. Seferos, D.S., Giljohann, D.A., Hill, H.D., Prigodich, A.E., and Mirkin, C.A. (2007) Nano-flares: probes for transfection and mRNA detection in living cells. *J. Am. Chem. Soc.*, **129**, 15477–15479.
 131. Maxwell, D.J., Taylor, J.R., and Nie, S. (2002) Self-assembled nanoparticle probes for recognition and detection of biomolecules. *J. Am. Chem. Soc.*, **124**, 9606–9612.
 132. Chen, Z., Berciaud, S., Nuckolls, C., Heinz, T.F., and Brus, L.E. (2010) Energy transfer from individual semiconductor nanocrystals to graphene. *ACS Nano*, **4**, 2964–2968.
 133. Chen, M.-L., Liu, J.-W., Hu, B., Chen, M.-L., and Wang, J.-H. (2011) Conjugation of quantum dots with graphene for fluorescence imaging of live cells. *Analyst*, **136**, 4277–4283.
 134. Hu, S.-H., Chen, Y.-W., Hung, W.-T., Chen, I.-W., and Chen, S.-Y. (2012) Quantum-dot-tagged reduced graphene oxide nanocomposites for bright fluorescence bioimaging and photothermal therapy monitored in situ. *Adv. Mater.*, **24**, 1748–1754.
 135. Kim, H., Namgung, R., Singha, K., Oh, I.-K., and Kim, W.J. (2011) Graphene oxide–polyethylenimine nanoconstruct as a gene delivery vector and bioimaging tool. *Bioconjugate Chem.*, **22**, 2558–2567.
 136. Chen, B., Liu, M., Zhang, L., Huang, J., Yao, J., and Zhang, Z. (2011) Polyethylenimine-functionalized graphene oxide as an efficient gene delivery vector. *J. Mater. Chem.*, **21**, 7736–7741.
 137. Zhang, L., Lu, Z., Zhao, Q., Huang, J., Shen, H., and Zhang, Z. (2011) Enhanced chemotherapy efficacy by sequential delivery of siRNA and anticancer drugs using PEI-grafted graphene oxide. *Small*, **7**, 460–464.
 138. Kong, W.H., Sung, D.K., Kim, K.S., Jung, H.S., Gho, E.J., Yun, S.H., and Hahn, S.K. (2012) Self-assembled complex of probe peptide – E. Coli RNA I conjugate and nano graphene oxide for apoptosis diagnosis. *Biomaterials*, **33**, 7556–7564.
 139. HaiQing, D., Zhao, Z., Wen, H., Li, Y., Guo, F., Shen, A., Pilger, F., Lin, C., and Shi, D. (2010) Poly(ethylene glycol) conjugated nano-graphene oxide for photodynamic therapy. *Sci. China Chem.*, **53**, 2265–2271.
 140. Bao, H., Pan, Y., Ping, Y., Sahoo, N.G., Wu, T., Li, L., Li, J., and Gan, L.H. (2011) Chitosan-functionalized graphene oxide as a nanocarrier for drug and gene delivery. *Small*, **7**, 1569–1578.
 141. Rana, V.K., Choi, M.-C., Kong, J.-Y., Kim, G.Y., Kim, M.J., Kim, S.-H., Mishra, S., Singh, R.P., and Ha, C.-S. (2011) Synthesis and drug-delivery behavior of chitosan-functionalized graphene oxide hybrid nanosheets. *Macromol. Mater. Eng.*, **296**, 131–140.
 142. Huang, P. (2011) Folic acid-conjugated graphene oxide loaded with photosensitizers for targeting photodynamic therapy. *Theranostics*, **1**, 240–250.
 143. O'Connor, A.E., Gallagher, W.M., and Byrne, A.T. (2009) Porphyrin and non-porphyrin photosensitizers in oncology: preclinical and clinical advances in photodynamic therapy. *Photochem. Photobiol.*, **85**, 1053–1074.
 144. Song, Y., Chen, Y., Feng, L., Ren, J., and Qu, X. (2011) Selective and quantitative cancer cell detection using target-directed functionalized graphene and its synergetic peroxidase-like activity. *Chem. Commun.*, **47**, 4436–4438.
 145. Cornelissen, B., Able, S., Kersemans, V., Waghorn, P.A., Myhra, S., Jurkshat, K., Crossley, A., and Vallis, K.A. (2013) Nanographene oxide-based radioimmunoconstructs for in vivo targeting and SPECT imaging of HER2-positive tumors. *Biomaterials*, **34**, 1146–1154.
 146. Liu, M., Zhao, H., Quan, X., Chen, S., and Fan, X. (2010) Distance-independent quenching of quantum dots by nanoscale-graphene in self-assembled sandwich immunoassay. *Chem. Commun.*, **46**, 7909–7911.

5

Immobilization of Enzymes and other Biomolecules on Graphene

Ioannis V. Pavlidis, Michaela Patila, Angeliki C. Polydera, Dimitrios Gournis, and Haralampos Stamatis

5.1

Introduction

Nanobiotechnology refers to the use of nanotechnology to further the goals of biotechnology. The synergistic interactions between these two technologies have resulted in innovative advances in two different ways, including the use of biological systems and macromolecules (cells, nucleic acids, and proteins including enzymes) for the production of functional nanosystems and the development of biological nanosystems. Nanobiocatalysis, in which enzymes are incorporated into nanostructured materials, is one typical example [1].

Enzymes are important biomacromolecules that are considered nature's versatile catalysts for chemical and biochemical reactions. Enzymes are able to perform and regulate the complex chemical processes that are the basis of the metabolism of all living organisms. The excellent functional properties of enzymes, such as high catalytic efficiency, as well as chemo-, regio-, and stereo-specificity, are rightly perceived as highly desirable properties for applications in various biotechnological processes, including:

- Biotransformation of natural and synthetic compounds and production of high value products,
- analytics and diagnostics, mainly in medicine, and
- environmental protection and bioremediation.

A large number of enzymes that catalyze a vast array of reactions have been identified and characterized and are in principle, available for use as biocatalysts. However, the common perception is that, enzymes, as well as other biocatalytic systems such as catalytic antibodies and whole cells, are sensitive, unstable, and have to be used in water; features that are not ideal for a catalyst and undesirable in most processes. In many cases, a way to avoid at least part of these drawbacks is to immobilize enzymes [2]. The use of immobilized enzymes and other biomolecules, instead of fully or partially soluble preparations, presents many advantages, such as enhanced stability, repeated use, easy separation from the reaction mixture, possible

modulation of the catalytic properties, prevention of protein contamination of the product, and simple performance and design of the bioreactor [3].

Immobilization of biomolecules was achieved by their inclusion into polymeric matrices or binding onto carrier materials via different types of interactions, including physical adsorption and covalent binding [4]. Among various immobilization supports used, nanostructured composite materials with large active surface area and desirable pore sizes, including nanoporous media, nanofibers, nanoparticles, and carbon-based nanomaterials (CBNs), are now the focus of intense fundamental and applied research in a number of areas, including biocatalysis. Biomolecules, enzymes included, are nanometer-scaled molecules, which benefit from the high surface area-to-volume ratio of these nanostructures; this is because it is possible to load higher amount of biocatalysts compared to conventional supports.

One of the particularly advantageous features of nanostructured materials is their efficacy in manipulating the nanoscale environment of the biomolecules and thus in their biological function and stability [5, 6]. The unique properties of nanomaterials, as immobilization supports for biomolecules, together with other desirable properties, such as conductivity and magnetism, offer particularly exciting opportunities in biocatalysis, molecular imaging, therapy, and delivery of biomolecules, as well as in construction of biosensors and biomedical devices [1, 7–9].

Recently, a new nanomaterial of high surface area-to-volume ratio, graphene, has attracted increasing attention as a fundamental building block for fullerenes, carbon nanotubes (CNTs), and graphite. Graphene is made of monolayers of two-dimensional honeycomb graphite type carbon [10, 11]. This unique nanostructure material has high surface area, excellent electrical conductivity and electron mobility at room temperature, robust mechanical properties, and flexibility [12]. The unique nanostructure and properties of graphene and its oxidized form, graphene oxide (GO), provide potential nanocomposite applications, including the immobilization of biomacromolecules.

The chemical functionalization of these carbon nanomaterials for grafting desirable functional groups (such as epoxide, carboxylic, and hydroxyl groups) onto their surface is used to obtain nanomaterials with tailor-made properties [13, 14]. The surface chemistry of the functionalized nanomaterials can affect their interactions with biomolecules and thus affect the structure and the biological function of biomolecules, providing potential applications in nanotechnology and biomedicine. Graphene nanomaterials have been used as immobilization support to prepare nanobiocatalytic systems or as a drug delivery vehicle by adsorption of the drug on its surface. Moreover, graphene nanomaterials have been exploited in cellular imaging, as well as in the preparation of biosensors and biofuel cells.

In this chapter, we will focus on the most recent developments in the use of graphene-based nanostructured materials for enzyme and other biomolecules immobilization, together with their potential applications in various fields, such as biocatalysis, biosensors, biofuel cells, intracellular biomolecules, and transportation.

5.2 Immobilization Approaches

Despite the fact that the graphite surface can be chemically functionalized to dope any functional groups on its surface, most of the research in the field of biomacromolecules immobilization focuses on GO as the immobilization matrix. The reason for this can be the ease of production of GO from graphite. A coarse categorization of the immobilization approaches could sort them into three groups: (i) physical adsorption, (ii) covalent attachment, and (iii) affinity interactions. In this paragraph, we discuss the protein/enzyme immobilization, but the approaches described here could also apply to other biomacromolecules, such as DNA and antibodies.

Physical adsorption is an easy approach for the immobilization of biomacromolecules onto graphene and graphene derivative surfaces, which seems to be favored by most researchers [15–19]. The approach followed in most cases is straight-forward [18, 20]; the nanomaterial is dispersed (or deposited on the surface of an electrode) and then an amount of enzyme is added to this dispersion; the mixture is incubated for a specific time interval and then the nanomaterial (or biosensor) is recovered, as rinsing steps are crucial for the removal of the loosely bound enzyme molecules. The physical adsorption is attributed mostly to hydrophobic and electrostatic interactions, although other factors, such as the geometry of the nanomaterial, can play an important role [14, 21, 22]. Hydrophobic interactions can be grown between the hydrophobic surface or any hydrophobic functional group of the graphene and the hydrophobic areas on the surface of the protein [23]. On the other hand, electrostatic interactions can either be between charged groups of the nanomaterial and the biomolecule, or by π - π stacking between the rings on the surface of graphene derivatives and any aromatic amino acids exposed on the surface of the protein. Until now, no adequate method has been proposed to predict the quota of these forces during physical adsorption. An interesting work of Zhang and coworkers [22] advocates that the electrostatic interactions are the driving force of the non-covalent immobilization; immobilization of horseradish peroxidase (HRP) and lysozyme, two enzymes of different pI, in variable pH revealed that the highest immobilization yield was attained in the pH that was predicted to grant the stronger electrostatic interactions. On the contrary, Azamian and coworkers [24] showed that the adsorption of protein onto CNTs is insensitive to protein pI, and thus the electrostatic interactions are not predominant in this case. Another interesting work compared the immobilization efficiency of GO and rGO (reduced graphene oxide) [15]; contrary to the initial hypothesis of the authors, rGO showed higher immobilization efficiency than the GO, which is more rich in chemical groups. This underlined the fact that the electrostatic interactions do not play a major role in this case. Moreover, using circular dichroism (CD) spectroscopy, they observed that the structure of the enzymes is altered when immobilized on GO and rGO and proposed that hydrophobic areas are exposed to the protein surface [15]. In order to improve the immobilization efficiency, other factors were also studied. Immobilization onto GO showed that there is no significant effect on

the number of graphene layers, so that the total exfoliation is not mandatory for efficient immobilization [16]. Decoration of graphene with calcium atoms [25] or ionic liquid (IL) [26] enhances the immobilization efficiency without disrupting the graphene surface. However, a major drawback of physical adsorption is that the protein is in equilibrium between the nanomaterial and the solution, and thus can be gradually detached [18, 23]. Surprisingly, there is no dedicated research on the dynamics of protein leakage.

Covalent immobilization can address this drawback, by the formation of a covalent bond between the nanomaterial and the protein; this leads to a more robust biomaterial, suggesting higher stability and preventing enzyme leakage [27]. Several approaches have been developed for the covalent immobilization of proteins and other biomacromolecules onto graphene derivatives. Two approaches are the most common; the use of carbodiimide as a “bridge molecule” between carboxylated materials, such as GO, and proteins [23] and the cross linking of amine groups on the protein and the nanomaterial surface with glutaraldehyde [20] (Figure 5.1).

The use of the carbodiimide chemistry is most often applied, usually using the 1-ethyl-3-(3-dimethylaminopropyl) carbodiimide (EDC) and *N*-hydroxysuccinimide (NHS) or the more hydrophilic *N*-hydroxysulfo-succinimide (sulfo-NHS). As shown in Figure 5.1, EDC attacks the carboxyl group of the nanomaterial to form an unstable reactive *o*-acylisourea ester. This can directly be used to form a stable amide bond with the free amine groups of the surface of the protein. However, as the water molecule can disrupt the ester and regenerate the carboxyl group, the use of NHS or sulfo-NHS is crucial to produce a semi-stable amine reactive ester that can be later replaced from the protein. This approach was successfully applied for the immobilization of various biomolecules such as nucleotides [28], RNA [29], single-stranded DNA (ssDNA) [30], glucose oxidase (GOD) [31], and bovine serum albumin [32]. In order to further improve the efficiency of this protocol, methods have been developed for the enrichment of the GO surface with carboxyl groups [29, 30]. Some researchers describe the use of non-functionalized graphene, for instance, the use of poly-L-lysine hydrobromide for the immobilization of HRP [33], the use of 10-perylene tetracarboxylic acid for the immobilization of ssDNA [34], the use of Au nanoparticles and sodium citrate for the covalent immobilization of GOD [35], or the more sophisticated use of 1-pyrenebutanoic acid succinimidyl ester for the immobilization of GOD [36]; pyrene is used for π - π stacking on graphene and then the semi-stable NHS ester is exchanged with the enzyme to form a covalent bond.

The alternative approach in covalent immobilization, which is not used as often, is the cross linking of free amine groups that should be present on the nanomaterial and the lysine residues on the surface of the proteins. In order to provide amine groups on the graphene surface, researchers functionalize graphene with several materials. For instance, bovine serum albumin was used to functionalize graphene, in order to provide the free amine groups and cross link with cholesterol oxidase and cholesterol esterase [37]. More sophisticated was the approach of Zue and coworkers, where, in order to have free amine groups on the surface of the

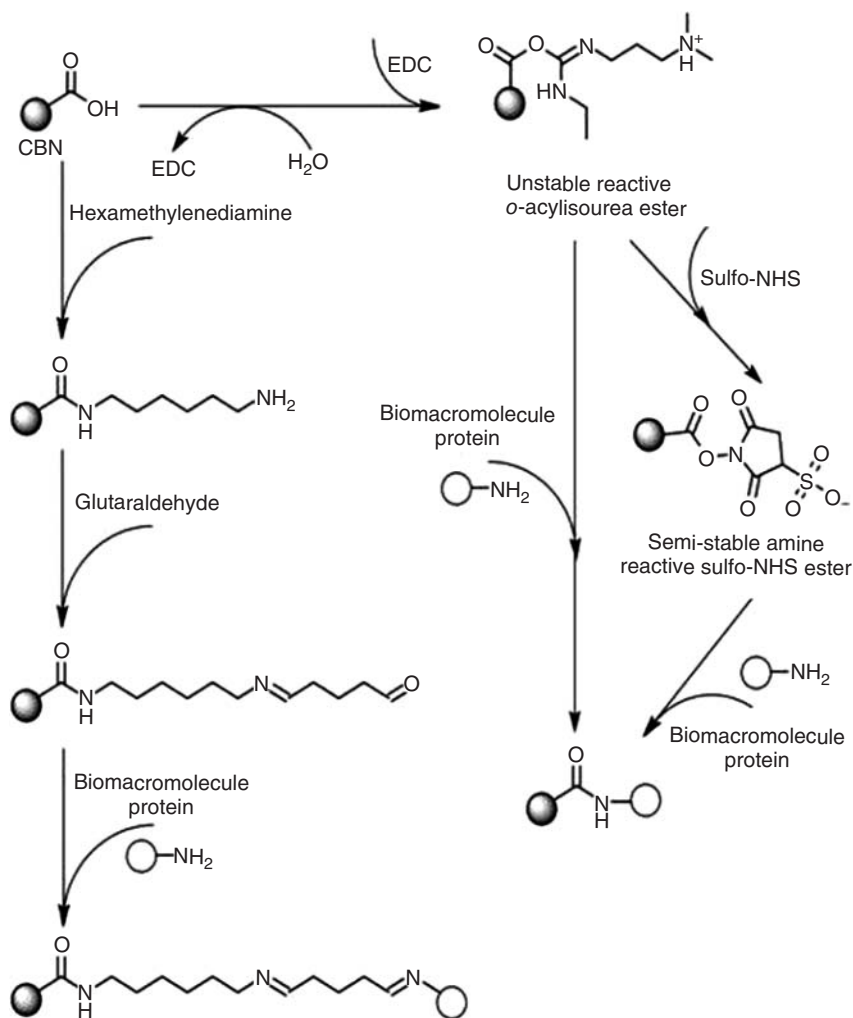


Figure 5.1 Schematic representation of various approaches for covalent immobilization onto carboxylated carbon-based nanomaterials (CBNs), such as GO; left side is an

approach with glutaraldehyde cross linking, while on the right branch there is the widely applied EDC/NHS approach.

nanomaterial, they first covalently bound Fe_3O_4 nanoparticles functionalized with aminopropyl-triethoxysilane on the surface of GO through EDC/NHS chemistry and then used glutaraldehyde to covalently immobilize hemoglobin on the silane derivative [38].

However, if we want to be critical of the field of covalent immobilization, there are some crucial gaps in most studies on this field. There is (i) no direct certification that the covalent bond is present, (ii) no or insufficient hindrance of the physical adsorption, and (iii) no rational optimization of the immobilization

process, regarding the incubation time, the amount of the cross-linker, and so on. The use of EDC for the immobilization of protein on single wall CNTs resulted in comparable levels of enzyme loading as without this coupling factor, leading to the conclusion that the immobilization in both cases is predominantly non-covalent [24]. A well-studied and detailed approach was on the immobilization of β -galactosidase onto GO with the use of cysteamine and glutaraldehyde [39]. Cysteamine is chemisorbed to the surface of GO and its free amine groups are used for cross linking to the enzyme with the use of glutaraldehyde. The researchers used the response surface methodology approach to optimize the amount of GO, enzyme, glutaraldehyde, and cysteamine. Despite the interesting approach to the problem, this group did not avoid the physical adsorption to monitor only the covalent immobilization. In an attempt to rationalize the covalent immobilization procedure and compare it with the non-covalent immobilization procedure, we have worked with GO functionalized with hexamethylenediamine in order to have free amine groups covalently fixed on the nanomaterial surface [20]. In order to hinder the nonspecific immobilization we used Tween 20, as we have found that the hydrophobic interactions are the predominant force for the nonspecific immobilization. Esterases and lipases of different pI were immobilized onto CNT-NH₂ (amine carbon nanotube) and GO-NH₂ (amine graphene oxide) using glutaraldehyde as a cross-linker and the covalent bond was certified through X-ray photoelectron spectroscopy. In our opinion, more detailed studies should be conducted on this perspective, in order to rationalize the covalent immobilization and try to predict the behavior of biomacromolecules.

The final immobilization approach is the affinity immobilization, which does not differ much from the previous approaches, but stands out for its reversible character. This method is usually based on the use of specific antibodies, in a sandwich approach. For instance, functionalized graphene with Au nanoparticles and L-cysteine were used to immobilize rabbit antihuman IgG antibody, which has affinity to human IgG [40]. In a more straight-forward approach, GO was functionalized with avidin and biotin-modified aptamer was immobilized through avidin–biotin affinity, in order to prepare a thrombin detector [41]. These are sophisticated techniques that involve a lot of steps and affinity interactions; however, with more intensive studies they could be used for the regeneration of the immobilized enzyme and the nanomaterial. Loo and coworkers performed an interesting comparative study of all three approaches [41]. This study revealed that physical adsorption leads to leakage of the aptamer, whereas covalent immobilization could counter this problem. The most interesting result, however, was that although the affinity-based immobilization was more stable than the physical adsorption, it led to less selective biosensors, questioning the accuracy of the affinity interactions.

All the aforementioned approaches are interesting and yielded significant results, however, more extensive studies are needed, as they are expected to provide us with a better insight of the immobilization process, thus facilitating the rational design of more effective biomaterials and biosensors.

5.3

Applications of Immobilized Biomolecules

5.3.1

Biosensors

A biosensor can be defined as a compact analytical device for transforming biological signals into analytical ones. It combines a bio-component with a physical element that is mainly used for converting the biologically derived message to quantitative information [42, 43]. A biosensor device consists of a highly selective and sensitive biological or biologically derived sensing element (e.g., microbial cells, cell receptors, enzymes, antibodies, nucleic acids, etc.) intimately associated with a physicochemical transducer that translates the biological recognition process between the receptor and the analyte into a measurable signal [44]. The intensity of the generated signal is directly or inversely proportional to the analyte concentration. Although antibodies and nucleic acids are widely employed, enzymes are by far the most commonly used bio-elements in biosensors [45].

Owing to the different signal detecting mechanisms, biosensors can be categorized into various types, including resonant, photometric, thermal detection, ion-sensitive field-effect transistors, and electrochemical sensors. Electrochemical sensors are often used to develop biosensors [46] because of their reproducibility, low cost, simple design, and small dimensions [47].

Biosensors have a wide range of applications in the biomedical and drug sensing field, for toxicity analysis in environmental monitoring, as well as in food and quality control. Health care is the main area in the biosensor applications, such as monitoring of glucose, cholesterol, and urea levels in biological fluids. Industrial applications for biosensors include monitoring fermentation broths or food processing procedures by detecting concentrations of glucose and other fermentative end products. In addition, the sensitive detection of toxic compounds, such as phenolic compounds in the industrial waste waters, is an important topic for environmental monitoring.

Great effort has been made to develop new mediator-free biosensors based on direct electron transfer by immobilizing enzymes on conducting substrates. However, the electroactive centers of enzymes are usually embedded deeply into the large 3D structure of protein molecules [48]. Hence various immobilizing matrices, especially nanomaterials, have been applied to immobilize biomolecules and optimize electron transfer of enzyme redox center on the surface of electrodes. Among these materials, carbon-based materials such as highly ordered mesoporous carbon [49], carbon nanofiber [50], and CNT [51, 52], have been studied to immobilize redox enzymes and used in the bioanalytical area for electrode design [53]. Recently, it has been found that graphene has the ability to promote electron transfer of metalloproteins including GOD, cytochrome *c* (cyt *c*), myoglobin, and HRP [54–56]. Figure 5.2 presents a GO-supported heme protein on a glassy carbon electrode (GCE) surface.

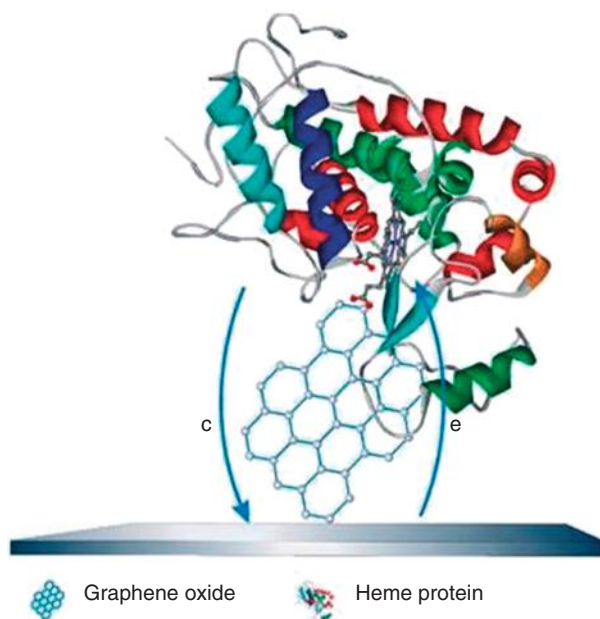


Figure 5.2 Schematic representation of a GO-supported heme protein on electrode surface. (Reprinted with permission from Ref. [54], Copyright 2010, American Chemical Society.)

Owing to their high surface area, unique heterogeneous electron transfer rate, remarkable electrical conductivity, chemical and electrochemical stability, and good biocompatibility, graphene and its derivatives have been used in several types of biosensors to detect different kinds of analytes including important electroactive compounds such as ethanol, glucose, nitrate, H_2O_2 , and nitric oxide [57–59]. Various organic solvents such as *N*-methyl-2-pyrrolidone, *N,N*-dimethylformamide, and ILs, and stabilizing reagents such as polymers (e.g., Nafion, sulfonated polyaniline, poly(methyl methacrylate)), chitosan, ssDNA, were used to avoid aggregating or facilitate the direct electron transfer reaction between protein and electrode. Various redox enzymes such as GOD, HRP, tyrosinase, and other proteins have been coupled with graphene to construct modified electrodes applicable in the production of third-generation electrochemical biosensors.

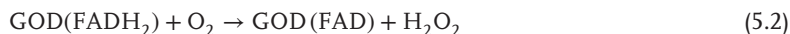
5.3.1.1 Glucose Oxidase-Based Biosensors

GOD is the most widely used enzyme in the field of biosensors. GOD catalyzes the oxidation of β -D-glucose to gluconic acid, by utilizing molecular oxygen as an electron acceptor with simultaneous production of hydrogen peroxide.

The reduction of the flavin adenine dinucleotide (FAD) in the enzyme with glucose results in the reduced form of the enzyme (FADH_2).



The reoxidation of the flavin with free oxygen generates the oxidized form of the enzyme FAD:



H_2O_2 produced during Equation 5.2 can be detected at the electrode surface:



GOD can oxidize β -D-glucose using other oxidizing substrates besides molecular oxygen, including quinones and one-electron acceptors. This enzyme has received considerable importance in real-time glucose monitoring, because of its high selectivity to glucose. The quantification of glucose can be achieved via electrochemical detection of H_2O_2 . Based on the high electrocatalytic activity of graphene toward H_2O_2 and the excellent performance of direct electrochemistry of GOD, graphene has shown great promise in applications as electrode material for GOD immobilization and improvement of its direct electron transfer on electrodes [53]. Several methods and graphene-based materials have been employed to effectively immobilize GOD on electrode surfaces, for the fabrication of electrochemical glucose biosensors.

The use of exfoliated graphite nanoplatelets (diameter of 1 μm and thickness of 10 nm) for the development of a glucose biosensor was reported by Lu and coworkers [60]. The biosensing interface was prepared by casting GOD and graphite nanoplatelets in a Nafion water–isopropyl-alcohol solution with a high concentration of organic solvent (85% alcohol). The resulting biosensor exhibits high sensitivity of 14.17 $\mu\text{A mM}^{-1} \text{cm}^{-2}$, a detection limit of 10 μM glucose and a linear detection range up to 6 mM. The direct electrochemistry of GOD immobilized in a modified electrode based on a composite film of exfoliated graphite nanoplatelets (nanosheets) and Nafion was reported [60, 61]. Nafion acts as both an effective solubilizing agent for graphite nanoplatelets and a biocompatible matrix for the immobilization of the biomolecule.

Shan and coworkers [56] reported the first graphene-based glucose biosensor. The biosensor was based on polyvinylpyrrolidone-protected graphene and exhibited high electrocatalytic activity toward the reduction of O_2 and H_2O_2 and could be dispersed well in water. This research team has constructed a glucose biosensor based on polyvinylpyrrolidone-protected graphene/polyethylenimine-functionalized (PEI) IL nanocomposites, which facilitated the direct electron transfer process between the immobilized GOD and electrode. The prepared biosensor had good stability and reproducibility with linear glucose response from 2 to 14 mM.

The immobilization through covalent amide linkage of GOD on graphene nanosheets was reported by Alwarappan *et al.* [62]. The conjugated graphene-GOD was immobilized onto the GCE surface. The GCE surface was already modified with polypyrrole (ppy) to form a stable matrix that facilitates the encapsulation of graphene–GOD on the electrode surface (Figure 5.3). The entire electrode

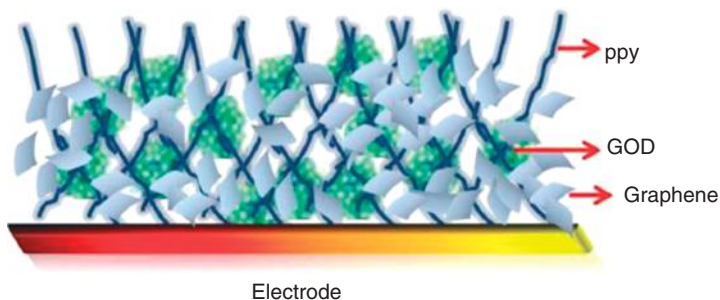


Figure 5.3 Representation of graphene–GOD entrapped within a porous polypyrrole matrix. (Reprinted with permission from Ref. [62], Copyright 2010, American Chemical Society.)

was employed for glucose detection exhibiting good sensitivity and stability (15% response decrease after three weeks storage).

Wang *et al.* [63] proposed the use of electrochemically *rGO* adsorbed on GCE and modified with GOD as biosensor to detect glucose. The enzyme was immobilized by covalent bonding via a polymer generated by electrografting N-succinimidyl acrylate. The direct electron transfer between enzyme and the electrode was realized, while the activity of GOD was maintained on the electrode.

The direct electron transfer reaction of GOD at a graphene–chitosan modified electrode was demonstrated by Kang and coworkers [64]. Graphene can be dispersed well in aqueous media with the help of natural biocompatible biopolymer chitosan, which provides a good biocompatible microenvironment for proteins or enzymes. It has been shown that the GOD–graphene–chitosan nanocomposite film can be used for sensitive detection of glucose with high sensitivity, a wide linear range, and low detection limit.

An efficient biosensing system for glucose detection, based on graphene sheets integrated with GOD, was presented by Wu and coworkers [65]. In this case, graphene was directly dispersed in water with the aid of ultrasonication. The GOD–graphene hybrid prepared in this work exhibited good electrocatalytic activity toward the reduction of oxygen. The response displayed linear range from 0.1 to 10 mM with sensitivity of $110 \mu\text{A mM}^{-1} \text{cm}^{-2}$ and a detection limit of $10 \mu\text{M}$. The values of the glucose concentration in human blood serum measured by the GOD–graphene/GCE are in good agreement with the data from the commercial monitor.

ILs have been widely used as an important material in enhancing performance of the modified electrode as a binder for biosensors. Owing to their electrochemical stability and biocompatibility, ILs are effective solubilizing agents for CBNs such as CNTs and graphene nanosheets, exhibiting improved sensitive signal for the detection of various analytes. A nanocomposite containing a typical IL (1-ethyl-3-methyl imidazolium ethyl sulfate) and GO nanosheets at room temperature has the ability to improve the direct electrochemistry and electrocatalytic activity of GOD [66]. When the obtained modified GCE was applied as a biosensor for glucose detection, a linear range of 2.5–45 nM with detection limit of 0.175 nM was

obtained. The enzyme electrode kept 95% of its original response after 2 months. In a similar manner, nanohybrids of chemically modified graphene and the ionic liquid 1-butyl-3-methylimidazolium hexafluorophosphate were prepared by sonication to modify the electrode [67]. The fabricated electrode can be used as selective glucose biosensor with respect to short response time (< 5 s), a sensitivity of $0.64 \mu\text{A mM}$ and detection limit of 0.376 mM .

A polymeric IL functionalized graphene, poly(1-vinyl-3-butylimidazolium bromide)-graphene (poly(ViBuIm⁺B⁻)-G) has been synthesized and utilized to fabricate an enzyme electrode for the determination of glucose [58]. The polymeric IL stabilizes graphene nanosheets well in an aqueous solution providing a positive charge in the aqueous solution, thus facilitating the immobilization of GOD via self-assembly under mild conditions. The negatively charged GOD was immobilized onto the (poly(ViBuIm⁺B⁻)-G) to form a GOD/(poly(ViBuIm⁺B⁻)-G)/GCE. The immobilized GOD exhibited fast direct electron transfer at the electrode and performed well for the electrocatalytic oxidation of glucose with good sensitivity and wide linear range of glucose from 0.8 to 20 mM.

The integration of graphene and metal nanoparticles showed potential applications in protein electrochemistry. The use of graphene–CdS nanocomposite as a novel immobilization matrix for GOD was reported by Wang and coworkers [68]. It was shown that the immobilized GOD on the modified electrode retains its native structure and electrocatalytic activities. The obtained glucose biosensor displays satisfactory analytical performance from 2 to 16 mM with a detection limit of 0.7 mM.

Zeng and coworkers [69] proposed the use of palladium nanoparticle/chitosan-grafted graphene nanocomposites for the construction of a glucose biosensor. The biosensor formed facilitated a high loading of GOD and exhibited good electrocatalytic activity toward H_2O_2 .

Xu *et al.* [70] proposed an electrochemical platform based on NiO nanoparticles and TiO_2 -graphene for the direct electrochemistry of GOD. A mediator-free GOD-based glucose biosensor was constructed through a layer-by-layer assembly approach. The biosensor exhibited specific and sensitive detection for glucose in the range of 1–12 mM, low detection limit ($1.2 \times 10^{-6} \text{ M}$), and high sensitivity ($4.129 \mu\text{A mM}^{-1}$).

A novel nanocomposite of rGO and gold-palladium (1:1) bimetallic nanoparticles, without the aid of any reducing reagent, was introduced by Yang *et al.* [71]. The nanocomposite showed good biocompatibility, fast electron transfer kinetics, large electroactive surface area, high sensitivity and stability against O_2 reduction. The GOD-based glucose biosensor prepared had a detection limit of $6.9 \mu\text{M}$, a linear range up to 3.5 mM and a sensitivity of $266.6 \mu\text{A mM}^{-1} \text{ cm}^{-2}$.

GOD was successfully covalently bound to the surface of the functionalized graphene–gold nanoparticles hybrid [35]. The direct and reversible electron transfer process between GOD and the hybrid electrode was realized without any supporting film or electron mediator. The model of the glucose biosensor was successfully used to determine the level of blood sugar concentration in a human serum sample.

rGO/PAMAM (poly(amido amine)) dendrimer–silver nanoparticles nanocomposite was used as a novel immobilization matrix for GOD and exhibited excellent direct electron transfer properties [72]. The fabricated glucose biosensor based on GOD electrode modified with this nanocomposite displayed satisfactory analytical performance with a wide linear range from 0.032 to 1.89 mM, high sensitivity ($75.72 \mu\text{A mM}^{-1} \text{cm}^{-2}$) and low detection limit (4.5 μM). Furthermore, the interference created by ascorbic and uric acid, which usually coexists with glucose in blood samples, is almost negligible to this biosensor.

The use of graphene quantum dots (GQD, graphene sheets smaller than 100 nm) coated on carbon ceramic electrode surface was introduced by Razmi and Mohammad-Rezaei [73] as a novel matrix for GOD immobilization for the preparation of glucose biosensor. The developed biosensor responds efficiently to glucose presence over a concentration range of 5–1270 μM , detection limit of 1.73 μM , and sensitivity of $0.085 \mu\text{A mM}^{-1} \text{cm}^{-2}$. The biosensor has been examined as a sensitive third-generation amperometric and voltametric glucose biosensor in human serum analysis with satisfactory results. The good performance of the biosensor is attributed to the porous nature of the electrode, high surface-to-volume ratio of GQD and strong interaction between enzyme and GQD.

A graphene-based amperometric glucose biosensor was developed by the covalent immobilization of GOD to graphene-functionalized GCE [74]. In this work, 3-aminopropyltriethoxysilane was employed for the dispersion of graphene as well as an amine surface modification agent for GCE and graphene. The developed biosensor was used for detecting glucose in the diabetic pathophysiological range 0.5–32 mM.

The direct immobilization of GOD on rGO without any cross-linking agents or modifiers was presented by Unnikrishnan *et al.* [75]. A solution phase approach was used to prepare exfoliated GO, followed by electrochemical reduction to get rGO–GOD biocomposite. The developed biosensor exhibits high catalytic activity toward glucose over a linear range of 0.1–27 mM, with a sensitivity of $1.85 \mu\text{A mM}^{-1} \text{cm}^{-2}$.

5.3.1.2 Horseradish Peroxidase-Based Biosensors

HRP is an important heme-containing protein that has been widely used for the fabrication of amperometric biosensors based on its direct electrochemistry to the detection of hydrogen peroxide. However, the direct electron transfer to the redox center of HRP is generally difficult because the redox center is buried within the three-dimensional structure of the enzyme [48]. Several works have been done to enhance the direct transfer of electrons from the redox center of the enzyme to the electrode, improving the sensitivity of the electrode with immobilized HRP. Graphene-based material has attracted tremendous attention for HRP immobilization because of its functional and electrochemical and electrical properties.

The use of graphene-modified electrodes for fabrication of H_2O_2 biosensors was demonstrated by several groups. Sun *et al.* [76] reported the preparation of graphene and double-stranded DNA composite material that was used for the

immobilization of HRP on the surface of a carbon IL electrode. The fabricated HRP modified electrode showed excellent electrocatalytic activity to the reduction of trichloroacetic acid over the concentration range of 1.0–21.0 mM with a detection limit of 0.133 mM.

Zhou *et al.* [77] described the construction of a H₂O₂ biosensor based on the co-immobilization of graphene and HRP onto biocompatible polymer chitosan. A GCE was modified by the biocomposite, followed by electrodeposition of Au nanoparticles on the surface. The biosensor showed high sensitivity and fast response upon the addition of H₂O₂. The linear range to H₂O₂ was from 0.005 to 5.13 mM with a detection limit of 1.7 μM.

The direct electrochemistry-based hydrogen peroxide biosensor was created with the utilization of the single-layer graphene nanoplatelet–enzyme composite film [78]. HRP was selected as a model for analysis. The composite film enhanced the direct electron transfer between the enzyme and the electrode surface, and can offer a third-generation biosensor with good properties, such as fast response and high sensitivity.

The direct electron transfer of HRP immobilized on GO–Nafion nanocomposite film, as well as its application as a new biosensor were investigated by Zhang *et al.* [79]. GO-based polymer composites provide a favorable microenvironment for HRP to carry out its direct electron transfer, which allows it to be used for H₂O₂ and O₂ sensing with great sensitivity.

The immobilization of HRP on electrochemically *r*GO or partially *r*GO was also demonstrated [80–82]. The electrochemically *r*GO–HRP modified screen printed carbon electrode showed good electroanalytical properties toward the amperometric determination of H₂O₂ with a linear range of detection of 9–195 μM [81]. In addition, a GCE modified with immobilized HRP on partially *r*GO can promote the electron transfer between enzyme and electrode. The modified electrodes have good stability, reusability, and high catalytic activity for the decomposition of H₂O₂, phenol, and *p*-chlorophenol and could find practical application as enzyme-based amperometric sensors used for the detection of phenolic pollutants in water [82].

5.3.1.3 Tyrosinase-Based Biosensors

Tyrosinase is a catechol oxidase containing a dinuclear copper center that catalyzes the oxidation of monophenols to *o*-diphenols and further to *o*-quinones in the presence of oxygen as an electron-acceptor. Based on the inhibition of tyrosinase activity from a molecule, tyrosinase biosensors have been developed for the determination of various pollutants. The use of graphene as a modification material on GCE and graphite electrodes in novel electrochemical tyrosinase biosensors was investigated by several groups. An amperometric biosensor for the detection of organophosphorus pesticides was prepared based on the tyrosinase immobilized on platinum nanoparticles and the use of a GCE modified with graphene [83]. Hydrophilic nanographene was prepared by ball milling of graphite and was used as support to construct a tyrosinase biosensor for the determination of bisphenol [84]. The nanographene-based tyrosinase biosensor displayed high performance over a linear range from 100 nM to 2 μM with a sensitivity of 3.1 A cm⁻² M⁻¹.

5.3.1.4 Cytochrome *c*-Based Biosensors

Cyt *c* is a heme protein found between the inner and outer membranes of mitochondria. The direct electrochemistry of cyt *c* has been studied at various graphene-based electrode surfaces [54, 85].

Hua *et al.* [17] reported the greatly improved catalytic and electrochemical properties of cyt *c* in a confined environment which has been achieved by assembling the protein within covalently modified sulfonated graphene nanosheets.

Wu *et al.* [86] studied the direct electron transfer of cyt *c* on GCE modified with chitosan-dispersed graphene nano-flakes. Cyt *c* immobilized on the surface of the electrode maintains its bioactivity and shows an enzyme-like activity for the reduction of nitric oxide.

Chen and Zhao [87] reported the preparation of a nanocomposite of polymerized IL-modified graphene nanosheet and its use as a modifier to a basal plane graphite electrode; this electrode was used for the immobilization of cyt *c* for the construction of graphene-based electrochemical biosensors.

5.3.1.5 Other Protein/Enzyme Biosensors

Graphene nanocomposite materials have also served as a basis for constructing not only GOD, HRP, and tyrosinase biosensors, which were described before, but several other types of biosensors based on the use of various proteins and enzymes such as hemoglobin and myoglobin for the detection of nitrate, nitrite, hydrogen peroxide, and so on, acetylcholine esterase for the detection of organophosphate pesticides and alcohol dehydrogenase for the detection of β -nicotinamide adenine dinucleotide (NADH). Moreover, various bienzymic biosensors based on the co-immobilization of various enzymes onto graphene nanocomposite materials have been investigated for the determination of cholesterol, maltose, or growth factor protein in human platelets. Table 5.1 presents several selected biosensors, designed by combining graphene nanocomposite materials with various proteins and enzymes.

5.3.1.6 DNA Sensors

Sensitive, selective, and cost-effective analysis of DNA is important in many fields such as clinical diagnostics and treatment, pathology, criminology, pharmacogenetics, food safety and so on. Several electrochemical sensing interface for high-performance DNA biosensing applications, based on the assembly between graphene and DNA molecules, were constructed. It was demonstrated that various dye-labeled or fluorophore labeled ssDNA or hpDNA (hairpin DNA), which were used as probes for DNA sensing, could be stably adsorbed or covalently attached on graphene-based materials [97–101]. Figure 5.4 shows a schematic representation of a detection graphene platform for the detection of DNA and proteins.

Lin *et al.* [102] demonstrated the preparation of an electrochemical DNA sensor based on simple graphene sensing platform based on the π - π stacking interaction between graphene and ssDNA probes. The biosensor was applied with high sensitivity and selectivity for special DNA sequence analysis based on the sandwich

Table 5.1 Graphene-based biosensors with various proteins and enzymes.

Protein/enzyme	Graphene-based material used	Compound detected	References
Hemoglobin	Graphene–poly(diallyldimethylammonium chloride)	Nitrate	[88]
	Graphene–chitosan	H ₂ O ₂	[89]
	Graphene–TiO ₂	Trichloroacetic acid	[90]
	Graphene–Pt	H ₂ O ₂	[91]
Myoglobin	Graphene-CTAB (cetyltrimethylammonium bromide)-IL	H ₂ O ₂	[92]
Alcohol dehydrogenase	Graphene-IL	NADH	[93]
Acetyl-cholinesterase	Graphene-IL	Organophosphate pesticides	[94]
Cholesterol oxidase/ cholesterol esterase	Functionalized graphene	Cholesterol, H ₂ O ₂	[37]
	Graphene–Pt	Cholesterol, H ₂ O ₂	[95]
GOD/glucoamylase	Modified graphene sheets	Maltose	[96]

assembly between graphene target DNA and DNA-conjugated gold nanoparticles. The immobilization based on physical adsorption of hpDNA probes on graphene platforms comprising different numbers of same-sized graphene layers was demonstrated by Bonanni and Pumera [100].

Dubuisson *et al.* [103] compared the results obtained by immobilizing DNA probes based on physical adsorption by π – π stacking interactions or covalent attachment on an anodized epitaxial graphene platform and found that covalently bound DNA provided a more sensitive response and larger detection range than physical adsorption.

For covalent binding, the DNA probe is attached to carboxylic group-functionalized graphene platforms or to graphene surfaces modified with various molecules [104]. The integration of oxidized graphene and polyaniline nanowires layer-by-layer for the fabrication of an electrochemical biosensor for monitoring DNA was reported by Bo *et al.* [105]. The oligonucleotide probe (ssDNA) was immobilized through the formation of phosphoramidate bonds between the amino group of the polyaniline and the phosphate group of the oligonucleotides. Sun *et al.* [106] demonstrated the development of a carboxyl-functionalized graphene oxide (GO-COOH) and electropolymerized poly-L-lysine modified GCE for the electrochemical sensing of DNA. In this case, the amine modified probe ssDNA sequences were immobilized on the surface of the electrode by covalent linking with the formation of amide bonds.

Hu *et al.* [34] demonstrated a graphene platform fabrication for the covalent grafting of ssDNA based on the decoration of GO sheets with perylene tetracarboxylic

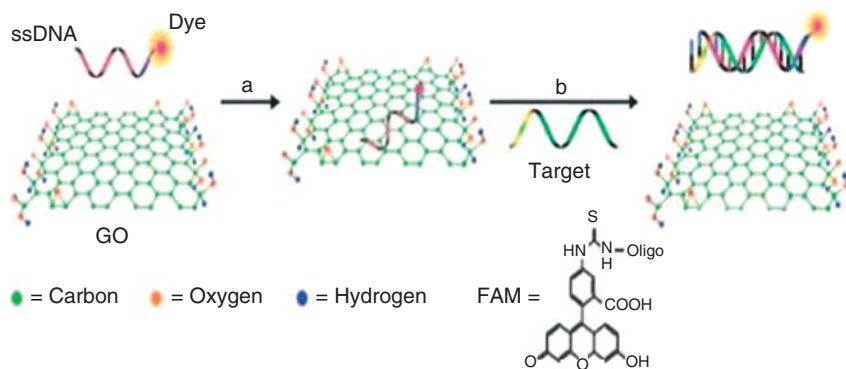


Figure 5.4 Schematic representation of the target-induced fluorescence change of dye-labeled ssDNA-GO complex. FAM (fluorescein-amidite) is a fluorescein-based fluorescent dye. Step (a) Dye-labeled ssDNA binds on GO and this interaction completely quenches the fluorescence of the dye.

Step (b) Target molecule interacts with the dye-labeled ssDNA, disturbing the interactions with GO, and thus the fluorescence is restored. (Reprinted with permission from Ref. [97], Copyright 2009, Wiley-VCH Verlag GmbH & Co KGaA, Weinheim.)

acid. A DNA impedance biosensing platform was constructed by the same group, in which a positively charged perylene bisimide derivatives (PDI) is anchored to graphene sheets [107]. In this platform, the electrostatic interaction between the positively charged imidazole rings of PDI and negatively charged phosphate backbones of ssDNA probes facilitates the latter's immobilization. ssDNA grafting on PDI/graphene occupied the phosphate backbones and left the bases available for efficient hybridization. This electrostatic grafting manner was easier compared to covalent grafting as no previous activation of graphene electrode was needed.

Bonanni *et al.* [30] demonstrated a strategy for covalent linking of ssDNA to chemically modified graphenes and applied it for the detection of DNA hybridization and DNA polymorphism by using impedimetric methods. Amino-modified DNA probe was used to form an amide bond with the carboxylic moiety that is present on the graphene surface using carbodiimide chemistry. The best sensitivity and reproducibility was obtained when electrochemically *rGO* was used. On this platform, a high amount of DNA probe was immobilized which is probably because of the higher availability of carboxyl groups on this surface.

5.3.1.7 Immunosensors and Aptasensors

The use of graphene platforms for the development of highly sensitive and selective immunoassays generates continual interest because it has become a major analytical tool in clinical diagnosis, environmental evaluation, and food analysis [99, 108, 109]. These immunoassays can be classified into two main categories based on the sensing approach adopted:

- 1) immunosensors, in which the target analyte (antigen) binds specifically to an antibody, which is immobilized on the surface of the electrode

Table 5.2 Graphene-based immunosensors and aptasensors.

Graphene-based material	Compound detected	References
<i>Immunosensors</i>		
Graphene–chitosan	Microcystin	[111]
GO	Rotavirus	[109]
Graphene sheet	α -Fetoprotein	[112]
Gold nanoparticles–graphene	Human IgG	[113]
Functionalized graphene	Cancer biomarkers	[114, 115]
rGO	Mouse IgG	[116]
GO initiated silver enhancement	Platelet-derived growth factor BB	[117]
Gold nanoparticles–graphene cross-linked with L-cysteine	IgG	[40]
Nanoporous gold foils–graphene sheets	Human serum chorionic gonadotropin	[118]
Biofunctionalized magnetic graphene nanosheets	Prostate specific antigen	[119]
<i>Aptasensors</i>		
Colloidal graphene	Microcystin-LR	[120]
Multi-labeled rGO sheets	Platelet-derived growth factor and thrombin	[121]
Gold nanoparticles–graphene	L-Histidine	[122]
Graphene	ATP	[123]

- 2) aptasensors, in which the target molecule binds specifically to an aptamer (artificial functional DNA or RNA) immobilized on the electrode surface

Graphene-based immunosensors and aptasensors have been developed to detect various target molecules, including proteins, nucleic acids, peptides, amino acids, cells, viruses, and small molecules [110]. Table 5.2 summarizes the application of various immunosensors and aptasensors based on the use of graphene nanomaterials, while Figure 5.5 shows a GO-based immunosensor system.

5.3.2

Biocatalysis

Nanobiocatalysis is a rapidly growing research field which refers to the development of new nanobiocatalytic systems based on the use of enzymes immobilized on nanostructured materials, using conventional approaches, such as covalent bonding and physical adsorption [1]. The ideal immobilization support should prevent enzyme aggregation or denaturation, but maintain the native conformation of enzymes [18]. The use of nanostructured materials as immobilization supports has been extensively reported [20, 124–126]. Among various nanomaterials used

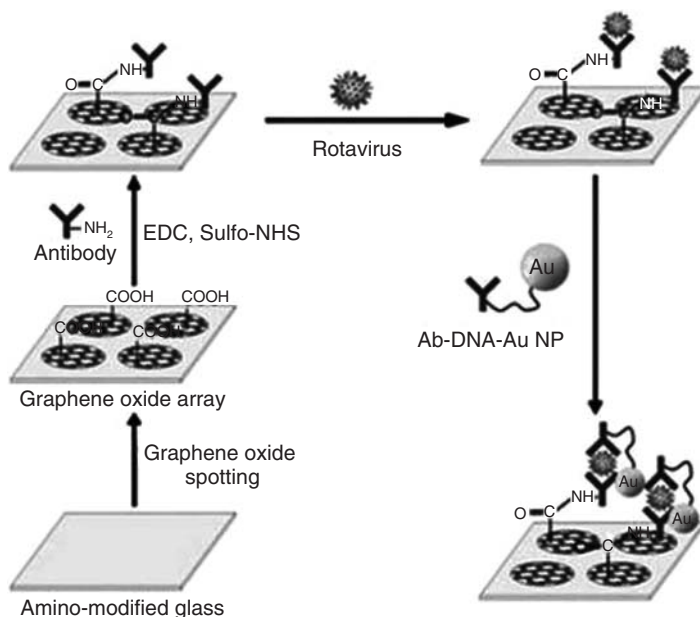


Figure 5.5 Illustration of a GO-based immunosensor. (Reprinted with permission from Ref. [109], Copyright 2010, Wiley-VCH Verlag GmbH & Co. KGaA, Weinheim.)

for this purpose, graphene and GO derivatives have attracted considerable interest as immobilization supports owing to their mechanical, thermal, and electrical properties. Their unique surface properties, such as large surface area and layered structure, as well as the ease of their functionalization render them ideal for use with various methods for enzyme immobilization.

Various enzymes were successfully immobilized on graphene and GO derivatives and were used to investigate their catalytic properties [19, 127]. Some of them are presented here, while some other interesting studies are listed in Table 5.3. In a previous work of our group [20] we have reported the immobilization of lipases and esterases on amino-functionalized GO. The enzymes were immobilized on the nanomaterial surface through physical adsorption and covalent bonding. The catalytic activity of the immobilized enzymes was determined through the esterification of caprylic acid with 1-butanol and in most cases was much higher than the activity of free enzymes. Covalently immobilized enzymes exhibited comparable or even higher activity, as well as higher operational stability compared to the physically adsorbed ones. Fourier transformed infrared (FT-IR) spectroscopy analysis showed that, all hydrolases studied underwent some conformational changes upon immobilization on functionalized GO, which could be related to specific interactions of enzymes with this nanomaterial.

Hua *et al.* [17] investigated the catalytic and electrochemical behavior of cytochrome *c* after its immobilization on sulfonated graphene nanosheets. The peroxidase

Table 5.3 List of researches on the immobilization of enzymes onto graphene and its derivatives for biocatalytic applications.

Enzymes	Nanomaterial	Immobilization	References
HRP	GO, rGO	NCI	[15, 18]
	Graphene/sodium dodecyl benzene sulfonate	NCI	[128]
	GO doped CTAB reverse micelles	NCI	[127]
OxOx	GO, rGO	NCI	[15]
GOD	GO	NCI	[129]
	GO	CI	[130]
Cyt <i>c</i>	Sulfonated graphene sheets	NCI	[17]
Soybean peroxidase	GO doped CTAB reverse micelles	NCI	[127]
Laccase	GO	NCI	[19]
Alkaline protease	GO	CI	[131]
Esterase	Amine-GO	NCI and CI	[20]
Lipase	Amine-GO	NCI and CI	[20]
	GO doped CTAB reverse micelles	NCI	[127]

CI, covalent immobilization; NCI, non-covalent immobilization.

activity of immobilized cyt *c* was determined due to *o*-phenylenediamine oxidation, and was almost eightfold higher than that of free cyt *c*. The V_{\max} of immobilized cyt *c* was almost 5-fold higher than free protein, whereas the Michaelis-Menten constant (K_m) was 7.5-fold lower than native cyt *c*, indicating that the electrostatic interactions between functionalized GO and cyt *c* may result in structural changes around the heme moiety leading to higher catalytic activity. These conformational changes were detected by CD measurements, where the typical bands for α -helix content were altered after cyt *c* immobilization on the sulfonated GO.

Zhang *et al.* [15] reported the immobilization of HRP and oxalate oxidase (OxOx) on rGO. Both enzymes were immobilized by physical adsorption on rGO and their catalytic behavior was investigated and compared to GO-enzymes conjugations. In the case of immobilized OxOx, the catalytic activity was higher compared to the free enzyme and retained up to 90% of its activity after 10 cycles of use. Further, the rGO-enzyme conjugates exhibited higher enzyme activity and stability than the GO-enzyme conjugates, suggesting that the adsorption of enzymes on the surface of graphene is governed by hydrophobic interactions instead of electrostatic interactions, leading to better catalytic behavior.

The properties of GO-alkaline protease bio-composites were demonstrated by Su *et al.* [131]. Alkaline protease was covalently immobilized on GO using glutaraldehyde as cross-linker. The optimum pH of alkaline protease shifted by 1 unit toward the alkaline compared to the free enzyme, suggesting an alteration in the microenvironment of the enzyme because of the immobilization

process or immobilization support. The thermostability and reusability of the immobilized enzyme was significantly improved, as it retained almost 90% of its initial activity after 20 days storage, whereas free alkaline protease retained 75% of its initial activity, indicating that GO is a promising support for enzyme immobilization.

Covalent immobilization of β -galactosidase on functionalized graphene has also been reported [39]. The thermal stability of immobilized enzyme was significantly higher than that of free enzyme solution. Immobilized β -galactosidase retains its catalytic activity after 10 min incubation at 6 °C, whereas free enzyme loses 64% of its initial activity after 4 min incubation at the same temperature. K_m values for the free enzyme were calculated 1.73 mM with *o*-nitrophenyl- β -D-galactopyranoside and 10 mM with lactose, whereas for immobilized enzyme they were changed to 1.28 and 5.78 mM, respectively. The rate of whey and milk lactose hydrolysis was determined and found to be 0.0413 and 0.0238 h⁻¹, respectively. The storage stability of immobilized enzyme was found to be more than 94% after 4 months storage at 4 °C. Finally, the functionalized graphene–enzyme conjugates showed great reusability, as more than 92% enzymatic activity was maintained after 10 cycles of repeated use.

The immobilization of HRP on GO and its applications in phenolic compound removal was reported by Zhang *et al.* [18]. HRP was immobilized via physical adsorption, mainly through electrostatic interactions. The immobilized enzyme exhibited about 50% remaining activity, whereas the free enzyme solution exhibited only 20% residual activity after 2 h incubation at 50 °C. In addition, storage stability of immobilized HRP was much higher than that of the native enzyme (4.6-fold). The catalytic efficiency for the phenolic compound removal of immobilized enzyme was comparable and in some cases even higher than that of the free enzyme solution.

Immobilized trypsin on functionalized GO has been used in proteolysis and protein digestion [132, 133]. GO functionalized with amino-Fe₃O₄ nanoparticles was used as support for trypsin immobilization [134]. Trypsin was immobilized via π – π stacking and hydrogen bonding interaction with an immobilization capacity of 0.275 mg enzyme mg⁻¹ nanomaterial. As this nanomaterial is an excellent irradiator absorber, the immobilized enzyme reactor developed was able to efficiently digest standard proteins within 15 s, while the conventional in-solution digestion may occur for 12 h. During the digestion of bovine serum albumin and myoglobin, no peptide residue was observed, a result correlated with the high hydrophilicity of GO. The bioreactor was used for 5 min to perform digestion of proteins extracted from rat liver. A total of 456 protein groups were identified, a result comparable to the 12 h in-solution digestion, which indicated that the bioreactor developed has a great potential for proteome studies. Another group has used functionalized GO with poly-L-lysine and PEG-diglycolic acid (polyethylene glycol) for the immobilization of trypsin and the use of the biocatalyst as protein digestion reactor [135]. The microwave-assisted on-plate proteolysis with the immobilized trypsin followed by matrix-assisted laser desorption-ionization

time-of-flight (MALDI-TOF) mass spectrometry (MS) analysis resulted in high efficiency, as hundreds of samples could be digested within a short time (about 15 s), indicating that the enzyme–GO conjugates are a promising strategy for protein digestion and peptide mapping.

5.3.3

Biofuel Cells

Enzyme-based biofuel cells (EBFCs) are devices capable of directly transforming chemical to electric energy via electrochemical reactions involving enzymatic catalysis [136, 137]. EBFC use biomass-derived energy carriers, such as glucose, fructose, ethanol, and oil for the generation of electricity. Various oxidoreductases, such as GOD and alcohol dehydrogenase, are used for the oxidation of fuels at the anode of a biofuel cell in order to generate protons and electrons. At the cathode, oxidases, such as laccase or bilirubin oxidase, are used to catalyze the reaction of an oxidant (usually oxygen) with these electrons and protons, generating water. The two main application areas that are being considered for EBFC are *in vivo* implantable power supplies for electronic medical devices such as pacemakers, micro drug pumps, deep brain stimulators, and *ex vivo* power supplies for small portable power devices [1, 138, 139].

However, EBFCs remain limited because of short lifetimes and low power densities. CBNs, such as CNTs and graphene, are conductive materials that support direct electron transfer of enzymes that are immobilized by either adsorption or covalent attachment [138, 140, 141]. Among CBNs used so far, graphene has a rich surface chemistry, which is different from that of other kinds of carbon structures and exhibits an excellent conductivity that is approximately 60 times higher than that of single wall CNTs [142, 143]. Further, the electrons on the very large surface area of graphene move ballistically over the sheet without any collisions with mobility as high as $10.000\text{ cm}^2\text{ V}^{-1}\text{ s}^{-1}$ at room temperature [11, 144]. The distinct properties of graphene have evoked great interest in the development of many kinds of graphene-based electronic devices, including biofuel cells [145, 146].

The use of graphene sheets for the construction of membraneless biofuel cell is reported by Liu *et al.* [147] (Figure 5.6). The anode consisted of a gold electrode on which graphene–GOD from *Aspergillus niger* were co-immobilized using silica sol–gel matrix. The cathode was constructed in a similar manner except for the immobilized enzyme used, which was bilirubin oxidase from *Myrothecium verrucaria*. This graphene-based EBFC yields a maximum power density of about $24\ \mu\text{W cm}^{-2}$ with a lifetime of 7 days, which is two times larger than the maximum power density generated by the single wall CNT-based EBFC.

A similar enzymatic glucose/oxygen biofuel cell system based on immobilized enzyme on graphene sheets was prepared by the same group [145]. The biofuel cell employs the gold plate electrodes modified by specific graphene–enzyme conjugations. The bioanode was prepared by co-immobilization of GOD and graphene using electrogenerated polypyrrole film. The biocathode was fabricated using the

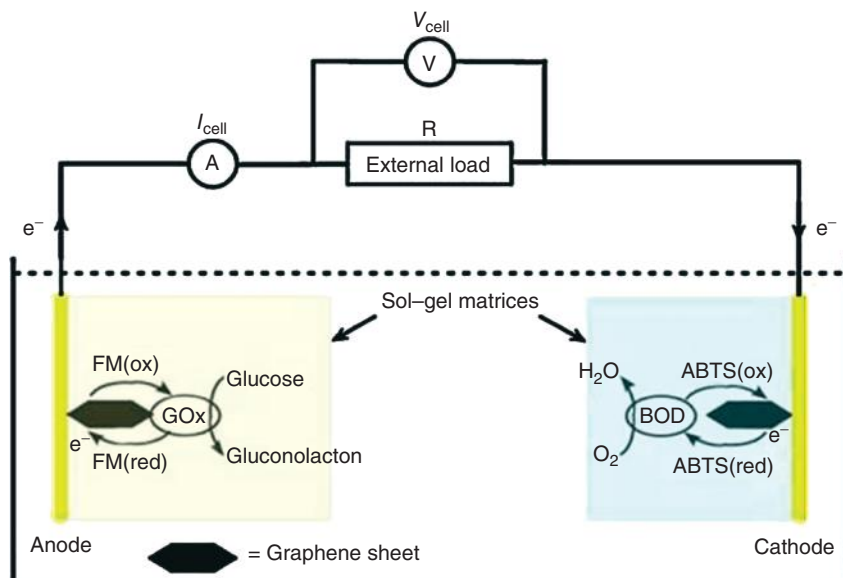


Figure 5.6 Schematic representation of a graphene-based membraneless EBFC. (Reprinted with permission from Ref. [147], Copyright 2010, Elsevier B.V.)

same procedure with bilirubin oxidase used as biocatalyst. The electrochemical activity of these electrodes was superior to the electrodes immobilized with sol-gel.

The capability of graphene as a spacer to assemble electrochemically functionalized nanostructures onto electrodes was demonstrated by Wang *et al.* [146] (Figure 5.7). By using graphene as spacer, the multilayered nanostructures of graphene/methylene green (MG) and graphene/multiwall carbon nanotubes (MWCNTs) were formed onto electrodes through layer-by-layer chemistry on the basis of the electrostatic and/or π - π interactions between graphene and the electrochemically useful components.

Using glucose dehydrogenase-based bioanode with graphene/MWCNT nanostructure assembled on the GCE and a laccase-based biocathode, a glucose/O₂ biofuel cell was prepared. The cell has an open-circuit voltage of 0.69 V and a maximum power density of 22.50 $\mu\text{W cm}^2$ at 0.48 V in 10 mM phosphate buffer (pH 6.0) containing 10 mM NAD⁺ and 30 mM glucose. The electrochemical and electrocatalytic properties of the assembled nanostructures indicate that these graphene-based nanostructures could serve as electronic transducers for molecular bioelectronic devices such as biosensors and biofuel cells.

The use of the yeast surface display system of redox enzymes has demonstrated several advantages in biofuel cells, such as the ability to regenerate the enzyme on the surface once it becomes inactive, the use of both yeast metabolism and the displayed enzyme for complete fuel oxidation, the possibility to digest a complex fuel without the need for the fuel to cross the cellular membrane [148–150]. The

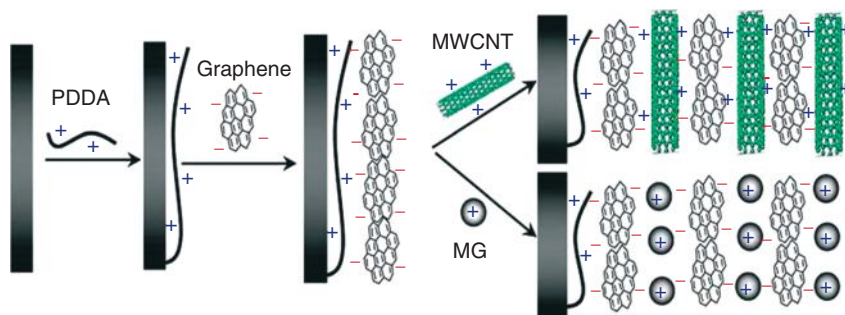


Figure 5.7 Schematic illustration of the controllable formation of electrochemically functional electrodes with graphene as spacer. PDDA: poly-(diallyldimethylammonium chloride). (Reprinted with permission from Ref. [146], Copyright 2011, American Chemical Society.)

encapsulation of a living microorganism, such as *Saccharomyces cerevisiae* yeast, displaying GOD in electrochemically active GO hydrogels was reported [151]. In this case, GO enabled direct communication between the displayed enzyme active site and the surface of the electrode, which is very important for the use of this system for biofuel cell applications [151].

5.3.4

Drug and Gene Delivery

Graphene-based nanomaterials have recently attracted much interest for their potential applications in biomedicine fields such as cellular imaging, photothermal therapy, biosensor-based disease markers and drug, as well as, gene delivery. GO offers a lot of advantages against other vectors for drug and gene delivery, such as the high content of oxygen groups on its surface that leads in oriented functionalization for biological applications. This characteristic surface makes GO biocompatible because of the hydrophilicity of the oxygen-containing groups. In addition, the production of GO can be achieved easily and inexpensively. The delocalized π -electrons on the graphene plane enable the binding of various aromatic drug molecules via π - π stacking. The conjugations of targeting ligands with graphene derivatives can result in selective drug delivery toward specific types of cells. Since 2008, a lot of studies have been carried out using GO as carrier for drug and gene delivery with very interesting results [152–156].

Liu and coworkers [157] used for the first time GO functionalized with PEG (PEG-GO) as a nanocarrier for anticancer drugs loading. In this work, SN38, a camptothecin analog, was non-covalently immobilized on PEG-GO via van der Waals interactions. SN38 is a water-insoluble topoisomerase I inhibitor produced by the hydrolysis of camptothecin. After SN38 was conjugated with PEG-GO, its solubility was increased at concentrations up to 1 mg ml^{-1} . Cell proliferation assay showed that PEG-GO-SN38 afforded highly potent cancer cell killing *in vitro*

against human colon cancer cell line HCT-116. The IC₅₀ of the immobilized drug was 6 nM for HTC-116 cells, 1000-fold higher than that of camptothecin and free SN38, indicating that GO can be used as promising material for drug delivery and biological applications.

Zhang *et al.* [158] investigated the controlled loading and targeted delivery of doxorubicin and camptothecin, two anticancer drugs. Nanoscale GO covalently functionalized with folic acid was used as the drug carrier. Doxorubicin and camptothecin were physically adsorbed on folic acid-functionalized GO mainly via π - π stacking and hydrophobic interactions. It was found that the loading of doxorubicin was much higher than that of camptothecin, which is ascribed to the difference in their structures and thus the difference in the interactions developed between the drugs and GO. The drug loading was concentration-dependent, which can result in controlled loading on the GO sheets. Furthermore, the loading of both drugs on the GO was investigated. The doxorubicin loading in this case was 5.1-fold higher, whereas the camptothecin loading remained constant. This result suggests that the loading of the drugs depends mainly on the distribution coefficient of the drug dissolved in solution and that adsorbed on the graphene carriers. The cytotoxicity of the immobilized drugs was investigated using MCF-7 and A549 cells. The functionalized GO loaded with both drugs exhibited higher cytotoxicity to MCF-7 cells than that observed with only one drug loaded, demonstrating the utility of functionalized GO as a carrier for controlled drug loading and targeted delivery of multiple drugs.

The same research group has also reported the use of GO in gene delivery [159]. GO was first functionalized with PEI (PEI-GO) via electrostatic interactions developed between the negatively charged GO and the positively charged PEI. The cytotoxicity of PEI-GO was investigated as it is a crucial factor for vectors used in gene delivery. Human cervical carcinoma cells (HeLa cells) retained their viability up to 90% when they were incubated with 10 mg ml⁻¹ PEI-GO, whereas in the presence of the same concentration of PEI they retained only 40% of their viability. The capability of PEI-GO to deliver foreign plasmid DNA into cells was also investigated. PEI-GO showed an excellent transfection efficiency in HeLa cells, which was comparable or even higher than free PEI, indicating that PEI-GO has great potential as a novel vector for efficient gene delivery.

5.4

Interactions between Enzymes and Nanomaterials

The interactions between enzymes and nanomaterials is a crucial factor for the function of biomolecules and therefore for the design of effective nanobiocatalytic systems. Nanomaterials can interact with biomolecules through electrostatic and/or hydrophobic interactions, π - π stacking interactions, van der Waals forces, or hydrogen bond forming. These interactions depend on the structure, the surface chemistry, the charge and the hydrophilicity of the nanomaterials [160]

and may affect the conformational state of the biomolecules. Altering the structure of biomolecules may result in a change in their catalytic properties. The influence of CBNs, such as graphene, GO, and their derivatives, on the catalytic properties and structure of proteins, especially enzymes, has been reported [134, 161].

Our group has investigated the interactions developed between GO-derivatives and *cyt c* [162]. GO-derivatives (reduced and nonreduced) functionalized with carboxyl, amine, and alkyl groups were used. These nanomaterials enhance the peroxidase activity of *cyt c*. This activation can be attributed to hydrophobic, as well as electrostatic interactions. It has been shown that the functionalization of GO with different alkyl chains enhance the peroxidase activity of *cyt c*, as well as its stability. The presence of the alkyl chains on the surface of GO makes these materials more hydrophobic and results in a decrease of the peroxidase activity of *cyt c*. This result seems to be governed by hydrophobic interactions developed between the nanomaterials and the proteins. In addition, the different functional groups seem to interact through electrostatic interactions with the protein, as the negatively charged functional groups seem to interact better with the positively charged *cyt c*. CD studies were used to investigate the influence of functionalized GO on the secondary structure of *cyt c*, as well as on the heme microenvironment. The far-UV CD results showed that the secondary structure of *cyt c* in the presence of these nanomaterials is retained. Instead, changes in the Soret region of *cyt c* were observed, indicating the reorientation of heme active center to a more accessible conformation, which leads to higher protein activity.

Zuo and colleagues [54] have also reported the electrostatic and hydrophobic interactions developed between GO and *cyt c*. *Cyt c* was used in a GCE in order to investigate the electron transfer potential. It was shown that the presence of GO facilitates *cyt c* electron transfer, as a result of the electrostatic and hydrophobic interactions developed between the nanomaterial and the protein. UV-vis and fluorescence studies showed that *cyt c* retains its active site conformation upon interaction with GO.

In a previous study of our group [163], we have reported the influence of functionalized GO on the structure of lipases and esterases. The interaction of functionalized GO was studied by steady-state fluorescence spectroscopy and CD. The fluorescence study showed that in the case of esterase Bs2, the highest quenching was observed in the presence of GO, which led to full deactivation of the enzyme, whereas the lowest quenching was observed in the presence of amine-functionalized GO, which did not significantly affect the enzyme activity. The conformational changes of the secondary structure of hydrolases were further investigated through CD studies. The far-UV CD results showed a slight decrease of the α -helix content and an increase of the β -sheet content in the presence of GO in case of lipases, whereas the biggest conformational changes were observed in the case of esterase Bs2 in the presence of GO and amine-functionalized GO, where the α -helix content was significantly decreased with the simultaneous increase of the β -sheet content.

The conformational changes of GOD upon non-covalent conjugation with GO have been reported by Shao *et al.* [129]. The UV–vis studies of the GO–GOD conjugates in the FAD moiety showed a slight blueshift of the FAD band and an increase in the absorbance, which suggests that the FAD moiety of the conjugation becomes more exposed than in the case of free enzyme. Fluorescence spectroscopic studies of the bioconjugates demonstrated that tryptophan fluorescence of GOD is significantly quenched upon immobilization onto GO. A blueshift was observed as the concentration of GO increased, which indicates conformational changes on the tertiary structure.

GO has been used for non-covalent immobilization of HRP by Zhang *et al.* [22]. The interactions developed upon immobilization were studied. Changing the pH of the immobilization media, the interactions between HRP and GO were also changed. At pH 4.8–7.2 where the HRP is positively charged, the immobilization was much higher as a result of the electrostatic interactions developed with the negatively charged GO, whereas at pH higher than 7.2, the enzyme is negatively charged, leading to the repelling of GO, thus lowering immobilization efficiency. Atomic force microscopy experiments showed that the average diameter of immobilized HRP was larger and its height was shorter compared to the free enzyme, which reveals that immobilization induces some conformational changes on the enzyme molecule.

The same group investigated the nature of the interactions developed between *rGO* and HRP and OxOx [15]. The enzyme loading on chemically *rGO* was insensitive to pH changes, leading to the conclusion that the interactions between the enzymes and the nanomaterials are not electrostatic. To further reinforce their theory, the contact angle of water of the *rGO* was evaluated. The contact water angle was increased with increase in the reduction agent, confirming the high hydrophobic area of *rGO*, which leads to enzyme adsorption through hydrophobic interactions rather than electrostatic. However, HRP and OxOx are both soluble proteins, thus the most hydrophobic residues should be located in the interior of the enzymes. The high immobilization yield observed suggests that the chemically *rGO* induces conformational changes on the enzyme molecules, resulting in interruption of the hydrophobic interior balance. CD studies confirm the changes in the protein structure. The secondary structure of HRP was partially lost, leading to the lowest peroxidase activity observed.

The oriented covalent immobilization of GOD on concanavalin A-functionalized GO was investigated and compared with nonspecific binding of the enzyme on GO by Zhou *et al.* [130]. The immobilized GOD showed better thermal stability at the temperature range of 25–70 °C than the free enzyme. It was proposed that upon immobilization the enzyme can restrict unfolding and nonspecific aggregation resulting in more improved thermal stability. The storage stability of immobilized GOD was higher compared to that of the free enzyme, indicating probably a conformational change as a result of interactions developed between the enzyme and GO during immobilization process.

5.5 Conclusions

Graphene has rapidly become one of the most widely studied carbon-based materials because of its unique structural features and exceptional chemical, electrical, and mechanical properties that lead to many potential applications. Graphenes obtained with various procedures were successfully employed in different applications in various fields, including biotechnology and biomedicine. In this chapter, we presented an overview of the recent advances of the use of graphene and its derivatives for a wide variety of practical applications based on the immobilization of enzymes and other biomolecules. We have selectively reviewed the rapid and exciting advances in the applications of graphene and its water-soluble derivative, GO, with focus on biosensors and biofuel cell construction, the preparation of nanobiocatalytic systems as well as in biomedicine with focus on gene and drug delivery. We believe that this trend will continue and even speed up in the years to come. However, while other CBNs, such as CNTs, have been studied for the past two decades, graphene-based materials have been developed only recently, and still much has to be done in terms of producing graphene-based chemical structures suitably functionalized for the specific tasks required in the search for practical purposes. For further exploration and better optimization of the application of graphene-based materials on biomedicine and nano-biotechnology, one critical and fundamental question still needs to be addressed, that is, the effect of graphene-based materials on structure and function of various biomolecules and biological systems. It is, therefore, very important to gain more insight into the interactions between graphene-based materials and active biomolecules, such as enzymes and other proteins, as well as to understand their regulating factors in order to expand the biotechnological and biomedical applications of graphene-based materials.

Abbreviations

CBNs	Carbon-based nanomaterials
CD	Circular dichroism
CI	Covalent immobilization
CNT	Carbon nanotubes
CNT-NH ₂	Amine carbon nanotubes
Cyt <i>c</i>	Cytochrome <i>c</i>
EBFC	Enzyme-based biofuel cells
EDC	1-Ethyl-3-(3-dimethylaminopropyl) carbodiimide
FAD	Flavin adenine dinucleotide
FT-IR	Fourier transformed infrared
GCE	Glassy carbon electrode
GO	Graphene oxide
GO-COOH	Carboxyl-functionalized graphene oxide
GO-NH ₂	Amine graphene oxide

GOD	Glucose oxidase
GQD	Graphene quantum dots
HeLa cells	Immortal cell line derived from cervical cancer cell from Henrietta Lacks (HeLa)
	Henrietta Lacks (HeLa)
hpDNA	Hairpin DNA
HRP	Horseradish peroxidase
IL	Ionic liquid
MALDI-TOF	Matrix-assisted laser desorption-ionization time-of-flight
MG	Methylene green
MWCNT	Multiwall carbon nanotubes
MS	Mass spectrometry
NCI	Non-covalent immobilization
NHS	<i>N</i> -Hydroxysuccinimide
OxOx	Oxalate oxidase
PDI	Perylene bisimide derivative
pDNA	Plasmidic DNA
PEG	Polyethylene glycol
PEI	Polyethylenimine
ppy	Polypyrrole
PDDA	Poly(diallyldimethylammonium chloride)
rGO	Reduced graphene oxide
ssDNA	Single strand DNA
Sulfo-NHS	<i>N</i> -Hydroxysulfosuccinimide
SWCNT	Single wall carbon nanotubes
UV-vis	Ultraviolet-visible

References

- Kim, J., Grate, J.W., and Wang, P. (2008) *Trends Biotechnol.*, **26** (11), 639–646.
- Guisan, J.M., Betancor, L., Fernandez-Lorente, G., and Flickinger, M.C. (2009) Immobilized enzymes, in *Encyclopedia of Industrial Biotechnology*, John Wiley & Sons, Inc., Hoboken, NJ.
- Sheldon, R.A. (2007) *Adv. Synth. Catal.*, **349** (8-9), 1289–1307.
- Hanefeld, U., Gardossi, L., and Magner, E. (2009) *Chem. Soc. Rev.*, **38** (2), 453–468.
- Gupta, M.N., Kaloti, M., Kapoor, M., and Solanki, K. (2011) *Artif. Cells, Blood Substitutes, Biotechnol.*, **39** (2), 98–109.
- Wang, P. (2006) *Curr. Opin. Biotechnol.*, **17** (6), 574–579.
- Feng, W. and Ji, P. (2011) *Biotechnol. Adv.*, **29** (6), 889–895.
- Vamvakaki, V. and Chaniotakis, N.A. (2007) *Biosens. Bioelectron.*, **22** (11), 2650–2655.
- Willner, I., Basnar, B., and Willner, B. (2007) *FEBS J.*, **274** (2), 302–309.
- Geim, A.K. and Novoselov, K.S. (2007) *Nat. Mater.*, **6** (3), 183–191.
- Novoselov, K.S., Geim, A.K., Morozov, S.V., Jiang, D., Zhang, Y., Dubonos, S.V., Grigorieva, I.V., and Firsov, A.A. (2004) *Science*, **306** (5696), 666–669.
- Stankovich, S., Dikin, D.A., Dommett, G.H.B., Kohlhaas, K.M., Zimney, E.J., Stach, E.A., Piner, R.D., Nguyen, S.T., and Ruoff, R.S. (2006) *Nature*, **442** (7100), 282–286.

13. Bourlinos, A.B., Gournis, D., Petridis, D., Szabó, T., Szeri, A., and Dékány, I. (2003) *Langmuir*, **19** (15), 6050–6055.
14. Shim, M., Kam, N.W.S., Chen, R.J., Li, Y., and Dai, H. (2002) *Nano Lett.*, **2** (4), 285–288.
15. Zhang, Y., Zhang, J., Huang, X., Zhou, X., Wu, H., and Guo, S. (2012) *Small*, **8** (1), 154–159.
16. Alwarappan, S., Boyapalle, S., Kumar, A., Li, C.Z., and Mohapatra, S. (2012) *J. Phys. Chem. C*, **116** (11), 6556–6559.
17. Hua, B.Y., Wang, J., Wang, K., Li, X., Zhu, X.J., and Xia, X.H. (2012) *Chem. Commun.*, **48** (17), 2316–2318.
18. Zhang, F., Zheng, B., Zhang, J., Huang, X., Liu, H., Guo, S., and Zhang, J. (2010) *J. Phys. Chem. C*, **114** (18), 8469–8473.
19. Park, J.H., Xue, H., Jung, J.S., and Ryu, K. (2012) *Korean J. Chem. Eng.*, **29** (10), 1409–1412.
20. Pavlidis, I.V., Vorhaben, T., Tsoufis, T., Rudolf, P., Bornscheuer, U.T., Gournis, D., and Stamatidis, H. (2012) *Bioresour. Technol.*, **115**, 164–171.
21. Gómez, J.M., Romero, M.D., and Fernández, T.M. (2005) *Catal. Lett.*, **101** (3–4), 275–278.
22. Zhang, J., Zhang, J., Zhang, F., Yang, H., Huang, X., Liu, H., and Guo, S. (2010) *Langmuir*, **26** (9), 6083–6085.
23. Gao, Y. and Kyrtatzis, I. (2008) *Bioconjug. Chem.*, **19** (10), 1945–1950.
24. Azamian, B.R., Davis, J.J., Coleman, K.S., Bagshaw, C.B., and Green, M.L.H. (2002) *J. Am. Chem. Soc.*, **124** (43), 12664–12665.
25. Cazorla, C., Rojas-Cervellera, V., and Rovira, C. (2012) *J. Mater. Chem.*, **22** (37), 19684–19693.
26. Jiang, Y., Zhang, Q., Li, F., and Niu, L. (2012) *Sens. Actuators B*, **161** (1), 728–733.
27. Stavriannoudaki, V., Vamvakaki, V., and Chaniotakis, N. (2009) *Anal. Bioanal. Chem.*, **395** (2), 429–435.
28. Shen, J., Yan, B., Shi, M., Ma, H., Li, N., and Ye, M. (2011) *J. Colloid Interface Sci.*, **356** (2), 543–549.
29. Hu, X., Mu, L., Wen, J., and Zhou, Q. (2012) *J. Hazard. Mater.*, **213–214**, 387–392.
30. Bonanni, A., Ambrosi, A., and Pumera, M. (2012) *Chem. Eur. J.*, **18** (6), 1668–1673.
31. Liu, Y., Yu, D., Zeng, C., Miao, Z., and Dai, L. (2010) *Langmuir*, **26** (9), 6158–6160.
32. Shen, J., Shi, M., Yan, B., Ma, H., Li, N., Hu, Y., and Ye, M. (2010) *Colloids Surf., B*, **81** (2), 434–438.
33. Shan, C., Yang, H., Han, D., Zhang, Q., Ivaska, A., and Niu, L. (2009) *Langmuir*, **25** (20), 12030–12033.
34. Hu, Y., Li, F., Bai, X., Li, D., Hua, S., Wang, K., and Niu, L. (2011) *Chem. Commun.*, **47** (6), 1743–1745.
35. Chen, Y., Li, Y., Sun, D., Tian, D., Zhang, J., and Zhu, J.J. (2011) *J. Mater. Chem.*, **21** (21), 7604–7611.
36. Kodali, V.K., Scrimgeour, J., Kim, S., Hankinson, J.H., Carroll, K.M., De Heer, W.A., Berger, C., and Curtis, J.E. (2011) *Langmuir*, **27** (3), 863–865.
37. Manjunatha, R., Shivappa Suresh, G., Savio Melo, J., D’Souza, S.F., and Venkatarangaiah Venkatesha, T. (2012) *Talanta*, **99**, 302–309.
38. Zhu, J., Xu, M., Meng, X., Shang, K., Fan, H., and Ai, S. (2012) *Process Biochem.*, **47** (12), 2480–2486.
39. Kishore, D., Talat, M., Srivastava, O.N., and Kayastha, A.M. (2012) *PLoS ONE*, **7** (7), e40708.
40. Wang, G., Huang, H., Zhang, G., Zhang, X., Fang, B., and Wang, L. (2010) *Anal. Method Instrum.*, **2** (11), 1692–1697.
41. Loo, A.H., Bonanni, A., and Pumera, M. (2013) *Chem. Asian J.*, **8** (1), 198–203.
42. Zhou, Y., Chiu, C.W., and Liang, H. (2012) *Sensors-Basel*, **12** (11), 15036–15062.
43. Newman, J.D. and Setford, S.J. (2006) *Mol. Biotechnol.*, **32** (3), 249–268.
44. Le Goff, A., Holzinger, M., and Cosnier, S. (2011) *Analyst*, **136** (7), 1279–1287.
45. Sassolas, A., Blum, L.J., and Leca-Bouvier, B.D. (2012) *Biotechnol. Adv.*, **30** (3), 489–511.

46. Sarma, A.K., Vatsyayan, P., Goswami, P., and Minter, S.D. (2009) *Biosens. Bioelectron.*, **24** (8), 2313–2322.
47. Grieshaber, D., MacKenzie, R., Vörös, J., and Reimhult, E. (2008) *Sensors*, **8** (3), 1400–1458.
48. Andreu, R., Ferapontova, E.E., Gorton, L., and Calvente, J.J. (2007) *J. Phys. Chem. B*, **111** (2), 469–477.
49. Zhou, M., Ding, J., Guo, L.P., and Shang, Q.K. (2007) *Anal. Chem.*, **79** (14), 5328–5335.
50. Wu, L., Zhang, X., and Ju, H. (2007) *Biosens. Bioelectron.*, **23** (4), 479–484.
51. Gooding, J.J., Wibowo, R., Liu, J., Yang, W., Losic, D., Orbons, S., Mearns, F.J., Shapter, J.G., and Hibbert, D.B. (2003) *J. Am. Chem. Soc.*, **125** (30), 9006–9007.
52. Cai, C. and Chen, J. (2004) *Anal. Biochem.*, **332** (1), 75–83.
53. Zhu, Z., Garcia-Gancedo, L., Flewitt, A.J., Xie, H., Moussy, F., and Milne, W.I. (2012) *Sensors-Basel*, **12** (5), 5996–6022.
54. Zuo, X., He, S., Li, D., Peng, C., Huang, Q., Song, S., and Fan, C. (2010) *Langmuir*, **26** (3), 1936–1939.
55. Wang, Y., Li, Y., Tang, L., Lu, J., and Li, J. (2009) *Electrochem. Commun.*, **11** (4), 889–892.
56. Shan, C., Yang, H., Song, J., Han, D., Ivaska, A., and Niu, L. (2009) *Anal. Chem.*, **81** (6), 2378–2382.
57. Chen, D., Tang, L., and Li, J. (2010) *Chem. Soc. Rev.*, **39** (8), 3157–3180.
58. Zhang, Q., Wu, S., Zhang, L., Lu, J., Verproot, F., Liu, Y., Xing, Z., Li, J., and Song, X.M. (2011) *Biosens. Bioelectron.*, **26** (5), 2632–2637.
59. Ping, J., Wu, J., Wang, Y., and Ying, Y. (2012) *Biosens. Bioelectron.*, **34** (1), 70–76.
60. Lu, J., Drzal, L.T., Worden, R.M., and Lee, I. (2007) *Chem. Mater.*, **19** (25), 6240–6246.
61. Fu, C., Yang, W., Chen, X., and Evans, D.G. (2009) *Electrochem. Commun.*, **11** (5), 997–1000.
62. Alwarappan, S., Liu, C., Kumar, A., and Li, C.Z. (2010) *J. Phys. Chem. C*, **114** (30), 12920–12924.
63. Wang, Z., Zhou, X., Zhang, J., Boey, F., and Zhang, H. (2009) *J. Phys. Chem. C*, **113** (32), 14071–14075.
64. Kang, X., Wang, J., Wu, H., Aksay, I.A., Liu, J., and Lin, Y. (2009) *Biosens. Bioelectron.*, **25** (4), 901–905.
65. Wu, P., Shao, Q., Hu, Y., Jin, J., Yin, Y., Zhang, H., and Cai, C. (2010) *Electrochim. Acta*, **55** (28), 8606–8614.
66. Tasviri, M., Ghasemi, S., Ghourchian, H., and Gholami, M.R. (2013) *J. Solid State Electrochem.*, **17** (1), 183–189.
67. Yang, M.H., Choi, B.G., Park, H., Hong, W.H., Lee, S.Y., and Park, T.J. (2010) *Electroanal.*, **22** (11), 1223–1228.
68. Wang, K., Liu, Q., Guan, Q.M., Wu, J., Li, H.N., and Yan, J.J. (2011) *Biosens. Bioelectron.*, **26** (5), 2252–2257.
69. Zeng, Q., Cheng, J.S., Liu, X.F., Bai, H.T., and Jiang, J.H. (2011) *Biosens. Bioelectron.*, **26** (8), 3456–3463.
70. Xu, C.X., Huang, K.J., Chen, X.M., and Xiong, X.Q. (2012) *J. Solid State Electrochem.*, **16** (12), 3747–3752.
71. Yang, J., Deng, S., Lei, J., Ju, H., and Gunasekaran, S. (2011) *Biosens. Bioelectron.*, **29** (1), 159–166.
72. Luo, Z., Yuwen, L., Han, Y., Tian, J., Zhu, X., Weng, L., and Wang, L. (2012) *Biosens. Bioelectron.*, **36** (1), 179–185.
73. Razmi, H. and Mohammad-Rezaei, R. (2013) *Biosens. Bioelectron.*, **41** (1), 498–504.
74. Zheng, D., Vashist, S.K., Al-Rubeaan, K., Luong, J.H.T., and Sheu, F.S. (2012) *Talanta*, **99**, 22–28.
75. Unnikrishnan, B., Palanisamy, S., and Chen, S.M. (2013) *Biosens. Bioelectron.*, **39** (1), 70–75.
76. Sun, W., Guo, Y., Li, T., Ju, X., Lou, J., and Ruan, C. (2012) *Electrochim. Acta*, **75**, 381–386.
77. Zhou, K., Zhu, Y., Yang, X., Luo, J., Li, C., and Luan, S. (2010) *Electrochim. Acta*, **55** (9), 3055–3060.
78. Lu, Q., Dong, X., Li, L.J., and Hu, X. (2010) *Talanta*, **82** (4), 1344–1348.
79. Zhang, L., Cheng, H., Zhang, H.M., and Qu, L. (2012) *Electrochim. Acta*, **65**, 122–126.
80. Li, M., Xu, S., Tang, M., Liu, L., Gao, F., and Wang, Y. (2011) *Electrochim. Acta*, **56** (3), 1144–1149.

81. Palanisamy, S., Unnikrishnan, B., and Chen, S.-M. (2012) *Int. J. Electrochem. Sci.*, **7**, 7935–7947.
82. Zhang, Y., Zhang, J., Wu, H., Guo, S., and Zhang, J. (2012) *J. Electroanal. Chem.*, **681**, 49–55.
83. Liu, T., Xu, M., Yin, H., Ai, S., Qu, X., and Zong, S. (2011) *Microchim. Acta*, **175** (1-2), 129–135.
84. Wu, L., Deng, D., Jin, J., Lu, X., and Chen, J. (2012) *Biosens. Bioelectron.*, **35** (1), 193–199.
85. Alwarappan, S., Joshi, R.K., Ram, M.K., and Kumar, A. (2010) *Appl. Phys. Lett.*, **96** (26), 263702.
86. Wu, J.F., Xu, M.Q., and Zhao, G.C. (2010) *Electrochem. Commun.*, **12** (1), 175–177.
87. Chen, H. and Zhao, G. (2012) *J. Solid State Electrochem.*, **16** (10), 3289–3297.
88. Liu, K., Zhang, J., Yang, G., Wang, C., and Zhu, J.-J. (2010) *Electrochem. Commun.*, **12** (3), 402–405.
89. Xu, H., Dai, H., and Chen, G. (2010) *Talanta*, **81** (1-2), 334–338.
90. Sun, W., Guo, Y., Ju, X., Zhang, Y., Wang, X., and Sun, Z. (2013) *Biosens. Bioelectron.*, **42** (1), 207–213.
91. Feng, X., Li, R., Hu, C., and Hou, W. (2011) *J. Electroanal. Chem.*, **657** (1-2), 28–33.
92. Liao, H.G., Wu, H., Wang, J., Liu, J., Jiang, Y.X., Sun, S.G., and Lin, Y. (2010) *Electroanal.*, **22** (19), 2297–2302.
93. Shan, C., Yang, H., Han, D., Zhang, Q., Ivaska, A., and Niu, L. (2010) *Biosens. Bioelectron.*, **25** (6), 1504–1508.
94. Li, Y. and Han, G. (2012) *Analyst*, **137** (13), 3160–3165.
95. Dey, R.S. and Raj, C.R. (2010) *J. Phys. Chem. C*, **114** (49), 21427–21433.
96. Zeng, G., Xing, Y., Gao, J., Wang, Z., and Zhang, X. (2010) *Langmuir*, **26** (18), 15022–15026.
97. Lu, C.H., Yang, H.H., Zhu, C.L., Chen, X., and Chen, G.N. (2009) *Angew. Chem. Int. Ed.*, **48** (26), 4785–4787.
98. Song, B., Li, D., Qi, W., Elstner, M., Fan, C., and Fang, H. (2010) *ChemPhysChem*, **11** (3), 585–589.
99. Bonanni, A., Loo, A.H., and Pumera, M. (2012) *Trends Anal. Chem.*, **37**, 12–21.
100. Bonanni, A. and Pumera, M. (2011) *ACS Nano*, **5** (3), 2356–2361.
101. Chen, Y., Jiang, B., Xiang, Y., Chai, Y., and Yuan, R. (2011) *Chem. Commun.*, **47** (48), 12798–12800.
102. Lin, L., Liu, Y., Tang, L., and Li, J. (2011) *Analyst*, **136** (22), 4732–4737.
103. Dubuisson, E., Yang, Z., and Loh, K.P. (2011) *Anal. Chem.*, **83** (7), 2452–2460.
104. Bo, Y., Wang, W., Qi, J., and Huang, S. (2011) *Analyst*, **136** (9), 1946–1951.
105. Bo, Y., Yang, H., Hu, Y., Yao, T., and Huang, S. (2011) *Electrochim. Acta*, **56** (6), 2676–2681.
106. Sun, W., Zhang, Y., Ju, X., Li, G., Gao, H., and Sun, Z. (2012) *Anal. Chim. Acta*, **752**, 39–44.
107. Hu, Y., Wang, K., Zhang, Q., Li, F., Wu, T., and Niu, L. (2012) *Biomaterials*, **33** (4), 1097–1106.
108. Roy, S., Soin, N., Bajpai, R., Misra, D.S., McLaughlin, J.A., and Roy, S.S. (2011) *J. Mater. Chem.*, **21** (38), 14725–14731.
109. Jung, J.H., Cheon, D.S., Liu, F., Lee, K.B., and Seo, T.S. (2010) *Angew. Chem. Int. Ed.*, **49** (33), 5708–5711.
110. Ohno, Y., Maehashi, K., and Matsumoto, K. (2010) *J. Am. Chem. Soc.*, **132** (51), 18012–18013.
111. Zhao, H., Tian, J., and Quan, X. (2013) *Colloids Surf., B*, **103**, 38–44.
112. Wei, Q., Mao, K., Wu, D., Dai, Y., Yang, J., Du, B., Yang, M., and Li, H. (2010) *Sens. Actuators B*, **149** (1), 314–318.
113. Yang, Y.C., Dong, S.W., Shen, T., Jian, C.X., Chang, H.J., Li, Y., and Zhou, J.X. (2011) *Electrochim. Acta*, **56** (17), 6021–6025.
114. Du, D., Zou, Z., Shin, Y., Wang, J., Wu, H., Engelhard, M.H., Liu, J., Aksay, L.A., and Lin, Y. (2010) *Anal. Chem.*, **82** (7), 2989–2995.
115. Yang, M., Javadi, A., Li, H., and Gong, S. (2010) *Biosens. Bioelectron.*, **26** (2), 560–565.
116. Haque, A.M.J., Park, H., Sung, D., Jon, S., Choi, S.Y., and Kim, K. (2012) *Anal. Chem.*, **84** (4), 1871–1878.

117. Qu, F., Lu, H., Yang, M., and Deng, C. (2011) *Biosens. Bioelectron.*, **26** (12), 4810–4814.
118. Li, R., Wu, D., Li, H., Xu, C., Wang, H., Zhao, Y., Cai, Y., Wei, Q., and Du, B. (2011) *Anal. Biochem.*, **414** (2), 196–201.
119. Liu, F., Zhang, Y., Ge, S., Lu, J., Yu, J., Song, X., and Liu, S. (2012) *Talanta*, **99**, 512–519.
120. Liu, M., Zhao, H., Chen, S., Yu, H., and Quan, X. (2012) *Environ. Sci. Technol.*, **46** (22), 12567–12574.
121. Bai, L., Yuan, R., Chai, Y., Zhuo, Y., Yuan, Y., and Wang, Y. (2012) *Biomaterials*, **33** (4), 1090–1096.
122. Liang, J., Chen, Z., Guo, L., and Li, L. (2011) *Chem. Commun.*, **47** (19), 5476–5478.
123. Wang, L., Xu, M., Han, L., Zhou, M., Zhu, C., and Dong, S. (2012) *Anal. Chem.*, **84** (17), 7301–7307.
124. Ray, M., Chatterjee, S., Das, T., Bhattacharyya, S., Ayyub, P., and Mazumdar, S. (2011) *Nanotechnology*, **22** (41), 415705.
125. Pang, H.L., Liu, J., Hu, D., Zhang, X.H., and Chen, J.H. (2010) *Electrochim. Acta*, **55** (22), 6611–6616.
126. Shang, W., Nuffer, J.H., Muñoz-Papandrea, V.A., Colón, W., Siegel, R.W., and Dordick, J.S. (2009) *Small*, **5** (4), 470–476.
127. Das, K., Maiti, S., Ghosh, M., Mandal, D., and Das, P.K. (2013) *J. Colloid Interface Sci.*, **395** (1), 111–118.
128. Zeng, Q., Cheng, J., Tang, L., Liu, X., Liu, Y., Li, J., and Jiang, J. (2010) *Adv. Funct. Mater.*, **20** (19), 3366–3372.
129. Shao, Q., Wu, P., Xu, X., Zhang, H., and Cai, C. (2012) *Phys. Chem. Chem. Phys.*, **14** (25), 9076–9085.
130. Zhou, L., Jiang, Y., Gao, J., Zhao, X., Ma, L., and Zhou, Q. (2012) *Biochem. Eng. J.*, **69**, 28–31.
131. Su, R., Shi, P., Zhu, M., Hong, F., and Li, D. (2012) *Bioresour. Technol.*, **115**, 136–140.
132. Jiao, J., Miao, A., Zhang, X., Cai, Y., Lu, Y., Zhang, Y., and Lu, H. (2013) *Analyst*, **138** (6), 1645–1648.
133. Bao, H., Chen, Q., Zhang, L., and Chen, G. (2011) *Analyst*, **136** (24), 5190–5196.
134. Jiang, B., Yang, K., Zhao, Q., Wu, Q., Liang, Z., Zhang, L., Peng, X., and Zhang, Y. (2012) *J. Chromatogr. A*, **1254**, 8–13.
135. Xu, G., Chen, X., Hu, J., Yang, P., Yang, D., and Wei, L. (2012) *Analyst*, **137** (12), 2757–2761.
136. Minteer, S.D., Liaw, B.Y., and Cooney, M.J. (2007) *Curr. Opin. Biotechnol.*, **18** (3), 228–234.
137. Willner, I., Yan, Y.M., Willner, B., and Tel-Vered, R. (2009) *Fuel Cells*, **9** (1), 7–24.
138. Gao, F., Yan, Y., Su, L., Wang, L., and Mao, L. (2007) *Electrochem. Commun.*, **9** (5), 989–996.
139. Barton, S.C., Gallaway, J., and Atanassov, P. (2004) *Chem. Rev.*, **104** (10), 4867–4886.
140. Li, C.Z., Choi, W.B., and Chuang, C.H. (2008) *Electrochim. Acta*, **54** (2), 821–828.
141. Liu, Y. and Dong, S. (2007) *Biosens. Bioelectron.*, **23** (4), 593–597.
142. Alwarappan, S., Erdem, A., Liu, C., and Li, C.Z. (2009) *J. Phys. Chem. C*, **113** (20), 8853–8857.
143. Dai, J., Wang, Q., Li, W., Wei, Z., and Xu, G. (2007) *Mater. Lett.*, **61** (1), 27–29.
144. Geim, A.K. and MacDonald, A.H. (2007) *Phys. Today*, **60** (8), 35–41.
145. Liu, C., Chen, Z., and Li, C.Z. (2011) *IEEE Trans. Nanotechnol.*, **10** (1), 59–62.
146. Wang, X., Wang, J., Cheng, H., Yu, P., Ye, J., and Mao, L. (2011) *Langmuir*, **27** (17), 11180–11186.
147. Liu, C., Alwarappan, S., Chen, Z., Kong, X., and Li, C.Z. (2010) *Biosens. Bioelectron.*, **25** (7), 1829–1833.
148. Fishilevich, S., Amir, L., Fridman, Y., Aharoni, A., and Alfonta, L. (2009) *J. Am. Chem. Soc.*, **131** (34), 12052–12053.
149. Szczupak, A., Kol-Kalman, D., and Alfonta, L. (2012) *Chem. Commun.*, **48** (1), 49–51.
150. Bahartan, K., Amir, L., Israel, A., Lichtenstein, R.G., and Alfonta, L. (2012) *ChemSusChem*, **5** (9), 1820–1825.
151. Bahartan, K., Gun, J., Sladkevich, S., Prikhodchenko, P.V., Lev, O., and

- Alfonta, L. (2012) *Chem. Commun.*, **48** (98), 11957–11959.
152. Lu, Y.J., Yang, H.W., Hung, S.C., Huang, C.Y., Li, S.M., Ma, C.C.M., Chen, P.Y., Tsai, H.C., Wei, K.C., and Chen, J.P. (2012) *Int. J. Nanomedicine*, **7**, 1737–1747.
153. Zheng, X.T. and Li, C.M. (2012) *Mol. Pharm.*, **9** (3), 615–621.
154. Bao, H., Pan, Y., Ping, Y., Sahoo, N.G., Wu, T., Li, L., Li, J., and Gan, L.H. (2011) *Small*, **7** (11), 1569–1578.
155. Kakran, M., Sahoo, N.G., Bao, H., Pan, Y., and Li, L. (2011) *Curr. Med. Chem.*, **18** (29), 4503–4512.
156. Wang, Y., Li, Z., Hu, D., Lin, C.T., Li, J., and Lin, Y. (2010) *J. Am. Chem. Soc.*, **132** (27), 9274–9276.
157. Liu, Z., Robinson, J.T., Sun, X., and Dai, H. (2008) *J. Am. Chem. Soc.*, **130** (33), 10876–10877.
158. Zhang, L., Xia, J., Zhao, Q., Liu, L., and Zhang, Z. (2010) *Small*, **6** (4), 537–544.
159. Chen, B., Liu, M., Zhang, L., Huang, J., Yao, J., and Zhang, Z. (2011) *J. Mater. Chem.*, **21** (21), 7736–7741.
160. Mu, Q., Liu, W., Xing, Y., Zhou, H., Li, Z., Zhang, Y., Ji, L., Wang, F., Si, Z., Zhang, B., and Yan, B. (2008) *J. Phys. Chem. C*, **112** (9), 3300–3307.
161. Jin, L., Yang, K., Yao, K., Zhang, S., Tao, H., Lee, S.T., Liu, Z., and Peng, R. (2012) *ACS Nano*, **6** (6), 4864–4875.
162. Patila, M., Pavlidis, I.V., Diamanti, E.K., Katapodis, P., Gournis, D., and Stamatis, H. (2013) *Process Biochem.*, **48** (7), 1010–1017.
163. Pavlidis, I.V., Vorhaben, T., Gournis, D., Papadopoulos, G.K., Bornscheuer, U.T., and Stamatis, H. (2012) *J. Nanopart. Res.*, **14** (5), 1–10.

6

Halogenated Graphenes: Emerging Family of Two-Dimensional Materials

Kasibhatta Kumara Ramanatha Datta and Radek Zbořil

6.1

Introduction

Graphene, the first two-dimensional crystal to enjoy supremacy, is undoubtedly the most studied and sought after material in interdisciplinary science and technology in the last decade [1–3]. The extraordinary properties of this sp^2 bonded carbon hexagonal crystal include high surface area, transparency, electrical conductivity, carrier mobility, surface reactivity, strength, flexibility, and so on, making it an emerging, forefront candidate for diverse applications [2–7]. Because of its vast potential, material scientists, physicists, and chemists are interested in engineering graphene's electronic properties, that is, in the opening up the bandgap for various optoelectronic-related applications [2, 8–10]. Significant attention is also being devoted to the exploration of surface reactivity of graphene, which is a direct consequence of its unique atomic structure [11, 12]. The high surface reactivity of graphene is utilized in designing novel functional derivatives either by covalent or noncovalent approaches [9, 10, 13].

There are several ways to tailor the functionalities of graphene depending on the choice and type of reaction or application. Graphene oxide (GO), fluorographene (FG, C_1F_1), and graphane are some prime examples of functionalized graphenes in which the added atom such as oxygen, fluorine, and hydrogen, respectively, are covalently bonded to graphene [9, 13–19]. During covalent modification of graphene, carbon atoms are converted from sp^2 to sp^3 , which prefer to establish tetrahedral geometry with longer bond lengths. GO has a complicated chemical structure with carboxyl groups at the edges and hydroxyl and epoxide groups at the basal plane, along with topological defects [14]. These oxygen-containing functional groups make GO an easily water-dispersible material that would be advantageous for various catalytic, biological, and green chemistry applications. Graphane can be prepared by exposing graphene to cold hydrogen plasma yielding 1 : 1 carbon-to-hydrogen ratio [18]. Graphane behaves as an insulator with charge carrier mobility that is three orders less as compared to graphene. FG can be prepared by fluorinating graphene by using fluorine precursors [15, 16] or mechanical or chemical exfoliation of bulk graphite fluoride (GrF) [15, 17]. Fluorination of

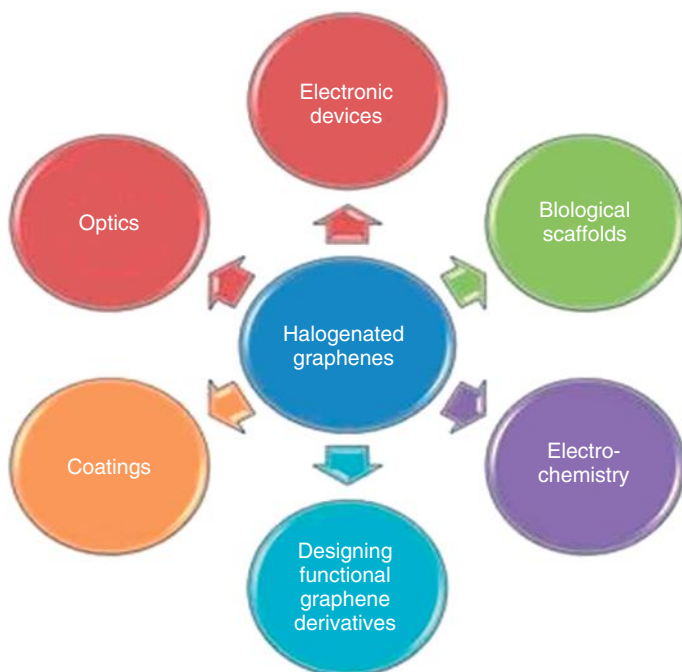


Figure 6.1 Diverse applications of halogenated graphenes.

graphene is similar to hydrogenation as fluorine forms a single bond with carbon, however, with a reversed dipole and increased binding strength. In the case of graphane, the bonding (C–H) is essentially only of covalent character, while in the case of other carbon materials and FG (C–F), the bonding type can vary from covalent, through semicovalent to ionic and van der Waal’s interactions [20].

There has been a lot of experimental and theoretical progress achieved in the field of stoichiometric FG, fluorinated, and other halogenated graphenes [21]. The halogen content in graphene dictates electronic, optical, thermal, electrocatalytic, magnetic, rheological, biological, and chemical properties of the resultant materials (Figure 6.1). Furthermore, there are a few reports on patterned halogenated graphenes and fabricated devices with fluorinated graphene or in combination with graphene nanostructures. In this chapter, we focus on the synthesis, characterization, properties, and applications of FG, other halogenated graphenes, and their hybrid derivatives.

6.2

Synthesis of Halogenated Graphenes

There are two important ways to prepare mono- or few-layered halogenated graphenes either by halogenating graphene or chemical/mechanical exfoliation of

bulk halogenated graphite. The two approaches are complementary to each other. The former methods involve halogenating graphene by appropriate gas [22, 23], polymers [24, 25], halogen precursor [16, 26], and interhalogen compounds [27]. The other approach utilizes the isolation of single- or few-layered halogenated graphene from bulk halogenated graphite (containing variable halogen content) by either solvents or by mechanical exfoliation [15, 17, 28, 29]. Detailed synthetic procedures of FG and various other halogenated graphenes are discussed below.

6.2.1

Fluorographene

6.2.1.1 Mechanical or Chemical Exfoliation – from Graphite Fluoride to Fluorographene

GrF is used as a starting material for the preparation of FG by the top-down approach either by mechanical [15, 30] or chemical exfoliation [17, 31]. Owing to the harsh experimental conditions involved in the synthesis of GrF, its monolayers were found to be very fragile and prone to rupture, resulting in low-quality FG during mechanical cleavage [30]. Single- and few-layered FG in the form of colloidal suspensions can be isolated by chemical etching from bulk GrF under sonication in the presence of sulfolane [17], dimethylformamide (DMF) [32], *N*-methyl-2-pyrrolidone (NMP) (Figure 6.2a–d) [31], or isopropyl alcohol [22]. Owing to the intercalation of solvent molecules within the interlayers of GrF, a weakening of the van der Waal's interactions between neighboring layers is observed, resulting in the isolation of colloidal FG. Chemical exfoliation facilitates the isolation of FG in large yields having polydisperse systems containing one- and few-layered FG. However, solution processability of FG suspensions is beneficial in the fields of coatings, polymer hybrids, and inks.

6.2.1.2 Fluorination of Graphene – from Graphene to Fluorographene

Till date, several methods have been reported to prepare FG by fluorination of graphene. At various temperatures under an inert environment (Figure 6.2e) [15, 33] or at room temperature (30 °C) [16], FG can be prepared using XeF₂ as a fluorinating agent. The room-temperature preparation of FG involves fluorinating graphene supported on silicon-on-insulator (SiO₂/Si) substrate using XeF₂ gas, which selectively etches the Si underlayer, consequently fluorinating both sides of the graphene to form stoichiometric C_{1.0}F_{1.0} [16]. Furthermore, fluorination of highly oriented pyrolytic graphite (HOPG) by F₂ gas at a temperature of 600 °C, followed by chemical exfoliation, yields a nonstoichiometric FG (C_{0.7}F₁) of a low quality [22].

6.2.2

Nonstoichiometric Fluorinated Graphene and Fluorinated Graphene Oxide

Fluorinated graphene with different fluorine coverage can be prepared by fluorinating graphene or by chemical or mechanical etching of nonstoichiometric

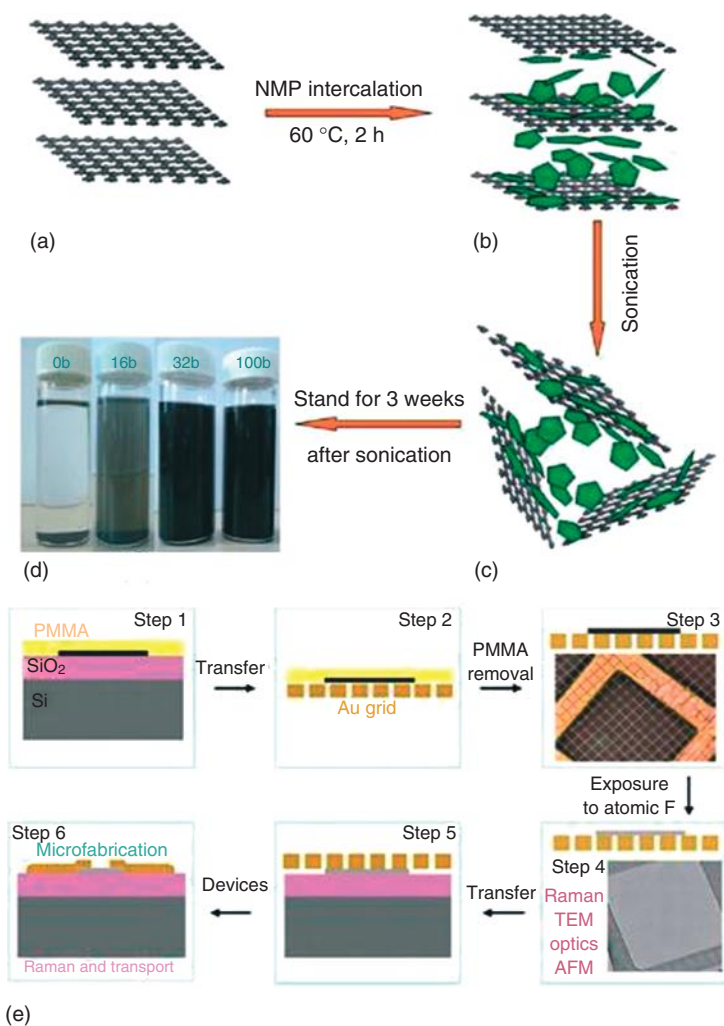


Figure 6.2 (a–d) Schematic representation of the NMP intercalation and exfoliation fabrication processes used to prepare CF dispersions. (Reproduced from Ref. [31].) (e) Various steps involved in the fluorination of graphene (PMMA–poly(methyl methacrylate)). (Reproduced from Ref. [15].)

GrF. Fluorination of single- or few-layered graphene is usually carried out in plasmas containing CF₄ [34], SF₆ [35], XeF₂ [16, 36], fluoropolymers [25], or Ar/F₂ [37] as fluorinating agents. To minimize ion bombardments and to improve the reaction with fluorine radicals on graphene, the substrate can be placed *face down* in the Ar/F₂ plasma chamber [37]. The extent of fluorine loading in the resultant fluorinated graphenes can be controlled by the plasma treatment time or by changing the precursor. Interhalogen compounds such as ClF₃ and BrF₃ can simultaneously intercalate and fluorinate graphite, followed by subsequent

exfoliation or heat treatment, resulting in semifluorinated graphenes with the composition C_2F [27, 38–40]. Polymers containing fluorine in their structure also serve as fluorinating precursors. The fluorination of graphene with a composition of C_4F can be carried out using fluoropolymer CYTOP[®] on graphene by laser irradiation (Figure 6.3a). In this approach, direct contact between CYTOP and the graphene surface is secured by transferring graphene films on Cu foil onto a SiO_2/Si substrate coated with CYTOP. After laser irradiation, photon-induced decomposition of CYTOP generates many active intermediates, such as CF_x and F radicals, which react with graphene yielding single-side fluorination as the active fluorine species are impermeable through the substrate (SiO_2/Si substrate) [25]. Similar to the isolation of graphene from bulk graphite and FG from bulk GrF, mono- or few-layered fluorinated graphenes can be obtained by mechanical or chemical exfoliation of bulk GrF with variable fluorine contents in

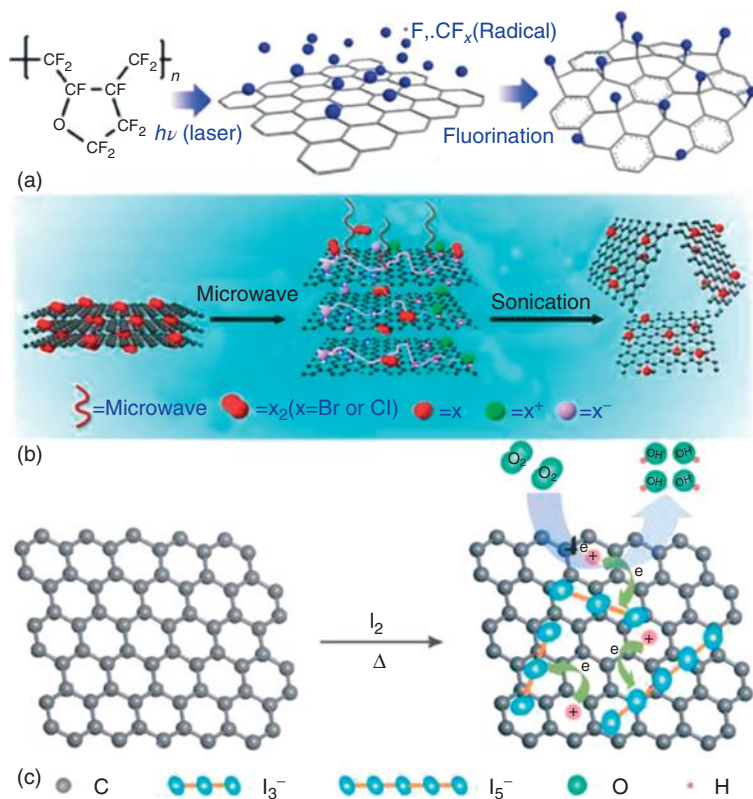


Figure 6.3 Scheme showing (a) the mechanism of fluorination using CYTOP and laser irradiation. (Reproduced from Ref. [25].) (b) Chlorination and bromination processes. The halogen was first intercalated between the graphite layers. With the assistance of

MiW-S, the halogen then reacted with the graphite directly. In the solution-phase sonication step, the graphite halide was exfoliated to single-layer G-X. (Reproduced from Ref. [29].) (c) I-doped graphene preparation. (Reproduced from Ref. [44].)

a variety of solvents with/without surfactants assisted via sonication [41, 42]. Ionic liquids such as 1-butyl-3-methylimidazolium bromide ([bmim]Br) and 1-methyl-3-octyl-imidazolium tetrafluoroborate ([omim]BF₄) were used to obtain mono- and few-layered fluorinated graphenes with compositions of CF_{0.25} and CF_{0.5} [28]. High temperatures generated in the arc discharge process are utilized in the preparation of multilayered fluorine-doped graphene (6.6 at. %) [43].

All the methods discussed above employ pure graphene or bulk GrF for the preparation of fluorinated graphenes. However, there are a few reports on the preparation of reduced fluorinated graphene oxide (FGO). FGO can be synthesized by fluorinating GO using hydrofluoric acid (HF) as a fluorine precursor by heat treatment [45, 46], photochemical treatment [47], by CF₄ plasma [48], or by oxidizing bulk semifluorinated GrF [49, 50]. By changing the reaction parameters such as temperature, HF concentration, and so on, the fluorine content of the resulting FGOs can be varied.

6.2.3

Other Halogenated Graphenes

To date, there have been no reports on the preparation of stoichiometric chloro-, bromo-, and iodographenes as compared to FG; the highest achieved loadings of halogen in graphene are in the order of 45, 5, and 3 at.% for Cl, Br, and I, respectively. Single- and few-layered chlorinated graphenes were prepared by the reaction between graphene and chlorine gas either by photochemical/plasma treatment at room temperature [23, 51, 52] or by ultraviolet (UV) irradiation in a liquid chlorine medium at 250 °C [26]. Dresselhaus and coworkers [52] used plasma-based chlorination to achieve single-side chlorinated graphene with a chlorine content of 45.3 at.% (close to C₂Cl). The C:Cl ratio can be tuned by altering the DC bias and treatment time in the plasma chamber [52]. Rao and coworkers reported brominated graphenes (5 at.%) by allowing graphene to react with liquid Br₂ in carbon tetrabromide at 250 °C by simultaneous UV irradiation [26]. Zheng *et al.* [29] reported microwave-spark (MiW-S)-assisted reaction that allows the direct production of halogenated graphite, which, on subsequent exfoliation in organic solvents, resulted in monolayer halogen-derived graphene with Cl (21 at.%) and Br (4 at.%) compositions, respectively. Owing to its strong microwave absorption, graphite expands its original volume (~200 times) with a rise in temperature accompanied by luminous sparks (Figure 6.3b). The hot graphite flakes directly react with moderately ionized halogens (X⁺) resulting in the halogenation of graphite via electrophilic substitution. Chlorination of graphene was found to be more effective than bromination as liquid Cl₂ is more reactive than Br₂ [26, 29].

Iodine-functionalized (3 at.%) graphenes have been prepared by direct annealing of camphor and I₂ [53]. Further, direct heating of GO with iodine (Figure 6.3c) at 500–1100 °C in inert conditions results in iodine-doped graphene (~0.1 at.%). The content of iodine can be varied by changing the carbonization temperature or mass ratio of GO and iodine [44]. A series of halogenated graphenes [54] have been prepared by thermal treatment of bulk graphite oxide under different

gaseous halogen atmospheres (chlorine, bromine, or iodine) yielding halogenated graphenes with doping levels of 2.1, 1.6, and 0.2 at.% for Cl, Br, and I, respectively. Edge-selective halogenated graphenes with the Cl, Br, and I contents of 5.89, 2.78, and 0.95 at. %, respectively, was demonstrated by ball milling graphite flakes in the presence of various halogen gases [55] except fluorine (owing to its high reactivity). In addition to mechanochemical cleaving of graphitic C–C bonds and edge-selective halogen functionalization of graphitic layers, ball milling also involves delamination of graphite into graphene nanoplatelets (GnPs). This results in high Brunauer–Emmett–Teller (BET) surface areas of 471, 579, and 662 m² g⁻¹ for ClGnP, BrGnP, and IGnP, respectively.

6.3

Characterization of Halogenated Graphenes

The structural characteristics, composition, bonding environment, morphology, and thermal stability of various halogenated graphenes are commonly evaluated by various characterization techniques along with strong theoretical support.

6.3.1

Fluorographene

Transmission electron microscope (TEM) images of FG obtained by exfoliation of GrF with sulfolane exhibited transparent nature with lateral dimensions ranging between 0.2 and 2 μm with a few sheets being twisted (Figure 6.4a–c). The structural characteristics of FG, obtained from selected area electron diffraction (SAED) analysis, confirmed the existence of a hexagonal crystalline structure [15, 17, 22] and stoichiometry equivalent to that of bulk GrF (Figure 6.4d,e). It has been shown that the retention of hexagonal crystalline order for FG is similar to that of graphene with 1% expansion of the unit cell (Figure 6.4f) [15, 22]. The experimental lattice constant (a) of C₁F₁ is 2.48 Å while for graphene, this is 2.46 Å.

This is in contrast to the case of graphane, which showed a compressed lattice with $a = 2.42$ Å [18]. The increase in unit cell and in-plane lattice constant of FG is expected as carbon atoms forming C–C bonds are converted from a sp² to sp³ configuration during the fluorination process accompanied by an increase in the C–C bond length. The thickness of FG layers can be directly investigated from atomic force microscopy (AFM) measurements. Chemical exfoliation of GrF using sulfolane showed the presence of FG monolayers with a thickness ranging from 6.7 to 8.7 Å (Figure 6.5).

The changes in composition, bonding, and electronic properties of graphene upon fluorine exposure can be clearly monitored by X-ray photoelectron spectroscopy (XPS), Fourier transform infrared spectroscopy (FTIR), high-resolution electron energy loss spectroscopy (HREELS), and Raman spectroscopy (Figure 6.6) [56]. Fluorination of graphene leads to remarkable changes in Raman spectra, that is, upon increasing the fluorination rate (using XeF₂), there is an increase

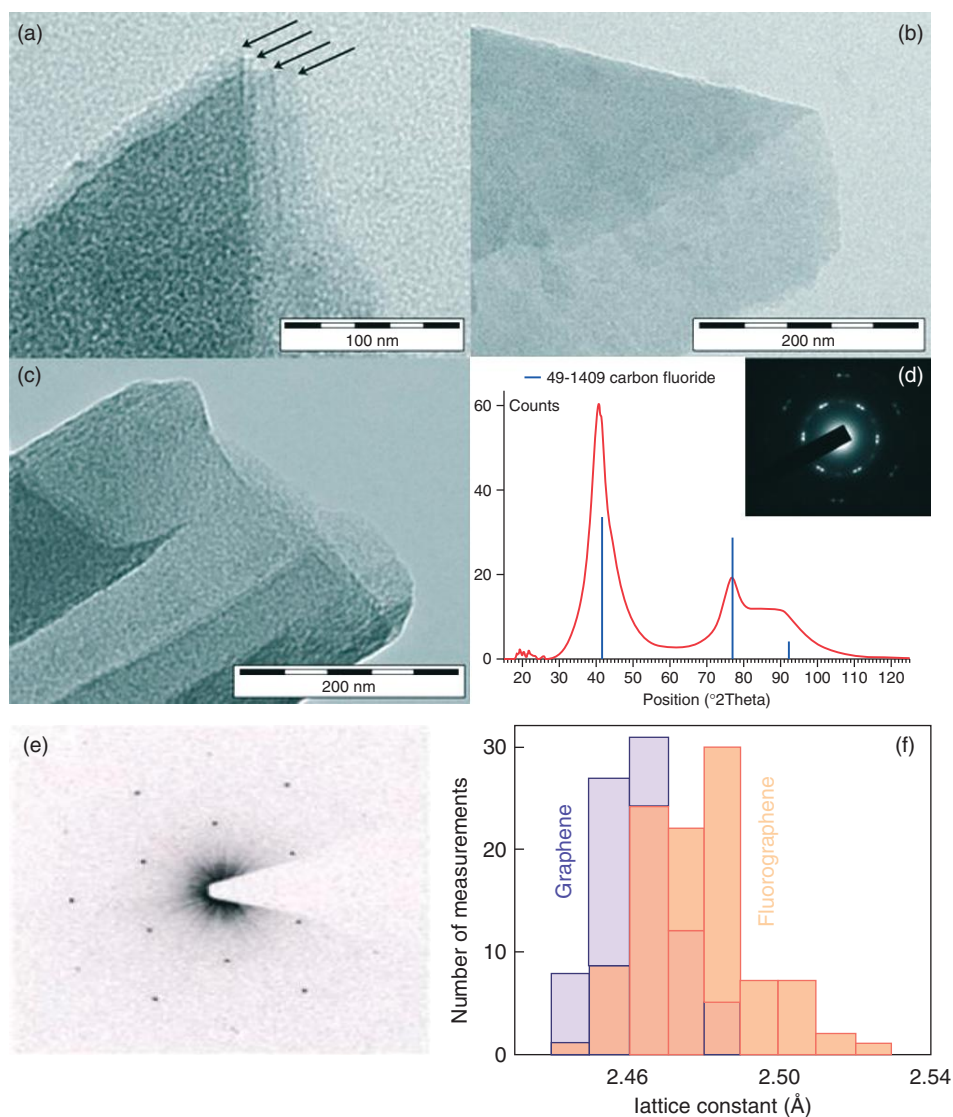


Figure 6.4 (a–c) TEM images of FG sheets obtained after GrF exfoliation in sulfolane. Arrows in the HRTEM image (a) indicate highly transparent FG monolayers; and (d) the SAED pattern confirms the stoichiometry and structure of the layers corresponding to the original GrF. (Reproduced from Ref. [17].) (e) Diffraction pattern from a FG

membrane; and (f) lattice constants measured using microscopy images, such as that shown in (e). For comparison, similar measurements were taken for membranes before fluorination (left histogram). The dotted line indicates the lattice constant for graphite. (Reproduced from Ref. [15].)

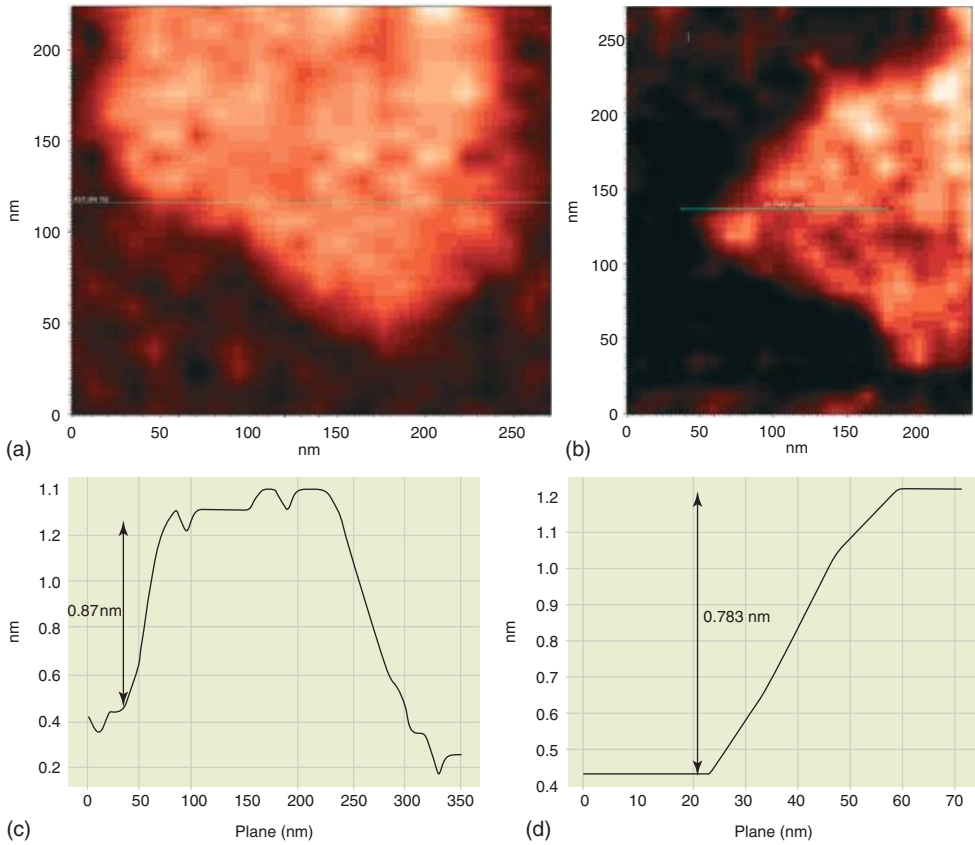


Figure 6.5 Two independent AFM images of FG monolayers (a,b) and their height profiles (c,d), providing evidencing for the layers being <math><0.9\text{ nm}</math> thick. (Reproduced from Ref. [17].)

in the appearance of a D-peak at 1350 cm^{-1} and broadening of the G (1587 cm^{-1}) and D'-peaks (1618 cm^{-1}), along with a decrease in the 2D band intensity. Also, when the exposure time is increased to 1 h where the formation of FG occurs, the characteristic Raman signals of pristine graphene fully disappear as a result of the destruction of aromatic π -conjugation (Figure 6.6a). UV-vis spectra of graphene showed a steady blueshift ($\sim 43\text{ nm}$) upon an increase in fluorine concentration (Figure 6.6b). The high electronegativity of fluorine induces strong chemical shifts in the C 1s binding energy (BE) allowing the use of XPS to quantify composition and bonding type. XPS analysis performed on FG, obtained by the fluorination of graphene on SiO_2/Si using XeF_2 , showed the major bonding of essentially C-F (86%) type, with smaller fractions of C-F₂ and C-F₃ species (owing to defects at the free edges) [16]. The carbon peak, observed at 284.6 eV for pure graphene, shifts to 287.5 eV, which can be assigned to a C-F binding state (Figure 6.6c). The change of C-F bonding type occurs from semi-ionic (685.5 eV) to covalent (687.5 eV), which is observed from the F 1s spectra with an increase in fluorination

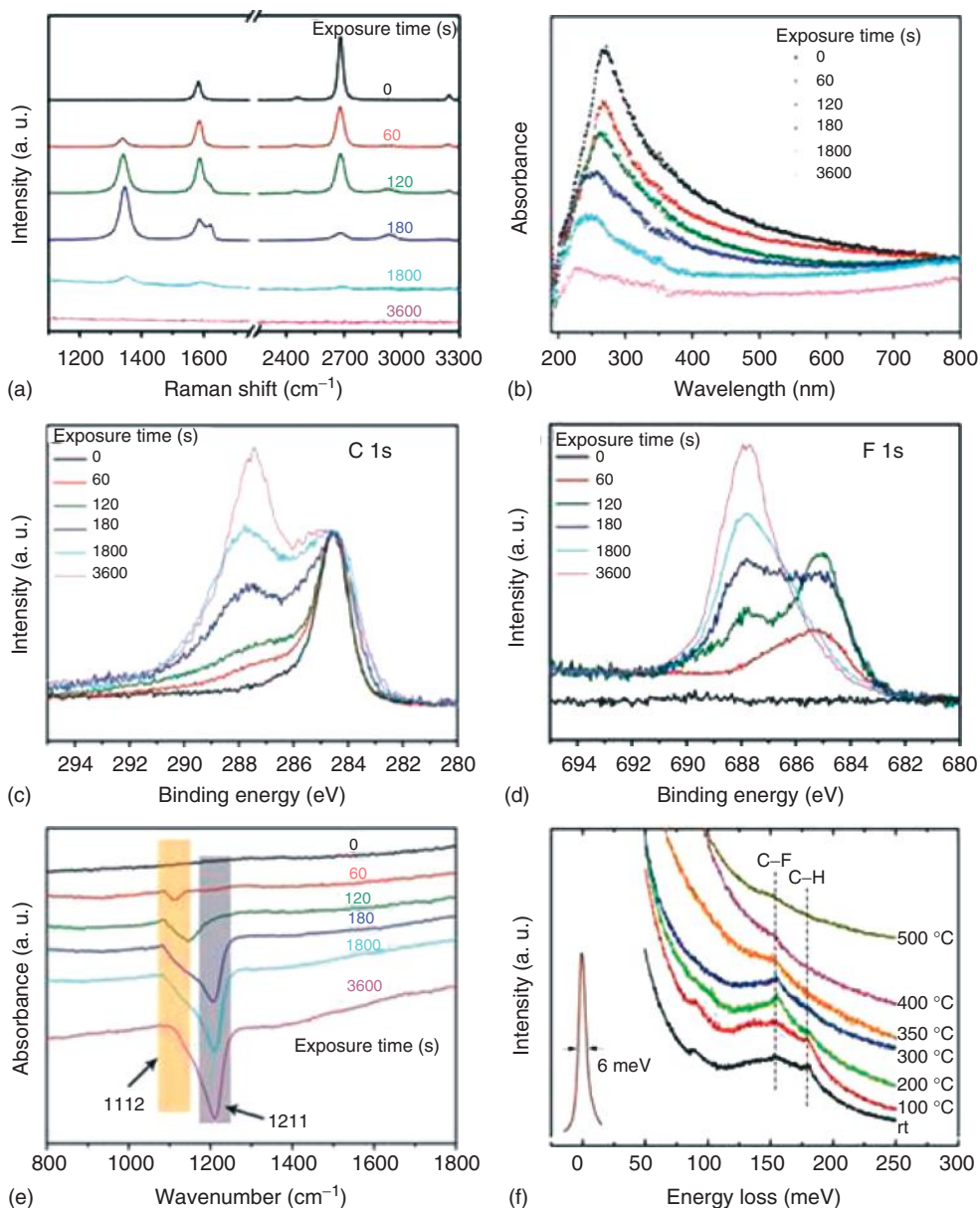


Figure 6.6 Evolution of C-F phases on graphene with increasing exposure time to XeF_2 characterized by (a) Raman spectra (514 nm), (b) UV-visible spectra, (c,d) XPS

C 1s and F 1s core-level spectra, (e) FTIR spectra, and (f) HREELS showing defluorination of FG by thermal annealing. (Reproduced from Ref. [56].)

time (Figure 6.6d). Moreover, with the increase in fluorine content, the stretching vibration of the C–F semi-ionic (1112 cm^{-1}) bonds progressively changes to covalent (1211 cm^{-1}) C–F bonds (Figure 6.6e). In order to observe the stability of C–F bonds, annealing of fluorinated graphene was done in vacuum and the changes were monitored using HREELS. The retention of loss peaks at around 154 meV (attributed to the C–F bond) even after the samples were annealed at $300\text{ }^\circ\text{C}$ for 1 h (10^{-10} Torr) in vacuum, suggesting the good thermal stability of fluorinated graphenes (Figure 6.6f). In addition, Robinson and coworkers observed that the chemical reduction of FGs by hydrazine vapor is more efficient for defluorination than via thermal annealing [16].

6.3.2

Partially Fluorinated and Halogenated Graphenes

To evaluate the structure and quality of the partially halogenated graphene, Raman spectroscopy is used as an important tool. To get detailed information regarding the bonding environment, structure, and composition, NMR, XPS, and FTIR spectroscopy were used. ^{19}F NMR spectra recorded for room-temperature GrF compounds (with different fluorine coverage ratios) revealed a minimum of six different environments for each sample [57]. The effect of fluorination on a number of graphene layers were evaluated by Yang *et al.* using SF_6 plasma treatment [35]. Owing to their high surface reactivity, single-layered graphenes can easily be fluorinated in contrast to the multilayered graphenes. This is due to the larger corrugations of the single-layered graphenes that reduce for thicker or multilayered graphenes. Further, the lattice defects and p-doping of graphene can be controlled by plasma treatment. For example, fluorination of graphene by CF_4 plasma induces a lower quantity of lattice defects and higher degree of p-doping to graphene than CHF_3 plasma treatment [34].

For chlorinated ($\sim 8\text{ at.}\%$) graphene, the characteristic D-peak appears at 1330 cm^{-1} , the G-peak at 1587 cm^{-1} , and the 2D-peak at 2654 cm^{-1} [23]. On increasing the loading of chlorine content in graphene, the D-peak redshifts to higher wavenumber owing to the formation of large quantity of covalent C–Cl bonds, thus creating a high degree of disorder [29]. Chlorinated graphene with a chlorine coverage of $\sim 30\text{ at.}\%$ showed a band at 790 cm^{-1} , which was assigned to the C–Cl stretching vibration [26]. FTIR spectra for chlorinated graphenes ($\sim 30\text{ at.}\%$), recorded at lower frequencies, show a peak near 790 cm^{-1} , which was assigned to the C–Cl stretching vibration. Brominated ($4\text{ at.}\%$) graphenes exhibit a weaker D-peak ($\sim 1350\text{ cm}^{-1}$) than chlorinated graphene, possibly due to a lower degree of modification of graphene. The 2D-peak of G-Br was blueshifted (8 cm^{-1}) and became broader as compared with pristine graphene, consistent with the small extent of modification by Br on graphene lattice [29]. The IR spectrum of the brominated graphene ($1.6\text{ at.}\%$) obtained from thermal reduction of graphene oxide (TRGO) showed a vibration at 600 cm^{-1} , indicative of a C–Br bond in TRGO-Br [54].

The variations in electronic properties of few-layered graphene doped by adsorption and intercalation of Br_2 and I_2 vapors have been systematically investigated by

Raman spectroscopy [58]. The aromatic network of graphene remained unaffected after halogen doping. Adsorption of bromine on single-layered graphene (SLG) promoted a high hole-doped density. The bilayer spectra indicated that doping by adsorbed I_2 and Br_2 was symmetrical on the top and bottom layers. The combination of surface as well as inside doping with Br_2 in three and four layers created a relatively constant doping level per layer. Also, the 2D Raman band of these systems was completely quenched. The presence of elemental iodine in the form of triiodide (I_3^- , peak at 117 cm^{-1}) and pentaiodide (I_5^- , peak at 154 cm^{-1}) has been confirmed by Raman and XPS spectroscopy for iodine-doped graphene samples [44, 53], which is not surprising as iodographene (graphene iodide) has been identified as an unstable intermediate and spontaneously decomposing compound [17].

6.4

Chemistry, Properties, and Applications of Fluorographene and Fluorinated Graphenes

The chemical stability of FG is similar to that of GrF and Teflon, making it extremely hydrophobic [15]. Thus, with the help of surfactants, FG nanosheets can be easily dispersible in various solvents [17, 31, 42]. Conversely, Wang and coworkers reported FG to be hydrophilic [56] with a water contact angle of $\sim 1^\circ$. It is believed that the reduced water contact angle of FG can be a result of a high coverage of fluorine atoms on monolayered carbon giving rise to an ordered array of oriented dipoles that can interact with molecular dipoles of water along with H-bonding ($C-F \cdots H-O$) interactions.

The introduction of fluorine into the graphene lattice significantly alters the electronic properties of graphene by reducing the charge in the conducting π -orbitals [16, 22]. Fluorination has been shown to cause a significant increase in the resistance in the electroneutral region due to the creation of a mobility gap in the electronic spectrum where electron transport occurs through the localized states. The resistance of the fluorinated graphene can be tuned by the extent of fluorine amount. For example, fluorinated graphene with a composition of $CF_{0.25}$ has been shown to have a sixfold higher resistance than graphene, while completely fluorinated graphene (C_1F_1) is a high-quality insulator (with resistivity of $>10^{12}\ \Omega$ at room temperature) suggesting the presence of a bandgap. For applications related to device fabrication, single-side fluorination of graphene would be sufficient as it opens a significant bandgap [25]. Furthermore, the electronic transport properties of fluorinated graphene can be tuned by adjusting the fluorine content [59].

The effect of incorporation of fluorine into graphene has a profound impact on its optical properties. The high electronegativity of fluorine atoms enables efficient doping or bandgap opening of graphene (bandgap engineering). The absorption spectra of pure, partially fluorinated, or fully fluorinated graphene are shown in Figure 6.7. Graphene exhibits an absorption spectrum that is relatively flat for light energies of $<2.5\text{ eV}$, which strongly increases in the blue region and has an absorption peak in the UV range (4.6 eV). In comparison, partially fluorinated graphene

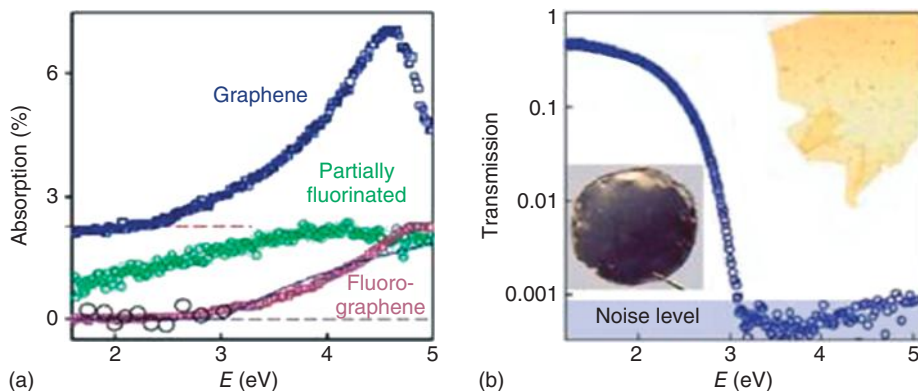


Figure 6.7 (a) Changes in optical transparency of graphene due to fluorination. The solid curve shows the absorption behavior expected for a 2D semiconductor with bandgap of 3 eV. (b) Graphene paper before and after fluorination (left and right insets,

respectively). The plot shows the optical transparency of fluorographene paper as a function of energy for a sample of 1 cm size and 5 μm thick in the photograph. (Reproduced from Ref. [15].)

shows a higher transparency, whereas FG appears to be transparent at visible frequencies and starts absorbing light only in the violet range (Figure 6.7) [15].

The absence of Raman signals for FG also corroborates the complete optical transparency. This proves that FG is a wide-gap semiconductor or insulator with bandgap of ≥ 3.0 eV. The optical photographs of graphene and FG laminates of macroscopic size are shown in Figure 6.7. FG was found to be optically transparent with a yellowish color corresponding to absorption in the violet light region. This also provides the direct visual evidence of FG being a wide-gap material. The light transmission spectra exhibited an onset at ~ 3.1 eV, in agreement with the gap value obtained from the absorption spectra of individual FG crystals [15]. Further, the bandgaps of fluorinated graphenes (obtained by exfoliating GrF by ionic liquids) having compositions of $\text{CF}_{0.25}$ and $\text{CF}_{0.5}$, measured by diffuse reflectance spectroscopy (DRS), were found to be 1.8 and 2.2 eV, respectively [28]. A bandgap of 2.9 eV was reported from dI/dV measurements on $\text{CF}_{0.25}$ obtained by fluorinating graphene by XeF_2 .

Photoluminescence measurements of FG dispersion in acetone carried out at room temperature showed emission peaks at 3.80 and 3.65 eV (Figure 6.8) [33]. The peak at 3.8 eV is associated with the band-to-band recombination of free electrons and holes as the same energy was measured for the bandgap of FG by near-edge X-ray absorption fine structure (NEXAFS) spectroscopy. The 3.645 eV peak (156 meV below the bandgap emission) is attributed to phonon-assisted radiative recombination across the bandgap, for which the C–F vibration mode is excited when the electron–hole pair recombines. With a lower degree of fluorination, an additional emission peak appearing at 2.88 eV was observed, which was also accompanied by a second peak located 157 meV lower in energy (Figure 6.8). The optical bandgap of FG is close to 3.8 eV, adequate for optoelectronic applications in the blue/UV region [33]. NEXAFS is also a powerful technique for assessing

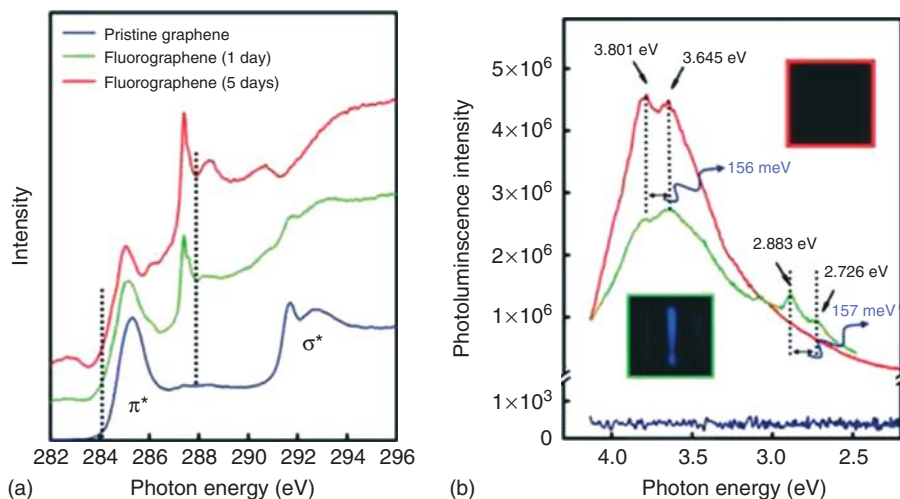


Figure 8.8 Bandgap opening of FG. (a) NEXAFS spectra of pristine graphene and fluorographene with two different contents of fluorine. The dashed lines at 284.1 and 287.9 eV mark the leading edges of the π^* resonance for the pristine and fluorinated samples, respectively. (b) Room-temperature photoluminescence emission of the pristine graphene/FG dispersed in acetone

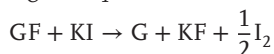
using 290 nm (4.275 eV) excitation. The dotted lines are used for guiding the eye. The interval of the dotted line is ~ 156 meV wide. Optical images (top view) of the blue emission observed after the PL (photolithography) emission was recorded with the samples in 3.5 ml quartz cuvettes. The blue light persists ~ 30 s after the excitation laser is turned off. (Reproduced from Ref. [33].)

the anisotropy in the chemical bonding of semifluorinated graphite ($\text{CF}_{0.5}$), which confirmed that half the carbon atoms are covalently bonded with fluorine, while the rest of the carbon atoms preserve π -electrons [40].

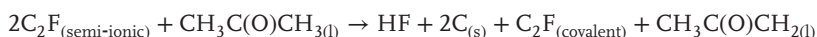
Fluorinated reduced graphene oxide (rGO) obtained by CF_4 plasma treatment was found to be a better substrate for surface-enhanced Raman spectroscopy (SERS) of molecules than pure rGO [48]. The chemical enhancement factor of fluorinated rGO can be tuned by changing the fluorine/carbon content (17–27%) due to the presence of a strong local electric field induced by the local dipoles of F-containing groups on the rGO surface [48]. In addition, fluorinated GO has a high nonlinear absorption and nonlinear scattering and its optical limiting threshold is about an order of magnitude better than that of GO. Furthermore, water-dispersible fluorinated graphene ($\text{CF}_{0.5}$) was isolated with the aid of a fluorosurfactant via aqueous phase exfoliation of GrF, which displayed third-order nonlinear optical response [42].

Defluorination of FG and fluorinated graphenes either by annealing in inert atmosphere in the presence of H_2 gas or by exposure to hydrazine vapors restored the conductivity and ambipolar nature analogous to graphene. Thermal defluorination (400–600 °C) of FG results in the removal of carbons and evolution of C–F products (e.g., CF_4 , C_2F_4 , C_2F_6) similar to that of bulk GrF [16, 60, 61]. Addition of KI to colloidal FG dispersion resulting in the formation of graphene is also an interesting approach to defluorination [17]. In this reaction, FG transforms into

unstable graphene iodine that quickly disproportionates into graphene and iodine following the equation



Interestingly, acetone was used to restore the conducting property of semi-ionic fluorinated graphene (s-FG). Multilayered s-FG with high insulating properties, on reduction with acetone (for a week), showed an increase of 10^9 times in the current from 10^{-13} to 10^{-4} Å, indicating an insulator-to-graphene (semimetal) like transition. This is due to selective elimination of ionic C–F bonds from the as prepared s-FG. The reduction of s-FG happens only with acetone, while solvents like methanol and water failed to show any change in electrical properties. The bond dissociation energy of ionic C–F is 54 kJ mol^{-1} and that of covalent C–F is $<460 \text{ kJ mol}^{-1}$, and the probable reduction mechanism of s-FG in acetone is given below.



The reduced multilayered C_2F film displayed p-type doping with holes as majority carriers. The reduction process of multilayered s-FG film with acetone is systematically characterized by Raman spectroscopy, XPS, and transport measurement analysis [27].

Fluorination of graphene with increasing fluorine coverage ratios results in a strong paramagnetism, that is, in CF_x samples with x increasing from 0.1 to 1 (FG), an increase of more than an order of magnitude in the low- T saturation magnetization is observed (Figure 6.9a) [62]. For the stoichiometric FG, a considerable decrease in the magnetization was observed compared to $\text{CF}_{0.75}$

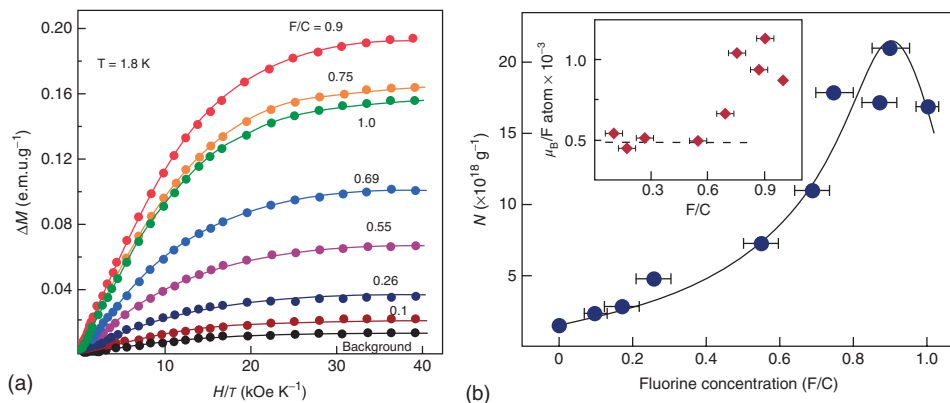


Figure 6.9 (a) Magnetic moment ΔM (after subtracting linear diamagnetic background) as a function of the parallel field strength H for different F/C ratios and (b) main panel: number of spins N extracted from the fits in panel (a) as a function of the F/C ratio. The solid curve is for guidance only. Inset: the same N normalized to

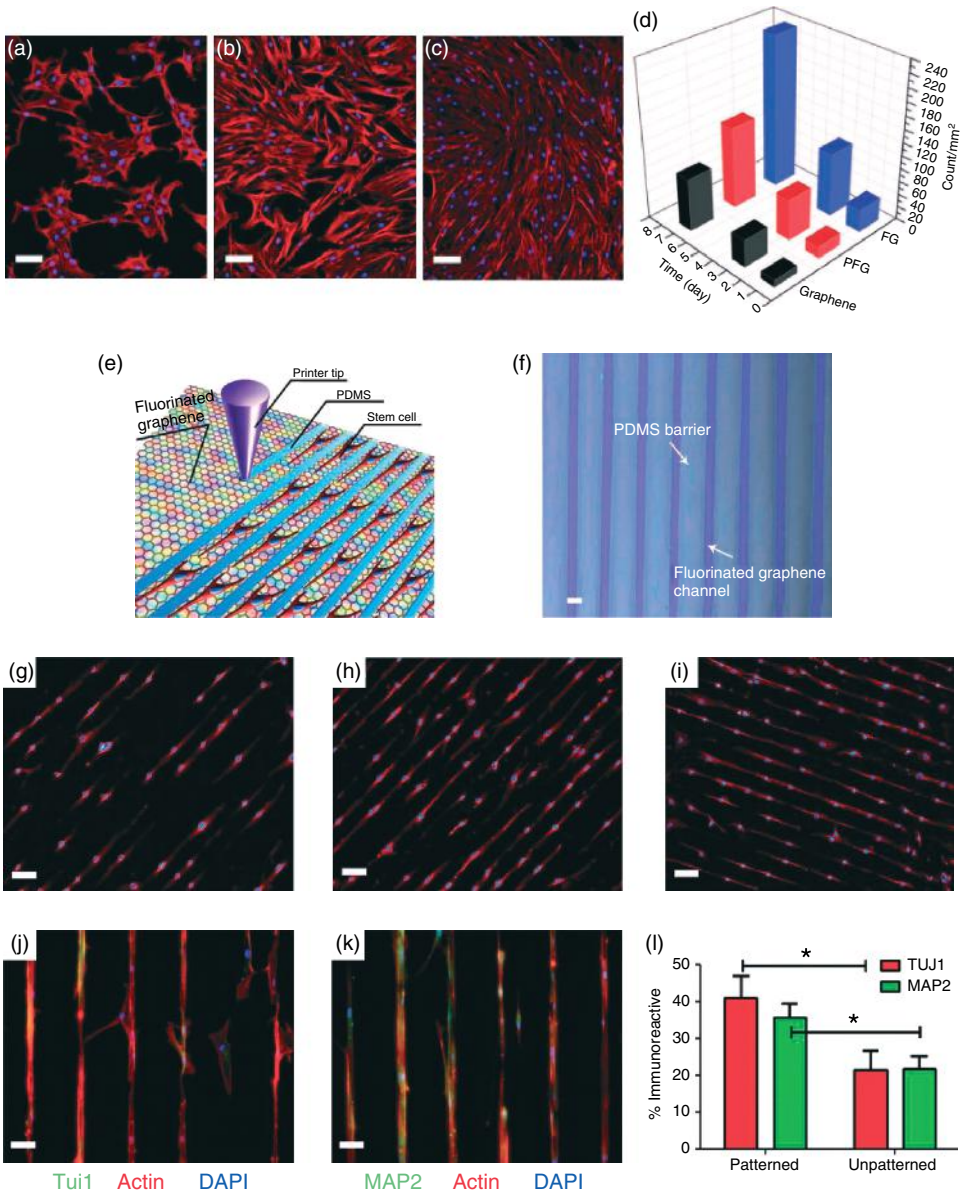
the concentration of adatoms in each sample ($\mu_B/F \text{ atom}$ is obtained by dividing the number of moments N , assuming that each carries $1 \mu_B$, by the number of F atoms per gram of fluorinated graphene). Error bars indicate the accuracy of determination of the fluorine concentrations. (Reproduced from Ref. [62].)

or $\text{CF}_{0.9}$, even though the material showed strong paramagnetism. The number of spins, N , increased monotonically with an increase in fluorine coverage, x , up to $x \approx 0.9$, and then decreased slightly for the FG (Figure 6.9b). A plot of the number of Bohr magnetons, μ_B , per attached F atom (inset in Figure 6.9b) clearly showed that the initial increase (up to $x \approx 0.5$) in the number of paramagnetic centers was proportional to x , but a more complicated relation between the number of atoms and N applied at higher x .

FG is three times less stiff than pure graphene, owing to the longer sp^3 -type bonding. Nair *et al.* have conducted nano-indentation experiments on FG by recording the bending of an AFM cantilever as a function of its displacement, and calculated the force acting on the membrane giving a value of $100 \pm 30 \text{ N m}^{-1}$ or 0.3 TPa for the 2D Young's modulus. The experimental Young's modulus was approximately half of that of the theoretical value (226 N m^{-1}) [63]. Friction force microscopy measurements on fluorinated graphene having a composition of C_4F exhibited a sixfold enhanced nanoscale friction on its surface in comparison to pristine graphene for applied normal forces up to 150 nN [64]. The adhesion force between the AFM tip and graphene was reduced (by about 25%) upon fluorination [65]. Furthermore, density functional theory (DFT) calculations confirmed that the reduction of adhesive properties was mainly governed by out-of-plane bending [64]. On the contrary, low interlayer friction was observed for multilayer FG from dispersion-corrected DFT calculations [66].

Owing to the high electronegativity of fluorine atoms, C–F bonds have high polarity and low surface free energy that stimulates interesting biological responses [56]. Human bone marrow derived mesenchymal stem cells (MSCs) cultured on FG proliferated faster and were more confluent after 7 days than cells cultured on partially fluorinated graphene and graphene (Figure 6.10a–d). FG was associated with a nearly threefold increase in cell density, showing that the introduction of C–F bonds on the surface of graphene facilitates cell adhesion and proliferation. Owing to their high density and close packing, the MSCs on FG are more spindly and elongated than those on partially fluorinated graphene (PFG) and graphene. To understand the effect of surface texture of the cell growth, water contact angle measurements were carried out on these materials. The water contact angle of graphene reduces from 83 to $\sim 1^\circ$ with increasing fluorine content. The distribution

Figure 6.10 (a–c) Fluorescence images of actin cytoskeleton of MSCs cultured on graphene, partially fluorinated graphene (PFG), and FG stained with rhodamine-phalloidin at day 7 (scale bar = $100 \mu\text{m}$); (d) proliferation of MSCs cultured on the graphene films, showing the controlled growth of MSCs on fluorinated graphene with different coverage of fluorine; (e) schematic drawing of patterning MSCs by printing PDMS barriers on graphene films directly; (f) optical microscope image of printed PDMS on fluorinated graphene film (scale bar = $50 \mu\text{m}$); (g–i) the aligned growth of stem cell on graphene, PFG, and FG with printed PDMS pattern, respectively (scale bar = $100 \mu\text{m}$); (j,k) MSCs preferentially attached on the FG strips and their F-actin aligned (red) and expressed neural specific markers – Tuj1 and MAP2 (green) (scale bar = $50 \mu\text{m}$); and (l) percentage of immunoreactive cells for Tuj1 and MAP2 on unpatterned and patterned FG strips. Note that the patterned FG strips induce higher expression of Tuj1 and MAP2 in the absence of retinoic acid ($n = 6, p < 0.05$). (Reproduced from Ref. [56].)



of fluorine, H-bonding interactions, and the surface roughness contribute to the reduction in the contact angle of fluorinated graphenes. Furthermore, selective attachment of MSCs over microchannels of FG (Figure 6.10e–k) was achieved via patterning FG with poly-dimethylsiloxane (PDMS). The density of the aligned MSCs is associated with the amount of fluorine on the graphene. In comparison with the cells cultured under nonpatterned FG, those cultured in patterned FG microchannels displayed improved expression of Tuj1 and MAP2 even in the absence of a neuron-inductive agent (Figure 6.10l).

6.5

Chemistry and Properties of Chlorinated and Brominated Graphenes

Partially chlorinated graphene (8 at.%) exhibited a nonzero bandgap that displayed four orders of magnitude higher sheet resistance than graphene [23]. This is due to the disruption of the conjugated system, reduction of the conducting π -orbital, and opening up of the bandgap. However, chlorinated graphene obtained by chlorine plasma treatment with a composition of C_2Cl displayed decrease in sheet resistance from 678 to 342 Ω /square, as a result of chlorination along with high mobility of 1535 $cm^2 (Vs)^{-1}$ [52]. Furthermore the dielectric constant (ϵ) of the chlorinated *r*GO composite film ($\epsilon = 169$) was found to be much higher than that for untreated reduced GO composite film ($\epsilon = 24$) [24]. The interfacial polarization between the chlorinated *r*GO platelets and the polymer, along with the polar and polarizable C–Cl bonds, was suggested to be the reason for the increase. Also, these materials displayed a 93% increase in conductivity due to p-type doping effect [51] induced by Cl atoms. Interestingly, either by thermal annealing or by laser irradiation, the covalently bonded chlorine can be easily removed for the recovery of reduced graphene derivatives [26, 29, 51].

The Br atom in graphene bromide (G-Br) can be substituted by various organic functional groups under conventional organic reaction environments [29, 67]. G-Br was found to be more reactive than G-Cl and the halide group can be almost completely substituted [29]. These organically modified new functional graphene derivatives can have attractive properties with promising applications. Iodine-modified graphene samples show fine electrocatalytic activity, long-term stability, and better methanol tolerance for the oxygen reduction reaction (ORR) [53, 44]. The high electrocatalytic activity of these samples is due to the formation of I_3^- within the structure and plays an important role in the enhancement of the ORR activity of graphene.

6.6

Other Interesting Properties of Halogenated Graphenes and Their Applications

Zhang *et al.* reported nonsymmetrically modified SLG – Janus graphene – that includes two types of functional groups separated by the single-mediated carbon layer (Figure 6.11A) [68]. The important step in the preparation of Janus graphene

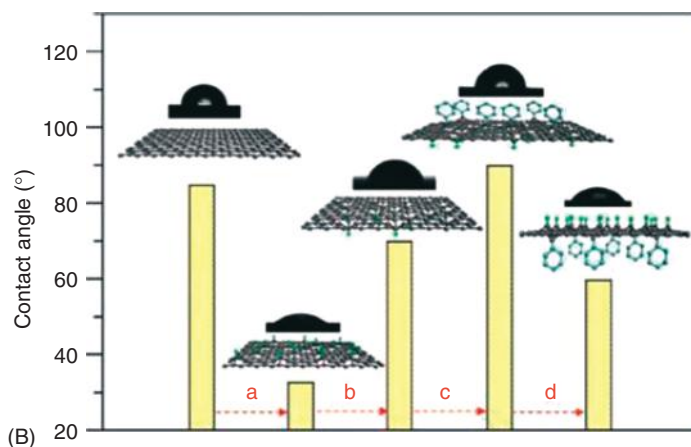
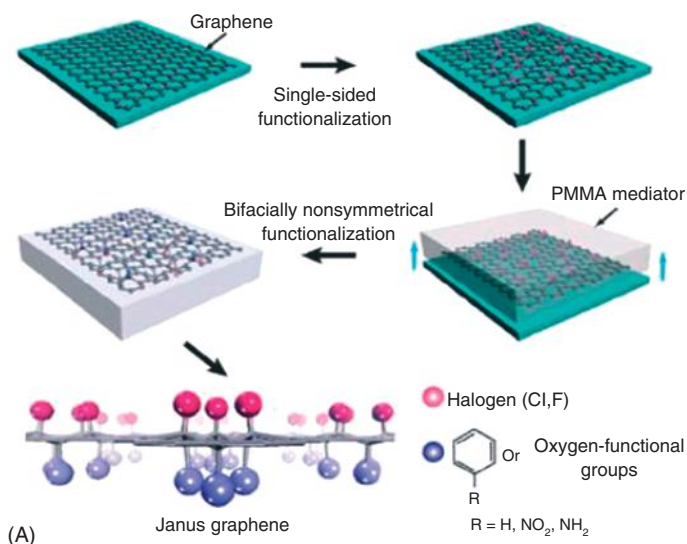


Figure 6.11 (A) Schematic illustration to fabricate Janus graphene. Spin coating a PMMA film on the single-sided functionalized graphene layer, peeling off PMMA/graphene from the substrate, turning over to nonsymmetrically modify the other side of graphene with the protection of PMMA as the substrate, and finally removing the PMMA to obtain Janus graphene. (B) The functional graphene derivative with

bifacially anisotropic wettability. Static water contact angle measurements in the fabrication procedures of Janus graphene: (a) single-sided photochlorination, (b) exposure of graphene fresh side, (c) single-sided phenylation, and (d) release of Janus graphene. The insets exhibit images of water droplets and schematic illustrations of the related surfaces. (Reproduced from Ref. [68].)

is to expose the clean side that was protected by the substrate in the first modification process. Four different types of Janus graphene have been fabricated by co-grafting halogen or aryl or oxygen-containing functional groups on each side by photochlorination, fluorination, phenylation, diazotization, and oxygenation reactions (Figure 6.11A). Interestingly, the functionalities on one side influence the chemical reactivity and surface wettability (water contact angle) of the opposite side because of the influence of the chemical groups and communication between them (Figure 6.11B). These materials are potential candidates for applications in sensors, actuators, and also in designing new functional derivatives of graphene.

Cheng *et al.* have carried out *ab initio* molecular dynamics (AIMD) simulations at room temperature on hydrogen adsorption on graphite-intercalated compounds (GICs) with fluoride anions [69]. Their calculations, along with experimental results, showed that these compounds exhibited significantly higher isosteric heats of adsorption for H_2 than porous carbon-based materials. In these materials, the strong interaction with hydrogen arises from the semi-ionic nature of C–F bonds. Furthermore, superior storage prospects of GIC can be envisaged by heteroatom doping to promote a higher level of charge transfer from graphene to fluoride anions.

Dilute fluorinated graphene sheets with a F/C ratio of 1:2000 carried out by CF_4 plasma in a reactive ion-etching system exhibits anisotropic, colossal negative magnetoresistance, and unusual “staircase” behavior at low temperatures (<5 K) [70]. At the charge neutrality point, the resistance improved by three orders of magnitude from 25 k Ω at 200 K to 2.5 M Ω at 5 K, displaying a strong insulating behavior at dilute F concentration [70]. In addition, the presence of adatom-induced local magnetic moments has been reported in dilute fluorinated graphene as a result of observed spin-flip scattering [71]. The spin-flip rate was tunable via fluorine coverage and carrier density. The surface chemistry associated with CF_4 and chlorine-based inductively coupled plasma-reactive ion etching (ICP-RIE) of the 6H-SiC (0001) surface followed by thermal annealing results in the growth of large area graphene-on-insulator films [72].

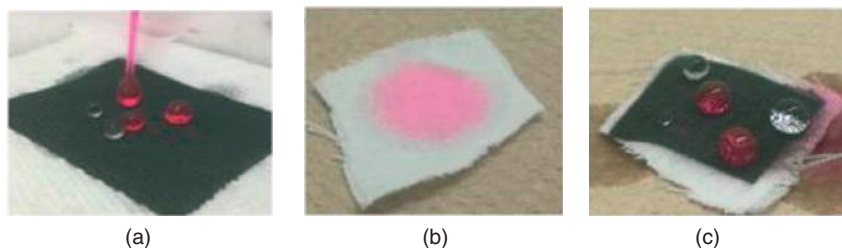


Figure 6.12 Highly fluorinated graphene oxide (HFGO) inks were spray-painted onto a variety of porous substrates to induce amphiphobicity. (a) Painted paper towels repel both deionized water and 30 wt% MEA

(pink), (b) a fabric is innately amphiphilic but upon spray-painting, shows self-cleaning characteristics as solvents and (c) water do not penetrate the fabric. (Reproduced from Ref. [49].)

A multistep approach was used to prepare fluorinated (15 at.%) graphene quantum dots (F-GQDs) that exhibited blue photoluminescence with a quantum yield of 6% comparable to GQDs. These F-GQDs display up-conversion photoluminescence properties [73]. FGO (23 at.%) obtained by oxidizing bulk GrF displayed a hydrophobic nature with a contact angle of 151° . The low surface free energy of the C–F bonds and the solution processability of these materials were advantageous in creating amphiphobic inks that can be sprayed on various substrates (both porous and nonporous substrates). Water and mono ethanolamine (MEA, pink) droplets were repelled from an amphiphobic paper towel (Figure 6.12) [49]. Such self-cleaning materials have important applicability in textiles and coatings.

6.7

Halogenated Graphene–Graphene Heterostructures – Patterned Halogenation

The fabrication of graphene-based electronic devices or designing halogenated graphene heterostructures requires patterned or selective halogenation. A lot of progress has been made in the direction of patterned fluorinated or chlorinated graphenes [15, 16, 25, 48]. By placing suitable masks or metal grids over graphene, patterned halogenation can be accomplished. The grids or masks that are placed over graphene protect it from being halogenated, while the rest gets halogenated resulting in patterned halogenation. The masked regions of graphene can be used as conductive pathways for various device applications.

A device comprising of a graphene nanoribbon (GNR) surrounded by fluorinated graphene with a composition of C_4F was shown to have an electron mobility of $\sim 2700 \text{ cm}^2 (\text{V s})^{-1}$ [74]. By using scanning probe lithography, GNRs as narrow as 35 nm were fabricated using a polystyrene mask, followed by fluorination to isolate the masked graphene from the surrounding wide bandgap fluorinated graphene (Figure 6.13a). The fluorinated regions of the device retained the starting carrier mobility and exhibited p-doping of 0.17 eV, while the polymer mask containing GNR showed stable performance. The same group utilized thermochemical nanolithography (TCNL) to locally reduce fluorinated graphene (C_4F) resulting in chemically isolated GNRs enclosed by fluorinated graphene [75]. For TCNL reduction, fluorinated graphene is a better substrate as it possesses majority of C–F bonds and the fluorine cannot incorporate into the lattice as compared to GO (which shows remains of residual oxygen even after annealing at high temperatures). TCNL uses hot AFM probe to locally convert highly insulating fluorinated graphene to conductive GNR. The sheet resistance of GNR of width 40 nm was close to $23 \text{ k}\Omega/\text{square}$ under ambient conditions. These methods open up possibilities of engineering conducting and semiconducting nano/micro-structured graphene-based transparent and flexible electronic devices. In addition, patterned channels with different conductivities may lead to the design of novel resistive memory and data storage devices.

Interestingly, the resistivity of insulating fluorinated graphenes can be progressively decreased by several orders of magnitude by electron beam irradiation due

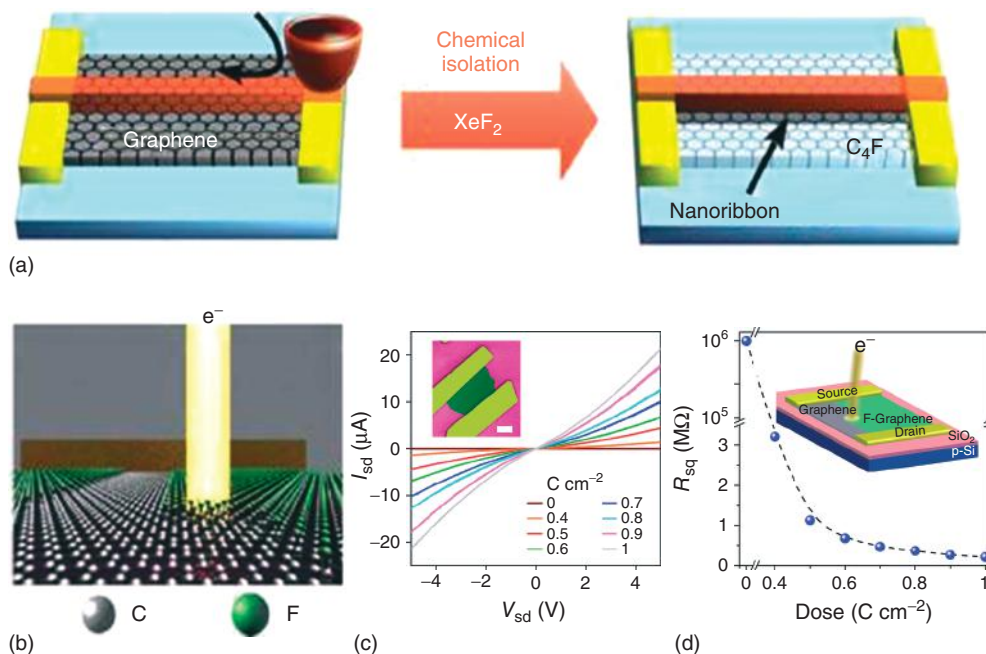


Figure 6.13 (a) Schematic diagram of the masking and isolation process. (Left) Thermal dip-pen nanolithography (tDPN) of polystyrene on SLG across the electrodes. (Right) Chemical isolation of GNR structure by XeF_2 fluorination. (Reproduced from Ref. [74].) (b) Scheme showing the nanopatterning of fluorinated graphene by electron beam irradiation; and (c) I - V characteristics for the C_4F graphene device reported in the inset after different electron beam irradiation doses. Inset: false color SEM (scanning

electron microscope) image of a typical C_4F graphene device, the white bar corresponds to 1 μm. The green area corresponds to the C_4F graphene flake, whereas the yellow parts are the Au/Cr electrodes. (d) The measured sample resistance per square plotted against the electron irradiation dose (the dashed black line is a guideline for the eye). The inset shows an illustration of the device configuration under irradiation with a beam of electrons. (Reproduced from Ref. [76].)

to the fragmentation of C–F bonds (Figure 6.13b) [76]. The improvement of the DC source–drain current versus voltage characteristics for a fluorinated graphene device after a uniform electron beam irradiation of the entire flake area up to a dose of 1 C cm^{-2} is shown in Figure 6.13c. For low doses, the source–drain I - V characteristics are mainly nonlinear with decreasing nonlinearity for higher doses. Upon electron beam irradiation dosing, the resistance decreases up to seven orders of magnitude from 1 TΩ down to 100 kΩ (Figure 6.13d). The properties of graphene nanoroads and QDs within FG, semifluorinated graphene [77] and in FG ribbons [78] have been theoretically studied by *ab initio* and first-principles DFT calculations.

DFT calculations showed the existence of significant C–H···F–C bonding between graphane and a FG bilayer with a small energy gap (of 0.5 eV at PBE, Perdew–Burke–Ernzerhof, GGA, generalized gradient approximation, level),

much lower than those of individual graphane and FG. The binding strength of this bilayer can be enhanced by applying an external electrical field. The energy gap of the graphene/FG bilayer (0–3.0 eV) can be modulated by changing the polarity and strength of the electric field, resulting in the semiconductor-metal transition [79].

6.8

Conclusion and Future Prospects

There are several interesting properties and emerging applications exhibited by halogenated graphenes. Halogenation of graphene opens the bandgap that can be tuned depending on the halogen coverage. Among various halogenated graphenes, stoichiometric FG has been isolated by several chemical and physical approaches. FG is already, with graphane and GO, a well-established member of the family of graphene derivatives. More importantly, the composition, structure, and homogeneity of FG are well defined compared to oxygenated and hydrogenated graphene counterparts.

The future prospects in the field of halogenated graphenes related to patterned halogenation enabling the preparation of graphene derivatives are highly promising in various electronic and sensing applications. Similarly, the controlled design of mixed graphene halides and simpler routes for the synthesis of partially halogenated graphenes would result in the development of two-dimensional semiconductors suitable for the commercial practice. In addition, interesting electronic and transport properties may arise due to stacking of FG/graphene or graphene/fluorographene/graphene (G/FG/G) layers. Future directions in the area of halogenated graphenes would be also in storage, biology, electrochemistry, coatings, and optics. Furthermore, the intrinsic functional groups associated with the halogenated graphenes could also be exploited for the stabilization of various inorganic nanoparticles. Hybrids of halogenated graphenes decorated with magnetic, metal, and semiconducting nanoparticles would be applicable in advanced catalytic, magnetic, and optical technologies.

References

1. Geim, A.K. and Novoselov, K.S. (2007) *Nat. Mater.*, **6**, 183–191.
2. Schwierz, F. (2010) *Nat. Nanotechnol.*, **5**, 487–496.
3. Novoselov, K.S., Fal'ko, V.I., Colombo, L., Gellert, P.R., Schwab, M.G., and Kim, K. (2012) *Nature*, **490**, 192–200.
4. Novoselov, K.S., Geim, A.K., Morozov, S.V., Jiang, D., Zhang, Y., Dubonos, S.V., Grigorieva, I.V., and Firsov, A.A. (2004) *Science*, **306**, 666–669.
5. Novoselov, K.S., Jiang, D., Schedin, F., Booth, T.J., Khotkevich, V.V., Morozov, S.V., and Geim, A.K. (2005) *Proc. Natl. Acad. Sci. U.S.A.*, **102**, 10451–10453.
6. Rao, C.N.R., Maitra, U., and Matte, H.S.S.R. (2012) *Graphene*, Wiley-VCH Verlag GmbH & Co. KGaA, Weinheim, pp. 1–47.
7. Castro Neto, A.H., Guinea, F., Peres, N.M.R., Novoselov, K.S., and Geim, A.K. (2009) *Rev. Mod. Phys.*, **81**, 109–162.

8. Balog, R., Jorgensen, B., Nilsson, L., Andersen, M., Rienks, E., Bianchi, M., Fanetti, M., Laegsgaard, E., Baraldi, A., Lizzit, S., Sljivancanin, Z., Besenbacher, F., Hammer, B., Pedersen, T.G., Hofmann, P., and Hornekaer, L. (2010) *Nat. Mater.*, **9**, 315–319.
9. Georgakilas, V., Otyepka, M., Bourlinos, A.B., Chandra, V., Kim, N., Kemp, K.C., Hobza, P., Zboril, R., and Kim, K.S. (2012) *Chem. Rev.*, **112**, 6156–6214.
10. Johns, J.E. and Hersam, M.C. (2013) *Acc. Chem. Res.*, **46**, 77–86.
11. Haddon, R.C. (2013) *Acc. Chem. Res.*, **46**, 1–3.
12. Loh, K.P., Bao, Q.L., Ang, P.K., and Yang, J.X. (2010) *J. Mater. Chem.*, **20**, 2277–2289.
13. Tang, Q., Zhou, Z., and Chen, Z.F. (2013) *Nanoscale*, **5**, 4541–4583.
14. Chen, D., Feng, H.B., and Li, J.H. (2012) *Chem. Rev.*, **112**, 6027–6053.
15. Nair, R.R., Ren, W.C., Jalil, R., Riaz, I., Kravets, V.G., Britnell, L., Blake, P., Schedin, F., Mayorov, A.S., Yuan, S.J., Katsnelson, M.I., Cheng, H.M., Strupinski, W., Bulusheva, L.G., Okotrub, A.V., Grigorieva, I.V., Grigorenko, A.N., Novoselov, K.S., and Geim, A.K. (2010) *Small*, **6**, 2877–2884.
16. Robinson, J.T., Burgess, J.S., Junkermeier, C.E., Badescu, S.C., Reinecke, T.L., Perkins, F.K., Zalalutdniov, M.K., Baldwin, J.W., Culbertson, J.C., Sheehan, P.E., and Snow, E.S. (2010) *Nano Lett.*, **10**, 3001–3005.
17. Zboril, R., Karlicky, F., Bourlinos, A.B., Steriotis, T.A., Stubos, A.K., Georgakilas, V., Safarova, K., Jancik, D., Trapalis, C., and Otyepka, M. (2010) *Small*, **6**, 2885–2891.
18. Elias, D.C., Nair, R.R., Mohiuddin, T.M.G., Morozov, S.V., Blake, P., Halsall, M.P., Ferrari, A.C., Boukhvalov, D.W., Katsnelson, M.I., Geim, A.K., and Novoselov, K.S. (2009) *Science*, **323**, 610–613.
19. Butler, S.Z., Hollen, S.M., Cao, L.Y., Cui, Y., Gupta, J.A., Gutierrez, H.R., Heinz, T.F., Hong, S.S., Huang, J.X., Ismach, A.F., Johnston-Halperin, E., Kuno, M., Plashnitsa, V.V., Robinson, R.D., Ruoff, R.S., Salahuddin, S., Shan, J., Shi, L., Spencer, M.G., Terrones, M., Windl, W., and Goldberger, J.E. (2013) *ACS Nano*, **7**, 2898–2926.
20. Touhara, H. and Okino, F. (2000) *Carbon*, **38**, 241–267.
21. Karlicky, F., Datta, K.K.R., Otyepka, M., and Zboril, R. (2013) *ACS Nano*, **7**, 6434–6464.
22. Cheng, S.-H., Zou, K., Okino, F., Gutierrez, H.R., Gupta, A., Shen, N., Eklund, P.C., Sofo, J.O., and Zhu, J. (2010) *Phys. Rev. B*, **81**, 205435.
23. Li, B., Zhou, L., Wu, D., Peng, H.L., Yan, K., Zhou, Y., and Liu, Z.F. (2011) *ACS Nano*, **5**, 5957–5961.
24. Kim, J.Y., Lee, W.H., Suk, J.W., Potts, J.R., Chou, H., Kholmanov, I.N., Piner, R.D., Lee, J., Akinwande, D., and Ruoff, R.S. (2013) *Adv. Mater.*, **25**, 2308–2313.
25. Lee, W.H., Suk, J.W., Chou, H., Lee, J.H., Hao, Y.F., Wu, Y.P., Piner, R., Aldnwande, D., Kim, K.S., and Ruoff, R.S. (2012) *Nano Lett.*, **12**, 2374–2378.
26. Gopalakrishnan, K., Subrahmanyam, K.S., Kumar, P., Govindaraj, A., and Rao, C.N.R. (2012) *RSC Adv.*, **2**, 1605–1608.
27. Lee, J.H., Koon, G.K.W., Shin, D.W., Fedorov, V.E., Choi, J.-Y., Yoo, J.-B., and Özyilmaz, B. (2013) *Adv. Funct. Mater.*, **23**, 3329–3334.
28. Chang, H.X., Cheng, J.S., Liu, X.Q., Gao, J.F., Li, M.J., Li, J.H., Tao, X.M., Ding, F., and Zheng, Z.J. (2011) *Chem. Eur. J.*, **17**, 8896–8903.
29. Zheng, J., Liu, H.-T., Wu, B., Di, C.-A., Guo, Y.-L., Wu, T., Yu, G., Liu, Y.-Q., and Zhu, D.-B. (2012) *Sci. Rep.*, **2**, 662.
30. Withers, F., Dubois, M., and Savchenko, A.K. (2010) *Phys. Rev. B*, **82**, 073403.
31. Gong, P.W., Wang, Z.F., Wang, J.Q., Wang, H.G., Li, Z.P., Fan, Z.J., Xu, Y., Han, X.X., and Yang, S.R. (2012) *J. Mater. Chem.*, **22**, 16950–16956.
32. Bourlinos, A.B., Safarova, K., Siskova, K., and Zboril, R. (2012) *Carbon*, **50**, 1425–1428.
33. Jeon, K.J., Lee, Z., Pollak, E., Moreschini, L., Bostwick, A., Park, C.M., Mendelsberg, R., Radmilovic, V., Kostecki, R., Richardson, T.J., and Rotenberg, E. (2011) *ACS Nano*, **5**, 1042–1046.

34. Chen, M.J., Zhou, H.Q., Qiu, C.Y., Yang, H.C., Yu, F., and Sun, L.F. (2012) *Nanotechnology*, **23**, 115706.
35. Yang, H.C., Chen, M.J., Zhou, H.Q., Qiu, C.Y., Hu, L.J., Yu, F., Chu, W.G., Sun, S.Q., and Sun, L.F. (2011) *J. Phys. Chem. C*, **115**, 16844–16848.
36. Wheeler, V., Garces, N., Jernigan, G., L., Myers-Ward, R., Jernigan, G., Culbertson, J., Eddy, C., and Gaskill, D.K. (2012) *Carbon*, **50**, 2307–2314.
37. Tahara, K., Iwasaki, T., Matsutani, A., and Hatano, M. (2012) *Appl. Phys. Lett.*, **101**, 163105.
38. Fedorov, V.E., Grayfer, E.D., Makotchenko, V.G., Nazarov, A.S., Shin, H.J., and Choi, J.Y. (2012) *Croat. Chem. Acta*, **85**, 107–112.
39. Grayfer, E.D., Makotchenko, V.G., Kibis, L.S., Boronin, A.I., Pazhetnov, E.M., Zaikovskii, V.I., and Fedorov, V.E. (2013) *Chem. Asian J.*, **8**, 2015–2022.
40. Okotrub, A.V., Yudanov, N.F., Asanov, I.P., Vyalikh, D.V., and Bulusheva, L.G. (2012) *ACS Nano*, **7**, 65–74.
41. Wang, Z., Wang, J., Li, Z., Gong, P., Ren, J., Wang, H., Han, X., and Yang, S. (2012) *RSC Adv.*, **2**, 11681–11686.
42. Bourlinos, A.B., Bakandritsos, A., Liaros, N., Couris, S., Safarova, K., Otyepka, M., and Zboril, R. (2012) *Chem. Phys. Lett.*, **543**, 101–105.
43. Shen, B.S., Chen, J.T., Yan, X.B., and Xue, Q.J. (2012) *RSC Adv.*, **2**, 6761–6764.
44. Yao, Z., Nie, H.G., Yang, Z., Zhou, X.M., Liu, Z., and Huang, S.M. (2012) *Chem. Commun.*, **48**, 1027–1029.
45. Pu, L.Y., Ma, Y.J., Zhang, W., Hu, H.L., Zhou, Y., Wang, Q.L., and Pei, C.H. (2013) *RSC Adv.*, **3**, 3881–3884.
46. Wang, Z., Wang, J., Li, Z., Gong, P., Liu, X., Zhang, L., Ren, J., Wang, H., and Yang, S. (2012) *Carbon*, **50**, 5403–5410.
47. Gong, P.W., Wang, Z.F., Li, Z.P., Mi, Y.J., Sun, J.F., Niu, L.Y., Wang, H.G., Wang, J.Q., and Yang, S.R. (2013) *RSC Adv.*, **3**, 6327–6330.
48. Yu, X.X., Lin, K., Qiu, K.Q., Cai, H.B., Li, X.J., Liu, J.Y., Pan, N., Fu, S.J., Luo, Y., and Wang, X.P. (2012) *Carbon*, **50**, 4512–4517.
49. Mathkar, A., Narayanan, T.N., Alemany, L.B., Cox, P., Nguyen, P., Gao, G.H., Chang, P., Romero-Aburto, R., Mani, S.A., and Ajayan, P.M. (2013) *Part. Part. Syst. Char.*, **30**, 266–272.
50. Chantharasupawong, P., Philip, R., Narayanan, N.T., Sudeep, P.M., Mathkar, A., Ajayan, P.M., and Thomas, J. (2012) *J. Phys. Chem. C*, **116**, 25955–25961.
51. Wu, J., Xie, L.M., Li, Y.G., Wang, H.L., Ouyang, Y.J., Guo, J., and Dai, H.J. (2011) *J. Am. Chem. Soc.*, **133**, 19668–19671.
52. Zhang, X., Hsu, A., Wang, H., Song, Y., Kong, J., Dresselhaus, M.S., and Palacios, T. (2013) *ACS Nano*, **7**, 7262–7270.
53. Kalita, G., Wakita, K., Takahashi, M., and Umeno, M. (2011) *J. Mater. Chem.*, **21**, 15209–15213.
54. Poh, H.L., Šimek, P., Sofer, Z., and Pumera, M. (2013) *Chem. Eur. J.*, **19**, 2655–2662.
55. Jeon, I.-Y., Choi, H.-J., Choi, M., Seo, J.-M., Jung, S.-M., Kim, M.-J., Zhang, S., Zhang, L., Xia, Z., Dai, L., Park, N., and Baek, J.-B. (2013) *Sci. Rep.*, **3**, 1810.
56. Wang, Y., Lee, W.C., Manga, K.K., Ang, P.K., Lu, J., Liu, Y.P., Lim, C.T., and Loh, K.P. (2012) *Adv. Mater.*, **24**, 4285–4290.
57. Vyalikh, A., Bulusheva, L.G., Chekhova, G.N., Pinakov, D.V., Okotrub, A.V., and Scheler, U. (2013) *J. Phys. Chem. C*, **117**, 7940–7948.
58. Jung, N., Kim, N., Jockusch, S., Turro, N.J., Kim, P., and Brus, L. (2009) *Nano Lett.*, **9**, 4133–4137.
59. Withers, F., Russo, S., Dubois, M., and Craciun, M.F. (2011) *Nanoscale Res. Lett.*, **6**, 526.
60. Kita, Y., Watanabe, N., and Fujii, Y. (1979) *J. Am. Chem. Soc.*, **101**, 3832–3841.
61. Watanabe, N., Koyama, S., and Imoto, H. (1980) *Bull. Chem. Soc. Jpn.*, **53**, 2731–2734.
62. Nair, R.R., Sepioni, M., Tsai, I.L., Lehtinen, O., Keinonen, J., Krasheninnikov, A.V., Thomson, T., Geim, A.K., and Grigorieva, I.V. (2012) *Nat. Phys.*, **8**, 199–202.

63. Leenaerts, O., Peelaers, H., Hernandez-Nieves, A.D., Partoens, B., and Peeters, F.M. (2010) *Phys. Rev. B*, **82**, 195436.
64. Ko, J.H., Kwon, S., Byun, I.S., Choi, J.S., Park, B.H., Kim, Y.H., and Park, J.Y. (2013) *Tribol. Lett.*, **50**, 137–144.
65. Kwon, S., Ko, J.H., Jeon, K.J., Kim, Y.H., and Park, J.Y. (2012) *Nano Lett.*, **12**, 6043–6048.
66. Wang, L.-F., Ma, T.-B., Hu, Y.-Z., Wang, H., and Shao, T.-M. (2013) *J. Phys. Chem. C*, **117**, 12520–12525.
67. Gao, J., Bao, F., Zhu, Q.D., Tan, Z.F., Chen, T., Cai, H.H., Zhao, C., Cheng, Q.X., Yang, Y.D., and Ma, R. (2013) *Polym. Chem. UK*, **4**, 1672–1679.
68. Zhang, L.M., Yu, J.W., Yang, M.M., Xie, Q., Peng, H.L., and Liu, Z.F. (2013) *Nat. Commun.*, **4**, 1443.
69. Cheng, H.S., Sha, X.W., Chen, L., Cooper, A.C., Foo, M.L., Lau, G.C., Bailey, W.H., and Pez, G.P. (2009) *J. Am. Chem. Soc.*, **131**, 17732–17733.
70. Hong, X., Cheng, S.H., Herding, C., and Zhu, J. (2011) *Phys. Rev. B*, **83**, 085410.
71. Hong, X., Zou, K., Wang, B., Cheng, S.H., and Zhu, J. (2012) *Phys. Rev. Lett.*, **108**, 226602.
72. Raghavan, S., Denig, T.J., Nelson, T.C., and Stinespring, C.D. (2012) *J. Vac. Sci. Technol., B*, **30**, 030605.
73. Feng, Q., Cao, Q., Li, M., Liu, F., Tang, N., and Du, Y. (2013) *Appl. Phys. Lett.*, **102**, 013111.
74. Lee, W.K., Robinson, J.T., Gunlycke, D., Stine, R.R., Tamanaha, C.R., King, W.P., and Sheehan, P.E. (2011) *Nano Lett.*, **11**, 5461–5464.
75. Lee, W.-K., Haydell, M., Robinson, J.T., Laracuente, A.R., Cimpoiasu, E., King, W.P., and Sheehan, P.E. (2013) *ACS Nano*, **7**, 6219–6224.
76. Withers, F., Bointon, T.H., Dubois, M., Russo, S., and Craciun, M.F. (2011) *Nano Lett.*, **11**, 3912–3916.
77. Ribas, M.A., Singh, A.K., Sorokin, P.B., and Yakobson, B.I. (2011) *Nano Res.*, **4**, 143–152.
78. Shi, H.L., Pan, H., Zhang, Y.W., and Yakobson, B.I. (2012) *J. Phys. Chem. C*, **116**, 18278–18283.
79. Li, Y.F., Li, F.Y., and Chen, Z.F. (2012) *J. Am. Chem. Soc.*, **134**, 11269–11275.

7

Noncovalent Functionalization of Graphene

Kingsley Christian Kemp, Yeonchoo Cho, Vimlesh Chandra, and Kwang Soo Kim

Noncovalent functionalization of graphene has been discussed in our recent review [1]. Here, we present the discussion in a more concise and updated theoretical and experimental form.

7.1

Noncovalent Functionalization of Graphene – Theoretical Background

Pristine graphene has attractive properties such as high electron mobility and mechanical flexibility [2, 3]. From the perspective of electronics, the zero bandgap of graphene prevents its application to transistors [4]. To overcome this problem, noncovalent functionalization of graphene is carried out. Noncovalent functionalization is a powerful means to minimize loss of desired properties while inducing desired properties. Graphene offers exposed π -electrons that can be exploited to form noncovalent bonding. Noncovalent intermolecular interactions are very important in understanding molecular clusters, supramolecular assembly, ionophores, biomolecular structures, crystal packing, and nanomaterial engineering [5–10]. Pristine graphene sheets are hydrophobic in nature, so they cannot be dissolved in polar solvents. However, functionalization of graphene sheets can make graphene dispersible and even soluble in aqueous solution as well as organic solvents [11]. Since it is necessary to avoid stacking for this purpose, noncovalent functionalization with organic compounds using π -interactions would be highly desirable, as noted in water-soluble fullerenes [12]. In this regard, the competition and cooperation between specific interactions are important in designing new nanomaterials and fabricating novel nanodevices. Even small differences in electronic properties of π -electron molecular systems may cause significant changes of geometries and molecular properties of the nanosystems. We begin with a brief discussion of the theoretical background. Graphene is adsorbed to gas molecules, aromatic molecules, and metals. Before discussing graphene, however, we start from benzene, the simplest graphitic system, where decades of extensive studies provide insights into the characteristics of noncovalent interactions of π -electrons.

7.1.1

Insight into the π -Interaction of Benzene

Noncovalent interaction with a benzene moiety has been intensively studied in the quantum chemistry community. This type of molecular systems encompasses rare gas- π , H- π , π - π , cation- π , and anion- π systems [13–15]. One of the reasons for the interest in this field is that the smallness of the complex makes high-level computations, such as coupled cluster theory with singles, doubles, and perturbative triples excitations (CCSD(T)) and symmetry-adapted perturbation theory (SAPT), affordable. In SAPT, the total interaction energy of a duplex can be decomposed into electrostatic, dispersion, induction, and exchange repulsion terms. Such analysis provides a lot of insights into interacting systems. In some cases, the formation of complexes is driven by electrostatic forces, while in other cases the interaction is mostly governed by dispersion forces. These methods give accurate energetics and insights into these aspects, but are only applicable to clusters at the current stage.

The benzene dimer is a model system used to investigate the π -interactions in aromatic complexes. It has been extensively studied both experimentally and theoretically. The experimental binding energy of the benzene dimer is 2–3 kcal mol⁻¹ [16]. The theoretical calculations show that the benzene dimer can form two stable structures: T-shaped (H- π interaction [17–22]) and parallel-displaced stacked (π - π interaction [13, 14, 22, 23]). Both conformers are nearly isoenergetic. Their formation is driven by dispersion forces. According to the experimental data obtained for the isolated benzene dimer, the edge-to-face conformer is slightly more stable than the parallel-displaced structure. However, it is important to note that the benzene dimer is a very flexible system, thus both forms can coexist.

However, as the aromatic systems become larger, the dispersion energy components dominate because the magnitude of the dispersion energies tends to be proportional to the number of electrons participating in the interaction. In this regard, as the π -systems are bigger, the H- π interaction is less important than the π - π interactions, which have larger dispersion energies due to larger contact area between the two π -systems. Therefore, in graphene systems, the π - π interaction becomes much more important.

The noncovalent π - π interactions play a crucial role in the investigation of the aromatic complexes. In the case of such systems, there are two significantly different situations. In the first case, both aromatic moieties have very similar or identical electron density distributions. The aromatic systems are characterized by negative and highly delocalized π -electron clouds. According to chemical intuition, the interaction between such molecular systems should be repulsive. However, π - π interactions are not driven by electrostatic forces but by dispersion forces, as the electrostatic energy contribution is significantly smaller than that of the dispersion energy. The detailed analysis of energy components in π - π interactions is helpful in the design of novel nanostructures and new nanomaterials.

As already discussed, in large aromatic systems such as graphene, the π - π interactions are much more important than the H- π interaction. Thus, most

π -conjugated molecules such as aromatic compounds and nucleobases tend to have π - π stacking conformations.

The cation- π interactions between metal cations and highly delocalized π -electron clouds of aromatic systems are driven by electrostatic and induction forces [24–26]. The role of dispersion energy is rather small as compared to that of π - π interactions. The strength of the interaction is determined by polarizabilities and dispersion interactions of the counter molecule (cation) and π -electron systems. The interactions of alkali metal and transition metal (TM) cations with aromatic systems are substantially different. The alkali metal cations prefer interactions where the metal is located above the centroid of the aromatic ring (C_{6v} symmetry). In the case of TM cations such as Au^+ , Pd^{2+} , Pt^{2+} , and Hg^{2+} , the off-center π -coordination is favored. The different behavior of TM cations is caused by $TM^{n+} \leftarrow \pi$ donation phenomenon [27–29]. In the case when a counterion is a positively charged aromatic compound, the $\pi^+ - \pi$ stacking interaction [15, 30, 31] is significantly smaller than the cation- π interaction (such as in alkali metal cations) but much larger than the π - π interaction.

The π -anion systems are important in anion recognition, structures of host-guest complexes, and supramolecular chemistry [32–36]. The π -electron cloud and anion are negatively charged, thus the electrostatic interaction is repulsive in the case of π -anion molecular systems. The total binding energies of anion- π systems are close to that of cation- π complexes. However, while the cation- π formation is driven by large contributions of electrostatic and induction energy terms, the formation of anion- π systems tends to be driven by dispersion forces.

7.1.2

Adsorption on Graphene

Studies of adsorption on graphene can be classified into two types: adsorption of an isolated molecule and that of many molecules forming an interfacial layer. The former usually focuses on bonding character and strength, whereas the latter aims at tuning of the graphene electronic structure. Hydrogen on graphene has been studied for hydrogen storage or graphene functionalization. The affinity of graphene to hydrogen is smaller than that of carbon nanotubes [37]. However, when hydrogen is chemisorbed to graphene, that is, when graphene is hydrogenated, interesting electronic properties appear. For example, when graphene is half-hydrogenated, it becomes a ferromagnetic semiconductor with a small indirect bandgap [38].

Aromatic molecules interact with graphene via the π - π interaction unless the H- π interaction is not strong [39]. The electrostatic interaction due to charge transfer often strengthens bonding between graphene and the adsorbed molecule. It is also charge transfer that shifts the Dirac cone and dopes graphene. Nucleobases on graphene received special attention because of possible application in supramolecular chemistry and DNA sequencing [40–42]. The predicted binding energy order is $G > A > T > C$. The binding energy is ~ 18 – 22 kcal mol⁻¹

and the distances between graphene and nucleobases are predicted to be $\sim 3.2 \text{ \AA}$.

Metal–graphene interactions are of particular importance in applications. The hydrogen storage capacity of graphene is significantly increased when light TM atoms are adsorbed onto it [43]. The graphene-metal interface deserves special attention because transport properties of graphene including the Dirac cone position can be significantly modified. Such modifications of electronic structure can as well be applied to bilayer graphene. For example, FeCl_3 and K sandwich bilayer graphene to open a bandgap without significant shifting of the Dirac point [44]. A recent report illustrates that Rashba splitting, an important character for spintronics, can be induced by metal, specifically Au [45]. Other interfaces were also considered. A graphene layer directly interfaced with SiC completely loses the Dirac cone [46]. A graphene bilayer on SiC acts as a freestanding single-layer graphene, and a graphene trilayer on SiC as a freestanding bilayer graphene. On the other hand, the interface with hexagonal boron nitride does not induce significant changes [47]. The bandgap is opened (about 0.1 eV) only when graphene is aligned with respect to hexagonal boron nitride.

We conclude this section with remarks on van der Waals corrections. The graphene surface has become a test bed for van der Waals correction methods. The surface is strongly anisotropic, so anisotropy of polarizability and nonadditive many-atom interactions should be accounted for [48–49]. This poses a challenge for future van der Waals correction methods.

7.2

Graphene–Ligand Noncovalent Interactions – Experiment

7.2.1

Polycyclic Molecules

Owing to the aromaticity afforded to graphene by its π -conjugation, we are able to functionalize graphene noncovalently with aromatic molecules. These molecules then lie along the basal surface of graphene and interact through π – π stacking interactions. A graphite surface could be functionalized by the strong affinity of pyrene toward the basal plane of graphite. This result has led to the functionalization of graphene using pyrene derivatives being explored by multiple research groups [50–60]. These functionalizations have led to water-soluble graphene [50, 52, 58, 59, 61], increased power conversion in solar cells [51, 60], and n/p-type doped graphene [55, 57] among many other properties.

Graphene/reduced-graphene-oxide (rGO) can be made water soluble [50, 52, 58, 59, 61, 62]. This water stability is obtained by sonication of graphite/or rGO in the presence of the pyrene stabilizer. Interestingly, these types of materials have been shown not to aggregate even when destabilized by extreme pH conditions or freeze drying [58]. This effect is believed to be due to the pyrene stabilizer moieties still being attached to the surface, which does not allow the material to aggregate.

Graphene can also be stabilized in aqueous medium using coronene carboxylate molecules [61]. In this study, the authors noted that there was strong molecular charge transfer taking place between the coronene moiety and the graphene sheet in solution, which shows the potential for these kinds of materials to be applied in nanoelectronics.

The flexibility and transparency of graphene materials make them desirable for application in electronics and solar cells. The transparency of a graphene electrode modified with pyrenebutanoic acid-succinimidyl ester is negligibly altered in the visible region [51]. However, by inclusion of this modified graphene in an organic solar cell, the solar efficiency could be improved by 88% compared to the use of graphene alone. It should be noted that even though this is an impressive result, this material still only affords 55% of the efficiency compared to a indium tin oxide (ITO)-based solar cell. By functionalizing graphene using pyrenene-1-sulfonic acid sodium salt (electronic donor) or a disodium salt of 3,4,9,10-perylenetetracarboxylic diimide bis-benzenesulfonic acid (electronic acceptor), the power efficiency in solar cells can be greatly improved [50].

Graphene can be functionalized using 1-pyrenecarboxylic acid and this water-stable solution can be used to create sensitive and selective sensors for gaseous ethanol, as well as ultracapacitors with a specific capacitance of $\sim 120 \text{ F g}^{-1}$ [52]. In a similar manner, graphene functionalized with pyrenebutanoic acid-succinimidyl ester can then be used as a platform to create micropatterned biosensors. This can be achieved by the covalent interactions between the amine groups of proteins and the reactive succinimide ester group on the graphene surface [53]. The use of graphene as an excellent sensing template has been shown by an enhanced Raman signal for terbium single-molecule magnets when non-covalently attached to a graphene surface through pyrene moieties [54]. This attachment allows analysis of a few isolated molecules on the surface of the graphene, which shows that the graphene and the molecule attached through van der Waals forces essentially retain the electronic properties of the pristine samples.

The electronic modulation of graphene is of high importance for graphene application. Using noncovalent functionalization, the carrier type in graphene can be changed. Graphene n–p junctions can be obtained by partial modification of a graphene surface using 1,5-diaminonaphthalene or polyethylenimine as an n-type dopant and 1-nitropyrene as a p-type dopant [55]. When spiropyran is used to n-dope graphene, the Dirac point of the graphene could be modulated using light [57]. Graphene and perylene bis-imide can communicate not only in the solid state but also in aqueous solution through noncovalent interactions [63].

Functionalization with 1-pyrenebutyric acid allows graphene to be evenly dispersed in polymer matrices [56]. These composite materials were then shown to have improved thermal conductance and mechanical properties compared to the pure conductive polymers. Metal oxides can only be coated on 3,4,9,10-perylene tetracarboxylic acid-functionalized graphene using atomic layer deposition [64]. In contrast, in pristine graphene, the metal oxide deposition only occurs on defect and edge sites. It is important to note that this method of atomic layer deposition is not

destructive to the graphene layer. Monolayers of perylene-3,4,9,10-tetracarboxylic dianhydride on a graphene sheet can be obtained by utilizing self-assembly [65].

Graphene can also be noncovalently functionalized using aromatic macrocycles such as porphyrins and phthalocyanines [62, 66–74]. Water solubility can be afforded to graphene using noncovalent functionalization with water-soluble porphyrins [67]. These solutions are then used to form highly conductive and transparent graphene films (sheet resistance $\sim 5 \text{ K}\Omega/\square^{-1}$) using a vacuum filtration method followed by thermal annealing. Light harvesting graphene sheets can be obtained by functionalization using phthalocyanine or porphyrin, which act as photosensitizers [72]. The charge separation between the photosensitizer and the graphene sheet acceptor was in the order of 10^{11} – 10^{12} s^{-1} , which could be applied in light energy harvesting. Graphene functionalized with water-soluble picket fence iron containing porphyrin [68] or metal-free 5,10,15,20-tetra(4-pyridyl)-21H,23H-porphyrin [70] have been used to electrochemically detect chlorite and nitro aromatic compounds, respectively. Both these materials displayed extremely low detection limits (0–1 ppb range) for the respective analytes, which makes them extremely useful in the detection of explosive compounds. This enhanced detection limit is believed to be due to the synergy between the fast electron conductance of the graphene and the molecular adsorptive properties of the porphyrin.

Graphene/porphyrin materials can also be used to detect a wide range of biomolecules [62, 71, 73, 74]. Using a simple wet-chemical strategy, a hemin-graphene hybrid material can be synthesized through π - π interactions [62]. This new nanomaterial exhibits peroxidase-like activity, high solubility, and stability in water and was used to differentiate between single-stranded (ss)- and double-stranded (ds)- DNA. On the basis of this information, an assay for sensitive single-nucleotide polymorphism detection using visual detection at room temperature was developed. DNA could be electrochemically detected at the molar level when the hemin-graphene material was functionalized with streptavidin and combined with a biotinylated molecular beacon [71]. By utilizing a similar wet-chemistry approach, a highly selective and sensitive electrochemical sensor was synthesized for dopamine [74]. A glassy carbon electrode coated with the graphene/meso-tetra (4-carboxyphenyl) porphyrin composite material was able to avoid the ascorbic acid and uric acid interference usually associated with dopamine sensing. This is believed to be due to preferable π - π interactions between the positively charged dopamine and the negatively charged porphyrin. A selective and sensitive label-free adenosine triphosphate electrochemical sensor has been produced through the noncovalent interaction between meso-tetrakis(4-methoxyl-3-sulfonatophenyl) porphyrin and graphene [73]. This material could be used to selectively determine between adenosine triphosphate and cytidine/guanosine/uridine triphosphate nucleosides with a detection limit of 0.7 nM.

Glucose can be detected at very low levels when graphene is functionalized with iron(III) meso-tetrakis(*N*-methylpyridinium-4-yl) porphyrin [68]. In addition, this material shows catalytic activity toward the oxygen reduction reaction (ORR),

which is believed to be due to efficient electron communication between the porphyrin and graphene. By using a pyridine-functionalized graphene, a graphene-metalloporphyrin metal organic framework could be synthesized [69]. These materials were then applied as Pt-free ORR catalysts that showed slow degradation after an initial loss in activity of 39%.

7.2.2

Biomolecules

Graphene can be functionalized using thiolated DNA, which binds noncovalently to both graphene/graphene oxides surfaces [75]. This water-soluble DNA/graphene material can then be used to anchor gold nanoparticles that could allow these types of materials to be applied in catalysis, field effect devices, and biodetection platforms. Graphene oxide/DNA material can be used to create a 3D hydrogel through a self-assembly process [76]. This self-assembly proceeds through the heating of the material in solution to 90 °C, which leads to unwinding of the DNA strands that are then able to bridge separate graphene oxide sheets as ss-DNA. This material was shown to exhibit self-healing upon heating, a large dye-adsorption capacity, environmental stability, and a large mechanical strength. DNA-functionalized graphene has also been used to direct the uniform growth of <2 nm Pt nanoclusters on the graphene surface [77]. In particular, this method affords an electrochemically active surface area that is several times that of the non-DNA-functionalized Pt-graphene sample. When this material was applied in the oxygen reduction reaction (ORR), it was shown to exhibit a larger ORR half wave potential and current density in comparison with the Pt-graphene and commercial Pt/C catalyst.

A phospholipid monolayer can be easily assembled on a graphene sheet by noncovalent interactions between the graphene sheet and the lipid tail, affording a unique planar mimic of the cellular membrane [78] (Figure 7.1). By incorporating a fluorescein-labeled phospholipid into the monolayer, a novel biosensor for the phospholipase D enzyme activity can be achieved by reactivation of the fluorescence of the fluorescein label. Lipid monolayer-coated graphene can also be used to immobilize enzymes and these types of material can subsequently be used as electrochemical biosensor [79]. The enzyme Microperoxidase-11 when entrapped in the lipid/graphene system exhibits very sensitive and reproducible hydrogen peroxide detection with a detection limit of 7.2×10^{-7} M. The benefit of using these types of lipid/graphene systems is that they are biocompatible, thereby creating a desirable environment for the entrapment of enzymes that are able to retain their structure and bioactivity.

Graphene monolayers can also be functionalized directly with enzymes [80]. In their study, Lu *et al.* showed that rGO sheets noncovalently functionalized with β -lactoglobulin make the graphene pH-dependent and soluble in water. Interestingly, the attached β -lactoglobulin helps in the reduction of the graphene oxide sheets besides offering anchoring sulfhydryl groups that can be used to anchor gold nanoparticles. The Au-functionalized β -lactoglobulin/graphene material was

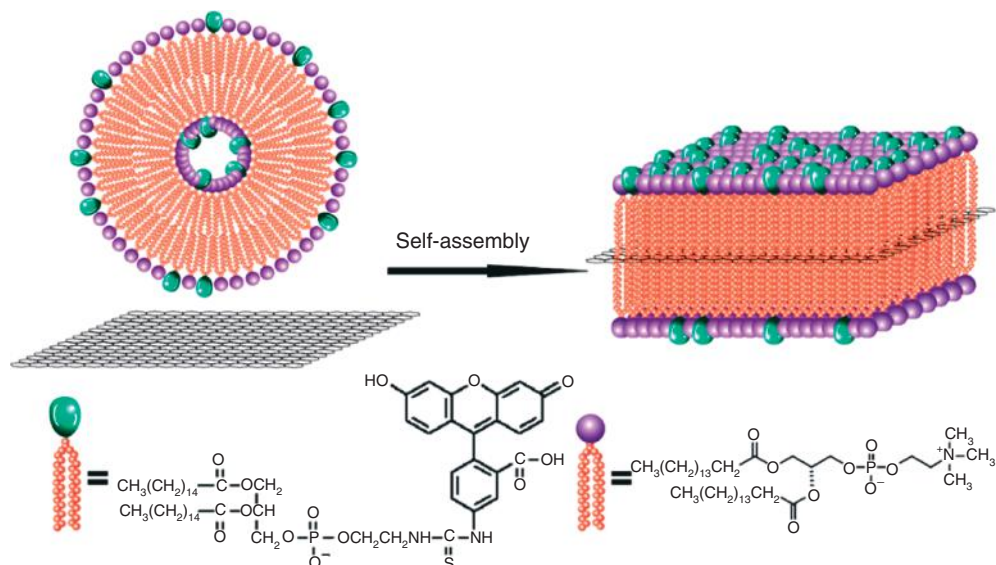


Figure 7.1 Phospholipid self-assembled monolayers on a graphene surface. (Reprinted with permission from Ref. [78]. Copyright 2012 American Chemical Society.)

additionally shown to exhibit a surface-enhanced Raman spectroscopy effect. Negatively charged sodium dodecyl benzene sulfonate-functionalized graphene can self-assemble with positively charged horseradish peroxidase through electrostatic interactions [81]. This material was shown to be sensitive and stable in the detection of hydrogen peroxide, as its structure was not compromised by the noncovalent bonding with the graphene surface [79].

In the complexation study of graphene-binding peptide and dodecameric carbon nanotube-binding peptide to graphene, the graphene-binding peptide binds to the edges of graphene, while the carbon nanotube-binding peptide binds to the basal surface of graphene [82]. These peptide/graphene materials can then be used to direct selective nanoparticle growth on the graphene sheet. The graphene-binding peptide shows a different conformation to its native form when bound with graphene [83]. This insight allows the functionalization of graphene using different peptides to create specific structures that should display interesting sensing selectivity and sensitivity among other applications.

The anticoagulant heparin was used to functionalize a graphene surface, allowing the graphene to become water soluble and biocompatible [84]. The heparin/graphene material showed a decreased anticoagulation antifactor Xa activity of 29.6 IU ml^{-1} compared to the pure heparin, which used 85.6 IU ml^{-1} . This is promising for biomedical applications as the heparin is able to retain its activity when functionalized to graphene. Graphene can be functionalized with heparin, where the heparin acts as a reducing agent for the graphene oxide substrate

[85]. Graphene that is noncovalently functionalized using pyrene-based glycoconjugates can be used for selective lectin detection [86]. These graphene devices were compared to similarly manufactured single-wall nanotube devices, owing to the dimensional structural differences between the carbon materials that effect electron conduction.

7.2.3

Polymers

Noncovalent polymer functionalization of graphene affords materials that can be applied in green chemistry, electronics, capacitors, and so on. Graphene could be made water stable using sulfonated polyaniline owing to the π – π stacking between the aromatic backbone of sulfonated polyaniline and the graphene basal plane [87]. This material was also shown to display high electrocatalytic activity, conductivity, and stability. In a similar manner, an electrode formed from a polyaniline/graphene composite was shown to have flexibility and high conductivity [88]. The gravimetric capacitance of this material was calculated to be 233 F g^{-1} , which is much larger than that of pure graphene paper (145 F g^{-1}) and other carbon-based flexible materials. A polypyrrole-functionalized graphene material can be applied in water remediation as well as gas adsorption [89, 90]. The polypyrrole/graphene material was shown to selectively adsorb Hg(II) ions in an aqueous solution containing a mixture of Hg(II), Cu(II), Cd(II), Pb(II), and Zn(II) ions [89] (Figure 7.2). The chemically activated polypyrrole/graphene material was used for the selective adsorption of CO_2 , with a maximum adsorption capacity of 4.3 mmol g^{-1} at 25°C and 1 atm [90].

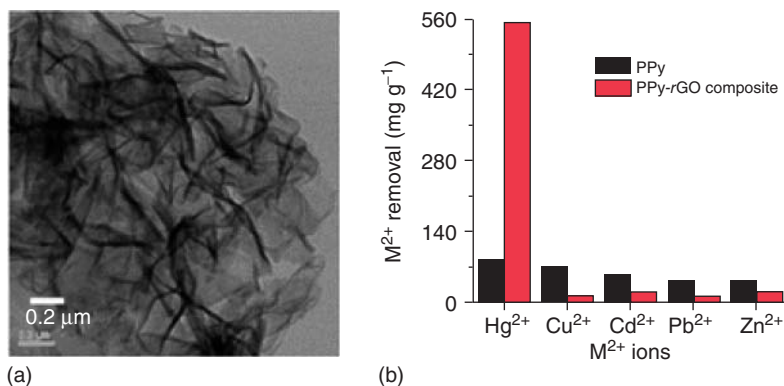


Figure 7.2 (a) Transmission electron microscope (TEM) image of the polypyrrole/rGO composite. (b) Bar graph showing the selective adsorption of mercury from aqueous

solution using the polypyrrole/graphene composite. (Reproduced from Ref. [89] with permission from The Royal Society of Chemistry.)

A polystyrene/graphene composite material can be manufactured by *in situ* peeling of graphite nanoplates in the presence of a polystyrene solution [91]. The composite formed was shown to be electrically conductive as a result of even dispersion of graphene in the matrix; interestingly, the polystyrene backbones stopped the graphene nanoplates from aggregating owing to strong π - π interactions. In a similar manner, the backbone of Nafion[®] allows it to functionalize graphene sheets [92]. This material was used to create a thin film that could be used in the sensitive electrochemical sensing of organophosphates. The conductivity of the material can be increased by the presence of Nafion[™] nanochannels in the material [93]. This material has also been used as a sensitive Cd(II) ion sensor when it is applied as an electrode during anodic stripping voltammetry with a detection limit of $0.005 \mu\text{g ml}^{-1}$ [94].

In a transparent polyimide/graphene composite film that displays enhanced mechanical strength, no phase separation occurs during thermal imidization owing to the strong noncovalent bonds between the graphene carboxylic acid and the polyimide precursor [95]. The increased mechanical strength in these samples is believed to be due to the 2D orientation of the graphene sheets parallel to the polyimide films, as well as the even dispersion of graphene in the polymer matrix. The polyimide/graphene material displays shape memory above the glass transition temperature ($\sim 250^\circ\text{C}$) where the addition of graphene improved the recovery rate [96].

Poly(3,4-ethylenedioxythiophene) (PEDOT) can be embedded with graphene-based electrolytes used in the polymerization process [97]. The electrolytes used were *rGO* and ionic liquid-functionalized graphene. It was shown that in the case of the ionic liquid-functionalized graphene electrolyte, the material displayed increased conductivity and faster switching kinetics compared to the *rGO* sample. Graphene can be stabilized in aqueous solution using a PEDOT/poly-(styrene sulfonate) conducting polymer dispersant [98]. A transparent thin film of this material displayed a large conductance that could be increased by simple Cl doping using SOCl_2 . The thermoelectric properties of PEDOT/poly-(styrene sulfonate) could be increased by the addition of a small amount of graphene (2 wt%), whereas a higher weight percent leads to a decrease in thermal conductivity [99]. The thermoelectric performance of this material is lower than that of PEDOT/poly-(styrene sulfonate) thin films containing 35 wt% single-wall nanotubes. This behavior is believed to be due to graphene multilayers that act as phonon-scattering centers.

By reducing graphene oxide in the presence of chitosan, an *rGO*/chitosan material could be synthesized [100]. This material displayed pH-driven water solubility, which is believed to be due to ionic interactions and hydrogen bonds between the graphene and the chitosan functional groups. In a related study, it was shown that this material can be used as a pH sensor owing to its reversible pH switch between dispersion and agglomerate (Figure 7.3) [101]. In a similar manner, cellulose and lignin derivatives can be used to stabilize graphene in aqueous solutions [102].

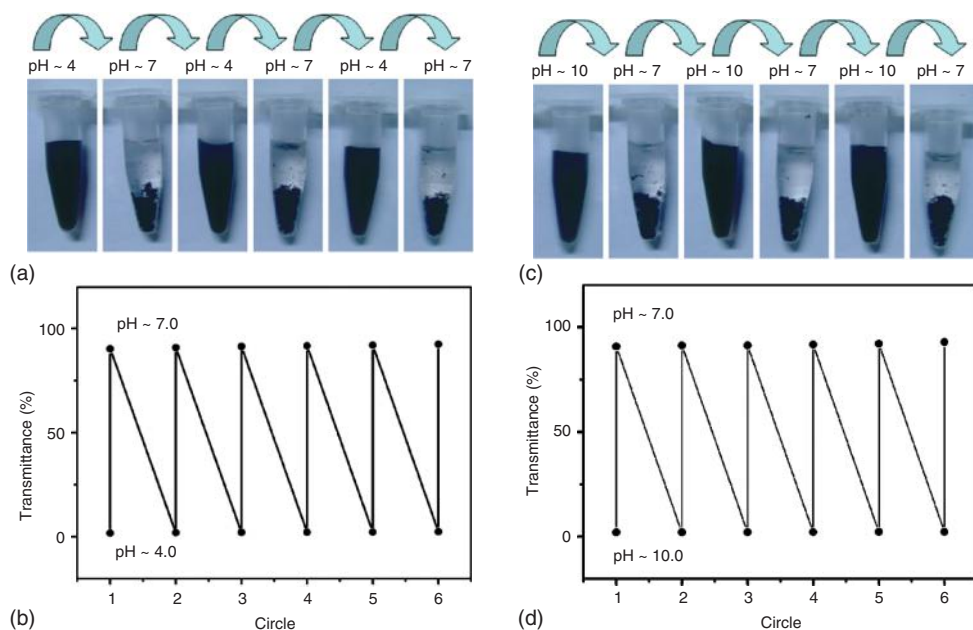


Figure 7.3 Pictures showing the reversible pH-response of a chitosan/graphene suspension between pH 7.0 and 4.0 (a,b) and between 7.0 and 10.0 (c,d). (Reprinted with permission from Ref. [101], Copyright (2012), with permission from Elsevier.)

A thermosensitive graphene/poly-(*N*-isopropylacrylamide) has been synthesized by simple sonication of the precursors [103]. This material could be dispersed in aqueous solution below the lower critical solution temperature of the material, which was determined to be 24 °C. The π - π stacking that occurs between poly-(2,5-bis(3-sulfonatopropoxy)-1,4-ethynyl-phenylene-alt-1,4-ethynylphenylene) sodium salt (PPE-SO₃⁻Na⁺) and graphene was used to disperse graphene in water [104]. The excess negative charges afforded to the material through the (PPE-SO₃⁻) sodium salt offers a novel way to further functionalize the graphene-based material. Graphene can be stabilized in aqueous solution using poly oxy-ethylene sorbitan laurate [105]. From this solution, a film could be made, which displayed stability in water as well as nontoxicity to mammalian cell lines; therefore, this material could be used in biomedical applications where high mechanical strength is desired.

The formation of a pluronic copolymer/graphene material has been shown to be highly stable in aqueous solution [106]. Interestingly, a mixture of this material with a cyclodextrin solution gives a hydrogel that displays a gel–sol transition at 45 °C. Poly-[(2-ethyl-dimethylammonioethyl methacrylate ethyl sulfate)-*co*-(1-vinylpyrrolidone)] (PQ11) could be used to functionalize graphene, thereby making it dispersible and stable [107]. The PQ11 polyelectrolyte displays reducing abilities, and as such it can be used to reduce Ag(II) ion in solution, thereby

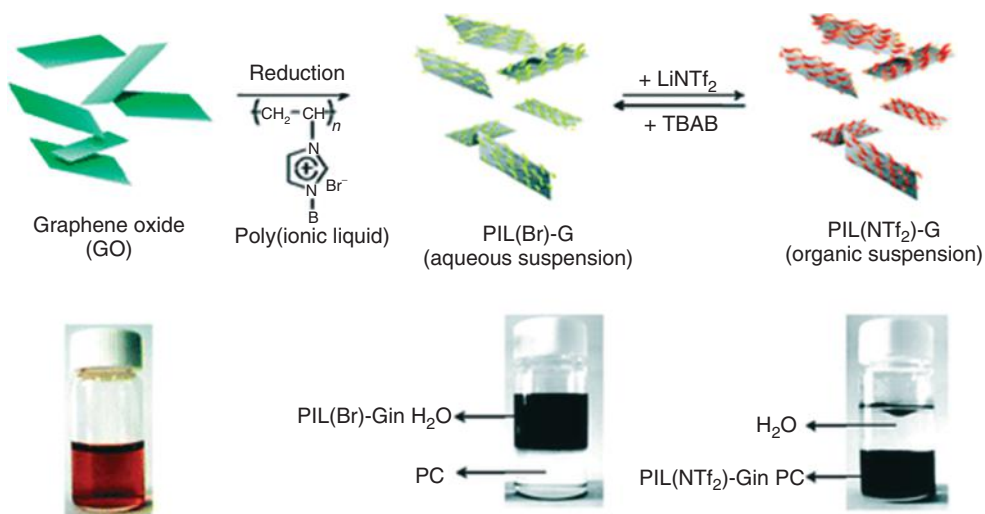


Figure 7.4 Schematic showing the synthetic process for the ionic liquid polymer (PIL)/graphene sheets. Anion exchange of the ionic liquid polymer leads to the phase

transfer between aqueous and organic solvents. (Reprinted with permission from Ref. [109], Copyright (2010) American Chemical Society.)

decorating the graphene surface with Ag nanoparticles. This Ag-functionalized graphene/PQ11 material could then be used to detect hydrogen peroxide in solution. This is in contrast to normal methods, which utilize enzymes.

Besides the water-soluble graphene materials, it is also possible to produce amphiphilic graphene materials [108]. The *r*GO can be functionalized using a polyethylene glycol (PEG) polyethylene oxide (OPE) triblock copolymer, thereby making this material soluble in a large number of polar and nonpolar organic solvents. Graphene can be made to undergo phase transfer between immiscible solvents by functionalization using ionic liquid polymers (Figure 7.4) [109].

By functionalizing a graphene surface with sulfonated poly-(ether-ether-ketone), a water-stable dispersion of graphene could be obtained [110]. An electrode manufactured using this material was tested as a supercapacitor electrode, and a high specific capacitance of 476 F g⁻¹ was obtained. This observed capacitance was stable over 10 charge/discharge cycles. The biofunctional polymer poly-(2-methoxystyrene) can be noncovalently bonded to a graphene surface [111]. This material was shown to maintain its bioactivity on binding with the graphene and this is attributed to the polymer maintaining a space between the graphene and the solution, in effect isolating the graphene.

7.2.4

Other Molecules

A variety of other organic and inorganic molecules can be noncovalently bonded onto graphene surfaces through π - π stacking, electrostatic interactions, hydrogen

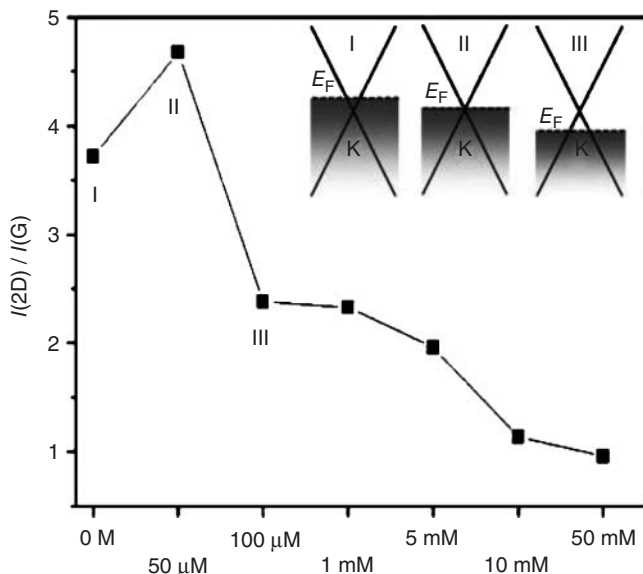


Figure 7.5 Evaluation of the Fermi-level changes of graphene upon functionalization using 4-bromobenzene diazonium tetrafluoroborate. The $I(2D)/I(G)$ ratio changes as a function of doping concentration. Insets depict the Fermi-level positions of

graphene before (I) and after functionalization with 50 μ M (II) and 100 μ M (III) of 4-bromobenzene diazonium tetrafluoroborate. (Reprinted with permission of Ref. [112], Copyright (2010) American Chemical Society.)

bonds, and so on. The functionalization of graphene sheets using 4-bromobenzene diazonium tetrafluoroborate allows the graphene material to be doped, without the need for high temperatures [112]. In particular, in this study, the amount of doping in the sample was shown to correlate to the change in the intensity ratio between the G and 2D Raman bands characteristic of single-layer graphene (Figure 7.5). Functionalization of graphene using pentacene self-assembled monolayers allows for graphene being doped using molecular engineering (Figure 7.6) [113].

A conductive thionine/graphene material displays a high degree of dispersability in aqueous solution [114]. This material offers further modification opportunities, as the thionine molecules can be further modified. Bidirectional conductive thin films produced from the thionine/graphene material show a nonvolatile resistive switching behavior [115]. The films produced display ON/OFF ratios of 10^4 as well as an excellent endurance over 350 cycles. This result shows that various low-temperature methods can be used to employ graphene in future electronics. The thionine/graphene material can be functionalized with Au nanoparticles by the solution reduction of HAuCl_4 in the presence of the graphene oxide/thionine precursor [116]. This material was then applied as an enzymeless electrochemical biosensor for glucose with a detection limit of $0.05 \mu\text{mol l}^{-1}$.

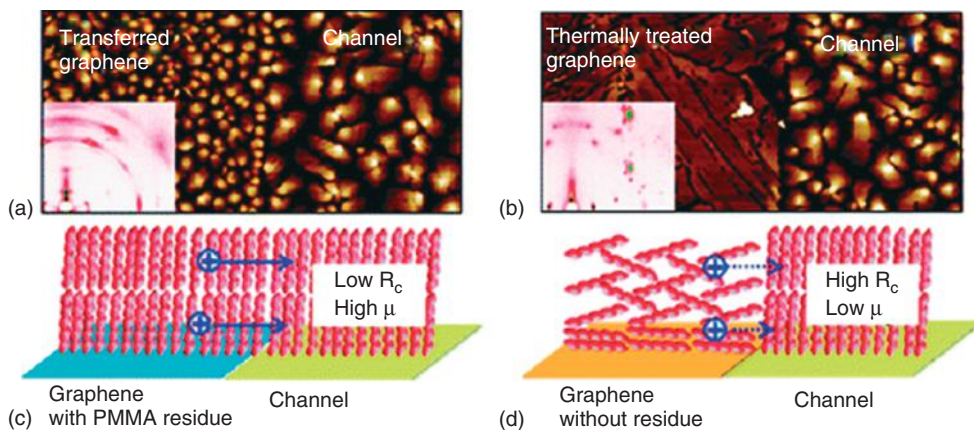


Figure 7.6 Atomic force microscope (AFM) images of the pentacene films near the interface between SiO₂ and untreated graphene electrodes (a) and thermally treated graphene electrodes (b). Schematic of the possible molecular packing orientations near

the interface between SiO₂ and untreated graphene electrodes (c) and thermally treated graphene electrodes (d). (Reprinted with permission of Ref. [113], Copyright (2011) American Chemical Society.)

The functionalization of graphene using organic dyes has yielded some interesting properties. Graphene could be functionalized using Congo red dye, and the resulting conductive composite material was dispersible in the polar solvents dimethylformamide, methanol, dimethyl sulfoxide, ethanol, and water [117]. This material can be used to direct even Au nanoparticle growth on the graphene surface, due to the multiple $-\text{SO}_3\text{Na}$ groups introduced on the surface by the Congo red dye. Functionalized graphene using the electroactive methylene green dye becomes a water-stable composite [118]. A glassy carbon electrode coated with the methylene green/graphene composite material was shown to increase the electrocatalytic activity of the methylene green toward nicotinamide adenine dinucleotide.

Graphene can be stabilized in aqueous medium by noncovalent π - π stacking with an imidazolium-modified hexa-peri-hexabenzocoronene derivative [119]. This composite material could be used as a graphene organic/aqueous phase-transfer agent by simple anion exchange. Graphene nanoribbons are stable in solution when functionalized with poly-(*m*-phenylenevinylene-*co*-2,5-dioctoxy-*p*-phenylenevinylene) [120]. It should be noted that this polymeric stabilization is a factor in the synthesis of these high-quality semiconducting nanoribbons from graphite. By using green tea phenols as reducing agents, the graphene oxide could be reduced while making the reduced graphene water stable by π - π interactions between the green tea phenol aromatic groups and the graphene [121].

To prepare a chemiluminescent graphene material, *N*-(aminobutyl)-*N*-(ethylisoluminol) was mixed with graphene oxide and self-reduction was allowed to take place to afford the *N*-(aminobutyl)-*N*-(ethylisoluminol)/graphene chemiluminescent material. In addition, this material was applied as a sensor

for hydrogen peroxide based on its chemiluminescence intensity [122]. The self-assembly of amine layers on a graphene surface can dope the graphene, as well as offering anchoring groups for further functionalization of the material [123]. The further functionalization of the material was shown for the evenly dispersed Au nanoparticle decoration of the diaminodecane/graphene material, as well as the atomic layer deposition of alumina onto these self-assembled amine layer/graphene sheets.

7.3

Conclusions

We have discussed noncovalent functionalization of graphene in terms of π -interactions, and reviewed these applications using polycyclic molecules, biomolecules, polymers, and other molecules. In the future, we expect that the functionalization of graphene would have more useful applications for molecular sensors, electronic materials, water remediation, light harvesting, and ORR catalysts.

References

- Georgakilas, V., Otyepka, M., Bourlino, A.B., Chandra, V., Kim, N., Kemp, K.C., Hobza, P., Zboril, R., and Kim, K.S. (2012) *Chem. Rev.*, **112**, 6156.
- Novoselov, K.S., Geim, A.K., Morozov, S.V., Jiang, D., Zhang, Y., Dubonos, S.V., Grigorieva, I.V., and Firsov, A.A. (2004) *Science*, **306**, 666.
- Kim, K.S., Zhao, Y., Jang, H., Lee, S.Y., Kim, J.M., Kim, K.S., Ahn, J.-H., Kim, P., Choi, J.-Y., and Hong, B.H. (2009) *Nature*, **457**, 706.
- Park, J., Jo, S.B., Yu, Y.-J., Kim, Y., Yang, J.W., Lee, W.H., Kim, H.H., Hong, B.H., Kim, P., Cho, K., and Kim, K.S. (2012) *Adv. Mater.*, **24**, 407.
- Meyer, E.A., Castellano, R.K., and Diederich, F. (2003) *Angew. Chem. Int. Ed.*, **42**, 1210.
- Lee, J.Y., Hong, B.H., Kim, W.Y., Min, S.K., Kim, Y., Jouravlev, M.V., Bose, R., Kim, K.S., Hwang, I.-C., Kaufman, L.J., Wong, C.W., Kim, P., and Kim, K.S. (2009) *Nature*, **460**, 498.
- Hong, B.H., Small, J.P., Purewal, M.S., Mullochandov, A., Sfeir, M.Y., Wang, F., Lee, J.Y., Heinz, T.F., Brus, L.E., Kim, P., and Kim, K.S. (2005) *Proc. Natl. Acad. Sci. U.S.A.*, **102**, 14155.
- Kim, H.G., Lee, C.-W., Yun, S., Hong, B.H., Kim, Y.-O., Kim, D., Ihm, H., Lee, J.W., Lee, E.C., Tarakeshwar, P., Park, S.-M., and Kim, K.S. (2002) *Org. Lett.*, **4**, 3971.
- Hong, B.H., Lee, J.Y., Lee, C.W., Kim, J.C., Bae, S.C., and Kim, K.S. (2001) *J. Am. Chem. Soc.*, **123**, 10748.
- Singh, N.J., Lee, H.M., Hwang, I.-C., and Kim, K.S. (2007) *Supramol. Chem.*, **19**, 321.
- Chandra, V., Park, J., Chun, Y., Lee, J.W., Hwang, I.-C., and Kim, K.S. (2010) *ACS Nano*, **4**, 3979.
- Chun, Y., Singh, N.J., Hwang, I.-C., Lee, J.W., Yu, S.U., and Kim, K.S. (2013) *Nat. Commun.*, **4**, 1797.
- Kim, K.S., Tarakeshwar, P., and Lee, J.Y. (2000) *Chem. Rev.*, **100**, 4145.
- Riley, K.E., Pitonak, M., Jurecka, P., and Hobza, P. (2010) *Chem. Rev.*, **110**, 5023.
- Singh, N.J., Min, S.K., Kim, D.Y., and Kim, K.S. (2009) *J. Chem. Theory Comput.*, **5**, 515.

16. Krause, H., Ernstberger, B., and Neusser, H.J. (1991) *Chem. Phys. Lett.*, **184**, 411.
17. Burley, S.K. and Petsko, G.A. (1985) *Science*, **229**, 23.
18. Lee, E.C., Hong, B.H., Lee, J.Y., Kim, J.C., Kim, D., Kim, Y., Tarakeshwar, P., and Kim, K.S. (2005) *J. Am. Chem. Soc.*, **127**, 4530.
19. Grabowski, S.J. (2007) *J. Phys. Chem. A*, **111**, 13537.
20. Kim, E., Paliwal, S., and Wilcox, C.S. (1998) *J. Am. Chem. Soc.*, **120**, 11192.
21. Tarakeshwar, P., Choi, H.S., and Kim, K.S. (2001) *J. Am. Chem. Soc.*, **123**, 3323.
22. Lee, E.C., Kim, D., Jurecka, P., Tarakeshwar, P., Hobza, P., and Kim, K.S. (2007) *J. Phys. Chem. A*, **111**, 3446.
23. Hunter, C.A. and Sanders, J.K.M. (1990) *J. Am. Chem. Soc.*, **112**, 5525.
24. Dougherty, D.A. and Stauffer, D.A. (1990) *Science*, **250**, 1558.
25. Kim, K.S., Lee, J.Y., Lee, S.J., Ha, T.-K., and Kim, D.H. (1994) *J. Am. Chem. Soc.*, **116**, 7399.
26. Kim, D., Hu, S., Tarakeshwar, P., Kim, K.S., and Lisy, J.M. (2003) *J. Phys. Chem. A*, **107**, 1228.
27. Yi, H.-B., Lee, H.M., and Kim, K.S. (2009) *J. Chem. Theory Comput.*, **5**, 1709.
28. Yi, H.B., Diefenbach, M., Choi, Y.C., Lee, E.C., Lee, H.M., Hong, B.H., and Kim, K.S. (2006) *Chem. Eur. J.*, **12**, 4885.
29. Youn, I.S., Kim, D.Y., Singh, N.J., Park, S.W., Youn, J., and Kim, K.S. (2012) *J. Chem. Theory Comput.*, **8**, 99.
30. Singh, N.J., Shin, D., Lee, H.M., Kim, H.T., Chang, H.-J., Cho, J.M., Kim, K.S., and Ro, S. (2011) *J. Struct. Biol.*, **174**, 173.
31. Das, A., Jana, A.D., Seth, S.K., Dey, B., Choudhury, S.R., Kar, T., Mukhopadhyay, S., Singh, N.J., Hwang, I.-C., and Kim, K.S. (2010) *J. Phys. Chem. B*, **114**, 4166.
32. Quinonero, D., Garau, C., Rotger, C., Frontera, A., Ballester, P., Costa, A., and Deya, P.M. (2002) *Angew. Chem. Int. Ed.*, **41**, 3389.
33. Mascal, M., Armstrong, A., and Bartberger, M.D. (2002) *J. Am. Chem. Soc.*, **124**, 6274.
34. Kim, D., Tarakeshwar, P., and Kim, K.S. (2004) *J. Phys. Chem. A*, **108**, 1250.
35. Xu, Z., Singh, N.J., Kim, S.K., Spring, D.R., Kim, K.S., and Yoon, J. (2011) *Chem. Eur. J.*, **17**, 1163.
36. Kim, D.Y., Geronimo, I., Singh, N.J., Lee, H.M., and Kim, K.S. (2012) *J. Chem. Theory Comput.*, **8**, 274.
37. Henwood, D. and Carey, J.D. (2007) *Phys. Rev. B*, **75**, 245413.
38. Zhou, J., Wang, Q., Sun, Q., Chen, X.S., Kawazoe, Y., and Jena, P. (2009) *Nano Lett.*, **9**, 3867.
39. Chakarova-Kack, S.D., Schroder, E., Lundqvist, B.I., and Langreth, D.C. (2006) *Phys. Rev. Lett.*, **96**, 146107.
40. Min, S.K., Kim, W.Y., Cho, Y., and Kim, K.S. (2011) *Nat. Nanotechnol.*, **6**, 162.
41. Cho, Y., Min, S.K., Yun, J., Kim, W.Y., Tkatchenko, A., and Kim, K.S. (2013) *J. Chem. Theory Comput.*, **9**, 2090.
42. Min, S.K., Cho, Y., Mason, D.R., Lee, J., and Kim, K.S. (2011) *J. Phys. Chem.*, **C115**, 16247.
43. Durgun, E., Ciraci, S., and Yildirim, T. (2008) *Phys. Rev. B*, **77**, 085405.
44. Yang, J.W., Lee, G., Kim, J.S., and Kim, K.S. (2011) *J. Phys. Chem. Lett.*, **2**, 2577.
45. Marchenko, D., Varykhalov, A., Scholz, M.R., Bihlmayer, G., Rashba, E.I., Rybkin, A., Shikin, A.M., and Rader, O. (2012) *Nat. Commun.*, **3**, 1232.
46. Varchon, F., Feng, R., Hass, J., Li, X., Nguyen, B.N., Naud, C., Mallet, P., Veuillen, J.Y., Berger, C., Conrad, E.H., and Magaud, L. (2007) *Phys. Rev. Lett.*, **99**, 126805.
47. Kharche, N. and Nayak, S.K. (2011) *Nano Lett.*, **11**, 5274.
48. Tkatchenko, A., Alfè, D., and Kim, K.S. (2012) *J. Chem. Theory Comput.*, **8**, 4317.
49. Kim, K.S., Karthikeyan, S., and Singh, N.J. (2011) *J. Chem. Theory Comput.*, **7**, 3471.
50. Xu, Y., Bai, H., Lu, G., Li, C., and Shi, G.Q. (2008) *J. Am. Chem. Soc.*, **130**, 5856.

51. Wang, Y., Chen, X., Zhong, Y., Zhu, F., and Loh, K.P. (2009) *Appl. Phys. Lett.*, **95**, 063302.
52. An, X., Butler, T.W., Washington, M., Nayak, S.K., and Kar, S. (2011) *ACS Nano*, **5**, 1003.
53. Kodali, V.K., Scrimgeour, J., Kim, S., Hankinson, J.H., Carroll, K.M., de Heer, W.A., Berger, C., and Curtis, J.E. (2011) *Langmuir*, **27**, 863.
54. Lopes, M., Candini, A., Urdampilleta, M., Plantey, A.R., Bellini, V., Klyatskaya, S., Marty, L., Ruben, M., Affronte, M., Wernsdorfer, W., and Bendiab, N. (2010) *ACS Nano*, **4**, 7531.
55. Cheng, H.C., Shiue, R.J., Tsai, C.C., Wang, W.H., and Chen, Y.T. (2011) *ACS Nano*, **5**, 2051.
56. Song, S.H., Park, K.H., Kim, B.H., Choi, Y.W., Jun, G.H., Lee, D.J., Kong, B.-S., Paik, K.-W., and Jeon, S. (2013) *Adv. Mater.*, **25**, 732.
57. Jang, A.-R., Jeon, E.K., Kang, D., Kim, G., Kim, B.-S., Kang, D.J., and Shin, H.S. (2012) *ACS Nano*, **6**, 9207.
58. Parviz, D., Das, S., Ahmed, H.S.T., Irin, F., Bhattacharia, S., and Green, M.J. (2012) *ACS Nano*, **6**, 8857.
59. Malig, J., Romero-Nieto, C., Jux, N., and Guldi, D.M. (2012) *Adv. Mater.*, **24**, 800.
60. Su, Q., Pang, S., Alijani, V., Li, C., Feng, X., and Mullen, K. (2009) *Adv. Mater.*, **21**, 3191.
61. Ghosh, A., Rao, K.V., George, S.J., and Rao, C.N.R. (2010) *Chem. Eur. J.*, **16**, 2700.
62. Guo, Y., Deng, L., Li, J., Guo, S., Wang, E., and Dong, S. (2011) *ACS Nano*, **5**, 1282.
63. Kozhemyakina, N.V., Englert, J.M., Yang, G., Spiecker, E., Schmidt, C.D., Hauke, F., and Hirsch, A. (2010) *Adv. Mater.*, **22**, 5483.
64. Wang, X., Tabakman, S.M., and Dai, H. (2008) *J. Am. Chem. Soc.*, **130**, 8152.
65. Wang, Q.H. and Hersam, M.C. (2009) *Nat. Chem.*, **1**, 206.
66. Tu, W., Lei, J., Zhang, S., and Ju, H. (2010) *Chem. Eur. J.*, **16**, 10771.
67. Geng, J. and Jung, H.T.J. (2010) *Phys. Chem. C*, **114**, 8227.
68. Zhang, S., Tang, S., Lei, J., Dong, H., and Ju, H. (2011) *J. Electroanal. Chem.*, **656**, 285.
69. Jahan, M., Bao, Q., and Loh, K.P. (2012) *J. Am. Chem. Soc.*, **134**, 6707.
70. Guo, C.X., Lei, Y., and Li, C.M. (2011) *Electroanalysis*, **23**, 885.
71. Ju, H., Wang, Q., Lei, J., Deng, S., and Zhang, L. (2012) *Chem. Commun.*, **49**, 916.
72. Bikram, K.C., Das, S.K., Ohkubo, K., Fukuzumi, S., and D'Souza, F. (2012) *Chem. Commun.*, **48**, 11859.
73. Zhang, H., Han, Y., Guo, Y., and Dong, C. (2012) *J. Mater. Chem.*, **22**, 23900.
74. Wu, L., Feng, L., Ren, J., and Qu, X. (2012) *Biosens. Bioelectron.*, **34**, 57.
75. Liu, J., Li, Y., Li, Y., Li, J., and Deng, Z. (2010) *J. Mater. Chem.*, **20**, 900.
76. Xu, Y., Wu, Q., Sun, Y., Bai, H., and Shi, G. (2010) *ACS Nano*, **4**, 7358.
77. Tiwari, J.N., Nath, K., Kumar, S., Tiwari, R.N., Kemp, K.C., Le, N.H., Youn, D.H., Lee, J.S., and Kim, K.S. (2013) *Nature Commun.*, **4**, 2221.
78. Liu, S.-J., Wen, Q., Tang, L.-J., and Jiang, J.-H. (2012) *Anal. Chem.*, **84** (14), 5944–5950.
79. Liu, J., Han, L., Wang, T., Hong, W., Liu, Y., and Wang, E. (2012) *Chem. Asian J.*, **7**, 2824.
80. Lu, F., Zhang, S., Gao, H., Jia, H., and Zheng, L. (2012) *ACS Appl. Mater. Interfaces*, **4**, 3278.
81. Zeng, Q., Cheng, J., Tang, L., Liu, X., Liu, Y., Li, J., and Jiang, J. (2010) *Adv. Funct. Mater.*, **20**, 3366.
82. Kim, S.N., Kuang, Z., Slocik, J.M., Jones, S.E., Cui, Y., Farmer, B.L., McAlpine, M.C., and Naik, R.R. (2011) *J. Am. Chem. Soc.*, **133**, 14480.
83. Katoch, J., Kim, S.N., Kuang, Z., Farmer, L., Naik, R.R., Tatulian, S.A., and Ishigami, M. (2012) *Nano Lett.*, **12**, 2342.
84. Lee, D.Y., Khatun, Z., Lee, J.-H., Lee, Y.-K., and In, I. (2011) *Biomacromolecules*, **12**, 336.
85. Wang, Y., Zhang, P., Liu, C.F., Zhan, L., Li, Y.F., and Huang, C.Z. (2012) *RSC Adv.*, **2**, 2322.
86. Chen, Y., Vedala, H., Kotchey, G.P., Audfray, A., Cecioni, S., Imberty, A.,

- Vidal, S., and Star, A. (2012) *ACS Nano*, **6**, 760.
87. Bai, H., Xu, Y., Zhao, L., Li, C., and Shi, G. (2009) *Chem. Commun.*, **45**, 1667.
88. Wang, D.W., Li, F., Zhao, J., Ren, W., Chen, Z.G., Tan, J., Wu, Z.S., Gentle, I., Lu, G.Q., and Cheng, H.M. (2009) *ACS Nano*, **3**, 1745–1752.
89. Chandra, V. and Kim, K.S. (2011) *Chem. Commun.*, **47**, 3942.
90. Chandra, V., Yu, S.U., Kim, S.H., Yoon, Y.S., Kim, D.Y., Kwon, A.H., Meyyappan, M., and Kim, K.S. (2012) *Chem. Commun.*, **48**, 735.
91. Wu, H., Zhao, W., Hu, H., and Chen, G. (2011) *J. Mater. Chem.*, **21**, 8626.
92. Choi, B.G., Park, H., Park, T.J., Yang, M.H., Kim, J.S., Jang, S.-Y., Heo, N.S., Lee, S.Y., Kong, J., and Hong, W.H. (2010) *ACS Nano*, **4**, 2910.
93. Ansari, S., Kelarakis, A., Estevez, L., and Giannelis, E.P. (2010) *Small*, **6**, 205.
94. Lia, J., Guoa, S., Zhaia, Y., and Wang, E. (2009) *Electrochem. Commun.*, **11**, 1085.
95. Kim, G.Y., Choi, M.-C., Lee, D., and Ha, C.-S. (2012) *Macromol. Mater. Eng.*, **297**, 303.
96. Yoonessi, M., Shi, Y., Scheiman, D.A., Colon, M.L., Tigelaar, D.M., Weiss, R.A., and Meador, M.A. (2012) *ACS Nano*, **6**, 7644.
97. Saxena, A.P., Deepa, M., Joshi, A.G., Bhandari, S., and Srivastava, A.K. (2011) *ACS Appl. Mater. Interfaces*, **3**, 1115.
98. Jo, K., Lee, T., Choi, H.J., Park, J.H., Lee, D.J., Lee, D.W., and Kim, B.S. (2011) *Langmuir*, **27**, 2014.
99. Kim, G.H., Hwang, D.H., and Woo, S.I. (2012) *Phys. Chem. Chem. Phys.*, **14**, 3530.
100. Fang, M., Long, J., Zhao, W., Wang, L., and Chen, G. (2010) *Langmuir*, **26**, 16771.
101. Liu, J., Guo, S., Han, L., Ren, W., Liu, Y., and Wang, E. (2012) *Talanta*, **101**, 151–156.
102. Yang, Q., Pan, X., Huang, F., and Li, K. (2010) *J. Phys. Chem. C*, **114**, 3811.
103. Liu, J., Yang, W., Tao, L., Li, D., Boyer, C., and Davis, T.P. (2010) *J. Polym. Sci., Part A: Polym. Chem.*, **48**, 425.
104. Yang, H.F., Zhang, Q.X., Shan, C.S., Li, F.H., Han, D.X., and Niu, L. (2010) *Langmuir*, **26**, 6708.
105. Park, S., Mohanty, N., Suk, J.W., Nagaraja, A., An, J., Piner, R.D., Cai, W., Dreyer, D.R., Berry, V., and Ruoff, R.S. (2010) *Adv. Mater.*, **22**, 1736.
106. Zu, S.-H. and Han, B.-H. (2009) *J. Phys. Chem. C*, **113**, 13651.
107. Liu, S., Tian, J., Wang, L., Li, H., Zhang, Y., and Sun, X. (2010) *Macromolecules*, **43**, 10078.
108. Qi, X., Pu, K.Y., Li, H., Zhou, X., Wu, S., Fan, Q.-L., Liu, B., Boey, F., Huang, W., and Zhang, H. (2010) *Angew. Chem. Int. Ed.*, **49**, 9426.
109. Kim, T.Y., Lee, H.W., Kim, J.E., and Suh, K.S. (2010) *ACS Nano*, **4**, 1612–1618.
110. Kuila, T., Mishra, A.K., Khanra, P., Kim, N.H., Uddin, M.E., and Lee, J.H. (2012) *Langmuir*, **28**, 9825.
111. Reuven, D.G., Suggs, K., Williams, M.D., and Wang, X.-Q. (2012) *ACS Nano*, **6**, 1011.
112. Lim, H., Lee, J.S., Shin, H.J., Shin, H.S., and Choi, H.C. (2010) *Langmuir*, **26** (14), 12278–12284.
113. Lee, W.H., Park, J., Sim, S.H., Lim, S., Kim, K.S., Hong, B.H., and Cho, K. (2011) *J. Am. Chem. Soc.*, **133**, 4447–4454.
114. Chen, C., Zhai, W., Lu, D., Zhang, H., and Zheng, W. (2011) *Mater. Res. Bull.*, **46**, 583.
115. Hu, B., Quhe, R., Chen, C., Zhuge, F., Zhu, X., Peng, S., Chen, X., Pan, L., Wu, Y., Zheng, W., Yan, Q., Lu, J., and Li, R.-W. (2012) *J. Mater. Chem.*, **22**, 16422.
116. Kong, F.-Y., Li, X.-R., Zhao, W.-W., Xu, J.-J., and Chen, H.-Y. (2012) *Electrochem. Commun.*, **14**, 59.
117. Li, F., Bao, Y., Chai, J., Zhang, Q., Han, D., and Niu, L. (2010) *Langmuir*, **26**, 12314.
118. Liu, H., Gao, J., Xue, M., Zhu, N., Zhang, M., and Cao, T. (2009) *Langmuir*, **25**, 12006.

119. Wei, H., Li, Y.-Y., Chen, J., Zeng, Y., Yang, G., and Li, Y. (2012) *Chem. Asian J.*, **7**, 2683.
120. Li, X.L., Wang, X.R., Zhang, L., Lee, S.W., and Dai, H.J. (2008) *Science*, **319**, 1229.
121. Wang, Y., Shi, Z., and Yin, J. (2011) *ACS Appl. Mater. Interfaces*, **3**, 1127.
122. Shen, W., Yu, Y., Shu, J., and Cui, H. (2012) *Chem. Commun.*, **48**, 2894.
123. Long, B., Manning, M., Burke, M., Szafranek, B.N., Visimberga, G., Thompson, D., Greer, J.C., Povey, I.M., MacHale, J., Lejosne, G., Neumaier, D., and Quinn, A.J. (2012) *Adv. Funct. Mater.*, **22**, 717.

8

Immobilization of Metal and Metal Oxide Nanoparticles on Graphene

Germán Y. Vélez, Armando Encinas, and Mildred Quintana

8.1

Introduction

Graphene is a two-dimensional sheet of sp^2 -hybridized carbon atoms in a honeycomb lattice. The long-range π -conjugation in the graphene structure yields extraordinary thermal, mechanical, and electrical properties predicted by theoretical calculations. Recently, the isolation of a single-layer graphene made possible the observation of a large amount of these interesting physical properties, for example, graphene's ambipolar field effect [1], the quantum Hall effect at room temperature [2], extremely high carrier mobility [3], and the first ever detection of single-molecule adsorption event [4]. Besides, graphene is the thinnest known material and the strongest ever measured, it shows record thermal conductivity and stiffness, it is impermeable to gases, and it has the right proportion between brittleness and ductility [1–4]. These extraordinary properties have generated a huge interest in the possible application of graphene in a myriad of devices. To this end, one of the many strategies implemented for the use of graphene as a platform to develop new materials, is the immobilization of metal and metal oxide nanoparticles (NPs) on its surface [5]. The physical and chemical properties of NPs, such as large surface area and their interaction with the electromagnetic field, are of great interest in catalysis, optoelectronic devices, biotechnology, biomedicine, magnetic resonance imaging (MRI), environmental remediation, and so on [6]. It is generally accepted that the amazing properties of graphene might enhance the effects of NPs in the composite material. In this chapter, we describe the most representative approaches for the immobilization of metal and metal oxide NPs on graphene sheets (GSs) and some of the applications of the ensuing composite nanomaterials.

8.2

Graphene Production

There are a number of methods for generating graphene and chemically modified graphene [7]. Until now, most procedures have remained as demonstration

techniques, mainly for basic research and for providing proof of concept devices. However, a prerequisite for exploiting the proposed applications for graphene is the availability of processable GSs in large quantities [8]. Next, we briefly refer to the most commonly used procedures for graphene production.

8.2.1

Graphene Oxide (GO)

In the production of graphene-NP composites, the most common source for graphene is graphene oxide (GO) [9]. This material is produced through graphite exfoliation using strong oxidizing agents. The exact structure of GO is difficult to determine, but it is clear that the aromatic lattice of graphene is disrupted by the presence of epoxides, alcohols, ketone, carbonyls, and carboxylic groups. The existence of these moieties covalently attached to the graphene hexagonal lattice is reflected in its conductivity properties, making GO an isolator rather than conductor material.

8.2.2

Functionalized Graphene (f-Graphene)

The ultrasonication of graphite in different organic solvents such as *N,N*-dimethylformamide (DMF), *N*-methyl-2-pyrrolidone (NMP), benzyl benzoate, isopropyl alcohol, acetone, and mixtures of water surfactants has led to the production of stabilized graphene layers in dispersions [10]. This approach provides graphene on a more preparative scale, opening the way to solution/dispersion chemistry. With this, it is expected that many problems in graphene processing could be at least partially solved, for example, scalability, dispersibility, stability, and the control of the electronic structure by introducing chemical changes locally. In particular, graphene prepared as colloidal suspensions is especially prone to further chemical processing, for example, functionalization with molecules and NPs, which is advantageous for the synthesis of hybrid structures and composite materials. Colloidal graphene suspensions, before their transfer to solid substrates or their integration with other materials, have to be stabilized by means of molecular chemical derivatization or by supramolecular interactions, resulting in functionalized graphene (*f*-graphene) [5].

8.2.3

Graphene Growth on Metal Surfaces

Graphene films can be produced by chemical vapor deposition (CVD) or epitaxial growth on different metal surfaces. However, achieving large graphene domains with uniform thickness still remains a challenge. In addition, surface bonding may strongly affect the electronic properties of GSs [11].

8.2.4

Micromechanical Cleavage of Graphite

Micromechanical cleavage was the first method used for the isolation of graphene. The procedure involves rubbing the surface of a graphite crystal against another surface. This process results in a variety of flakes getting attached to the latter surface. From the resulting flakes, it is always possible to find single layers. Despite its simplicity, this technique results in graphene layers with a very low density and defects, keeping intact the main intrinsic properties of the single GS [12, 13]. However, this procedure is still considered a model technique for basic research. The laborious and time-consuming process of layer-by-layer cleavage is considered a major hurdle for scaling up this method to large-scale production.

A large number of publications have been produced in recent years that are related to the assembly and fabrication of graphene-NP nanohybrids that use one of the above techniques for the production of GSs. Next, we collate this information to discuss what we consider to be the most representative strategies for the immobilization of metal and metal oxide NPs on graphene layers.

8.3

Graphene Functionalized with Metal Nanoparticles (M-NPs)

Owing to the rich spectrum of physical properties added by different graphene-metal nanoparticles (M-NPs) such as Au, Pd, Pt, Ag, among others, M-NP composites can be designed for several important applications [6]. For example, graphene-Au NPs are used in the fabrication of optoelectronic devices, while composites of graphene functionalized with Pt are used as a catalytic system in the elaboration of fuel cells [14]. Most of the numerous methods that have been developed for immobilizing M-NPs on graphene layers are mainly based on three different strategies: (i) reducing a metal salt in the presence of GO [15, 16], (ii) anchoring the M-NPs on previously formed *f*-graphene [17–20], and (iii) the growth of M-NPs on graphene supported on diverse metal surfaces [21].

8.3.1

GO-Reducing Approach

There is no single route to immobilize M-NPs on GO. However, a general way to synthesize these composites can be seen in Figure 8.1. All procedures involve the reduction of a metal salt and GO. During the reduction process, the NPs grow and normally adhere to the GO surface [22]. Sodium borohydride (NaBH_4) and hydrazine hydrate (HH) are commonly used as reducing agents. The reduction process normally takes place rapidly with both solutions. However, it has been shown that reduced graphene oxide (*r*GO) exhibits higher conductivity when the

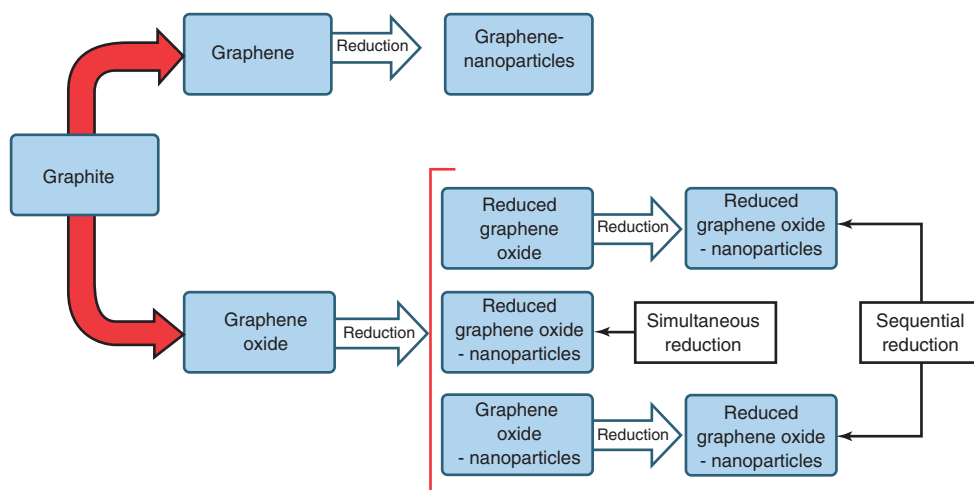


Figure 8.1 Experimental diagram for immobilizing M-NPs on the graphene layers.

reduction process is assisted by HH solution [23, 24]. In addition, reduction can be conducted in the presence of GO or rGO. The final product can be varied according to the required needs. For example, if the conductivity of the composite is important, then oxide content should be avoided in the final product [25].

8.3.1.1 Reduction Assisted by Sonication

Another method used for the immobilization of M-NPs on GO is reduction assisted by sonication. The advantage of this method lies in the stability achieved in the GO layers when reduced [26]. Several studies have demonstrated that sonication of metal salts in the presence of surfactants leads to the formation of M-NPs [27]. The sonication frequency used for this purpose normally ranges from 20 to 1000 kHz. However, it was found that the optimal reduction frequency, at least for Au salts, is approximately 200 kHz [28]. Another advantage of using high-frequency ultrasound is that the reduction of the GO and the metal salt can be carried out in two ways - sequential and simultaneous reduction [14]. Figure 8.2 shows transmission electron microscopy (TEM) images of GO-Au NP composites for sequential (a) and simultaneous reduction (b), respectively. The reduction was activated by ultrasound at a frequency of 211 kHz. For the sequential method, GO was reduced in a 2% aqueous solution of polyethylene glycol (PEG) for 3 h, then was mixed with a HAuCl₄ solution and the sonication was continued for a further 2 h. For simultaneous reduction, the solution containing GO and HAuCl₄ was sonicated for 4 h. As is seen in Figure 8.2, the morphology of GO-Au NP composites depends strongly on the route of oxidation. When the reduction is sequential, Au NPs are small and stick to the graphene surface in the form of small clusters; however, when the reduction is simultaneous, the particles are large and evenly and individually dispersed on the graphene surface [14].

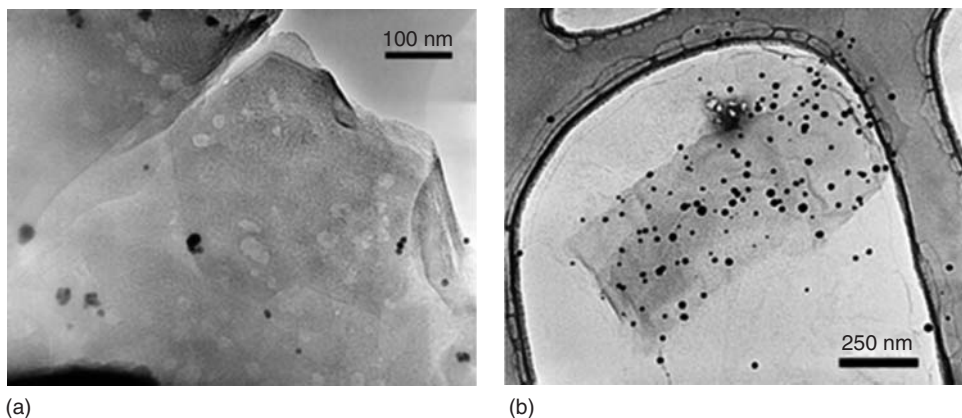


Figure 8.2 TEM micrograph of the rGO-Au NP composite at low resolution on a holey carbon grid; (a) corresponds to the sequentially reduced sample, while (b) corresponds to the simultaneous reduction. The initial HAuCl_4 concentration used was 0.1 mM in both cases. (Reprinted with permission from Ref. [14]. Copyright 2010 American Chemical Society.)

8.3.2

Anchoring NPs on *f*-Graphene

Chemical organic reactions are mainly performed on graphene for the production of stable dispersions. To this end, a successful approach is the reaction of dienophiles with the sp^2 carbon lattice of graphene. For example, azomethine ylides reacts through a 1,3-dipolar cycloaddition, a reaction performed for the functionalization of different carbon nanostructures such as fullerenes, nanotubes, onions, and nanohorns [29]. The reaction affords a variety of organic derivatives that display interesting applications in several areas including polymer composites, biotechnology, nanoelectronic devices, drug delivery, and solar cells. Thus, after the production of GSs dispersed in organic solvents by the ultrasonication of graphite, 1,3-dipolar cycloaddition was applied to the GSs by employing paraformaldehyde and a specifically designed NH_2 -terminated α -amino acid as precursors [17, 18]. The protonated terminal amino groups were shown to selectively bind Au nanorods (NRs), Figure 8.3. The presence of the particles reduced the aggregation of the final functionalized graphene-Au NP composites, as shown in Figure 8.3.

Later, the functionalization of exfoliated graphene in DMF using dendrons in two different reactions was completed with the 1,3-dipolar cycloaddition and amide-bond condensation reaction on the preexisting carboxylic groups [19]. The free amino groups at the tips of the dendrons act as ligands in the complexation of Au NPs, which were then introduced as contrast markers for the identification of the reactive sites. With this strategy, it was demonstrated that GSs could be selectively functionalized on the edges or in the entire lattice, Figure 8.4. For the 1,3-dipolar cycloaddition reaction, TEM images show Au NPs distributed all over the graphene surface. However, for the amidation reaction, the NPs seem to be

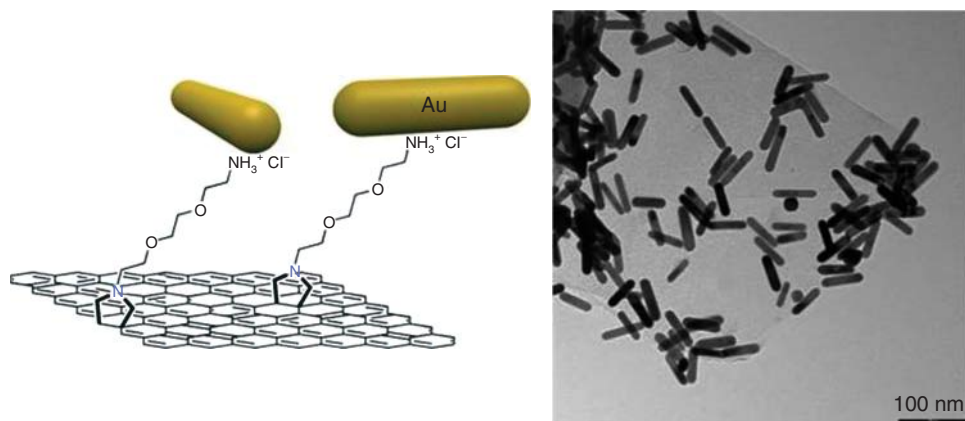


Figure 8.3 Anchoring of Au NPs on *f*-graphene sheets.

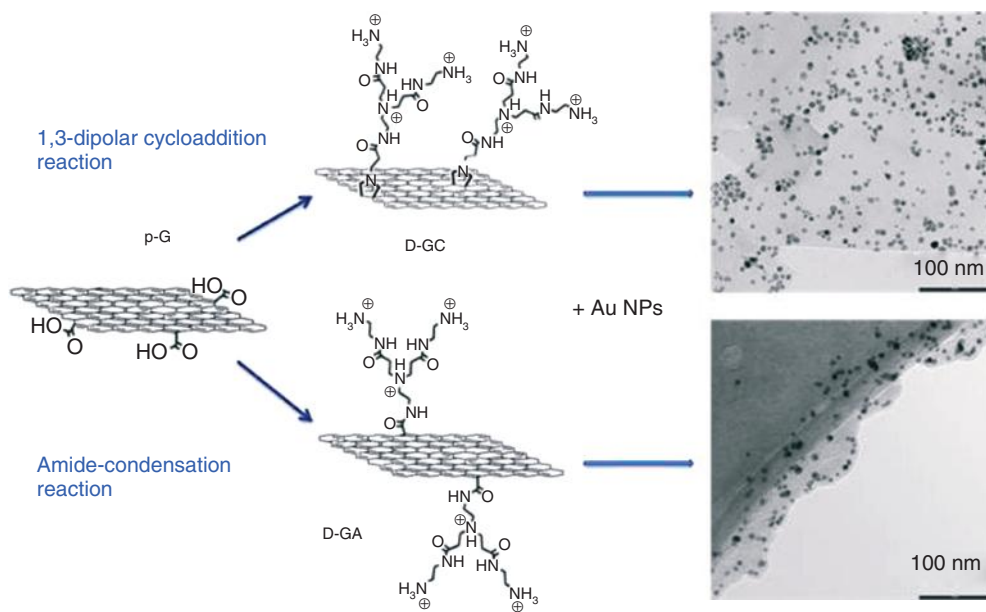


Figure 8.4 Selective functionalization of bulk graphene or graphene edges. p-G, pristine graphene; D-GC, graphene functionalized by a 1,3-dipolar cycloaddition

reaction; D-GA, graphene functionalized by an amide condensation reaction (Reprinted with permission from Ref. [19]. Copyright 2010 Royal Society of Chemistry.)

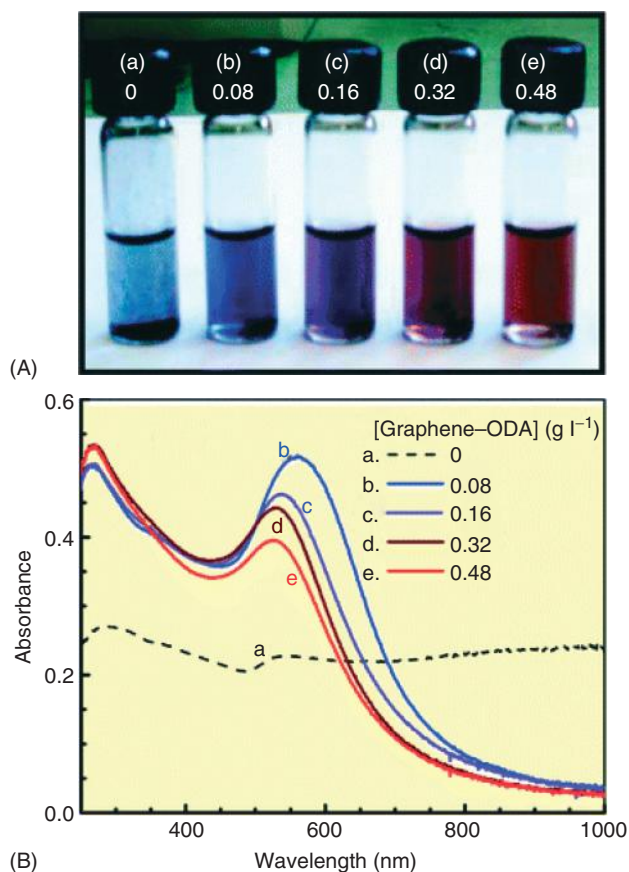


Figure 8.5 Photograph (A) and absorption spectra (B) of 1 mM Au NPs in THF containing different concentrations of graphene-ODA. (Reprinted with permission from Ref. [20]. Copyright 2008 American Chemical Society.)

deposited mainly at the edges of the exfoliated material. In the last material, the lack of functional groups and consequently of Au NPs in the central part of the sheets induced fast aggregation. Thus, an advantage of using *f*-graphene is the possibility of tuning the graphene properties for specifically desired applications.

In addition, the functionalization of graphene allows the controlled growth of the NPs. For example, Au NPs were obtained by AuCl_4^- chemical reduction in a NaBH_4 solution. Before the reduction process, the NaBH_4 solution was mixed with a suspension of graphene that had first been functionalized with octadecylamine (graphene-ODA) and dispersed in tetrahydrofuran (THF) [20]. This process was performed for five different concentrations of *f*-graphene in THF, 0, 0.08, 0.16, 0.32, and 0.48 g l^{-1} . A photograph of these five samples is presented in Figure 8.5A, while Figure 8.5B shows their corresponding absorption spectra. From the last graph, it

was possible to establish that the NP size depends on the concentration of graphene-ODA in THF. In this work, the authors observed that in the absence of *f*-graphene, Au NPs remain aggregated and deposited at the bottom of the THF solution. For higher concentrations of graphene-ODA, Au NP aggregates disappear and yielded individual NPs, this was reflected in the pronounced sharp surface plasmon absorption that corresponded to NPs with diameters between 10 and 20 nm.

8.3.2.1 Controlling Size of NPs

Evidently, in all nanosystems, the size of the NP is very important; an illustration focused on the study of the size of the NPs deposited on the graphene films is described next [21]. Graphene films were produced on an oxidized substrate by the method of micromechanical cleavage. Then, a 0.3 nm layer of gold was deposited on its surface using a thermal evaporation method. Finally, Au NPs were formed on the graphene surface after a heating treatment that consisted of annealing the samples at 400 °C for 3 h in a controlled atmosphere. Using this procedure, Luo *et al.* demonstrated that the mean diameter of the Au NPs depends on the number of layers of GSs. This fact was observed in high-resolution scanning transmission microscopy (HR-SEM) images for films with one-, two-, and three-layer thickness (Figure 8.6a). By plotting the mean Au NP diameter, D , as a function of film thickness, m , the authors adjusted their observations to a theoretical model (Figure 8.6b). The model is based on the long-range electrostatic interactions that are a consequence of charge exchange between the graphene and the Au NPs.

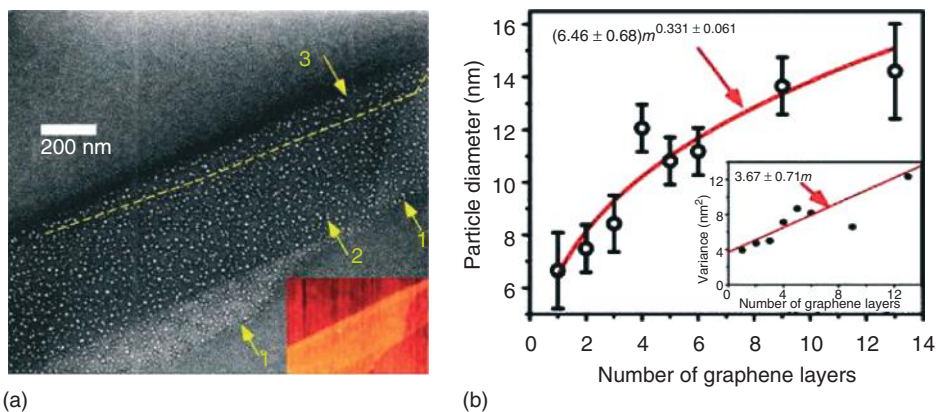


Figure 8.6 (a) HR-SEM images of Au NPs prepared on graphene with few layers on a SiO_2/Si substrate. The numbers and arrow indicate the number of graphene layers. The inset is the atomic force microscope (AFM) image of the same region before nanoparticle growth. (b) Average diameter of Au NPs as a function of the number of graphene layers. The red line is a power law fit suggested

by theory. The inset is the corresponding dependence of the variance of the diameter distribution; the curve shows the theoretically predicated linear dependence. The data points for nine layers are shown in the graph but omitted from the fit. (Reprinted with permission from Ref. [21]. Copyright 2010 American Chemical Society.)

These interactions limit the growth of NPs and predict that the dependence of the particle diameter with respect to the film thickness is of the form:

$$D = Am^{\nu} \quad (8.1)$$

where, in this case, $A = 5.9$ nm and $\nu = 1/3$. A polynomial fit of the experimental data shown in the inset of Figure 8.6b leads to $A = 6.46 \pm 0.67$ nm and $\nu = 0.33 \pm 0.06$, in agreement with the theoretical prediction. Experimentally, HR-SEM images established that the surface morphology of graphene depends considerably on its thickness. When the thickness of the graphene film was about 700 lines, the diameter of the Au NPs was between 100 and 300 nm and their faces were oriented preferentially. For graphene films with few lines, the situation was completely different. The NP density on the surface of graphene was increased while the diameter of the NPs was observed to range between 5 and 20 nm, with the particle shape spherical, and so no preferential orientation was observed.

8.3.3

Applications of M-NPs/Graphene Nanohybrids

8.3.3.1 Optoelectronic Devices

The high transparency and good conductivity of graphene, make it an excellent candidate for the development of optoelectronic devices [15, 30]. However, besides these qualities, semiconductor optoelectronic devices must have a high charge carrier flow between the electrodes and the semiconductor layer; this is achieved by controlling the work function of the electrode [31]. The immobilization of Au NPs on the surface of graphene allows this. Experiments have shown that the work function depends on the time of deposition of the Au NPs [32]. To this end, graphene was obtained by the CVD method and then it was placed in an aqueous solution of AuCl_4^- for inducing reduction of the metal salt and obtaining decorated graphene (graphene-Au NPs). The reduction process (or doping) is performed for times ranging between 0 and 1200 s. By means of scanning Kelvin probe microscopy (SKPM) measurements, it was established that the work function of the graphene-Au NP films can be modified with time doping; specifically, it was observed that the surface potential of the Au NPs is larger than that of graphene. This observation suggested that doping in the GSs is p-type and indicates that the work function changes with doping. Thus, photodetector diodes can be fabricated using graphene-Au NP composites. Building electrodes with tunable work function significantly improves the performance of these devices. Figure 8.7a shows the current density as a function of voltage applied for photodetector diodes fabricated with electrodes of pristine graphene and graphene-Au NPs produced by doping for 20 s. Measurements were performed with and without the AM (air mass coefficient, solar energy) at 1.5 illumination. Before the AM 1.5 illumination, both devices exhibit the characteristic curve of a diode. However, in the device elaborated with graphene-Au NPs, the open-circuit voltage is greater than that in the device elaborated with pristine graphene. When the devices were illuminated, the differences between them were more drastic. In graphene-Au NPs, both the short-circuit current and

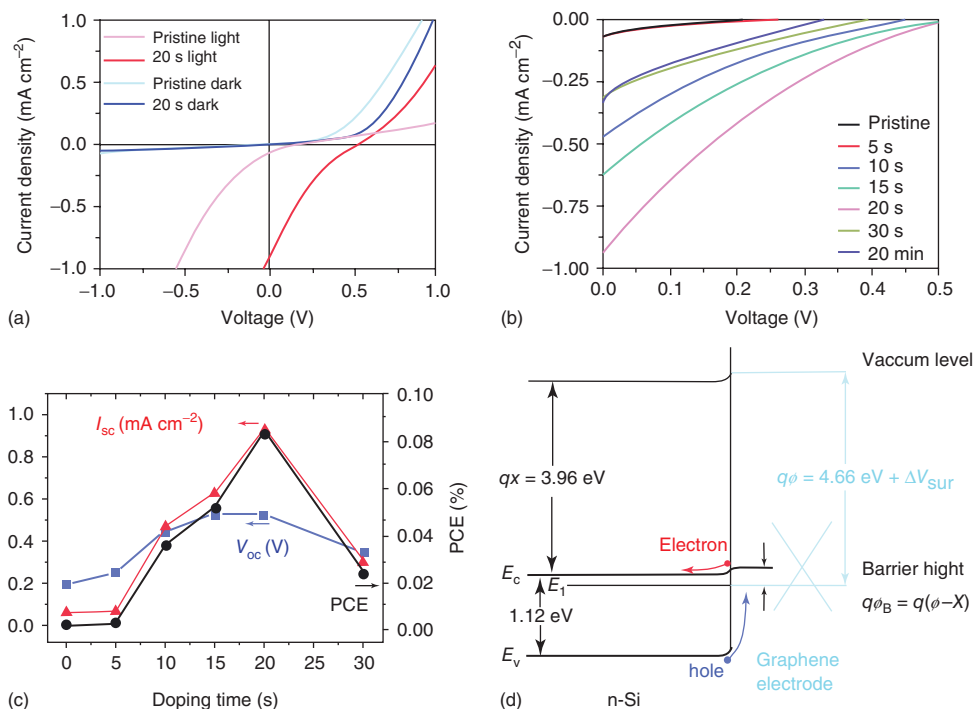


Figure 8.7 (a) Typical electrical measurement of pristine and 20 s AuCl_3 doped CVD-G/n-Si photovoltaic devices; (b) current-voltage plots of the devices with different doping times from 5 s to 20 min under AM 1.5 illumination; (c) comparison of I_{sc} ,

V_{oc} , and PCE for different doping times; and (d) schematic illustration of the photovoltaic devices' band energy diagram (values obtained from Ref. [33]). (Reprinted with permission from Ref. [32]. Copyright 2010 American Chemical Society.)

the open-circuit voltage were much higher than in the device produced with the pristine graphene film. The behavior of the current density as a function of voltage for the device elaborated with different Au NPs doping is shown in Figure 8.7b. It can be clearly seen that 20 s doping yields the highest short-circuit current and open-circuit voltage. From Figure 8.7c, it can be observed that the evolution with respect to doping time of three quantities that characterize the performance of a photovoltaic diode, namely, the short-circuit current (red line), the open-circuit voltage (blue line), and the power converter efficiency (PCE, black line), evidently shows that the best performance was obtained when the electrodes of photovoltaic diode have been doped for 20 s. This result is in agreement with results obtained by the SKPM where the largest shift was obtained in the surface potential for 20 s doping. The authors also found that the doping time affects the amount and size of the Au NPs deposited on the graphene surface. The graphene-Au NP electrodes depend on the surface morphology, hence controlling the size of the Au NPs deposited on the graphene surface will optimize the performance of optoelectronic devices.

8.3.3.2 Applications in Catalysis

Important technological applications arise when it is possible to obtain materials with high specific surface area [1–4]. Among the most important is the development of catalyst materials that are used in the production of fuel cells. In recent years, Pt and other precious metals have been used as catalysts in fuel cells; however, with the arrival of graphene, new materials with indisputable advantages have been developed. Besides, these new materials have high catalytic surface, they reduce the use of costly metals, and present higher catalytic activity [33–35]. Usually, catalytic activity depends directly on the specific surface area of the composite, which is related to the dispersion, the size of the deposited NPs, and so on. For example, the optimal size of Pt NPs for electrocatalysts used in fuel cells has been determined to in range 3–5 nm [34].

One way to determine whether a material is a good or bad catalyst is to measure its electrochemically active surface area (ECSA); this is easily achieved through cyclic voltammetry (CV) measurements. Electrodes made from graphene-Pt are the most used to develop proton exchange membrane (PEMs) fuel cells [25] and direct methanol fuel cells (DMFCs) [34, 36]. In the PEM fuel cell, electricity is produced through oxidation of hydrogen on the catalyst system, while methanol is the fuel used in the DMFC. We illustrate each case with an example.

The PEM fuel cell was prepared by the simultaneous addition of H_2PtCl_6 and GO in a NaBH_4 reduction [25]. This resulted in Pt NPs adhering partially to the surface of the rGO. The material obtained was used to cover a glassy carbon electrode for which the ECSA was measured. These measurements were compared with two other electrodes that differed only in their coating. One electrode was coated with Pt,

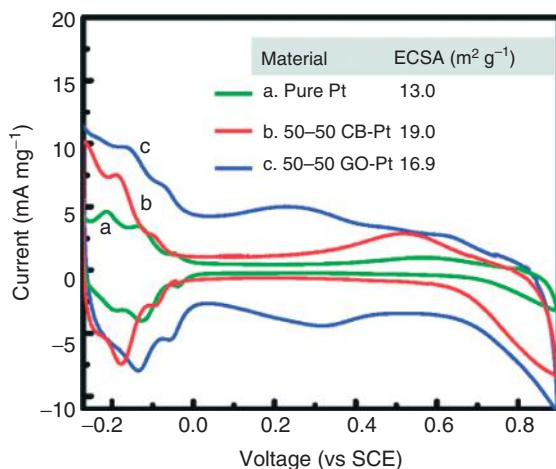


Figure 8.8 Cyclic voltammetry graphs of Pt, 50–50 (by weight) carbon black-Pt, and 50–50 (by weight) partially reduced graphene oxide-Pt. Twenty micrograms per square centimeter of Pt was deposited on each

electrode. 0.1 M H_2SO_4 was used as the electrolyte and the scan rate was 20 mV s^{-1} . (Reprinted with permission from Ref. [25]. Copyright 2009 American Chemical Society.)

while the other was coated with a carbon black film decorated with Pt NPs. Figure 8.8 shows the voltammetry cycles for the three electrodes. The values of ECSA were obtained from these curves. The GO-Pt NP electrodes exhibit higher ECSA than Pt NP electrodes but less than the carbon black-Pt NP electrodes. A further reduction assisted by HH was performed in order to completely reduce the GO. This process was followed by a heat treatment that considerably improved the conductive properties of the GO-Pt NP composite. To optimize the heat treatment time, rGO samples were annealed at 300 °C for different time intervals (2, 4, 8, and 16 h). New electrodes were prepared with these samples in a substrate of Toray™ carbon paper instead of a glassy carbon substrate. Figure 8.9 shows the cyclic voltammogram of these new electrodes. The inset in the figure shows the relative increase in ECSA as a function of annealing time. Before the heat treatment, these electrodes exhibited an ECSA of 11.5 m² g⁻¹. Later it was observed that ECSA decreases during the first few hours of annealing; however, when 8 h of annealing was reached, the highest relative increase (80%) was achieved, equivalent to an ECSA of approximately 20 m² g⁻¹.

For the DMFC [37], the NPs adhered to the graphene layers by the simultaneous electrochemical reduction of GO and H₂PtCl₆. The SEM images, not presented here, confirmed the high dispersion of NPs in the electrodes, as well as a mean diameter of approximately 10 nm. The authors also used GO and metal salt sequential reduction, but the dispersion of the NPs was poor and their mean size greater than 200 nm. Thus, only those electrodes that were produced by simultaneous reduction were useful in the preparation of DMFC. Electrocatalytic activity of the GO-Pt NP electrodes was studied in comparison with conventional Vulcan-Pt electrodes using oxidation of methanol as a model. In Figure 8.10a, the cyclic voltammogram for both catalysts

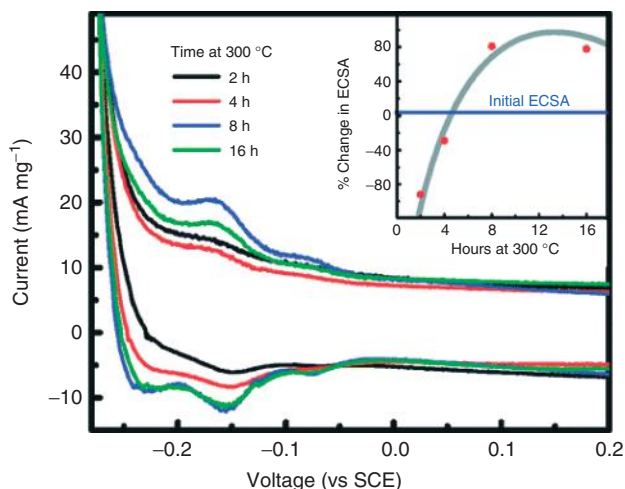


Figure 8.9 Cyclic voltammograms of hydrazine-treated GO-Pt in 0.1 M H₂SO₄ and annealed at 300 °C for different periods of time (scan rate = 20 mV s⁻¹ and catalyst concentration = 10 μg cm⁻² of Pt). The inset

shows the relative increase of ECSA in these samples. (Reprinted with permission from Ref. [25]. Copyright 2009 American Chemical Society.)

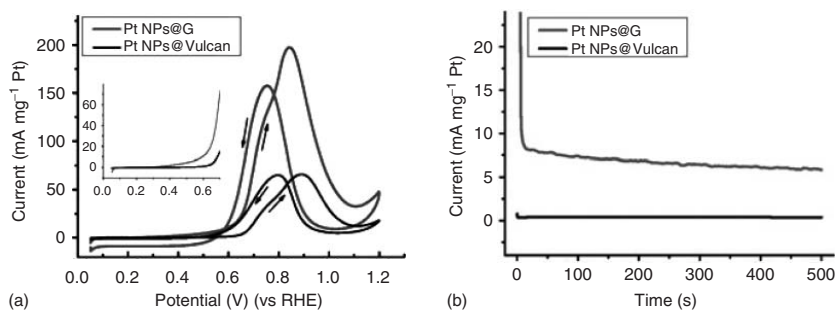


Figure 8.10 (a) CVs of Pt NPs@G/GCE (glassy carbon electrode) and Pt NPs@Vulcan/GCE in a N_2 -saturated solution of 0.5 M H_2SO_4 solution containing 1 M CH_3OH at a scan rate of 10 mV s^{-1} . The inset shows the zoom-in CV in the potential range from 0.05 to 0.80 V and (b) current-time profiles of these electrodes at 0.6 V (vs reversible hydrogen electrode, RHE) in a N_2 -saturated solution of 0.5 M H_2SO_4 solution containing 1 M CH_3OH . (Reprinted with permission from Ref. [37]. Copyright 2010 Royal Society of Chemistry.)

are shown. The peak current for electrooxidation of methanol was approximately three times larger in the GO-Pt NP electrode ($197 \text{ mA mg Pt}^{-1}$) than in the Vulcan-Pt electrode (67 mA mg Pt^{-1}). The inset in the figure shows that the onset potential for the electrooxidation of methanol was lower in GO-Pt NP electrodes (0.35 V) than in Vulcan-Pt electrodes (0.60 V). From the current versus time graph (for an operating voltage of 0.6 V) shown in Figure 8.10b, it is observed that GO-Pt NP electrodes exhibit higher current flow and good stability over time. The findings clearly demonstrated that GO-Pt NP composites exhibit superior electrocatalytic activity toward the electrooxidation of methanol rather than Vulcan-Pt composites.

8.3.3.3 Applications in Biology

Raman spectroscopy is a widely used technique for the identification of materials, in particular, for large molecules. When the molecule has a small cross section, normally, the Raman signal is weak. Surface-enhanced Raman spectroscopy (SERS) can improve the sensitivity in the detection of molecules. The SERS concept dates from 1977 [38], however 3 years before that the first enhancement media [39], commonly known as the *SERS substrate*, had already been obtained.

Recently, Huang *et al.* [40] have used the SERS technique to study the cellular uptake of GO-Au nanocomposites. Au NPs and GO were used as SERS proof and SERS substrate, respectively. Au NPs were prepared according to Frens' approach [33] and then covered with *meso*-2,3-dimercapto-succinic acid (DMSA). On the other hand, GO was functionalized with PEG to ensure stability of the GO-Au NP structure inside the cell. The GO-Au NP hybrid was consolidated after stirring a solution that contained Au NPs, GO-PEG, and *N*-ethyl-*N'*-[(dimethylamino)-propyl]carbodiimide hydrochloride (EDC) for 48 h.

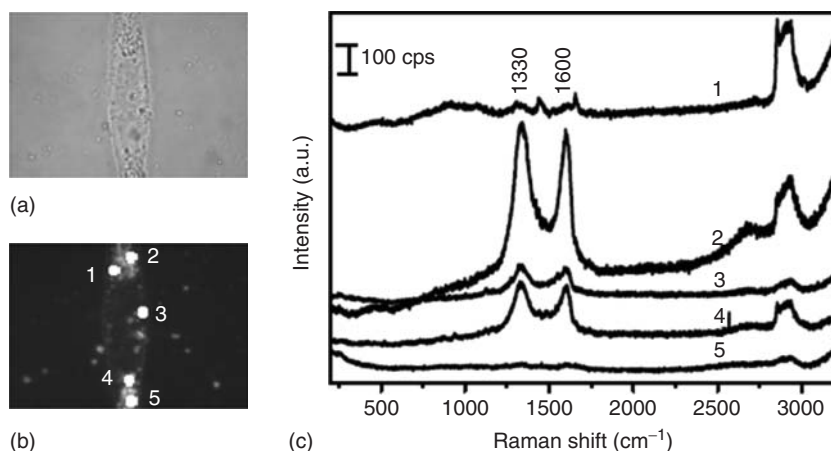


Figure 8.11 (a) Bright- and dark-field microscopic images of Ca Ski cells incubated with Au-GO for 4 h. (c) Raman spectra of the different spots marked in (b) in the Ca Ski cell. (Reprinted with permission from Ref. [40]. Copyright 2012 Wiley-VCH.)

Ca Ski cells (Human Caucasian cervical carcinoma) were incubated with GO and bright- and dark-field microscopy images confirmed the presence of GO inside the cell; but in the Raman spectra performed in places where the GO appeared, the peaks corresponding to the D- and G-bands of graphene were not detected. Instead, when Ca Ski cells were incubated with GO-Au NPs the presence of GO-Au NP hybrids inside the cell was also noted (Figure 8.11a,b). Figure 8.11c shows the Raman spectra taken at different points marked in the dark-field microscope image (Figure 8.11b). Peaks at 1330 and 1600 cm^{-1} (peaks D and G), characteristic of graphene are clearly observed in the spectra, which confirms that the Au NPs act as SERS substrate. The variation in the intensity of the peaks D and G are evidence of the inhomogeneous distribution of graphene within the cell. The results obtained by Huang *et al.* allow the use of SERS technique in the study of intracellular events owing its high spatial resolution.

8.4

Graphene Functionalized with Metal Oxide Nanoparticles

The present technological revolution requires the elaboration of rechargeable electric batteries with good features. For example, cell phones, electronic agendas, photocameras, lap tops, and cars require these devices. A high ability to store charge, discharge resistance, and long shelf life are some of the essential features for a good rechargeable electric battery. At present, these needs are supplemented by lithium ion batteries. Nevertheless, efforts are constantly being made to improve their properties, specifically by working on ways to improve the physical properties of the cathodes and anodes that are responsible for storing electric charge. Recent progress in graphene/metal oxide composites highlights the importance of synergistic effects between these nanomaterials for the development of new batteries [41, 42].

8.4.1

Lithium Batteries

Recent studies have shown that the performance of lithium ion batteries can be improved when the anodes are made with graphene- SnO_2 NP composites as the excellent physical properties of graphene along with the high capacity of SnO_2 make the resulting material highly efficient [43]. Although replacing carbon-based materials by graphene leads to better results, the deposition of metal oxides on GSSs is not easy owing to the poor interaction between them; hence, there is a need to design efficient methods for synthesizing these materials. Usually, it is desired to obtain a significant number of particles attached to GSSs as well as high dispersion of the particles.

Recently, a very efficient method was developed to attach SnO_2 NPs to graphene monolayers. In this method, the amount of SnO_2 in the anode was close to 65%, almost three times greater than that obtained in carbon nanotube material (CNT- SnO_2)-based anodes, leading to improved stability of the anode during charge and

discharge cycles [44]. Graphene-SnO₂ composites were obtained by two simple steps: initially, GO was produced by the modified Hummer method [9]. GO was then mixed with water, producing GO monolayers highly dispersed in the solution owing to the presence of oxygenated groups. By the addition of SnCl₂ solution, Sn⁺² ions bonded to oxygen groups. This was followed by washing with deionized water and SnO₂ NPs were formed that were attached on both sides of the GO monolayer. In order to increase the conductivity of the composite, it was necessary to reduce the presence of oxygenated groups. Reduction was carried out by a heat treatment. After chemical reduction, oxygenated groups still existed in a small proportion, however, the presence of these favored the high dispersion of SnO₂ NPs on the graphene surface as confirmed by the high-resolution transmission electron microscopy (HR-TEM) images that showed NPs with an average size of 3 nm. Li ion batteries with graphene-SnO₂ anodes exhibited improved electrochemical properties compared to the batteries made from other materials. For example, in graphene-SnO₂ (60% SnO₂) and CNT-SnO₂ (25% SnO₂) anodes the initial capacity was 786 and 720 mAh g⁻¹, and after 50 cycles, approximately 71% and 61% of the initial charge was retained, respectively (Figure 8.12).

A very interesting approach for the elaboration of anodes for Li ion batteries is based on the use of Mn₃O₄ as precursor material [42]. Although this oxide has low conductivity, it is an attractive material mainly due to its elevated natural abundance and consequentially, low cost. Anodes made with Mn₃O₄ have little ability to store electric charge; it has been experimentally determined that about 300 mAh g⁻¹ decays to 38% of its initial value after 10 cycles of operation. The advantages of using Mn₃O₄ appear when it is functionalized with few layers graphene. Anodes prepared under these conditions exhibit superior performance, that is, the storage capacity doubles in values and the anodes showed stable performance during the charge and discharge cycles. For the production of this material, GO was obtained by the modified method of Hummer [9]. Graphene-Mn₃O₄ anodes were then

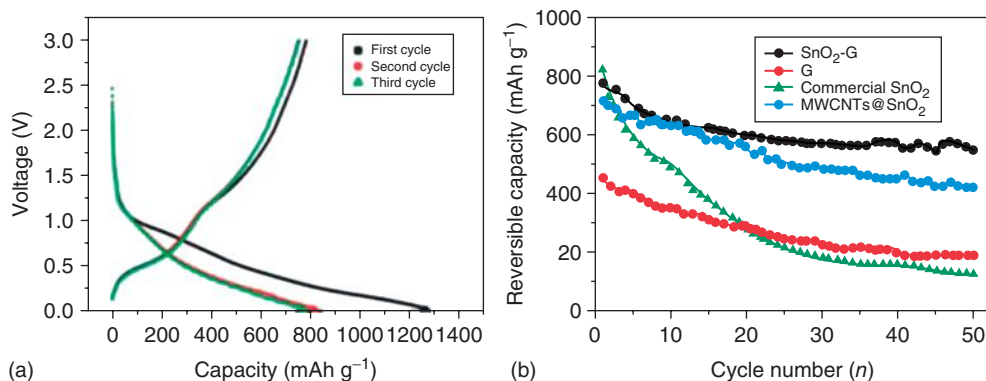


Figure 8.12 (a) A charge/discharge profile of the SnO₂-G composite and (b) the cycle performance of SnO₂-G, commercial SnO₂, and as-prepared G at a rate of C/5. (Reprinted with permission from Ref. [44]. Copyright 2010 Royal Society of Chemistry.)

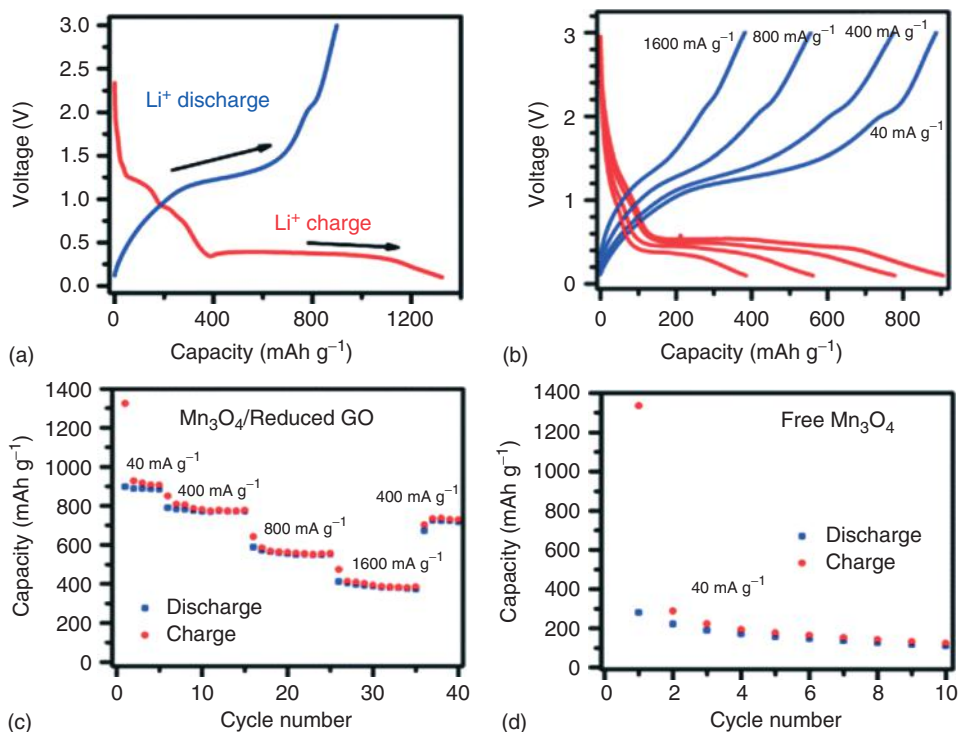


Figure 8.13 Electrochemical characterizations of a half-cell composed of Mn₃O₄/rGO and Li. The specific capacities are based on the mass of Mn₃O₄ in the Mn₃O₄/rGO hybrid. (a) Charge (red) and discharge (blue) curves of Mn₃O₄/rGO for the first cycle at a current density of 40 mA g⁻¹; (b) representative charge (red) and discharge (blue) curves

of Mn₃O₄/rGO at various current densities; (c) capacity retention of Mn₃O₄/rGO at various current densities; and (d) capacity retention of free Mn₃O₄ nanoparticles without graphene at a current density of 40 mA g⁻¹. (Reprinted with permission from Ref. [42]. Copyright 2010 American Chemical Society.)

produced, with the first step consisting in the hydrolysis of GO and Mn(CH₃COO)₂ assisted by a solution of DMF and water. Mn₃O₄ NPs adhering to the GO layers were thus obtained [41]. The reduction of GO was conducted by a hydrothermal treatment in which the solution obtained in the first step was mixed with deionized water and heated to 180 °C for 10 h. The final product consisted of Mn₃O₄ NPs highly dispersed on the graphene layers. Through SEM and TEM images, the size of the Mn₃O₄ NPs was determined to range between 10 and 20 nm.

Figure 8.13 shows some electrochemical measurements performed in Li ion battery anodes made from graphene-Mn₃O₄. Some interactions between the materials making up the battery can be observed through the profiles of the first charge and discharge cycle (Figure 8.13a). The behavior between 1.2 and 0.4 V during the first charge cycle was due to the irreversible reaction between Li⁺ ions and rGO as well as to the decomposition of the electrolyte solvent. The

plateau observed close to 0.4 V reflects the interactions between Li^+ and Mn_3O_4 . During the first discharge cycle a plateau due to the reverse reaction also appeared close to 1.2 V. After several cycles of operation, the charge-discharge profiles were measured for different current densities (Figure 8.13b). From Figure 8.13, it can be observed that, during the charging process, the potential of the anodes decreases as current density increases, while during the discharge process, the potential increases with current density. Figure 8.13c shows the behavior of the specific storage capacity as a function of the number of operating cycles. The storage capacities reported in Figure 8.13 were calculated relative to the mass of Mn_3O_4 and not with respect to the total mass of the hybrid. Figure 8.13 also shows that the initial storage capacity of the anode is 900 mAh g^{-1} for a current density of 40 mA g^{-1} . An important fact to be noted is that storage capacity remained stable with the number of cycles and decreased to 390 mAh g^{-1} when the current density was increased to 1600 mA g^{-1} . Then 50 cycles of operation the measurement was performed with a current density of 400 mA g^{-1} and the anode retained approximately 81% of the initial charge. Through Figure 8.13d the performance of graphene- Mn_3O_4 anode can be compared with that of Mn_3O_4 anode, where the storage capacity decreased from 300 to 115 mAh g^{-1} in only 10 cycles of operation.

Other materials based on graphene and metal oxides such as CuO , Co_3O_4 , CoO , Fe_3O_4 , TiO_2 , and $\text{Li}_4\text{Ti}_5\text{O}_{12}$ have also shown interesting electrochemical properties for the development of lithium ion batteries [45–49]. The current goal in this field is to obtain anodes with larger storage capacity as well as a good performance of the device for long operating cycles. In some cases, the aim is to optimize the process variables, such as the size of the metal oxide NPs and graphene concentration, whereas in other cases, the objective is simply to find a new material.

8.4.2

Optical Properties

TiO_2 and ZnO are currently considered to be excellent photocatalytic materials. This is due to their easy electric response when they are subjected to UV irradiation. In addition, these semiconductor materials offer other interesting features such as thermal stability and nontoxicity. Under UV illumination, electrons of the valence band are excited to the conduction band, creating electron-hole pairs. The energy required to produce such excitement in TiO_2 and ZnO is approximately 3.1–3.6 and 3.4 eV, respectively [50–52].

Several applications have arisen from these optical properties; however, there are two limitations when these oxides are used as photocatalysts. The first is the rapid recombination between the electrons and holes, while the second has to do with the small amount (approximately 5%) of UV radiation contained in sunlight. Both aspects reduce the efficiency of the photocatalyst and therefore preventing recombination of electrons and holes as well as expanding the range of light absorption to the visible region are two objectives to take into account in the development of new photocatalytic materials. With this aim, TiO_2 has been doped with different

elements, including precious metals such as Pt, Au, and Ag [53–55], nonmetallic elements such as S, N, and C [56–58], and even carbon-based composites [59, 60].

Since the photocatalytic behavior of carbon-semiconductor-based composites was good, it was expected that graphene could also serve as a support for the semiconductor particles. In these structures, graphene acts as an efficient means to transport electrons, thus preventing electron-hole recombination. Applications of graphene-based photocatalysts are innumerable, for example, graphene-TiO₂ and graphene-ZnO nanostructures are used in the production of hydrogen by water splitting [61], degradation of organic solvents [62], and optoelectronic devices [63]; they are even used as photocatalytic reducers [51, 64, 65]. Herein, we discuss some examples.

8.4.2.1 Water Splitting

TiO₂ thin films have been used as materials for the photocatalytic water splitting [66] as in this material the photoelectrons generated through UV irradiation have sufficient energy (~ 2 eV) to split water and produce oxygen and hydrogen. The efficiency of the TiO₂ photocatalyst is affected by the rapid photogenerated recombination of electrons and holes. However, this limitation was overcome when graphene was added as precursor material. Figure 8.14 shows that the amount of hydrogen produced is dependent on the concentration of graphene in the photocatalyst. With the TiO₂ photocatalyst, hydrogen is produced at a constant rate of 4.5 mol h^{-1} , photocatalyst efficiency increases to a maximum (8.6 mol h^{-1}) when the concentration of graphene is 5 wt%. For higher concentrations of graphene, the hydrogen production is less efficient, probably because an excess of graphene favors collisions between the charge carriers, which leads to recombination between electron-hole pairs. Graphene-TiO₂ NPs composites were synthesized by the hydrolysis of tetra-butyl orthotitanate (TBOT) in a dispersion of rGO followed by a short

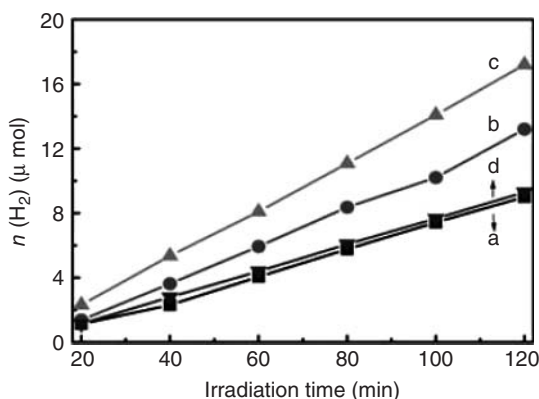


Figure 8.14 Reaction time profiles of H₂ evolution under UV-vis illumination over the photocatalysts using 200 ml 0.1 mol l^{-1} Na₂S to 0.04 mol l^{-1} Na₂SO₃ as a sacrificial agent: P25 (a), TiO₂/1 wt% GSs (b),

TiO₂/5 wt% GSs (c), and TiO₂/10 wt% GSs (d). (Reprinted with permission from Ref. [61]. Copyright 2010 Royal Society of Chemistry.)

heat treatment (450 °C for 2 h). GO was obtained by the method of Hummer [9] and the chemical reduction was assisted by NaBH₄ [61].

8.4.2.2 *f*-Graphene-POM

In a completely different approach, inorganic components are synthesized in advance and then attached to the surface of graphene via linking agents that utilize covalent or noncovalent interactions (van der Waals interactions, hydrogen bonding, π - π stacking, or electrostatic interactions). In this approach, either the inorganic components or graphene (or both) require modification with functional groups, as we have previously described. The type of functionalization and thus, the strength of interaction, determine the loading of the inorganic nanomaterials on the graphene surface. This self-assembly-based method is excellent at overcoming any incompatibilities between nanomaterials syntheses and the formation of nanocomposites. Compared to *in situ* growth, a better distribution, size, and feeding amount control of the second components on graphene could be obtained by the self-assembly of NPs on *f*-graphene. Using this method, we have produced *f*-graphene with a tailored distribution of polycationic, quaternized, ammonium pendants that provided an sp² carbon nanoplatform to anchor a totally inorganic tetraruthenate catalyst, mimicking the oxygen-evolving center of natural PSII in photosynthetic systems, Figure 8.15 [67]. The resulting hybrid material displayed oxygen evolution at overpotential as low as 300 mV at neutral pH with negligible loss of performance after 4 h testing. This multilayer electroactive asset enhances the turnover frequency by 1 order of magnitude with respect to the isolated catalyst, and provides a definite upgrade of the carbon nanotube material, with a similar surface functionalization.

8.4.3

Photocatalytic Reduction of GO

Photocatalytic reduction of GO was possible by UV irradiation of both TiO₂ [50] and ZnO NPs [63]. When the semiconductor was irradiated in the presence of methanol, the holes are scavenged to produce ethoxy radicals, while electrons were accumulated within semiconductor NPs. Subsequently, the electrons reacted with certain functional groups of GO and caused its reduction. The above reactions for the TiO₂ and ZnO can be expressed as follows:



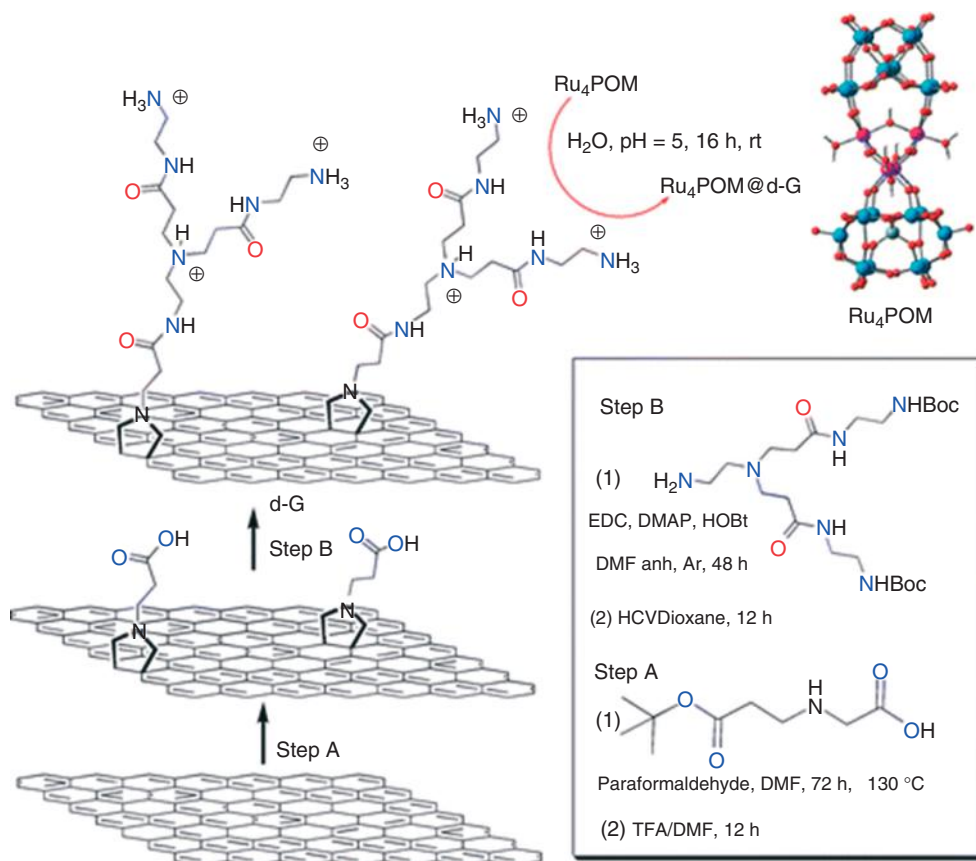


Figure 8.15 Synthesis of graphene nanoplatform supporting Ru_4POM (polyoxometalate). Reagents and conditions: Step A: (1) paraformaldehyde, N,N -dimethylformamide (DMF), 72 h, $130\text{ }^\circ\text{C}$; (2) trifluoroacetic acid/ N,N -dimethylformamide, 12 h, room temperature. Step B: (1)

dendron **d**, N -(3-dimethylaminopropyl)- N_0 -ethylcarbodiimide, 4-(dimethylamino)pyridine, 1-hydroxybenzotriazole, anhydrous N,N -dimethylformamide, 48 h, room temperature, inert atmosphere. (Reprinted with permission from Ref. [67]. Copyright 2013 American Chemical Society.)

In addition to the reduction of the GO, it was possible to estimate the number of electrons transferred to the GO through measures of UV-absorption and UV-decay, both per unit mass of GO [63] as well as per unit time [42], respectively. In essence, the procedure to reduce the GO did not differ with the semiconductor employed: in both cases, a suspension of ethanol that contained the semiconductor NPs and GO was irradiated. The suspension was stirred constantly through nitrogen bubbles to ensure uniform irradiation. Semiconductor NPs were obtained by hydrolysis using titanium isopropoxide ($Ti(OCH(CH_3)_2)_4$) and zinc acetate ($Zn(O_2CCH_3)_2$), respectively, as precursor materials.

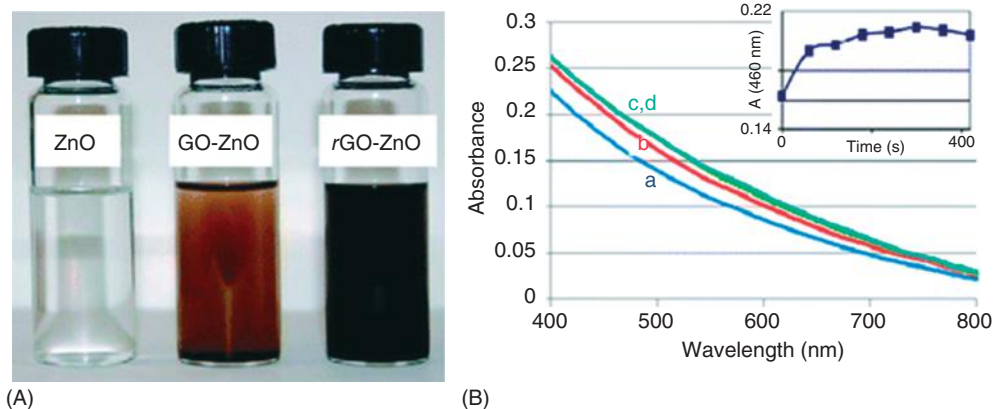


Figure 8.16 (A) Suspensions of ZnO, ZnO-GO, and ZnO-rGO. The color changes from brown (middle vial) to dark brown (right vial) as we irradiate the ZnO-GO sample with UV light. (B) Absorption spectra of 0.5 mg/ml GO and 1 Mm ZnO in deaerated ethanol at different UV irradiation times of (a) 0 s, (b) 60 s, (c) 180 s, and (d) 420 s. The inset shows the growth of absorption with UV irradiation time. (Reprinted with permission from Ref. [50]. Copyright 2009 American Chemical Society.)

Figure 8.16a illustrates the color change when the GO-ZnO composite suspended in ethanol was irradiated. This color change from light brown to black indicates partial restoration of the π -network in the GSs, which occurs in the chemical reduction of GO. In the absence of ZnO, the ethanol-GO solution remained unchanged in color, indicating that the reduction of GO was assisted by semiconductor NPs. As shown in Figure 8.16b, UV light absorption of the GO-ZnO nanocomposite increased when the irradiation time increased from 0 to 420 s. In the inset to the figure, the variation of the absorption with respect to time of exposure to irradiation for a wavelength of 460 nm is shown. The absorption increased during the first 200 s of exposure and from there on remained approximately constant. GO-TiO₂ nanocomposites exhibited a change in color behavior similar to that observed in Figure 8.16.

According to Equation 8.2a, TiO₂ accumulates electrons when irradiated in the presence of ethanol. If the composite is irradiated to trap a maximum number of photoelectrons and then GO is added to the suspension, photocatalytic reduction process starts and the number of electrons trapped in the TiO₂ decreases with GO concentration. This behavior was clearly seen in the absorption spectrum of the TiO₂ composite that had previously been irradiated until absorption saturation (Figure 8.17A). Monitoring the behavior of the intensity of this peak with respect to the GO content and using the molar absorbance of electrons trapped in TiO₂ at 650 nm (760 M⁻¹ cm⁻¹), it was possible to establish that there is a linear relationship between the number of electrons involved in the reduction and the amount of rGO. Through a linear fit, it is estimated that about 0.01 mol of electrons are required to reduce 1 g of GO (Figure 8.17B).

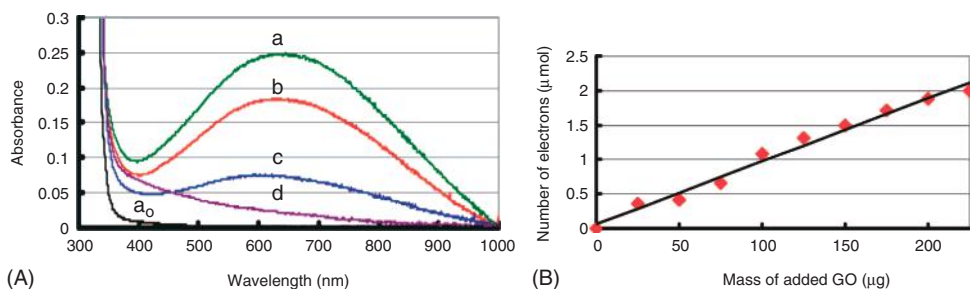


Figure 8.17 (A) Absorption spectra of UV-irradiated 10 mM TiO₂ suspension in ethanol (spectrum a) and after the addition of graphene oxide suspension (deaerated): (a) 0 μg, (b) 50 μg, (c) 150 μg, and (d) 300 μg GO (a₀ corresponds to TiO₂ suspension

prior to UV irradiation); (B) the dependence of electrons extracted from TiO₂ on the amount of GO added to the suspension. (Reprinted with permission from Ref. [64]. Copyright 2008 American Chemical Society.)

The charge transfer between the semiconductor particles and the GO was also evident through the emission spectrum. In the absence of GO, the emission peak was intense and could be located around the wavelength characteristic of the semiconductor NPs; for ZnO, the wavelength is approximately 530 nm (Figure 8.18). Figure 8.18 shows that as GO is added, the fluorescence decreases because the electrons are transferred to the GO and this initiates the chemical reduction process (Equation 8.3b). Measures of emission at 530 nm as a function of time for different GO concentrations (not shown in this chapter) reveal that the emission exhibits a multiexponential decay; specifically, the decay has two components - one associated with fast decay and other with slow decay. The charge transfer between

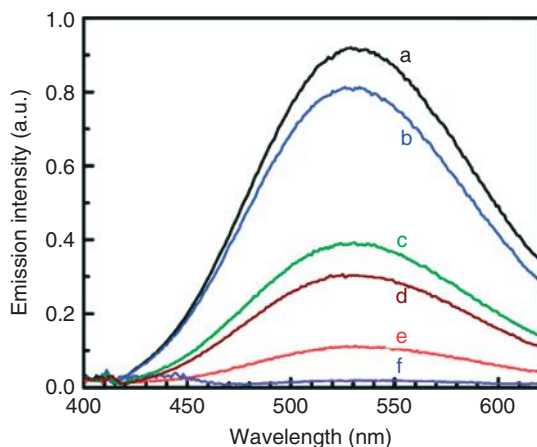


Figure 8.18 Emission spectra of a 1 mM ZnO suspension at different GO concentrations: (a) 0 mg ml⁻¹, (b) 0.035 mg ml⁻¹, (c) 0.09 mg ml⁻¹, (d) 0.14 mg ml⁻¹, (e)

0.20 mg ml⁻¹, and (f) 0.24 mg ml⁻¹. (Reprinted with permission from Ref. [52]. Copyright 2009 American Chemical Society.)

ZnO and GO relates to the fast decay component, therefore it was possible to obtain information about the dynamics of the transfer through the development of the rapid decay constant with respect to the GO concentration. For the system under discussion, it was determined that when the GO concentration in ethanol is 0.025 mg ml^{-1} , the electrons are transferred at a constant rate of $1.2 \times 10^9 \text{ s}^{-1}$.

8.5

Graphene Functionalized with Magnetic NPs

GO and *r*GO functionalized with magnetic NPs (GO-Mag NPs) have also received considerable attention as they provides a platform to combine the electronic and physicochemical properties of GO with the magnetic response of the NPs.

A key property of these materials is their sensibility to externally applied magnetic fields that can be used to remotely move and guide the material as required for a wide range of applications. In this sense, these materials are susceptible for use as magnetic carriers that can be separated from mixtures using low field magnetic-separation techniques that make them potentially attractive in applications that range from the biomedical and physicochemical domains to water treatment, metal, and pollutant removal.

A wider application potential for these materials appears on adding other materials to the composite where one can functionalize either the GO or the magnetic NPs to gain chemical or biological specificity, while the material maintains its magnetic response.

By far, the most commonly used magnetic NPs are made of magnetite, Fe_3O_4 [68]. However, NPs of other materials that have been successfully anchored to GO or *r*GO include $\text{Ni}_x\text{Co}_{100-x}$, Co [69], Ni [70], NiB [71], Co_3O_4 [72], MFe_2O_3 ferrites (with $M = \text{Mn, Co, Ni, and Zn}$) [73, 74], Fe-core/Au-shell [75], and NiFe [76]. However, not all these materials have been used to exploit the magnetic properties of the GO-Mag NPs, but rather as electrodes for sensors as well as for Li ion batteries, which have been discussed in the previous section. In this section, only those applications that exploit the magnetic response of the system are discussed.

As recently reviewed by Liu *et al.* [77], there are mainly three different strategies for the synthesis of graphene–magnetite composites. The first one involves a two-step process that starts with GO that is chemically reduced and functionalized with a surfactant or a polymer that allows binding of the NPs. The second strategy also involves a two-step process where the magnetic NPs are reduced in the presence of GO. In this case, the iron ions are captured by carboxylate anions via coordination and precipitation by the addition of an alkaline solution, leading to magnetite–GO composites. These composites can be further treated thermally or in the presence of chemical agents, to remove the oxygen-containing groups of GO leading to magnetic NPs and *r*GO composites. The third approach is a single-step procedure, in which the chemical reduction of GO and the deposition of Fe_3O_4 NPs on the carbon basal plane are combined in one step.

8.5.1

Magnetic Properties

Applications that are based on the interaction between the material and the externally applied magnetic field require certain characteristic magnetic properties, and much of the success of a given magnetic material is determined by these properties. From a very general standpoint, there are two properties that are fundamental, a zero or very low magnetic remanence and a reasonably high value of the saturation magnetization. A zero, or very low, remanence material is ideal for the implementation of any magnetic-separation process, as it would have a strong response to the applied field and no magnetic response when the field is switched off. This will reduce or eliminate the aggregation of the magnetic carriers in the absence of the applied field, which facilitates the dispersion and reuse of the material. On the other hand, the total or effective saturation magnetization of the material is the other key parameter as it determines the magnetic field intensity required in the separation process, which plays a major role in the complexity and cost of the process.

Zero or very low remanence can be achieved with superparamagnetic (SPM) or very soft ferromagnetic materials. GO-Mag NPs exhibit very different magnetic responses depending on the type of material, average particle size, and its concentration on the GO. The existing experimental results suggest that, in fact, the optimal GO-Mag NPs are obtained from the trade-off between the specific function or property required for a given application and the adequate magnetization strength required to magnetically separate the compound.

Magnetite NPs with average diameter below 20–30 nm are known to be SPM at room temperature and several groups have reported SPM GO-Mag NPs. Figure 8.19 illustrates the hysteresis loop measured in an SPM $\text{Fe}_3\text{O}_4/\text{GO}$ composite, where

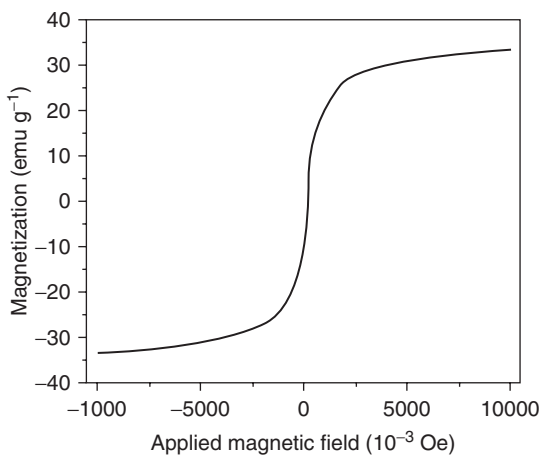


Figure 8.19 Magnetization loops of GO- Fe_3O_4 -PEG. The absence of a hysteresis loop indicates the superparamagnetic properties. (Reprinted with permission from Ref. [78]. Copyright 2012 Springer.)

one can see that the system has zero remanence at 300 K [78]. Moreover, despite the fact that the magnetization continues increasing even at 10 kOe (1 T), about 60–70% of the saturation magnetization is reached at low field values (1–2 kOe). This is very important as it shows that magnetic separation can be done using low field strengths.

The effective magnetization of the material can be further tailored without loss of the SPM properties by changing either the particle size, keeping it below the critical SPM diameter, or the particle coverage on the GO, which can be controlled during synthesis of the NPs. This is exemplified in Figure 8.20a,b where the dependence on the average diameter of the Fe_3O_4 particles, their coverage density, and the saturation magnetization are plotted as a function of the feed ratio of NaOH and in Figure 8.20b, the corresponding hysteresis loops [80]. As seen in these figures, the magnetic response in all cases is consistent with an SPM material and the total saturation magnetization shows a clear variation with particle size and coverage.

These variations simply reflect that the total saturation magnetization of the GO-Mag NPs is proportional to the total volume of magnetic material contained in the composite. In this sense, it worth noting that when other materials are added to the GO-Mag NPs to gain chemical or biological functionality, the volume of magnetic material in the final composite changes [70, 80]. This is illustrated in the hysteresis loops shown in Figure 8.21 that compares the magnetization loops measured on the Fe_3O_4 NPs, the GO-Mag NPs, and the carbon-coated Fe_3O_4 NP/GO composite (labeled GFC 190) [80]. This example shows that the composite has less magnetic material per mass unit and the magnetization mass density decreases.

Introducing magnetic NPs made of alloys allows changing and controlling both the remanence and the saturation magnetization of the material [69, 73, 74, 76]. For example, this has been done using $\text{Ni}_x\text{Co}_{100-x}$ alloy NPs. Figure 8.22 shows

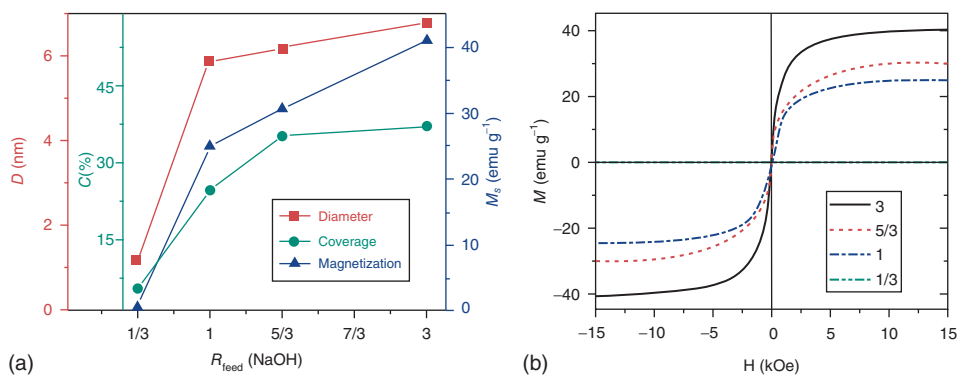


Figure 8.20 (a,b) Dependence of the average diameter (D) of Fe_3O_4 nanoparticles, the coverage density (C) of Fe_3O_4 nanoparticles on graphene nanosheets, and the saturated magnetization (M_s) of graphene@ Fe_3O_4

on R_{feed} -NaOH (at fixed R_{feed} - $\text{FeCl}_3 = 2$ and $t = 1$ h). (Reprinted with permission from Ref. [79]. Copyright 2010 American Chemical Society.)

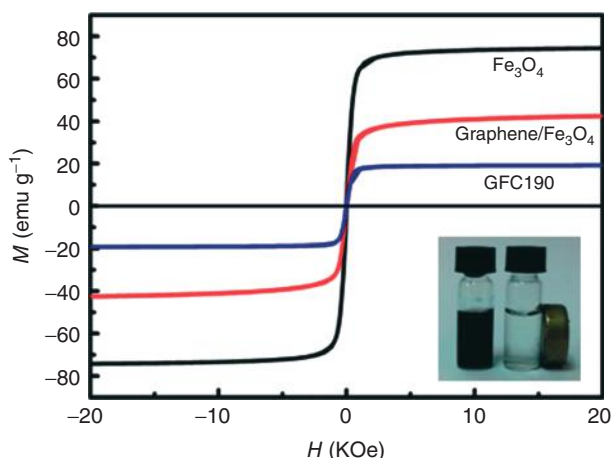


Figure 8.21 Magnetization curves of Fe_3O_4 nanoparticles, $\text{Fe}_3\text{O}_4/\text{GO}$, and carbon-coated $\text{Fe}_3\text{O}_4/\text{GO}$ composite (named GFC190). (Reprinted with permission from Ref. [80]. Copyright 2012 Royal Society of Chemistry.)

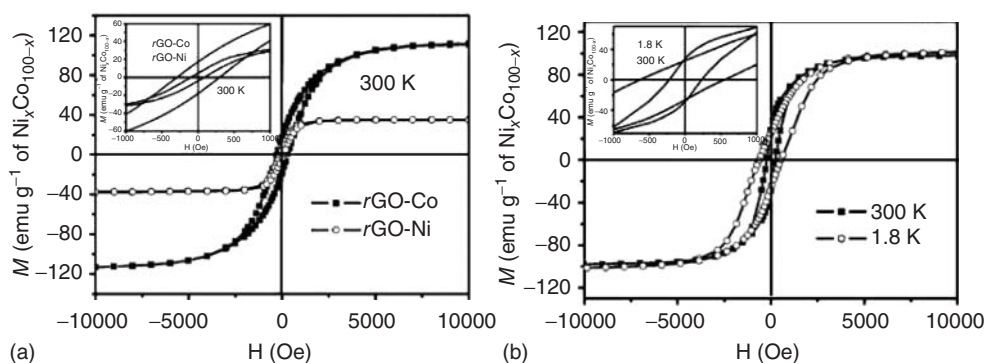


Figure 8.22 Magnetic hysteresis loops of $r\text{GO-Ni}_x\text{Co}_{100-x}$ nanocomposites at 1.8 and 300 K: (a) pure Co and Ni (300 K) and (b) $\text{Ni}_{25}\text{Co}_{75}$. (Reprinted with permission from Ref. [69]. Copyright 2012 American Chemical Society.)

the hysteresis loop measured in GO-Mag NPs with (a) pure Ni and Co NPs and (b) $\text{Ni}_{25}\text{Co}_{75}$ alloy NPs [69]. As seen from the results obtained at 300 K, there is a noticeable difference in the hysteresis loops between pure Ni, Co, and their alloy. In particular, for all cases, the material exhibits a finite remanence and, as expected, the saturation magnetization is different for each material.

In general, the particle shape is practically spherical, so the particles have no magnetic shape anisotropy. However, the packing of magnetic NPs on the GO surface produces a two-dimensional array of nearly spherical particles, which, at moderate and high concentrations, as a consequence of the dipolar interaction between particles, can result in the modification of the hysteresis loops when

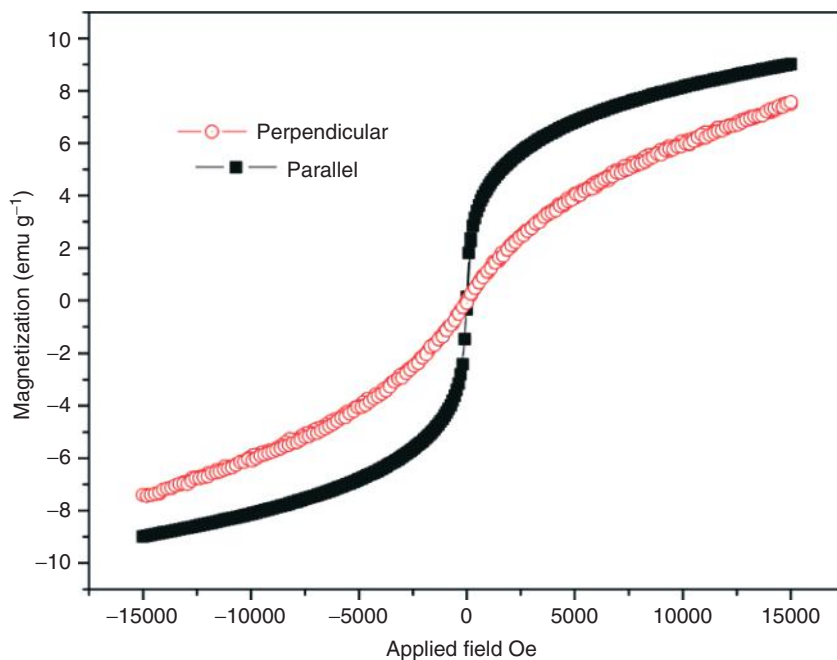


Figure 8.23 Magnetization curve for a *rGO*/iron oxide freestanding film measured with the field applied parallel and perpendicular to the film. (Reprinted with permission from Ref. [81]. Copyright 2012 Elsevier.)

the field is applied parallel to the plane of the sample [81], as illustrated in Figure 8.23.

In this figure, there is a clear difference between the hysteresis loops measured with the magnetic field applied parallel and perpendicular to the plane of the sample. Although in both directions, the remanence vanishes, consistent with an SPM material, it is clear that it is easier to magnetize the material when the field is applied parallel to the plane as compared to the perpendicular direction.

The examples mentioned above underline the fact that these composites have magnetic properties that can be widely modified and provide evidence that there is a very large margin to fine-tune these properties according to the specific needs and applications envisaged.

8.5.2

Applications of GO-Mag NPs

Applications of GO-Mag NPs include removal of metals and pollutants from water [88–90], catalysis, hydrogen storage, drug and gene transport and delivery, photothermal treatment, immobilization of molecules, MRI, and magnetically controlled actuators.

8.5.2.1 Magnetic Separation of Metals and Pollutants with GO-Mag NPs

Recovery and removal of metals and pollutants from wastes and wastewater is increasingly important both from the perspective of materials recovery and recycling and as pollutant removal. This is due to several factors such as material scarcity, energy saving, and environmental control that figure among the most important. Magnetic-field-based separation and elimination of diverse substances and compounds is very attractive, as it enables fast, cost effective, and easy removal of these substances from complex heterogeneous mixtures at small or large scale. For example, magnetic-separation techniques have been applied for wastewater treatment since the early 1940s [82]. On the other hand, carbon nanomaterials, such as activated carbons, carbon nanotube composites, and graphene possess high sorption capacities. The surface of GO contains functional groups such as carboxyl, hydroxyl, and epoxy that have strong complexation capacities and thus are attractive as a platform for the removal of metals and pollutants.

GO-Mag NPs have been shown to combine attractive physicochemical and magnetic properties that make them suitable for their use as a platform for magnetic separation of organic dyes, metal ions, and aromatic compounds. Specific examples include removal of metal ions such as U(VI) [91], Co(II) [83], arsenic [84] (arsenate) [85], and chromium(VI) [86, 87], organic dyes such as methylene blue (MB) [73, 80, 88], rhodamine B (RhB) [89], malachite green [89], pararosaniline [89], and aromatic compounds such as benzene, toluene, and dimethylbenzene [70].

The results presented in Figure 8.24 exemplify the removal by magnetic separation of organic dyes from water using an iron oxide/*r*GO composite [89]. The figure shows the UV-vis absorption spectra of rhodamine B at 554 nm and malachite green at 625 nm as a function of the Mag-GO concentration (Figure 8.24a,b). The results show that the absorbance decreases as the concentration of GO-Mag NPs is increased. Furthermore, from these measurements the percentage of dye removed has been determined and this is shown in Figure 8.24d for rhodamine B and malachite green, respectively. As seen from these results, for the maximal concentration of GO-Mag NPs used (0.7 g l^{-1}) a removal percentage of 90% is attained for both substances. Finally, the insets in Figure 8.24a,c show the photographs of the dye solutions before and after using 0.7 g l^{-1} of GO-Mag NPs.

From the examples found in the literature, GO-Mag NPs are also attractive as there is little or no need to add other materials to the composites in order to improve their sorption properties. This simplifies material synthesis and its optimization is limited to finding the best compromise between the sorption capacity and the quantity of magnetic material required to facilitate the magnetic separation of the material.

As mentioned in the previous section, increasing the concentration of magnetic NPs on the graphene increases the total magnetization, making the material more susceptible to magnetic separation. However, the effective surface area of the graphene decreases as the concentration of the magnetic NPs increases, which reduces the sorption capacity of the composite, so the performance of the GO-Mag NPs will be a trade-off between sorption capacity and magnetic response.

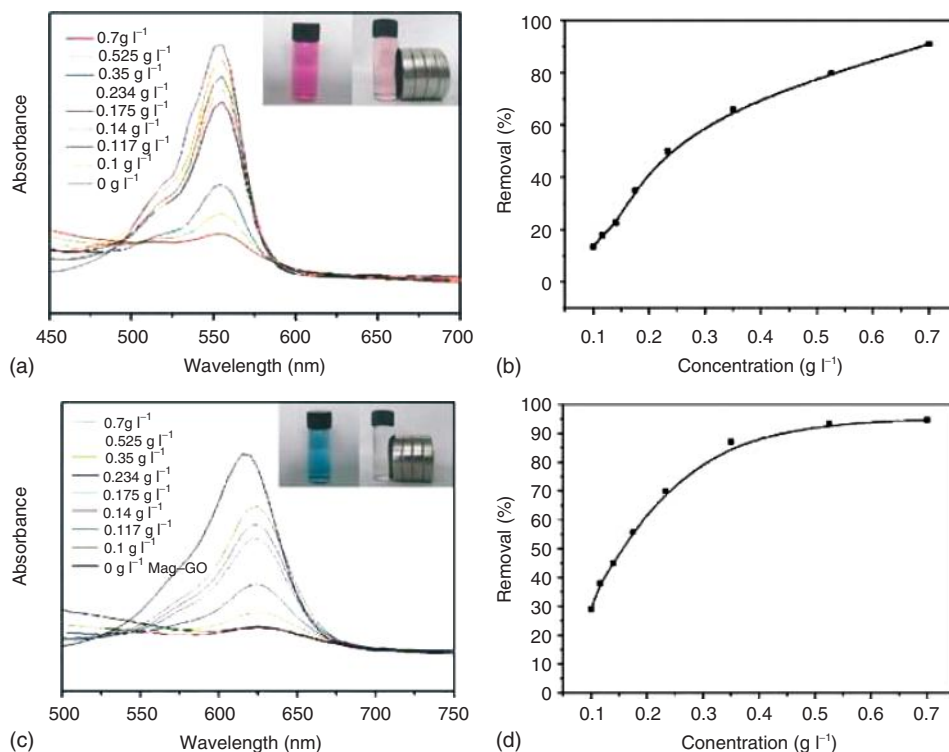


Figure 8.24 Removal of rhodamine B (a,b) and malachite green (c,d) at different concentrations of GO-MagNPs. Insets in (a,c) show the photos of dye solutions before and after using GO-Mag NPs (0.7 g l⁻¹). (Reprinted with permission of Ref. [89]. Copyright 2011 Springer.)

This has been shown by Zong *et al.* [91] while studying the removal of U(IV) from aqueous solutions using GO-Mag NPs. In their experiments, they tried to determine the optimal proportion of GO and iron oxide on U(IV) sorption performance using GO-Mag Fe₃O₄ NP contents of 0%, 20%, 40%, 60%, 80%, and 100%. The results shown in Figure 8.25 clearly show that as the content of Fe₃O₄ increases, sorption performance decreases. Without doubt, GO alone has excellent sorption properties, however, in order to magnetically remove the material from solution, it is necessary to sacrifice the high performance values of GO by using some fraction of its surface to anchor the magnetic NPs. As these authors conclude, the best compromise was the 20% iron oxide content, as it allows having good sorption while possessing a magnetic response high enough to make the material separable with an external magnetic field.

8.5.2.2 Biomedical Applications of GO-Mag NPs

Many reports have demonstrated the potential of carbon nanostructures and their hybrid structures for a variety of biomedical applications ranging from biosensing,

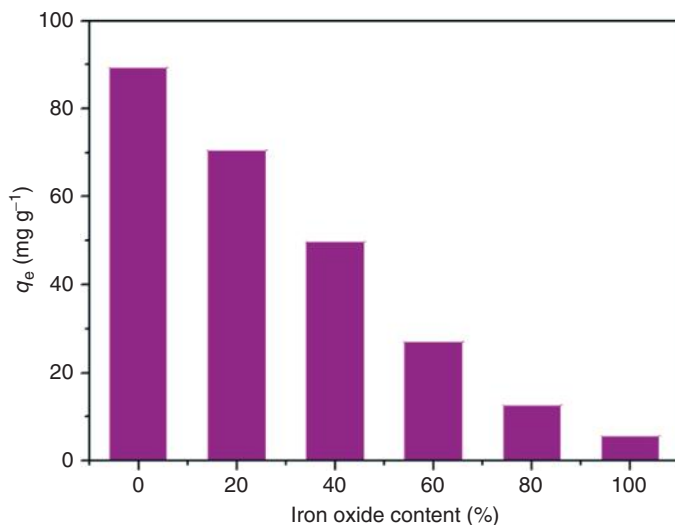


Figure 8.25 Influence of the percentage of iron oxide on GO on the sorption of U(IV). (Reprinted with permission of Ref. [91]. Copyright 2013 American Chemical Society.)

drug delivery, and diagnostics, to cancer treatment and tissue engineering. On the other hand, magnetic NPs have been extensively studied for biomedical applications. As for carbon nanostructures, an appropriate physicochemistry and controllable surface properties represent the biggest hurdle that needs to be surpassed in order to produce biomedical materials. For magnetic NPs, however, there has been significant progress in this regard and they have been extensively investigated for various applications such as drug delivery, hyperthermia, MRI, tissue engineering and repair, biosensing, biochemical separations, and bioanalysis [82, 92].

Drug Delivery A very promising application of magnetic-responsive nanomaterials is in the field of drug and reagent delivery and release. Here again, the magnetic response of the material to an externally applied magnetic field allows guiding and immobilizing the material to the targeted tissue.

While magnetic NPs have been extensively studied for drug delivery, it is well known that the integration of heterostructures combining magnetic NPs and other materials offer distinct surfaces and properties that can confer them with multiple functions. In this sense, carbon-based nanomaterials have been shown to have excellent uptake qualities for aromatic molecules including many chemotherapy drugs that may be easily loaded on the surface of sp^2 -carbon nanomaterials such as carbon nanotubes and graphene by π - π stacking. So the combination of magnetic NPs and GO open the possibility of envisaging a new and vast range of possibilities to develop magnetically guided heterostructures for drug delivery and theranostics.

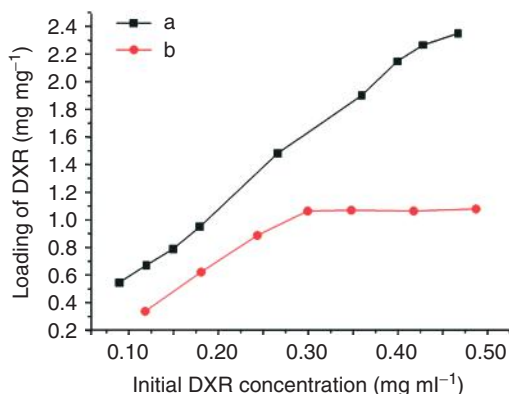


Figure 8.26 Loading capacity of DXR on GO (a) and GO-Mag NPs (b) with different initial DXR concentrations. (Reprinted with permission of Ref. [93]. Copyright 2009 Royal Society of Chemistry.)

To date, only a few examples of GO-Mag NPs for drug delivery have been reported. These tests were based on common anticancer drugs such as doxorubicin (DOX) [93], doxorubicin hydrochloride (DXR) [78], and 5-fluorouracil (5-FU) [93].

The strategy for loading of the drug into the GO-Mag NP carriers can vary. For example, DOX [93] and 5-FU [94] were directly conjugated on the GO, while Ma *et al.* [78] conjugated DXR on PEG-functionalized GO-Mag NPs. In all cases, the complexes demonstrated being SPM and showed high drug-loading capacity. However, as shown by Yang *et al.*, the loading capacity is lower in the Mag-GO when compared with pristine GO. Figure 8.27 compares the loading capacity of DXR on both GO (a) and GO-Mag NPs (b) with different initial DXR concentrations [93], where one can note the loading saturation in GO-Mag NPs, which is attributed to the reduced effective surface area of GO due to the magnetic NPs.

The drug-release tests were done by triggering their release by adjusting the pH of the dispersion. Figure 8.26 shows the measured release of 5-FU from the GO-Mag NPs at different pH values [94]. For these experiments, the authors investigated the release kinetics at 37 °C using a Na₂HPO₄-KH₂PO₄ buffer solution with pH 4.0 and 6.9, respectively. These pH values were chosen in order to mimic the acidic environment of tumors. As shown in Figure 8.27, the release rate of 5-FU is much faster in acidic conditions than in neutral conditions. Specifically, 54.72% and 14.74% of the total amount of 5-FU were released over 8 h at pH 4.0 and 6.9, respectively. These results are analogous to those obtained with DRX [78] and DOX [93], which clearly suggests that this is a viable mechanism for drug release.

GO-Mag NPs Applied in Magnetic Resonance Imaging Magnetic NPs have been extensively studied as an MRI T_2 contrast agent for contrast enhancement and signal amplification as they are much more efficient promoters of relaxation than

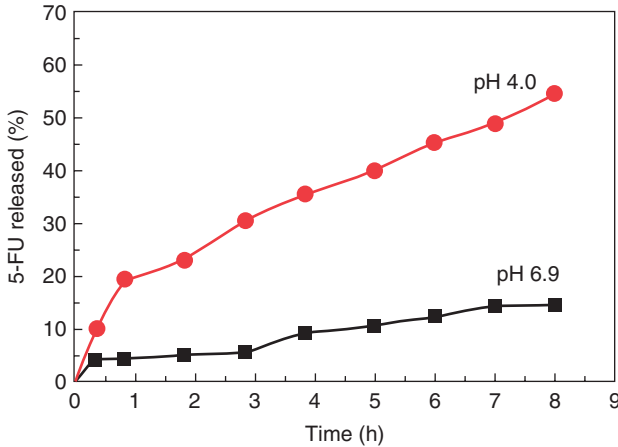


Figure 8.27 Release of 5-FU on GO-Mag NPs at different pH values. (Reprinted with permission of Ref. [94]. Copyright 2013 Wiley.)

the MRI T_1 contrast agent gadolinium-diethylenetriamine pentaacetic acid, and their magnetic properties can be managed by controlling their size and surface coatings [82]. However, as already mentioned, there is an enormous potential for heterostructures made of two or more materials with different physicochemical properties that can show multifunctional characteristics. For example, the imaging enhancement property of magnetic NPs can be used in conjunction with drug delivery applications for real-time monitoring of drug distribution to the target tissue, as well as to follow the effect of therapeutics on the progression of disease. Recently, several authors have tested *in vitro* the effectiveness of GO-Mag NPs as MRI contrast agents.

Cong *et al.* [95], have produced poly(sodium 4-styrenesulfonate) (PSS) to produce a stable PSS-coated rGO sheet aqueous dispersion that was subsequently decorated with Fe_3O_4 NPs. Cong *et al.* [95] have used carboxymethyl dextran (CMD) and aminodextran (AMD)-coated $\text{Fe}_3\text{O}_4/\text{GO}$. More recently, Ma *et al.* [78] have used PEG-functionalized GO-Mag NPs.

Evaluation of the effectiveness of the GO-Mag NPs as a contrast agent is evaluated by analyzing the T_2 -weighted MR imaging with varying either the GO-Mag NPs or simply the magnetic material concentration. Figure 8.28 shows the results obtained with the GO-Mag PSS as a function of the concentration [95]. From the T_2 -weighted MR imaging shown in the Figure 8.28, it is concluded that magnetic NPs are responsible for the contrast enhancement; as seen here, pure graphene provides no contrast enhancement. The contrast enhancement with GO-Mag NP concentration has been confirmed by these three studies [78, 95, 96].

The results found to date show that GO-Mag NPs are a suitable platform for applications in biomedicine. GO-Mag NPs are an exciting class of novel materials that have large potential in this field and further efforts are expected in order to combine more functionality.

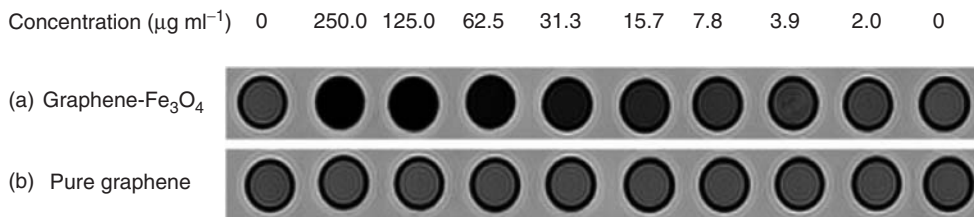


Figure 8.28 T_2 -weighted MR imaging of the magnetic-functionalized graphene (a) and pure graphene (b). No enhancement of contrast was observed at different concentrations of graphene. (Reprinted with permission of Ref. [95]. Copyright 2010 Wiley.)

8.6

Conclusions

As we have shown, a number of novel composite materials have been prepared using graphene and metal or metal oxide NPs. Many authors have demonstrated that graphene-based composite materials present better properties than polymer matrices or other carbon-based composites. Normally, the improved materials are obtained at very low graphene contents, which makes them easier to be commercialized and cheaper to be produced. However, until now, most of the procedures used for the synthesis of these composites involve the production of GO followed by its reduction. These processes diminish the main properties of graphene, that is, chemical stability and conductivity. Thus, it is expected that improved production of graphene might enhance the performance of metal or metal oxide graphene composites.

References

- Novoselov, K.S., Geim, A.K., Morozov, S.V. *et al.* (2004) *Science*, **306**, 666.
- Novoselov, K.S., Geim, A.K., Morozov, S.V. *et al.* (2005) *Nature*, **438**, 197.
- Geim, A.K. (2009) *Science*, **324**, 1530.
- Wehling, T.O., Novoselov, K.S., Morozov, S.V. *et al.* (2008) *Nano Lett.*, **8**, 173.
- Georgakilas, V., Otyepka, M., Bourlinos, A. *et al.* (2012) *Chem. Rev.*, **112**, 6156.
- El-Sayed, M.A. (2001) *Acc. Chem. Res.*, **34**, 257.
- Compton, O.C. and Nguyen, S.T. (2010) *Small*, **6**, 711.
- Quintana, M., Vazquez, E., and Prato, M. (2013) *Acc. Chem. Res.*, **46**, 138.
- Marcano, D.C., Kosynkin, D.V., Berlin, J.M. *et al.* (2010) *ACS Nano*, **4**, 4806.
- Hernandez, Y., Nicolosi, V., Lotya, M. *et al.* (2008) *Nat. Nanotechnol.*, **3**, 563.
- Choi, W., Lahiri, I., Seelaboyina, R. *et al.* (2010) *Crit. Rev. Solid State*, **35**, 52.
- Novoselov, K.S., Jiang, D., Schedin, F. *et al.* (2005) *Proc. Natl. Acad. Sci. U.S.A.*, **102**, 10451.
- Geim, A.K. and Novoselov, K.S. (2007) *Nat. Mater.*, **6**, 183.
- Wan, X., Huang, Y., and Chen, Y. (2012) *Acc. Chem. Res.*, **45**, 598.
- Vinodgopal, K., Neppolian, B., Lightcap, I.V. *et al.* (2010) *J. Phys. Chem. Lett.*, **1**, 1987.
- Dai, L. (2013) *Acc. Chem. Res.*, **46**, 31.
- Quintana, M., Spyrou, K., Grzelczak, M. *et al.* (2010) *ACS Nano*, **4**, 3527.

18. Quintana, M., Grzelczak, M., and Prato, M. (2010) *Phys. Status Solidi B*, **247**, 2645.
19. Quintana, M., Montellano, A., del Rio, A.E. *et al.* (2011) *Chem. Commun.*, **47**, 9330.
20. Muszynski, R., Seger, B., and Kamat, P.V. (2008) *J. Phys. Chem. C*, **112**, 5263.
21. Luo, Z., Somers, L., Dan, Y. *et al.* (2010) *Nano Lett.*, **10**, 777.
22. Xu, C., Wang, X., and Zhu, J. (2008) *J. Phys. Chem. C*, **112**, 19841.
23. Stankovich, S., Dikin, D.A., Piner, R.D. *et al.* (2007) *Carbon*, **45**, 1558.
24. Si, Y. and Samulski, E.T. (2008) *Nano Lett.*, **8**, 1679.
25. Seger, B. and Kamat, P.V. (2009) *J. Phys. Chem. C*, **113**, 7990.
26. He, Y., Vinodgopal, K., Ashokkumar, M. *et al.* (2006) *Res. Chem. Intermed.*, **32**, 709.
27. Gedanken, A. (2004) *Ultrason. Sonochem.*, **11**, 47.
28. Okitsu, K., Ashokkumar, M., and Grieser, F. (2005) *J. Phys. Chem. B*, **109**, 20673.
29. Georgakilas, V., Bourlinos, A.B., Gournis, D. *et al.* (2008) *J. Am. Chem. Soc.*, **130**, 8733.
30. Gomez De Arco, L., Zhang, Y., Schlenker, C.W. *et al.* (2010) *ACS Nano*, **4**, 2865.
31. Crispin, X., Geskin, V., Crispin, A. *et al.* (2002) *J. Am. Chem. Soc.*, **124**, 8131.
32. Shi, Y., Kim, K.K., Reina, A. *et al.* (2010) *ACS Nano*, **4**, 2689.
33. Frens, G. (1973) *Nat. Phys. Sci.*, **241**, 20.
34. Yoo, E., Okata, T., Akita, T. *et al.* (2009) *Nano Lett.*, **9**, 2255.
35. Dong, L., Reddy, R., Gari, S. *et al.* (2010) *Carbon*, **48**, 781.
36. Li, Y., Gao, W., Ci, L. *et al.* (2010) *Carbon*, **48**, 1124.
37. Zhou, Y.G., Chen, J.J., Wang, F. *et al.* (2010) *Chem. Commun.*, **46**, 5951.
38. Albrecht, M.G. and Creighton, J.A. (1977) *J. Am. Chem. Soc.*, **99**, 5215.
39. Fleischmann, M., Hendra, P.J., and McQuillan, A.J. (1974) *Chem. Phys. Lett.*, **26**, 163.
40. Huang, J., Zong, C., Shen, H. *et al.* (2012) *Small*, **8**, 2577.
41. Yoo, E., Kim, J., Hosono, E. *et al.* (2008) *Nano Lett.*, **8**, 2277.
42. Wang, H., Cui, L.F., Yang, Y. *et al.* (2010) *J. Am. Chem. Soc.*, **132**, 13978.
43. Paek, S.M., Yoo, E., and Honma, I. (2009) *Nano Lett.*, **9**, 72.
44. Zhang, L.S., Jiang, L.Y., Yan, H.J. *et al.* (2010) *J. Mater. Chem.*, **20**, 5462.
45. Wang, B., Wu, X.L., Shu, C.Y. *et al.* (2010) *J. Mater. Chem.*, **20**, 10661.
46. Wu, Z.S., Ren, W., Wen, L. *et al.* (2010) *ACS Nano*, **4**, 3187.
47. Wang, D., Choi, D., Li, J. *et al.* (2009) *ACS Nano*, **3**, 907.
48. Shen, L., Yuan, C., Luo, H. *et al.* (2011) *Nanoscale*, **3**, 572.
49. Xiao, L., Yang, Y., Yin, J. *et al.* (2009) *J. Power Sources*, **194**, 1089.
50. Lambert, T.N., Chavez, C.A., Hernandez-Sanchez, B. *et al.* (2009) *J. Phys. Chem. C*, **113**, 19812.
51. Zhou, K., Zhu, Y., Yang, X. *et al.* (2011) *New J. Chem.*, **35**, 353.
52. Williams, G. and Kamat, P.V. (2009) *Langmuir*, **25**, 13869.
53. Kowalska, E., Remita, H., Colbeau-Justin, C. *et al.* (2008) *J. Phys. Chem. C*, **112**, 1124.
54. Zhang, L., Yu, J.C., Yip, H.Y. *et al.* (2003) *Langmuir*, **19**, 10372.
55. Oros-Ruiz, S., Pedraza-Avella, J.A., Guzmán, C. *et al.* (2011) *Top. Catal.*, **54**, 519.
56. Ohno, T., Akiyoshi, M., Umebayashi, T. *et al.* (2004) *Appl. Catal. A*, **265**, 115.
57. Asahi, R., Morikawa, T., Ohwaki, T. *et al.* (2001) *Science*, **293**, 269.
58. Sakthivel, S. and Kisch, H. (2003) *Angew. Chem. Int. Ed.*, **42**, 4908.
59. Robel, I., Bunker, B.A., and Kamat, P.V. (2005) *Adv. Mater.*, **17**, 2458.
60. Zhang, L.W., Fu, H.B., and Zhu, Y.F. (2008) *Adv. Funct. Mater.*, **18**, 2180.
61. Zhang, X.Y., Li, H.P., Cui, X.L. *et al.* (2010) *J. Mater. Chem.*, **20**, 2801.
62. Zhang, H., Lv, X., Li, Y. *et al.* (2010) *ACS Nano*, **4**, 380.
63. Chang, H., Sun, Z., Ho, K.Y.F. *et al.* (2011) *Nanoscale*, **3**, 258.
64. Williams, G., Seger, B., and Kamat, P.V. (2008) *ACS Nano*, **2**, 1487.
65. Lightcap, I.V., Kosel, T.H., and Kamat, P.V. (2010) *Nano Lett.*, **10**, 577.
66. Murphy, A.B. (2007) *Sol. Energy Mater. Sol. Cells*, **91**, 1326.

67. Quintana, M., Montellano, A., Rapino, S. *et al.* (2013) *ACS Nano*, **7**, 811.
68. Zhang, Y., Chen, B., Zhang, L., Huang, J., Chen, F., Yang, Z., Yao, J., and Zhang, Z. (2011) *Nanoscale*, **3**, 1446.
69. Bai, S., Shen, X., Zhu, G., Li, M., Xi, H., and Chen, K. (2012) *ACS Appl. Mater. Interfaces*, **4**, 2378.
70. Li, S., Niu, Z., Zhong, X., Yang, H., Lei, Y., Zhang, F., Hu, W., Dong, Z., Jin, J., and Ma, J. (2012) *J. Hazard. Mater.*, **229**, 42.
71. Wang, Y., Guo, C.X., Wang, X., Guan, C., Yang, H., Wang, K., and Li, C.M. (2010) *Energy Environ. Sci.*, **4**, 195.
72. Zhang, H., Bai, Y., Feng, Y., Li, X., and Wang, Y. (2013) *Nanoscale*, **5**, 2243.
73. Bai, S., Shen, X., Zhong, X., Liu, Y., Zhu, G., Xu, X., and Chen, K. (2012) *Carbon*, **50**, 2337.
74. Fu, Y. and Wang, X. (2011) *Ind. Eng. Chem. Res.*, **50**, 7210.
75. Pham, T.A., Kumar, N.A., and Jeong, Y.T. (2010) *Synth. Met.*, **160**, 2028.
76. Bai, S., Shen, X., Zhu, G., Xu, Z., and Yang, J. (2012) *Cryst. Eng. Commun.*, **14**, 1432.
77. Liu, Y.W., Guan, M.X., Feng, L., Deng, S.L., Bao, J.F., Xie, S.Y., Chen, Z., Huang, R.B., and Zheng, L.S. (2013) *Nanotechnology*, **24**, 025604.
78. Ma, X., Tao, H., Yang, K., Feng, L., Cheng, L., Shi, X., Li, Y., Guo, L., and Liu, Z. (2012) *Nano Res.*, **5**, 199.
79. He, H. and Gao, C. (2010) *ACS Appl. Mater. Interfaces*, **2**, 3201.
80. Fan, W., Gao, W., Zhang, C., Tjiu, W.W., Pan, J., and Liu, T. (2012) *J. Mater. Chem.*, **22**, 25108.
81. Narayanan, T., Liu, Z., Lakshmy, P., Gao, W., Nagaoka, Y., Sakthi Kumar, D., Lou, J., Vajtai, R., and Ajayan, P. (2012) *Carbon*, **50**, 1338.
82. Yang, H.W., Hua, M.Y., Liu, H.L., Huang, C.Y., and Wei, K.C. (2012) *Nanotechnol. Sci. Appl.*, **2012**, 73.
83. Liu, M., Chen, C., Hu, J., Wu, X., and Wang, X. (2011) *J. Phys. Chem. C*, **115**, 25234.
84. Chandra, V., Park, J., Chun, Y., Lee, J.W., Hwang, I.C., and Kim, K.S. (2010) *ACS Nano*, **4**, 3979.
85. Wu, X.L., Wang, L., Chen, C.L., Xu, A.W., and Wang, X.K. (2011) *J. Mater. Chem.*, **21**, 17353.
86. Fan, L., Luo, C., Sun, M., and Qiu, H. (2012) *J. Mater. Chem.*, **22**, 24577.
87. Jabeen, H., Chandra, V., Jung, S., Lee, J.W., Kim, K.S., and Kim, S.B. (2011) *Nanoscale*, **3**, 3583.
88. Ai, L., Zhang, C., and Chen, Z. (2011) *J. Hazard. Mater.*, **192**, 1515.
89. Sun, H., Cao, L., and Lu, L. (2011) *Nano Res.*, **4**, 550.
90. Wu, Q., Feng, C., Wang, C., and Wang, Z. (2013) *Colloids Surf. B Biointerfaces*, **101**, 210.
91. Zong, P., Wang, S., Zhao, Y., Wang, H., Pan, H., and He, C. (2013) *Chem. Eng. J.*, **220**, 45.
92. Reddy, L.H., Arias, J.L., Nicolas, J., and Couvreur, P. (2012) *Chem. Rev.*, **112**, 5818.
93. Yang, X., Zhang, X., Ma, Y., Huang, Y., Wang, Y., and Chen, Y. (2009) *J. Mater. Chem.*, **19**, 2710.
94. Fan, X., Jiao, G., Zhao, W., Jin, P., and Li, X. (2013) *Nanoscale*, **5**, 1143.
95. Cong, H.P., He, J.J., Lu, Y., and Yu, S.H. (2010) *Small*, **6**, 169.
96. Chen, W., Yi, P., Zhang, Y., Zhang, L., Deng, Z., and Zhang, Z. (2011) *ACS Appl. Mater. Interfaces*, **3**, 4085.

9

Functionalization of Graphene by other Carbon Nanostructures

Vasilios Georgakilas

9.1

Introduction

An interesting class of graphene derivatives has been developed over the past few years as a result of the combination of pristine graphene or graphene oxide (GO) and other carbon nanostructures especially C_{60} , carbon nanotubes (CNTs) and nanospheres. These derivatives can all be seen as carbon hybrid nanocomposites or superstructures and are usually studied with respect to their use in several applications such as supercapacitors, lithium-ion batteries, photocatalytic cells, polymer enhancement, as a result of the advanced characteristics and properties that occurs by the combination of the components. The most frequently used, carbon nanohybrids, are prepared by a combination of GO and CNTs. In most cases the analogous combination of the physicochemical properties of the two characteristic carbon nanostructures such as electrical conductivity, active surface area, and mechanical strength are remarkably enhanced in the hybrid nanocomposite owing to a synergistic effect that is often observed.

9.2

Graphene- C_{60} Nanocomposites

Graphene or GO and C_{60} are two of the most well studied carbon nanostructures that have remarkable differences with respect to their structure, their chemical reactivity, and their physical, optical, and electronic properties. Their common characteristic is that are constructed by sp^2 carbon atoms arranged in hexagonal rings; however C_{60} is the smallest carbon nanostructure with spherical shape that induces a high strain and consequently high reactivity to the C-C bonds of C_{60} instead of graphene, which is ideally a 2D layer extended by several micrometers. In addition, the aromatic character of graphene is usually interrupted locally in several areas of the surface by defect sites and at the edges of the layer. The large surface area of graphene is offered as substrate for the dispersion of C_{60} molecules or C_{60} small aggregates, avoiding accumulation of larger C_{60}

crystals that usually limit the activity of C_{60} . The combination of C_{60} with pristine graphene or GO has shown better nonlinear optical properties than the separated components [1], improved photovoltaic (PV) performance [2, 3], and photoconductivity [4]. Functionalization of graphene or GO by C_{60} can be performed either by the covalent binding of a C_{60} derivative or by a simple deposition of C_{60} on graphene.

9.2.1

Covalent Bonding of C_{60} on GO

The structures of graphene and C_{60} do not allow a direct connection between the two components even if GO, which is enriched with oxygen groups, is used in the place of pristine graphene. There is only a weak interaction, which is not always enough to guarantee the stability of a hybrid material because of the different character (size, solubility of C_{60} , etc.) of the two components. However, C_{60} derivatives with reactive amines or other nitrogen groups such as pyrrolidine rings can bind covalently through amide bond formation with carboxyl groups of GO [5, 1]. The nature of C_{60} functionalized GO is described by Fourier transform infrared (FTIR) and Raman spectroscopy and high-resolution transmission electron microscopy (HRTEM) microscopy and thermogravimetric analysis (TGA) measurements. The Raman spectrum consists of the two characteristic peaks of D and G bands of GO at 1354 and 1600 cm^{-1} and a third intense peak that is located between these two at 1469 cm^{-1} assigned to the $A_g(2)$ mode of C_{60} . A relative shift of the C_{60} band by 13 cm^{-1} related to pyrrolidine functionalized C_{60} indicates a strong interaction between the two species, which is explained by the covalent attachment of the two species. HRTEM images of GO- C_{60} showed spherical species, with a diameter of about 0.8 nm that is very close to the diameter of C_{60} molecule, attached to GO edges [5]. The appearance of C_{60} at the edges is in agreement with the fact that most carboxylic groups of GO are also located also at the edges. GO- C_{60} has shown enhanced nonlinear optical performance superior to those of the two separate materials [1] (Figure 9.1).

9.2.2

Deposition of C_{60} on Graphene

C_{60} is a well studied 0D carbon nanostructure and subsequently a reactive organic molecule. Because of its electron acceptor character and other interesting physicochemical properties, C_{60} and its organic derivatives are considered as attractive nanomaterials for several optoelectronic applications, especially in organic PV cells [2]. On the other hand, the graphene surface can be seen as a conductive substrate where C_{60} can be easily dispersed, helping in the successful electron transfer, which is the central action in PV systems, from an electron donor to C_{60} . As a result the decoration of graphene nanoplatelets by finely dispersed C_{60} could be used for the improvement of the yield of PV cells.

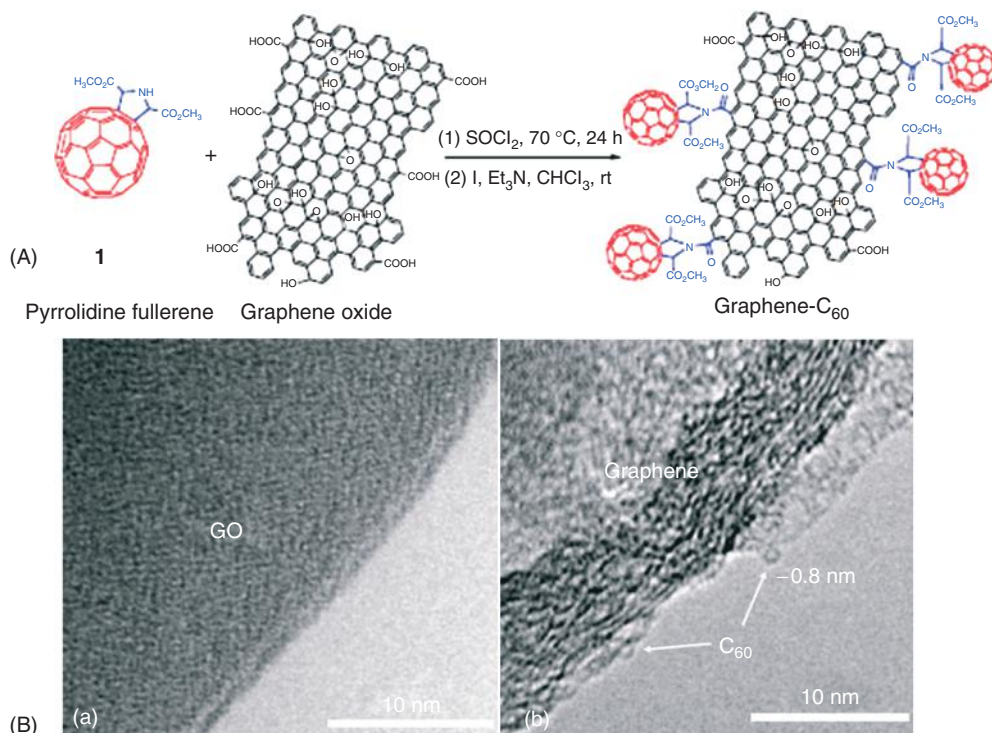
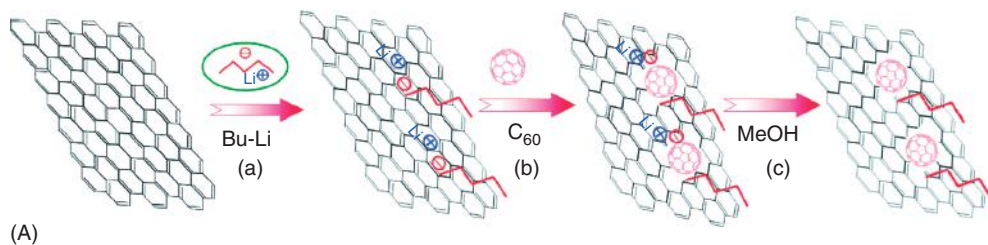


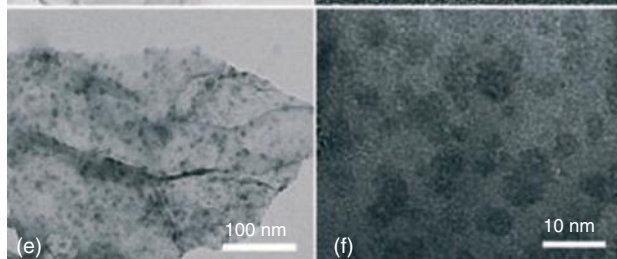
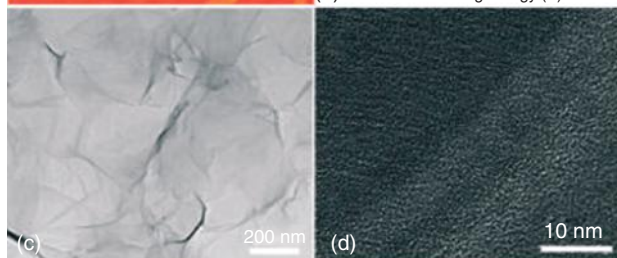
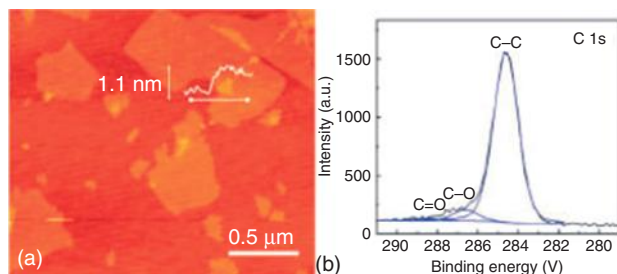
Figure 9.1 (A) Covalent attachment of C₆₀ on GO. (B) HRTEM images of GO (a) and GO-C₆₀ (b) hybrid. (Reprinted with permission from Ref. [5], Copyright 2009, Elsevier B.V.)

Graphene nanoplatelets are activated through lithiation by the nucleophilic addition of butyl lithium (*n*-BuLi) and then decorated by C₆₀ molecules (see Figure 9.2.A). The use of C₆₀ decorated graphene (C₆₀/Graphene) hybrid in bulk heterojunction solar cells as electron acceptor in combination with poly(3-hexylthiophene) (P3HT) as electron donor resulted in a remarkable increase of the power conversion efficiency [3]. The graphitic material here is chemically reduced graphene oxide (*r*GO) while C₆₀ molecules are aggregated in larger clusters as presented in Figure 9.2B.

The appearance of C₆₀ on graphitic surface is indicated by the FTIR and Raman spectra of the hybrid, which are presented as a combination of the analogous spectra of the two separated components (Figure 9.3). More characteristic is the Raman spectrum of the hybrid, which apart from the two characteristic D and G bands at 1354 and 1601 cm⁻¹, respectively, contains a single sharp band between those two at 1476 cm⁻¹ assigned to the Ag(2) mode of C₆₀ shifted up slightly compared to the band that appears in the spectrum of pure C₆₀. The hybrid composite C₆₀/*r*GO is combined with P3HT and applied in PV cells as this combination is among others favored by the enlargement of the range of absorbed energy and the



(A)



(B)

Figure 9.2 (A) Deposition of C_{60} on graphene activated by BuLi. (B) (a) atomic force microscope (AFM) image of GO nanoplatelets. (b) High-resolution XPS (X-ray photoelectron spectroscopy) spectrum of

graphene produced by chemical reduction of GO. (c,d) TEM images of rGO. (e,f) TEM images of C_{60} /rGO. (Reprinted with permission from Ref. [3], Copyright 2011, American Chemical Society.)

facilitation of the energy transfer. The broadening of the absorbed UV–vis energy range is attributed to the better ordering of the P3HT polymer on the graphene substrate.

The deposition of alkylated C_{60} derivatives on a graphene monolayer has been used to study the photoconductivity and the enhanced memory effect of the as-prepared material because of the electron acceptor properties of C_{60} molecules.

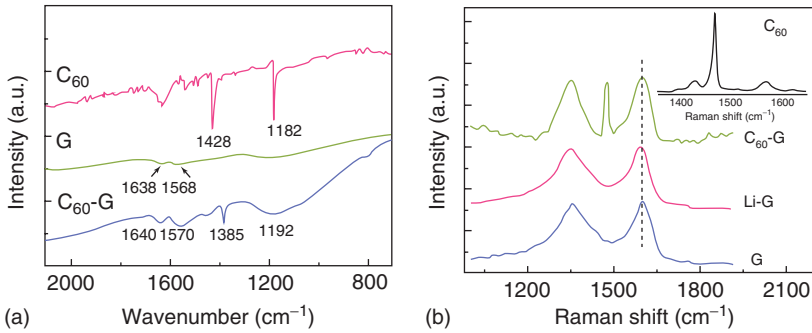


Figure 9.3 (a) FTIR spectra and (b) Raman spectra of C₆₀/rGO and the separated components. (Reprinted with permission from Ref. [3], Copyright 2011, American Chemical Society.)

The graphene monolayer was grown by low-pressure chemical vapor deposition (LPCVD) on a copper foil and then transferred to a Si wafer with a thick SiO₂ layer. C₆₀ molecules functionalized by long alkyl chains dissolved in an aprotic solvent were deposited on the graphene layer and self organized in flake-like nanostructures [4] (Figure 9.4).

The monolayer character of the chemical vapor deposition (CVD) growth of graphene is indicated by the Raman spectrum of the related structure where the single graphene monolayer is characterized by a strong sharp peak near 2700 cm⁻¹ which is usually two times higher than G band. After the absorption of C₆₀ molecules the Raman spectrum is enriched by the characteristic band at 1462 cm⁻¹ assigned to C₆₀. The device showed high reproducible electrical conductivity upon

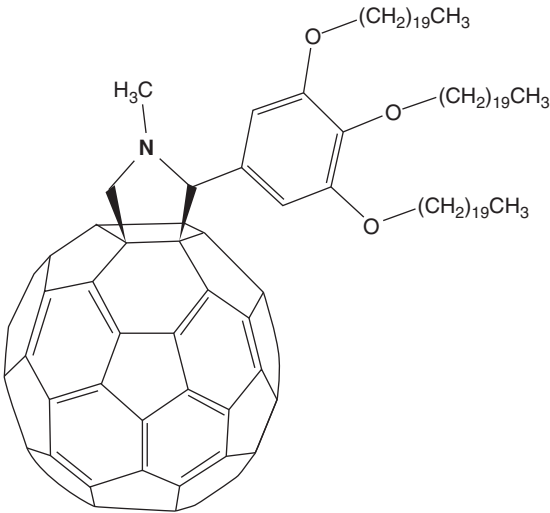


Figure 9.4 The structure of the alkylated C₆₀ [4].

visible light illumination, which is attributed to the generation of holes in C_{60} and their transfer to graphene.

Another interesting all carbon nanocomposite is formed between rGO and C_{60} when rGO is wrapped around C_{60} aggregates forming long C_{60}/rGO nanowires [6]. The driving force of this aggregation is the π - π interactions between rGO and C_{60} . C_{60} wires are formed in a solution of C_{60} by a simple evaporation of the solvent or in the interface between two immiscible solvents by liquid-liquid interfacial precipitation (LLIP). C_{60} nanowires prepared by the last method have higher strength and electrical conductivity because of the shorter intermolecular distance between C_{60} molecules. The wrapping of C_{60} wires by rGO is performed when a solution of rGO in isopropyl alcohol is added in a dispersion of C_{60} in m -xylene. The C_{60}/rGO nanowires are formed in the interface between isopropanol and m -xylene and isolated by centrifugation (Figure 9.5).

The as-prepared nanowires have a diameter range of 200–800 nm and a length that exceed $10\ \mu\text{m}$. The composition of the product is confirmed by Raman spectroscopy by the characteristic peaks of GO and C_{60} that are present in the product also – the D and G bands assigned to GO at 1350 and $1600\ \text{cm}^{-1}$, respectively, as well as a peak at $1469\ \text{cm}^{-1}$ from C_{60} . Interesting information about the properties of nanowires is provided by the UV-vis spectroscopy of C_{60}/rGO in comparison with that of the two components. The $3^1T_{1u} \rightarrow 1^1A_g$ transition of C_{60} at $340\ \text{nm}$ is shifted to $380\ \text{nm}$ in C_{60}/rGO . This $40\ \text{nm}$ shift

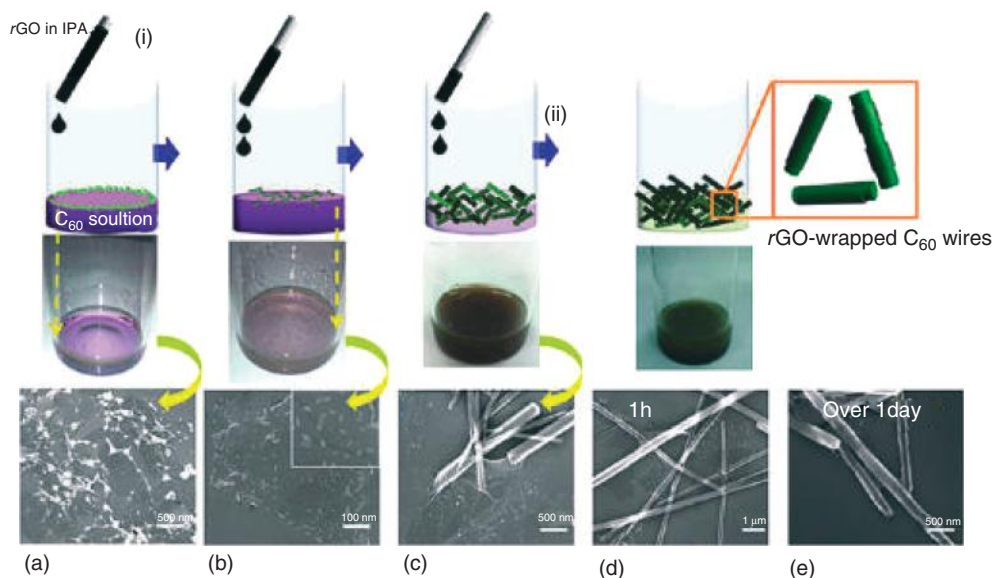


Figure 9.5 The LLIP preparation of C_{60}/rGO nanowires. (i) Dropping slowly rGO solution into C_{60} solution and (ii) keeping the mixed solution at 4°C . (Reprinted with permission from Ref. [6], Copyright 2011, American Chemical Society.)

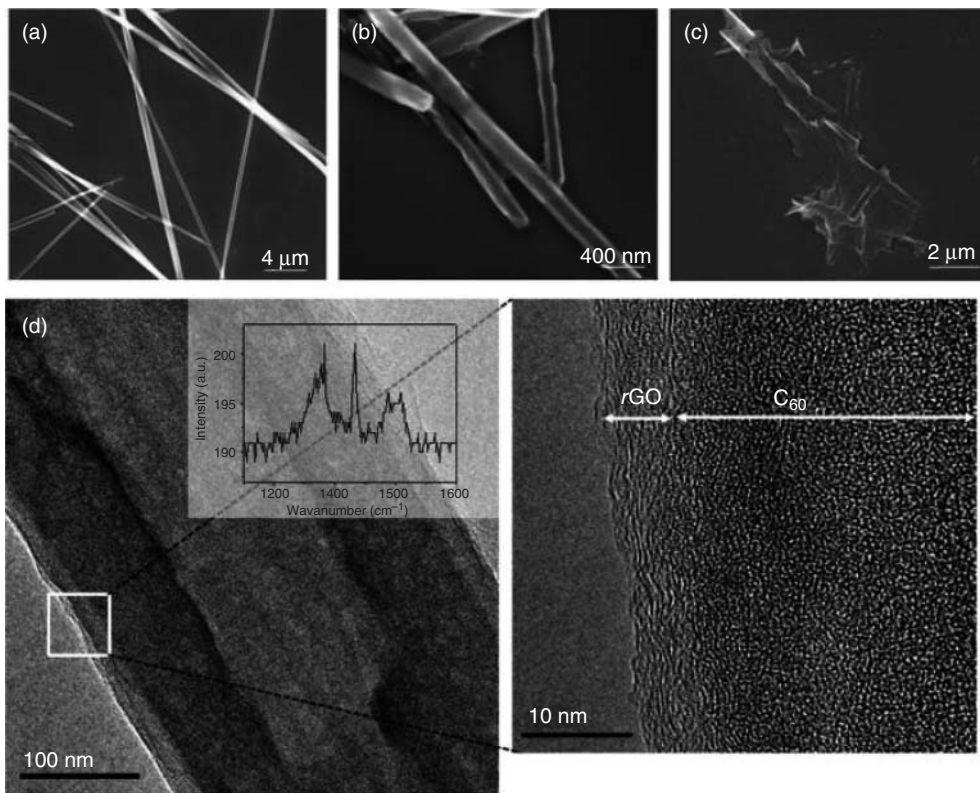


Figure 9.6 SEM images of (a) C_{60} wires, (b) C_{60}/rGO wires, (c) rGO after dissolving C_{60} in xylene, and (d) TEM image of C_{60}/rGO wires. The magnified image of

(d) shows rGO layers. The inset in (d) shows the Raman spectra of C_{60}/rGO wires. (Reprinted with permission from Ref. [6], Copyright 2011, American Chemical Society.)

is attributed to the strong delocalization of the π electron system of rGO in the vicinity of C_{60} wires. This is an indication of the strong π - π interaction between the two components. The C_{60}/rGO wires showed p-type semiconducting behaviors indicating charge transfer between rGO and C_{60} and hole transport through rGO (Figure 9.6).

Analogous composites by the further involvement of CNTs are also promising nanostructured materials in solar cells [7]. The employment of CNTs together with C_{60} and GO in one complex combination leads to all carbon nanocomposites that exhibit interesting physicochemical properties that are produced by the combination of the different roles of the three components in such a complex product. First of all the role of GO is determined by its amphiphilic character and its dispersibility in water because of the number of carboxylates that are located in the areas near the edges of the graphitic surface. A significant number of these carboxylates remain in the graphene layer even after the reduction of GO to rGO .

The dispersibility of GO in water, in combination with the existence of aromatic parts that exist on the graphitic surface, make it a suitable surfactant for the dispersion of single-wall nanotube (SWNT) in water but it is not enough for the dispersion of C_{60} . In fact, SWNTs suspended by sonication in a dispersion of GO in water are attached onto GO through van der Waals interactions with the graphitic parts of GO and the as-produced GO/SWNTs composite remains dispersed in water. The suspension of C_{60} in a dispersion of GO in water did not end with the dispersion of C_{60} , but the last is dispersed in water by the presence of SWNTs upon sonication although SWNTs are not dispersible in water. However the C_{60} /SWNTs composite that is formed by the attachment of C_{60} on SWNT surface is not solution processable since it is not stable in water and is precipitated slowly after the end of the sonication process. These obstacles are eliminated by the use of GO as surfactant for the stable dispersion of C_{60} /SWNTs. In fact C_{60} /SWNT is well dispersed in GO dispersion in water by sonication without precipitation as presented in Figure 9.10. The final complex structure is a ternary all carbon composite C_{60} /SWNTs/GO that was studied in solar cell devices in this form as well as with C_{70} in the place of C_{60} and rGO in place of GO. The use of C_{70} /SWNTs/rGO as active layer in solar cell increases the power conversion by 0.85%. The most promising idea that is related to this ternary nanocomposite is the development of an all carbon solar cell that could be constructed by the combination of carbon nanostructures in different combinations (Figure 9.7).

9.3

Graphene–CNT Hybrid Nanostructures

The common graphitic structure of pristine graphene or GO and CNT is the driving force of their interaction. The combination of a 2D carbon nanomaterial such as graphene with a 1D wire-like carbon nanostructure such as SWNTs or multiwall nanotubes (MWNTs), leads to interesting nanoarchitectures, which could be seen as 3D hybrids with combined properties. Among other things the combination of graphene or GO with CNTs offers to the produced hybrids increased electrical conductivity, enhanced mechanical properties, and high active surface area. Such hybrids have been used in the form of transparent conductive films for the improvement of organic light-emitting diodes (OLEDs), solar cells, field emission transistors, and other optoelectronic applications or as electrodes in sensors, and so on.

In the case of graphene or GO and CNTs, thanks to the large size and surface of both components, the non-covalent interactions are strong enough to keep them tightly aggregated ensuring the stability of the hybrid. In general these two components can usually be combined in three different ways. The easiest and most often used procedure is by mixing together pristine graphene or GO and CNTs or their organic derivatives dispersed in a common solvent or in miscible solvents. The way that the composite is isolated from the liquid phase depends on its use.

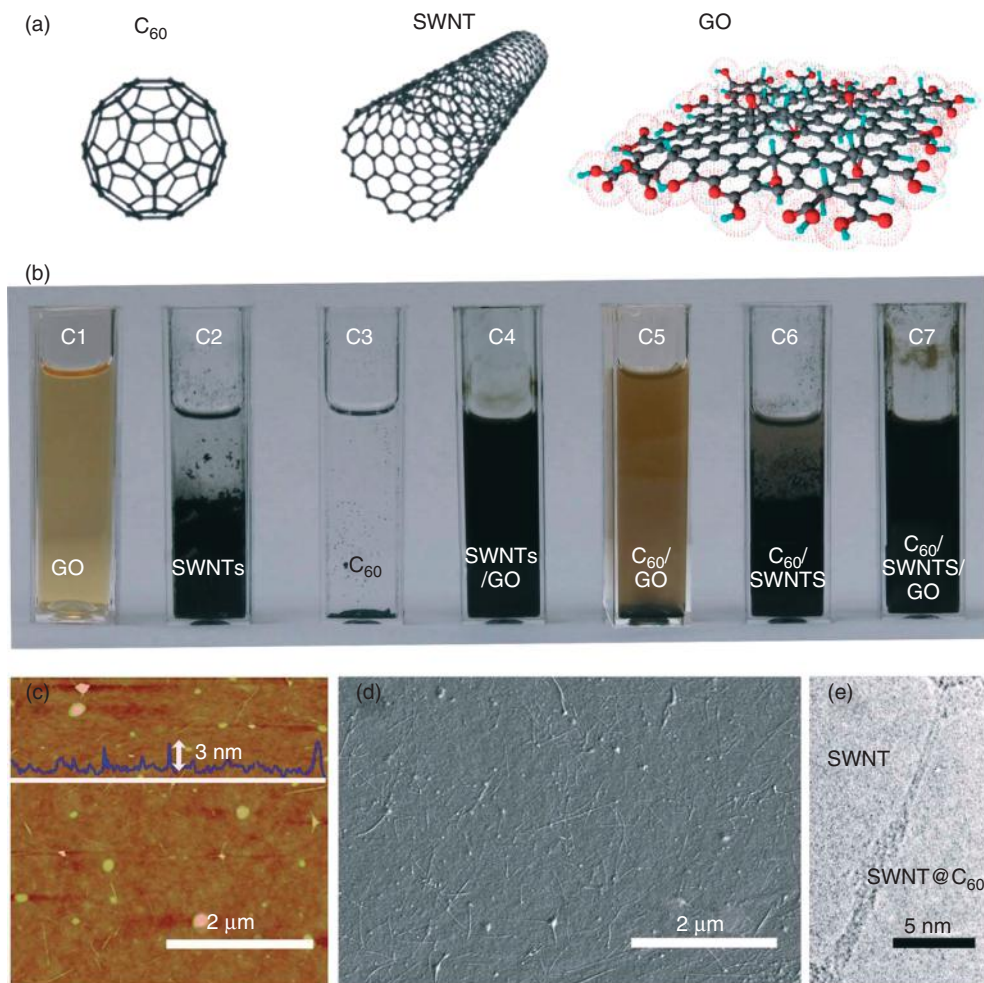


Figure 9.7 (a) The structures of carbon nanoallotropes that involved in these composites. (b) Dispersion of carbon nanostructures (GO and SWNTs: 1 mg ml^{-1} and C_{60} : 0.5 mg ml^{-1}) in water and the composites that are formed by sonication in several

mixtures. AFM (c) and SEM (d) images of a spin-coated thin film of $\text{C}_{60}/\text{SWNTs}/\text{GO}$. (e) High-resolution TEM of $\text{C}_{60}/\text{SWNTs}$. (Reprinted with permission from Ref. [7], Copyright 2012, Royal Chemical Society.)

For example, when a transparent thin film of the hybrid nanocomposite is needed, the later can be isolated by vacuum filtration on a membrane or by spraying on a substrate.

The next method is the direct development of CNTs on graphene surfaces by CVD or other technique. In this case CNTs are grown perpendicular to the graphene surface forming a more characteristic 3D nanostructure. The last method is the

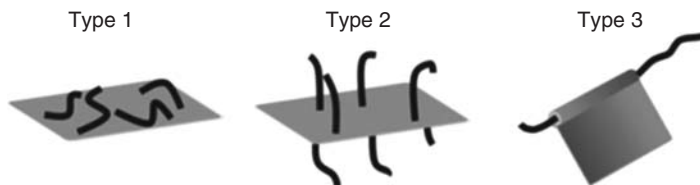


Figure 9.8 The three different types of graphene/CNT composites. (Reprinted with permission from Ref. [8], Copyright 2012, Springer.)

wrapping of CNTs by graphene or GO nanosheets that can cover partly or totally the CNT surface (Figure 9.8).

9.3.1

Graphene–CNT Composites by Simple Mixing

The amphiphilic character of GO originates from by the combination of strong hydrophilic areas, because of the presence of oxygen groups, with strong hydrophobic areas where the graphitic structure is dominant. The hydrophilic character of GO is expressed by its high dispersibility in water. CNTs on the other hand are not dispersible in water; however in the presence of GO, they become dispersible. GO here has the role of the surfactant that covers, by its hydrophobic areas, the external surface of CNTs after their debundling and stabilizes them in water because of its high hydrophilicity.

The interactions between the two components are usually π – π or van der Waals type and rarely are they covalently bonded by the intervention of an organic linker. Usually in these GO/CNTs composites that are prepared by mixing of pre-synthesized components, CNTs are lying on the GO surface and ideally could function as interconnectors between the separated GO nanosheets and as a conductive bridge increasing effectively the electrical conductivity of the composite [9–26]. In addition, such conformation offers the largest interface between them which means also the largest potential interaction between the two nanostructures. In most cases, GO is preferred as starting material because it is easily prepared in high yield from the abundant graphite. In a further step, after the formation of the GO/CNT hybrid, GO can be transformed to rGO by a chemical reduction, restoring its aromatic character partially. As a consequence the electrical conductivity, the thermal stability, and the mechanical strength of rGO are enhanced remarkably compared to GO (Figure 9.9).

In a characteristic example GO nanosheets and oxidized CNTs are suspended in anhydrous hydrazine where GO is partly reduced to rGO and simultaneously the composite formation is followed affording a dark gray stable dispersion [10]. The rGO/CNTs hybrid can be deposited in several substrates by spin coating leaving a thin conductive film after the solvent evaporates. Depending on the spin speed, the thickness of the film can be controlled in order to achieve the preferable optical transmittance. A thin film prepared this way showed very low sheet resistance of

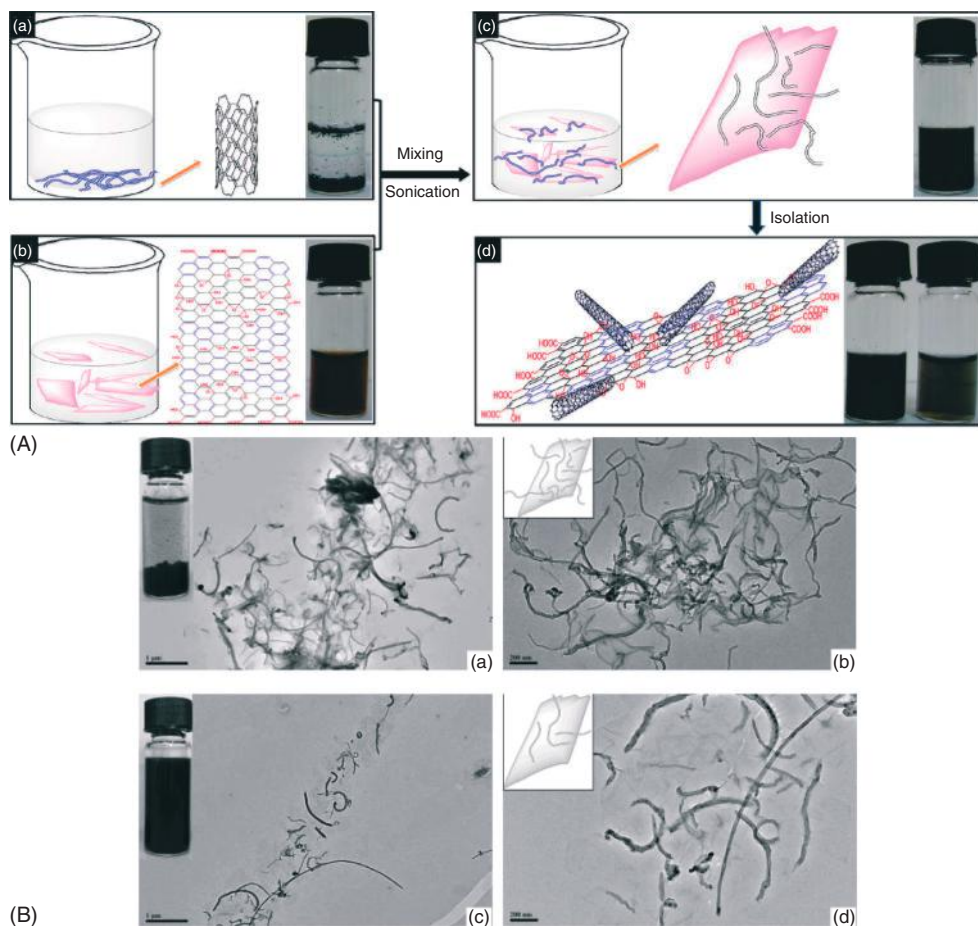


Figure 9.9 (A) Functionalization of GO by CNTs by mixing and sonication of two separated suspension of the two components. (B) TEM images of GO/MWNT composites with different ratios. The inset in (b,d) is

the schematic description of the MWNT-GO complexes. (Reprinted with permission from Ref. [9], Copyright 2010, American Chemical Society.)

$636 \Omega \text{sq}^{-1}$ with optical transmittance of 92%. For comparison, similar films of the CNTs and *r*GO components showed sheet resistance of 22 and $490 \text{ k}\Omega \text{sq}^{-1}$, respectively. The high decrease in the resistivity of *r*GO/CNTs is promoted by the morphology of the film where *r*GO is spread homogeneously on the total area of the film and CNTs are deposited on the graphitic surfaces and interconnect the separated *r*GO nanosheets like wires. The conductivity can be further increased by a chemical anion doping of the composite film that is achieved by exposing it to thionyl chloride (SOCl_2) vapor. Actually, the sheet resistance of a film is decreased by this anion doping from 636 to $240 \Omega \text{sq}^{-1}$ whereas the optical transmittance is changed only slightly [10] (Figure 9.10).

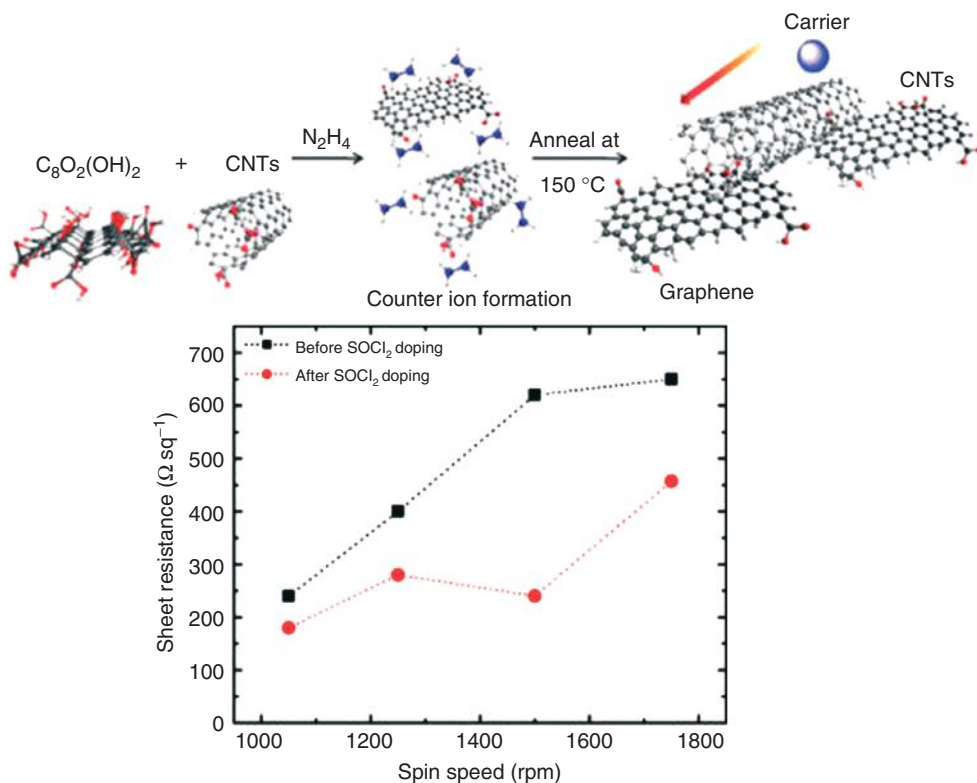


Figure 9.10 The formation of $rGO/CNTs$ in hydrazine. The influence of $SOCl_2$ doping on the sheet resistance of $rGO/CNTs$ composites. The different spin speeds correspond to analogous film thickness. (Reprinted with permission from Ref. [10], Copyright 2009, American Chemical Society.)

In a similar procedure SWNT and GO have been dispersed in water with the assistant of RNA molecules that act as surfactants. The transparent conductive $GO/SWNTs$ film formed by filtration is reduced by sodium boron hydride to $rGO/SWNTs$ and showed slightly better results than the previews work with a conductivity of $655\ \Omega\text{ s}^{-1}\text{q}$ and transparency at 95.6% [11] (Figure 9.10).

Similar $rGO/CNTs$ can be prepared, among other ways, by the vacuum filtration of a suspension of the two components through a polytetrafluoroethylene (PTFE) membrane, which can then be dissolved leaving a thin film of the composite with different morphology depending on the method of the filtration. When the two components are filtered consecutively from two different suspensions a double layered thin film is formed. On the other hand, after the filtration of a suspension of both components, the morphology of the formed film can be described as an interconnected network. The filtered mixture is prepared by the dispersion of GO and oxidized MWNTs in water with the assistance of sodium dodecyl sulfate (SDS) surfactant. The filtration is followed by the dissolving of polyethylene terephthalate

(PET) membrane in acetone, the reduction of GO/CNTs film to *r*GO/CNTs by hydrogen iodide (HI) and finally a p-type doping of the *r*GO/CNTs film by HNO₃ treatment with simultaneous removal of the surfactant. The HNO₃ treatment has a significant contribution to the increase in the conductivity because of the induced p-doping and the transparency by the removal of metal impurities, amorphous carbon, and surfactant.

The thickness of the film can be tuned by the volume of the filtered suspension. The conductivity of the film is increased as the thickness increases whereas the transparency is decreased. Both characteristics are also dependent on the ratio of the two components. An important advantage of the *r*GO/CNTs film against indium tin oxide (ITO) is the ability to function even after repeated flexures without serious changes in the conductivity. The two different films showed similar sheet resistance ($R_s = 240 \Omega \text{sq}^{-1}$ for the interconnected network and $R_s = 180 \Omega \text{sq}^{-1}$ for the double layered film) and optical transparency (about 80%) [12] (Figure 9.11).

GO and acid treated MWNTs dispersed in ethanol by sonication can be combined in a hybrid composite through π – π interactions and then incorporated in TiO₂ based photoanode for application in dye sensitized solar cells (DSSCs). The ratio of the two components is not predetermined and it depends on the surface morphology of graphene and MWNTs surfaces. A ratio of GO/MWNTs at 2 : 1 has been shown to produce the optimal dispersion in a solution. The incorporation of carbon hybrid in TiO₂ matrix resulted in the highest adsorption of dye in comparison with pure TiO₂ or mixed with the separated components. The advantage of the hybrid modified TiO₂ is attributed to the higher active surface area and the more uniform distribution of pores (Figure 9.12).

The photogeneration of electron/hole pairs in dye sensitized TiO₂, which is the first step of the energy conversion in DSSCs, is significantly reduced

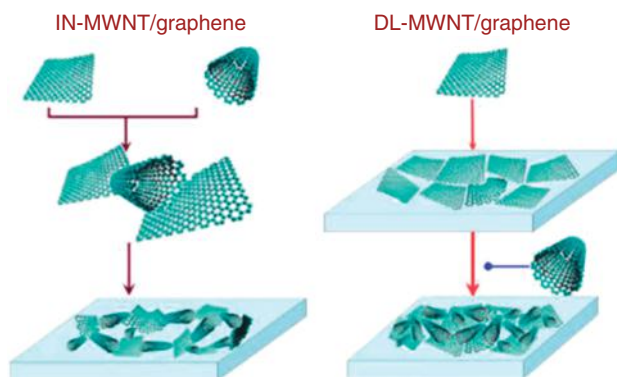


Figure 9.11 Two different ways to prepare thin films of the *r*GO/CNTs composites. The IN-MWNT/graphene described as interconnected network and DL-MWNT/graphene as double layered film. (Reprinted with permission from Ref. [12], Copyright 2012, American Chemical Society.)

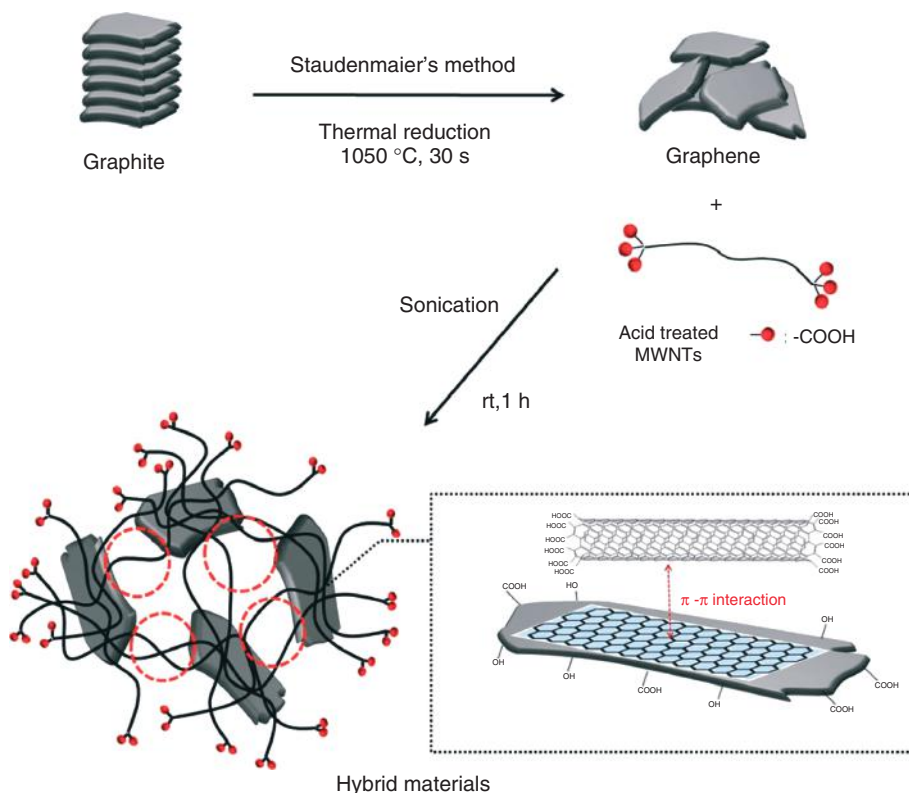


Figure 9.12 GO/MWNTs hybrid composite formation by sonication of a mixture of GO and acid treated MWNTs. (Reprinted with permission from Ref. [13], Copyright 2011, American Chemical Society.)

by charge recombination. This effect is suppressed by the insertion of a conductive carbon nanostructure between TiO_2 and the conductive glass. Here the use of the highly conductive GO/MWNTs hybrid showed the lowest recombination effect as indicated by the lowest photoluminescence emission band assigned to the electron/holes recombination. Finally the use of GO/MWNTs hybrid as photoanode in DSSC device showed the highest photocurrent density and conversion efficiency increase, 35% and 31%, respectively [13] (Figure 9.13).

In several cases GO/CNTs hybrids have been used in sensor devices for the voltammetric determination of organic compounds, such as hydrogen peroxide (H_2O_2), β -nicotinamide adenine dinucleotide (NADH) [14], tyrosine and paracetamol [15] which have a pharmaceutical interest, or are used as pesticides like carbendazim [16]. The voltammetric sensor is a three electrode system; glassy carbon, saturated calomel, and Pt, which are working sensors, references, and counter electrodes, respectively. The role of the hybrid GO/MWNTs in the voltammetric

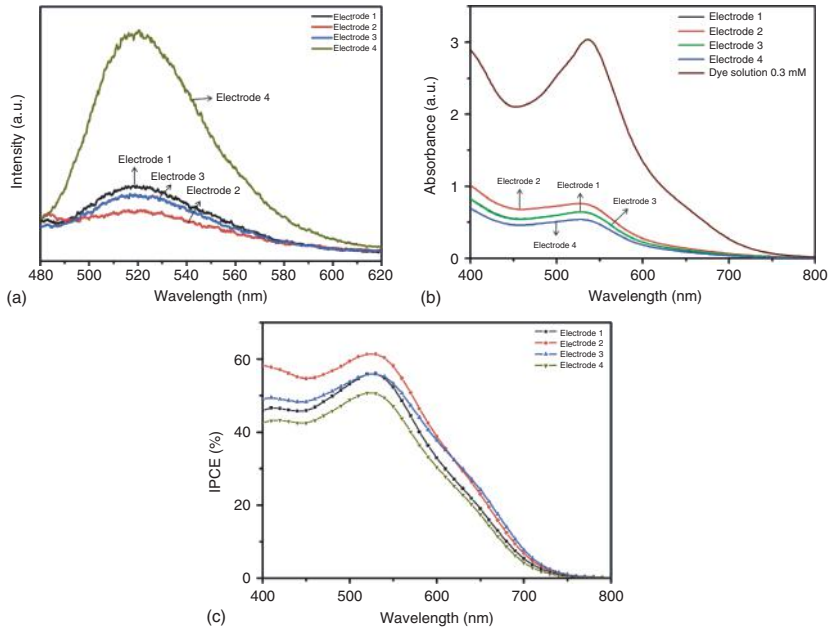


Figure 9.13 (a) UV-vis spectra of a dye solution and dye desorbed from composite working electrodes. The electrodes are made by pure TiO_2 (electrode 4) or TiO_2 and MWNTs (electrode 1), GO (electrode 3), and GO/MWNTs hybrid (electrode 2); (b) photolithography (PL) spectra and the incident photoconversion efficiency (IPCE) spectra; and (c) of DSSCs with the prepared electrodes. (Reprinted with permission from Ref. [13], Copyright 2011, American Chemical Society.)

measurements is examined with the use of a modified working electrode of glassy carbon that is surface covered by GO/MWNTs composite [15, 16]. The contribution of the hybrid in the voltammetric sensor is based on its high electrical conductivity, high surface area, which also means significant increase of the electroactive interaction sites, and finally high porosity of the modified glassy carbon electrode, all of which make the active sites more accessible and facilitate the transport of the detected molecules. As a consequence the modification of the voltammetric sensor by GO/MWNTs hybrid leads to the great improvement of the electrochemical response [15]. A GO/MWNTs modified voltammetric device for the determination of carbendazim showed a wider linear range from 10 nM to 4 μ M with a detection limit at 5 nM [16].

A rGO/SWNT hybrid modified glassy carbon electrode has been used in a biosensor for the detection of H₂O₂ and NADH. The modified electrode showed remarkable improvement in the performance of the biosensor that is attributed to the high conductivity of the hybrid and the better coverage of the electrode by the hybrid composite in comparison to the relative coverage that is offered by the single components. The linear detection range of H₂O₂ and NADH was ranged between 0.5 and 5 M and 20 and 400 μ M, while the limit of detection was 1.3 and 0.078 μ M, respectively [14].

The voltammetric technique has been also used for the detection of trinitrotoluene (TNT) with the assistance of a rGO/MWNT hybrid modified electrochemical system. A screen printed electrode in this system is covered by the hybrid formed by GO and MWNT in a water suspension and reduced electrochemically. The graphitic surface is further functionalized by ethylenediamine (EDA) through amidation with carboxylic acids of GO. The electron rich free primary amine groups are then responsible for the capture of the electron deficient TNT through the formation of a charge transfer system known as Jackson–Meisenheimer (JM) complex. The optical and electrochemical traces of this complex are used for the detection and the monitoring of trace levels of TNT [17] (Figure 9.14).

The use of the modified electrode in the electrochemical detection of TNT showed promising results such as the detection limit of TNT, which is decreased to 0.01 ppb. The colorimetric determination of TNT is based on the absorption JM complex formed and showed a linear detection range from 1 ppt to 1 pm (Figure 9.15).

In a different approach GO can be used as a protective surface to a CNT-based field effect transistor (FET), which is used as biosensor for the detection and determination of biomolecules such as proteins and DNA molecules. The role of GO here is to protect the SWNT surface from the physisorbed or chemisorbed biomolecules that cause degradation of the performance of the biosensor during the measurement. A thin film of GO is deposited on the SWNT/Au electrode and the biosensor device is completed by the deposition of Au nanoparticles and the immobilization of the 2-aminoethanethiol/biotin *N*-hydroxysuccinimide (NHS) probe [14] on it. The result of this SWNT passivation with GO layers is the improvement of the biosensor device sensitivity through the increase of the on/off ratio of the FET (Figure 9.16).

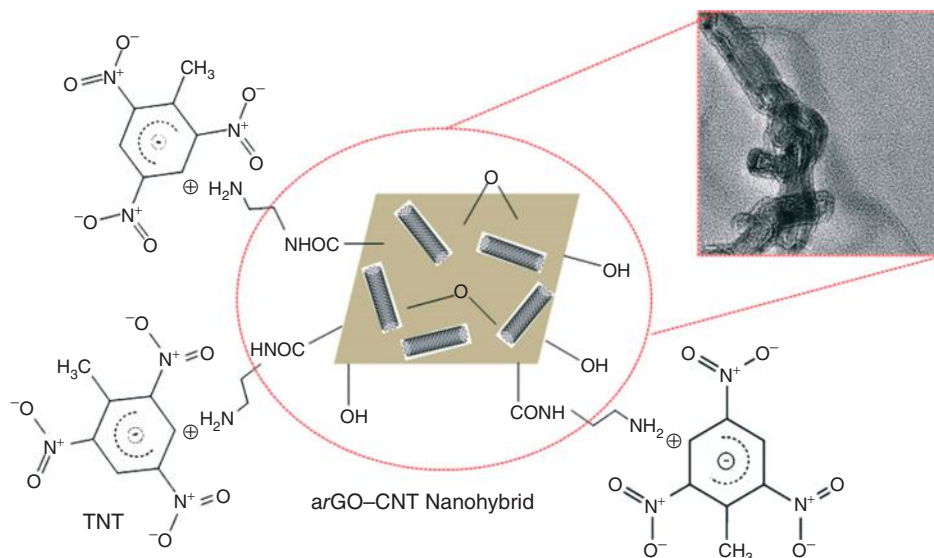


Figure 9.14 Schematic representation of the JM complex between TNT and amine modified *r*GO/MWNT hybrid. (Reprinted with permission from Ref. [17], Copyright 2011, Elsevier V.B.)

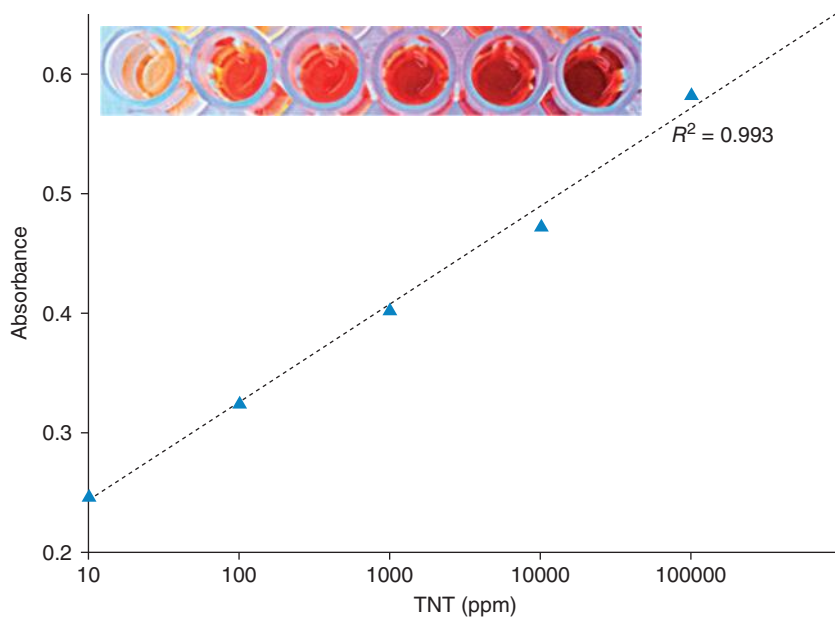


Figure 9.15 UV-vis calibration curve from several concentrations of TNT solutions. The inset photo of several samples with increased TNT concentration from left to right. (Reprinted with permission from Ref. [17], Copyright 2011, Elsevier V.B.)

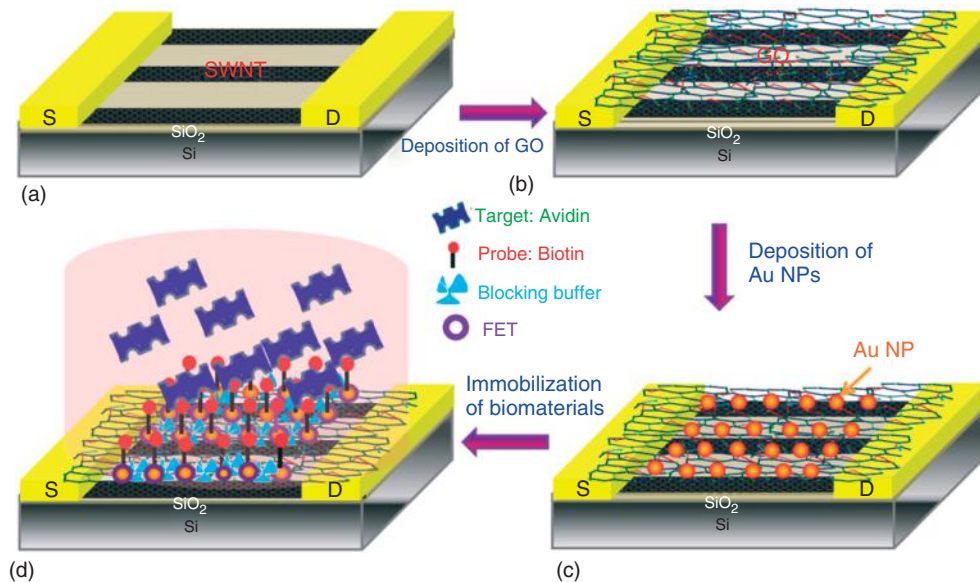


Figure 9.16 Schematic illustration of the SWNT/GO FET biosensor fabrication process. (Reprinted with permission from Ref. [18], Copyright 2013, Elsevier V.B.)

9.3.2

Graphene–CNTs Hybrid Nanostructures by Direct Development of CNTs on Graphene Surface

The role of graphene here is to be the substrate where CNTs are developed perpendicular to the surface and forming a 3D all carbon nanostructure. The most important advantage of this type lies in the extremely high active area, which is highly preferable in catalytic applications. The most suitable way for the perpendicular development of CNTs on the graphene surface is the catalytic growth by CVD technique [27–31]. In a characteristic procedure the growth of CNTs is performed by the decomposition of methane over Fe catalytic nanoparticles at high temperature [27] (Figure 9.17).

The iron catalytic centers are provided *in situ* by the reduction of a layered double hydroxide (LDH) FeMgAl lamellar substrate by the hydrogen that is generated from the decomposition of hydrocarbons at high temperature. Few-layer graphene nanosheets and SWNTs are then grown with the latter being developed perpendicular to the graphene surface. The SWNTs functionalized graphene hybrid (Graphene/SWNT) is obtained after the removal of the calcined LDH flakes. The high temperature – over 950 °C – is responsible for the appearance of graphene nanosheets in the product. CVD growth at temperatures lower than 900 °C produced only SWNTs (Figure 9.18).

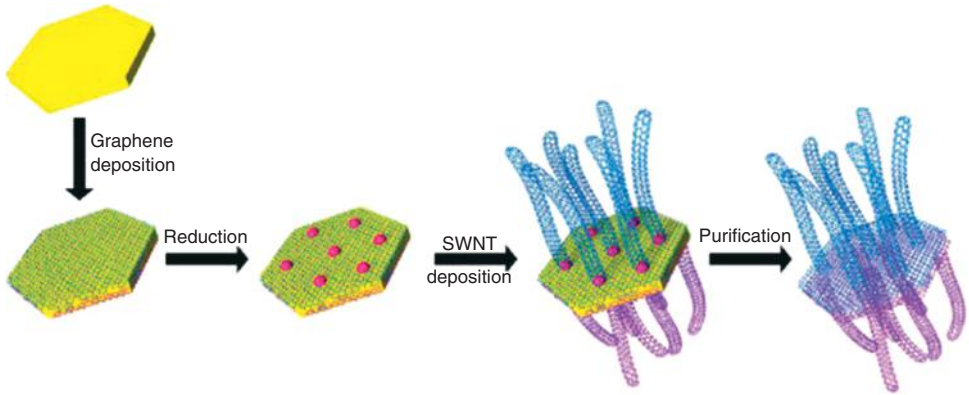


Figure 9.17 Schematic representation of the growth of graphene/SWNT hybrid on LDH flakes by catalytic CVD. (Reprinted with permission from Ref. [27], Copyright 2012, American Chemical Society.)

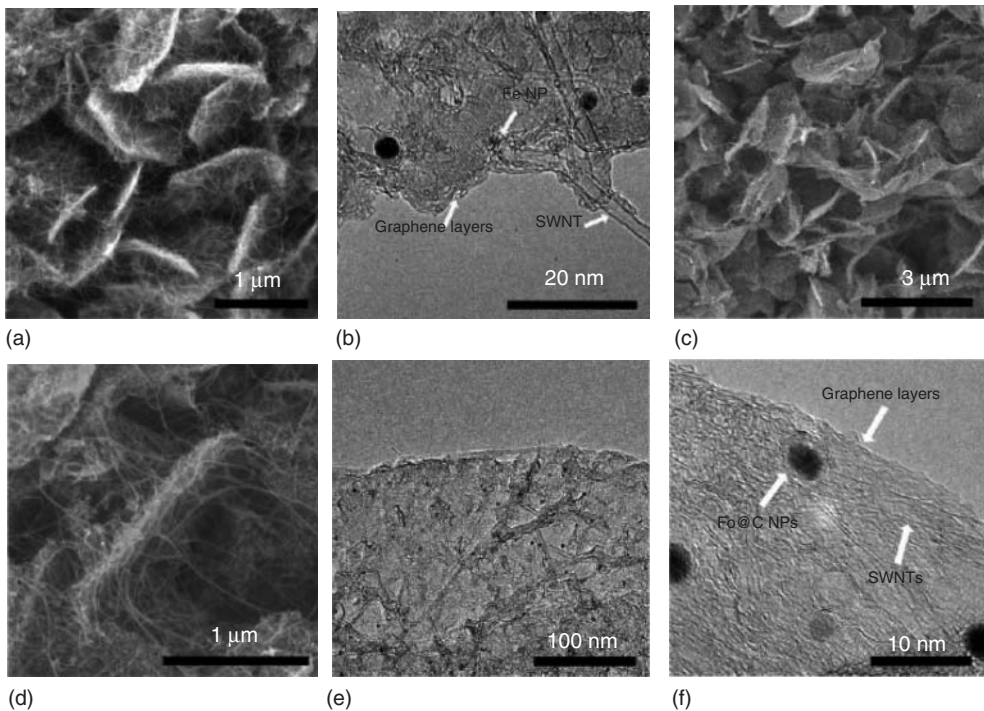


Figure 9.18 (a) SEM and (b) TEM images of graphene/SWNT/LDO hybrids. LDO is the layered double oxide by-product that has not yet been removed. (c,d) TEM images of

graphene/SWNT hybrid and (e,f) HRTEM images of graphene/CNTs nanostructure. (Reprinted with permission from Ref. [27], Copyright 2011, American Chemical Society.)

The Raman spectra of the hybrid product composed of the D and G bands that are common for both nanostructures and a group of radial breathing mode (RBM) peaks that revealed the existence of SWNTs in the composite. The I_D/I_G ratio is increased to 0.28 from 0.12 in SWNTs as a result of the increased number of defects that are observed in the graphene surface and at the graphene/SWNT junctions as well. The TGA diagram of the hybrid product reveals a sharp weight loss near 500 °C in a very short temperature range. The absence of weight loss below 500 °C is attributed to the low percentage of amorphous carbon impurities whereas the sharp weight loss is explained by the similar thermal stability of the as-prepared graphene and SWNT.

Although the way of the connection of SWNT on graphene is not directly indicated, it seems that C–C covalent bonds are formed at the junction between the two parts. The graphene/SWNT product have excellent properties such as large specific surface area, high electrical conductivity, structural stability, and high porosity, that can be valuable for the use of this hybrid in fabricating electrodes for energy storage. For example graphene/SWNT hybrid can host effectively large quantities of sulfur improving the capacity of a Li–S battery. Sulfur can be incorporated homogeneously into graphene/SWNT in a ratio of 60%, where it is stabilized thermally as shown by the relative TGA diagram (see Figure 9.23). A Li–S battery with S enriched graphene/SWNT as a cathode showed a high charge capacity of 650 mA h g⁻¹, which is almost stable after 100 cycles at a high current rate of 5 C (Figure 9.19).

A different approach to prepare graphene/CNT hybrid materials includes the CVD growth of CNTs on graphene substrates by the catalytic action of Ni nanoparticles that are dispersed on the graphene surface. The first step of this procedure is the formation of Ni nanoparticles on exfoliated rGO nanosheets. Then using CVD method with acetonitrile as carbon feed, CNTs are grown perpendicular to the rGO surface as pillars between the graphitic layers [28]. The CNT pillared graphene has a robust 3D porous structure with high specific surface area as high as 352 m² g⁻¹ (Figure 9.20).

9.4

Graphene–Carbon Nanospheres

GO has been functionalized by carbon nanospheres (CNSs) in a 3D all carbon pillared nanostructure with high surface area and electrical conductivity, where metallic nanoparticles can be deposited creating an efficient catalytic system for proton exchange membrane (PEM) fuel cells [32]. The low cost commercially available CNSs are conductive spherical nanoparticles with a diameter of 35 nm and a Brunauer–Emmett–Teller (BET) surface area of 232 m² g⁻¹. The incorporation of CNS between the GO layers is performed by mixing separate suspensions of both GO nanosheets and CNSs in water followed by the removal of the solvent by evaporation and lyophilization. The hybrid nanostructure was then heated under H₂ in order to remove oxygen groups from GO layers. The as-prepared partly

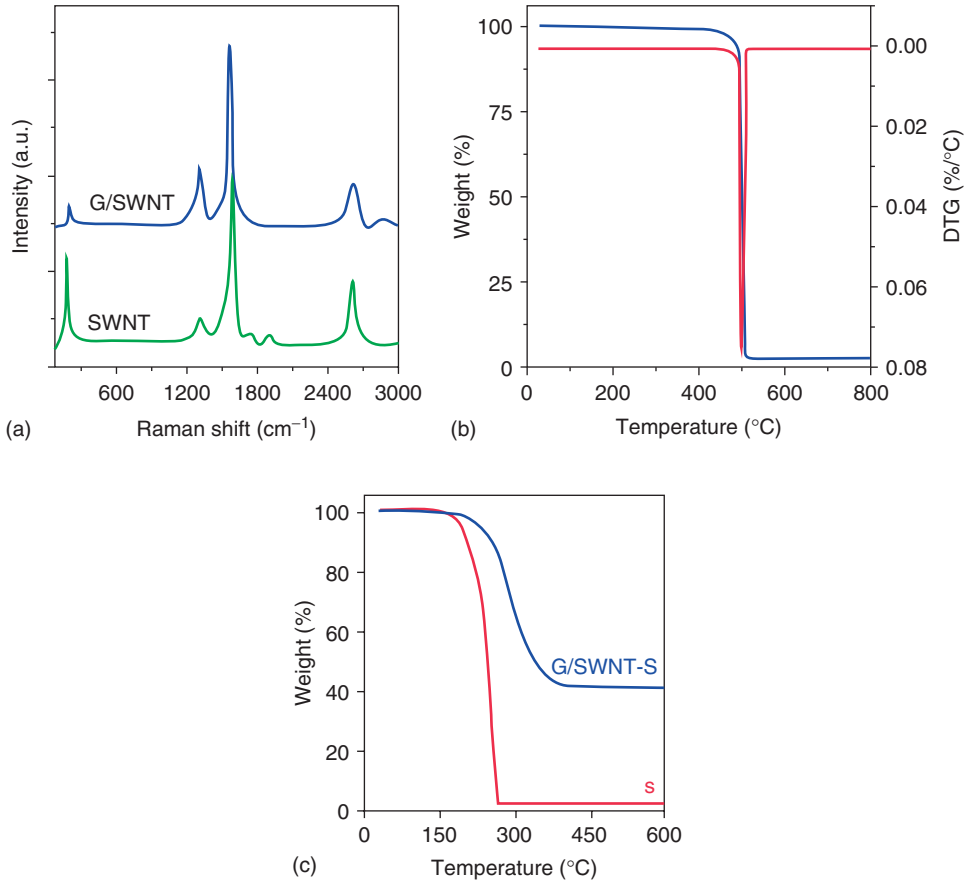


Figure 9.19 (a) Raman spectra of SWNT and graphene/SWNT prepared by CVD method. (b) TGA curve of graphene/SWNT hybrid under O₂. (c) TGA curves of sulfur and graphene/SWNT-S nanostructures. (Reprinted with permission from Ref. [27], Copyright 2012, American Chemical Society.)

reduced nanocomposite (*rGO*–CNS) is finally decorated by platinum nanoparticles through the reduction of Pt cations by ethylene glycol, leading to a 3D *rGO*–CNS nanoassembly enriched with Pt catalytic nanoparticles finely dispersed in its interlayer space (see Figures 9.21).

The subsequent dispersion of CNSs and GO nanosheets in water leads to stable aqueous colloids even though CNSs are not hydrophilic and water-dispersible by themselves. This result indicates the strong interaction between the two nanostructures in the liquid phase and before the removal of the water. It is not clear if this interaction leads to the formation of 3D nanoassembly already in the water phase or CNSs are just immobilized on the hydrophilic GO single layers which are dispersed in water, which is the most possible situation.

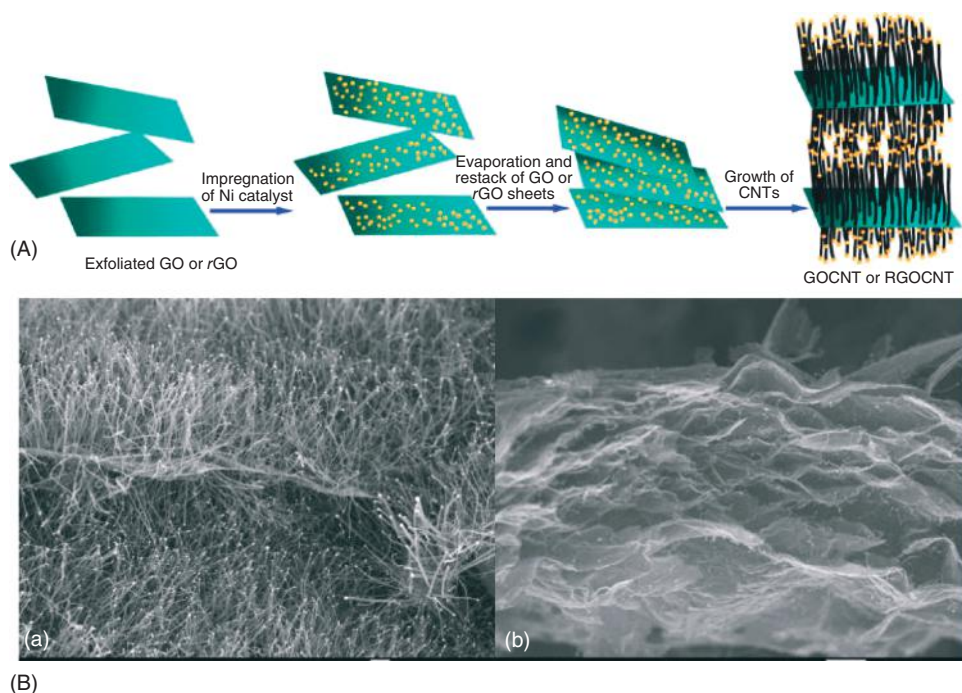


Figure 9.20 (A) CVD growth of CNTs on reduced GO layers; (B) Field emission scanning electron microscope (FESEM) images of the as prepared reduced graphene/CNTs hybrid material. (Reprinted with permission from Ref. [28], Copyright 2010, American Chemical Society.)

The hybrid nanocomposite showed an increased BET area because of the increased distance between the graphitic layers that is induced by the insertion and stabilization of CNSs into the interlayer space of *rGO*–CNSs nanoassembly. On the other hand the presence of GO nanosheets between the CNSs prevent them from overlapping and coalescence during the high temperature treatments. The porous structure of the all carbon *rGO*–CNS nanoassembly facilitates the dispersion of the water soluble Pt cation precursor into the interlayer space leading to the fine dispersion of Pt nanoparticles after the reduction step. A careful examination of TEM image shows that Pt nanoparticles are better dispersed in *rGO*–CNS nanoassemblies than in GO or commercial Carbon (see Figure 9.22).

In addition the porous structure of the final product improve the catalytic processes by facilitating the diffusion of the reaction gases and their access to the catalytic centers and the transportation of the products at high rates. The final Pt functionalized *rGO*–CNS showed much better stability and higher activity compared to Pt/CNS or Pt/C during electrochemical tests that supports the use of Pt/GCG (graphene–carbon–graphene) in PEM fuel cells (Figure 9.23).

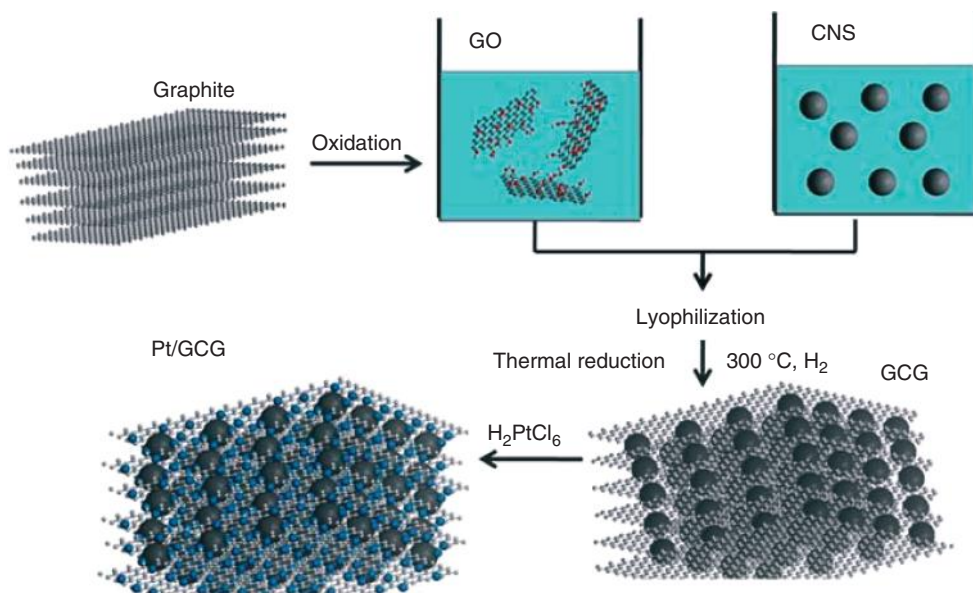


Figure 9.21 The formation of *rGO*–CNS nanoarchitecture (here symbolized as GCG by the authors) and its decoration with Pt catalytic nanoparticles. (Reprinted with permission from Ref. [32], Copyright 2013, Royal Society of Chemistry.)

9.5

Graphene–Carbon Nitride Dots Hybrid Nanocomposite

Carbon nitride dots (CNDs) have been recently developed as a new class of carbon nanomaterials [33–35]. They consist of carbon and nitrogen atoms organized in dots with diameters of several nanometers, interesting photoluminescence emission, and high dispersibility in water. An interesting hybrid material has been constructed by the deposition of CNDs on GO nanosheets and used as a substrate for the immobilization of glucose oxidase (GOD) for the preparation of a glucose biosensor. The CNDs are formed by polymerization of carbon tetrachloride (CCl_4) and EDA under reflux heating. CNDs and GO nanosheets are both suspended in water where they are organized into a composite material by the deposition of CNDs on GO surfaces. After the reduction of GO by hydrazine the final product is produced as *rGO*/CNDs hybrid composite [36]. Although *rGO* loses its hydrophilicity after the reduction, the presence of the highly hydrophilic CNDs offer excellent stability to the hybrid in water. The last step in the construction of the glucose biosensor is the immobilization of the negatively charged GOD on the graphitic surface with the assistance of the negatively charged CNDs and the electrostatic forces that are developed between them. The as-prepared GOD modified *rGO*/CNDs (GOD/*rGO*/CNDs) are deposited

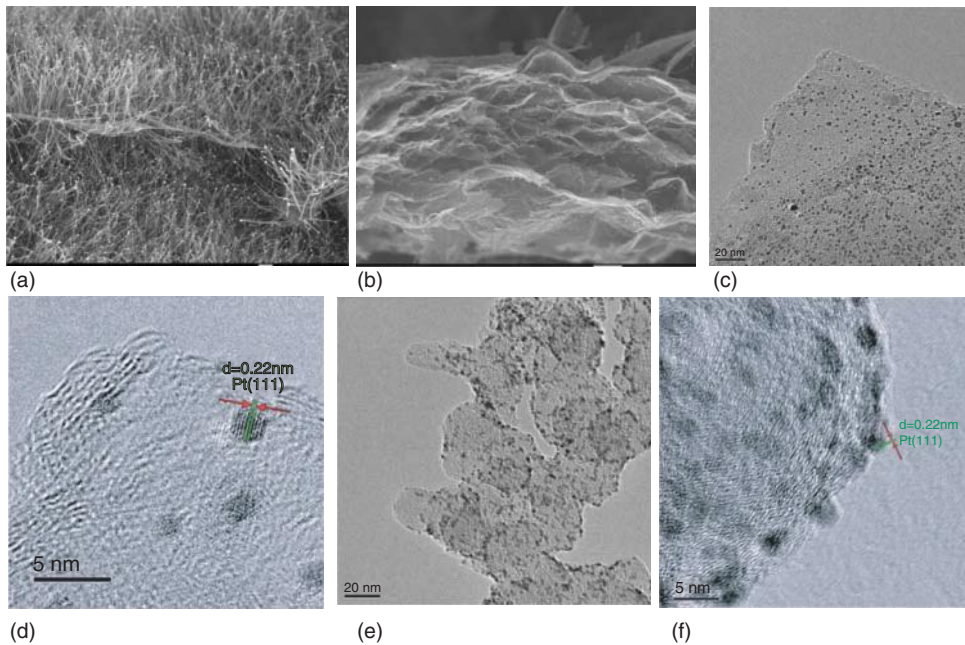


Figure 9.22 TEM images of Pt decorated rGO-CNS nanoassembly (a,b), GO (c,d), and commercial carbon (e,f). (Reprinted with permission from Ref. [32], Copyright 2013, Royal Society of Chemistry.)

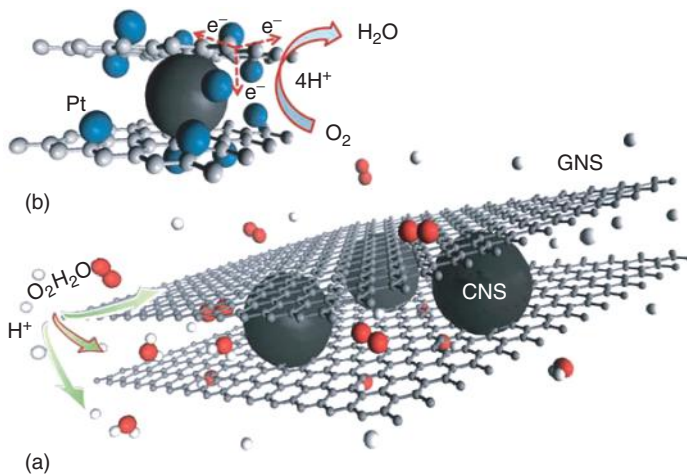


Figure 9.23 Schematic illustration of the nanoassembly and its catalytic activity for the oxygen reduction reaction. (Reprinted with permission from Ref. [32], Copyright 2013, Royal Society of Chemistry.)

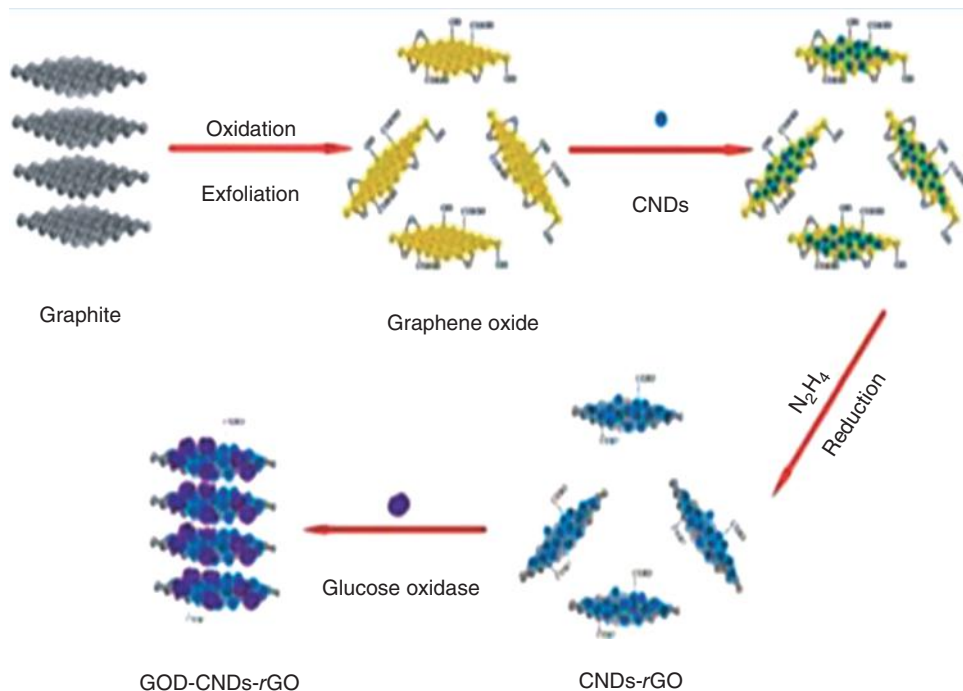


Figure 9.24 The schematic representation of the preparation of glucose biosensor by the immobilization of GOD on rGO/CNDs. (Reprinted with permission from Ref. [36], Copyright 2013, Elsevier V.B.)

on a glassy carbon electrode. The detection limit of glucose by this method is recorded at $40\ \mu\text{M}$ and the linear detection range is between $40\ \mu\text{M}$ and $20\ \text{mM}$ (Figure 9.24).

9.6

Conclusions

All carbon composites are represented by a new category of carbon nanomaterials that are formed either as a nanocomposite by the combination of already prepared simple carbon nanostructures or are constructed directly as happens when CNT are developed on graphene surfaces. All carbon composites are suitable for a variety of applications and in most cases their properties are superior to those of the single carbon nanostructures. The role of graphene in these nanocomposites is crucial and as a consequence a large number of carbon nanostructures are based on graphene or GO nanosheets. The main advantages that necessitate the presence of graphene in these nanostructures are that it has the largest active surface among carbon nanostructures, higher conductivity,

and it is provided easily from an abundant and cheap precursor. The further chemical functionalization is expected to lend a dominant role to all carbon nanostructures.

References

- Liu, Z.B., Xu, Y.F., Zhang, X.Y., Zhang, X.L., Chen, Y.S., and Tian, J.G. (2009) *J. Phys. Chem. B*, **113**, 9681.
- Wudl, F. (2002) *J. Mater. Chem.*, **12**, 1959.
- Yu, D., Park, K., Durstock, M., and Dai, L. (2011) *J. Phys. Chem. Lett.*, **2**, 1113.
- Jeon, E.K., Yang, C.S., Shen, Y., Nakanishi, T., Jeong, D., Kim, J.J., Ahn, K., Kong, K., Jeon, J.O., Yang, C.S., Shen, Y., Nakanishi, T., Jeong, D., Kim, J.J., Ahn, K., Kong, K., and Lee, J.O. (2012) *Nanotechnology*, **23**, 455202.
- Zhang, X., Huang, Y., Wang, Y., Ma, Y., Liu, Z., and Chen, Y. (2009) *Carbon*, **47**, 334.
- Yang, J., Heo, M., Lee, H.J., Park, S.M., Kim, J.Y., and Shin, H.S. (2011) *ACS Nano*, **10**, 8365.
- Tung, V.C., Huang, J.H., Kim, J., Smith, A.J., Chu, C.W., and Huang, J. (2012) *Energy Environ. Sci.*, **5**, 7810.
- Chao, Z. and Xi, L.T. (2012) *Chin. Sci. Bull.*, **57**, 3010.
- Zhang, C., Ren, L., Wang, X., and Liu, T. (2010) *J. Phys. Chem. C*, **114**, 11435.
- Tung, V.C., Chen, L.M., Allen, M.J., Wassei, J.K., Nelson, K., Kaner, R.B., and Yang, Y. (2009) *Nano Lett.*, **9**, 1949.
- Wang, R., Sun, J., Gao, L., Xu, C., Zhang, J., and Liu, Y. (2011) *Nanoscale*, **3**, 904.
- Peng, L., Feng, Y., Lv, P., Lei, D., Shen, Y., Li, Y., and Feng, W. (2012) *J. Phys. Chem. C*, **116**, 4970.
- Yen, M.Y., Hsiao, M.C., Liao, S.H., Liu, P., Tsai, H.M., Ma, C.C.M., Pu, N.W., and Ger, M.D. (2011) *Carbon*, **49**, 3597.
- Huang, T.Y., Huang, J.H., Wei, H.Y., Ho, K.C., and Chu, C.W. (2013) *Biosens. Bioelectron.*, **43**, 173.
- Arvand, M. and Gholizadeh, T.M. (2013) *Colloids Surf., B: Biointerfaces*, **103**, 84.
- Luo, S., Wu, Y., and Gou, H. (2013) *Ionics*, **19**, 673.
- Sablok, K., Bhalla, V., Sharma, P., Kaushal, R., Chaudhary, S., and Raman Suri, C. (2013) *J. Hazard. Mater.*, **248–249**, 322.
- Chang, J., Mao, S., Zhang, Y., Cui, S., Steeber, D.A., and Chen, J. (2013) *Biosens. Bioelectron.*, **42**, 186.
- Tian, L., Meziari, M.J., Lu, F., Kong, C.Y., Cao, L., Thorne, T.J., and Sun, Y.P. (2010) *Appl. Mater. Interfaces*, **2**, 3217.
- Shao, J.J., Lv, W., Guo, Q., Zhang, C., Xu, Q., Yang, Q.H., and Kang, F. (2012) *Chem. Commun.*, **48**, 3706.
- Velten, J., Mozer, A.J., Li, D., Officer, D., Wallace, G., Baughman, R., and Zakhidov, A. (2012) *Nanotechnology*, **23**, 085201.
- Chen, S., Yeoh, W., Liu, Q., and Wang, G. (2012) *Carbon*, **5**, 4557.
- Zheng, Z., Du, Y., Wang, Z., Zhang, F., and Wang, C. (2012) *J. Mol. Catal. A: Chem.*, **363**, 481.
- Vinayan, B.P., Nagar, R., Raman, V., Rajalakshmi, N., Dhathathreyan, K.S., and Ramaprabhu, S. (2012) *J. Mater. Chem.*, **22**, 9949.
- Kim, J.Y., Jang, J.W., Youn, D.H., Kim, J.Y., Kim, E.S., and Lee, J.S. (2012) *RSC Adv.*, **2**, 9415.
- Sui, Z., Meng, Q., Zhang, X., Ma, R., and Cao, B. (2012) *J. Mater. Chem.*, **22**, 8767.
- Zhao, M.Q., Liu, X.F., Zhang, Q., Tian, G.L., Huang, J.Q., Zhu, W., and Wei, F. (2012) *ACS Nano*, **6**, 10759.
- Zhang, L.L., Xiong, Z., and Zhao, X.S. (2010) *ACS Nano*, **7030**.
- Fan, Z., Yan, J., Zhi, L., Zhang, Q., Wei, T., Feng, J., Zhang, M., Qian, W., and Wie, F. (2010) *Adv. Mater.*, **22**, 3723.
- Fan, Z.J., Yan, J., Wei, T., Ning, G.Q., Zhi, L.J., Liu, J.C., Cao, D.X., Wang, G.L., and Wei, F. (2011) *ACS Nano*, **5**, 2787.

31. Sridhar, V., Kim, H.J., Jung, J.H., Lee, C., Park, S., and Oh, I.K. (2012) *ACS Nano*, **6**, 10562–10570.
32. He, D., Cheng, K., Peng, T., Pan, M., and Mu, S. (2013) *J. Mater. Chem. A*, **1**, 2126.
33. Liu, S., Tian, J., Wang, L., Luo, Y., Zhai, J., and Sun, X. (2011) *J. Mater. Chem.*, **21**, 11726.
34. Liu, S., Wang, L., Tian, J., Zhai, J., Luo, Y., Lu, W., and Sun, X. (2011) *RSC Adv.*, **1**, 951.
35. Liu, S., Tian, J., Wang, L., Luo, Y., and Sun, X. (2012) *RSC Adv.*, **2**, 411.
36. Qin, X., Asiri, A.M., Alamry, K.A., Al-Youbi, A.O., and Sun, X. (2013) *Electrochim. Acta*, **95**, 260–267.

10

Doping of Graphene by Nitrogen, Boron, and Other Elements

Achutharao Govindaraj and C.N.R. Rao

10.1

Introduction

Graphene can be doped with boron and nitrogen as well as with other heteroatoms. B_2H_6 is generally used as the boron source, whereas NH_3 or pyridine is employed as the nitrogen source for doping graphene by chemical vapor deposition (CVD) and arc-discharge techniques. Urea as a nitrogen source is also found to be very effective. Substitutional doping of graphene with boron and nitrogen brings about significant changes in their electronic structure and properties. Doping with boron and nitrogen causes marked changes in the Raman spectra of the carbon nanostructures. Such doping not only results in desirable properties but allows manipulation of properties for specific purposes. In this article, we present the synthesis, characterization, and properties of graphene doped with boron, nitrogen, and other elements and also discuss their important applications.

The discovery of graphene has opened a new era in the science of two-dimensional (2D) materials [1–3]. As the mother of all graphitic forms, graphene is the building block for carbon materials of all dimensionalities. One atom-thick graphene sheets with a 2D planar geometry exhibit novel electron transport properties [4]. Several procedures for the preparation of graphenes have been described in the literature [5, 6]. By doping, one can alter the electronic and quantum transport properties of graphene. We have recently presented the highlights of some of the research on the synthesis and selected properties of graphene and graphene mimics [7]. Doping of graphenes can be classified into the following categories [8]: electrical doping, such as gate-controlled doping [9, 10], metallic cluster-induced doping [11] or substrate-induced doping [12], chemical doping, occurring when the lattice structures of graphene are changed by chemical routes, such as substitutional doping with heteroatoms [13], and molecular doping [14]. These modifications strongly depend on the type of dopants, their concentrations, and location within the graphene structure.

10.2

Nitrogen-Doped Graphene

Nitrogen doping has been an effective way to modify the properties of graphene and render its potential use for various applications. Three common C–N bonding configurations are normally obtained when doping nitrogen into the graphene lattice; pyridinic N, pyrrolic N, and graphitic N. Attempts have also been made to introduce nitrogen and boron into graphene sheets in order to modify their electronic properties [15–19].

10.2.1

DC Arcing

Nitrogen-doped graphene (NG) composed of two to three layers is prepared by carrying out DC arc discharge experiments in the presence of H_2 + pyridine or H_2 + ammonia [16]. The method makes use of the fact that in the presence of hydrogen, graphene sheets do not readily roll into nanotubes. Transformation of nanodiamond in the presence of pyridine also yields a nitrogen-doped graphene. One set of nitrogen doped graphene samples (NG1) was prepared by carrying out DC arc discharge (38 V, 75 A) of graphite electrodes in the presence of H_2 , He, and pyridine vapor. In a typical experiment, pyridine vapor is carried to the arc chamber by passing hydrogen (200 Torr) through a pyridine bubbler and subsequently by passing He (500 Torr). A second set of nitrogen doped samples (NG2) was prepared by carrying out arc discharge of graphite electrodes in the presence of H_2 (200 Torr), He (200 Torr), and NH_3 (300 Torr). Transformation of nanodiamond was also carried out in the presence of He and pyridine vapor at 1650 °C to obtain N-doped graphene (NG3). All the doped samples were characterized by a variety of physical methods along with an undoped sample prepared by arc-discharge in hydrogen (HG) for comparison. Figure 10.1 shows TEM (transmission electron microscope) images of pure and N-doped graphene prepared by the arc-discharge method, as well as calculated scanning tunneling microscopy (STM) image of N-doped graphene bilayer. X-ray photoelectron spectroscopic (XPS) analysis show NG1, NG2, and NG3 to contain 0.6, 0.9, and 1.4 at.% of nitrogen, respectively.

In Figure 10.2a, we show XPS data of the NG2 sample along with electron energy loss spectroscopy (EELS) elemental mapping. The asymmetric shape of the N 1s peak indicates the existence of at least two components. On deconvolution, we find peaks at 398.3 and 400 eV, the first one being characteristic of pyridinic nitrogen (sp^2 hybridization) and the second of nitrogen in the graphene sheets.

Raman spectroscopy is ideally suited for the characterization of graphene and doped graphene. Pure graphene shows three main features in the 1000–3000 cm^{-1} region in the Raman spectrum (with 632.8 nm excitation): G-band characteristic of the sp^2 -network ($\sim 1570\text{ cm}^{-1}$), defect-related D-band ($\sim 1320\text{ cm}^{-1}$), and 2D-band ($\sim 2640\text{ cm}^{-1}$). Raman spectra of pure and doped graphenes are shown in

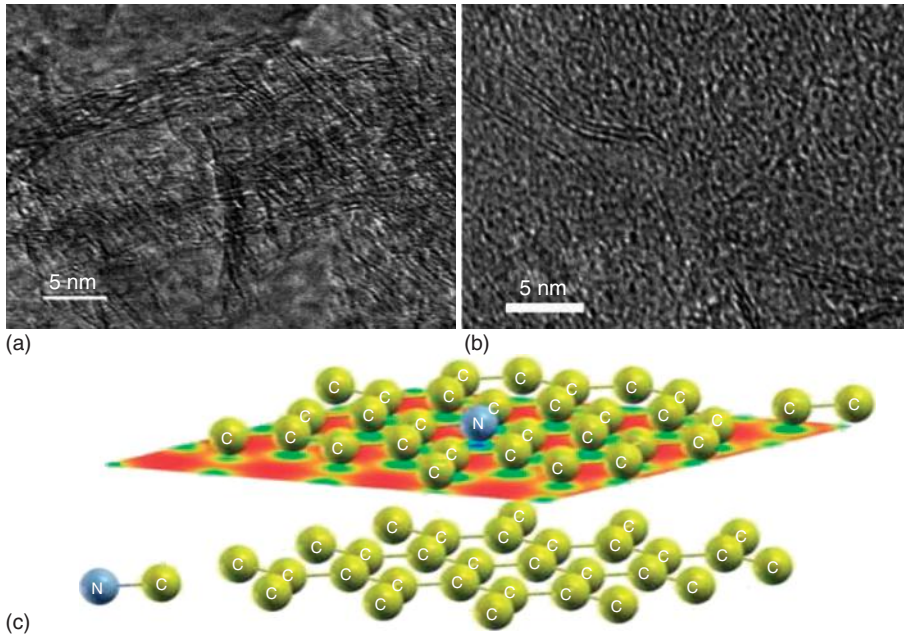


Figure 10.1 TEM images of (a) undoped (HG), (b) nitrogen-doped (NG) graphenes, and (c) calculated scanning tunneling microscopy (STM) image of N-doped bilayers. N doping results in addition of electronic charge on carbon atoms on the sublattice of the substituted dopant, as evident in weaker blue color (N). (Reproduced from Ref. [16].)

Figure 10.3. The G-band stiffens both with nitrogen doping. This is similar to what happens with electrochemical doping [9], but differs from what occurs when the doping is through molecular charge-transfer [20, 21]. Stiffening of the G-band arises from the nonadiabatic removal of the Kohn anomaly at the G-point, and its broadening is because of the absence of blockage of the decay channels of the phonons into electron–hole pairs [22]. The intensity of the D-band is higher with respect to that of the G-band in doped samples. On doping, the relative intensity of the 2D-band generally decreases with respect to that of the G-band. N and B-doped graphenes exhibit higher electrical conductivity than undoped graphene.

Gopalakrishnan *et al.* [23] studied the effect of interaction of tetracyanoethylene (TCNE) and tetrathiafulvalene (TTF) with boron- and nitrogen-doped graphene prepared by employing Raman spectroscopy. The G and 2D bands of boron- and nitrogen-doped graphenes in the Raman spectra show significantly different changes on interaction with electron-donor and electron-acceptor molecules. Thus, TCNE and TTF have different effects on the Raman spectra of boron- and nitrogen-doped graphenes. The changes in the Raman spectra brought about by electron-donor and electron-acceptor molecules can be understood

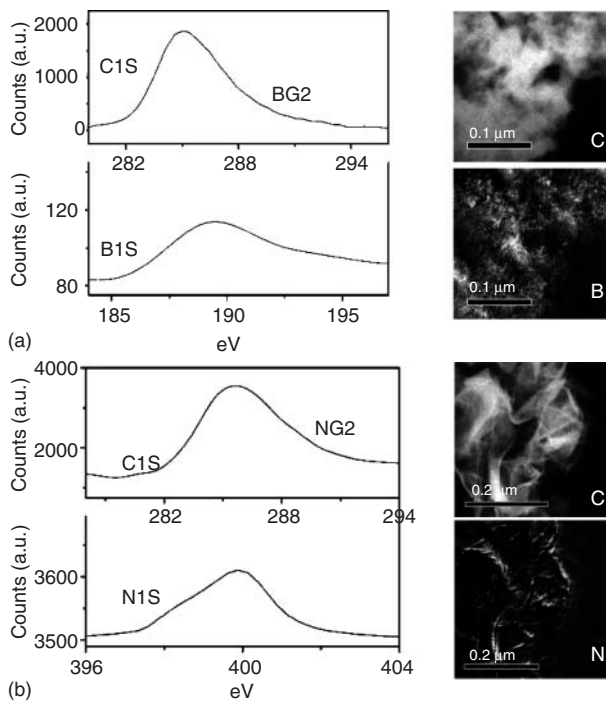


Figure 10.2 (a) C 1s and N 1s XPS signals of N-doped graphene (NG2), EELS elemental mapping of C and N of NG2. (b) C 1s and B 1s XPS signals of B-doped graphene (BG2), EELS elemental mapping of C and B of BG2. (Reproduced from Ref. [16].)

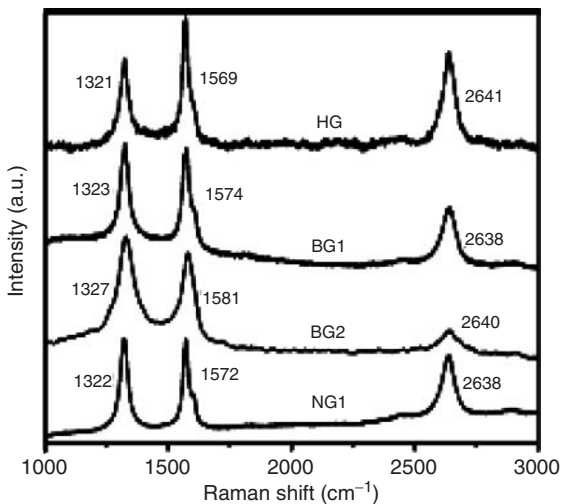


Figure 10.3 Raman spectra of undoped (HG) and doped (BG and NG) graphene samples. (Reproduced from Ref. [16].)

on the basis of molecular charge transfer. Guan *et al.* synthesized few-layer nitrogen-doped graphene nanosheets (N-GNSs) by a DC arc discharge under a nitrogen atmosphere at high temperature [24]. The cathode was a pure graphite rod and the anode was a composite graphite rod (6 mm diameter) filled with a mixture of Fe_2O_3 , Co_2O_3 , NiO , and graphite powder, wherein each of the Fe, Co, and Ni elements was 1.5 wt% in the mixture. The nitrogen (purity > 99.9 vol%, 50 sccm flow rate) was first heated to 800 °C before flowing into the arc discharge chamber. The gap between the graphite electrodes was kept constant in the range of 0.5–1 mm by manually advancing the consumed anode and the discharge voltage and current varied between 30–32 V and 25–30 A, respectively. N-doped graphene sheets formed inside the inner core of the column-shaped deposits on the top of the cathode. The content of few-layer N-GNSs in the column-shaped deposits formed on the top of the cathode is larger than 50 wt%.

10.2.2

Heating with Ammonia, Hydrazine, and Other Reagents

The formation of the C–N bond occurs mostly at the edges of graphene where chemical reactivity is high. Li *et al.* developed a simultaneous doping and reduction technique to obtain bulk quantities of N-doped (up to 5% doping), reduced graphene oxide (RGO) sheets through thermal annealing of graphene oxide (GO) in ammonia [18]. XPS study of GO sheets annealed at various reaction temperatures reveals that N-doping occurs at a temperature as low as 300 °C, whereas the highest doping level of ~5% N is achieved at 500 °C. N-doping is accompanied by the reduction of GO which decreases the oxygen level from ~28% in as-made GO down to ~2% in 1100 °C NH_3 -reacted GO. XPS analysis of the N binding configurations of doped GO finds pyridinic N in the doped samples, with increased quaternary N (N that replaces the carbon atoms in the graphene plane) in GO annealed at higher temperatures (≥ 900 °C). Oxygen groups in GO are generally responsible for reactions with NH_3 and C–N bond formation. Pre-reduced GO with fewer oxygen groups by thermal annealing in H_2 reduces the reactivity of NH_3 and gives lower N-doping level. Electrical measurements of individual GO sheet devices demonstrate that GO annealed in NH_3 exhibits higher conductivity than those annealed in H_2 , suggesting more effective reduction of GO by annealing in NH_3 rather than in H_2 , consistent with the XPS data. Wang *et al.* covalently functionalized individual graphene nanoribbons with nitrogen by high-power electrical Joule heating/annealing in NH_3 gas, leading to n-type electronic doping consistent with theory [19]. Li *et al.* prepared N-doped graphene (NG) by annealing reduced graphene oxide (RGO) in an ammonia atmosphere and in vacuum respectively and examined the photoluminescence properties of RGO and NG [25]. The results show that doping RGO with N can quench its fluorescence and the fluorescence quenching of NG obtained in vacuum being more efficient than that prepared in atmosphere.

Huan *et al.* have demonstrated a simple and efficient method to enhance the quaternary nitrogen doping (N-doping) of graphene oxide via chemical reduction prior to thermal annealing [26]. The strategy employed was to modify graphene oxide (GO) prior to thermal annealing so as to provide a more efficient structure for quaternary N doping. GO was first chemically reduced with hydrazine to substantially increase the formation of C=C bonds and simultaneously decrease the atomic oxygen concentration. The reduced graphene oxide (RGO) was then annealed in the presence of NH_3 . Although N-doping via the replacement of oxygen is preferred, the probability of carbon being substituted with N dopants in the graphitic structure of RGO could increase because of the higher content of C=C. Park *et al.* performed experiments to investigate the chemical structures evolved from hydrazine-treated graphene oxide [27]. The chemical structures of ^{15}N -labeled hydrazine-treated ^{13}C -labeled graphite oxide (produced by the modified Hummer's method) and unlabeled hydrazine-treated graphene oxide studied by different spectroscopic techniques confirm the insertion of an aromatic nitrogen in a five-membered ring at the platelet edges, restoring the graphitic network in the basal planes.

10.2.3

Chemical Functionalization Route

Jeon *et al.* prepared large-area nitrogen-doped graphene films from simple solution casting of edge-selectively functionalized graphite [28]. In the first step, graphite is edge-selectively functionalized with 4-aminobenzoic acid by a "direct" Friedel-Crafts acylation reaction in a polyphosphoric acid/phosphorus pentoxide medium to produce 4-aminobenzoyl edge-functionalized graphite (EFG). In the second step, EFG is dispersed in *N*-methyl-2-pyrrolidone (NMP), followed by solution casting to yield large-area graphene films on silicon wafers. Upon heat treatment, the EFG film becomes an N-doped graphene (N-graphene) film to display outstanding electrocatalytic activity for oxygen reduction reaction (ORR). Chang *et al.* report an efficient method for preparing nitrogen-doped graphene nanoplatelets via wet-chemical reactions from simple solution edge-functionalization of graphene [29]. The reaction between the monoketone (C=O) in graphene oxide (GO) and monoamine containing compound produces imine functionalized GO (iGO) (Figure 10.4). The reaction between a-diketone in GO and 1,2-diamine (ortho-diamine)-containing compound gives stable pyrazine ring functionalized GO (pGO). Subsequent heat-treatment of iGO and pGO results in high-quality nitrogen-doped graphene nanoplatelets to be designated as hiGO and hpGO, respectively. Interestingly hpGO displays n-type field-effect transistor (FET) behavior with a charge neutral point (Dirac point) located at $\sim -16\text{ V}$. hpGO also showed hole and electron mobilities ~ 11.5 and $12.4\text{ cm}^2\text{ V}^{-1}\text{ s}^{-1}$, respectively.

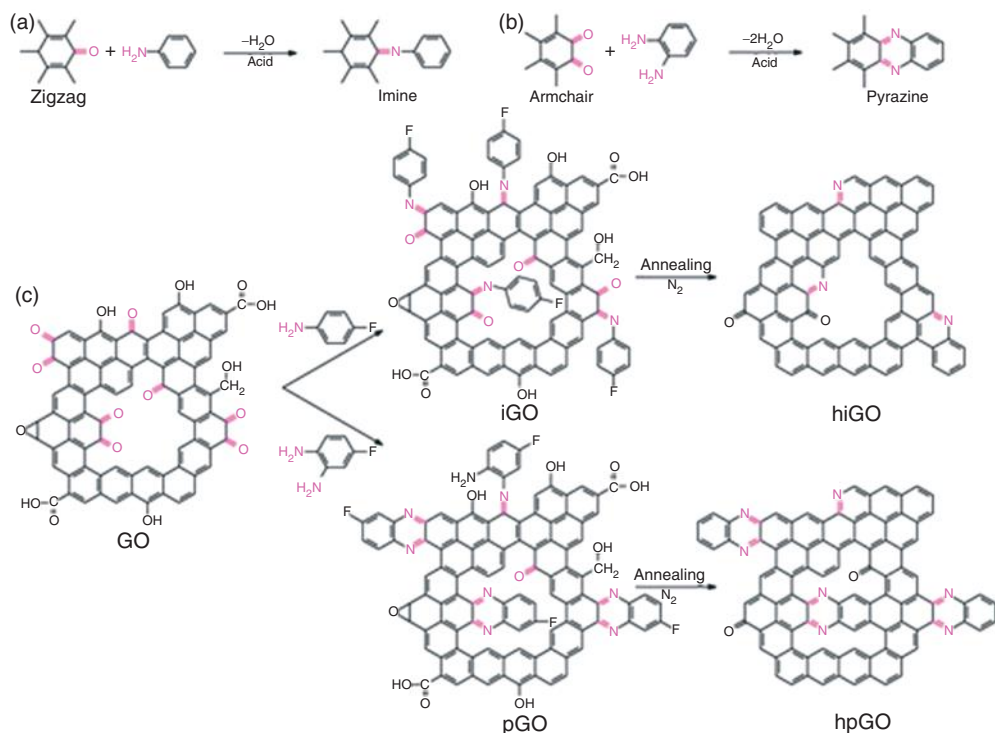


Figure 10.4 Schematic representations: (a) GO and 4-fluoroaniline or 1,2-diamino-4-fluorobenzene to yield iGO or pGO, respectively. Subsequent heat treatment of iGO and pGO under nitrogen atmosphere produced hiGO and hpGO, respectively. (Reproduced with permission from [29]. Copyright © 2013 American Chemical Society.)

10.2.4

Solvothermal Synthesis

Deng *et al.* [30] developed a solvothermal method for one-pot direct synthesis of N-doped graphene via the reaction of tetrachloromethane with lithium nitride under mild conditions at 250 °C for 10 h in a stainless steel autoclave in nitrogen, which renders fabrication in gram scale. The product was washed sequentially with 18 wt% HCl aqueous solution, water, and ethanol, followed by drying at 120 °C for 12 h. Alternatively, cyanuric chloride was mixed with lithium nitride instead of tetrachloromethane and the reaction carried out at 350 °C for 6 h and the product washed and dried. The distinct electronic structure perturbation induced by the incorporation of nitrogen (4.5–16.4%) in the graphene network was observed by STM (Figure 10.5). The enhanced catalytic activity of N-doped graphene was

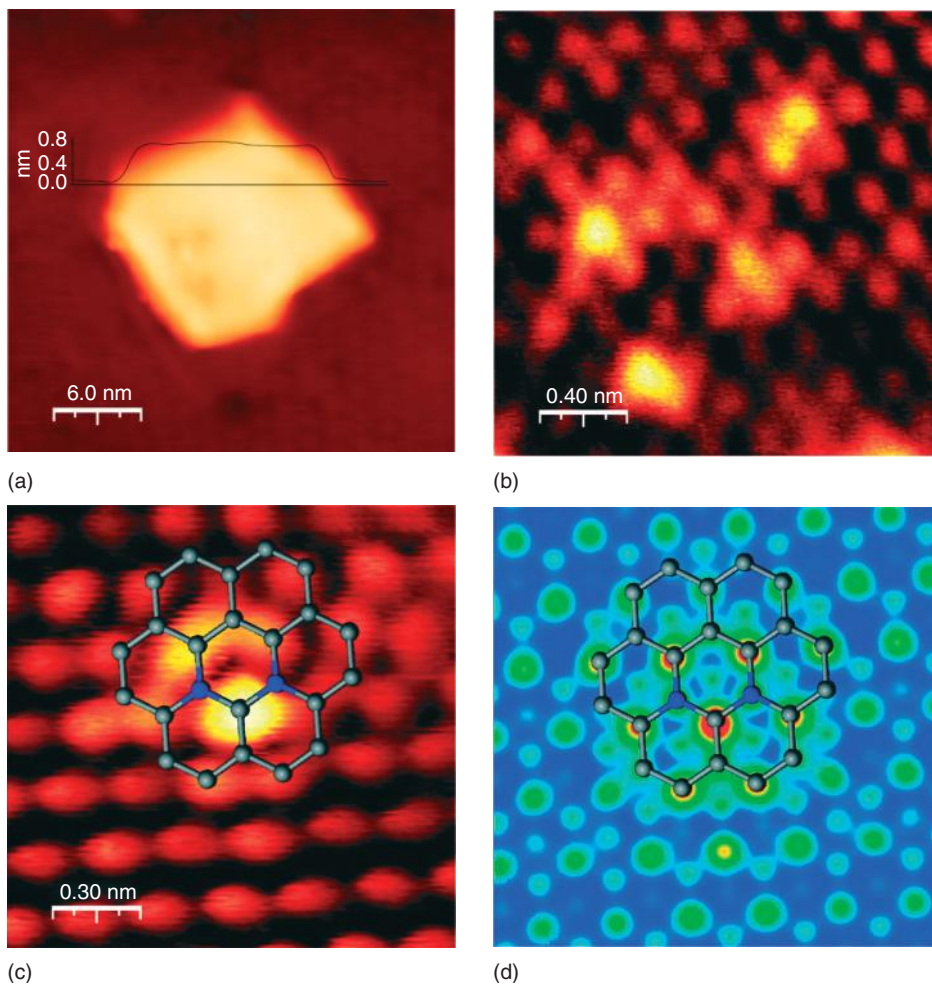


Figure 10.5 STM images of NG-2. (a) Isolated bilayer N-doped graphene and the black curve on top showing the height measurement across this bilayer. (b,c) High resolution images with defects arranged in different configurations, measured at a Bias = 0.5 V, current $I = 53.4$ pA, and Bias = 0.9 V, $I = 104$ pA, respectively. (d)

Simulated STM image for (c). The inserted schematic structures represent N-doping graphene, with the hexagons in gray balls highlighting the atomic network of graphene and deep blue balls labeling N atoms. (Reproduced with permission from [30]. Copyright © 2011 American Chemical Society)

demonstrated in a fuel cell cathode ORR with respect to pure graphene and commercial carbon black XC-72.

Nitrogen-doped graphene sheets are prepared through a combined chemical and hydrothermal reduction of colloidal dispersions of graphene oxide in the presence of hydrazine and ammonia at pH of 10 [31]. Oxygen reduction and nitrogen doping were achieved simultaneously under hydrothermal conditions.

Up to 5 wt% nitrogen-doped graphene sheets with slightly wrinkled and folded features were obtained at a relatively low hydrothermal temperature. With increase in hydrothermal temperature, the nitrogen content decreased slightly and more pyridinic N was incorporated into the graphene network. A jellyfish-like graphene structure was formed by self-organization of graphene sheets at a hydrothermal temperature of 160 °C. On further increase of the temperature to 200 °C, graphene sheets self-aggregate into agglomerate particles but still contained a doping level of 4 wt% N. Hassan *et al.* [32] report the preparation of pyrrolic-structure enriched N-doped graphene by hydrothermal synthesis at varied temperatures. Initially the pH of the aqueous solution of graphitic oxide was adjusted to 10–11 using ammonia before adding 1.75 ml of aqueous hydrazine. The mixture was transferred to a Teflon-lined autoclave and subjected to hydrothermal treatment for 3 h at three different temperatures including 80, 130, and 180 °C. Doping graphene with N increased the electrical double layer supercapacitance to $\sim 194 \text{ F g}^{-1}$ and density functional theory (DFT) calculation showed the proper level of binding energy found between the pyrrolic-N structure and the electrolyte ions, thus explaining the highest contribution of the pyrrolic-structure to the capacitance.

N-GNSs with a nitrogen level as high as 10.13 at.% has been synthesized via a simple hydrothermal reaction of graphene oxide (GO) and urea [33]. An aqueous dispersion of GO with urea (prepared under sonication for 3 h) was sealed in a 50 ml Teflon-lined autoclave and maintained at 180 °C for 12 h. The solid products (N-doped graphene sheets) were filtered and washed with distilled water several times and dried at 80 °C. N-doping and reduction of GO were achieved simultaneously by the hydrothermal reaction. During the hydrothermal process, urea releases NH_3 in a sustained manner, which reacts with the oxygen functional groups of the GO and the nitrogen atoms then doping into graphene skeleton, leading to the formation of nitrogen doped graphene sheets. In 6 M KOH electrolyte, the synthesized N-GNSs with both high nitrogen (10.13 at.%) and large surface area ($593 \text{ m}^2 \text{ g}^{-1}$) exhibits excellent capacitive behavior (326 F g^{-1} , 0.2 A g^{-1}), superior cycling stability, and coulombic efficiency (99.58%) after 2000 cycles. An energy density of 25.02 Wh kg^{-1} could be achieved at a power density of 7980 W kg^{-1} by a two-electrode symmetric capacitor test.

Wu *et al.* report the preparation of NG materials by hydrothermal reaction of graphene oxide (GO) with urea, and their electrocatalytic properties toward oxygen reduction in 0.1 M KOH [34]. The introduction of urea leads to successful nitrogen insertion in the form of pyridinic, pyrrolic, and graphitic bonding configurations with enhanced reduction of GO, and an increase in the mass ratio between urea and GO gives higher nitrogen contents, which is accompanied by more defects in the microstructure. Reduction of O_2 to OH^- at lower overpotentials is favored by the incorporation of nitrogen, and the activity of NG is closely associated with the nitrogen content and the microstructure. NG with about 7% nitrogen and moderate defect density prepared from mass ratios of 1 : 200 and 1 : 300 (GO/urea) showed the best performance. Guo *et al.* synthesized nitrogen-doped graphene hydrogels (NGHs) through a one-pot hydrothermal route with graphene oxide

(GO) as raw material and urea as the reducing-doping agent [35]. The results demonstrate that nitrogen was doped into the graphene plane at the same time as the GO sheets were reduced, and the nitrogen content incorporated into the graphene lattice to be in the range of 3.95–6.61 at.% with pyrrolic N as the main component. The NGHs contained about 97.6 wt% water and have a large specific surface area (SSA) of $>1300 \text{ m}^2 \text{ g}^{-1}$ in the wet state. The sample NGH-4 with a nitrogen content of 5.86 at.% and SSA of $1521 \pm 60 \text{ m}^2 \text{ g}^{-1}$ in the wet state showed excellent capacitive behavior (308 F g^{-1} at 3 A g^{-1}) and superior cycling stability (i.e., 92% retention after 1200 cycles) in $6 \text{ mol l}^{-1} \text{ KOH}$. Zhang *et al.* prepared ORR active N-doped carbon catalysts via a wet chemical reaction between a reactive graphitic carbon template (e.g., graphene oxide) and N-containing molecules (e.g., dicyandiamide) at temperatures as low as 180°C [36]. Without any high-temperature treatments, the as-prepared Nitrogen-doped reduced graphene oxide (NrGO) with additional Fe-containing nanoparticles (NPs) showed an impressive ORR catalytic activity, comparable to N-doped carbon from high-temperature pyrolysis. N-doped graphene sheets were obtained using a hydrothermal reaction of graphene oxide and hexamethylenetetramine (HMT) in a Teflon-lined autoclave at 180°C for 12 h [37]. HMT plays important roles in both reducing the graphene oxide and doping N (8.62 at.%) into the graphene sheets. Geng *et al.* [38] have obtained nanoflower-like nitrogen-doped graphene sheets having about 6–10 layers by a low temperature solvothermal process using pentachloropyridine and metallic potassium reactants. Qian *et al.* have obtained nitrogen-doped (N-doped) few-layer graphene sheets by reaction in supercritical (SC) acetonitrile at $\geq 310^\circ \text{C}$ for various time intervals from 2 to 24 h, using expanded graphite as the starting material (Figure 10.6) [39]. XPS analysis revealed that the level of nitrogen-doping (N-doping) increased from 1.57 to 4.56 at.% when the reaction time was tuned from 2 to 24 h. Cao *et al.* report a relatively low-temperature preparation method for the synthesis of

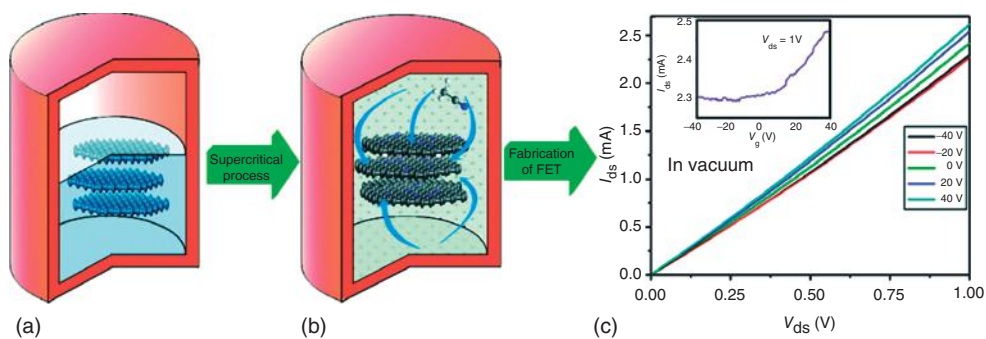


Figure 10.6 Schematic illustration of N-doped graphene sheets prepared via SC reaction with ACN at 310°C : (a) Few-layer graphene sheets were obtained by solvothermal-assisted exfoliation process and centrifugation, and then were mixed with ACN in corundum-lined autoclave

(b) N-doped graphene sheets were formed after SC reaction with ACN at 310°C for designated time. (c) Electrical properties of N-doped graphene FET. (Reproduced with permission from [39]. Copyright © 2011 American Chemical Society)

N-doped graphene (NG) with >10% N by heating graphene oxide and NH_4HCO_3 in a sealed autoclave at a temperature $\sim 150^\circ\text{C}$ [40]. The product exhibits a specific capacitance of 170 F g^{-1} at 0.5 A g^{-1} in 5 M KOH , and a high retention rate of 96.4% of its initial capacitance after 10 000 charge–discharge cycles at a charge density (c.d) of 10 A g^{-1} .

10.2.5

Chemical Vapor Deposition and Pyrolysis

Wei *et al.* [17] synthesized the N-doped graphene with few layers (up to 9 at.% N) by a CVD process over a Cu/Si substrate using CH_4 and NH_3 as the C and N sources, respectively. The substrate was placed in a quartz tube with a flow of hydrogen (20 sccm) and argon (100 sccm). When the center of the furnace reached 800°C , 60 sccm CH_4 , and 60 sccm NH_3 were introduced into the flow as the C source and N source, respectively, and then the substrate was rapidly moved to the high temperature region. After 10 min of growth, the sample was cooled to room temperature under H_2 ambience. As doping accompanies the recombination of carbon atoms into graphene in the CVD process (Figure 10.7), N atoms can be substitutionally doped into the graphene lattice and the electrical measurements show that the N-doped graphene exhibits an n-type behavior, indicating substitutional doping modulates the electrical properties of graphene (Figure 10.8).

Qu *et al.* synthesized nitrogen-doped graphene (N-graphene) by CVD of methane in the presence of ammonia [41]. A Ni-coated SiO_2/Si wafer was heated up to 1000°C in a quartz tube furnace in high-purity argon atmosphere and thereafter, a nitrogen-containing reaction gas mixture ($\text{NH}_3:\text{CH}_4:\text{H}_2:\text{Ar} = 10:50:65:200$ standard cubic centimeters per minute) was introduced into the quartz tube and kept flowing for 5 min. The resultant N-graphene film could be etched off from the substrate by dissolving the residual Ni catalyst layer in an aqueous solution of HCl, allowing the freestanding N-graphene sheets to be transferred onto substrates for subsequent investigation. The resultant N-graphene could act as a metal-free electrode with good electrocatalytic activity, long-term operation stability, and tolerance to crossover effect being better than platinum for oxygen reduction via a four-electron pathway in alkaline fuel cells. Dai *et al.* deposited single- and multilayer N-doped graphene on TEM copper grids by CVD from NH_3 and CH_4 [42]. The reactor temperature was first increased to 1000°C under hydrogen gas flow, and CH_4 (30–150 sccm) and NH_3 (6–20 sccm) were then introduced into the reactor system. By controlling the gas mixture ratio, the N atomic percentage in the graphene could be regulated in the 0.7–2.9% range. Zhao *et al.* has grown nitrogen-doped graphene monolayers on pre-cleaned copper substrates by heating a mixture of CH_4 , H_2 , and NH_3 at a pressure of 1.9 Torr and a temperature of 1000°C for 18 min [13]. While all the samples were grown with CH_4 and H_2 flow rates of 170 and 10 sccm respectively, different doping concentrations were achieved using different NH_3 partial pressures (0 Torr (pristine graphene, PG), 0.04 Torr (NG4), 0.07 Torr (NG7), 0.10 Torr (NG10), and 0.13 Torr (NG13)). A close-up topography has revealed

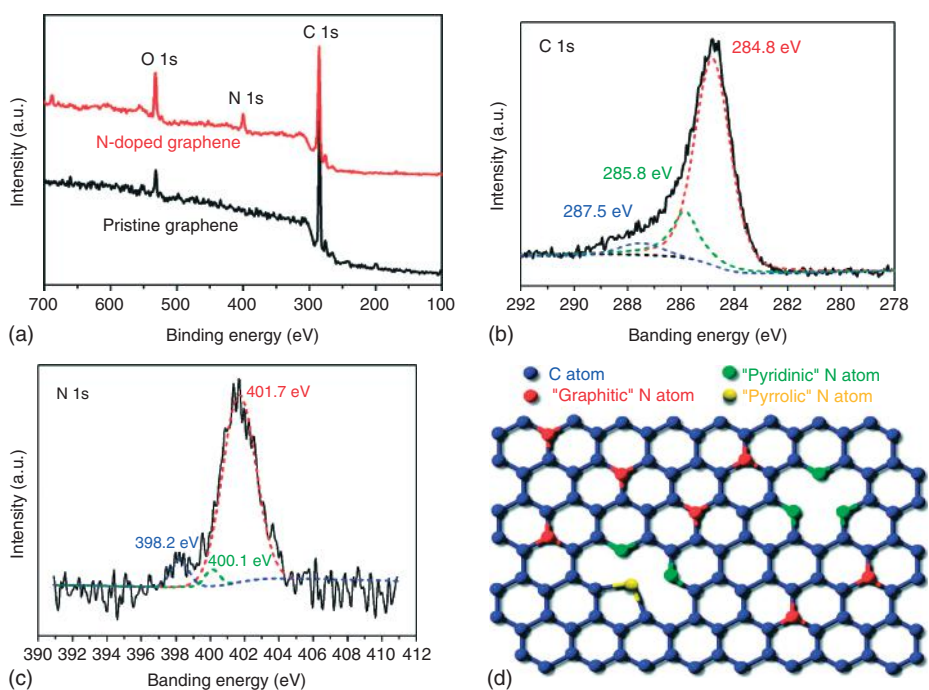


Figure 10.7 (a) XPS spectra of the pristine graphene and the N-doped graphene. (b) XPS C 1s spectrum and (c) XPS N 1s spectrum of the N-doped graphene. The C 1s peak can be split to three Lorentzian peaks at 284.8, 285.8, and 287.5 eV, which are labeled by red, green, and blue dashed lines. The N 1s peak can be split to three Lorentzian peaks at 401.7, 400.1, and

398.2 eV, which are labeled by red, green, and blue dashed lines. (d) Schematic representation of the N-doped graphene. The blue, red, green, and yellow spheres represent the C, “graphitic” N, “pyridinic” N, and “pyrrolic” N atoms in the N-doped graphene, respectively. (Reproduced with permission from [17]. Copyright © 2009 American Chemical Society)

three bright spots forming a triangle (Figure 10.9), the distance between the bright spots being equal to the graphene lattice constant (2.5 \AA). An STM line scan through the dopant (inset in Figure 10.9a) shows an apparent out-of-plane height of $0.6 \pm 0.2 \text{ \AA}$, consistent with the N atom substitution in the plane of the graphene.

Luo *et al.* [43] report the synthesis of single-layer graphene (SLG) doped with pyridinic N by thermal CVD of hydrogen and ethylene on Cu foils in the presence of ammonia at $900 \text{ }^\circ\text{C}$ for 30 min. The Cu foil was heated at $900 \text{ }^\circ\text{C}$ for 30 min in flowing 10 sccm H_2 at 1 Torr. The gas mixture of H_2 and C_2H_4 was then flowed at 4.6 Torr with a rate of 30 and 10 sccm for 30 min, respectively. After the growth, the samples were cooled down to room temperature ($\sim 20 \text{ }^\circ\text{C min}^{-1}$) with flowing H_2 under the pressure of 1 Torr. For the growth of CN_x -graphene, NH_3 diluted in He (NH_3/He , v/v 10%) with the flow rate of 3–12 sccm was introduced into the

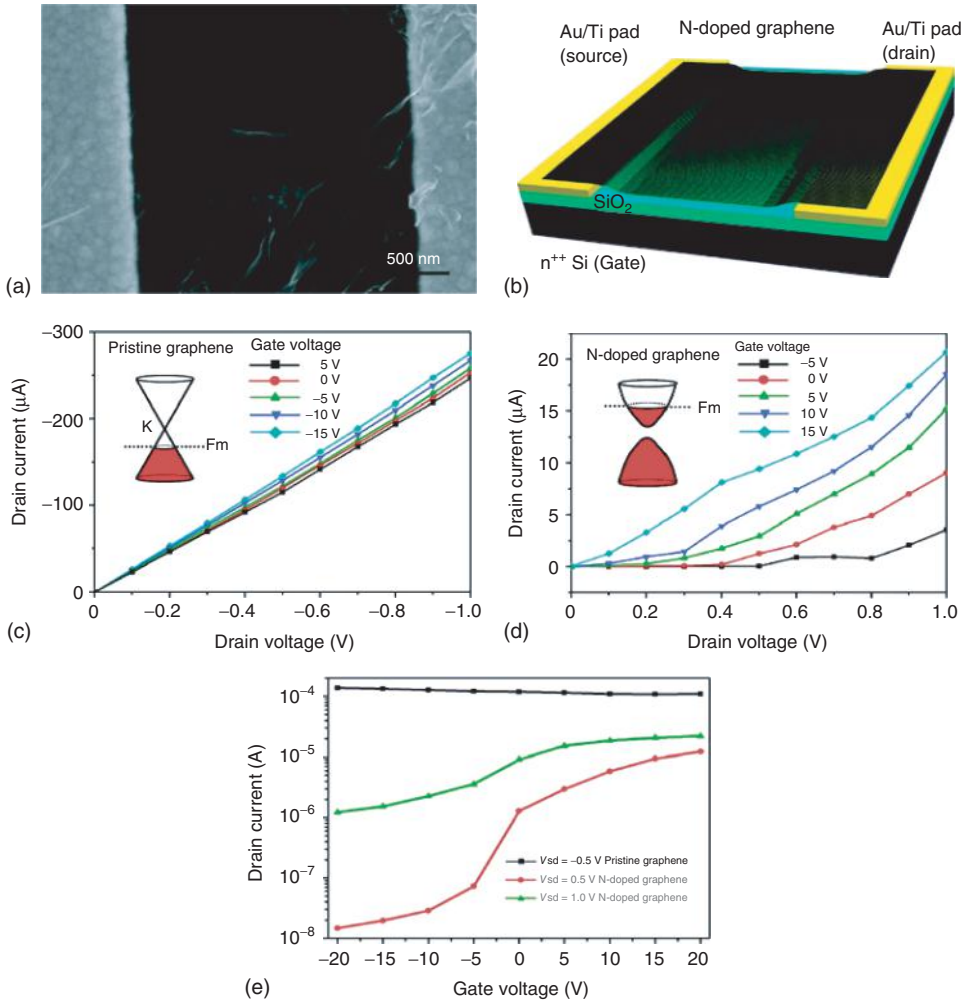


Figure 10.8 Electrical properties of the N-doped graphene. (a) SEM image of an example of the N-doped graphene device. (b) Bird's-eye view of a schematic device configuration. (c,d) I_{ds}/V_{ds} characteristics at various V_g for the pristine graphene and the N-doped graphene FET device, respectively. The

insets are the presumed band structures. (e) Transfer characteristics of the pristine graphene (V_{ds} at -0.5 V) and the N-doped graphene (V_{ds} at 0.5 and 1.0 V). (Reproduced with permission from [17]. Copyright © 2009 American Chemical Society)

reactor during the graphene growth process without changing the flow rates of H_2 and C_2H_4 . By adjusting the flow rate of ammonia, the atomic ratio of N and C can be modulated from 0 to 16%. The domain-like distribution of N incorporated in graphene was revealed by Raman spectroscopy and time-of-flight secondary ion mass spectrometry. UV photoemission spectroscopy demonstrated that the

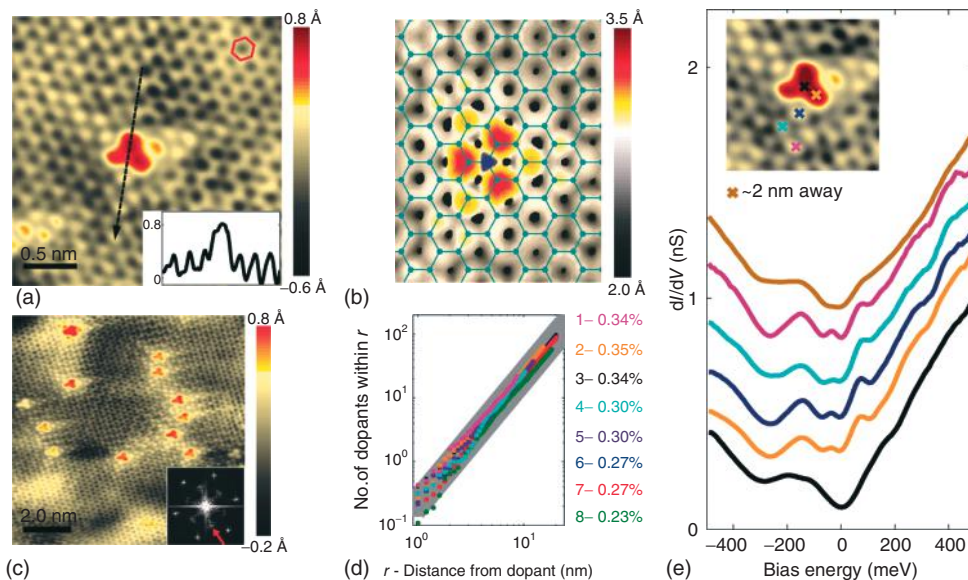


Figure 10.9 Visualizing individual nitrogen dopants in monolayer graphene, STM imaging of nitrogen dopants. (a) STM image of the most common doping form observed on N-doped graphene on copper foil, corresponding to a single graphitic N dopant. (Inset) Line profile across the dopant shows atomic corrugation and apparent height of the dopant ($V_{\text{bias}} = 0.8 \text{ V}$, $I_{\text{set}} = 0.8 \text{ nA}$). (b) Simulated STM image of graphitic N dopant ($V_{\text{bias}} = 0.5 \text{ V}$), based on DFT calculations. Also superposed is a ball-and-stick model of the graphene lattice with a single N impurity. (c) STM image of N-doped graphene on copper foil showing 14 graphitic dopants and strong intervalley scattering tails. (Inset) FFT of topography shows atomic peaks (outer hexagon) and intervalley scattering peaks (inner hexagon, indicated

by red arrow) ($V_{\text{bias}} = 0.8 \text{ V}$, $I_{\text{set}} = 0.8 \text{ nA}$). (d) Spatial distribution of N–N distances from eight samples on copper foils with different N concentrations. The distributions are all fit well by a quadratic power law (expected error bands in gray) overall length scales indicating that N dopants incorporate randomly into the graphene lattice. (e) dI/dV curves taken on a N atom (bottom) and on the bright topographic features near the nitrogen atom on N-doped graphene on copper, offset vertically for clarity. The top curve is the dI/dV spectrum taken $\sim 2 \text{ nm}$ away from the dopant. (Inset) Positions where the spectra were taken ($V_{\text{bias}} = 0.8 \text{ V}$, $I_{\text{set}} = 1.0 \text{ nA}$). (Reproduced with permission from [13]. Copyright © 2011 American Association for the Advancement of Science)

pyridinic N efficiently changed the valence band structure of graphene, including raising the density of π states near the Fermi level and the reduction of work function. Gao *et al.* [44] have grown large area, nitrogen-doped single atomic layer graphene films on copper foils by CVD, which can be easily transferred to a variety of substrates with N atoms present mainly as pyrrolic-nitrogens. The doping level of N was $\sim 3.4 \text{ at.}\%$. Reddy *et al.* [45] carried out a controlled growth of nitrogen-doped graphene layers on Cu substrate using acetonitrile based CVD. Initially the Cu foil was loaded in a quartz tube of a CVD furnace and evacuated to a base pressure of 10^{-2} Torr and the furnace was then heated to 950°C , while flowing Ar/H_2

and maintaining a pressure of 5 Torr. Once the desired temperature was reached, Ar/H₂ flow was stopped and acetonitrile vapors passed while maintaining the tube pressure at 500 mTorr. Around 3–15 min of vapor flow typically resulted in one or few-layer graphene. The NG was thus grown directly on Cu current collectors and studied for reversible Li-ion intercalation properties. Reversible discharge capacity of NG is almost double compared to PG due to the large number of surface defects induced due to N-doping. Cui *et al.* [46] also investigated the production of NG from liquid acetonitrile and demonstrated the need for a critical feed rate of acetonitrile. Lv *et al.* describe the synthesis of large-area, crystalline monolayer NG sheets on Cu foils using methane (CH₄) and ammonia (NH₃) as precursors via atmospheric-pressure chemical vapor deposition (AP-CVD) (Figure 10.10), yielding a N-doping site composed of two quasi-adjacent substitutional nitrogen atoms within the same graphene sub-lattice (N₂^{AA}) [47].

Figure 10.10a shows a photograph of the as-synthesized NG on Cu foil. Owing to the high transparency of single graphene layers, the NG-covered Cu foil exhibits the intrinsic appearance of copper. In addition, the underneath Cu foil could

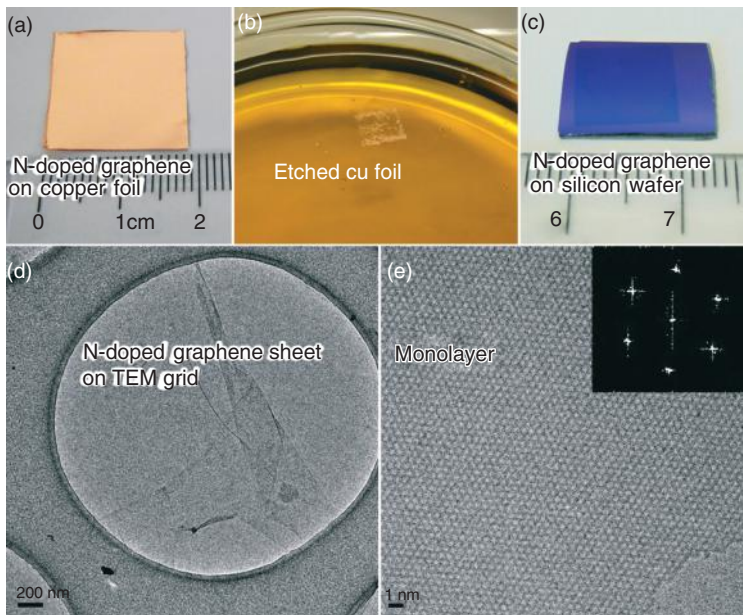


Figure 10.10 Morphology of as-synthesized N-doped graphene (NG) sheets. (a) Photograph of as-synthesized NG sample on Cu foil. (b) PMMA-coated NG with Cu residues floating on FeCl₃/HCl aqueous solution, which is used as Cu etchant. Cu foil can be completely etched away within ~20 min. (c) NG sheet (1 cm × 1 cm) on silicon wafer with 300 nm-thick SiO₂ coating. This NG sheet

was only part of the prepared NG sample shown in (a). It could be any size depending on the dimension of original NG-covered Cu foil for transfer. (d,e) Typical HRTEM images of as-synthesized monolayer NG. The inset of (e) is the corresponding fast Fourier transform (FFT) depicting the hexagonal pattern characteristic of the graphene framework [47].

be easily etched away in an aqueous FeCl_3/HCl solution (Figure 10.10b). NG samples were then transferred onto other substrates (e.g., SiO_2/Si wafers) using a polymethylmethacrylate (PMMA)-assisted method in order to keep large-area NG sheets from breaking during the transfer process. Figure 10.10c shows a transferred NG sheet with a $1\text{ cm} \times 1\text{ cm}$ area. It is noteworthy that the size of the NG sample could be much larger depending only on the size of the original Cu foil used for the transfer. STM and scanning tunneling spectroscopy (STS) of NG (Figure 10.11) revealed the presence of localized states in the conduction band induced by N_2^{AA} -doping, which was confirmed by ab initio calculations.

Jin *et al.* have demonstrated the growth of monolayer of NG in centimeter-scale sheets on copper foils, using CVD with pyridine as the sole source of both carbon and nitrogen [48]. These workers evacuated the reactor furnace tube and then heated it to 1000°C in 400 sccm H_2 flow under a H_2 gas pressure of ~ 6 Torr. After annealing for 20 min, pyridine vapor was introduced into the reactor by passing a 40 sccm Ar gas flow through a bubbler containing liquid pyridine. The temperature and gas flows were maintained in the furnace tube for 10 min with a total pressure of ~ 7 Torr. After the growth period, the Ar gas flow was stopped and the sample cooled to room temperature under H_2 gas flow. NG was fabricated on a Pt(111) surface through CVD [49]. The heated substrate was exposed to N-containing organic molecules such as pyridine and acrylonitrile. Analysis by XPS and Raman spectroscopy revealed that NG was formed on a Pt(111) surface from pyridine at the substrate temperature (T_s) $> 500^\circ\text{C}$, while nitrogen was not doped at $T_s > 700^\circ\text{C}$. Exposing the heated substrate to acrylonitrile also led to formation of graphene but nitrogen was not incorporated at any T_s . Koch *et al.* obtained nitrogen-doped graphene on Ni(111) by CVD using pyridine as the precursor [50], by exposing the substrate to 1×10^{-5} Torr pyridine at substrate temperatures of 400, 580, or 800°C for 2 min. The so-obtained NG layers were investigated using photoelectron spectroscopy. The nitrogen content was found to be influenced by the growth temperature and determined the atomic arrangement of the nitrogen atoms. The graphene produced with pyridine at a substrate temperature of $T_s = 800^\circ\text{C}$ contains no nitrogen, and this may be owing to temperature-induced decomposition of the pyridine precursor followed by the recombination and desorption of molecular nitrogen. Corresponding measurements on graphene grown by pyridine CVD at a substrate temperature of $T_s = 580^\circ\text{C}$ indicate nitrogen content of 0.02 monolayers, that is, 1% also at $T_s = 400^\circ\text{C}$ yields nitrogen concentration of 0.05 monolayers. Valence-band photoelectron spectra showed that the incorporation of nitrogen leads to a broadening of the photoemission lines and a shift of the π band. Density functional calculations for two possible geometric arrangements, the substitution of carbon atoms by nitrogen and vacancies in the graphene sheet with pyridinic nitrogen at the edges, reveal that the two arrangements have opposite effects on the band structure. Xue *et al.* [51] demonstrate a self-assembly approach that gave single-layer, single crystal, and highly NG domain arrays by self-organization of pyridine molecules on Cu surface at $\geq 300^\circ\text{C}$. These NG domains have a tetragonal-shape, reflecting the single crystal nature confirmed by electron-diffraction measurements. Lin *et al.* [52] report a synthetic method for the

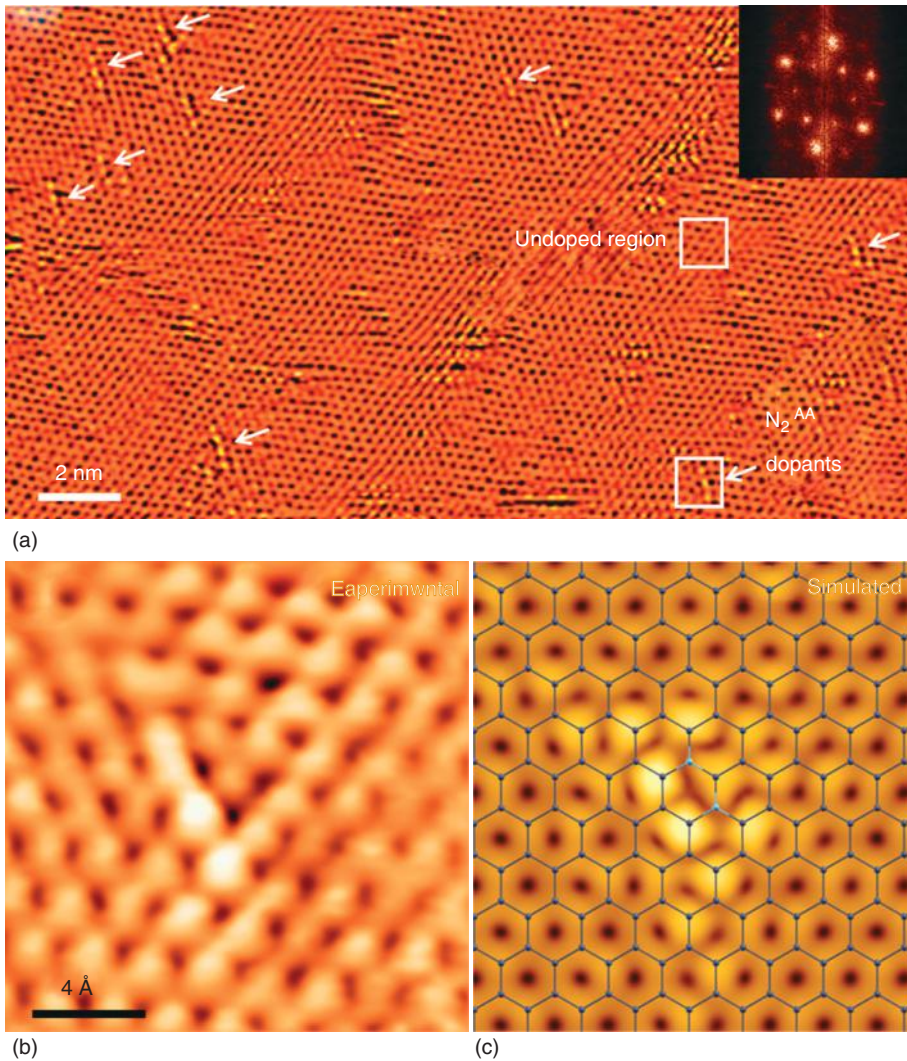


Figure 10.11 Experimental and simulated STM images of as-synthesized NG sheets. (a) Large-area STM image of the NG illustrating the presence of numerous N-dopants with similar peapod-like configuration (highlighted by white arrows), V_{bias} 5275 mV, I_{set} 5100 pA. The upper and lower squares are used to indicate the undoped region and N₂ dopants. (Inset) FFT of topography presents reciprocal lattice (outer hexagon) and inter-valley scattering (inner hexagon). The STM

image shown here is obtained in flattening mode to remove the overall roughness of the substrate and enhance the atomic contrast of dopants. (b) Highly resolved STM image of a N₂^{AA} dopant. (c) Ball-stick structural model of the N₂^{AA} dopant and simulated STM image obtained using first-principles calculations. The bias is 21.0 eV. The carbon and nitrogen atoms are illustrated using gray and cyan balls, respectively [47].

preparation of NG via pyrolysis of GO with polypyrrole (PPy). Oehzelt *et al.* [53] developed a strategy for efficient growth of NG on a large scale *in situ* by CVD of *s*-triazine on a Ni(111) surface. The synthesis was carried out by exposing triazine vapor ($\sim 1 \times 10^{-6}$) in the 540–635 °C range for ~ 30 min. In the incipient reaction of *s*-triazine molecules with the Ni(111) surface, a graphene monolayer, containing a variety of nitrogen atom environments, is formed. A band gap of 300 meV and a charge-carrier concentration of $\sim 8 \times 10^{12}$ electrons per cm^2 , induced by 0.4 at.% of graphitic nitrogen are reported.

10.2.6

Pyrolysis Methods

Xu *et al.* [54] synthesized NG by pyrolysis of metal (Fe, Ni) tetrapyrrolineporphyrazine, a nitrogen-rich metal phthalocyanine derivative with four pyridine substituents above 850 °C. The NG analog is nitrogen-rich with atomic ratio of N/C about 20.5% and has uniform distribution of C and N atoms with a majority of N atoms present in a pyridine type environment. The material exhibits a one-step, four-electron pathway for ORR, and shows almost identical voltammetric responses before and after about 100 000 cycles, indicating that it has high and stable electrocatalytic activity for oxygen reduction.

Sheng *et al.* [55] report a catalyst-free thermal annealing approach for the large-scale synthesis of NG via thermal annealing of graphite oxide with a low-cost industrial material melamine as the N source at a temperature of 700–1000 °C in a tubular furnace. In a typical procedure, graphite oxide (prepared by the modified Hummers' method) and melamine were mixed together with a mass ratio of 1 : 5 by grinding, forming a uniform gray mixture. This mixture in a crucible was then placed into a corundum tube with a flow of argon atmosphere and heated to 800 °C at a rate of 5 °C min^{-1} . After the temperature was maintained for 1 h, the furnace was cooled to room temperature and the product was collected from the crucible. The possible doping process is illustrated in scheme in Figure 10.12.

Nitrogen atoms or other nitrogen species formed by decomposition of carbon nitride can attack these active sites and form NGs. To a certain extent, NGs with different nitrogen atomic percent can be achieved by controlling the mass ratio of graphite oxide and melamine, the annealing temperature, and time. The resultant product shows that the atomic percentage of N in doped graphene samples can be adjusted up to 10.1% which mainly contains pyridine-like N atoms. It exhibits excellent electrocatalytic activity of NG toward the ORR in alkaline electrolytes, which is independent of N doping level. Lin *et al.* [56] also report the preparation of NG via pyrolysis of graphene oxide with melamine. The resulting NG shows high electrocatalytic activity toward ORR in an alkaline solution with an onset potential of -0.10 V versus Ag/AgCl reference electrode. Li *et al.* [57] report preparation of NG with large surface area by combining the ultrafast thermal exfoliation and covalent transformation from the melamine–graphene oxide (GO) mixture at different temperatures. As shown in Figure 10.13a, preparation at 300 °C (NG300) shows a high percentage of pyridinic-N and pyrrolic-N structures but a

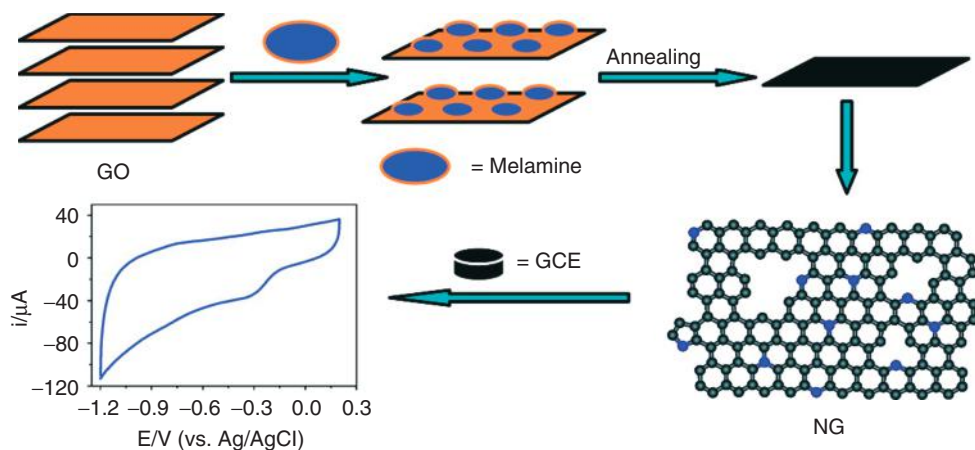


Figure 10.12 I: Schematic illustration of the nitrogen doping process of melamine into GO layers. (1) Melamine adsorbed on the surfaces of GO when temperature is $<300^\circ\text{C}$. (2) Melamine condensed and formed carbon nitride when temperature is $<600^\circ\text{C}$. (3) Carbon nitride decomposed and doped into graphene layers when temperature is $>600^\circ\text{C}$. II: (A) Typical cyclic voltammograms (CVs) for ORR obtained at a bare glassy carbon electrode (GCE)

(a), graphene/GCE (b), and NG5/GCE ($\text{N}\% = 7.1\%$) (c) in O_2 saturated 0.1 M KOH aqueous solution. (B) CVs for ORR at NGs, synthesized with different mass ratio of GO and melamine (1:1, 1:2, 1:5, 1:10, 1:50) at 800°C , modified GCE in O_2 saturated 0.1 M KOH aqueous solution. Scan rate: 100 mV s^{-1} . (Reproduced with permission from [55]. Copyright © 2011 American Chemical Society)

low percentage of graphitic-N. When the temperature was increased to 600°C , a decrease in the percentage of pyrrolic-N and an increase in the percentage of graphitic-N is observed (Figure 10.13b). At 900°C , the major components of NG900 are pyridinic-N and graphitic-N (Figure 10.13c). When GO alone (i.e., in the absence of melamine) was thermally exfoliated/reduced at 900°C by this procedure, yields only un-doped graphene, showing no obvious peaks in the N1s spectrum of graphene (Figure 10.13d). The above results for the XPS N1s spectra confirm that by this procedure the nitrogen atoms can be doped into graphene and transformed into four nitrogen-doped structures in the graphene layers.

Parvez *et al.* [58] have developed a cost-effective synthesis of NG by using cyanamide and graphene oxide leading to high and controllable nitrogen content (4.0–12.0%) after pyrolysis. NG thermally treated at 900°C shows a stable methanol crossover effect, high c.d (6.67 mA cm^{-2}), and durability ($\sim 87\%$ after 10 000 cycles) when catalyzing ORR in alkaline solution. Iron NPs could be incorporated into NG with the aid of Fe(III) chloride in the synthetic process. This allows one to examine the influence of non-noble metals on the electrocatalytic performance. NG supported with 5 wt% Fe NPs displayed an excellent methanol crossover effect and high c.d (8.20 mA cm^{-2}) in an alkaline solution. Moreover, Fe-incorporated NG showed good stability in both alkaline ($\sim 94\%$) and acidic ($\sim 85\%$) solutions, which out-performed the platinum and NG-based catalysts.

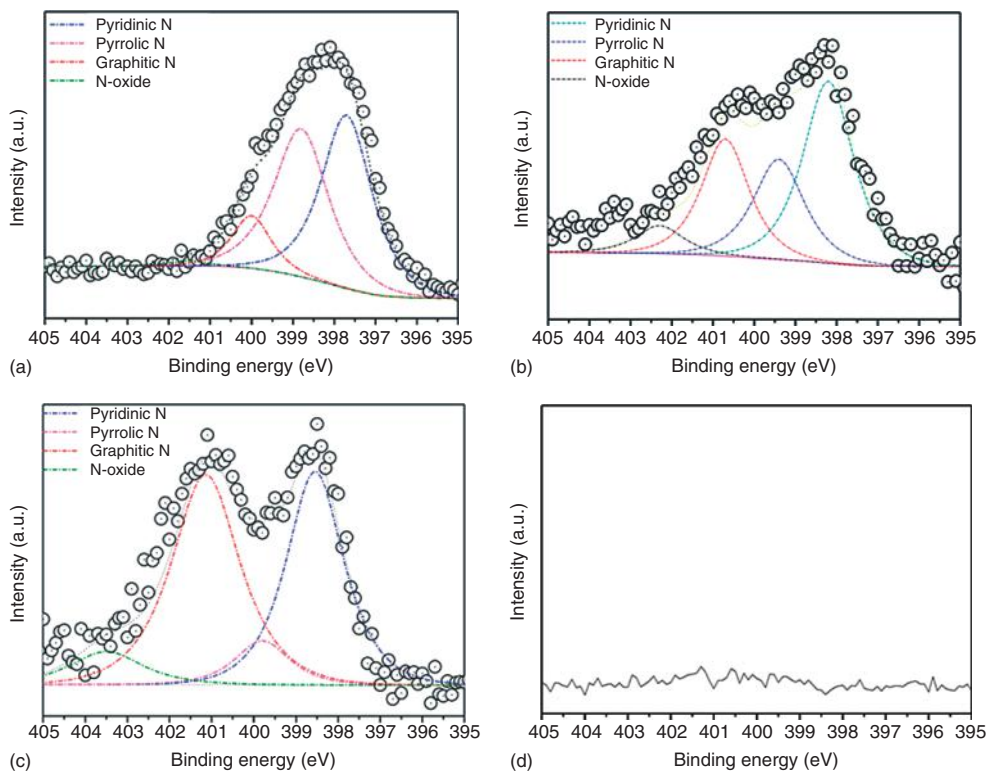


Figure 10.13 XPS N 1s core level spectra of (a) NG300, (b) NG600, (c) NG900, and (d) graphene. (Reproduced with permission from [57]. Copyright © 2013 Elsevier)

Gopalakrishnan *et al.* [59] have prepared heavily nitrogenated graphene oxide containing ~ 18 wt% nitrogen by microwave synthesis with urea as the nitrogen source. In a typical procedure, graphene oxide was ground with different proportions of urea and the pelletized mixture heated in a microwave reactor (900 W) for 30 s. The graphene oxide gets simultaneously reduced and doped with nitrogen. The products obtained with graphene:urea mass ratios of 1 : 0.5, 1 : 1, and 1 : 2, designated as NGO-1, NGO-2, and NGO-3, respectively, possess nitrogen contents of 14.7, 18.2, and 17.5 wt%, respectively. This nitrogen content is considerably higher than those found in earlier reports. Typical TEM and atomic force microscopy (AFM) images in Figure 10.14a,b show that the graphene sheets appear somewhat like scrolls due to microwave treatment. These materials show outstanding performance as a supercapacitor electrode material (*see for details*; Section 10.6), with the specific capacitance going up to 461 F g^{-1} .

Li *et al.* [60] report the synthesis of NG from glucose by adding dicyandiamide to form layered graphitic carbon nitride ($\text{g-C}_3\text{N}_4$), which serves as a sacrificial template. In a typical synthesis, the two-step heating of a mixture of dicyandiamide

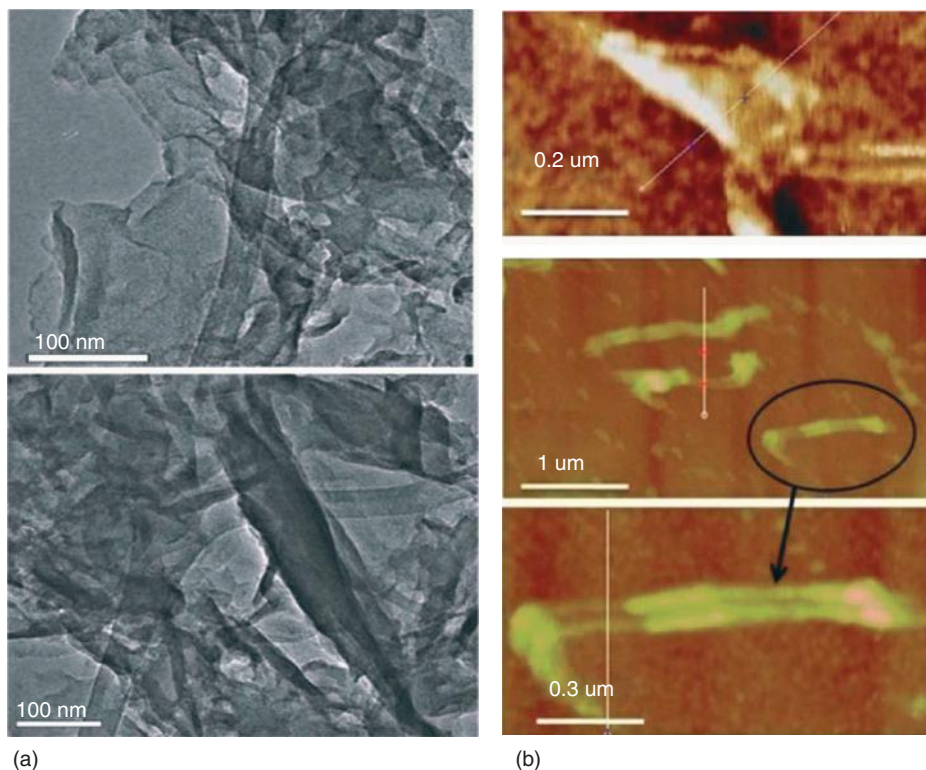


Figure 10.14 (a) TEM and (b) AFM images of N-doped graphene (NGO-3) [59].

and glucose under a protective flow of N_2 directly results in freestanding graphene with a yield of 28–60% (calculated based on added C from glucose). During the process, the thermal condensation of dicyandiamide creates a layered $g-C_3N_4$ template, which binds the as-formed aromatic carbon intermediates to its surface by means of donor–acceptor interactions and finally confines their condensation in a cooperative process to the interlayer gaps of $g-C_3N_4$ at $600^\circ C$. The stacking heights of the two phases are controlled by the relative amounts of the two monomers, glucose and dicyandiamide. Because the $g-C_3N_4$ template undergoes complete thermolysis at $>750^\circ C$, graphene-like sheets are liberated and the observed nitrogen content was 4.3 at.% (at $1000^\circ C$). This approach allows for gradually tuning the concentration of the nitrogen dopant in a broader range without disturbing the morphology of graphene. There has been some effort to develop routes for obtaining large sheets of monolayer or bilayer graphene. Sun *et al.* [61] report that large area, high-quality graphene with controllable thickness can be grown from different solid carbon sources such as polymer films or small molecules-deposited on a metal catalyst substrate at temperatures $\geq 800^\circ C$. The

growth of monolayers of NG was carried out from solid carbon sources atop metal catalysts by a one-step process (Figure 10.15).

Melamine was mixed with PMMA and spin-coated onto the Cu substrate. At a temperature as low as 800 °C or as high as 1000 °C (tested limit) for 10 min, with a reductive gas flow (H_2/Ar) and a atmospheric pressure conditions, a

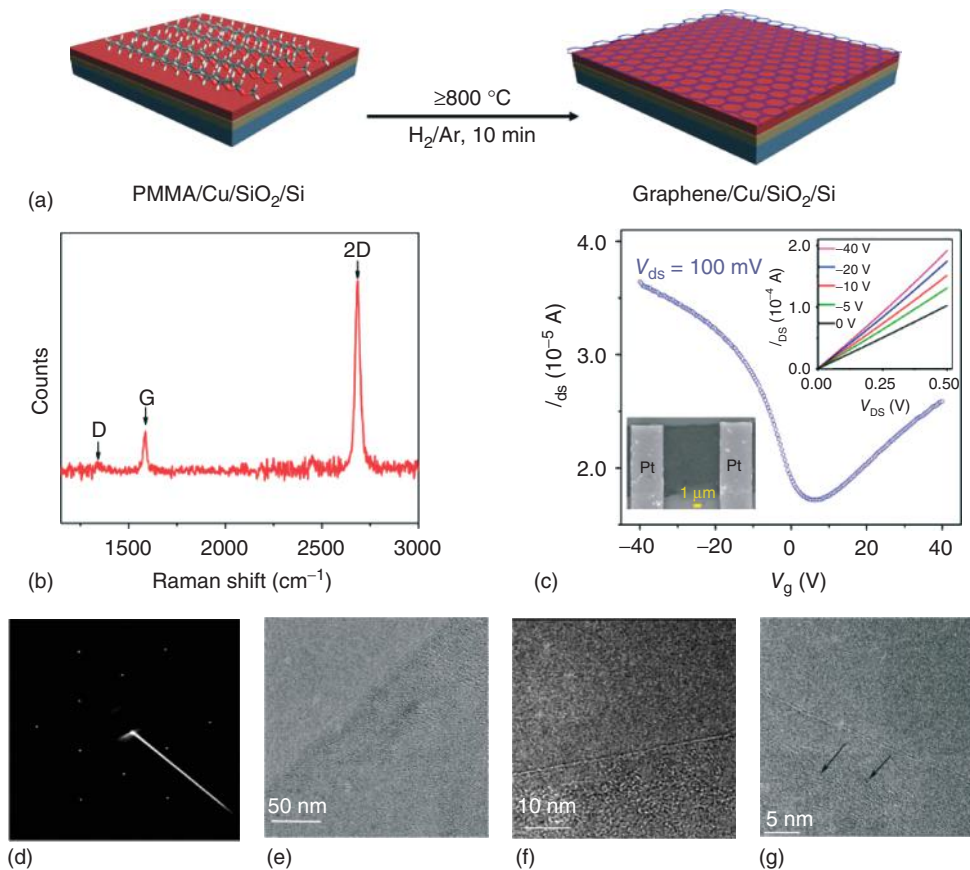


Figure 10.15 Synthetic protocol, spectroscopic analysis, and electrical properties of PMMA-derived graphene. (a) Monolayer graphene is derived from solid PMMA films on Cu substrates by heating in an H_2/Ar atmosphere at 800 °C or higher (up to 1000 °C). (b) Raman spectrum (514 nm excitation) of monolayer PMMA-derived graphene obtained at 1000 °C. (c) Room temperature $I_{ds}-V_g$ curve from a PMMA-derived graphene-based back-gated FET device. Top inset, $I_{ds}-V_{ds}$ characteristics as a function of V_g ; V_g changes from 0V

(bottom) to 240 V (top). Bottom inset, SEM (JEOL-6500 microscope) image of this device where the PMMA-derived graphene is perpendicular to the Pt leads. I_{ds} , drain-source current; V_g , gate voltage; V_{ds} , drain-source voltage. (d) Selected-area electron diffraction (SAED) pattern of PMMA-derived graphene. (e–g) HRTEM images of PMMA-derived graphene films at increasing magnification. In (g) black arrows indicate Cu atoms. (Reproduced with permission from [61]. Copyright © 2010 Nature Publishing Group)

single uniform layer of graphene was formed on the substrate. The prepared polymer films were successfully converted into NG, with an N content of 2–3.5% (Figure 10.16). The graphene material thus produced can be easily transferred to different substrates. Lin *et al.* synthesized NG via pyrolysis of graphene oxide with urea and studied its electrocatalytic activity toward the ORR [62]. The total nitrogen content in the graphene was as high as 7.86%, with a high proportion of N + G. The

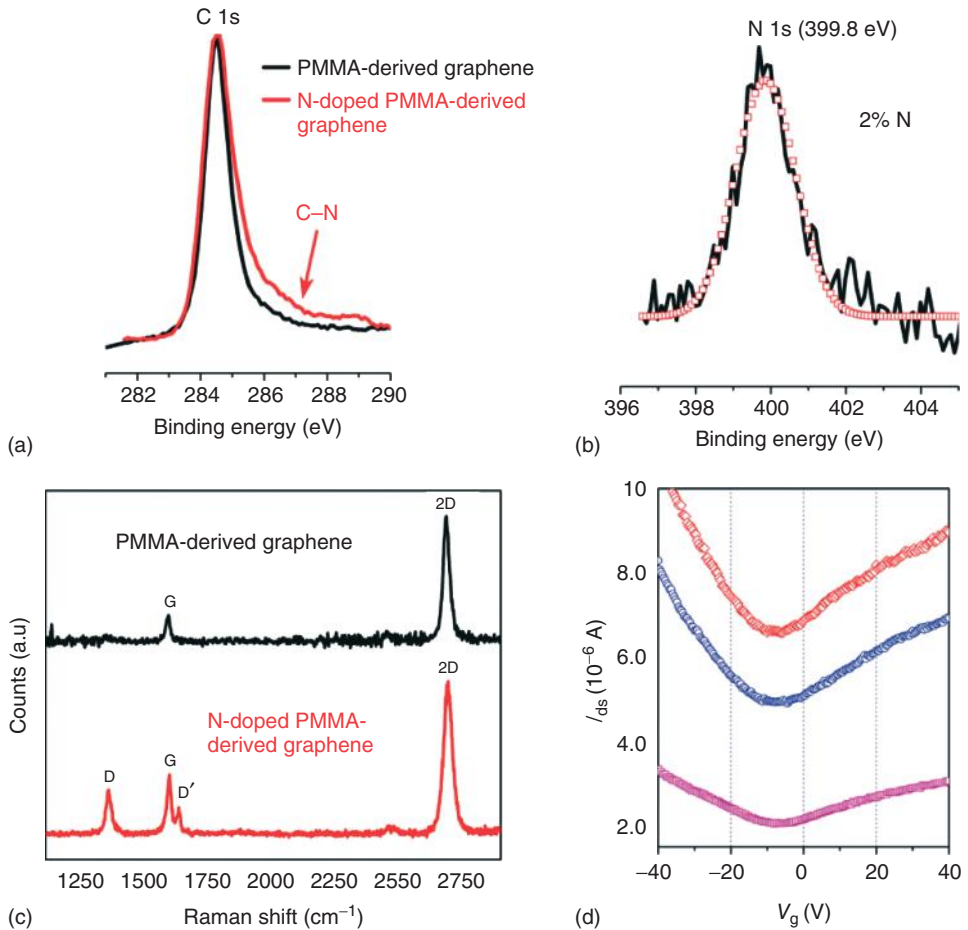


Figure 10.16 (a) XPS analysis from the C 1s peak of PMMA-derived graphene (black) and N-doped PMMA-derived graphene (red); the shoulder can be assigned to the C–N bond. (b) XPS analysis, showing the N 1s peak (black line) and its fitting (squares), of N-doped PMMA-derived graphene. The atomic concentration of N for this sample is about 2% (C is 98%). No N 1s peak

was observed for pristine PMMA-derived graphene. (c) Raman spectra of pristine and N-doped PMMA-derived graphene. (d) Room temperature $I_{ds}-V_g$ curves ($V_{ds} = 500$ mV) showing n-type behavior obtained from three different N-doped graphene-based back-gated FET devices. (Reproduced with permission from [61]. Copyright © 2010 Nature Publishing Group)

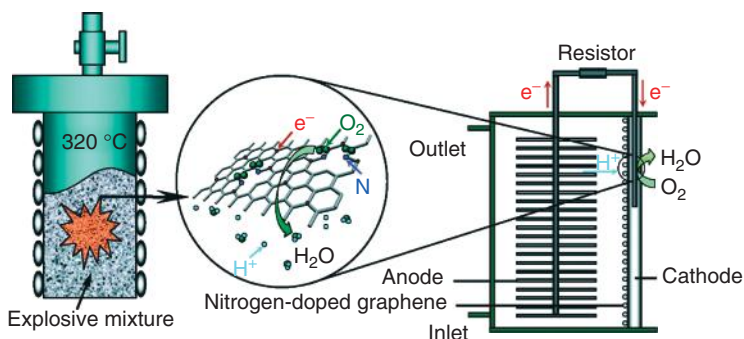


Figure 10.17 A low-temperature method to synthesize nitrogen doped graphene in gram-scale quantities with a denotation process and NG was applied as the cathode catalyst of microbial fuel cells (MFCs). (Reproduced with permission from [61]. Copyright © 2010 Nature Publishing Group)

resulting graphene exhibited high catalytic activity toward the ORR and preferred a four-electron pathway.

Feng *et al.* [63] report an easy-to-operate and low-temperature method to synthesize NG in gram-scale quantities with a denotation process (Figure 10.17). In a typical procedure, the detonation reaction of cyanuric chloride (2 g) and trinitrophenol (3 g) was carried out at 320 °C with a momentary pressure of 60 MPa and an equilibrium pressure of 30 MPa in a 20 ml stainless steel autoclave (Figure 10.17). After the autoclave was cooled to room temperature, the gaseous products were discharged and black solid NG was collected. In the graphene sheets the existence of the nitrogen substitute with an atomic ratio of N/C 12.5% was greater than those reported in the literature. In the neutral phosphate buffer solution, NG was demonstrated to act as a metal-free electrode with excellent electrocatalytic activity and long-term operation stability for oxygen reduction via a combination of two-electron and four-electron pathways. When NG was used as the cathode catalyst of microbial fuel cells, the obtained maximum power density was comparable to that of conventional platinum catalyst.

10.2.7

Other Methods

Zhang *et al.* [64] report a method for growing NG using embedded C and N source with the aid of a boron mediator during the electron beam deposition process, wherein boron atoms prefer to stay in the bulk of nickel and nitrogen atoms tend to segregate out onto the nickel surface. As shown schematically in Figure 10.18, NG is obtained through vacuum annealing of a sandwiched Ni(C)/B(N)/SiO₂/Si substrate at high temperature. With the utilization of the segregation phenomenon, the trace amount of C species involved in the Ni film as well as the B-trapped N species are simultaneously squeezed out via thermal annealing, forming uniform NG film (scheme in Figure 10.18).

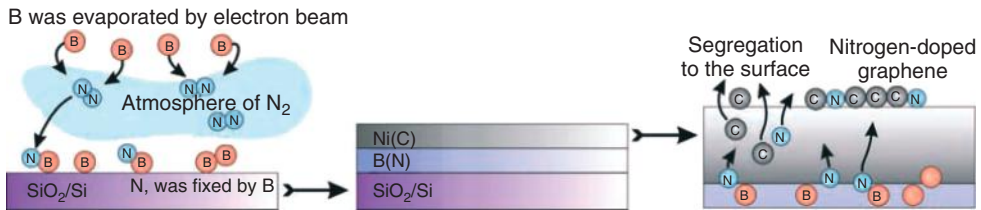


Figure 10.18 Schematic illustration of our concurrent segregation technique for growing nitrogen-doped graphene. The electron beam evaporated boron layer was used as the nitrogen trap and the top nickel layer containing a trace amount of carbon as the

segregation medium and carbon source. Nitrogen-doped graphene was formed on nickel surface after vacuum annealing at high temperature. (Reproduced with permission from [64]. Copyright © 2011 Wiley-VCH)

Compared with PG, such NG exhibits a remarkable n-type behavior with an effective bandgap of 0.16 eV, suggesting that the N-doping could tune the electrical properties of graphene (Figure 10.19).

Zheng *et al.* have demonstrated a general transfer-free method to directly grow large areas of uniform bilayer graphene on insulating substrates such as SiO₂, h-BN, Si₃N₄, and Al₂O₃ from solid carbon sources such as polymer films of poly(2-phenylpropyl)methylsiloxane (PPMS), PMMA, polystyrene (PS), and poly(acrylonitrile-*co*-butadiene-*co*-styrene) (ABS). The polymer polyABS leads to N-doped bilayer graphene due to its inherent nitrogen content [65]. Alternatively, the carbon feeds can be prepared from a self-assembled monolayer of butyltriethoxysilane atop a SiO₂ layer. The carbon feedstocks were deposited on the insulating substrates and then capped with a layer of nickel. At 1000 °C, under low pressure and a reducing atmosphere, the carbon source was transformed into a bilayer graphene film on the insulating substrates. The Ni layer is removed by dissolution, producing the bilayer graphene directly on the insulator with no traces of polymer left from a transfer step.

Vinayan *et al.* [66] devised a synthesis procedure to obtain nitrogen-doping in hydrogen-exfoliated graphene (HEG) sheets. An anionic polyelectrolyte-conducting polymer duo is used to form a uniform coating of the polymer over graphene sheets (scheme in Figure 10.20). Pyrolysis of graphene coated with PPy, at 800 °C in an inert argon atmosphere leads to the incorporation of nitrogen atoms in the graphene network with the simultaneous removal of the polymer yielding nitrogen-doped hydrogen-exfoliated graphene (N-HEG). These N-HEG sheets are used as catalyst support for dispersing platinum and platinum-cobalt alloy NPs synthesized by the modified-polyol reduction method, yielding a uniform dispersion of the catalyst NPs. Compared to commercial Pt/C electrocatalyst, Pt-Co/N-HEG cathode electrocatalyst exhibits four times higher power density in proton exchange membrane fuel cells (PEMFCs), which is attributed to the excellent dispersion of Pt-Co alloy NPs on the N-HEG support, the alloying effect of Pt-Co, and the high electrocatalytic activity of the N-HEG support. A stability study shows that

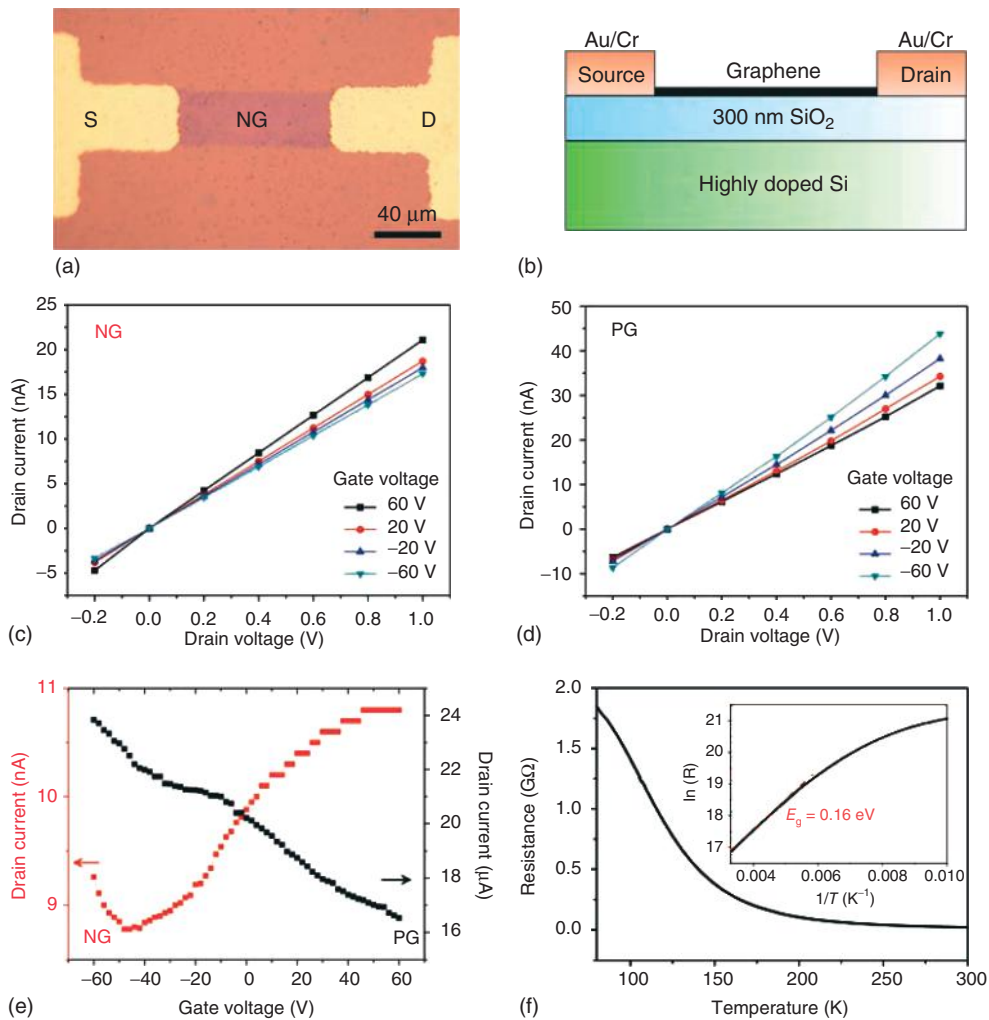


Figure 10.19 Electrical properties of nitrogen-doped graphene (NG) and pristine graphene (PG) in vacuum. (a) Optical microscope image of NG FET device. (b) Sketch of the device structure. (c,d) $I_{ds}-V_{ds}$ output characteristics of NG3 (N/C=1.6 at.%) and PG at variable back-gate voltages starting from -60 to 60 V in a step of 40 V, respectively. (e) Transfer

characteristics ($I_{ds}-V_g$) of NG3 (red) and PG (black) devices at $V_{ds}=0.5$ V. (f) Temperature dependence of the electrical resistance of NG2 (N/C=2.9 at.%). The inset shows the change of $\ln(R)$ as a function of T^{-1} in the temperature range from 100 to 300 K. (Reproduced with permission from [64]. Copyright © 2011 Wiley-VCH)

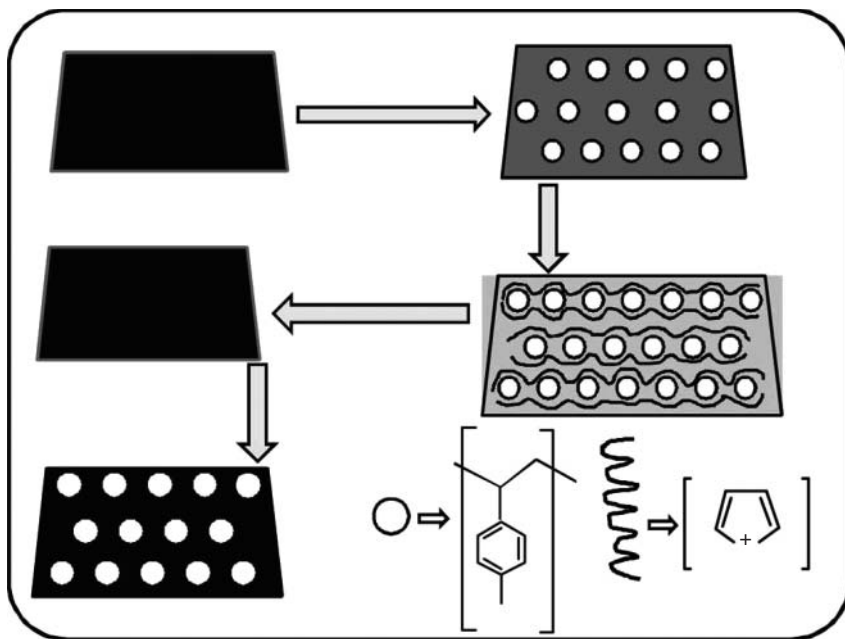


Figure 10.20 Schematic illustration of the synthesis procedure of Pt/N-HEG or Pt₃Co/N-HEG. (Reproduced with permission from [66]. Copyright © 2012 Wiley-VCH)

Pt/N-HEG and Pt–Co/N-HEG cathode electrocatalysts are highly stable in acidic media.

Chandra *et al.* produced N-doped porous carbon via chemical activation of PPy functionalized graphene sheets at 400 °C (a-NDC4), 500 °C (a-NDC5), 600 °C (a-NDC6), and 700 °C (a-NDC7) in N₂ flow (100 sccm), using a 7 M KOH solution, which shows selective adsorption of CO₂ (4.3 mmol g⁻¹) over N₂ (0.27 mmol g⁻¹) at 298 K [67]. The PPy functionalized graphene sheets (with different graphene oxide loadings (weight% = 25, 50, and 75) in pyrrole) were synthesized via chemical polymerization of pyrrole in graphene oxide using ammonium persulfate and subsequent reduction using hydrazine. Sun *et al.* [68] used nanoporous nitrogen doped carbon to modify the surfaces of graphene sheets by carbonizing a mixture of graphene oxide and phenol-melamine-formaldehyde (PMF) pre-polymer in the presence of a soft template (Pluronic F127). For fabricating graphene sheets sandwiched by nanoporous N-doped carbon layers, a simple soft template method was adapted, by using a triblock copolymer, Pluronic F127, as the template for guiding the growth of nanoporous structures of PMF pre-polymer on graphene sheets. After carbonization at 700 °C, graphene-based catalysts with a sandwich structure (G-PMFs) were obtained. The resulting graphene based composite sheets (G-PMFs) have a sandwich structure with one graphene layer and two nanoporous N-doped C layers. G-PMFs have large SSAs of 190–630 m² g⁻¹ and exhibit high

electrocatalytic activity, good durability, and high selectivity for the ORR. The performance of the Zn-air fuel cell with a G-PMF anode was tested and is comparable to that of the Zn-air cell with a com. Pt/C anode. Lin *et al.* [69] prepared NG by the pyrolysis of GO-PANI (polyaniline) composite at 1000 °C for 30 min in an Ar atmosphere. The reaction was carried out for 24 h, and the resulting NG contained 2.4 at.% N, of which as high as 1.2 at.% is quaternary N. Electrochemical characterization reveals that the NG has excellent catalytic activity toward ORR in an alkaline electrolyte, including a desirable four-electron pathway for the formation of water, large kinetic-limiting current density, long-term stability, and good tolerance to methanol crossover. In addition, NG also had high catalytic activity toward oxygen evolution reaction (OER), rendering its potential application as a bifunctional catalyst for both ORR and OER. Lai *et al.* [70] produced NG by annealing of GO under ammonia or by annealing of a N-containing polymer/reduced graphene oxide (RGO) composite (PANI/RGO or PPy/RGO) at different temperatures. The active center structure resulting from the bonding state of the N atom of NG-based catalysts was found to have a significant effect on the selectivity and catalytic activity for ORR. Annealing of GO with ammonia preferentially formed graphitic N and pyridinic N centers, while annealing of PANI/RGO and PPy/RGO tended to generate pyridinic and pyrrolic N moieties, respectively. Most significantly, the electrocatalytic activity of the catalyst was dependent on the graphitic N content which determined the limiting c.d, while the pyridinic N content improved the onset potential for ORR.

Wen *et al.* [71] synthesized crumpled NG nanosheets (C-NGNSs) with ultrahigh pore volume, by heating a solution of cyanamide (NH_2CN) and GO under stirring at 90 °C (until completely dry), followed by heating of the product at 400 °C and finally calcined at 750 or 900 °C to obtain the products C-NGNSs-750 or C-NGNSs-900, respectively (Figure 10.21). The GO- NH_2CN product heated at 400 °C induces the polymerization of cyanamide and thus forms a thin C_3N_4 polymer layer on the surface of the GO ($\text{GO}@p\text{-C}_3\text{N}_4$).

Hwang *et al.* [72] demonstrate a controlled, systematic method to tune the charge transport in graphene FETs based on alternating layer-by-layer assembly of positive and negative charged GO followed by thermal reduction (Figures 10.22 and 10.23). Nitrogen atoms from the functional groups of positively charged GO are incorporated into the reduced graphene oxide films and substitute carbon atoms during the thermal reduction. The nitrogen-doping process occurs to different degrees in graphene multilayers with varying numbers of bilayers and thereby resulting in the interesting transition in the electronic behavior in graphene multilayer transistors.

Palaniselvam *et al.* [73] developed a simple way to simultaneously create pores and N-doped active sites on graphene for performing electrochemical ORR. The main aspect of the process is the *in situ* generation of Fe_2O_3 NPs and their concomitant dispersion on graphene by pyrolyzing GO with the Fe phenanthroline complex. The deposited Fe_2O_3 NPs thus act as seeds for pore generation by etching the carbon layer along the graphene- Fe_2O_3 interface (Figure 10.24). Detection of

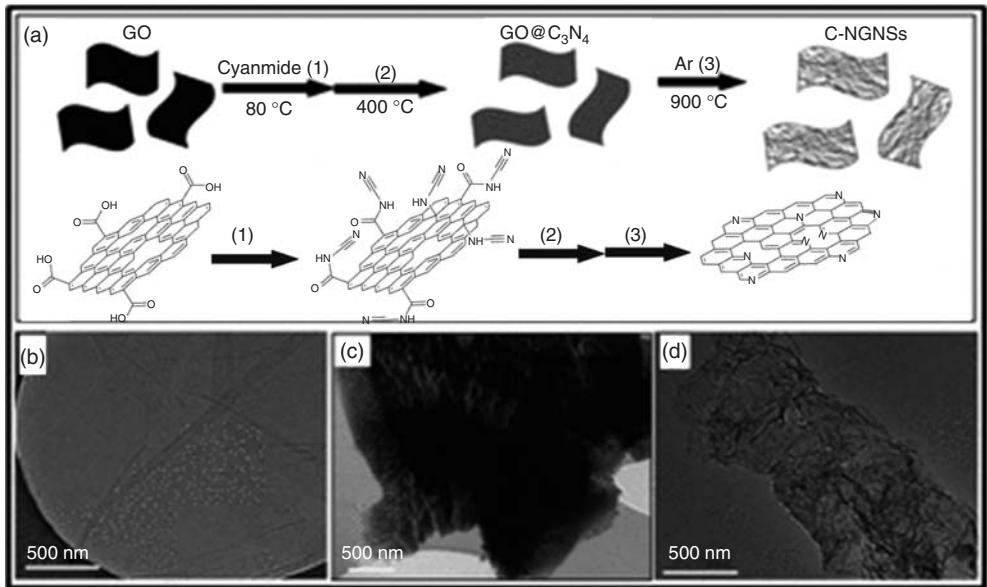


Figure 10.21 Schematic illustration for fabricating crumpled nitrogen-doped graphene (a); TEM images of the GO (b); GO@p-C₃N₄ (c); and C-NGNSs-900 (d). (Reproduced with permission from [71]. copyright © 2012 Wiley-VCH)

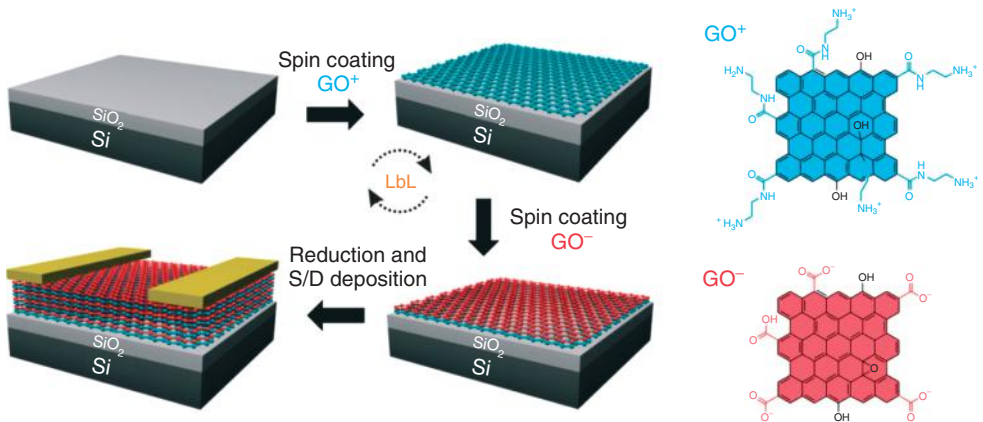


Figure 10.22 Schematic representation of LbL-assembled graphene-based FETs. (Reproduced with permission from [72]. Copyright © 2012 American Chemical Society)

Fe₃C along with Fe₂O₃ confirms C spill-over from graphene as a plausible step involved in the pore engraving process. Since the process offers a good control on the size and dispersion of the Fe₂O₃ NPs, the pore size and distribution also could be managed very effectively in this process. As the phenanthroline complex decomposes and gives Fe₂O₃ NPs and subsequently the pores on graphene, the

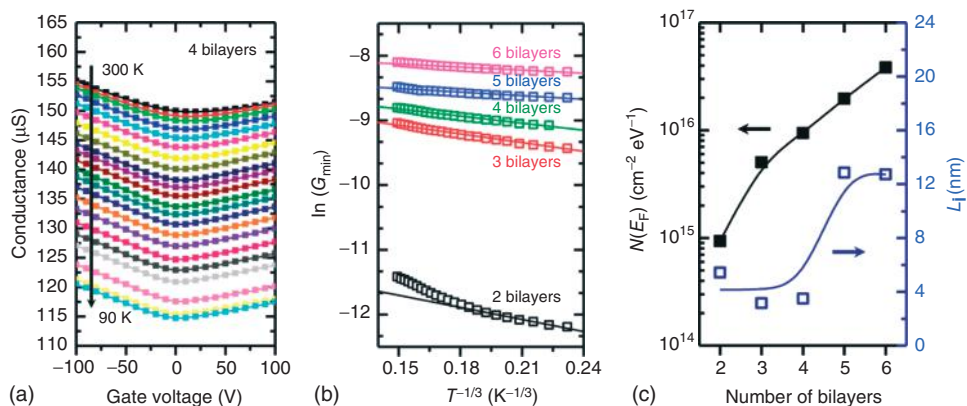


Figure 10.23 (a) Temperature-dependent conductance versus gate voltage plots of thermal reduction of graphene oxide (TrGO) FETs with four-bilayer TrGO FET. (b) $\ln(G_{\min})$ versus $T^{-1/3}$ plots of TrGO FETs with different numbers of graphene bilayers. (c) $N(E_F)$ and L_I of TrGO films as a function of number of bilayers. (Reproduced with permission from [72]. Copyright © 2012 American Chemical Society)

unsaturated carbons along the pore openings simultaneously capture N of the phenanthroline complex and provide very efficient active sites for ORR under alkaline conditions. The degree of N doping and hence the ORR activity could be improved by subjecting the porous material for a second round of N doping using Fe-free phenanthroline.

Unni *et al.* [74] report a template-free synthetic route for the preparation of mesoporous NG containing a high weight percentage of pyrrolic nitrogen, large SSA, and comparable electrochemical oxygen reduction activity as that of the state-of-the-art 40 wt% Pt/C catalyst. In a typical synthesis, initially GO was functionalized with pyrrole by dispersing GO in deionized water, followed by the addition of pyrrole monomer and refluxing for 15 h at 95 °C. After completion of the reaction, the resulting black solution was filtered using polytetrafluoroethylene (PTFE) filter paper and the wet cake was washed with solvents and was dried in a vacuum oven. This composite GPPy obtained at this stage was used for preparing various NG samples. In the next step, NG was prepared by simple heat treatment of reduced graphene oxide, which has oxidized products of pyrrole anchored on the surface, in an argon atmosphere at different heating temperatures such as 700, 800, 900, and 1000 °C. The desired coordination of nitrogen in the carbon framework of graphene has been conceived by a mutually assisted redox reaction between GO and pyrrole, followed by thermal treatment at elevated temperatures. The heat treatment plays an important role in establishing the desired pyrrolic coordination of nitrogen in graphene for the electrochemical ORR. The NG sample obtained after heat treatment at 1000 °C (NG-1000) has 53% pyrrolic nitrogen content compared to similar samples prepared by treating at low temperatures. Because the oxygen reduction activity is strongly a function of the

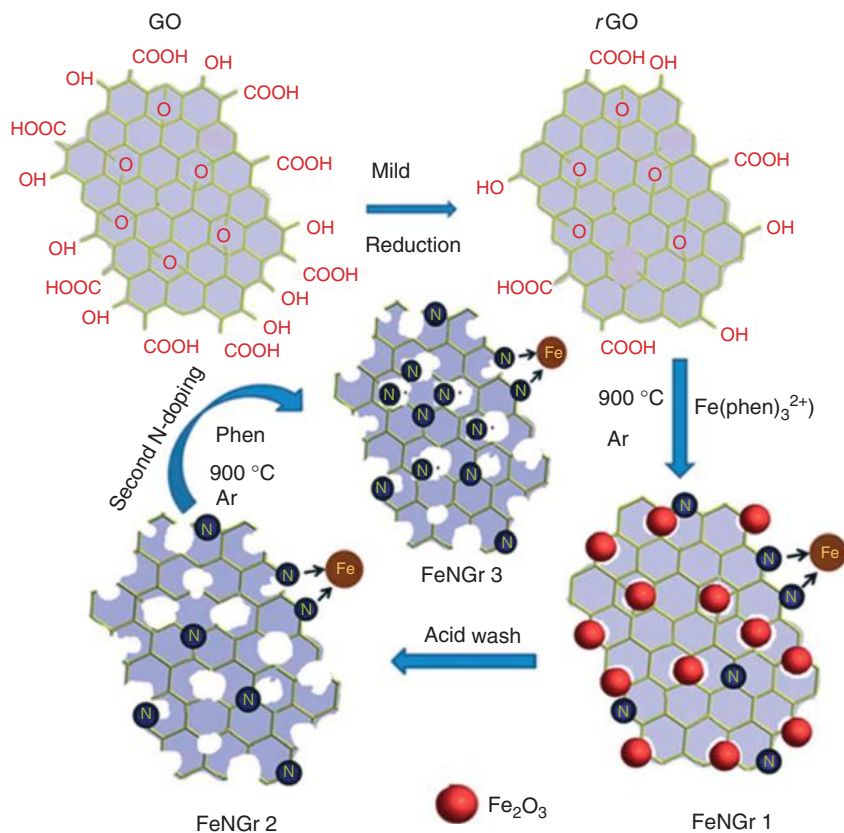


Figure 10.24 Schematic representation of the process involved in the creation of pores and the nitrogen and iron nitride doped active sites on graphene. (Reproduced with permission from [73]. Copyright © 2012 Royal Society of Chemistry)

heat treatment temperature, the electrochemical ORR activities of the different heat treated catalysts were individually evaluated. Saleh *et al.* [75] have synthesized N-doped microporous carbon consisting of NG sheets via chemical activation of polyindole-modified graphene oxide (PIG) hybrids at temperatures of $400\text{--}800\text{ }^\circ\text{C}$ (Figure 10.25, schematic illustration). The NG sheets are microporous with an adsorption pore size of 0.6 nm for CO_2 and show a maximum surface area of $936\text{ m}^2\text{ g}^{-1}$ (Figure 10.26). The polyindole-modified graphene oxide hybrid activated at $600\text{ }^\circ\text{C}$ (PIG6) possesses a surface area of $534\text{ m}^2\text{ g}^{-1}$ and a micropore volume of $0.29\text{ cm}^3\text{ g}^{-1}$. PIG6 shows a maximum CO_2 adsorption capacity of 3.0 mmol g^{-1} at $25\text{ }^\circ\text{C}$ and 1 atm . This high CO_2 uptake is due to the highly microporous character of the material and its N content.

Three-dimensional N-doped graphene-carbon nanotube networks (NGCs) are obtained by hydrothermal treatment, freeze-drying, and subsequent carbonization of graphene oxide-dispersed pristine carbon nanotubes (CNTs) in the presence

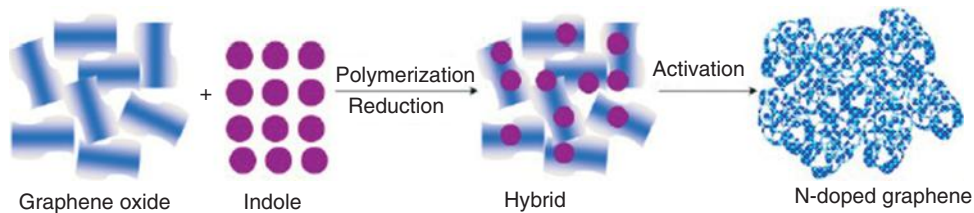


Figure 10.25 Schematic illustration of synthesis of N-doped graphene. (Reproduced from Ref. [75].)

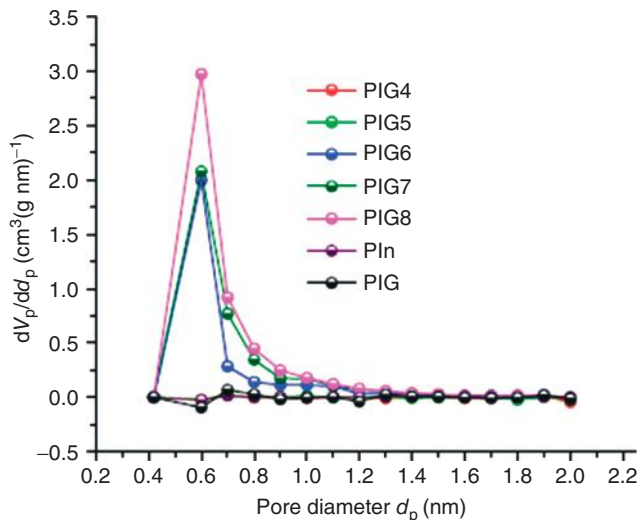


Figure 10.26 Pore size distribution for Polyindole (PIn) and PIG samples. (Reproduced from Ref. [75].)

of pyrrole (Figure 10.27) [76]. The overall synthetic procedure is illustrated in Figure 10.27. GO is used as the surfactant to directly disperse pristine CNTs without any additives and the CNTs prevent the aggregation of graphene as well as improve the whole conductivity of NGCs. Figure 10.28 (a) and (b) shows SEM and TEM images of the GO-dispersed pristine CNTs respectively. After hydrothermal self-assembly with pyrrole, freeze-drying, and subsequent carbonization process, the resulting NGCs-0.5 possesses 3D interconnected frameworks with randomly opened macropores (Figure 10.28c,d) due to the effective cross linking of sufficient PPy polymerization during the hydrothermal treatment. The TEM image in Figure 10.28e reveals that the NGCs-0.5 also possesses numerous mesopores and micropores, which is possibly caused by the addition of pristine CNTs. The inserted CNTs not only prevent the aggregation of NG, but also improve its conductivity. The intensity ratio of the G band at 1350 cm^{-1} relative to the D band at 1587 cm^{-1} in the Raman spectra (I_G/I_D) reliably increases (Figure 28(f)), indicating the integration of pristine CNTs. The resulting NGCs used as a supercapacitor show high specific



Figure 10.27 Fabrication of NGCs. (Reproduced with permission from [76]. Copyright © 2013 Royal Society of Chemistry)

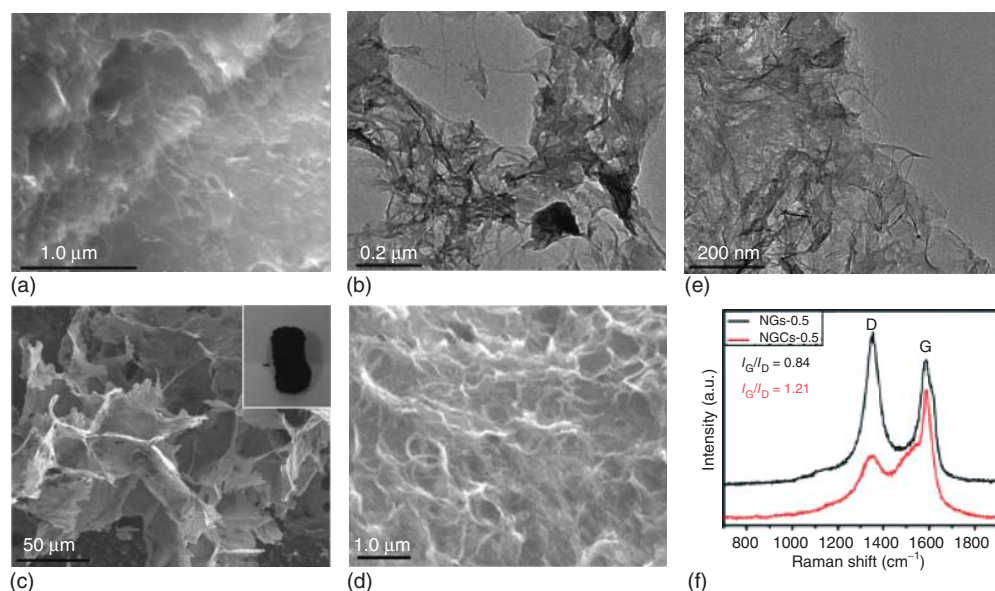


Figure 10.28 (a,b) Representative SEM and TEM images of the GO-dispersed pristine CNTs. (c,d) SEM images of NGCs-0.5 at different magnification. (e) TEM images of NGCs-0.5. (f) Raman spectra of

NGCs-0.5 and the benchmark sample, NGCs-0.5. The inset of (c) is the digital photograph of NGCs-0.5. (Reproduced with permission from [76]. Copyright © 2013 Royal Society of Chemistry)

capacitance, good rate capability, and still retain ~96% of the initial capacitance even after 3000 cycles.

Chen *et al.* [77] report a hydrothermal process for the synthesis and structural adjustment of the NGH, which can be readily scaled-up for mass production of NGH by using an organic amine and GO as precursors (see scheme in Figure 10.29).

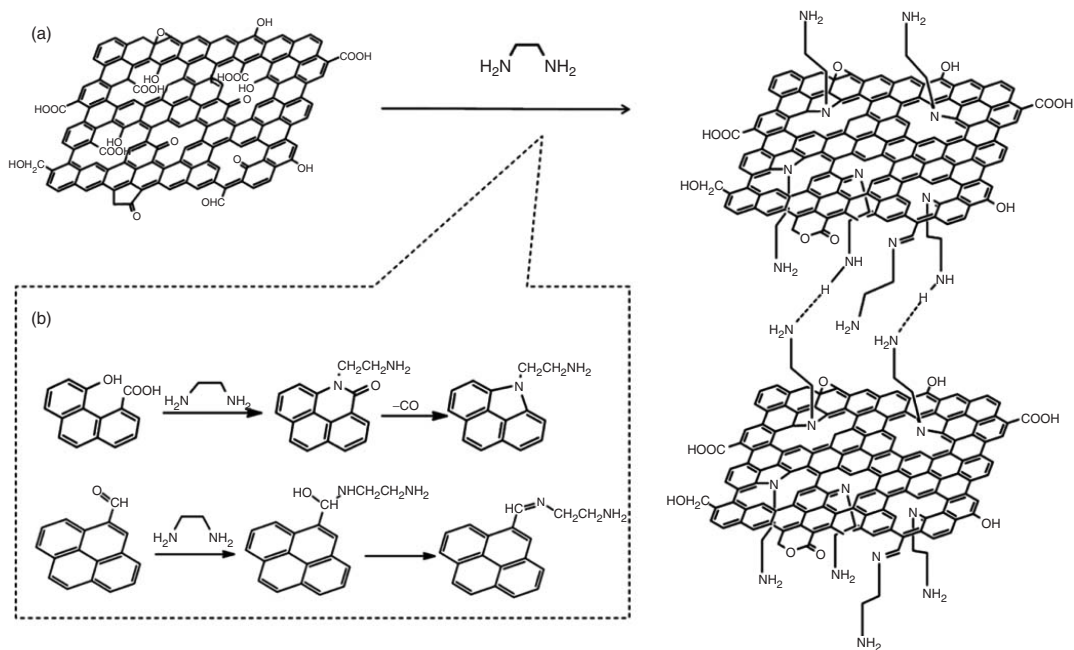


Figure 10.29 Schematic illustration of the controlled assembly of the 3DGN-GH, (a) illustration of the enhancement of the distance between graphene layers by ethylene diamine and (b) the possible reaction pathways for nitrogen doping. (Reproduced with permission from [77]. Copyright © 2013 Elsevier)

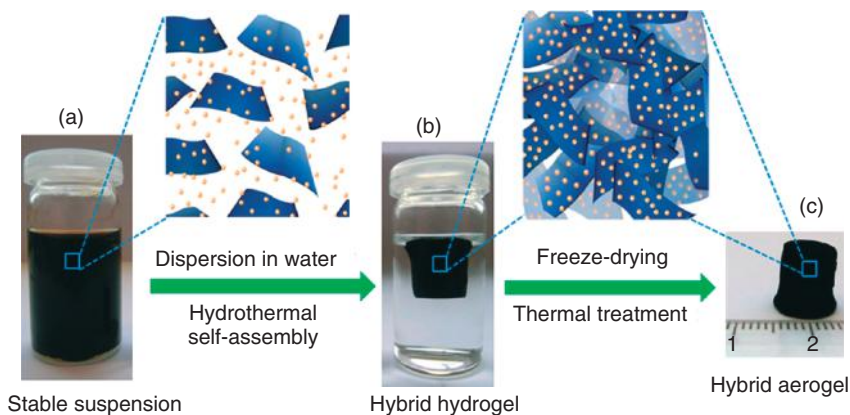


Figure 10.30 Fabrication process for the 3D $\text{Fe}_3\text{O}_4/\text{N-GAs}$ catalyst. (a) Stable suspension of GO, iron ions, and PPy dispersed in a vial. (b) Fe- and PPy-supporting graphene hybrid hydrogel prepared by hydrothermal self-assembly and floating on water in a vial, and its ideal assembled model. (c) Monolithic $\text{Fe}_3\text{O}_4/\text{N-GAs}$ hybrid aerogel obtained after freeze-drying and thermal treatment. (Reproduced with permission from [78]. Copyright © 2012 American Chemical Society)

The structure of the hydrogel and the content of nitrogen in the graphene are easily adjusted by organic amine. The supercapacitor performance was found to be remarkably enhanced. At an ultrafast charge–discharge rate of 185.0 A g^{-1} , a high power density of 205.0 kW kg^{-1} was obtained. The c.d of 100.0 A g^{-1} , 95.2% of its capacitance was retained for 4000 cycles.

Wu *et al.* [78] reported three-dimensional nitrogen-doped graphene aerogel (N-GA)-supported Fe_3O_4 NPs ($\text{Fe}_3\text{O}_4/\text{N-GAs}$) and utilized it as catalysts for the ORR. The fabrication process for 3D $\text{Fe}_3\text{O}_4/\text{N-GAs}$ is demonstrated in Figure 10.30. Fe_3O_4 NPs nucleated and grew on the graphene surface with simultaneous incorporation of nitrogen species into the graphene lattice. The as-prepared hydrogel was directly dehydrated via a freeze-drying process to maintain the 3D monolithic architecture and then heated at 600°C for 3 h under nitrogen (Figure 10.30c). The final product from this process was a black monolithic hybrid aerogel composed of NG networks and Fe_3O_4 NPs. These graphene hybrids exhibit an interconnected macroporous framework of graphene sheets with uniform dispersion of Fe_3O_4 NPs (Figure 10.31).

In studying the effects of the carbon support on the Fe_3O_4 NPs for the ORR, they found that $\text{Fe}_3\text{O}_4/\text{N-GAs}$ show a more positive onset potential, higher cathodic density, lower H_2O_2 yield, and higher electron transfer number for the ORR in alkaline media than Fe_3O_4 NPs supported on N-doped carbon black or NG sheets, highlighting the importance of the 3D macropores and high SSA of the GA support for improving the ORR performance. Furthermore, $\text{Fe}_3\text{O}_4/\text{N-GAs}$ showed better durability than the commercial Pt/C catalyst. He *et al.* demonstrate a novel resin-based methodology for large-scale self-assembly of the NG obtained by using a precursor containing N and metal ions (Figure 10.32) [79]. In a

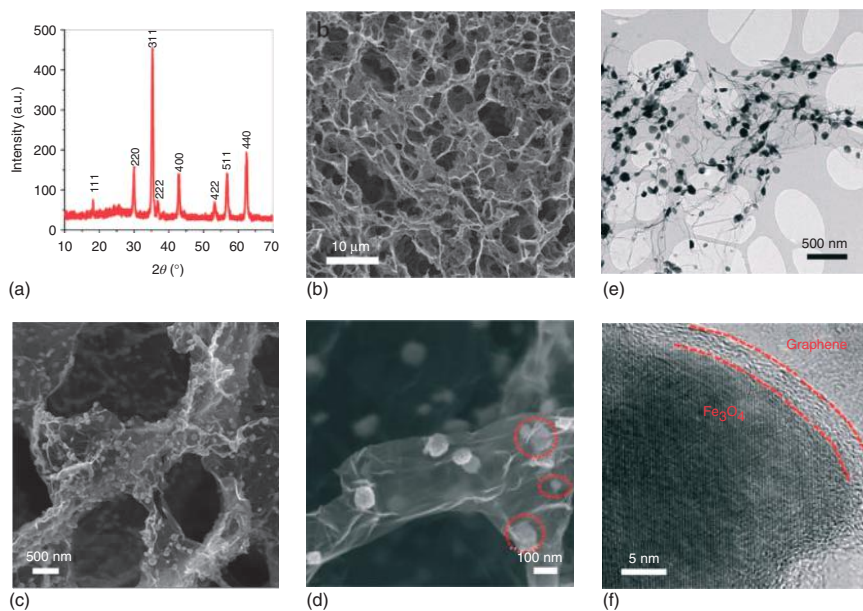


Figure 10.31 Structure and morphology of $\text{Fe}_3\text{O}_4/\text{N-GAs}$ catalysts. (a) XRD pattern and (b–d) typical SEM images of $\text{Fe}_3\text{O}_4/\text{N-GAs}$ revealing the 3D macroporous structure and uniform distribution of Fe_3O_4 NPs in the GAs. The red rings in (d) indicate Fe_3O_4 NPs encapsulated in thin graphene layers. Representative (e) TEM and (f) HRTEM images of $\text{Fe}_3\text{O}_4/\text{N-GAs}$ revealing an Fe_3O_4 NP wrapped by graphene layers. (Reproduced with permission from [78]. Copyright © 2012 American Chemical Society)

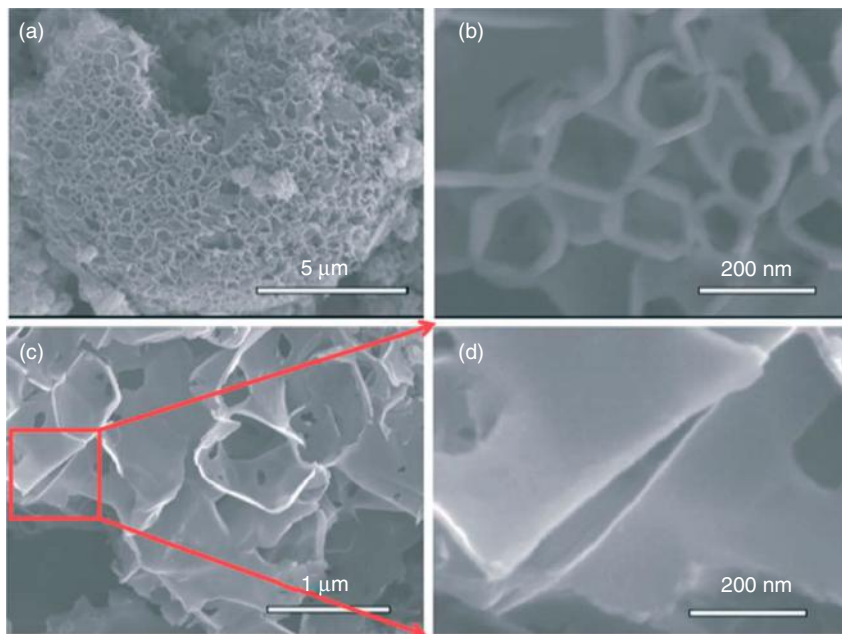


Figure 10.32 SEM micrographs of N-doped graphene. (a) SEM image of the as synthesized N-doped graphene structures before sonication, (b) high magnification SEM image of the N-doped graphene before sonication, (c) SEM image of the

as-synthesized N-doped graphene after simple sonication in ethanol for several minutes and (d) a close-up of the red square in (c). (Reproduced with permission from [79]. Copyright © 2012 Royal Society of Chemistry)

typical procedure, 20 g of nitrogen-containing resin (N-resin), poly-(acrylonitrile-divinylbenzene-triallyl isocyanurate), was immersed in 200 ml of 1 mol l^{-1} HCl solution to remove impurities. The solution of $\text{CoCl}_2 \cdot 6\text{H}_2\text{O}$ (4.72 g) dissolved in 100 ml of deionized (DI) water and 20 g of the purified N-resin was then mixed under magnetic stirring at 80°C until the mixture was dried. The cobalt containing N-resin was further heated in a tube furnace at 1100°C under flowing argon at a rate of 30 ml min^{-1} for 1 h. The product was finally post-treated with 3.0 M HCl solution for more than 12 h with magnetic stirring to completely remove cobalt. The electrochemical performance of the NG catalyst was studied by a rotating ring-disk electrode (RRDE) system and showed an outstanding electrocatalytic activity, long-term stability, and good MeOH and CO tolerance for ORR.

Zhao *et al.* have reported the hydrothermal preparation of N-doped, ultralight, 3D graphene framework (GF), by hydrothermally treating a mixture of a low concentration ($0.35\text{--}0.4 \text{ mg ml}^{-1}$) of aqueous GO suspension with 5 vol% pyrrole in a Teflon-lined autoclave at 180°C for 12 h [80]. The so formed N-containing gel was then freeze-dried and annealed at 1050°C for 3 h under Ar atmosphere. Because of the conjugated structure of pyrrole with its electron-rich N atom, it can attach to the surfaces and galleries of GO sheets through hydrogen-bonding

or π - π interactions, thus providing an N source. The pyrrole also works as swelling agent to effectively prevent GO from self-stacking during the hydrothermal process, thus leading to the formation of the large volume GF. A low concentration (e.g., 0.35 mg ml^{-1}) of GO dispersion with pyrrole allows the assembly of 3D porous graphene networks; this does not occur in the absence of pyrrole.

10.3

Boron Doping

Luo *et al.* [81], adopting a global optimization method, performed particle-swarm optimization (PSO) simulations, to predict new stable nanostructures of 2D boron-carbon (B-C) compounds for a wide range of boron concentrations. The calculations show that (i) all 2D B-C compounds are metallic except for BC_3 , which is a magic case where the isolation of carbon six-membered ring by boron atoms results in a semiconducting behavior, (ii) for C-rich B-C compounds, the most stable 2D structures can be viewed as boron doped graphene (BG) structures, where boron atoms typically form 1D zigzag chains except for BC_3 in which boron atoms are uniformly distributed, (iii) the most stable 2D structure of BC has alternative carbon and boron ribbons with strong in-between B-C bonds, which possesses a high thermal stability above 2000 K, and (iv) for B-rich 2D B-C compounds, there is a novel planar-tetracoordinate carbon motif with an approximate C_{2v} symmetry.

Panchakarla *et al.* carried out DC arc discharge experiments using graphite electrodes in the presence of $\text{H}_2 + \text{B}_2\text{H}_6$ or using boron-stuffed graphite electrodes yielding BG of two to four layers [16]. First set of BG samples (BG1) was prepared by carrying out arc discharge of graphite electrodes in the presence of hydrogen, helium, and diborane (B_2H_6). B_2H_6 vapor was carried to the arc chamber by passing hydrogen (200 Torr) through B_2H_6 generator and subsequently by passing He (500 Torr). A second set of boron doped samples (BG2) was prepared by carrying out arc discharge using a boron-stuffed graphite electrode (3 at.% boron) in the presence of H_2 (200 Torr) and He (500 Torr). Also all doped graphene samples were characterized by a variety of physical methods along with an undoped sample prepared by arc discharge in hydrogen (HG) for comparison. Figure 10.33 shows TEM image of BG prepared by the arc discharge method along with a calculated STM image.

XPS analysis showed that the BG1 and BG2 contained 1.2 and 3.1 at.% of boron, respectively, while the EELS data showed the content of boron in these samples to be 1.0 and 2.4 at.% respectively. In Figure 10.2b, we show typical core-level XPS data of BG2 along with the elemental mapping by EELS. Analysis of the (002) reflections in the X-ray diffraction (XRD) patterns showed that the B-doped samples contained two to three layers on an average, which is also confirmed by the TEM images (see Figure 10.33 for typical TEM images). AFM images also showed the presence of two to three layers in the BG and NG samples, with occasional presence of single layers. Raman spectra of all the BG and NG samples in comparison with

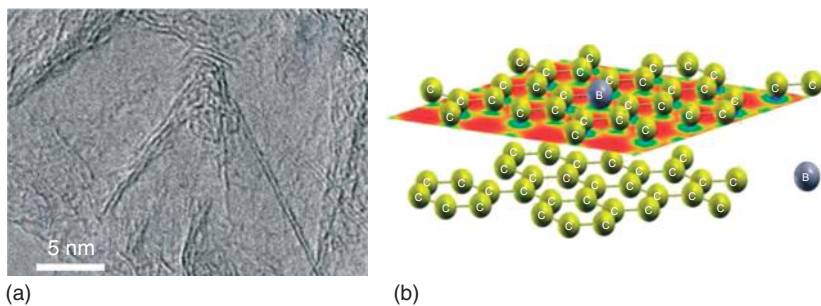


Figure 10.33 TEM images of (a) B-doped graphene (BG2), (b) calculated scanning tunneling microscopy (STM) image of B-doped graphene bilayers; B doping results in depletion of electronic charge on carbon atoms on the sublattice of the substituted dopant, as evident in weaker green (B) color. (Reproduced from Ref. [16].)

the spectrum of the pure graphene sample (HG), prepared by the H_2 -discharge method is shown in Figure 10.3. It is noteworthy that the G band stiffens both with boron and nitrogen doping. The shift in the case of BG2, with a higher B-content, is larger than with BG1. The intensity of the D band is higher with respect to that of the G band in all the doped samples. On doping, the relative intensity of the 2D band generally decreases with respect to the G band.

10.3.1

Mechanical Exfoliation

Kim *et al.* [82] reported SLG, substitutionally doped with boron by the mechanical exfoliation of boron-doped graphite. Boron-doped graphite was prepared by thermally treating graphite with a boron compound at 2450°C using a graphite furnace (Figure 10.34a). The amount of substitutional boron in graphite was ~ 0.22 at.% and the boron atoms were spaced 4.76 nm apart in SLG. The sevenfold higher intensity of the D-band when compared to the G-band was explained by the elastically scattered photoexcited electrons by boron atoms before emitting a phonon (Figure 10.34b). The frequency of the G-band in single-layer substituted BG was unchanged, which could be explained by the p-type boron doping (stiffening) counteracting the tensile strain effect of the larger carbon-boron bond length (softening).

10.3.2

Thermal Annealing

Sheng *et al.* doped boron atoms into GFs via a catalyst-free thermal annealing approach in the presence of boron oxide [83]. In a typical procedure, graphite oxide (synthesized by the modified Hummers' method) powder was put onto the surface of B_2O_3 in a corundum crucible, which was then placed in the center of a corundum tube with a continuous flow of argon to guarantee an

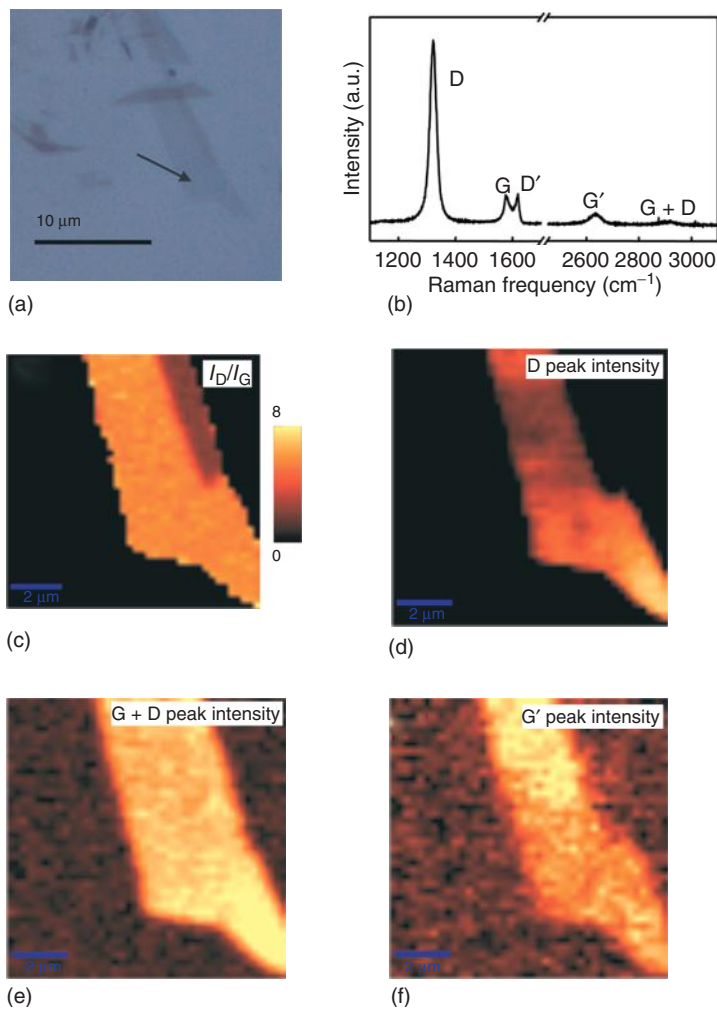


Figure 10.34 (a) Optical microscope image of the boron-doped single-layer graphene (indicated by the arrow) on an SiO_2/Si substrate; (b) Raman spectrum obtained using a 633 nm laser line, and spatial maps of (c) I_D/I_G , the intensities of the (d) D-band, (e) G + D-band, and (f) G' -band. The integrated intensity of the D-band is sevenfold that of the G-band. (Reproduced with permission from [82]. Copyright © 2012 American Chemical Society)

inert atmosphere in the tube furnace. The center temperature of the furnace was heated to 1200°C at a heating rate of 5°C min^{-1} . After maintaining at this temperature for 4 h, the sample was cooled to room temperature slowly under an Ar atmosphere. The obtained product was then refluxed in 3 M NaOH aqueous solution for 2 h to remove any of the unreacted boron oxide. After filtration and water washing, the product was dried in a vacuum at 60°C . The

as-prepared BG has a flake-like structure with an average thickness of about 2 nm and 3.2% atomic percentage of boron. Due to its particular structure and unique electronic properties, the resultant BG exhibits excellent electrocatalytic activity toward ORR in alkaline electrolytes, similar to the performance of Pt catalysts.

10.3.3

Chemical Vapor Deposition

Li *et al.* [84] synthesized BG directly by CVD using ethanol and boron powder as the precursors. First, boron powder was uniformly dispersed in ethanol by ultrasonication for 30 min, and the suspension mixture was then evenly spray-coated on the copper surface. After natural drying, the copper substrate was placed in the middle of a quartz tube located in a thermal CVD furnace. When the furnace was heated up to 950 °C, ethanol was introduced into the quartz tube as the carbon source at 10 $\mu\text{l min}^{-1}$. After 10 min reaction, the sample was cooled down to room temperature under argon flow. A mixed solution of FeCl_3/HCl was used to etch the copper away to obtain the free-standing BG film. The process schematic is shown in Figure 10.35. The BG so obtained shows p-type semiconductor features. Doped graphene films can form p–n junctions with n-Si to deliver power-conversion efficiencies of up to 3.4% under AM 1.5.

Cattelan *et al.* [85] employed a two-step procedure for the optimization growth of single layer BG nanostructures on polycrystalline copper foils by CVD using methane and diborane as carbon and boron source, respectively. BG films were deposited on electro-polished Cu foils in a homemade low-pressure cold-wall CVD system. The growth temperature was reached using a resistive heating system directly in contact with the Cu foils. The Cu foil surface was activated according to the following procedure: the system was evacuated by a scroll pump and a liquid nitrogen cold trap obtaining a base pressure of 5×10^{-2} mbar, and 200 sccm of Ar were introduced into the chamber for 20 min to replace air. The argon flux was then replaced by a 25 sccm flux of hydrogen during the annealing stage (950 °C) for 25 min. For BG, the growth was in two steps: 1 min of 25 sccm of methane dosing and 30 s of codosing of 25 sccm of methane and 10 sccm of diborane (1% in helium). Immediately after the growth, the resistive heating was shut down to rapidly decrease the substrate temperature (from 1000 to 200 °C in less than 30 s, and all the fluxes were stopped. In the first step, the copper surface is seeded with pure graphene islands, whereas the boron source is activated only in a second stage. In this case, the nonstoichiometric boron carbides formed on the bare copper areas between preseeded graphene patches can be exploited to easily release boron, which diffuses from the peripheral areas inward of graphene islands leading to the effective substitutional doping of the order of ~1%. Attempts to deposit doped layers in one-step were not successful since the formation of the reactive boron species as a consequence of diborane decomposition on the Cu surface leading to disordered nonstoichiometric carbides.

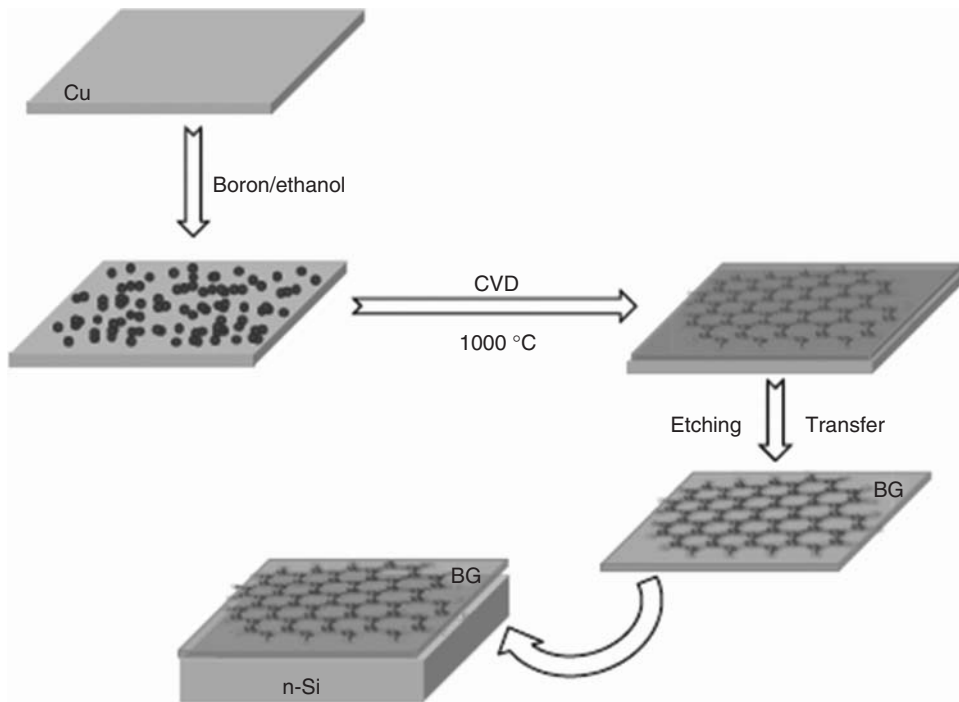


Figure 10.35 Schematic of BG preparation and solar cell assembly. (Reproduced with permission from [84]. Copyright © 2012 Wiley-VCH)

Gebhardt *et al.* report the synthesis of BG on Ni (111) in a CVD process of triethylborane (TEB), by segregating of boron from the bulk of the substrate crystal [86]. BG produced by CVD using TEB as precursor at temperatures between 600 and 950 K, leads to boron concentrations of typically 0.15 up to 0.35 ML after an exposure of 1800 L. Concentrations below 0.15 ML (monolayer) were prepared by segregating boron from the bulk, while exposing the nickel crystal to propene at 10^{-6} mbar at 900 K until saturation of the carbon signal. Boron is dissolved in the bulk by exposure to TEB and subsequent annealing to temperatures of 1100 K. Doping with boron leads to graphene preferentially adsorbed in the top-fcc geometry, since the boron atoms in the graphene lattice are then adsorbed at substrate fcc-hollow sites. The smaller distance of boron atoms incorporated into graphene compared to graphene carbon atoms leads to a bending of the doped graphene sheet in the vicinity of the boron atoms.

Wang *et al.* [87] synthesized wafer-scale BG monolayers using phenylboronic acid as a sole precursor in CVD. Typically B-doped graphene films were grown inside a horizontal tube furnace equipped with a 1-in.-diameter quartz tube, where a copper foil was loaded in the hot center of the furnace, whereas phenylboronic acid powder, was placed upstream at a location ~ 35 cm away from the center. A schematic representation of B-doped graphene growth is illustrated in Figure 10.36.

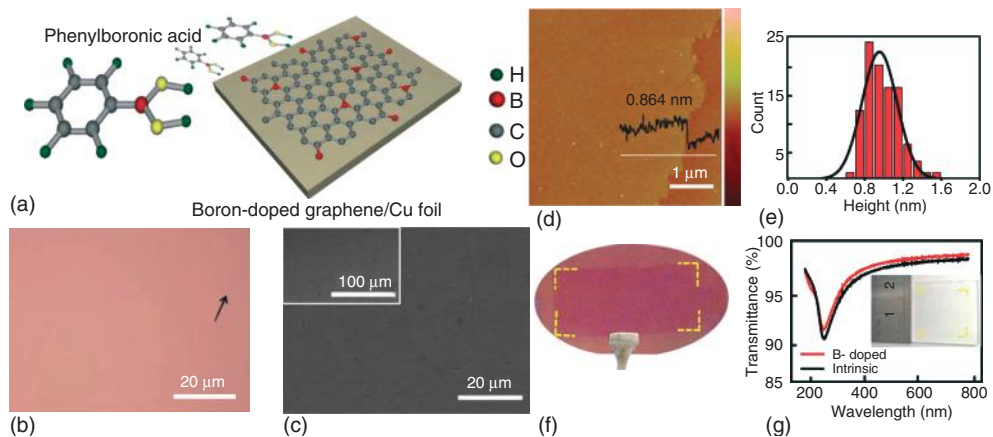


Figure 10.36 (a) Schematic diagram of CVD growth of boron-doped graphene on Cu surface with phenylboronic acid as the carbon and boron sources. The red, gray, yellow, and green spheres represent boron, carbon, oxygen, and hydrogen atoms, respectively. (b) Optical micrograph of a monolayer boron-doped graphene transferred onto SiO₂/Si substrate. The arrow points to blank SiO₂/Si substrate. (c) SEM image of the boron-doped graphene film transferred onto SiO₂/Si substrates. The inset shows the low-magnification SEM image of the same sample. (d) AFM image of the region pointed by black arrow in panel (b) with a

z-scale of 20 nm. (e) Histogram of thickness distribution from AFM height images. (f) Contrast enhanced photograph of the B-doped graphene sample on 4-in. Si/SiO₂ substrate. (g) UV-vis transmittance spectra of the boron-doped graphene and the reference intrinsic graphene on quartz substrate. The intrinsic graphene monolayer was CVD grown on copper using methane and then transferred on the quartz substrate. Inset: the photograph of boron-doped graphene monolayer on a quartz substrate. (Reproduced with permission from [87]. Copyright © 2013 Wiley-VCH)

After the copper foil was annealed at 1030 °C under 10 sccm H₂ with a pressure of 120 mbar for 30 min, the furnace was cooled down to 950 °C. Phenylboronic acid powder was heated with a heating tape to 130 °C for the gradual sublimation. H₂ (10 sccm) was used as the carrier gas to transport the vapor of phenylboronic acid downstream to the copper foil. After a 20-min growth, the furnace was cooled to room temperature under 10 sccm H₂.

B-doped graphene films grown on copper were then transferred onto SiO₂/Si with a dry transfer procedure to avoid the p-type doping caused by the adsorbed H₂O and O₂. Briefly, the graphene samples with PMMA films detached from the copper foil were cleaned by DI water, isopropyl alcohol, and then dried in air for 6 h before the graphene/PMMA films were placed onto the target substrates. The B-doped graphene film was transferred under dry conditions onto a SiO₂ substrate for Raman measurements (Figure 10.37). Both the G (1592 cm⁻¹) and 2D bands (2695 cm⁻¹) of the B-doped graphene show upshifts of 6 and 9 cm⁻¹, respectively. Meanwhile, the intensity ratio of the 2D and G bands (I_{2D}/I_G) decreases. The emergence of D and D' bands, the observed shifts in G and 2D band position as well as the decrease in I_{2D}/I_G ratios are consistent with the expected p-type doping

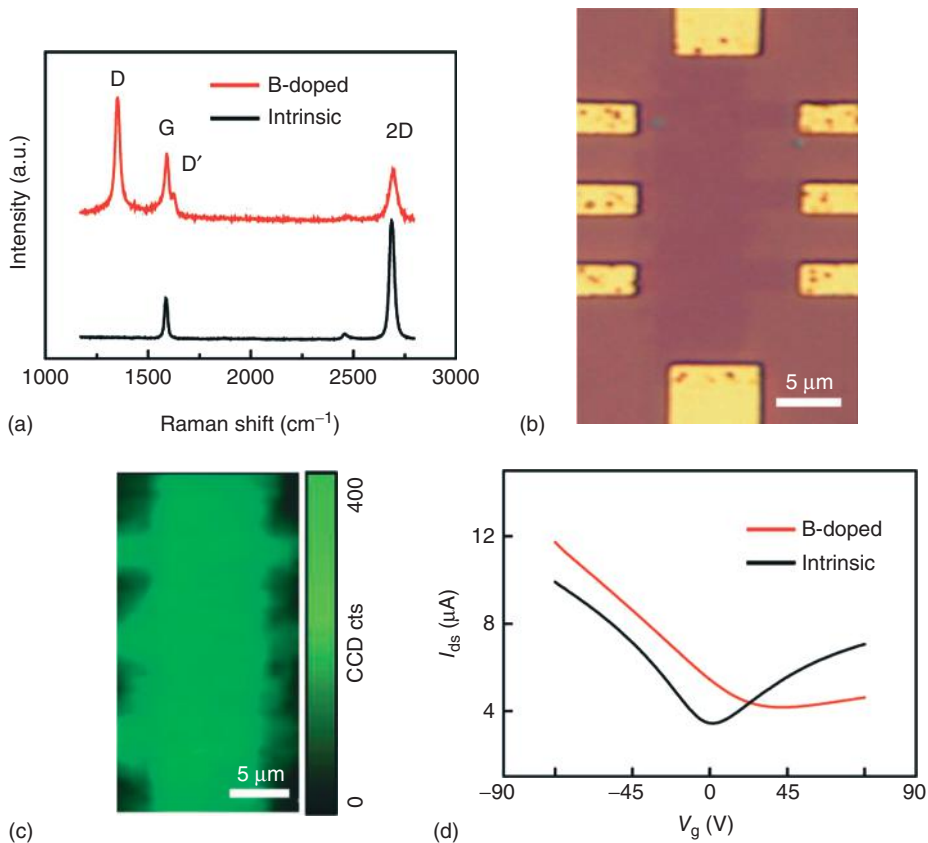


Figure 10.37 (a) Typical Raman spectra of the boron-doped (red) and intrinsic (black) graphene transferred on SiO_2/Si substrate by a dry transfer procedure. (b) Optical micrograph of a boron-doped graphene device. (c) Raman map of D band intensity the channel region of the boron-doped graphene

device shown in (b). (d) Source–drain current (I_{ds}) versus back gate voltage (V_g) with $V_{ds} = 0.1 \text{ V}$ of the boron-doped (red) and intrinsic (black) graphene device, respectively. (Reproduced with permission from [87]. Copyright © 2013 Wiley-VCH)

effect in B-doped graphene films. The uniform B-doped graphene exhibits a p-type doping behavior with a considerably high carrier mobility of about $800 \text{ cm}^2 \text{ V}^{-1} \text{ s}^{-1}$, confirmed by electric transport measurements. This method of B-doping may enable modulation-doped growth of mosaic graphene with p–i or p–n junctions.

10.3.4

Other Methods

Lue *et al.* prepared boron-doped graphene nanosheets (GNSs) via a rapid Wurtz-type reductive coupling (WRC) reaction without the assistance of any transition metal catalysts [88]. This method involves a nearly stoichiometric reaction of

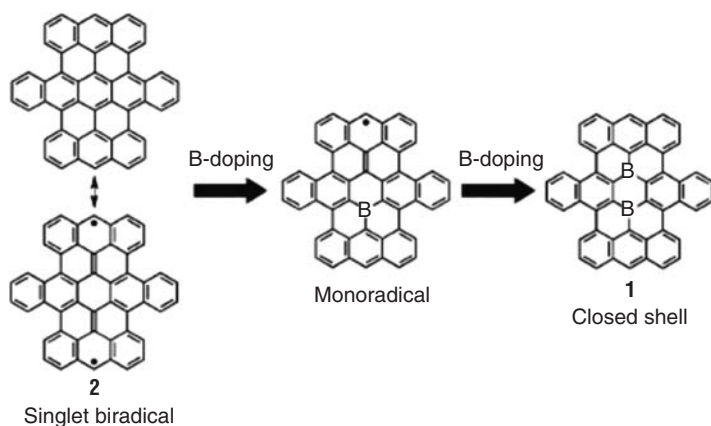


Figure 10.38 Schematic representation of stepwise boron doping of an extended polyaromatic hydrocarbon. (Reproduced with permission from [91]. Copyright © 2012 Wiley-VCH)

CCl_4 , and potassium (K) in the presence of an appropriate amount of BBr_3 at $150\text{--}210^\circ\text{C}$ for as short as 10 min, which possesses great advantages compared with the solvothermal method. The number of layers in the as-prepared graphene is <5 . Khai *et al.* [89] prepared BG oxide by annealing films obtained from suspensions of GO and H_3BO_3 in *N,N*-dimethylformamide. First-order Raman spectra revealed that the intensity ratio of the D and G bands of B-doped GO was significantly lower than those of as-synthesized and annealed GOs, suggesting more graphitization of the B-doped GO as a result of the doping effect. The C 1s XPS of B-doped GO films not only indicated that a considerable amount of functional groups has been removed but also exhibited the peak of C-B band at around 283.7 eV. Additionally, the B1s XPS spectrum of B-doped GOs could be deconvoluted into several peaks centered at 187.2, 188.9, 190.3, 192.0, and 193.7 eV, attributed to the presence of B atom in B_4C , B-sub-C, BC_2O , BCO_2 , and B_2O_3 , respectively. Comparison of the photoluminescence spectra of B-doped GO with that of 1100°C -annealed GO indicated that the overall intensity was decreased, presumably because of the B-induced graphitization. An additional band at around 600–700 nm from B-doped GO is attributed to the boron carbide phases.

Han *et al.* [90] produced B-doped nanoplatelets (borane-reduced graphene oxide, B-rGO) on a large scale using the solution process, via the reduction of GO by a boranetetrahydrofuran adduct under reflux, and studied their use for supercapacitor electrodes. The B-rGO had a high SSA of $466\text{ m}^2\text{ g}^{-1}$ and showed excellent supercapacitor performance including a high specific capacitance of 200 F g^{-1} in aqueous electrolyte as well as superior surface area-normalized capacitance to typical carbon-based supercapacitor materials and good stability after 4500 cycles. Two- and three-electrode cell measurements showed that energy storage in the B-rGO supercapacitors was by ion adsorption on the surface of the nanoplatelets in addition to electrochemical redox reactions.

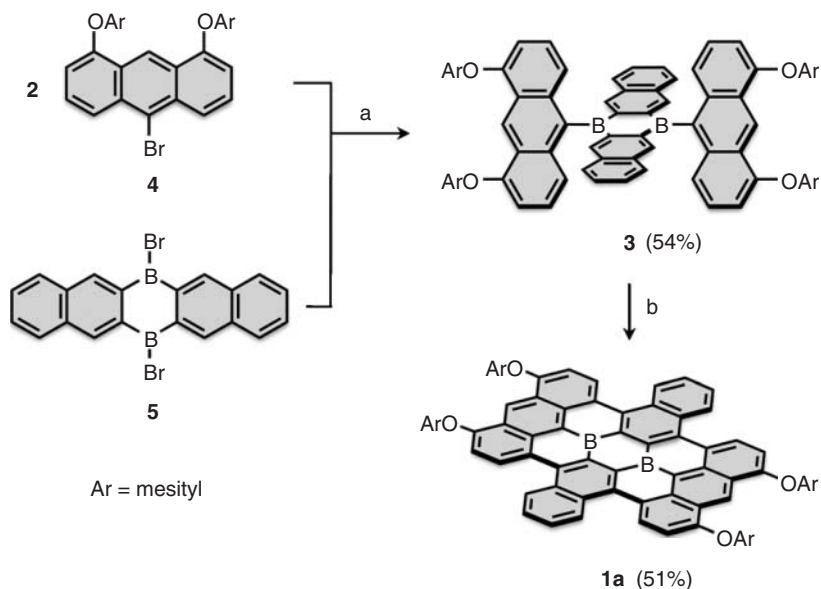


Figure 10.39 Synthesis of B-doped nanographene **1a**. Reagents and conditions: (a) *n*-BuLi, Et₂O, from 0 to 25 °C, then **5**, toluene, from 0 to 25 °C and (b) FeCl₃,

CH₃NO₂, and CH₂Cl₂. (Reproduced with permission from [91]. Copyright © 2012 Wiley-VCH)

Dou *et al.* [91] showed boron-containing polycyclic aromatic hydrocarbon as a substructure of BG, and achieved stable B-doped nanographene as a single closed-shell compound by a bottom-up organic synthesis (Figure 10.38). Because the replacement of a C atom by a B atom corresponds to a one-electron oxidation, namely hole doping, the doping of a single B atom into the skeleton will result in the formation of an unstable open-shell compound (Figure 10.38, schematic). Two boron atoms need to be introduced at the same time to produce a stable closed-shell structure. In compound **1**, two B atoms are placed in the central hexagon, and its closed-shell structure should produce unique properties that are totally different from those of the undoped congener **2** (Figure 10.39, schematic). The structure deviates from planarity because of steric overcrowding in the *cove* regions. The most important effect of B doping is the significant contribution of the p orbitals of the B atoms to both the relevant unoccupied and occupied orbitals, which play important roles in the broad absorption over the entire visible region as well as the fluorescence in the near-IR region.

Tang *et al.* [92] synthesized B-doped graphenes with tunable band gap and transport properties via controllable doping through reaction with the ion atmosphere of trimethylboron decomposed by reactive microwave plasma. The B content could be adjusted over the 0–13.85 at.% range by controlling the ion reaction time, from which the doping effects on transport properties were quantitatively evaluated. Electrical measurements from graphene FETs show that B-doped graphenes have

a distinct p-type conduction with a current on/off ratio higher than 10^2 . The band gap of graphene is changed from 0.0 to ~ 0.54 eV with increasing B content, leading to modulated transport properties.

10.4

BN Doping in Graphene

Pham *et al.* have shown ammonia borane is a highly efficient reducing agent instead of hydrazine for the reduction of GO in both aqueous and organic solvents, which is nontoxic and more effective than hydrazine [93]. More interestingly, ammonia borane reduction of GO in THF produced higher NG and BG, which exhibited high supercapacitor performance.

Wu *et al.* prepared N- and B-doped monolayer graphene by CVD using PS, urea, and boric acid as solid precursors [94]. The solid-state PS and dopant elemental precursors were subsequently heated to the setting value by a heating lamp under a mixture of H_2 and Ar gas, while the Cu foil substrate was kept at $1000^\circ C$ for a growth time of ~ 30 min. It was found that monolayer graphene could be synthesized by regulating the weight of the solid carbon precursor with the H_2/Ar gas flow rate. After the growth process, the furnace and heating lamp were cooled down to room temperature. By adjusting the elemental precursors, the nitrogen content could be modulated from 0.9 to 4.8% for N-doped graphene and the B content from 0.7 to 4.3% for B-doped graphene, as estimated by XPS. The mobilities of the N- and B-doped graphene-based back-gate FETs are about $350\text{--}550$ and $450\text{--}650\text{ cm}^2\text{ V}^{-1}\text{ s}^{-1}$, respectively. Bepete *et al.* [95] developed a method for growing a large area of graphene doped with small BN domains on copper foils using a single step CVD (at a temperature of $995^\circ C$) with methane, boric acid powder, and nitrogen gas as the carbon, boron, and nitrogen sources, respectively. This process avoids the use of boranes and ammonia and both B and N can be substituted into the graphene structure in the form of small BN domains to give a B-N-C system. Lin *et al.* [96] demonstrates the conversion of graphene oxide nanosheets into borocarbonitride (BCN) nanosheets by reacting them with B_2O_3 and ammonia at $900\text{--}1100^\circ C$, by which both the boron and nitrogen atoms are incorporated into the graphene lattice in randomly distributed BN nanodomains (Figure 10.40). The content of BN in BN-doped GNSs can be tuned by changing the reaction temperature, which in turn affects the optical bandgap of these nanosheets. Electrical measurements show that the BN-doped GNS exhibits an ambipolar semiconductor behavior and the electric bandgap is ≈ 25.8 meV.

Levendorf report a process, which they call patterned regrowth, that allows for spatially controlled synthesis of lateral junctions between electrically conductive graphene and insulating h-BN, as well as between intrinsic and substitutionally doped graphene (Figure 10.41) [97]. The films form mechanically continuous sheets across the heterojunctions. Conductance measurements confirm laterally insulating behavior for h-BN regions, whereas the electrical behavior of

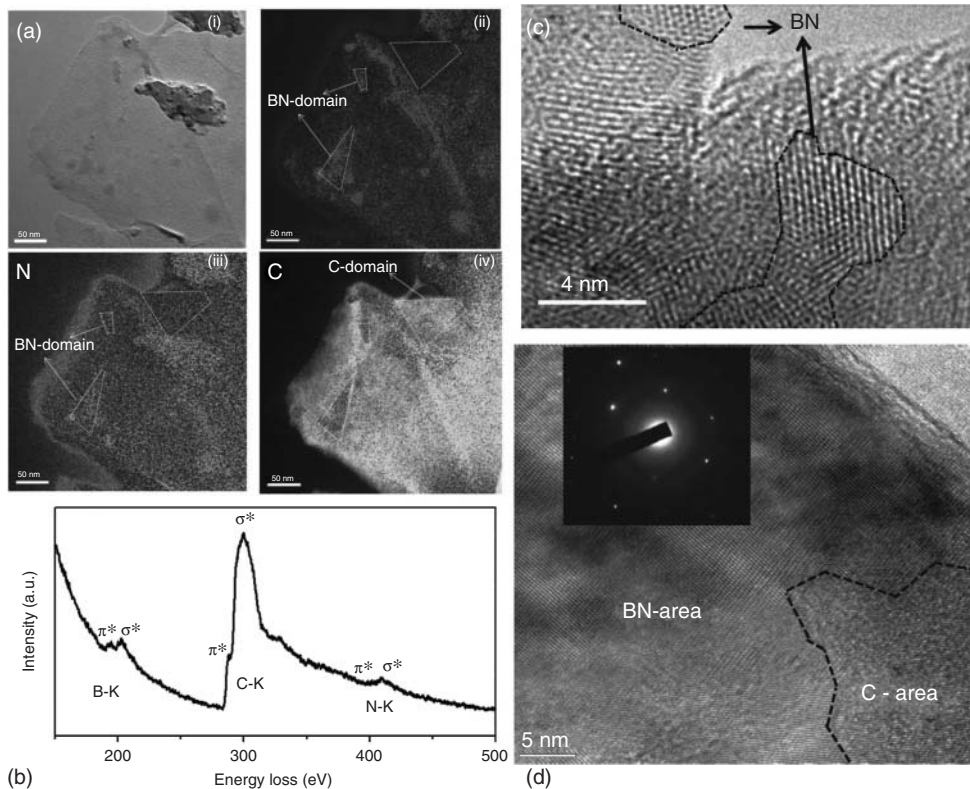


Figure 10.40 (a) EELS elemental maps acquired from the BCN nanosheets prepared at 900 °C. (i) bright-field image; (ii) boron mapping; (iii) nitrogen mapping; and (iv) carbon mapping. (b) EELS spectrum recorded from a single BCN nanosheet (the measured point was taken from the star marked in (a-i)). It shows the three distinct K-edges of the boron, carbon, and nitrogen

at 188, 284, and 398 eV, respectively. (c) HRTEM image of the BCN sheet prepared at 900 °C; the enclosed regime shows the BN lattice domain. (d) HRTEM image of the BCN sheet prepared at 1000 °C; the inset shows the selected-area electron diffraction pattern of the BN lattice domain. (Reproduced with permission from [96]. Copyright © 2012 Wiley-VCH)

both doped and undoped graphene sheets maintain excellent properties, with low sheet resistances and high carrier mobilities. Atomic sheets containing hybridized bonds involving elements B, N, and C over wide compositional ranges could result in new materials with properties complementary to those of graphene and h-BN, enabling a rich variety of electronic structures, properties, and applications.

Ci *et al.* [98] report the synthesis and characterization of large-area atomic layers of h-BN and C material, consisting of hybridized, randomly distributed domains of h-BN and C phases with compositions ranging from pure BN to pure graphene. Their studies reveal that their structural features and bandgap are distinct from those of graphene, doped graphene, and h-BN. Fan *et al.* [99] using first-principles

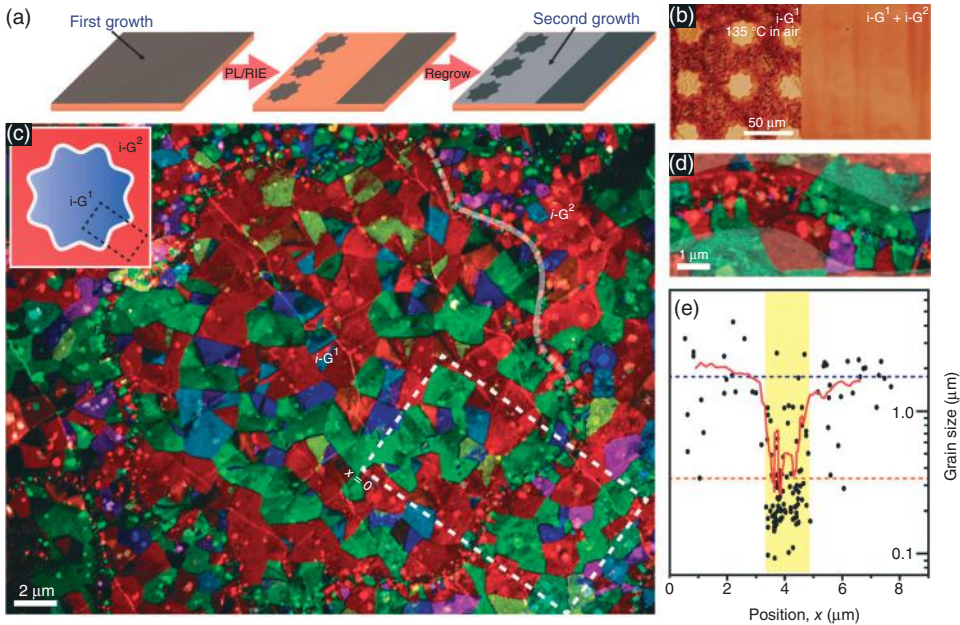


Figure 10.41 Process schematic and DF (dark field)-TEM characterization of graphene heterostructures. (a) Schematic for formation of atomically thin lateral heterojunctions using photolithography (PL) and reactive ion etching (RIE). (b) The left panel shows an optical image of a patterned Cu/G^1 foil oxidized to enhance contrast (the dark areas are Cu). The right panel shows an optical image after reduction of CuO_x and subsequent growth of intrinsic- G^2 ($i\text{-G}^2$).

(c) False-color DF-TEM image of an $i\text{-G}^1/i\text{-G}^2$ patterned area (schematic in inset). (d) Zoomed-in image of the junction region. (e) Plot of grain size versus position in the box outlined in (c). Dotted lines indicate average grain size away from (blue line) and near (highlighted region and orange line) the junction. Shading indicates the width of the region with smaller grains. (Reproduced with permission from [97]. Copyright © 2012 Nature Publishing Group)

calculations, show that the band gap of graphene can be opened effectively around K (or K') points by introducing small boron nitride (BN) domains. BN domains are easily formed in the basal plane of graphene because of phase separation. It is also found that by random doping with boron or nitrogen it is possible to open a small gap in the Dirac points, except for the modulation of the Fermi level. The surface charges, which belong to the π states near Dirac points, are found to be redistributed locally. The charge redistribution is attributed to the change of localized potential owing to doping effects and the band opening induced by the doped BN domain is found to be because of the breaking of localized symmetry of the potential. Chang *et al.* [100] report on the opening and scaling of band gap in *in situ* BN doped graphene (BNG) films grown by low-pressure CVD method. A significant band gap ~ 600 meV is observed for low BN concentrations

and is attributed to the opening of the π - π^* band gap of graphene as a result of the isoelectronic BN doping. As-grown films exhibit structural evolution from homogeneously dispersed small BN clusters to large sized BN domains with embedded diminutive graphene domains. The evolution is described in terms of competitive growth among h-BN and graphene domains with increasing BN concentration.

Xue *et al.* used a modified CVD to prepare a class of new graphene foams (GFs) doped with nitrogen, boron, or both [101]. Nitrogen-doped graphene foams (N-GFs) with a nitrogen doping level of 3.1 at.% were prepared by CVD of CH_4 in the presence of NH_3 while boron-doped graphene foams (B-GFs) with a boron doping level of 2.1 at.% were produced by using toluene and triethyl borate as a carbon and a boron source. On the other hand, GFs co-doped with nitrogen (4.5 at.%) and boron (3 at.%) (BN-GFs) were prepared by CVD using melamine diborate as the precursor. In all the cases, scanning electron microscope (SEM) images revealed well-defined foam-like microstructures, whereas electrochemical measurements showed higher electrocatalytic activities toward ORR for the doped GFs than their undoped counterparts.

Zheng *et al.* incorporated N and B sequentially into selected sites of the graphene domain to induce an enhanced synergistic coupling effect that facilitates the electrocatalytic ORR [102]. B,N-graphene was synthesized from solution-exfoliated GO by a two-step doping strategy: first, N was incorporated by annealing with NH_3 at an intermediate temperature (e.g., 500 °C), and then B was introduced by pyrolysis of the intermediate material (N-graphene) with H_3BO_3 at a higher temperature (e.g., 900 °C) (Figure 10.42). The resultant two-step N,B-doping in graphene showed improved electrochemical performance as compared to that of singly doped graphene and the hybrid electrodes synthesized in one step.

Wu *et al.* [103] demonstrate a simplified prototype device of high-performance all-solid-state supercapacitors based on three-dimensional nitrogen and boron co-doped monolithic graphene aerogels. The device possesses an electrode-separator-electrolyte integrated structure, in which the aerogel serves as an additive/binder-free electrode and a polyvinyl alcohol (PVA)/ H_2SO_4 gel as the solid-state electrolyte and thinner separator. As a consequence, the supercapacitor exhibits minimized device thickness and high specific capacitance as well as good rate capability and power density. Li and Antonietti [104] carried out the copolymerization/polycondensation of biomass (glucose) and boric acid as templated by dicyandiamide to fabricate high-quality boron- and nitrogen-codoped holey graphene monoliths with through-plane nanopores. The holey graphene monoliths had a high surface area and showed excellent performance as metal-free carbocatalysts for selective oxidation. Various aspects of BCNs, $\text{B}_x\text{C}_y\text{N}_z$, have been discussed in detail recently [105]. These materials can possess BCN type rings or domains of BN or graphene.

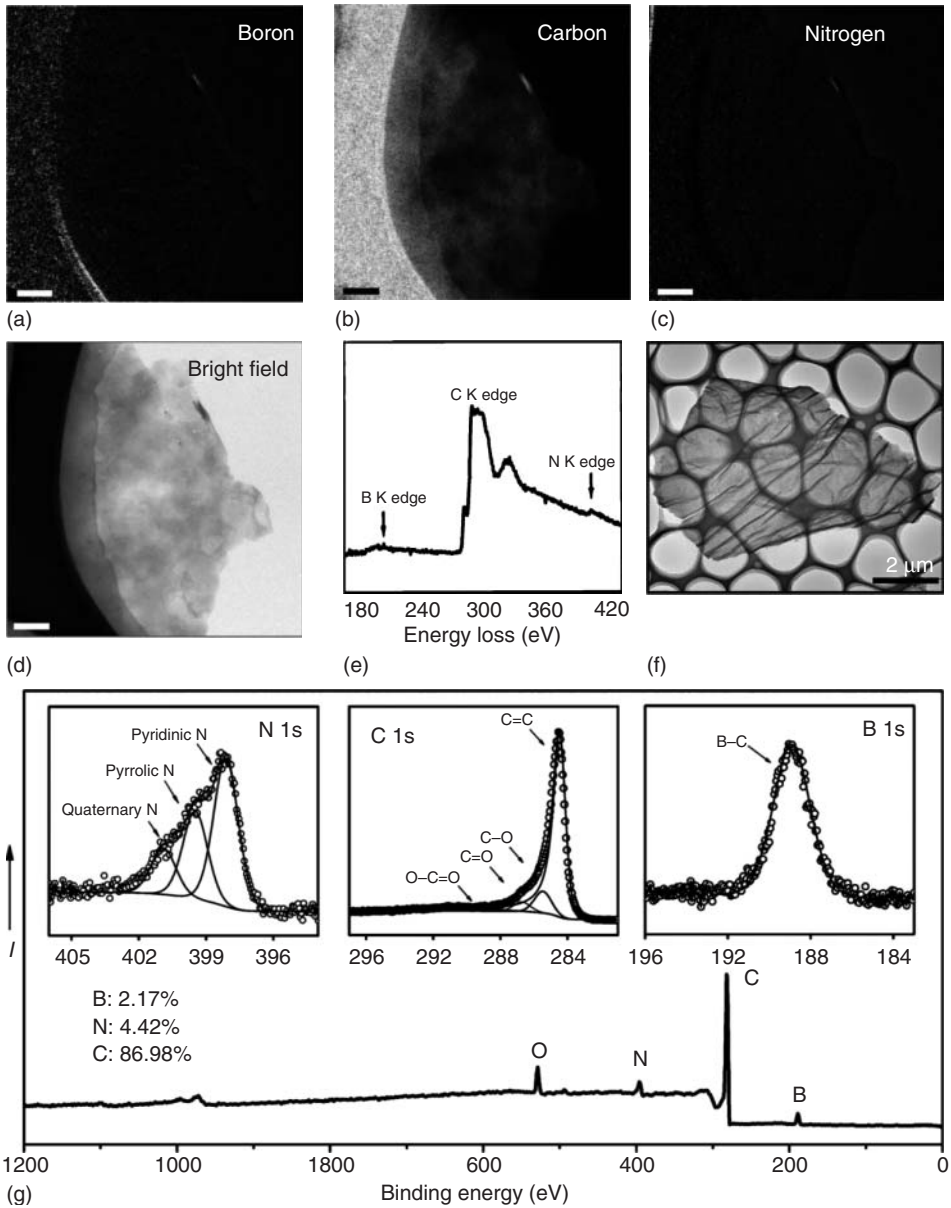


Figure 10.42 (a–d) Elemental mapping and (e) EELS spectrum of B,N-graphene (the scale bar is 100 nm). (f) Low-magnification TEM image of B,N-graphene. (g) XPS survey

and high-resolution spectra of N, C, and B 1s core levels in B,N-graphene. (Reproduced with permission from [102]. Copyright © 2013 Wiley-VCH)

10.5 Doping with Other Elements

Chemical doping involving the presence of chemical species other than B and N, such as sulfur [106], silicon [107], and adsorbed inorganic molecules (e.g., NO₂ [108]), HNO₃ [109] has been reported. Heteroatom (N or S)-doped graphene with high surface area has been prepared via thermal reaction between GO and guest gases (NH₃ or H₂S) from ultrathin graphene oxide-porous SiO₂ sheets at high temperatures (see schematic in Figure 10.43) [110]. Both N and S-doping can occur at annealing temperatures from 500 to 1000 °C to form the different binding configurations at the edges or on the planes of the graphene, such as pyridinic-N, pyrrolic-N, and graphitic-N for N-doped graphene, thiophene-like S, and oxidized S for S-doped graphene (Figure 10.44). Also, the resulting N and S-doped graphene sheets exhibit good electrocatalytic activity, long durability, and high selectivity when they are employed as metal-free catalysts for ORRs.

S-doped porous carbon hybridized with graphene (SPC@G) was prepared by choosing an ionic liquid (IL) as both the stabilizer for graphene and the medium to synthesize porous carbon doped with heteroatoms via a facile ionothermal method [111]. The synthesis route of the SPC@G nanocomposite is illustrated in Figure 10.45 with the D-glucose and GO as the starting materials and 1-butyl-3-methylimidazolium hydrosulfate [Bmim] [HSO₄] as the solvent (Figure 10.46). G-free SPC and reduced GO were prepared by the same ionothermal route as the control materials. Particularly, the as-obtained SPC@G nanocomposite shows ultrahigh reversible capacity (1400 mAh g⁻¹, much larger than commercial graphite), a long cycle life and excellent rate performances when being used as an anode material for lithium-ion batteries.

Choi *et al.* doped S and Se onto the N-doped graphene-CNT self-assembly (NGCA) by heat-treatment with diphenyldisulfide and/or diphenyldiselenide resulting in the dominant phases of -C-S-C- and -C-Se-C-, respectively, in the carbon lattice [112]. In the ORRs, the prepared materials exhibit similar onset potentials at ~0.85 V (vs RHE, reversible hydrogen electrode) regardless of chalcogenation. However, the additional doping of S and/or Se in the NGCA increases the current from ORRs in acid media. Specifically, additional Se-doping demonstrates significantly improved ORR activity with a high methanol tolerance and long-term stability in acid media compared to Pt/C. Poh *et al.* describe a scalable method of doping graphene lattice with sulfur atoms during the thermal exfoliation process of graphite oxides in the presence of gases/vapors such as H₂S, SO₂, or CS₂ [113]. The graphite oxides were first prepared by Staudenmaier, Hofmann, and Hummers methods followed by treatments in hydrogen sulfide, sulfur dioxide, or carbon disulfide. The level of doping is dramatically influenced by the type of graphite oxide used rather than by the type of sulfur-containing gas used during exfoliation. Yang *et al.* doped graphenes with the elements, which have the similar electronegativity with C such as S and Se, exhibit better catalytic activity (i.e., metal-free cathode catalyst for oxygen reduction), than the commercial Pt/C in alkaline media, indicating

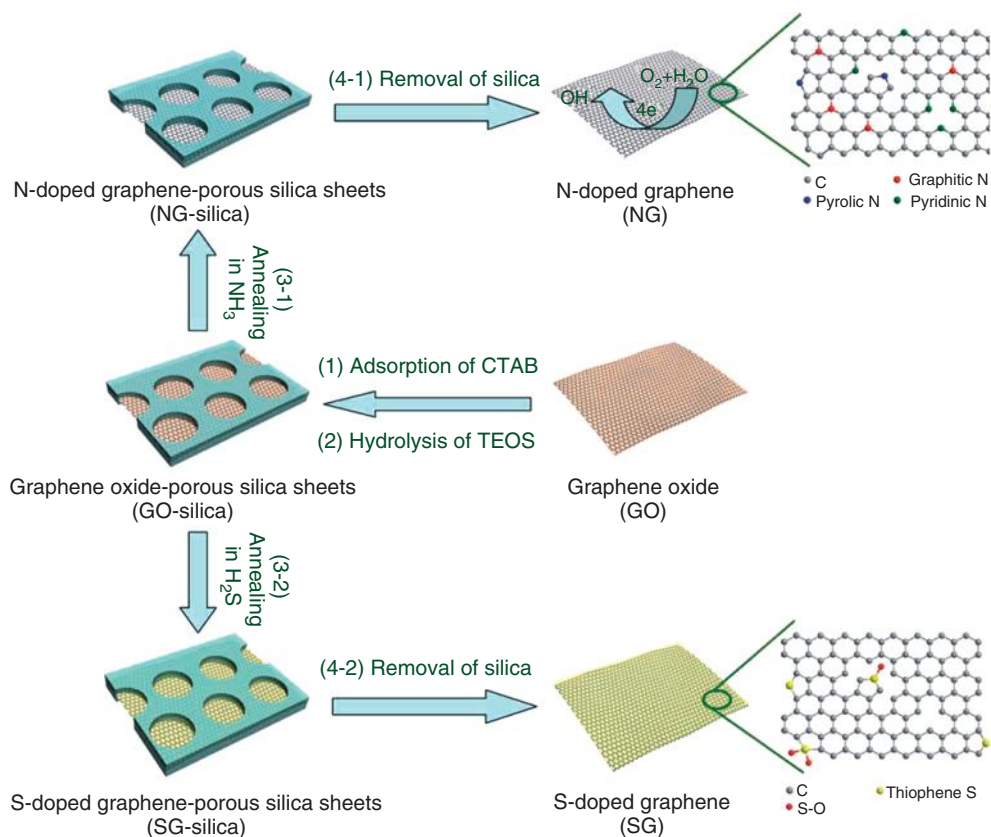


Figure 10.43 Schematic illustration of the fabrication of N and S-doped graphene: (1) and (2) hydrolysis of tetraethyl orthosilicate (TEOS) around the surface of graphene oxide with the aid of a cationic surfactant, cetyltrimethylammonium bromide (CTAB); (3-1) thermal annealing of GO-Silica sheets

in ammonia at 600, 800, 900, and 1000 °C, respectively; (3-2) thermal annealing of GO-Silica sheets in H₂S gas at 500, 700, and 900 °C, respectively; and (4-1 and 4-2) removal of silica by HF or NaOH solution. (Reproduced with permission from [110]. copyright © 2012 Wiley-VCH)

that these doped graphenes hold great potential as a substitute for Pt-based catalysts in fuel cells [114]. Liang *et al.* report one-step preparation of nitrogen and sulfur co-doped mesoporous graphene as metal-free electrocatalyst for ORR with synergistically enhanced performance [115]. This material shows excellent catalytic activity including a highly positive onset potential and very high kinetic limiting current, which makes it closely comparable to the com. Pt/C catalyst. DFT calculations have revealed that the synergistic performance enhancement results from the redistribution of spin and charge densities brought about by the dual doping of sulfur and nitrogen atoms, which leads to a large number of carbon atom active sites. This catalyst also shows a full fuel tolerance and much

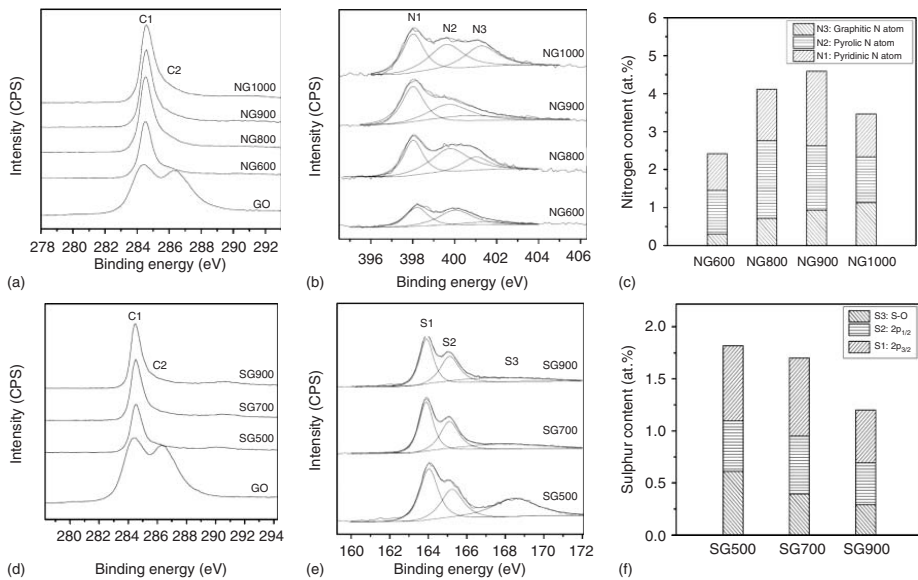


Figure 10.44 (a) High resolution C 1s XPS spectra of GO and NG with C1 (sp^2 carbon in graphene) and C2 (sp^3 carbon with C–O bonds, carbonyls (C=O), and carboxylates (O–C=O), originating from harsh oxidation). (b) High resolution N 1s XPS spectra of NG. The peaks are fitted to three energy components centered at around 398.0, 400.0, and 401.3 eV, corresponding to pyridinic-N (N1), pyrrolic-N (N2), and graphitic-N (N3), respectively. (c) The content of three nitrogen species (N1, N2, and N3) in NG sheets. (d) High resolution C 1s XPS spectra of GO and SG (sulfonated graphene) with C1 and C2. (e) High resolution S 2p XPS spectra of SG. The peaks are fitted to three energy components centered at around 163.9, 165.1, and 168.5 eV, corresponding to $Sp_{3/2}$ (S1), $Sp_{1/2}$ (S2), and S–O(S3), respectively. (f) The content of sulfur species (S1, S2, and S3) in SG sheets. (Reproduced with permission from [110]. copyright © 2012 Wiley-VCH)

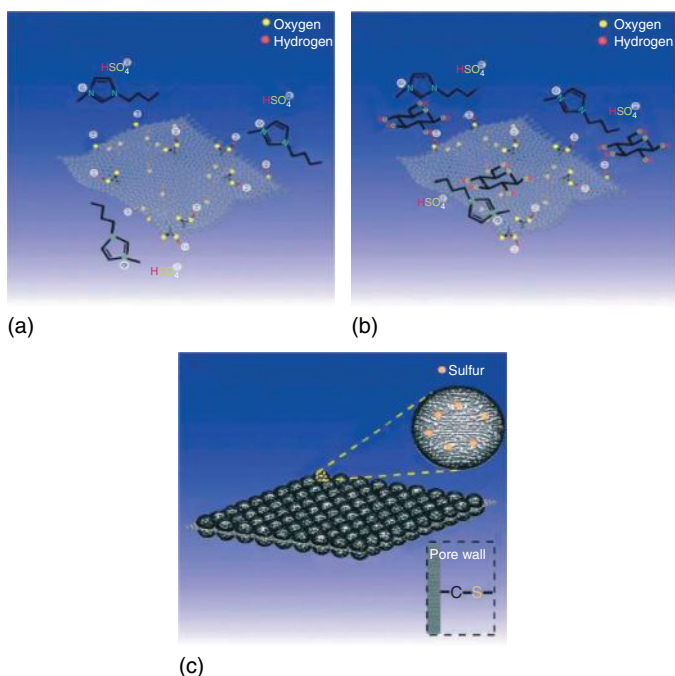


Figure 10.45 Schematic illustration of the synthesis route to SPC@G. (a) GO dispersed in IL, (b) D-glucose dissolved in the IL-GO mixture, and (c) as-obtained SPC@G after ionothermal carbonization. (Reproduced with permission from [111]. Copyright © 2012 Royal Society of Chemistry)

better long-term stability than Pt/C in alkaline environment. Lin *et al.* fabricated sulfur-doped graphene and demonstrated its influence on the discharge product formation in lithium–oxygen batteries [116]. The growth and distribution of the discharge products were studied and a mechanism was proposed. This will have significant implication for cathode catalysts and rechargeable battery performance. Li *et al.* by employing a mild phosphorus source for in situ doping the thermally reduced graphene oxide (TRG), have synthesized metal-free phosphorus-doped graphene nanosheets (P-TRG) with large surface area ($496.67 \text{ m}^2 \text{ g}^{-1}$) and relatively high P-doping level (1.16 at.%) by thermal annealing a homogeneous mixture of graphene oxide and 1-butyl-3-methylimidazolium hexafluorophosphate in an argon atmosphere [117]. The P atoms were substitutionally incorporated into the carbon framework and were partially oxidized, which created new active sites for the ORR. The ORR catalytic performance of the P-doped graphene is better or at least comparable to that of the benchmark Pt/C catalyst.

Liu *et al.* [118] have demonstrated a thermolysis approach for the synthesis of P-doped graphite layers with high electrocatalytic activity for the O₂ reduction in an alkaline medium. In this approach toluene was used as carbon precursor and

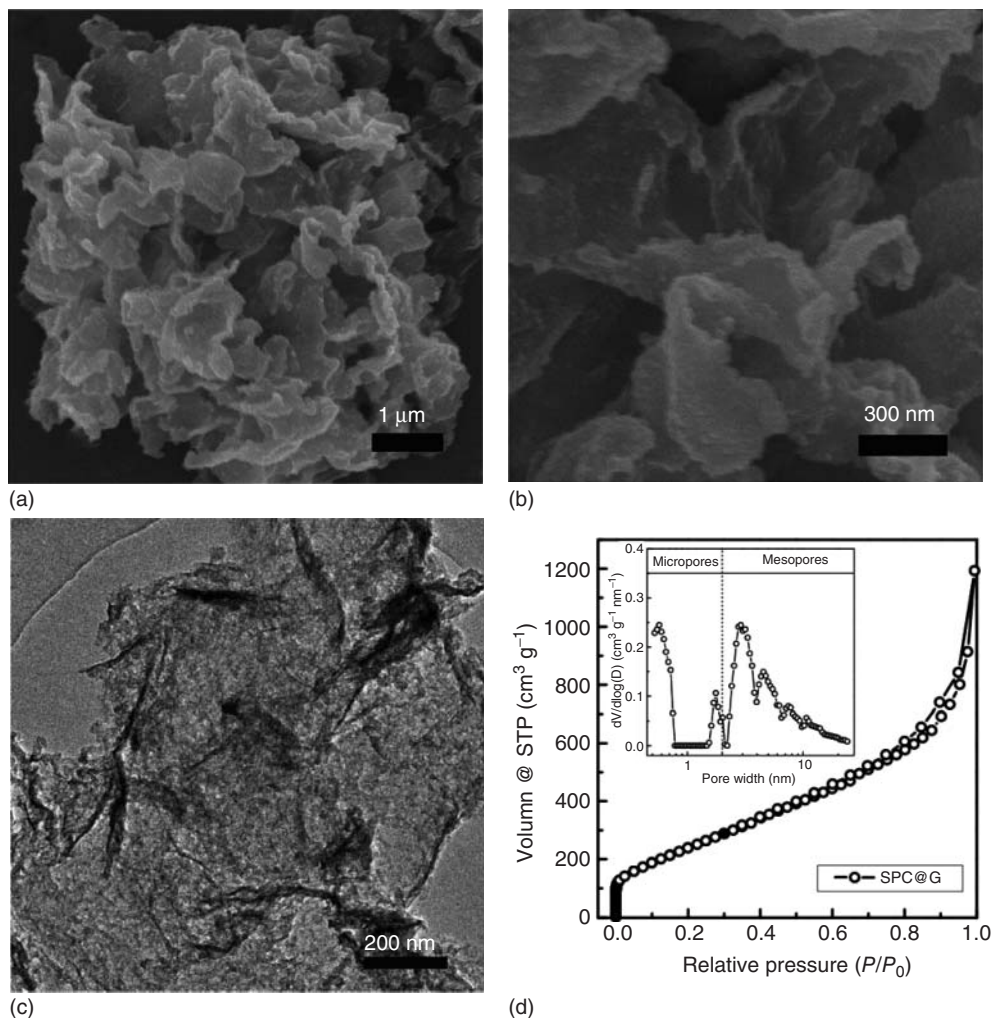


Figure 10.46 (a,b) SEM images and (c) TEM image of the SPC@G nanocomposite and (d) nitrogen adsorption–desorption isotherms of the SPC@G nanocomposite.

The inset shows the corresponding pore-size distribution. (Reproduced with permission from [111]. Copyright © 2012 Royal Society of Chemistry)

triphenylphosphine as phosphorus source. After a successful incorporation of phosphorus into the network of graphene sheets, the resulting P-doped graphite showed high electrocatalytic activity, long-thermal stability, and excellent tolerance to crossover effects of methanol in ORR in alkaline media. Yao *et al.* [119] synthesized iodine-doped graphene via a facile, catalyst-free thermal annealing process and used it for the electrocatalytic oxygen reduction in an alkaline medium. The new metal-free catalyst can exhibit a high catalytic activity, long-term stability, and an excellent methanol tolerance for the ORR. Nitrogen and silica co-doped graphene

nanosheets (NSi-GNSs) have been prepared via high-temperature annealing of N and Si-containing graphene oxide-IL (GO-IL) composite [120]. As a p-type semiconductor, the as-synthesized NSi-GNS shows excellent NO_2 gas sensing ability with high response value. Denis [121] investigated the chemical doping of monolayer and bilayer graphene with Al, Si, P, and S and observed band gap opening. Si-doped graphene has the lowest formation energy although it is semimetallic. P-doped graphene has a magnetic moment of $1 \mu_B$ and for 3 at.% of doping the band gap is 0.67 eV. Al-doped graphene is unstable but is an attractive material because it is metallic. To reduce the formation energies of the substitutional defects we investigated the formation of interlayer bonds in bilayer graphene. P forms the strongest bonds between layers giving particular stability to this material. P-doped bilayer graphene has a gap of 0.43 eV but it has no magnetic moment.

10.6 Properties and Applications

SLG is an ambipolar material with both hole and electron transport perpendicular to the surface. Late *et al.* [122] observed p-type or n-type behavior on doping graphene with boron or nitrogen. Figures 10.47 and 10.48 show the output characteristics (I_{ds} vs V_{ds}) and transfer characteristics (I_{ds} vs V_{gs}) of the FETs based on B-doped and N-doped graphenes, respectively, with p-type and n-type characteristics. The increase in the charge carrier concentration induced by gas molecules adsorbed on the surface of graphene can be used to fabricate sensitive gas sensors. On the basis of theoretical investigations, it has been predicted that

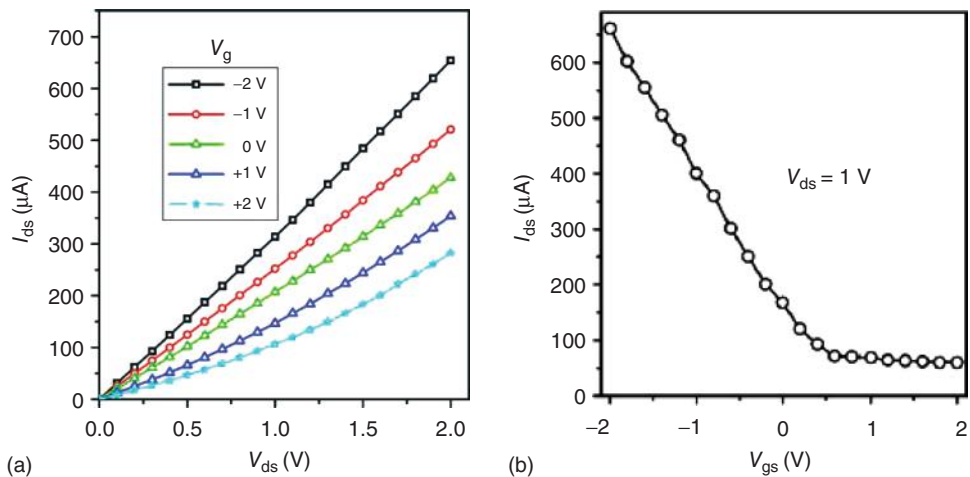


Figure 10.47 (a) Output characteristics (I_{ds} vs V_{ds}) and (b) transfer characteristics (I_{ds} vs V_{gs}) of the FET based on B-doped graphene. (Reproduced with permission from [122]. Copyright © 2010 Elsevier)

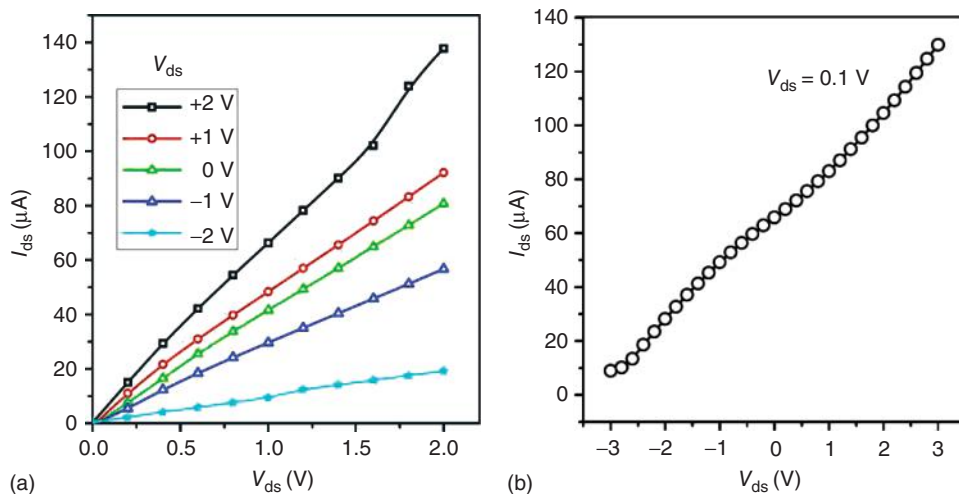


Figure 10.48 (a) Output characteristics (I_{ds} vs V_{ds}) and (b) transfer characteristics (I_{ds} vs V_{gs}) of the FET based on N-HG. (Reproduced with permission from [122]. Copyright © 2010 Elsevier)

doped graphene can be a good detector for gas molecules [123]. NG shows enhanced sensitivity for electron-withdrawing molecules such as NO_2 [124]. It appears that n-type graphene is a better sensor for NO_2 as it is an electron-withdrawing molecule.

NG or BG can be used as a promising anode for high-power and high-energy Li ion batteries under high-rate charge and discharge conditions [125]. The doped graphene shows a high reversible capacity of >1040 mAh g^{-1} at a low rate of 50 mA g^{-1} . More importantly, it can be quickly charged and discharged in a short time of 1 h to several tens of seconds together with high-rate capability and excellent long-term cyclability. For example, a high capacity of ~ 199 and 235 mAh g^{-1} was obtained for the NG and BG at 25 A g^{-1} (~ 30 s to full charge). Probably the unique two-dimensional structure, disordered surface morphology, heteroatom defects, better electrode/electrolyte wettability, increased inter-sheet distance, improved electrical conduction, and thermal stability of the doped graphene are beneficial to rapid surface Li^+ absorption and ultrafast Li^+ diffusion and electron transport. The doped materials are accordingly superior to pristine chemically derived graphene and other carbonaceous materials.

Wu *et al.* [126] present a synthesis approach for nitrogen-doped graphene-sheet-like nanostructures via the graphitization of a heteroatom polymer, in particular, PANI, under the catalysis of a cobalt species using multiwalled carbon nanotubes (MWCNTs) as a supporting template. The graphene-rich composite catalysts (Co-N-MWCNTs) exhibit substantially improved activity for oxygen reduction in nonaqueous lithium-ion electrolyte as compared to those of currently used carbon blacks and Pt/carbon catalysts, evidenced by both rotating disk electrode and Li- O_2 battery experiments. In particular, an optimal temperature for heat

treatment during synthesis is critical to creating a high-surface-area catalyst with favorable nitrogen doping. Li *et al.* [127], showed that nonaqueous lithium–oxygen battery fabricated with N-GNSs as cathode material, delivered a discharge capacity of $11\,660\text{ mAh g}^{-1}$, which is about 40% higher than that with the pristine GNSs. The electrocatalytic activity of N-GNSs for oxygen reduction in the nonaqueous electrolyte is 2.5 times as that of GNSs. Zhang *et al.* [128] synthesized N-doped MnO/GNSs (N-MnO) hybrid material by a hydrothermal method followed by NH_3 annealing and used them as high capacity anode material for Li-ion batteries. N-doped MnO (N-MnO) NPs were homogeneously anchored on the thin layers of N-doped GNS (N-GNS) to form an efficient electronic/ionic mixed conducting network. This nanostructured hybrid exhibits a reversible electrochemical Li storage capacity $\leq 772\text{ mAh g}^{-1}$ at 100 mA g^{-1} after 90 cycles, and an excellent rate capability of 202 mAh g^{-1} at a high c.d. of 5 A g^{-1} . Cai *et al.* [129] synthesized NG sheets with the nitrogen-doping level as high as 7.04 at.% by thermal annealing PG sheets and melamine and used them as anode materials for lithium-ion batteries. The high-level NG sheets exhibit a superhigh initial reversible capacity of 1123 mAh g^{-1} at a c.d. of 50 mA g^{-1} . More significantly, even at an extremely high c.d. of 20 A g^{-1} , highly stable capacity of about 241 mAh g^{-1} could still be obtained. This electrochemical performance is superior to that reported earlier for NG sheets. Their results indicate that the high-level NG sheets could be a promising anode material for high-performance lithium-ion batteries.

Xu *et al.* [130], synthesized monodisperse ultrathin SnO_2 nanorods on NG by a one-step hydrothermal strategy and studied its lithium storage properties. The uniform composites with high nitrogen content and ultrathin SnO_2 nanorods (2.5–4.0 nm in diameter and 10–15 nm in length) show high reversible specific capacity, superior rate capability, and outstanding cycling stability (803 mAh g^{-1}) as anode materials for lithium-ion batteries, owing to the synergistic effect between GS and SnO_2 and nitrogen-doping, which can greatly decrease the energy barrier for Li penetrating the pyridinic defects and improve the electronic structures.

Jeong *et al.* [131] developed ultracapacitors based on N-doped graphene produced by a plasma process, whose capacitance ($\sim 280\text{ F g}_{\text{electrode}}^{-1}$) is about four times larger than that of PG based counterparts and exhibits excellent cycle-life ($>200\,000$), high power capability, and compatibility with flexible substrates. Qiu *et al.* [132] showed that thermal nitridation of reduced graphene oxide sheets yields highly conductive ($\sim 1000\text{--}3000\text{ S m}^{-1}$) NG sheets, as a result of the restoration of the graphene network by the formation of C–N bonded groups and N-doping. Even without carbon additives, supercapacitors made of the NG electrodes can deliver remarkable energy and power when operated at higher voltages, at 0–4 V.

Gopalakrishnan *et al.* [59] have studied the electrochemical performance of heavily nitrogenated GO containing upto $\sim 18\text{ wt\%}$ nitrogen, prepared by microwave synthesis with urea as the nitrogen source by means of cyclic voltammetry (CV), galvanostatic charge–discharge curves, and electrochemical impedance

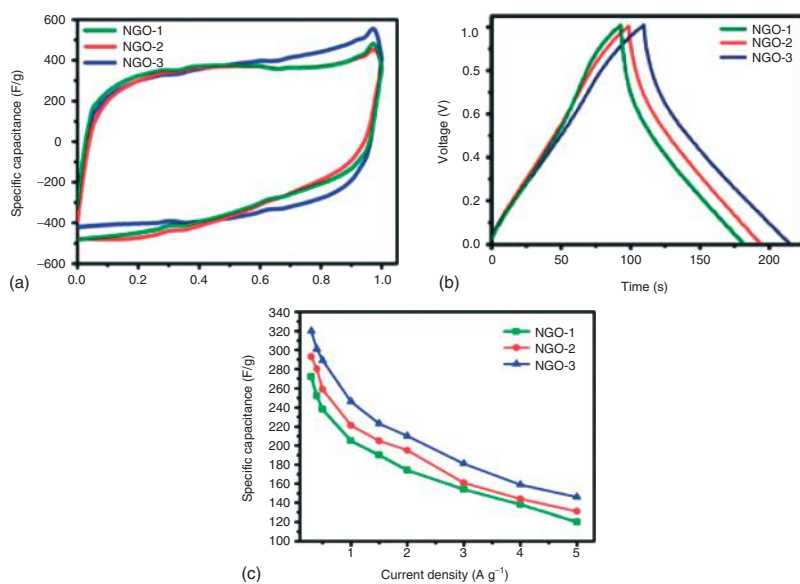


Figure 10.49 (a) Cyclic voltammograms of NGOs at a scan rate of 20 mV s^{-1} , (b) galvanostatic charge–discharge curves for NGO electrodes (at 0.5 mA g^{-1}), and (c) specific capacitance as a function of discharge current. (Reproduced with permission from [59]. Copyright © 2013 Royal Society of Chemistry)

spectroscopy (EIS) in a 6M KOH aqueous electrolyte without any binder or carbon additive. Cyclic voltammograms of the NGO samples measured at a scan rate of 20 mV s^{-1} for a sample loading of $\sim 2 \text{ mg}$ per electrode are shown in Figure 10.49a.

The CV curves remain rectangular even at high scan rates indicating excellent charge storage characteristics, resembling those of an ideal supercapacitor. We have found a maximum capacitance of 461 F g^{-1} at 5 mV s^{-1} in the case of NGO-3 (for synthesis details of GO, NGO-1 and NGO-2, NGO-3, refer [59] from earlier section). The values of specific capacitance of the NGO-3 electrode under scan rates of 100, 80, 40, 20, and 10 mV s^{-1} are 338, 349, 380, 401, and 434 F g^{-1} , respectively. The specific capacitance values of GO, NGO-1, and NGO-2 are 10, 438, and 442 F g^{-1} , respectively, at 5 mV s^{-1} . The galvanostatic charge–discharge curves of the NGO samples were measured in a potential window of 0–1 V at a current density of 0.5 A g^{-1} and are shown in Figure 10.49b. The discharge time of NGO-3 was longer compared to the other two materials at both high and low current densities. The galvanostatic charge–discharge curves of all the electrodes look nearly symmetric, indicating that these materials have good electrochemical capacitive characteristics. The specific capacitance values derived from the discharging curves at different current densities are shown in Figure 10.49c. We clearly see that the specific capacitance decreases with increase in current density for all the three materials. The specific capacitance of NGO-3 is 320 F g^{-1} at 0.3 A g^{-1} and for NGO-1 and NGO-2 the values are 272 and 293 F g^{-1} , respectively. EIS is an important measurement to determine the performances of supercapacitors. Figure 10.50a shows Nyquist plots in the frequency range 100 kHz to 0.01 Hz.

These plots show excellent capacitive behavior, as indicated by the near vertical line over the low frequency ranges. It is well known that the higher the slope value, the faster the formation of the electrical double layer. We clearly see that the slope of NGO-3 is greater than those of NGO-1 or NGO-2. The high frequency region is shown in the inset of Figure 10.50a. We observe small charge transfer resistance (C_t) in these materials. Equivalent series resistances (ESRs) of the samples are almost similar and the values are 0.35, 0.36, and 0.33Ω for NGO-1, NGO-2, and NGO-3, respectively. The ESR value follows the same trend as the graphitic nitrogen content. Cycling life is an important requirement for supercapacitor applications. Thus, we studied the cycling life tests for NGO-3 by repeating the galvanostatic charge–discharge between 0 and 1 V at a current density of 0.5 A g^{-1} for 1000 cycles. NGO-3 showed a loss of only 2.7% from the initial specific capacitance and showed good capacitance retention. The last few charge–discharge cycles looked almost similar when compared to the initial cycles (see Figure 10.50b, inset) illustrating long-term cyclic stability. Energy and power densities are important factors for evaluating power applications of electrochemical supercapacitors. Figure 10.50c shows the Ragone plots of all the NGO electrodes. The energy densities were calculated at various discharge current densities ranging from 0.3 to 5 A g^{-1} . The energy densities of the NGOs are remarkable, with NGO-3 showing the highest value of 44.4 Wh kg^{-1} at a current density of 0.3 A g^{-1} . NGO-1 and NGO-3 show

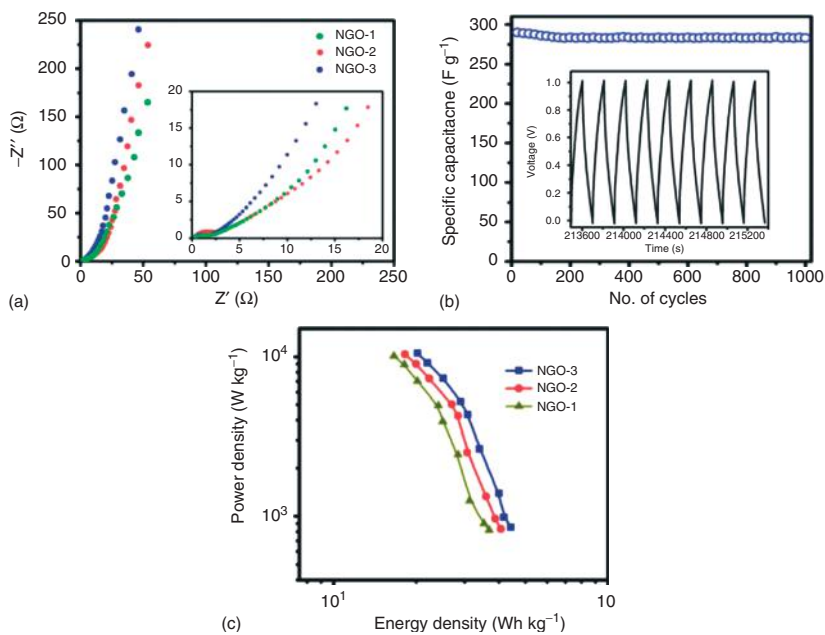


Figure 10.50 (a) Nyquist curves for NGO electrodes. (b) Specific capacitance versus the cycle number of NGO-3 measured at a current density of 0.5 A g^{-1} within an operational window of $0.0\text{--}1 \text{ V}$ (the inset shows the charge–discharge curves of the last few cycles for NGO-3). (c) Ragone plots of NGO based supercapacitors. (Reproduced with permission from [59]. Copyright © 2013 Royal Society of Chemistry)

energy densities of 40.7 and 36.9 Wh kg⁻¹, respectively, at a current density of 0.3 A g⁻¹. The power densities are in the range of 852–10 524 W kg⁻¹ for the NGO-3 electrode.

Nitrogen doped reduced graphene oxide (NRGO) samples with different nitrogen contents were prepared by two different methods and these samples are investigated as supercapacitor electrodes [133]. The NG samples are prepared by dispersing reduced graphene oxide (RGO) or HG (30 mg) in 50 ml absolute ethanol and urea (300 mg), followed by evaporation of ethanol at 50 °C resulting in a gray powder and further heating this pelletized powder to different temperatures (ranging from 600 to 900 °C for 90 min) in a nitrogen atmosphere yields the final NrGO product. The mass ratio between the graphene sample and urea was 1 : 10. NrGO samples prepared from RGO I (sodium borohydride reduced GO) and RGO II (hydrazine hydrate reduced GO) are designated as NrGO I and NrGO II, respectively. The temperature of the reaction is indicated in the sample as NrGO I-600, NrGO (I/II)-700, NrGO (I/II)-800, and NrGO (I/II)-900. The electrochemical performance of the nitrogen-doped graphene and reduced graphene oxides (NHG, NrGO I, and NrGO II) have been investigated in detail by means of CV, galvanostatic charge–discharge curves, and EIS, in comparison with measurements on the undoped graphene and RGO samples. Two electrode measurements have been carried out both in aqueous (6 M KOH) and in IL media. In Figure 10.51a, we show typical CV curves of rGO I and NrGO I (scan rate of 100 mV s⁻¹) for a sample loading of ~8 mg per electrode. The CV curve of rGO I shows Faradaic pseudo capacitance owing to the oxygen functionalities, but RGO I heated at 900 °C shows non-faradaic behavior because of the removal of most of the oxygen functionalities.

There is a significant increase in the capacitance of the nitrogen-doped sample with increase in nitrogen content. We have got maximum capacitance of 85 F g⁻¹ at a scan rate of 100 mV s⁻¹ for NrGO I-600 with a nitrogen content of 8.5 wt%. The specific capacitance values of the NrGO I-600 electrode under scan rates of 80, 40, 20, and 10 mV s⁻¹ are 89, 98, 110, and 126 F g⁻¹, respectively. The galvanostatic charge–discharge curves of rGO I and NrGO I samples were measured at a potential window of 0–1 V at a current density of 60 mA g⁻¹ and the results are shown in Figure 10.51b. The discharge time increases with the increase in nitrogen content. The charge–discharge curves of the NG samples are nearly symmetrical similar to those of ideal electrochemical double-layer capacitors. The specific capacitance values (at 60 mA g⁻¹) for rGO I and rGO I-900 are 24 and 30 F g⁻¹ while those of NrGO I-900, NrGO I-800, NrGO I-700, and NrGO I-600 are 48, 59, 71, and 84 F g⁻¹, respectively. Figure 10.51c shows the relationship between specific capacitance and discharge current. The specific capacitance decreases with increase in discharge current. In Figure 10.51d, we present Nyquist plots where rGO I shows a charge transfer resistance at the electrode/electrolyte interface while nitrogen-doped rGO I shows a vertical line in the low frequency region and the slope increases with increase in nitrogen content. The more vertical the curve, the more closely the electrochemical cell performs as an ideal capacitor. Magnified data of high frequency region shown in the inset of Figure 10.51d reveal

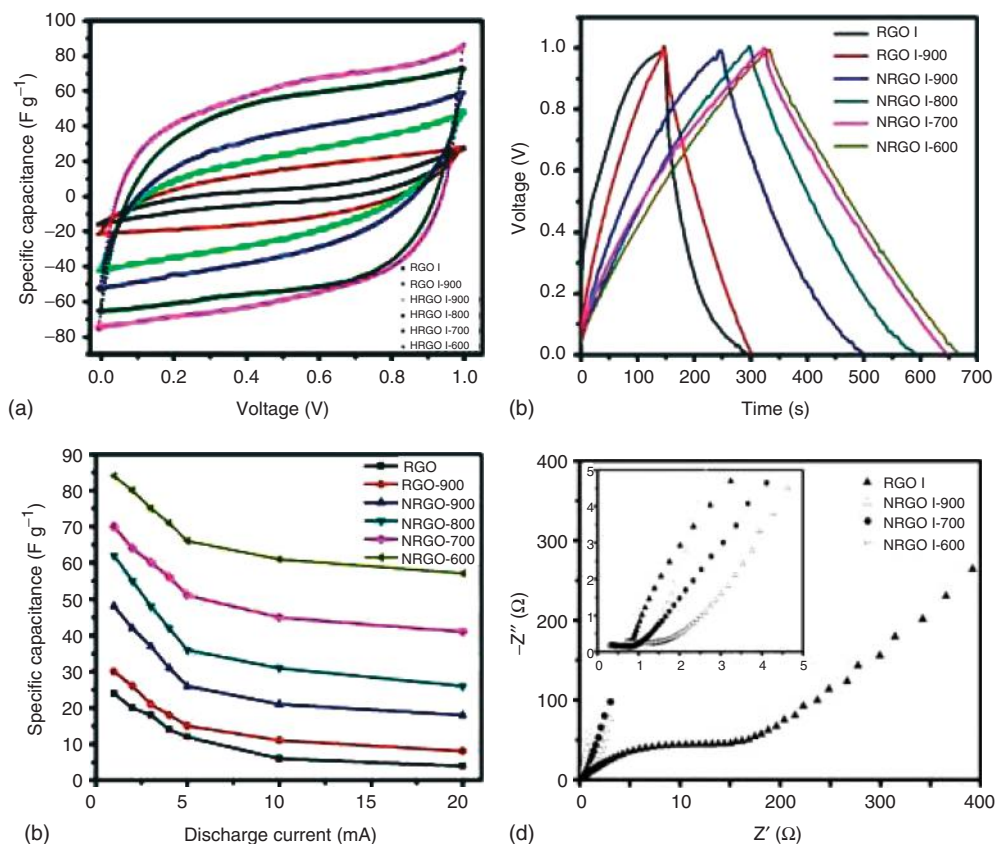


Figure 10.51 (a) Cyclic voltammograms of RGO I and NrGO I prepared at different temperatures (at scan rate 100 mV s^{-1}). (b) Galvanostatic charge–discharge curves for RGO I and NrGO I electrodes (at

60 mA g^{-1}). (c) Specific capacitance as a function of discharge current. (d) Nyquist curves for RGO I and NrGO I electrodes SSC. (Reproduced with permission from [133]. Copyright © 2013 Elsevier)

that NrGO electrodes associated with less resistance than undoped graphene. The high frequency region of the Nyquist plots shows small ESR, the value for rGOI being $0.70 \text{ } \Omega$. The values for NrGO I-900, NrGO I-700, and NrGO I-600 are 0.67 , 0.37 , and $0.29 \text{ } \Omega$, respectively. The specific capacitance of rGO II also increases with nitrogen doping, the values being 37 and 58 F g^{-1} for rGO II and NrGO II-900, respectively, at a scan rate of 100 mV s^{-1} . NrGO II-800 and NrGO II-700 samples showed capacitance values of 49 and 46 F g^{-1} , respectively, at a scan rate of 100 mV s^{-1} . Figure 10.52a shows the relationship between the specific capacitance and the discharge current. Specific capacitance decreases with increase in discharge current.

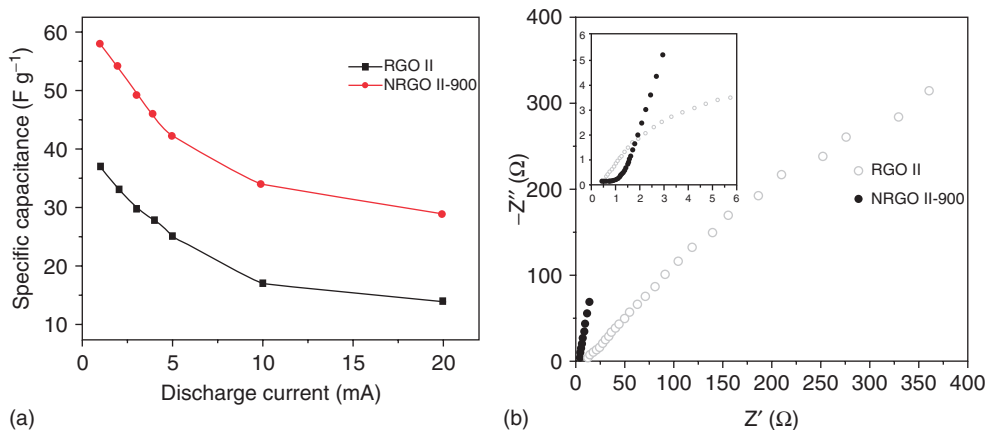


Figure 10.52 (a) Specific capacitance as a function of discharge current in aqueous media. (b) Nyquist curves for RGO and NrGO II-900 electrodes. (Reproduced with permission from [133]. Copyright © 2013 Elsevier)

The electrochemical impedance spectra are shown in Figure 10.52b. NrGO II-900 has less charge transfer resistance compared to rGO II. Magnified EIS data of high frequency region are shown in the inset of Figure 10.52b, the ESR value being 0.35 and 0.21 Ω for rGO I and NrGO II-900, respectively. We thus see that NrGO I-600 with the highest nitrogen content and surface area gives the best supercapacitor performance. Amongst the NrGO II samples, the one prepared at 900 °C with the highest nitrogen content and surface area gives the best results. NrGO I-600 and NrGO II-900 show a capacitance of 14.1 and 11.0 mF cm⁻², respectively. We studied the long-term cyclic stability of NrGO I-600 by repeating the galvanostatic charge–discharge test between 0 and 1 V at a current density of 0.5 A g⁻¹ for 1000 cycles. After 1000 cycles, the capacitance decreased by 13% of initial capacitance and exhibited excellent cycle stability. We obtained a maximum energy density of 11.8 Wh kg⁻¹ for NrGO II-600 at a current density of 60 mA g⁻¹. The specific capacitances of HG and NHG-900 are 4 and 15 F g⁻¹, respectively, at a current density of 100 mA g⁻¹ from galvanostatic charge–discharge curves. The ESR values of HG and NHG are 0.27 and 0.15 Ω, respectively. Thus NrGOs exhibit satisfactory specific capacitance, the values reaching 126 F g⁻¹ at a scan rate of 10 mV s⁻¹ in aqueous medium. Besides providing supercapacitor characteristics, the study has shown the nitrogen content and surface area to be important factors. In an IL medium, NrGO exhibit specific capacitance values of 258 and 240 F g⁻¹ at a scan rate of 5 mV s⁻¹. The IL enables a larger operating voltage range of 0.0–2.5 V compared to 0.0–1 V in aqueous medium.

Chen *et al.* [134] have reviewed development in synthesizing graphene materials for electrochemical capacitors (ECs) and discuss the strategies of fabricating graphene-based macroscopic electrodes. They highlighted the importance of SSA, conductivity, and heteroatom-doping of graphene sheets and the

micro/nanostructures of their electrodes for controlling the performances of graphene-based ECs. NG has great potential as a high-performance catalyst support for fuel cell electrocatalysis. Platinum-based catalysts represent a state of the art in the electrocatalysis of ORR from the point of view of their activity and durability in harnessing the chemical energy via direct electrochemical conversion. However, because platinum is both expensive and scarce, its widespread implementation in such clean energy applications is limited. Recent breakthroughs in the synthesis of high-performance nonprecious metal catalysts (NPMCs) make replacement of Pt in ORR electrocatalysts with earth-abundant elements, such as Fe, Co, N, and C, a realistic possibility.

Liang *et al.* [135] have reported a hybrid material consisting of Co_3O_4 nanocrystals grown on reduced graphene oxide and on N-doped graphene as a high-performance bifunctional catalyst for the ORR and OER in alkaline solutions. These hybrid materials exhibit high ORR activities in alkaline solutions, comparable to fresh commercial Pt/C catalyst but far exceeding Pt/C in stability and durability. The Co_3O_4 /N-doped graphene hybrid exhibits catalytic activity with superior stability to Pt (20 wt% Pt on Vulcan XC-72, Pt/C) in alkaline solutions, and is active for OER. Co_3O_4 /nitrogen doped reduced mildly oxidized graphene oxide (N-rmGO) hybrid with Co_3O_4 content of ~ 70 wt% exhibited a more positive ORR peak potential and higher peak current (Figure 10.53a) than Co_3O_4 /reduced graphene oxide (rmGO).

Rotating-disk electrode measurements reveal the ORR kinetics of Co_3O_4 /rmGO hybrid in 0.1 M KOH (Figure 10.53b). The kinetics follow first-order law toward the concentration of dissolved oxygen and show similar electron transfer numbers for ORR at different potentials (Figure 10.53b inset). The electron transfer number (n) was calculated to be ~ 3.9 at 0.60–0.75 V from the slopes of Koutecky–Levich plots, suggesting Co_3O_4 /rmGO hybrid favors a 4e oxygen reduction process, similar to ORR catalyzed by a high-quality commercial Pt/C catalyst measured in the same 0.1 M KOH electrolyte ($n \sim 4.0$ for Pt/C). RDE measurement revealed an electron transfer number of 4.0 at 0.60–0.75 V (Figure 10.53c). The half-wave potential at 1600 rpm was 0.83 V (Figure 10.53c), similar to that of Pt/C (0.86 V) and more positive than that of Co_3O_4 /rmGO (0.79 V; Figure 10.53b). N-doped graphene (N-rmGO) alone, without Co_3O_4 exhibits low ORR activity with electron transfer.

Wu and Zelenay [136] obtained M-N-C (M: Fe and/or Co) catalysts by simultaneously heat-treating precursors of nitrogen, carbon, and transition metals at 800–1000 °C. The activity and durability of resulting catalysts depend greatly on the selection of precursors and synthesis chemicals. In addition, they correlate quite well with the catalyst nanostructure. While chemists have presented no conclusive description of the active catalytic site for this class of NPMCs, they have developed a designed approach to making active and durable materials, focusing on the catalyst nanostructure. The approach consists of nitrogen doping, *in situ* carbon graphitization, and the usage of graphitic structures (possibly

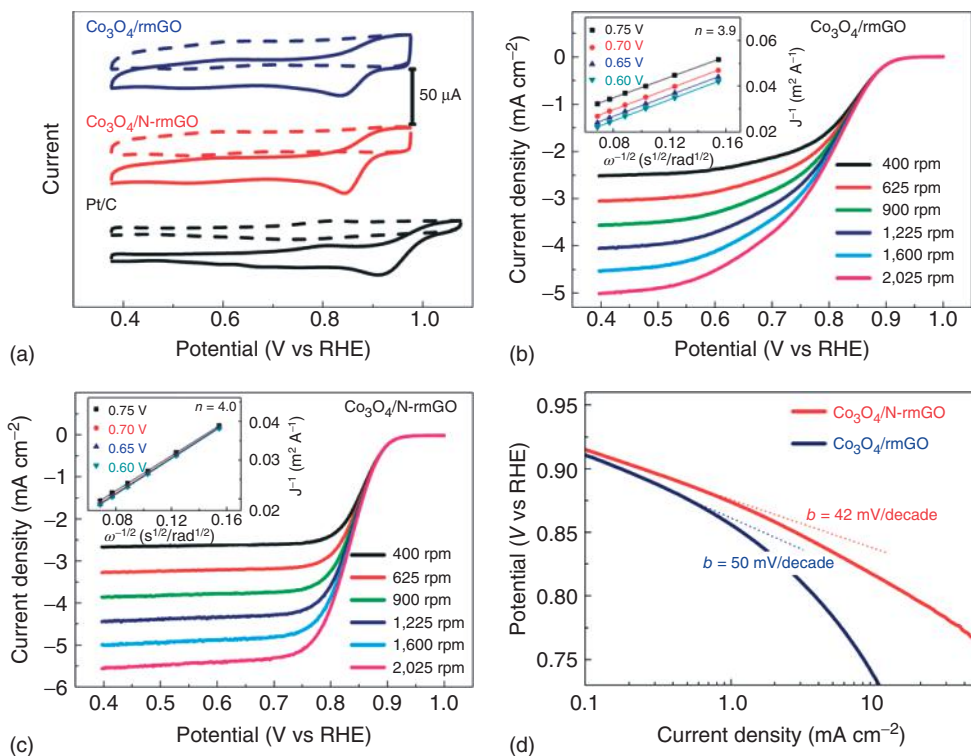


Figure 10.53 $\text{Co}_3\text{O}_4/\text{graphene}$ hybrid as oxygen reduction catalysts. (a) CV curves of $\text{Co}_3\text{O}_4/\text{rmGO}$ hybrid, $\text{Co}_3\text{O}_4/\text{N-rmGO}$ hybrid, and Pt/C on glassy carbon electrodes in O_2 -saturated (solid line) or Ar-saturated 0.1 M KOH (dash line). Catalyst loading was 0.17 mg cm^{-2} for all samples. (b) Rotating-disk voltammograms of $\text{Co}_3\text{O}_4/\text{rmGO}$ hybrid (loading $\sim 0.1 \text{ mg cm}^{-2}$) and (c) $\text{Co}_3\text{O}_4/\text{N-rmGO}$ hybrid (loading $\sim 0.1 \text{ mg cm}^{-2}$) in

O_2 -saturated 0.1 M KOH with a sweep rate of 5 mV s^{-1} at the different rotation rates indicated. The insets in (b) and (c) show corresponding Koutecký–Levich plots (J^{-1} versus $\omega^{-0.5}$) at different potentials. (d) Tafel plots of $\text{Co}_3\text{O}_4/\text{rmGO}$ and $\text{Co}_3\text{O}_4/\text{N-rmGO}$ hybrids derived by the mass-transport correction of corresponding RDE data. (Reproduced with permission from [135]. Copyright © 2011 Nature Publishing Group)

graphene and graphene oxides) as carbon precursors. Various forms of nitrogen, particularly pyridinic and quaternary, can act as n-type carbon dopants in the M-N-C catalysts, assisting in the formation of disordered carbon nanostructures and donating electrons to the carbon. The CN_x structures are likely a crucial part of the ORR active site(s). It is worth noting that the ORR activity is not necessarily governed by the amount of nitrogen, but by how the nitrogen is incorporated into the nanostructures. Apart from the possibility of a direct participation in the active site, the transition metal often plays an important role in the *in situ* formation of various carbon nanostructures by catalyzing the decomposition of the nitrogen/carbon precursor. We can control

the formation of different nanostructures during the synthesis of M-N-C catalysts. For example, *in situ* formed nitrogen-doped graphene sheets can only be derived from PANI, probably due to structural similarities between the aromatic structures of PANI and graphene. Highly graphitized carbon nanostructures may serve as a matrix for the formation of ORR-active groups with improved catalytic activity and durability, containing nitrogen and most probably metal atoms also.

NG films were synthesized by CVD of methane in the presence of ammonia showing good oxygen reduction characteristics in alkaline fuel cells [41]. The steady-state catalytic current at the N-graphene electrode is found to be around three times higher than that at the Pt/C electrode over a large potential range. The long-term stability, tolerance to crossover, and poison effect are also better than Pt/C for oxygen reduction in alkaline electrolyte. NG as a metal-free catalyst for oxygen reduction was synthesized by heat-treatment of graphene using ammonia and showed high oxygen reduction activity and durability [137]. It was found that at the optimum temperature of 900 °C, the resulting catalyst had a very high ORR activity through a four-electron transfer process in oxygen-saturated 0.1 M KOH. The electrocatalytic activity and durability of this material are comparable or better than the com. Pt/C (loading: 4.85 $\mu\text{g Pt cm}^{-2}$). Chung *et al.* demonstrate a new type of nitrogen-doped CNT/NP composite ORR electrocatalyst obtained from iron acetate as an iron precursor and from cyanamide as a nitrogen and CNT precursor in a simple, scalable, and single-step method [138]. The composite has the highest ORR activity in alkaline media of any NPMCs. When used at a sufficiently high loading, this catalyst outperforms the most active platinum-based catalysts.

Choi *et al.* [139] developed graphene-derived catalysts by restacking of N-doped single graphene layers for application in enhanced electrochemical ORRs in acidic media via heat-treatment with dicyandiamide and a small amount < 1 wt% of transition metal. In ORRs, bare graphene exhibits 0.58 V versus RHE of the onset potential; however, it increases to ~0.9 V through modification steps and records a mass activity of 1.28 mA mg^{-1} at 0.75 V. Through the correlation curve between the ORR activity and the number of restacked graphene layers, it is proposed that the stacking of a few layers is desirable in the ORRs rather than a single layer catalyst. The graphene-derived catalysts exhibit graphite properties of facile electron transfer as the restacking of graphene layers increases, without degradation of the pyridinic-N on the graphene edge. Choi *et al.* [140] developed NG for its application in ORRs in acidic media, and additional doping of B or P into the NGr is attempted to enhance the ORR performance. NG exhibits an onset potential of 0.84 V and a mass activity of 0.45 mA mg^{-1} at 0.75 V; however, the B, N-(BNG), and P, N-doped graphene (PNG) show onset potentials of 0.86 and 0.87 V, and mass activities of 0.53 and 0.80 mA mg^{-1} , respectively, which are correspondingly 1.2 and 1.8 times higher than those of the NG. Additional doping of B or P reduces the production of H_2O_2 in the ORRs, and shows higher stability than that of Pt/C in acidic media. It is proposed that the improvement in the ORR activity results from the enhanced asymmetry of the spin density

or electron transfer on the basal plane of the graphene, and the decrease in the energy gap between the highest occupied molecular orbital (HOMO) and the lowest unoccupied molecular orbital (LUMO) of the graphene through additional doping of B or P.

Xue *et al.* [141] prepared a three-dimensional N-GF and demonstrated its application as a metal-free electrocatalyst for the reduction of triiodide to replace the Pt cathode in dye-sensitized solar cells, leading to a power conversion efficiency up to 7.07%. This value of efficiency is among the highest efficiencies reported for dye-sensitized solar cells with carbon-based metal-free counter electrodes, comparable to that of a dye-sensitized solar cell with a Pt counter electrode constructed under the same conditions. Wang *et al.* [142] prepared nitrogen-doped graphene (NDG) sheets by a hydrothermal reduction of graphite oxide (prepared from graphite powder by the Hummer's method) using ammonia as the nitrogen source and as the catalyst for triiodide reduction to fabricate counter electrodes in dye-sensitized solar cells. Under one sun illumination (air-mass, AM, 1.5), the dye-sensitized solar cell with NDG electrode shows an energy conversion efficiency of 7.01%, which is comparable to that of the cell with Pt electrode. Field emission studies have been carried out on undoped as well as NG and BG samples prepared by arc-discharge method in a hydrogen atmosphere [143]. These graphene samples exhibit low turn-on voltages. NG shows the lowest turn-on voltage of $0.6 \text{ V } \mu\text{m}^{-1}$, corresponding to emission c.d. of $10 \mu\text{A cm}^{-2}$. These characteristics are superior to the other types of nanomaterials reported in the literature. Furthermore, emission currents are stable over the period of more than 3 h for the graphene samples. The observed emission behavior has been explained on the basis of nanometric features of graphene and resonance tunneling phenomenon. Vertically aligned few-layered graphene (FLG) nanoflakes have been synthesized on bare Si substrates by a microwave plasma enhanced CVD method showed enhanced and stable field emission [144]. *In situ* N_2 plasma treatment was carried out using electron cyclotron resonance plasma, resulting in various N_2 functionalities being grafted to the FLG surface. Compared with pristine FLGs, the N_2 plasma-treated FLGs showed significant improvement in field emission characteristics by lowering the turn-on field (defined at $10 \mu\text{A cm}^{-2}$) from 1.94 to $1.0 \text{ V } \mu\text{m}^{-1}$. Accordingly, the field emission current increased from $17 \mu\text{A cm}^{-2}$ at $2.16 \text{ V } \mu\text{m}^{-1}$ for pristine FLGs to about $103 \mu\text{A cm}^{-2}$ at $1.45 \text{ V } \mu\text{m}^{-1}$ for N-doped FLGs. Furthermore, N-doped FLG samples retained 94% of the starting current over a period of 10 000 s, during which the fluctuations were of the order of $\pm 10.7\%$ only. Long *et al.* [145] found that the NGNSs prepared by a high-temperature nitridation procedure represent a metal-free catalyst for aerobic selective oxidation of benzylic alcohols. The graphitic sp^2 N species are found to be catalytically active for the aerobic oxidation reaction based on good linear correlation with the activity results. Kinetic analysis showed that the N-doped graphene-catalyzed aerobic alcohol oxidation proceeds via a Langmuir–Hinshelwood pathway and has moderate activation energy ($56.1 \pm 3.5 \text{ kJ mol}^{-1}$ for the benzyl alcohol oxidation) close to that (51.4 kJ mol^{-1}) proceeding on the catalyst $\text{Ru}/\text{Al}_2\text{O}_3$ reported in literature.

Xin *et al.* [146] prepared NG via microwave heating in NH_3 atmosphere. Graphene, as an allotrope of C, is a good microwave-absorbing material and can reach a high temperature in minutes, facilitating N incorporation (5.04%) into the structure under NH_3 . For comparison, both plain graphene (G) and the NG were used as supporting materials for Pt to study their potential application in fuel cells. Also, Pt/NG catalysts exhibited higher electrochemical active surface area, MeOH catalytic activity and tolerance to CO poisoning than those of the Pt/G under fuel cell conditions. Some *et al.* [147] prepared highly air-stable phosphorus-doped n-type graphene field-effect transistors (PDG-FETs) and have demonstrated the relationship between the lone pair electron donating ability of the phosphorus atom, which is stronger than that of nitrogen due its higher nucleophilicity. The main inspiration of this study was to prove that the PDG-FET could create much stronger air-stable n-type behavior than NG FET. Kwon *et al.* [148] grown polypyrrole-converted nitrogen-doped few-layer graphene (PPy-NDFLG) on Cu substrate by CVD combined with vapor deposition polymerization and then transferred onto a flexible substrate. Furthermore, anti-vascular endothelial growth factor (anti-VEGF) RNA aptamer conjugated PPy-NDFLG was integrated into a liquid-ion gated FET geometry to fabricate a high-performance VEGF aptamer-based sensor. Field-induced high sensitivity was observed for the analyte-binding events, eventually leading to the recognition of the target molecules at an unprecedentedly low concentration (100 fM). Additionally, the aptasensor had excellent reusability, mechanical bendability, and durability in the flexible process.

Gopalakrishnan *et al.* [149] prepared the composites of TiO_2 NPs with pure graphene as well as BGs and NGs and studied the photodegradation of two dyes, methylene blue (MB), and rhodamine B (RB), adsorbed on them. MB which is a good electron donor and has a low ionization energy interacts strongly with electron-deficient BG resulting in fast degradation of the dye. However, RB which is not such a good electron donor and has a higher ionization energy, interacts strongly with electron-rich NG causing a faster degradation of the dye.

References

1. Geim, A.K. and Novoselov, K.S. (2007) *Nat. Mater.*, **6**, 183–191.
2. Tung, V.C., Allen, M.J., Yang, Y., and Kaner, R.B. (2009) *Nat. Nanotechnol.*, **4**, 25–29.
3. Robinson, J.T., Zhalutdinov, M., Baldwin, J.W., Snow, E.S., Wei, Z., Sheehan, P., and Houston, B.H. (2008) *Nano Lett.*, **8**, 3441–3445.
4. Wu, J., Pisula, W., and Mullen, K. (2007) *Chem. Rev.*, **107**, 718–747.
5. Novoselov, K.S., Geim, A.K., Morozov, S.V., Jiang, D., Zhang, Y., Dubonos, S.V., Grigorieva, I.V., and Firsov, A.A. (2004) *Science*, **306**, 666–669.
6. Rao, C.N.R., Sood, A.K., Subrahmanyam, K.S., and Govindaraj, A. (2009) *Angew. Chem. Int. Ed.*, **48**, 7752–7777.
7. Rao, C.N.R., Ramakrishna Matte, H.S.S., and Subrahmanyam, K.S. (2013) *Acc. Chem. Res.*, **46**, 149–159.

8. Lv, R. and Terrones, M. (2012) *Mater. Lett.*, **78**, 209–218.
9. Das, A., Pisana, S., Chakraborty, B., Piscanec, S., Saha, S.K., Waghmare, U.V., Novoselov, K.S., Krishnamurthy, H.R., Geim, A.K., Ferrari, A.C., and Sood, A.K. (2008) *Nat. Nanotechnol.*, **3**, 210–215.
10. Zhang, Y.B., Tang, T.T., Girit, C., Hao, Z., Martin, M.C., Zettl, A., Crommie, M.F., Shen, Y.R., and Wang, F. (2009) *Nature*, **459**, 820–823.
11. Santos, J.E., Peres, N.M.R., dos Santos, J.M.B.L., and Neto, A.H.C. (2011) *Phys. Rev. B*, **84**, 085430–085444.
12. Miwa, R.H., Schmidt, T.M., Scopel, W.L., and Fazzio, A. (2011) *Appl. Phys. Lett.*, **99**, 163108–163110.
13. Zhao, L.Y., He, R., Rim, K.T., Schiros, T., Kim, K.S., Zhou, H., Gutierrez, C., Chockalingam, S.P., Arguello, C.J., Palova, L., Nordlund, D., Hybertsen, M.S., Reichman, D.R., Heinz, T.F., Kim, P., Pinczuk, A., Flynn, G.W., and Pasupathy, A.N. (2011) *Science*, **333**, 999–1003.
14. Yu, W.J., Liao, L., Chae, S.H., Lee, Y.H., and Duan, X.F. (2011) *Nano Lett.*, **11**, 4759–4763.
15. Subrahmanyam, K.S., Panchakarla, L.S., Govindaraj, A., and Rao, C.N.R. (2009) *J. Phys. Chem. C*, **113**, 4257–4259.
16. Panchakarla, L.S., Subrahmanyam, K.S., Saha, S.K., Govindaraj, A., Krishnamurthy, H.R., Waghmare, U.V., and Rao, C.N.R. (2009) *Adv. Mater.*, **21**, 4726–4730.
17. Wei, D., Liu, Y., Wang, Y., Zhang, H., Huang, L., and Yu, G. (2009) *Nano Lett.*, **9**, 1752–1758.
18. Li, X., Wang, H., Robinson, J.T., Sanchez, H., Diankov, G., and Dai, H. (2009) *J. Am. Chem. Soc.*, **131**, 15939–15944.
19. Wang, X., Li, X., Zhang, L., Yoon, Y., Weber, P.K., Wang, H., Guo, J., and Dai, H. (2009) *Science*, **324**, 768–771.
20. Das, B., Voggu, R., Rout, C.S., and Rao, C.N.R. (2008) *Chem. Commun.*, 5155–5157.
21. Voggu, R., Das, B., Rout, C.S., and Rao, C.N.R. (2008) *J. Phys. Condens. Matter*, **20**, 472204–472208.
22. Pisana, S., Lazzeri, M., Casiraghi, C., Novoselov, K.S., Geim, A.K., Ferrari, A.C., and Mauri, F. (2007) *Nat. Mater.*, **6**, 198–201.
23. Gopalakrishnan, K., Moses, K., Dubey, P., and Rao, C.N.R. (2012) *J. Mol. Struct.*, **1023**, 2–6.
24. Guan, L., Cui, L., Lin, K., Wang, Y.Y., Wang, X.T., Jin, F.M., He, F., Chen, X.P., and Cui, S. (2011) *Appl. Phys. A*, **102**, 289–294.
25. Li, M., Tang, N., Ren, W., Cheng, H., Wu, W., Zhong, W., and Du, Y. (2012) *Appl. Phys. Lett.*, **100**, 233112/1–233112/3.
26. Huan, T.N., Van Khai, T., Kang, Y., Shim, K.B., and Chung, H. (2012) *J. Mater. Chem.*, **22**, 14756–14762.
27. Park, S., Hu, Y., Hwang, J.O., Lee, E.-S., Casabianca, L.B., Cai, W., Potts, J.R., Ha, H.-W., Chen, S., Oh, J., Kim, S.O., Kim, Y.-H., Ishii, Y., and Ruoff, R.S. (2012) *Nat. Commun.*, **3** (638), 1643/1–1643/8.
28. Jeon, I.-Y., Yu, D.-S., Bae, S.-Y., Choi, H.-J., Chang, D.-W., Dai, L.-M., and Baek, J.-B. (2011) *Chem. Mater.*, **23**, 3987–3992.
29. Chang, D.W., Lee, E.K., Park, E.Y., Yu, H., Choi, H.J., Jeon, I.-Y., Sohn, G.-J., Shin, D., Park, N., Oh, J.H., Dai, L., and Baek, J.-B. (2013) *J. Am. Chem. Soc.*, **135**, 8981–8988.
30. Deng, D., Pan, X., Yu, L., Cui, Y., Jiang, Y., Qi, J., Li, W.-X., Fu, Q., Ma, X., Xue, Q., Sun, G., and Bao, X. (2011) *Chem. Mater.*, **23**, 1188–1193.
31. Long, D., Li, W., Ling, L., Jin, M., Mochida, I., and Yoon, S.-H. (2010) *Langmuir*, **26**, 16096–16102.
32. Hassan, F.M., Chabot, V., Li, J., Kim, B.K., Ricardez-Sandoval, L., and Yu, A. (2013) *J. Mater. Chem. A*, **1**, 2904–2912.
33. Sun, L., Wang, L., Tian, C., Tan, T., Xie, Y., Shi, K., Li, M., and Fu, H. (2012) *RSC Adv.*, **2**, 4498–4506.
34. Wu, J., Zhang, D., Wang, Y., and Hou, B. (2013) *J. Power Sources*, **227**, 185–190.
35. Guo, H.-L., Su, P., Kang, X., and Ning, S.-K. (2013) *J. Mater. Chem. A*, **1**, 2248–2255.

36. Zhang, Y., Fugane, K., Mori, T., Niu, L., and Ye, J. (2012) *J. Mater. Chem.*, **22**, 6575–6580.
37. Lee, J.W., Ko, J.M., and Kim, J.-D. (2012) *Electrochim. Acta*, **85**, 459–466.
38. Geng, D., Hu, Y., Li, Y., Li, R., and Sun, X. (2012) *Electrochem. Commun.*, **22**, 65–68.
39. Qian, W., Cui, X., Hao, R., Hou, Y., and Zhang, Z. (2011) *ACS Appl. Mater. Interfaces*, **3**, 2259–2264.
40. Cao, H., Zhou, X., Qin, Z., and Liu, Z. (2013) *Carbon*, **56**, 218–223.
41. Qu, L., Liu, Y., Baek, J.-B., and Dai, L. (2010) *ACS Nano*, **4**, 1321–1326.
42. Dai, G.-P., Zhang, J.-M., and Deng, S. (2011) *Chem. Phys. Lett.*, **516**, 212–215.
43. Luo, Z., Lim, S., Tian, Z., Shang, J., Lai, L., MacDonald, B., Fu, C., Shen, Z., Yu, T., and Lin, J. (2011) *J. Mater. Chem.*, **21**, 8038–8044.
44. Gao, H., Song, L., Guo, W., Huang, L., Yang, D., Wang, F., Zuo, Y., Fan, X., Liu, Z., Gao, W., Vajtai, R., Hackenberg, K., and Ajayan, P.M. (2012) *Carbon*, **50**, 4476–4482.
45. Reddy, A.L.M., Srivastava, A., Gowda, S.R., Gullapalli, H., Dubey, M., and Ajayan, P.M. (2010) *ACS Nano*, **4**, 6337–6342.
46. Cui, T., Lv, R., Huang, Z.-H., Zhu, H., Kang, F., Wang, K., and Wu, D. (2012) *Carbon*, **50**, 3659–3665.
47. Lv, R., Li, Q., Botello-Mendez, A.R., Hayashi, T., Wang, B., Berkdemir, A., Hao, Q., Elias, A.L., Cruz-Silva, R., Gutierrez, H.R., Kim, Y.A., Muramatsu, H., Zhu, J., Endo, M., Terrones, H., Charlier, J.-C., Pan, M., and Terrones, M. (2012) *Sci. Rep.*, **2** (586), 1–8.
48. Jin, Z., Yao, J., Kittrell, C., and Tour, J.M. (2011) *ACS Nano*, **5**, 4112–4117.
49. Imamura, G. and Saiki, K. (2011) *J. Phys. Chem. C*, **115**, 10000–10005.
50. Koch, R.J., Weser, M., Zhao, W., Viñes, F., Gotterbarm, K., Kozlov, S.M., Höfert, O., Ostler, M., Papp, C., Gebhardt, J., Steinrück, H.-P., Görling, A., and Seyller, T. (2012) *Phys. Rev. B: Condens. Matter*, **86**, 075401/1–075401/6.
51. Xue, Y., Wu, B., Jiang, L., Guo, Y., Huang, L., Chen, J., Tan, J., Geng, D., Luo, B., Hu, W., Yu, G., and Liu, Y. (2012) *J. Am. Chem. Soc.*, **134**, 11060–11063.
52. Lin, Z., Waller, G.H., Liu, Y., Liu, M., and Wong, C.-P. (2013) *Nano Energy*, **2**, 241–248.
53. Usachov, D., Vilkov, O., Gr€uneis, A., Haberer, D., Fedorov, A., Adamchuk, V.K., Preobrajenski, A.B., Dudin, P., Barinov, A., Oehzelt, M., Laubschat, C., and Vyalikh, D.V. (2011) *Nano Lett.*, **11**, 5401–5407.
54. Xu, Z., Li, H., Yin, B., Shu, Y., Zhao, X., Zhang, D., Zhang, L., Li, K., Hou, X., and Lu, J. (2013) *RSC Adv.*, **3**, 9344–9351.
55. Sheng, Z.-H., Shao, L., Chen, J.-J., Bao, W.-J., Wang, F.-B., and Xia, X.-H. (2011) *ACS Nano*, **5**, 4350–4358.
56. Lin, Z., Song, M.-K., Ding, Y., Liu, Y., Liu, M., and Wong, C.-P. (2012) *Phys. Chem. Chem. Phys.*, **14**, 3381–3387.
57. Li, S.-M., Yang, S.-Y., Wang, Y.-S., Lien, C.-H., Tien, H.-W., Hsiao, S.-T., Liao, W.-H., Tsai, H.-P., Chang, C.-L., Ma, C.-C.M., and Hu, C.-C. (2013) *Carbon*, **59**, 418–429.
58. Parvez, K., Yang, S., Hernandez, Y., Winter, A., Turchanin, A., Feng, X., and Muellen, K. (2012) *ACS Nano*, **6**, 9541–9550.
59. Gopalakrishnan, K., Govindaraj, A., and Rao, C.N.R. (2013) *J. Mater. Chem. A*, **1**, 7563–7565.
60. Li, X.H., Kurasch, S., Kaiser, U., and Antonietti, M. (2012) *Angew. Chem. Int. Ed.*, **51**, 9689–9692, S9689/1–S9689/17.
61. Sun, Z., Yan, Z., Yao, J., Beitler, E., Zhu, Y., and Tour, J.M. (2010) *Nature (London)*, **468**, 549–552.
62. Lin, Z., Waller, G., Liu, Y., Liu, M., and Wong, C.-P. (2012) *Adv. Energy Mater.*, **2**, 884–888.
63. Feng, L., Chen, Y., and Chen, L. (2011) *ACS Nano*, **5**, 9611–9618.
64. Zhang, C., Fu, L., Liu, N., Liu, M., Wang, Y., and Liu, Z. (2011) *Adv. Mater.*, **23**, 1020–1024.
65. Yan, Z., Peng, Z.-W., Sun, Z.-Z., Yao, J., Zhu, Y., Liu, Z., Ajayan, P.M., and Tour, J.M. (2011) *ACS Nano*, **5**, 8187–8192.
66. Vinayan, B.P., Nagar, R., Rajalakshmi, N., and Ramaprabhu, S. (2012)

- Adv. Funct. Mater.*, **22**, 3519–3526, S3519/1–S3519/8.
67. Chandra, V., Yu, S.U., Kim, S.H., Yoon, Y.S., Kim, D.Y., Kwon, A.H., Meyyappan, M., and Kim, K.S. (2012) *Chem. Commun. (Cambridge, UK)*, **48**, 735–737.
 68. Sun, Y., Li, C., and Shi, G. (2012) *J. Mater. Chem.*, **22**, 12810–12816.
 69. Lin, Z., Waller, G.H., Liu, Y., Liu, M., and Wong, C.-P. (2013) *Carbon*, **53**, 130–136.
 70. Lai, L., Potts, J.R., Zhan, D., Wang, L., Poh, C.K., Tang, C., Gong, H., Shen, Z., Lin, J., and Ruoff, R.S. (2012) *Energy Environ. Sci.*, **5**, 7936–7942.
 71. Wen, Z., Wang, X., Mao, S., Bo, Z., Kim, H., Cui, S., Lu, G., Feng, X., and Chen, J. (2012) *Adv. Mater. (Weinheim)*, **24**, 5610–5616.
 72. Hwang, H., Joo, P., Kang, M.S., Ahn, G., Han, J.T., Kim, B.-S., and Cho, J.H. (2012) *ACS Nano*, **6**, 2432–2440.
 73. Palaniselvam, T., Aiyappa, H.B., and Kurungot, S. (2012) *J. Mater. Chem.*, **22**, 23799–23805.
 74. Unni, S.M., Devulapally, S., Karjule, N., and Kurungot, S. (2012) *J. Mater. Chem.*, **22**, 23506–23513.
 75. Saleh, M., Chandra, V., Christian, K.K., and Kim, K.S. (2013) *Nanotechnology*, **24**, 255702/1–255702/8.
 76. You, B., Wang, L., Yao, L., and Yang, J. (2013) *Chem. Commun. (Cambridge)*, **49**, 5016–5018.
 77. Chen, P., Yang, J.-J., Li, S.-S., Wang, Z., Xiao, T.-Y., Qian, Y.-H., and Yu, S.-H. (2013) *Nano Energy*, **2**, 249–256.
 78. Wu, Z.-S., Yang, S., Sun, Y., Parvez, K., Feng, X., and Muellen, K. (2012) *J. Am. Chem. Soc.*, **134**, 9082–9085.
 79. He, C., Li, Z., Cai, M., Cai, M., Wang, J.-Q., Tian, Z., Zhang, X., and Shen, P.K. (2013) *J. Mater. Chem. A*, **1**, 1401–1406.
 80. Zhao, Y., Hu, C., Hu, Y., Cheng, H., Shi, G., and Qu, L. (2012) *Angew. Chem. Int. Ed.*, **51**, 11371–11375.
 81. Luo, X., Yang, J., Liu, H., Wu, X., Wang, Y., Ma, Y., Wei, S.-H., Gong, X., and Xiang, H. (2011) *J. Am. Chem. Soc.*, **133**, 16285–16290.
 82. Kim, Y.A., Fujisawa, K., Muramatsu, H., Hayashi, T., Endo, M., Fujimori, T., Kaneko, K., Terrones, M., Behrends, J., Eckmann, A., Casiraghi, C., Novoselov, K.S., Saito, R., and Dresselhaus, M.S. (2012) *ACS Nano*, **6**, 6293–6300.
 83. Sheng, Z.-H., Gao, H.-L., Bao, W.-J., Wang, F.-B., and Xia, X.-H. (2012) *J. Mater. Chem.*, **22**, 390–395.
 84. Li, X., Fan, L., Li, Z., Wang, K., Zhong, M., Wei, J., Wu, D., and Zhu, H. (2012) *Adv. Energy Mater.*, **2**, 425–429.
 85. Cattelan, M., Agnoli, S., Favaro, M., Garoli, D., Romanato, F., Meneghetti, M., Barinov, A., Dudin, P., and Granozzi, G. (2013) *Chem. Mater.*, **25**, 1490–1495.
 86. Gebhardt, J., Koch, R.J., Zhao, W., Hoefert, O., Gotterbarm, K., Mammadov, S., Papp, C., Goerling, A., Steinrueck, H.-P., and Seyller, T. (2013) *Phys. Rev. B: Condens. Matter*, **87**, 155437/1–155437/9.
 87. Wang, H., Zhou, Y., Wu, D., Liao, L., Zhao, S., Peng, H., and Liu, Z. (2013) *Small*, **9**, 1316–1320.
 88. Lue, X., Wu, J., Lin, T., Wan, D., Huang, F., Xie, X., and Jiang, M. (2011) *J. Mater. Chem.*, **21**, 10685–10689.
 89. Khai, T.V., Na, H.G., Kwak, D.S., Kwon, Y.J., Ham, H., Shim, K.B., and Kim, H.W. (2012) *Chem. Eng. J. (Amsterdam)*, **211–212**, 369–377.
 90. Han, J., Zhang, L., Lee, S., Oh, J., Lee, K.-S., Potts, J.R., Ji, J., Zhao, X., Ruoff, R.S., and Park, S. (2013) *ACS Nano*, **7**, 19–26.
 91. Dou, C., Saito, S., Matsuo, K., Hisaki, I., and Yamaguchi, S. (2012) *Angew. Chem. Int. Ed.*, **51**, 12206–12210.
 92. Tang, Y.-B., Yin, L.-C., Yang, Y., Bo, X.-H., Cao, Y.-L., Wang, H.-E., Zhang, W.-J., Bello, I., Lee, S.-T., Cheng, H.-M., and Lee, C.-S. (2012) *ACS Nano*, **6**, 1970–1978.
 93. Pham, V.H., Hur, S.H., Kim, E.J., Kim, B.S., and Chung, J.S. (2013) *Chem. Commun. (Cambridge, UK)*, **49**, 6665–6667.
 94. Wu, T., Shen, H., Sun, L., Cheng, B., Liu, B., and Shen, J. (2012) *New J. Chem.*, **36**, 1385–1391.
 95. Bepete, G., Voiry, D., Chhowalla, M., Chiguvare, Z., and Coville, N.J. (2013) *Nanoscale*, **5**, 6552–6557.

96. Lin, T.-W., Su, C.-Y., Zhang, X.-Q., Zhang, W., Lee, Y.-H., Chu, C.-W., Lin, H.-Y., Chang, M.-T., Chen, F.-R., and Li, L.-J. (2012) *Small*, **8**, 1384–1391.
97. Levendorf, M.P., Kim, C.-J., Brown, L., Huang, P.Y., Havener, R.W., Muller, D.A., and Park, J. (2012) *Nature (London)*, **488**, 627–632.
98. Ci, L., Song, L., Jin, C., Jariwala, D., Wu, D., Li, Y., Srivastava, A., Wang, Z.F., Storr, K., Balicas, L., Liu, F., and Ajayan, P.M. (2010) *Nat. Mater.*, **9**, 430–435.
99. Fan, X., Shen, Z., Liu, A.Q., and Kuo, J.-L. (2012) *Nanoscale*, **4**, 2157–2165.
100. Chang, C.-K., Kataria, S., Kuo, C.-C., Ganguly, A., Wang, B.-Y., Hwang, J.-Y., Huang, K.-J., Yang, W.-H., Wang, S.-B., Chuang, C.-H., Chen, M., Huang, C.-I., Pong, W.-F., Song, K.-J., Chang, S.-J., Guo, J.-H., Tai, Y., Tsujimoto, M., Isoda, S., Chen, C.-W., Chen, L.-C., and Chen, K.-H. (2013) *ACS Nano*, **7**, 1333–1341.
101. Xu0065, Y., Yu, D., Dai, L., Wang, R., Li, D., Roy, A., Lu, F., Chen, H., Liu, Y., and Qu, J. (2013) *Phys. Chem. Chem. Phys.*, **15**, 12220–12226.
102. Zheng, Y., Jiao, Y., Ge, L., Jaroniec, M., and Qiao, S.Z. (2013) *Angew. Chem. Int. Ed.*, **52**, 3110–3116.
103. Wu, Z.-S., Winter, A., Chen, L., Sun, Y., Turchanin, A., Feng, X., and Muellen, K. (2012) *Adv. Mater. (Weinheim)*, **24**, 5130–5135, S5130/1–S5130/8.
104. Li, X.-H. and Antonietti, M. (2013) *Angew. Chem. Int. Ed.*, **52**, 4572–4576.
105. Kumar, N., Moses, K., Pramoda, K., Shirodkar, S.N., Mishra, A.K., Waghmare, U.V., Sundaresan, A., and Rao, C.N.R. (2013) *J. Mater. Chem. A*, **1**, 5806–5821.
106. Dai, J.Y., Yuan, J.M., and Giannozzi, P. (2009) *Appl. Phys. Lett.*, **95**, 232105–232107.
107. Zou, Y., Li, F., Zhu, Z.H., Zhao, M.W., Xu, X.G., and Su, X.Y. (2011) *Eur. Phys. J. B*, **81**, 475–479.
108. Wehling, T.O., Novoselov, K.S., Morozov, S.V., Vdovin, E.E., Katsnelson, M.I., Geim, A.K., and Lichtenstein, A.I. (2008) *Nano Lett.*, **8**, 173–177.
109. Kasry, A., Kuroda, M.A., Martyna, G.J., Tulevski, G.S., and Bol, A.A. (2010) *ACS Nano*, **4**, 3839–3844.
110. Yang, S., Zhi, L., Tang, K., Feng, X., Maier, J., and Muellen, K. (2012) *Adv. Funct. Mater.*, **22**, 3634–3640, S3634/1–S3634/6.
111. Yan, Y., Yin, Y.-X., Xin, S., Guo, Y.-G., and Wan, L.-J. (2012) *Chem. Commun. (Cambridge, UK)*, **48**, 10663–10665.
112. Choi, C.H., Chung, M.W., Jun, Y.J., and Woo, S.I. (2013) *RSC Adv.*, **3**, 12417–12422.
113. Poh, H.L., Simek, P., Sofer, Z., and Pumera, M. (2013) *ACS Nano*, **7**, 5262–5272.
114. Yang, Z., Yao, Z., Li, G., Fang, G., Nie, H., Liu, Z., Zhou, X., Chen, X., and Huang, S. (2012) *ACS Nano*, **6**, 205–211.
115. Liang, J., Jiao, Y., Jaroniec, M., and Qiao, S.Z. (2012) *Angew. Chem. Int. Ed.*, **51**, 11496–11500.
116. Li, Y., Wang, J., Li, X., Geng, D., Banis, M.N., Tang, Y., Wang, D., Li, R., Sham, T.-K., and Sun, X. (2012) *J. Mater. Chem.*, **22**, 20170–20174.
117. Li, R., Wei, Z., Gou, X., and Xu, W. (2013) *RSC Adv.*, **3**, 9978–9984.
118. Liu, Z.-W., Peng, F., Wang, H.-J., Yu, H., Zheng, W.-X., and Yang, J. (2011) *Angew. Chem. Int. Ed.*, **50**, 3257–3261, S3257/1-S3257/12.
119. Yao, Z., Nie, H., Yang, Z., Zhou, X., Liu, Z., and Huang, S. (2012) *Chem. Commun. (Cambridge, UK)*, **48**, 1027–1029.
120. Niu, F., Liu, J.-M., Tao, L.-M., Wang, W., and Song, W.-G. (2013) *J. Mater. Chem. A*, **1**, 6130–6133.
121. Denis, P.A. (2010) *Chem. Phys. Lett.*, **492**, 251–257.
122. Late, D.J., Ghosh, A., Subrahmanyam, K.S., Panchakarla, L.S., Krupanidhi, S.B., and Rao, C.N.R. (2010) *Solid State Commun.*, **150**, 734–738.
123. Ao, Z.M., Yang, J., Li, S., and Jiang, Q. (2008) *Chem. Phys. Lett.*, **461**, 276–279.
124. Ghosh, A., Late, D.J., Panchakarla, L.S., Govindaraj, A., and Rao, C.N.R. (2009) *J. Exp. Nanosci.*, **4**, 313–322.
125. Wu, Z.-S., Ren, W., Xu, L., Li, F., and Cheng, H.-M. (2011) *ACS Nano*, **5**, 5463–5471.

126. Wu, G., Mack, N.H., Gao, W., Ma, S., Zhong, R., Han, J., Baldwin, J.K., and Zelenay, P. (2012) *ACS Nano*, **6** (11), 9764–9776.
127. Li, Y., Wang, J., Li, X., Geng, D., Banis, M.N., Li, R., and Sun, X. (2012) *Electrochem. Commun.*, **18**, 12–15.
128. Zhang, K., Han, P., Gu, L., Zhang, L., Liu, Z., Kong, Q., Zhang, C., Dong, S., Zhang, Z., Yao, J., Xu, H., Cui, G., and Chen, L. (2012) *ACS Appl. Mater. Interfaces*, **4**, 658–664.
129. Cai, D., Wang, S., Lian, P., Zhu, X., Li, D., Yang, W., and Wang, H. (2013) *Electrochim. Acta*, **90**, 492–497.
130. Xu, C., Sun, J., and Gao, L. (2012) *Nanoscale*, **4**, 5425–5430.
131. Jeong, H.M., Lee, J.W., Shin, W.H., Choi, Y.J., Shin, H.J., Kang, J.K., and Choi, J.W. (2011) *Nano Lett.*, **11**, 2472–2477.
132. Qiu, Y., Zhang, X., and Yang, S. (2011) *Phys. Chem. Chem. Phys.*, **13**, 12554–12558.
133. Gopalakrishnan, K., Moses, K., Govindaraj, A., and Rao, C.N.R. (2013) *Solid State Commun.*, **175-176**, 43–50.
134. Chen, J., Li, C., and Shi, G. (2013) *J. Phys. Chem. Lett.*, **4**, 1244–1253.
135. Liang, Y., Li, Y., Wang, H., Zhou, J., Wang, J., Regier, T., and Dai, H. (2011) *Nat. Mater.*, **10**, 780–786.
136. Wu, G. and Zelenay, P. (2013) *Acc. Chem. Res.*, **46**, 1878–1889.
137. Geng, D., Chen, Y., Chen, Y., Li, Y., Li, R., Sun, X., Ye, S., and Knights, S. (2011) *Energy Environ. Sci.*, **4**, 760–764.
138. Chung, H.T., Won, J.H., and Zelenay, P. (2013) *Nat. Commun.*, **4**. doi: 10.1038/ncomms2944
139. Choi, C.H., Chung, M.W., Park, S.H., and Woo, S.I. (2013) *RSC Adv.*, **3**, 4246–4253.
140. Choi, C.H., Chung, M.W., Kwon, H.C., Park, S.H., and Woo, S.I. (2013) *J. Mater. Chem. A*, **1**, 3694–3699.
141. Xue, Y., Liu, J., Chen, H., Wang, R., Li, D., Qu, J., and Dai, L. (2012) *Angew. Chem. Int. Ed.*, **51**, 12124–12127.
142. Wang, G., Xing, W., and Zhuo, S. (2013) *Electrochim. Acta*, **92**, 269–275.
143. Palnitkar, U.A., Kashid, R.V., More, M.A., Joag, D.S., Panchakarla, L.S., and Rao, C.N.R. (2010) *Appl. Phys. Lett.*, **97**, 063102/1–063102/3.
144. Soin, N., Sinha, R.S., Roy, S., Hazra, K.S., Misra, D.S., Lim, T.H., Hetherington, C.J., and McLaughlin, J.A. (2011) *J. Phys. Chem. C*, **115**, 5366–5372.
145. Long, J., Xie, X., Xu, J., Gu, Q., Chen, L., and Wang, X. (2012) *ACS Catal.*, **2**, 622–631.
146. Xin, Y., Liu, J.-G., Jie, X., Liu, W., Liu, F., Yin, Y., Gu, J., and Zou, Z. (2012) *Electrochim. Acta*, **60**, 354–358.
147. Some, S., Kim, J., Lee, K., Kulkarni, A., Yoon, Y., Lee, S.M., Kim, T., and Lee, H. (2012) *Adv. Mater. (Weinheim)*, **24**, 5481–5486.
148. Kwon, O.S., Park, S.J., Hong, J.-Y., Han, A.-R., Lee, J.S., Lee, J.S., Oh, J.H., and Jang, J. (2012) *ACS Nano*, **6**, 1486–1493.
149. Gopalakrishnan, K., Joshi, H.M., Kumar, P., Panchakarla, L.S., and Rao, C.N.R. (2011) *Chem. Phys. Lett.*, **511**, 304–308.

11

Layer-by-Layer Assembly of Graphene-Based Hybrid Materials

Antonios Kouloumpis, Panagiota Zygouri, Konstantinos Dimos, and Dimitrios Gournis

11.1

Introduction

Layer-by-layer (LbL) assembly is an easy and inexpensive technique for the development of multilayer films [1–6]. Nevertheless, simplicity and low cost are not the only reasons why LbL has attracted so much of attention over the past two decades. The versatility of the process; the capability of using diverse types of materials; the tailoring of the final nanostructures with controlled architecture, thickness, and functionality; and lastly the potential of tuned, well defined, and desired properties determined by the multilayer number of the films produced are briefly the main advantages of LbL method [7–11]. Consequently, LbL assembly is considered to be a significant and unlimited bottom-up nanofabrication technique today [6].

Graphene, being a single-layered material, is an amazing and promising candidate for LbL assembly. Its superior electronic and mechanical properties can be modified, tuned, or enhanced by LbL assembly as has been reported in many studies over the last 3–4 years. The resulting LbL graphene-based hybrid films commonly attain extended and composite properties as various substances can be used for the intermediate layer, and are applicable mainly in electronic circuits and supercapacitors, and as sensors and so on.

The Langmuir–Blodgett (LB) technique is one of the most promising LbL methods for preparing monolayer and multilayer graphene-based thin films. This bottom-up approach enables the precise control of the monolayer thickness and allows homogeneous deposition over large areas and on almost any kind of solid substrate [12]. Although this emerging field of graphene nanoscience remains largely unexplored, several studies have demonstrated either the successful creation of high-quality graphene monolayers or the development of multilayer films of novel graphene hybrids by integrating a variety of guest species with the graphene matrix.

This chapter attempts to provide a comprehensive and critical overview of the most recent developments on the use of LbL and LB techniques for the design and construction of novel graphene-based hybrids. The structural, physicochemical,

electronic, mechanical, and tribological properties of these hybrid systems are discussed, while emphasis is placed on their potential applications in various fields such as electronics, sensors, and ion batteries.

11.2

LbL Graphene-Based Hybrid Films

LbL technique is generally based on the electrostatic interactions between the molecules/structures that form successive layers on a substrate. However, over the years, a variety of flexible synthetic approaches and processes have been reported that grant novelty to LbL assembly [10, 11, 13, 14]. In a typical LbL synthetic procedure, a substrate is immersed consecutively into two solutions of rather high concentrations of the substances that form the successive layers, with intermediate rinsing and stabilization of the layers. The whole process is repeated as many times as desired; the sequence of the layers can be modified with additional building blocks to acquire complex multicomponent nanostructures with novel properties [6].

Various LbL techniques have been developed recently in order to fabricate graphene-based hybrid films. Most of these techniques rely on modification of graphene sheets with polyelectrolytes (PEs) to acquire positively or negatively charged layers so that they are soluble in aqueous media for the production of multilayered films by subsequent immersion and adsorption from relevant solutions. In addition, other LbL procedures involve spin coating techniques, thermal evaporation, sputtering, electrodeposition, molecular beam epitaxy, chemical vapor deposition (CVD), and so on [15].

11.2.1

Hybrid Thin Films for Electronics

Since graphene's high importance lies in its electronic and transparency properties, most of the LbL graphene-based films reported in the literature report hybrid nanostructures with advanced relevant properties. In fact, the main aim of all related studies reported is to produce LbL-assembled graphene-based films with high uniformity, as low as possible sheet resistance for higher conductivity, and at least 80% optical transparency to meet the minimum requirement criteria for technological applicability. Graphene sheet is emerging as a potential substitute for conventional indium tin oxide (ITO) in flexible displays, touch screens, and solar cells. However, its sheet resistance is controlled by the number of the layers, and since the intrinsic sheet resistance of a single graphene layer is calculated to be $\sim 6 \text{ k}\Omega \text{ sq}^{-1}$ while ITO exhibits significantly lower sheet resistance ($\sim 10\text{--}20 \Omega \text{ sq}^{-1}$), functionalization is required to decrease this value drastically in final applicable materials. So, LbL assembling is a promising methodology for developing doped graphene multilayers in order to achieve higher extrinsic conductivity [16].

In this direction, Shen *et al.* [13] reported in 2009 one of the first successful uses of PEs for the modification of graphene sheets for subsequent LbL self-assembling procedure. Graphene surface was functionalized with poly(acrylic acid) (PAA) and poly(acrylamide) (PAM), which were covalently grafted on the graphene sheets by *in situ* living free radical polymerization. The functionalization allowed the development of negative charge in the case of PAA and positive charge for PAM on the surface of the graphene sheets. The two modified graphene materials formed stable dispersions in aqueous media, permitting their later use for LbL self-assembling through electrostatic interactions to produce a multilayer graphene-based structure. Various characterization techniques such as scanning electron microscopy (SEM), atomic force microscopy (AFM), and UV-vis spectroscopy proved not only the successful fabrication of the films but also their uniformity and tailoring capability. That way, the versatile LbL technique could be used for exploiting graphene's extraordinary properties by modification with a variety of agents that could be employed in such films, giving birth to applicable nanostructures.

Just a year later, Bae and his coworkers [17] reported the preparation and wet-chemical doping of large-area monolayered graphene sheets by CVD onto flexible copper substrates and their subsequent use via LbL assembly to fabricate doped graphene-based films with exceptional optoelectronic properties. The original films demonstrated sheet resistances as low as $\sim 125 \Omega \text{sq}^{-1}$ with 97.4% optical transmittance and exhibited the half-integer quantum Hall effect, indicating their high quality. Later, the monolayers could be stacked with LbL assembling to fabricate a doped four-layer film on various substrates such as silicon wafer, polyethylene terephthalate (PET), and quartz. The sheet resistance of the doped four-layer film was measured and found to be $\sim 30 \Omega \text{sq}^{-1}$ at $\sim 90\%$ transparency, which was superior to that of commercial transparent electrodes such as ITO. Moreover, the produced films displayed real application capabilities, as the constructed graphene-based electrodes were incorporated into a fully functional touch-screen panel device capable of withstanding high strain. For implementation of the applicable device, a transparent large-area graphene film was transferred on a 35 in. PET sheet and silver paste electrodes were patterned on the graphene/PET film, giving birth to a fully functional assembled graphene/PET touch panel with outstanding flexibility, which was connected to a computer with control software.

Li *et al.* [18] prepared advanced multilayered films via electrostatic LbL co-assembling of graphene oxide (GO) nanosheets and Keggin-type polyoxometalate clusters, $\text{H}_3\text{PW}_{12}\text{O}_{40}$ (phosphotungstate). Films were formed on various substrates such as quartz glass, silicon wafer, and flexible polymer supports. The substrates were pre-functionalized with a PEI (poly(ethyleneimine))/PW double layer as precursor films, and later different numbers of PAH/GO/PAH/PW layers were deposited on the modified substrates to construct GO-PW multilayer films, in which GO nanosheets and PW clusters were linked by poly(allylamine hydrochloride) (PAH) layers (Figure 11.1), where cationic PEs PEI and PAH were used as electrostatic linkers.

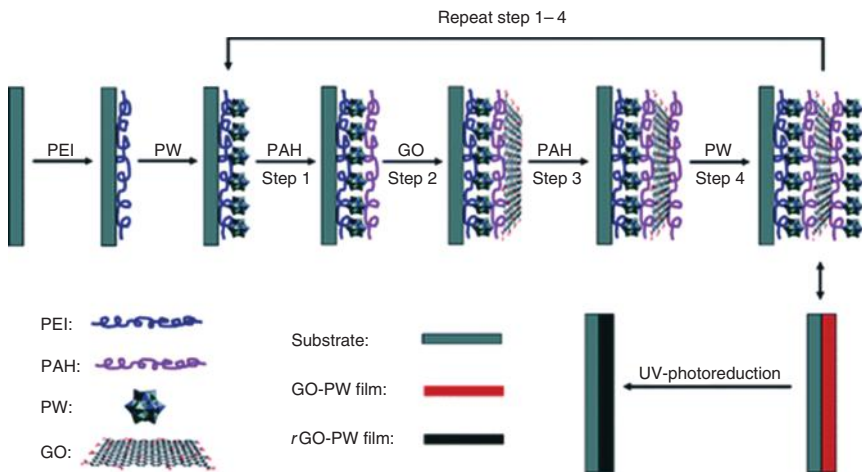


Figure 11.1 Schematic illustration of the fabrication procedure of rGO-PW multilayer films, which involves the LbL assembly of GO nanosheets and PW clusters using cationic polyelectrolytes PEI and PAH as electrostatic linkers, and a subsequent *in situ* photoreduction to convert GO to rGO. (Reproduced with permission from Ref. [18].)

In these films, the PW layers existed on both sides of the GO layers, aiming to realize an effective interaction between GO oxygen-containing groups and PW clusters, which would be favorable for electron transfer from photo-excited PW to GO. Hence, under UV irradiation, efficient *in situ* reduction of GO to reduced graphene oxide (rGO) occurred, assisted by the photocatalytic activity of the PW clusters. Thus, a mild and environmentally friendly photoreduction approach was followed to produce rGO sheets and large-area graphene-based hybrid films with high morphological uniformity and controlled thickness. Moreover, thin film field effect transistors (FETs) were fabricated using the composite films, which demonstrated typical ambipolar characteristics and good transport properties for both holes and electrons. The on/off ratios and the charge carrier mobilities of the transistors depended on the number of deposited layers and could be tuned easily. It is noteworthy that if photomasks were used to produce conductive patterns of rGO domains on the films, the rGO patterns could serve as efficient microelectrodes for photodetector devices. In this way, it is foreseen that the integration of various functional polyoxometalates could lead to novel multifunctional graphene-based devices. Finally, on the basis of this procedure of electrostatic LbL co-assembling of graphene sheets and polyoxometalate clusters presented by Li *et al.*, logic-gate devices with dual optical and electrical output functions could be fabricated by combining the luminescent property of polyoxometalate clusters with the electric response of the graphene sheets.

In contrast, while Li *et al.* used polyoxometalate clusters, Güneş and his coworkers [19] fabricated advanced doped graphene-based films according to a novel proposed LbL approach by using CVD and subsequent casting with a salt solution. Large-area graphene monolayers were synthesized on a Cu foil with CVD and later on, each layer was transferred on a PET substrate. An AuCl₃ solution was then spin-casted on it and the procedure was repeated several times to get LbL-doped thin layers (Figure 11.2).

For comparison, films with only the top layer of the film functionalized by doping were also prepared, and they exhibited significantly poorer environmental stability compared to the fully doped/modified films that additionally exhibited high uniformity. Doping of the graphene layers with Au particles or Au³⁺ cations resulted in enhanced conductivity with a relevant significant decrease up to ~80% of the sheet resistance, while transmittance was not noticeably affected. Specifically, a large-area (11 × 11 cm²) LbL-doped four-layer graphene-based film demonstrated a 54 Ω sq⁻¹ sheet resistance with a relatively high transmittance (85%) at 550 nm, when the pristine single graphene sheet showed a large sheet resistance of 725 Ω sq⁻¹ at a transmittance of 97.6% at the same wavelength. The combination of these characteristics of the fabricated films – low sheet resistance and high transparency – meets the technical requirements for industrial applications such as LCDs, thin film solar cells, flexible touch-screen panels, and electronic papers. Moreover, the graphene-based films produced display excellent bending stability showing superior performance in flexibility and stretchability compared to conventional ITO-based transparent conducting films. Considering

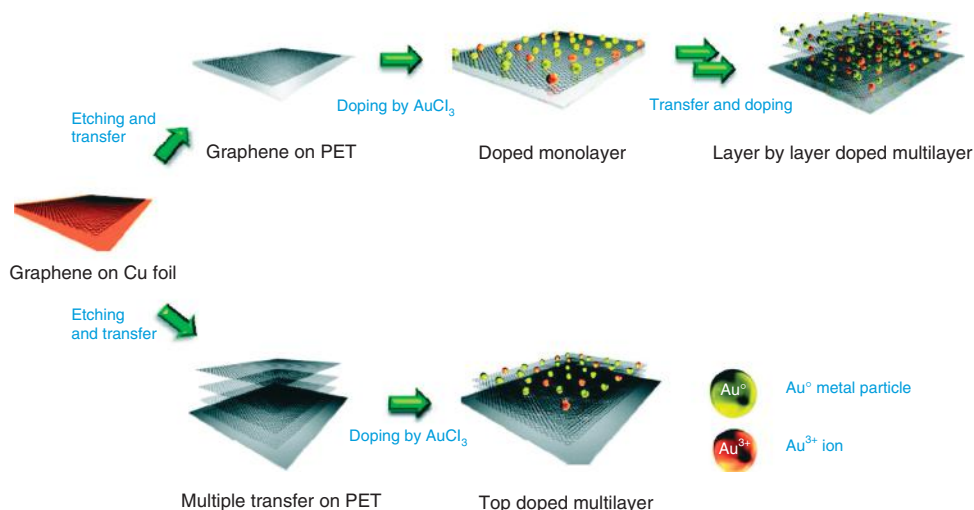


Figure 11.2 The schematic of the LbL-doping strategy. The top steps indicate LbL doping and the bottom steps indicate the topmost layer doping. Au atoms or ions are indicated by different colors. (Reproduced with permission from Ref. [19].)

the data above, an improvement in the synthesis and transfer procedures proposed by Güneş *et al.*, could result in even higher quality films with reduced defects leading to enhanced performance, thereby validating this methodology as a potential candidate for large-scale production of uniform large-area graphene-based films suitable for large-size displays.

As opposed to Güneş and his coworkers who used the CVD technique and spin-casting, Kong *et al.* [14] fabricated graphene-based films with gold nanoparticle (NP) layers by using vacuum filtration and simple immersion of the films in a gold salt solution. Sequential n -repetition of the two processes could be employed to form n -bilayer films. With the vacuum filtration process thin graphene films were deposited on a quartz glass substrate. Later, the films were immersed in a $\text{HAuCl}_4 \cdot 3\text{H}_2\text{O}$ solution where *in situ* spontaneous reduction of gold ions took place, forming Au NPs. The mechanism of the spontaneous reduction process that generated gold NPs on the graphene sheets likely involved galvanic displacement and redox reaction by the relative potential difference between gold ions and graphene while it was also promoted by the electrons present and donated by the negatively charged graphene sheets. As a consequence, the proposed LbL assembling process for hybrid graphene/gold NP films was not only simple but also inexpensive and environmentally friendly as no reducing agents or linkers were required or used, resulting in impurity-free transparent platforms that could potentially be employed to a variety of sensing applications, including probes for DNA microarrays and gold NP–oligonucleotide complexes for intracellular gene regulation.

On the contrary, Wang *et al.* [16] fulfilled a comprehensive study of varied modification methods for graphene sheets with the aim of optimizing its role as an anode for solar cells. In this context, a direct LbL transfer method of graphene sheets was developed that resulted in (poly(methyl methacrylate), PMMA) films that were free from residual impurity. According to the proposed methodology, a single layer by PMMA was spin-coated onto the first graphene sheet and these two layers were transferred onto another graphene layer (second) on a copper foil where the two graphene sheets bonded with a π - π interaction after annealing at 120 °C for 10 min. Subsequent etching of the copper foil allowed the direct transfer of the multilayers onto a third graphene sheet and thereby, pure graphene multilayers were produced without impurities between the layers as the top and only PMMA layer was removed in acetone. Prior to the PMMA removal, the multilayers could be transferred onto other substrates such as quartz glass. Individual layers were doped with HCl during the transfer process, while the top layer was doped with HNO₃ after PMMA elimination. The resulting LbL-assembled doped graphene multilayers remarkably exhibited a sheet resistance value as low as $\sim 80 \Omega \text{sq}^{-1}$ with a transmittance of $\sim 90\%$ at 550 nm, whereas conventional ITO has in general comparable sheet resistance for 80% optical transmittance and flexible PET demonstrates a higher sheet resistance of about $100\text{--}300 \Omega \text{sq}^{-1}$.

Furthermore, in order to get high-performance organic solar cells, additional modification of the films was realized with molybdenum oxide (MoO₃). Graphene films were coated with a thin MoO₃ layer of about 20 Å as it was evaporated on the graphene films and the films were tested as solar cell anodes after the spreading of a poly(3,4-ethylenedioxythiophene):poly(styrene sulfonate) (PEDOT:PSS) film on the MoO₃-coated graphene. A photovoltaic (PV) device based on that anode was constructed (Figure 11.3). The aforementioned graphene based PV device exhibited a 2.5% power conversion efficiency while a control device based on ITO had a 3% efficiency. This implies that compared to a control ITO based PV device, a $\sim 83.3\%$ of the power conversion efficiency could be attained. In fact, all key PV parameters for solar devices fabricated using the graphene anode were quite similar to those of the ITO anode.

Hong *et al.* [10] designed graphene-based films, studied their optoelectronic properties, and used them in a foldable printed circuit board. Films were formed by the successive layering of poly(allylamine)-(PAA) and poly(styrenesulfonate)-(PSS) on a quartz substrate. During the carbonization process, the PSS layers were transformed into graphene nanosheets (GNs) because of their inherent aromatic and highly ordered structure, while the PAA layers prevented the agglomeration of the GNs produced. Thus, PSS layers provided the carbon source and PAA layers acted as sacrificial layers for the stabilization of the structure. Furthermore, a metallic dopant (transition metal) was used during the LbL assembly that not only assisted the carbonization process but also formed an ionic crosslinking with neighboring sulfonate groups ($-\text{SO}_3\text{H}$) in the PSS layers, which acted as a pillaring agent that prevented agglomeration and shrinkage of the graphene-based films. The optical transmittance of the produced films at

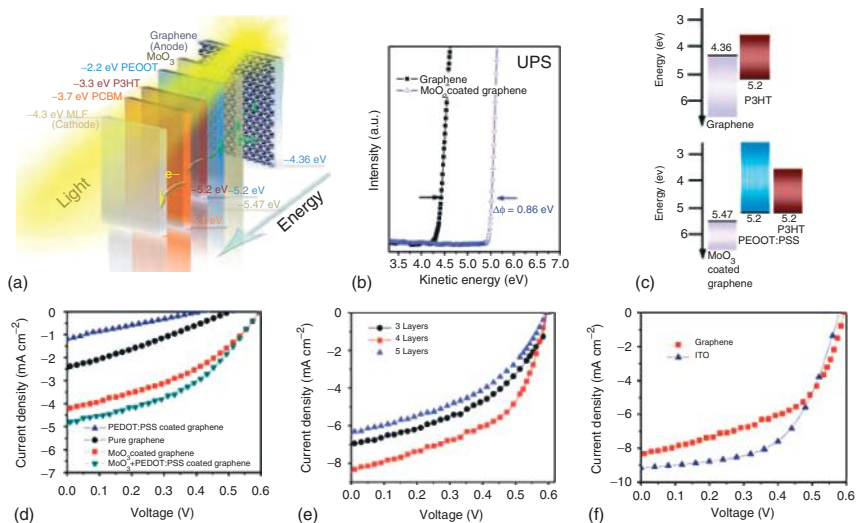


Figure 11.3 (a) Schematic diagram of photovoltaic device structure; (b) ultraviolet photoelectron spectroscopy (UPS) spectrum showing the secondary cut-off of four layers of graphene before (black line) and after modification with MoO_3 (blue line); (c) energy level diagram at the anode side of the photovoltaic cells without (top) and with (bottom) the MoO_3 + PEDOT:PSS layer; (d) current density–voltage (J – V) characteristics of devices under light illumination. Anode/P3HT:PCBM/LiF/Al (anode = four layers as-grown graphene and the same coated by PEDOT:PSS only, MoO_3 only, or MoO_3 + PEDOT:PSS); (e) three to five layers of acid-doped graphene/ MoO_3 + PEDOT:PSS/P3HT:PCBM/LiF/Al; and (f) anode/PEDOT:PSS/P3HT:PCBM/LiF/Al (anode is ITO or MoO_3 -coated graphene). (Reproduced with permission from Ref. [16].)

$\lambda = 550$ nm was controllable by the thickness (i.e., the number of the layers) and varied from 92% to 71% as the film thickness increased from 10 to 100 nm. In addition, the sheet resistance of the films decreased as the film thickness increased, obtaining its lowest value at $\sim 1.2 \text{ k}\Omega \text{ sq}^{-1}$, coupled with transmittance of $\sim 71\%$ for the most thick films (100 nm). All nanostructured films displayed linearity of the I - V curves over a voltage range from -0.1 to $+0.1$ V confirming their ohmic behavior. Moreover, the dV/dI values demonstrated dependence by the film thickness, as films of less than ~ 10 nm exhibited one to two orders of magnitude higher dV/dI values compared to those of relatively thick films.

The above characteristics of the prepared films render them as potential candidates for transparent electrodes and can display practical applicability in foldable printed circuit boards such as the one presented in Figure 11.4. For the production of the circuit board, an electrically conductive wire of 100% graphene-based films with thickness of 300 nm and width of 5 mm was patterned on a polyimide film. The pattern was designed on computer software (Figure 11.4a) and was inkjet-printed

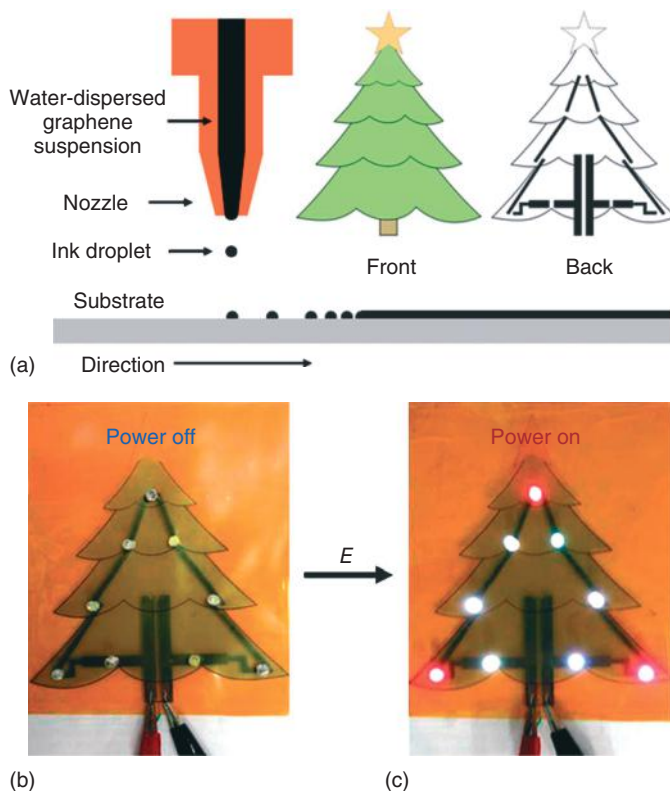


Figure 11.4 Graphene-based electronic circuit: (a) designed pattern for inkjet printing and (b,c) digital photographs of graphene-based electronic circuit turned off (b) and turned on (c). (Reproduced with permission from Ref. [10].)

repeatedly for 30 passes. The LEDs were connected in series and applied by a 27.0 V DC power supply. The electrically connected LEDs could be turned on by applying voltage, demonstrating the electrically conductive pathway of the graphene-based printed circuit.

A more complex, three-dimensional graphene-based nanostructure with electrocatalytic properties and possible electrochemical applications in nanodevices was prepared by Zhu and his coworkers [8]. Graphene sheets were functionalized with an imidazolium salt-based ionic liquid (IS-IL) and by using the LbL assembly, platinum NPs were attached through electrostatic interaction. The IL agent (1-(3-aminopropyl)-3-methylimidazoliumbromide) was covalently bonded on the surface of the GNs, modifying and providing them with positive charge. On the contrary, platinum NPs were stabilized and negatively charged with citrate allowing electrostatic interaction with the modified graphene sheets for the formation of the hybrid films. Nanostructures were developed on negatively charged substrates as ITO electrode, quartz slide, and freshly cleaved mica. The final films showed high electrocatalytic activity toward oxygen reduction, which could be further tuned by altering the number of the cycles in the LbL process. More specifically, for the determination of the electrocatalytic properties, cyclic voltammetry (CV) measurements were performed in a 0.5 M H_2SO_4 electrolyte saturated with oxygen solution at various millivolt per second scan rates. While in control experiments no catalytic reduction current was obtained, indicating that graphene was almost inert for the electrocatalytic oxygen reduction, the hybrid graphene-based nanostructured films exhibited remarkable catalytic reduction current in the range of 0.2–0.4 V. Furthermore, the catalytic oxygen reduction current varied with increasing millivolt per second scan rate. In fact, it demonstrated a linear function of the square root with the scan rate, indicating that the oxygen reduction was a diffusion control process.

Li *et al.* [20] managed to produce a relatively different class of multilayer films with the LbL assembly, once more for electrochemical properties and supercapacity. Three different building blocks were used to form the multicomponent graphene-based nanostructure – poly(sodium 4-styrenesulfonate)-mediated graphene sheets (PSS-GS), manganese dioxide (MnO_2) sheets, and poly(diallyldimethylammonium) (PDDA). Films were formed on an ITO electrode, and a full LbL assembly cycle contained one PSS-GS layer, one of MnO_2 , and two intermediate layers of PDDA, in a way producing an $\text{ITO}/(\text{PDDA}/\text{PSS-GS}/\text{PDDA}/\text{MnO}_2)_n$ electrode where n corresponds to the number of the LbL cycles. Electrochemical tests that were performed for the prepared multilayer film electrodes in a 0.1 M Na_2SO_4 solution demonstrated that the capacity increased with the number of bilayers. Specifically, for the $\text{ITO}/(\text{PDDA}/\text{PSS-GS}/\text{PDDA}/\text{MnO}_2)_n$ electrode, the larger the number n , the higher the capacity. In addition, ~90% of the specific capacitance for the 10-bilayer film electrode (263 F g^{-1} at a discharge current density of 0.283 A g^{-1}) still remained after 1000 times of cycling compared to the first cycle exhibiting very good cycling stability, while a high Coulombic efficiency of nearly 100% was also achieved. The exceptional characteristics of these multicomponent graphene-based films qualify them as potential candidates for novel electrode materials in supercapacitors.

Just a year before, Yu and Dai [21] achieved an average specific capacitance of 120 F g^{-1} and an almost rectangular cyclic voltammogram even at high scan rates of 1 V s^{-1} for a diverse graphene-based film. GO sheets were chemically reduced with hydrazine in the presence of PEI in aqueous solution. The water-soluble cationic PEI chains were attached on the surface of the resulting GNs (PEI-GNs), providing the necessary positive charge for the following LbL assembly procedure. Silicon or ITO glass were used as substrates for the formation of the hybrid films, and multiwalled nanotubes (MWNTs) that were negatively charged by acid oxidation (MWNT-COOH) were used as the intermediate building block of the film. LbL self-assembly process was executed until the desired thickness and architecture of the films was reached. Subsequently, the substrate-supported self-assembled hybrid films were heated at 150°C for 12 h in a vacuum oven, resulting in the formation of amide bonds between the amine groups of the PEI-modified graphene sheets and carboxylic acids on the acid-oxidized MWNT surface that further stabilized the structure and provided uniform films. The obtained hybrid films having interconnected network of carbon structures with well-defined nanopores, ideal for fast ion diffusion, are promising as supercapacitor electrodes. CV measurements were performed in a $1.0 \text{ M H}_2\text{SO}_4$ electrolyte solution, at room temperature and various scan rates, for heat-treated $[\text{PEI-GN/MWNT-COOH}]_n$ films with varied bilayer number n (3, 9, and 15). The electrochemical tests showed that an average specific capacitance of 120 F g^{-1} could be achieved, while it is worth noting that the CVs were still rectangular in shape even at high scan rates, indicating rapid charging and discharging with a low equivalent series resistance of the electrodes.

Another promising nanostructure for electrochromic devices was prepared by using GO as precursor for graphene-based LbL-assembled films by Sheng and his coworkers [22]. Graphene/polyaniline (PANI) multilayer films were successfully fabricated via sequential deposition of negatively charged GO and positively charged PANI upon electrostatic interaction, followed by the chemical reduction of GO with hydroiodic acid. PANI was selected for the LbL process, being a promising conductive polymer because of its environmental stability, low cost, controllable electrical conductivity, and interesting redox properties as it has four redox states with distinct colors. The thickness of the multilayer film increased linearly with the number of its bilayers, whereas each bilayer was measured to be $\sim 3 \text{ nm}$, yielding smooth and compact composite films with roughness less than 6 nm . CV studies indicated that these thin composite films were electroactive, and their redox reactions were related to the insertion–extraction of counter ions in PANI layers as anodic peak current density exhibited a linear relationship with the scan rate in the region of $0\text{--}30 \text{ mV s}^{-1}$. In addition, the thickness, conductivity, and transmittance of the multilayer film could be easily tuned by changing the alternate deposition steps. Moreover, the composite films were tested to be promising electrode materials for electrochromic devices even without using conductive transparent supporting electrodes such as the conventional ITO. An electrochromic device based on a 15 bilayer film showed improved electrochemical stability compared to a similar device with an ITO electrode.

Furthermore, after 300 cycles of potential switching, the optical contrast value decreased by 20% while the switching time was kept unchanged. Throughout this procedure, the (graphene/PANI)₁₅ film maintained good homogeneity and reliability.

In contrast, Lee *et al.* [23] developed a novel approach for constructing *rGO* films. According to their methodology, positively and negatively charged *rGO* sheets were LbL assembled with a spin-coating technique. Films were formed on silicon wafer or quartz slide substrates that were prior treated with oxygen plasma to introduce a hydrophilic surface. Negatively charged *rGO* was formed from GO that possessed carboxylic acid groups by hydrazine chemical reduction in the presence of ammonia to prevent the aggregation of the resulting *rGO* suspension (*rGO*-COO⁻). Positively charged *rGO* sheets were prepared by introducing amine groups (-NH₂) on the surface of negatively charged GO sheets through the *N*-ethyl-*N'*-(3-dimethyl aminopropyl)carbodiimidemethiodide (EDC) mediated reaction between carboxylic acids (and/or epoxides) and ethylenediamine excess, which led to a positively charged stable *rGO* suspension after hydrazine reduction (*rGO*-NH₃⁺). The LbL assembly provided highly controllable nanostructured films in terms of *thickness*, *transmittance*, and *sheet resistance*. Specifically, each *rGO* layer thickness could be controlled exactly in the sub-nanometer scale by simply varying the number of stacking sheets, which enabled tailoring of the optical and electrical properties in an outstanding manner. The final LbL-assembled *rGO* films exhibited sheet resistance of 8.6 and 32 kΩsq⁻¹ at 86% and 91% transmittance respectively. In addition, a real application for the implementation of these films as transparent electrodes in organic light-emitting diode (OLED) devices was tested. ITO-coated glass (10 Ωsq⁻¹) as reference and *rGO*-coated glass (3 kΩsq⁻¹) substrates were prepared and their electroluminescence properties were studied. The current density–voltage–luminance (*J–V–L*) characteristics of the two fabricated devices demonstrated that compared to the ITO electrode device, which showed the maximum luminance of ~7800 cd m⁻² at 6 V; the maximum luminance of the *rGO* electrode device was ~70 cd m⁻² at 18 V and increased with applied bias voltage. Furthermore, the maximum luminous efficiency of the *rGO* electrode device was ~0.10 cd A⁻¹, while that with the ITO electrode was ~0.38 cd A⁻¹.

A similar approach has been followed by Park *et al.* [24] GO was again used as starting material for the preparation of positively and negatively charged sheets, that were LbL self-assembled on the basis of electrostatic interactions to produce finally graphene-based films with thermal reduction of the assembled functionalized GO layers. The negatively charged GO was based on the carboxyl groups present while the positively charged GO sheets were synthesized in two steps: an intermediate acyl-chlorination reaction by thionyl chloride introduced chloride onto the GO sheets and a subsequent amidation reaction by ethylenediamine in pyridine modified the layers with amine groups. The final positively charged amine-functionalized GO sheets exhibited stable dispersibility within the polar organic solvent used for the reaction as well as in aqueous environment. By adjusting the LbL assembling cycles, controllable thickness, and tailored optical transparency

of the films was achieved while their electrical property was enhanced through a thermal treatment process apart from the p-doping effect by the adopted midstep acyl-chlorination reaction. Final films demonstrated sheet resistance of $1.4 \text{ k}\Omega \text{ sq}^{-1}$ with a light transmittance of 80% at 550 nm, meeting the minimum requirements for a practical transparent electrode application, validating this procedure as a potential route for developing LbL graphene-based films for transparent electrodes, flexible displays, or highly sensitive biosensors.

Yao *et al.* [25] made an effort to develop photoconductive patterns on GO/PDDA/TiO₂ hybrid films, which were constructed through LbL self-assembly. The aim of this study supported the photothermal and photocatalytic reduction of GO (*rGO*). In the first step, the fabrication of (PDDA/GO/PDDA/TiO₂)₂₀ films on a glass substrate was concluded. It was observed that the hybrid composite presented a relation between UV-vis absorption and layer numbers, revealing that the absorbance increased linearly as a function of deposition layer numbers. SEM images showed that the surface of the film was fluctuant. The procedure for the photothermal/photocatalytic reduction of GO (*rGO*) is based on the photocatalytic activity of TiO nanosheets. UV-vis measurements of the obtained film proved that the reduction of GO was successful and SEM images showed that the surface became smoother and changes were not observed in the lamellar structures. The *rGO* was used as an electronic transportation medium that presented high photocurrent generation and good reversibility in the generation of photoconductive pattern. The fabrication of the photoconductive pattern was realized by the illumination of the film. The results demonstrated that the hybrid films tested could be used in many microelectronic applications.

An effort to develop polymer-coated graphene nanoplatelets was overwhelmed by Rani and his coworkers [26]. In particular, they used two types of PEs, the positively charged PAH and the negatively charged poly sodium 4-styrenesulfonate (PSS). Consequently, they constructed the (PSS-G/PAH-G)_{*n*} through LbL assembly. In the first step, reduced graphene (*rG*) nanoplatelets were synthesized and afterwards they were coated with PSS and PAH. The attachment of PAH and PSS on the graphene sheets was a result of the electrostatic and the edge-to-face interactions, respectively. The procedure was realized by using two different substrates, more specifically a glass and a quartz substrate. In the experimental process the PDDA was used in order to provide positive charge to the substrate while four different concentrations of PSS and PAH solutions, 0.1, 0.2, 0.4, and 0.8 mg ml⁻¹ were tested. Electrical tests were performed to determinate the properties of each composite. Measurements showed that the conductivity between 0.1 and 0.2 mg ml⁻¹ was significantly increased, while between 0.4 and 0.8 mg ml⁻¹ a considerable reduction was observed. At the concentration of 0.2 mg ml⁻¹, the hybrid nanocomposite film presented the highest conductive behavior and after annealing for 2 h at 250 °C in nitrogen atmosphere, the material presented conductivity of around 0.2 S cm⁻¹ and 30 kΩ sheet resistance, in comparison with the pre-annealing film. AFM measurements showed that the coverage of surface is increased by altering the number of the deposition cycles

while the surface roughness was raised by increasing the concentration from 0.1 to 0.4 mg ml⁻¹.

Furthermore, Wang *et al.* [27] attempted to develop *via* the LbL approach well-ordered functional graphene-based nanostructures for application in bioelectronic field. More specifically, graphene/methylene green (MG) and graphene/multiwalled carbon nanotubes (MWCNTs) films were constructed in which graphene was used as a spacer. The synthetic process was performed by the usage of a glassy carbon electrode (GCE) as substrate which was modified five times for both nanocomposites, as the researchers considered that the five layers have the optimal electrocatalytic activity toward β -nicotinamide adenine dinucleotide (NADH). The choice of MG and carbon nanotubes (CNTs) was based on their exceptional electrochemical properties. The excellent electrocatalytic activity, the increased conductivity, and the high surface area that characterize these nanocomposites occurred by both the components and the graphene as a spacer; thus, these systems can be used in a variety of devices such as biosensors and biofuel cells.

Ishikawa *et al.* made an effort to develop a novel deposition's route based on the LbL method in order to construct graphene-based transparent conductive films (TCFs) [28]. They studied for the first time, the possible usage of (GO/GO-EDA)_n films as electrodes in silicon thin film solar cells. The LbL-assembled films suffered reduction by hydrazine vapor and thermal annealing at 600 °C in vacuum and were deposited on ZnO layers, which were produced by the metal organic chemical vapor deposition (MOCVD). In addition, on the three-layered graphene was fabricated a p-i-n single junction of solar cells, such as the amorphous silicon carbide (a-SiC_x:H), the hydrogenated amorphous silicon (a-Si:H), and the hydrogenated microcrystalline silicon oxide (μ c-SiO_x:H) (Figure 11.5).

The research group studied the optical and the electrical properties of the tested film. Table 11.1 presents comparatively the physical parameters of the LbL-assembled film and a sprayed graphene film. It was proved that increasing the number of LbL cycles, the film presented lowest values of optical transmittance and sheet resistance. However, the sheet resistance presented an improvement by

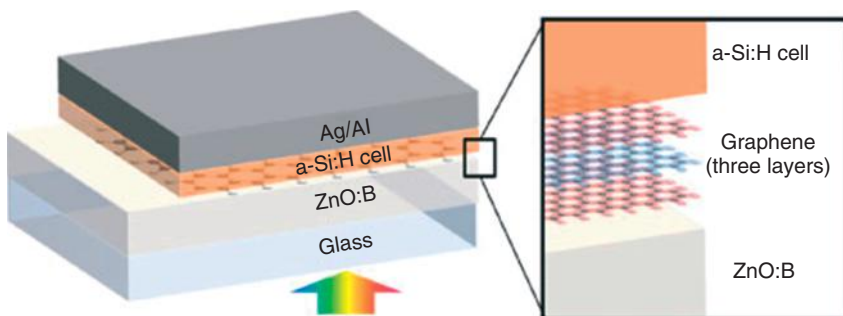


Figure 11.5 Illustration of silicon thin film solar cell using graphene-based window electrodes. (Reproduced with permission from Ref. [28].)

Table 11.1 Physical parameters of LbL-assembled and sprayed graphene films [28].

	Transmittance at 550 nm (%)	Sheet resistance ($\Omega \text{ sq}^{-1}$)	Sheet carrier concentration (cm^{-2})	Hall mobility ($\text{cm}^2 (\text{Vs})^{-1}$)
Spray	83.8	1.1×10^6	1.4×10^{12}	2.2
LbL assembly	84.0	5.8×10^4	3.8×10^{11}	57.5

an order of magnitude at the same optical transparency, originating from the good uniformity and stacking of graphene sheets.

The research of Seok *et al.* made an effort to improve the properties of PEDOT [29]. They constructed two-layered and three-layered PEDOT/graphene composite films via LbL assembly with a spin-coating technique (Figure 11.6).

PEDOT (3,4-ethylenedioxythiophene) is a conductive polymer that can be used in a variety of applications. On the other hand, single-layer graphene exhibits significantly electronic properties, mobility, transparency, and better mechanical properties than steel. Films were deposited on a glass wafer; however, the researchers succeeded also in generating a free-standing film by isolating it from the substrate by the usage of sodium hydroxide. The two-layered G/P nanocomposite showed increased conductivity (13 S cm^{-1}) compared to pristine PEDOT (6 S cm^{-1}) (Figure 11.7). The presence of graphene enhances the conductive properties of the PEDOT film and makes it possible for it to be used in electronic applications.

An ultrathin graphene supercapacitor based on “in plane” design was fabricated by Yoo and his coworkers [30]. The in-plane geometry provides the graphene sheets the ability to be used in energy storage devices. The combination of open architecture and the effect of graphene sheets attributes high capability values to the devices that consist of graphene electrodes. The specific capacity of one

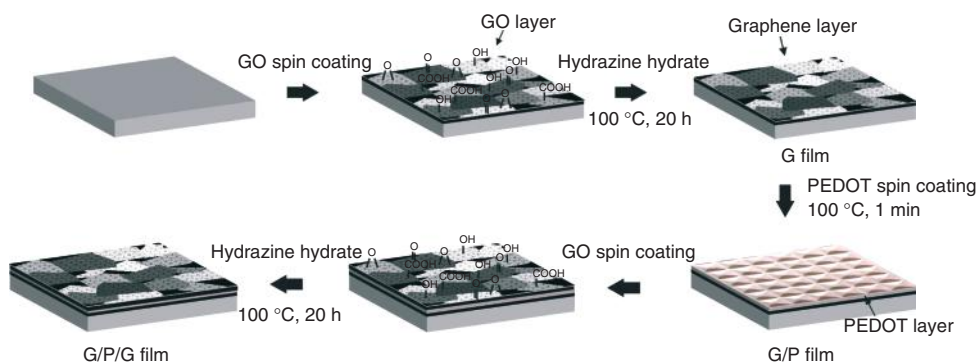


Figure 11.6 Fabrication process for the PEDOT and graphene composite film. (Reproduced with permission from Ref. [29].)

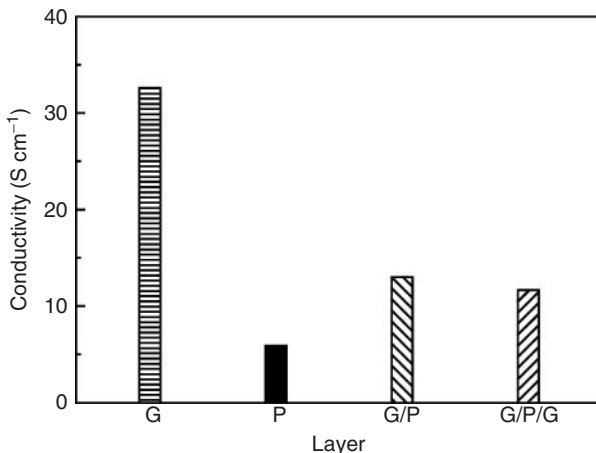


Figure 11.7 Conductivity data for graphene, PEDOT, G/P, and G/P/G composite films. While the graphene layer was spin-coated at 3000 rpm, PEDOT layer was deposited with 4000 rpm spin rate in a layer-by-layer manner. (Reproduced with permission from Ref. [29].)

to two layered graphene can be increased up to $80 \mu\text{F cm}^{-1}$, while in the case of multilayered graphene the value is higher than $394 \mu\text{F cm}^{-1}$. The studies are based on the development of *rGO* through LbL assembly. For comparison, graphene obtained via CVD was used. The internal resistance values of *rGO* and G were calculated to be 77 and 747 k Ω , respectively. From AFM measurements, it was proved that the *rGO* film had a thickness of ~ 10 nm. On the basis of theoretical estimates, 10 nm of thickness corresponds to 21 layers of graphene. The fact that the specific capacitance of the *rGO* device for a geometric area ($394 \mu\text{F cm}^{-2}$) was five times higher than the value of G ($80 \mu\text{F cm}^{-2}$) led to the conclusion that the new device with the “in plane” geometry can store more charge per unit area by increasing the number of layers. The researchers constructed stacked devices (conventional geometry) from the *rGO* electrode with the same area of the electrode containing similar amount of the polymer gel. The results of the comparison of the in plane and stacked device geometries are presented in Table 11.2. The new device geometry could be used with other thin-film-based supercapacitors and modulated in a variety of structural and hybrid designs for energy storage devices.

Table 11.2 Comparison of the specific capacity for the stacked versus in-plane device geometry for the *rGO* electrodes with ~ 10 nm thickness [30].

Geometry	Stacked ($\mu\text{F cm}^{-2}$)	In-plane ($\mu\text{F cm}^{-1}$)
<i>rGO</i>	140	394

11.2.2

Hybrid Thin Films as Sensors

Besides optoelectronic and electrode-related applications, LbL-assembled graphene-based films were also tested for gas or molecular sensing in recent years. It has been widely accepted that sensitivity and selectivity of sensors crucially depends on the host structure of the sensor. Graphene gathers some very important features that validate it as an ideal candidate for a sensing substrate. First of all, it is a 2D layered monoatomic structure with high uniformity that can be packed at will – with desirable and tailored functionalization groups, interlayer space, and cavities – in final films depending on the application. Secondly, it exhibits advanced electron conductivity as it contains extended systems of conjugated π -bonds that are vital for electron transfer phenomena and are also essential in sensing, and finally, it has inherent low electrical noise, which is important for achieving very low detection limits [31, 32]. For all these reasons, graphene-based electrodes have been recently reported to display superb electrocatalytic activity for H_2O_2 , O_2 , NADH, and other vital species as well as superior enzyme biosensing ability [33].

A related application has been reported by Zhang and Cui [31] who developed an ultrasensitive, low-cost, and label-free graphene-based cancer marker biosensor for the real-time detection of prostate-specific antigen (PSA) in a large detection range from 4 fg ml^{-1} to $4 \mu\text{g ml}^{-1}$. A PET flexible wafer was used as a substrate onto which a 50/200 nm thick chromium/gold layer was deposited with sputtering. Gold sensor electrodes were patterned photolithographically, whereas an additional lithography step was used to fabricate a window area on which the graphene film was LbL self-assembled while it protected the testing pads from the adsorption of graphene solutions. Poly(diallyldiamine chloride) (PDDA) and poly(styrene sulfonate) (PSS) were the two PEs used for the LbL assembly process of the graphene sheets on the window area of the chromium/gold layer (Figure 11.8).

Finally, the biosensor was immunized by immobilization of anti-PSA on the surface with label-free technique. For comparison, a horseradish peroxidase (HRP)-labeled PSA sensor and a CNT-based sensor were manufactured according to the same method. A five bilayer self-assembled graphene film displayed a $45 \pm 5 \text{ nm}$ thickness and a $0.9 \pm 0.01 \text{ k}\Omega$ resistance. By varying PSA concentration in testing solutions, a shift in the film conductivity was observed, indicating that label-free and labeled graphene sensors were capable of detecting very low concentrations of PSA down to 4 fg ml^{-1} (0.11 fM) and 0.4 pg ml^{-1} (11 fM) respectively, which were at least three orders of magnitude lower than achievable using CNT sensors (4 ng ml^{-1}) under the same conditions of design, fabrication, and measurement. The label-free sensor allowed the direct immunization reaction and therefore exhibited lower detection limit compared to the labeled sensor, at which a 300 nm thick PMMA passivation layer resulted in reduced PSA absorption. Moreover, both sensors do not require signal sampling amplification, which might easily induce a secondary electrical noise as in the case of sensors with higher detection limits. Furthermore, the low $1/f$ noise of

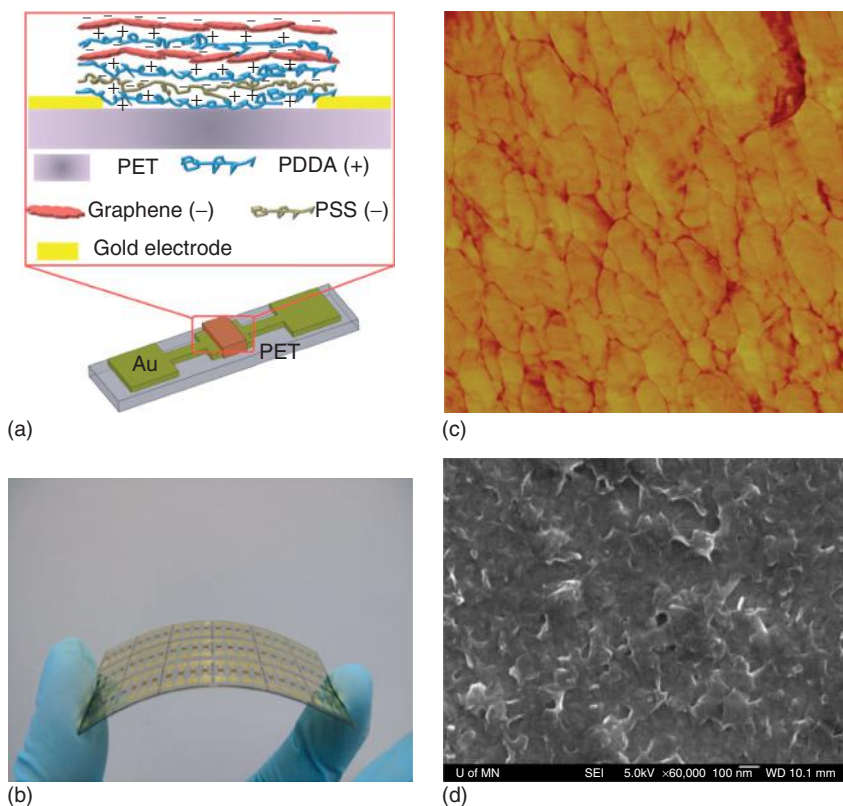


Figure 11.8 (a) Schematic illustration of LbL self-assembled graphene nanocomposite before immunization; (b) optical image of LbL self-assembled graphene cancer sensor on a flexible PET substrate; (c) AFM image of LbL self-assembled graphene

(scanning area is $1 \times 1 \mu\text{m}^2$); and (d) SEM image of LbL self-assembled graphene displaying its porous defoliation surface profile. The average graphene nanoplatelet is about $100 \times 100 \text{ nm}^2$. (Reproduced with permission from Ref. [31].)

graphene sensors due to the high quality of its crystal lattice and two-dimensional structure compared to the one-dimensional system of CNTs interpreted their higher performance. Conductance versus time measurements were also performed recording real-time trends, indicating that this methodology was capable of detecting real-time antigen concentrations, whereas with the appropriate modifications it could be used for the recognition of other antigens or complex diseases.

On the other hand, Ji *et al.* in 2010 [32] focused on fabricating LbL-assembled graphene-based films by functionalizing GO with nonvolatile ILs, *in situ* reduction of GO to graphene, and following electrostatic LbL assembly on quartz crystal microbalances (QCMs) (Figure 11.9). Subsequently, films were tested for selective gas sensing and found to possess higher affinity for toxic aromatic hydrocarbons

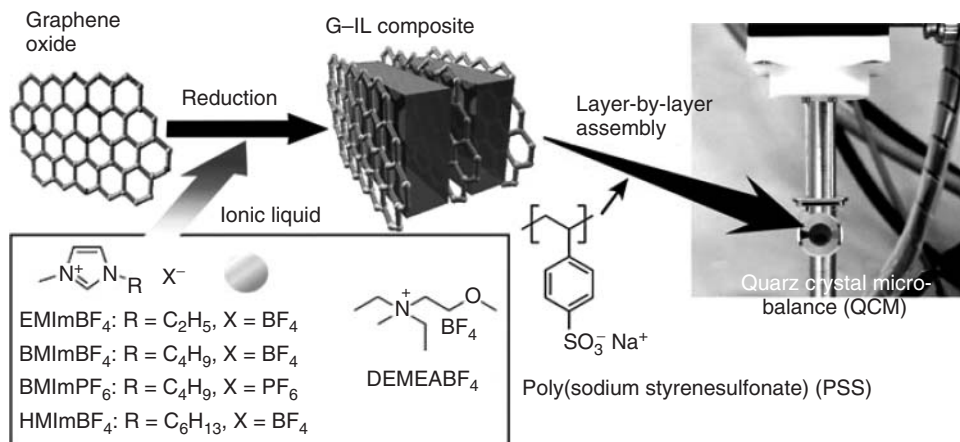


Figure 11.9 Schematic illustration of the preparation of graphene/ionic liquid (G-IL) composites and their LbL assembly on a quartz crystal microbalance (QCM). (Reproduced with permission from Ref. [32].)

than for their aliphatic analogs. This enhanced detection ability of aromatic molecules in contrast to aliphatic molecules was due to the well-defined π -electron-rich nanospace in the films. In addition, there was clear evidence of improved aromatic hydrocarbon gas adsorption with increasing interlayer spacing between the graphene sheets. More specifically, films exhibited high selectivity for benzene vapor as its adsorption was at least one order of magnitude higher compared to cyclohexane vapor adsorption despite their similar molecular sizes, molecular weights, and vapor pressures. Moreover, films with a 0.41 nm interlayer spacing also demonstrated higher benzene vapor adsorption compared to films with a 0.35 nm interlayer spacing.

Detection of vapors could be repeated through alternate exposure and removal of the guest solvents; a gradual degradation of the on/off response was noted for benzene detection, which was attributed to the strong interactions between aromatic compounds and the graphene layer, whereas the response to cyclohexane was fully reversible. Furthermore, the electric properties of the films depended on the gas adsorption since it was found that an original, unused film possessed a resistance of $178 \Omega \text{sq}^{-1}$ while after benzene adsorption it was decreased to $163 \Omega \text{sq}^{-1}$. The latter significantly indicated that gas detection could be converted into electrical signal and that these films were of vast practical applicability.

Another biosensor was fabricated by Zeng and his coworkers [33]. While most reports were based on covalent functionalization of graphene or GO sheets as precursor to yield oppositely charged sheets for sequential electrostatic LbL assembly, Zeng *et al.* followed a relatively different approach and developed a noncovalent modification. In fact, this methodology seemed to have a basic advantage as the intrinsic electronic properties of graphene sheets could be maintained or even

enhanced. The reported LbL assembly technique was based on a two-step procedure. At first, chemically rGO sheets were noncovalently modified by pyrene-grafted PAA in aqueous media based on intermolecular interactions, such as electrostatic interactions, hydrophobic forces, hydrogen bonds, and more specifically in this case, π - π stacking as well as van der Waals interactions. Secondly, the formed supramolecular assemblies were used as building blocks for LbL alternating deposition with PEI. Fabricated films were tested and found to display enhanced electron transfer for the redox reactions of $\text{Fe}(\text{CN})_6^{3-}$ and excellent electrocatalytic activity of H_2O_2 . Moreover, a bienzyme biosensing system for the detection of glucose and maltose was fabricated by successive LbL assembly of graphene, glucose oxidase (GOx), and glucoamylase (GA). Taking advantage of the electrocatalytic activity over H_2O_2 , the fabricated amperometric biosensor functioned as follows. GA catalyzed maltose hydrolysis to glucose, which was then oxidized by GOx producing H_2O_2 with the latter being detected by the graphene-based electrode. The bienzyme biosensor demonstrated detection limits for glucose and maltose of 0.168 and 1.37 mM respectively, while sensitivity was 0.261 and 0.00715 $\mu\text{A}\cdot\text{mM}^{-1}\cdot\text{cm}^{-2}$, respectively.

Chang *et al.* [34] investigated a simple method to detect the oxidative stress which occurred by hydrogen peroxide (H_2O_2) in tumor cells. For this purpose, an *in vitro* amperometric current-time technique was used, relying on an electrochemical sensor. A GCE (carbon glass electrode), which was modified via LbL electrochemical deposition technique, was used as the electrode. An rGO film covered the GCE and the Au NPs and poly(toluidine blue O) films were immobilized upon the graphene (rGO-Au-PTBO) (Figure 11.10). rGO, gold NPs, and poly(toluidine blue

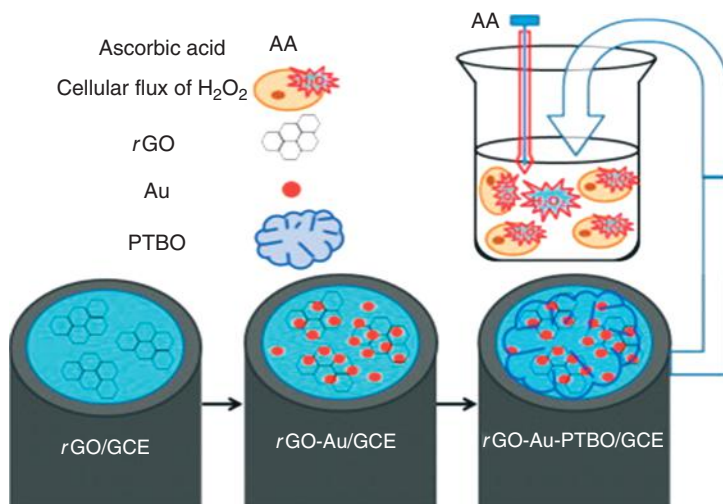


Figure 11.10 Schematic of the LbL assembly of rGO-Au-PTBO modified GCE used for detected H_2O_2 efflux from cells stimulated with ascorbic acid. (Reproduced with permission from Ref. [34].)

O) provide convenient properties to the composite. rGO displays excellent electrical conductivity at room and cryogenic temperatures. Au NPs provide exceptional catalytic ability to H_2O_2 and mediate the electron transfer between the analyte and the electrode. PTBO films play the role of the matrix that encases the Au NPs and obstruct some opposite-charged interference from penetrating into the surface of the electrode. It was observed that each layer of the graphene-based nanocomposite films presented enhanced catalytic effect toward electroreduction of H_2O_2 . The presence of PTBO films as well the low potential (-0.3 V) enabled high selectivity of the sensor for the detection of H_2O_2 efflux from tumor cells.

Qin *et al.* [35] studied the construction of a label-free aptasensor with extremely unique properties such as selectivity and sensitivity to different molecules, especially to peptides. For this reason, their research focused on graphene multilayer via LbL assembly. This sensor presents much more advantages compared with previous electrochemical aptasensors: high accumulation levels of methylene blue (MB), large surface area for target absorption, as well as high electrical conductivity. Furthermore, the detection of the target is independent of environmental factors. In this study, the main target is vasopressin (VP), a peptide hormone that plays an important role in the kidney's function. Using pulse voltammetry, it is possible to detect the lowest concentration of the target at a wide detection range from 1 to 265 ng ml^{-1} . Another advantage of the method is the use of aptamer, an oligonucleotide that has the ability to immobilize the peptide onto the electrode interface that inhibits electron transfer, resulting in a concentration-dependent decrease of voltage at differential pulse voltammetry (DPV). MB and the positively charged poly(diallyldimethylammonium chloride) (PDDA) were attached in the negative surface of the ITO electrode formatting the first layer. Then, the graphene layer coated with negatively charged PSS were connected with PDDA. After several steps, the multilayer graphene intercalated with MB. Aptamer as a negatively charged oligonucleotide attached in PDDA outer surface and after that the substrate connected on this (Figure 11.11). These LbL multilayers could bring more probes and aptamers that could improve the sensitivity of the biosensors.

On the other hand, the research of Shan *et al.* [36] was focused on graphene-based nanocomposite films and their possible applications. They prepared (Prussian blue/PEI-graphene)_n multilayers via the LbL method using an ITO electrode as a substrate. The procedure of the LbL method consisted of three parts. Firstly, the ITO substrate was immersed in PDDA in order to obtain positively charged surface. Secondly, the PDDA-modified substrate was immersed in Prussian blue (PB) solution and finally, the substrate was soaked in a PEI-graphene solution. After each immersion, the tested sample was rinsed three times with water. The multilayer film was taken by repeating the second and third steps. The presence of PEI-graphene, because of its good dispersibility and the existence of active amino groups, leads to the excellent properties of the composite and renders this suitable for many applications such as in medicine, catalysis, and energy. Study on its electrocatalytic ability toward H_2O_2 was

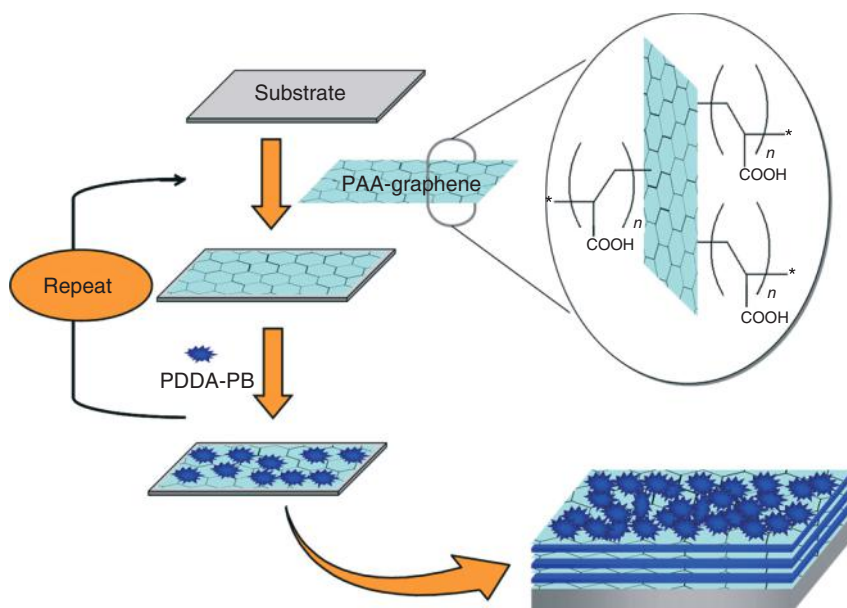


Figure 11.12 Schematic representation of the assembling process of (PAA-graphene/PDDA-PB)_n multilayer films. PAA-graphene: polyacrylic acid functionalized graphene (negatively charged), PDDA-PB:

poly(diallyldimethylammonium chloride) protective Prussian blue NPs (positively charged). (Reproduced with permission from Ref. [37].)

performed, revealing that the [PB/PEI-graphene]_n presents good electrochromic and electrocatalytic properties and for this reason could be promising in electro-sensing applications.

In addition, Ma *et al.* [37] also studied the use of graphene-based nanocomposite films in biosensing applications. More specifically, they constructed a (PAA-graphene/PDDA-PB)_n multilayer film via electrostatic LbL assembly. PAA modified the surface of graphene, which acted as a building block for the assembly and interacted electrostatically with the positively charged PDDA/PB. A GCE was used as a substrate (Figure 11.12). The group tried to study the performance of the tested system in electrocatalysis. Their results confirmed that the (PAA-graphene/PDDA-PB)_n film shows catalytic activity toward the reduction of H₂O₂. They also verified that the number of the bilayers and the electroactive species are important factors in studies that focus on the development of advanced biosensing devices.

In another study, Mao *et al.* investigated the role of the LbL-assembled film (PFIL-GS/PB)_n as a substrate to detect hydrogen peroxide by electrochemical surface plasmon resonance (EC-SPR) spectroscopy [38]. Decorated graphene sheets were initially synthesized with a cationic polyelectrolyte-functionalized ionic liquid (PFIL-GS), which presented high conductivity and a very stable aqueous

dispersion because of the electrostatic repulsion between the modified sheets. The bonds between the PFIL and the graphene sheets were not only because of their opposite charge but also of the π - π interactions between the imidazole ring of PFIL and the aromatic rings of graphene sheets. The usage of PB gave a significant advantage to the composite because of its excellent electrocatalytic activity toward H_2O_2 reduction. The experiment was facilitated by strong electrostatic interactions between positively charged PFIL-GS and negatively charged PB. An important observation was that the PFIL-GS/PB multilayer film presented the highest electrocatalytic activity toward reduction of H_2O_2 between PB and PFIL-GS.

Liu *et al.* [39] made an effort to construct an electrochemical immunosensor in order to detect the human IgG. For this purpose, in the first step they fabricated a three-dimensional composite film on a GCE via LbL assembly. More specifically, they synthesized rG and functionalized MWCNTs. The fabrication of the composite was realized by the electrostatic absorption of the positively charged poly(diallyldimethylammonium chloride) (PDDA) and the negatively charged carbon nanomaterials, rG, and MWCNTs. The multilayered composite film was characterized by electrochemical impedance spectroscopy (EIS) and CV. It was proved that the tested material presents a notably improvement in the interfacial electron transfer rate in comparison with chemically reduced graphene or MWCNTs modified electrode. A sandwich-type-electrochemical immunosensor, which is based on the rG-MWCNTs assembled interface, was constructed using human IgG as a model target. Experiments on the operation of the sensor showed that it exhibits exceptional selectivity, stability, and reproducibility with the detection limit of 0.2 ng ml^{-1} . Moreover, it displays good accuracy for the determination of the human IgG in serum samples. This modified electrode interface could be helpful in a variety of medical applications such as in the point-of-care diagnostics application of clinical screening of cancer biomarkers.

Furthermore, Liu and his coworkers [40] tried to develop an electrochemical sensor in order to detect dopamine. For this reason, they modified a GCE with a graphene-based composite through LbL assembly. The researchers synthesized rGO, which was functionalized with PSS and stabilized poly(amido amine) (PAMAM) on gold NPs. The LbL method was realized by the electrostatic interactions between the negatively charged rGO and positively charged solution of AuNPs. The electrode obtained positive charge by the immersions in PDDA solution. $(\text{AuNPs}/\text{rGO})_n/\text{GCE}$ was characterized by three different techniques – CV, EIS, and DPV. The assembled modified electrode presented good reproducibility, high stability, and a splendid sensing performance for the detection of dopamine. The improvement of the electrocatalytic activity toward the oxidation of dopamine was due to the synergistic effect of the rGO and the gold NPs. In addition, the electrochemical sensor proved that it can detect dopamine and uric acid simultaneously by using DPV, exhibiting high sensitivity and selectivity. This kind of sensors with the aforementioned properties could be used in many applications of medical and biotechnological fields.

11.2.3

Hybrid Films for Other Applications

While most of the research studies focused on the electro-optical properties of LbL-assembled graphene-based films, Zhao *et al.* [41] constructed poly(vinyl alcohol) (PVA) modified GO films and reported on their mechanical properties. Since individual graphene sheets exhibit extraordinary mechanical properties, it has been used as filler for the fabrication of polymeric films with enhanced mechanical properties. In that way, by a simple LbL self-assembly, thin multilayer (PVA/GO)_n films with high homogeneity and well-defined layered architecture were successfully fabricated, where the bilayer thickness was ~3 nm. Assembling was based on hydrogen bonding interactions between the oxygen functional groups of GO and the hydroxyl groups of the PVA chains. Final films possessed high degree of planar GO orientation in the lamella structure, resulting in a significant enhancement of the mechanical properties of the LbL nanocomposites compared to a parallel pure PVA film. In fact, the elastic modulus of the hybrid films (17.64 GPa) was improved by 98.7% compared to the pure PVA film whereas hardness (1.15 GPa) was increased by 240.4%. These values qualify LbL self-assembling technique as a potential method for the production of polymer/graphene hybrid films for mechanical applications.

Studies of the tribological properties of multilayer graphene-based LbL-assembled films were carried out from the research group of Liu *et al.* [42]. For the preparation of the hybrid composite, the negatively charged poly(sodium 4-styrenesulfonate) (PSS), which played the role of the mediator of graphene sheets (PSS-GS), and the PEI, which possesses positive charge, were used and deposited on a silicon wafer. Through AFM characterization it was observed that the monolayer PEI/PSS-GS film appeared to have small uncovered areas and some overlapped platelets which did not occur in the case of three and five-layered hybrid films (Figure 11.13). The surface of (PEI/PSS-GS)₃ and (PEI/PSS-GS)₅ were completely covered, making the materials more compact. Macrotribological measurements showed that by increasing the numbers of the layers, the tribological behavior of the (PEI/PSS-GS)_n hybrid film can be improved significantly. The exceptional tribological properties of the film, which were demonstrated using a universal material tester tribometer, allow it to operate as a low-friction and anti-wear coating in micro- and nanoelectromechanical systems. Generally, the material is expected to be ideal in plenty of applications such as nanoelectronics, sensors, batteries, supercapacitors, and hydrogen storage devices.

Xia and his coworkers [43] studied the possibility of improving the function of lithium-ion batteries. In this way, thin films of MoO₂ NPs and graphene sheets were formed by LbL assembly and were evaluated as binder-free anodes. The hybrid nanocomposite was created between the anionic polyoxometalate clusters and the oxygen functional group of the GO, in presence of a cationic PE. The researchers managed to compose, after consecutive treatment in an Ar-H₂ atmosphere, a hybrid material with three-dimensional interlocked nanopores, where ultrafine

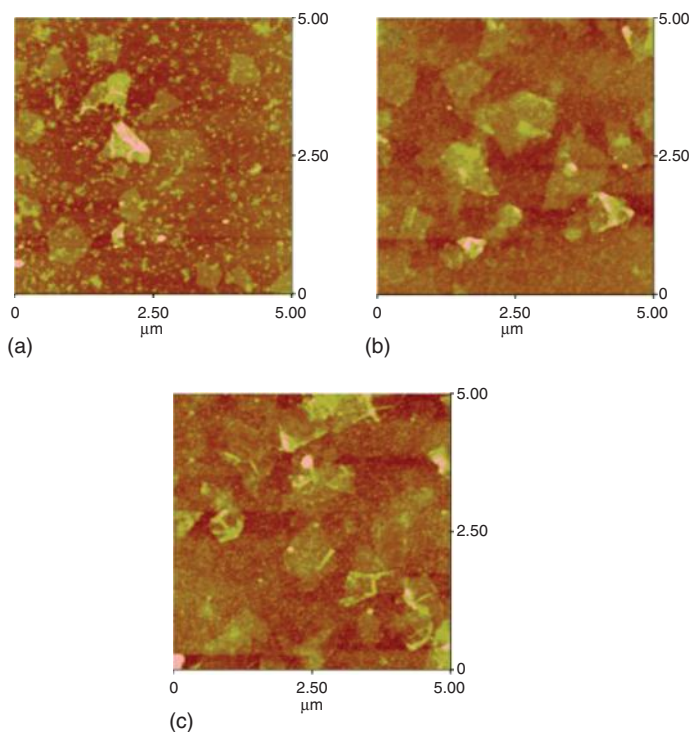


Figure 11.13 AFM images for different PEI/PSS-GS film samples ((a–c) represent the $(\text{PEI/PSS-GS})_n$, ($n=1, 3, 5$), respectively). (Reproduced with permission from Ref. [42].)

MoO_2 NPs were homogeneously deposited in the porous network of GNs. It was proved that the tested material, if used as an anode for lithium-ion batteries, would exhibit extraordinary electrochemical behavior with high specific capacity and fine cyclability. More specifically, the MoO_2 -graphene thin film electrode after 100 cycles of discharge-charge had specific capacity of around 675 mAh g^{-1} , rendering it extremely hopeful for lithium storage applications.

Finally, Jalili *et al.* made an effort to develop ultra-stiff and ultra-strong 3D architectures which could facilitate high elongation-at-break through LbL self-assembly [44]. They studied the usage of organic solvents as building blocks in order to construct self-assembled composites. More specifically, they tried to comprehend the solvophobic effect and the parameters of liquid crystalline graphene oxide (LC GO) dispersions in organic solvents, which directly affect the self-assembly technique. Toward this aim, they constructed GO-SWCNTs hybrid materials where the presence of *N*-cyclohexyl-2-pyrrolidone (CHP) in the dispersion of LC GO plays the role of a mediator between the LC GO and the SWCNTs. The attachment was realized through hydrophobic and π - π interactions. Moreover, the solvent of LC GO and CHP can debundle CNTs and might promote

the fabrication of fully ordered self-assembled CNTs-GO composites. This research could overcome many obstacles, such as solubility issues and water sensitivity, in the processability of a wide range of materials which require organic solvents.

11.3

Graphene-Based Hybrids through the Langmuir–Blodgett Approach

Thin films of thickness of a few nanometers (a monolayer) are the source of high expectations as being useful components in many practical and commercial applications such as sensors, detectors, displays, and electronic circuit components. The possibility to synthesize hybrid materials, almost without limitations, with desired structure and functionality in conjunction with a sophisticated thin film deposition technology enables the production of electrically, optically, and biologically active components on a nanometer scale. The LB technique is one of the most promising techniques for preparing such thin films as it enables

- the precise control of the monolayer thickness,
 - homogeneous deposition of the monolayer over large areas, and
 - the possibility of making multilayer structures with varying layer composition.
- An additional advantage of the LB technique is that monolayers can be deposited on almost any kind of solid substrate.

Many possible applications (optical, electrical, and biological) have been suggested over the years for LB films. Their characteristics include extremely thin films with high degree of structural order [45]. Among other layered materials, such as aluminosilicate nanoclays or layered double hydroxides, graphene has been widely used in the LB approach. High-quality graphene monolayers or multilayer films of novel graphene hybrids have been developed by integrating graphene matrices with a variety of guest species.

11.3.1

Monolayers of Graphene Oxide

Water-supported monolayers of graphene oxide single layers (GOSLs) can be made without any surfactant or stabilizing agent. Laura Cote *et al.* [46] in 2008 demonstrated LB assembly of GOSLs. The single layers formed stable dispersion against flocculation or coagulation when confined at the 2D air–water interface. The edge-to-edge repulsion between the single layers prevented them from overlapping during monolayer compression. The layers folded and wrinkled at their interacting edges at high surface pressure, leaving the interior flat. GOSL monolayers can be readily transferred to a solid substrate with density continuously tunable from dilute to closely packed and to overpacked monolayers of interlocking sheets. When single layers of very different sizes are brought together face to face, they can irreversibly stack to form double layers [46]. The geometry-dependent GOSL interaction revealed here should provide insight into the thin film processing

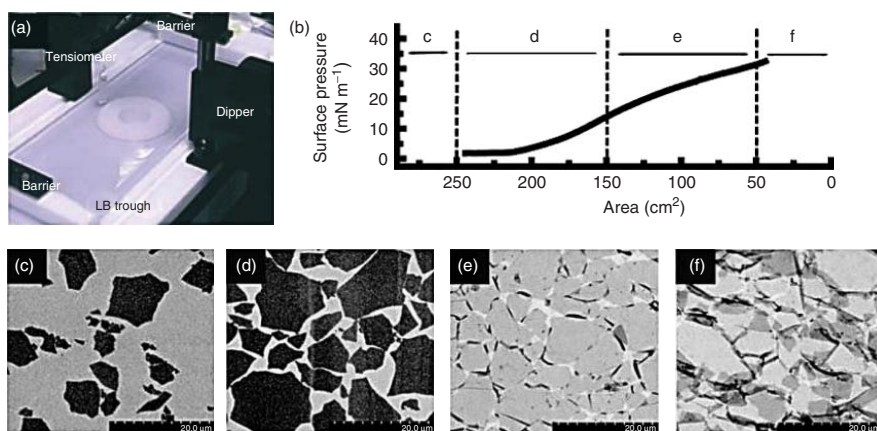


Figure 11.14 Langmuir-Blodgett assembly of graphite oxide single layers. (a–d) SEM images showing the collected graphite oxide monolayers on a silicon wafer at different regions of the isotherm. The packing density was continuously tuned: (a) dilute monolayer of isolated flat sheets, (b) monolayer of closely packed GO, (c) overpacked monolayer with sheets folded at interconnecting edges, and (d) overpacked monolayer with folded and partially overlapped sheets interlocking with each other. (e) Isothermal surface pressure–area plot showing the corresponding regions (a–d) at which the monolayers were collected. Scale bars in (a–d) represent 20 μm . (Reproduced with permission from Ref. [47].)

of GO materials since the packing of GOSLs affects surface roughness, film porosity, packing density, and so on. In addition, LB assembly readily creates a large-area monolayer of GOSL, which is a precursor for graphene-based electronic applications [46].

Amphiphilicity is a fundamental solution property of materials. The insight that GO is amphiphilic should lead to a better understanding of the processing and assembly of GO sheets. GO can be solution processed to form thin films by many techniques such as spin coating, drop casting, spraying, and dip coating. In 2009, Cote *et al.* [47] took advantage of GO surface activity and employed the classical molecular assembly methods such as the LB technique to create monolayers. In the classical LB technique, a surfactant monolayer is spread on the water surface and confined between two movable barriers (Figure 11.14a). As the barriers are closed, the surface density of molecules increases, leading to an increase in surface pressure or reduction in surface tension that can be continuously monitored by a tensiometer. The floating monolayers can then be transferred to a solid support by vertical dip coating.

Since GO is amphiphilic, it can be spread from alcohols that are even miscible with water, such as methanol. When methanol droplets are gently dropped on water surface, it can first spread rapidly on the surface before mixing with water. In this way, the GO surfactant sheets can be effectively trapped at the air–water interface [47]. The density of sheets can then be continuously tuned by moving the barriers. Upon compression, the monolayer exhibits a gradual increase in surface pressure, as shown in the surface pressure–area isotherm plot (Figure 11.14b). At the initial stage where the surface pressure is near zero, the collected film consists of dilute, well-isolated flat sheets (Figure 11.14c). As compression continues, a gradual increase in surface pressure begins to occur and the sheets start to close pack into a broken tile mosaic pattern over the entire surface (Figure 11.14d). Upon further compression, the soft sheets are forced to fold and wrinkle at their touching points in order to accommodate the increased pressure (Figure 11.14e). This is in stark contrast to traditional molecular or colloidal monolayers, which would collapse into double layers resulting in a constant or decreasing surface pressure when compressed beyond the close-packed regime. Even further compression resulted in interlocked sheets with nearly complete surface coverage (Figure 11.14f) [47]. The LB assembly produces flat GO thin films with uniform and continuously tunable coverage.

The LB technique was used by Xi Ling and Jin Zhang [48] the same year to construct mono- and multilayer ordered aggregates of protoporphyrin IX (PPP) as shown in Figure 11.15.

The Raman enhancement was dependent on the molecular configuration in contact with graphene, in which the functional group of PPP in direct contact with graphene has a stronger enhancement than other groups [48]. These results reveal that graphene-enhanced Raman scattering (GERS) is strongly dependent on the distance between graphene and the molecule, which is convincing evidence that the Raman enhancement effect based on graphene belongs to the chemical enhanced mechanism. This discovery provides a convenient system for the study

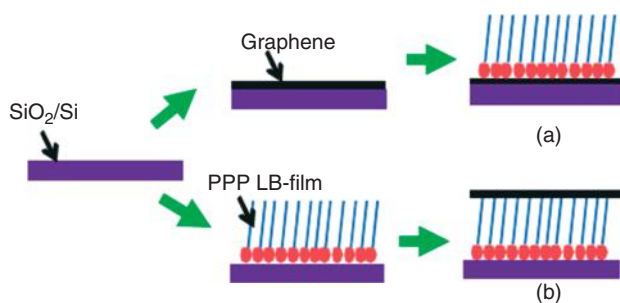


Figure 11.15 Schematic representation of the sample preparation. (Reproduced with permission from Ref. [48].)

of the chemical enhanced mechanism and will benefit further understanding of surface-enhanced Raman scattering (SERS).

Szabo *et al.* [49] observed a negligible amount of imperfections in LB films such as GO sheets folded back at interconnecting edges or face-to-face aggregates that were deposited in a hydrophilic substrate. These highly ordered monolayers are very promising for advanced electronic applications because very large areas can be covered by densely tiled GO nanosheets, which can provide continuous electrical pathways after reduction to conductive graphene [49]. LB films of chemically derived graphene may be especially beneficial for the fabrication of optically transparent flexible circuits, where the use of ITO is limited because of its rigidity and fragility.

Wang *et al.* [50] in 2011 developed a universal technique for size fractionation of GO sheets by just adjusting the pH value of GO dispersion. The hydrazine-reduced LB films of large lateral dimensions showed much higher conductivities than those of small lateral dimensions. Furthermore, the thin film of large lateral dimensions prepared by filtration exhibited a smaller d-space and much higher tensile strength and modulus than those of small lateral dimension films. The lateral dimensions of GO sheets have strong effects on the structures and properties of the self-assembled GO films. Larger GO sheets favor the formation of paper-like films with more tight and perfect structures, which greatly improved their mechanical properties. Furthermore, LB films of larger GO sheets also showed higher conductivities after chemical reduction because of their more compact morphology, fewer structural defects, and lower contact resistances [50].

A year later, Imperiali *et al.* [51] investigated the structure and properties of the GO interfacial layer and evaluated the conditions for the formation of freestanding films. The rheological properties have been shown to be responsible for the efficiency of such layers in stabilizing water–oil emulsions. Moreover, because of the mechanical integrity, large-area monolayers can be deposited by, for example, LB techniques using aqueous subphases. These films can be turned into TCFs upon subsequent chemical reduction.

Spectroscopic studies of large sheets of GO and rGO monolayers, which were prepared by LB technique, were investigated in the same year by Sutar *et al.* [52]. The GO monolayers were reduced by hydrazine exposure followed by heat treatment in vacuum and argon atmosphere to obtain rGO monolayers, without affecting the morphological stability of the sheets. Fourier transform infrared (FTIR) data have revealed that the reduction process results in a significant decrease in oxygen functionalities. The X-ray photoelectron spectroscopy (XPS) data showed that during the reduction process, I_D/I_G ratio decreases, which is also indicative of decrease in the fraction of non-graphitic carbon in the monolayers.

11.3.2

Nanocomposite Films

An LB approach for highly efficient fabrication of nanoscrolls from functionalized GO single sheets was reported by Yan Gao *et al.* [53]. Transmission electron microscope study revealed that the scroll has a tubular structure without caps at its ends. The scrolls align parallel to the moving barriers of the LB equipment and exhibit a loose–dense pattern during the LB compression process. They also realized that specific solvents can unwind the scrolled structures. This method opened up a new avenue for high-yield fabrication of carbon nanoscrolls using functionalized GO as the building block.

Two years later, in 2012 Ramesha *et al.* [54] initiated the possibility of 2D *in situ* electrochemical polymerization in a Langmuir trough. They spread exfoliated graphene oxide (EGO) on water surface to bring the anilinium cations present in the subphase to air–water interface through electrostatic interactions (Figure 11.16).

Subsequent electrochemical polymerization of aniline under applied surface pressure results in the EGO/PANI composite with PANI in planar polaronic form. For the deposition in a grassy carbon substrate, a Langmuir–Schaefer mode (horizontal deposition) was applied.

The same year, Narayanam and his coworkers [55] worked on GO–Cd composite LB monolayers by introducing Cd^{2+} ions into the subphase. The changes in the behavior of the Langmuir monolayer isotherm in the presence of Cd^{2+} ions are attributed to changes in the microstructure and density of the GO sheets on the subphase surface. The incorporation of Cd ions into the GO monolayers causes some overlapping of sheets and extensive formation of wrinkles. Sulphidation of the GO–Cd sheets results in the formation of uniformly distributed CdS nanocrystallites on the entire basal plane of the GO monolayers [55]. The de-bonding of Cd with oxygen functional groups results in a reduction of the wrinkles. The GO sheets act primarily as a platform for the interaction of metal ions with oxygen functionalities, and their structure and characteristic features are not affected by either uptake of Cd or formation of CdS.

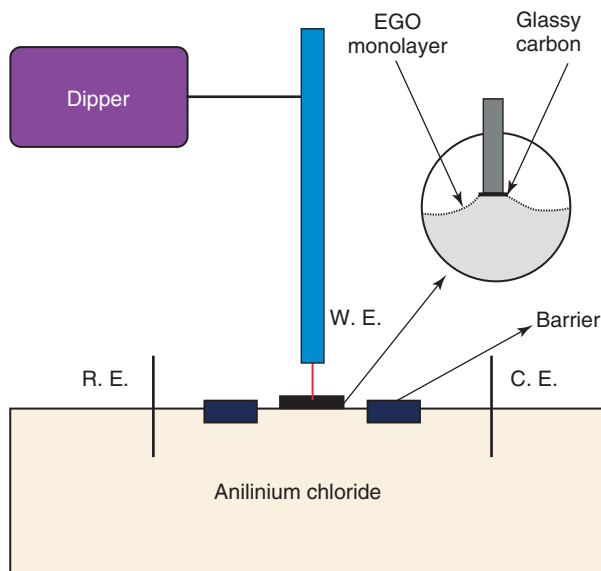


Figure 11.16 Experimental LB setup for *in situ* polymerization (R.E., Reference Electrodes; W.E., Working Electrodes; and C.E., Counter Electrodes). (Reproduced with permission from Ref. [54].)

11.3.3

Applications and Properties of LB Thin Films

Li and his coworkers [56] in 2008 reported that the exfoliation–reintercalation–expansion of graphite can produce high-quality single-layer graphene sheets stably suspended in organic solvents. The graphene sheets exhibit high electrical conductance at room and cryogenic temperatures. Large amounts of graphene sheets in organic solvents are made into large transparent conducting films by LB assembly in a layer by layer manner. The chemically derived, high-quality graphene sheets could lead to future scalable graphene devices.

Cao and his coworkers [57] in 2010, presented a new class of high-performance photoresponsive molecular FETs formed from LB monolayers of copper phthalocyanine (CuPc), using two-dimensional (2D) ballistically conductive single-layer graphene as planar contacts. The unique feature is the integration of LB technique with the fabrication of nanogap electrodes to build functional molecular electronic devices. LB technique offers a promising and reliable method to prepare large-area ordered ultrathin films with well-defined architectures (Figure 11.17).

The integration of LB technique with sophisticated micro/nanofabrication affords efficacious molecular FETs with bulk-like carrier mobility (as high as $0.04 \text{ cm}^2 (\text{V s})^{-1}$), high on/off current ratios (over 10^6), high yields (almost 100%),

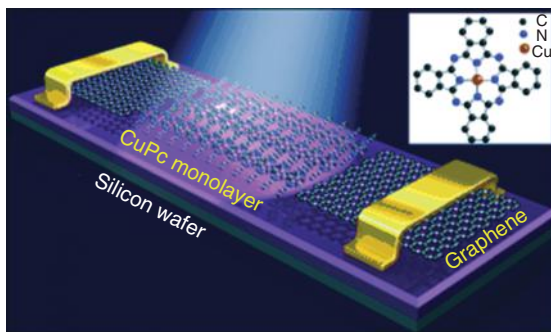


Figure 11.17 The structure of the CuPc monolayer transistor device with metal electrodes protected by a 50 nm layer of silicon dioxide. Inset: the molecular structure of copper phthalocyanine (CuPc). (Reproduced with permission from Ref. [57].)

and high reproducibility. These transistors are formed from self-assembled uniform monolayers of p-type CuPc semiconductors using single-layer graphene as planar contacts. Another important result is that these transistors are ultrasensitive to light, although their active channel consists of only a single 1.3 nm thick layer, forming the basis for new types of environmental sensors and tunable photodetectors. This method of incorporating molecular functionalities into molecular electronic devices by combining bottom-up self-assembly and top-down device fabrication should speed up the development of nanometer/molecular electronics in the future.

Negatively charged functionalized GO layers were incorporated into polyelectrolyte multilayers (PEMs) fabricated in an LbL assembly via LB deposition by Kulkarni *et al.* [58] (Figure 11.18) in the same year. These LbL-LB GO nanocomposite films were released as robust freely standing membranes with large lateral dimensions (centimeters) and a thickness of around 50 nm.

Micromechanical measurements showed enhancement of the elastic modulus by an order of magnitude, from 1.5 GPa for pure LbL membranes to about 20 GPa for only 8.0 vol% GO encapsulated LbL membranes. These tough nanocomposite PEMs can be freely suspended over large (few millimeters) apertures and sustain large mechanical deformations.

At the same time, Gengler and his coworkers [12] developed a straightforward method to deposit uniform single-layer graphene films on arbitrary substrates without size limitation and under ambient conditions. The fast high-yield method allows control of graphene coverage by simple adjustment of the applied surface pressure in an LB trough. The prepared films could sustain all physical and chemical treatments associated with the lithography process without any loss of material. Additionally, among all chemically exfoliated graphite, the flakes obtained show one of the lowest resistivities at the Dirac charge neutrality point (≈ 65 kV) and provide evidence for switching from a hole-conduction regime to an electron-conduction regime. The deposition method illustrated could also be applied to other types

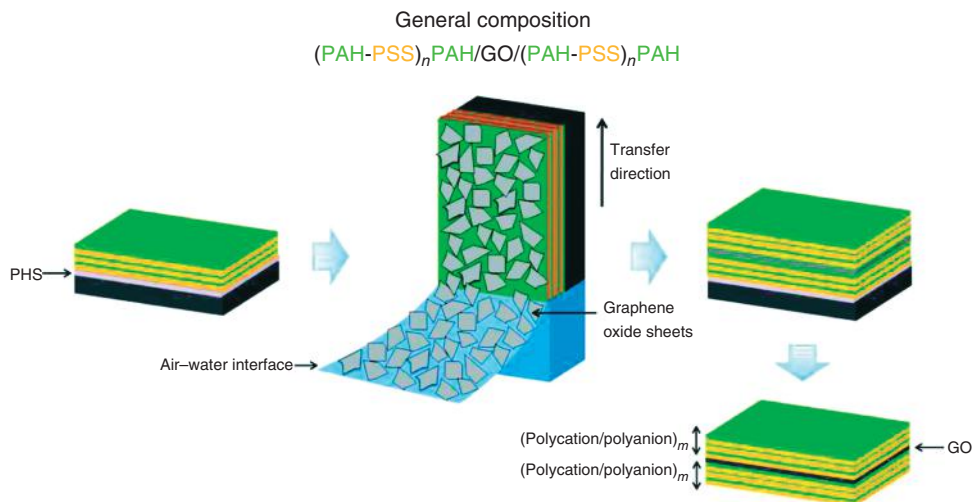


Figure 11.18 Schematic representation of fabrication and assembly of freestanding GO-LbL membrane. (Reproduced with permission from Ref. [58].)

of exfoliated graphene/graphite produced without passing through the graphite oxidation step.

A few-layer *r*GO thin film on a Si/SiO₂ wafer using the LB method, followed by thermal reduction, was fabricated by Yin *et al.* [59] in 2012 (Figure 11.19). After photochemical reduction of Pt NPs (Pt NPs) on *r*GO, the obtained Pt NPs/*r*GO composite is employed as the conductive channel in a solution-gated FET, which is then used for real-time detection of hybridization of single-stranded deoxyribonucleic acid (ssDNA) with high sensitivity (2.4 nM). Such a simple, but effective method for the fabrication of *r*GO-based transistors shows great potential for the mass production of graphene-based electronic biosensors.

In the same period, Sutar *et al.* [60] investigated the electronic structure of GO and *r*GO monolayers using photoelectron spectroscopy. The GO monolayers was obtained by the LB route and suitably treated to obtain *r*GO monolayers. In comparison with GO, *r*GO monolayers showed steeper Fermi edge, decrease in work function (WF), and increase in p electron density of states (DOS) because of the removal of oxygen functional groups or increase in graphitic carbon species. The *r*GO, as compared to GO, also exhibited Auger features attributable to the increase in p electron DOS. The effective number of valence electrons as obtained from plasmon loss features showed 28% increase upon reduction, associated with the increase in graphitic carbon content. Thus, by controlled reduction of GO, it should be possible to tune its electronic structure and hence electronic/optoelectronic properties.

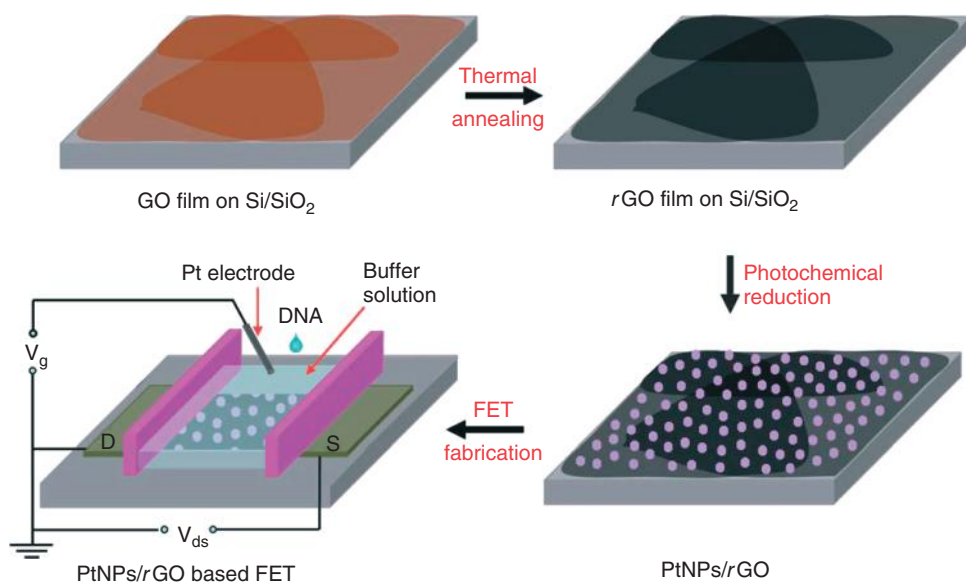


Figure 11.19 Schematic illustration of fabrication of a solution-gated FET device based on PtNPs/rGO films for DNA detection. (Reproduced with permission from Ref. [59].)

A study on composite electrode materials based on GO and transition metal oxide nanostructures for supercapacitor applications was presented by Lake *et al.* [61] in 2012. Electrophoretic deposition of GO on a conductive substrate was used to form rGO films through chemical reduction. The strong interaction of GO with Co₃O₄ and MnO₂ nanostructures was demonstrated in the self-assembled LB monolayer composite, showing the potential to fabricate thin film supercapacitor electrodes without using binder materials. They demonstrated a facile, two-step process of metal oxide and graphene nanocomposite to fabricate binder-free supercapacitor electrodes [61]. The potential high conductive pathways and high surface areas provided by the graphene layer interfaced with the electrolyte and the high electrochemical capacitive charge storage from Co₃O₄ and MnO₂ nanocomposites can be tuned to exhibit optimal energy and power densities. The initial hybrid electrode comprising of a Co₃O₄ and MnO₂ nanocomposite with a top rGO layer provides more efficient contact of electrolyte ions, electroactive sites, and shorter transport and diffusion path lengths, leading to high specific capacitances compared with traditional double layer supercapacitors [61]. The feasibility of such an electrode material is supported by the favorable interactions between the metal oxides as well as with rGO. This two-step composite nanostructure thin film process is nontoxic and scalable for binder-free supercapacitor processing.

Fragile organic LB films of C₂₂ fatty acid cadmium salts (cadmium (II) behenate) were covered by a compressed monolayer LB film of GO flakes by Petersen *et al.* [62].

The structure of the mGO-protected LB films was found to be perfectly preserved. The metal deposition completely destroys the first two LB layers of unprotected films. This study provides clear evidence of the efficient protection offered by a single atomic layer of GO.

TCFs were produced by Zheng *et al.* [63] in 2011 using the ultra-large graphene oxide (UL-GO) sheets that were deposited layer by layer on a substrate using the LB assembly technique. The density and degree of wrinkling of the UL-GO monolayers are turned from dilute, closely packed flat UL-GO to graphene oxide wrinkles (GOWs) and concentrated graphene oxide wrinkles (CGOWs) by varying the LB processing conditions [63]. The method demonstrated opens the way for high-yield fabrication of GOWs or CGOWs that are considered promising materials for hydrogen storage, supercapacitors, and nanomechanical devices. The films produced from UL-GO sheets with a closely packed flat structure exhibit exceptionally high electrical conductivity and transparency after thermal reduction and chemical doping treatments. A remarkable sheet resistance of $\sim 500 \Omega \text{sq}^{-1}$ at 90% transparency was obtained, which outperformed the graphene films grown on a Ni substrate by CVD [63]. The technique used to produce transparent conductive UL-GO thin films is facile, inexpensive, and tunable for mass production.

Continuing his research, Zheng *et al.* [64] composed large-area hybrid transparent films of UL-GO and functionalized single walled carbon nanotubes (SWCNTs) via a LbL-LB assembly process. The optoelectrical properties are much better than the corresponding of GO films prepared by the same technique, and the highest among all graphene, GO and/or CNT thin films reported in the literature (Figure 11.20).

The LB assembly technique developed is capable of controlling the film composition, structure, and thickness, while it is highly suitable for fabrication of transparent conducting optoelectronic devices on a large scale without extra post-transfer processes. With further refinement of the synthesis technique, this versatile material could offer the properties required for next generation optoelectronic devices.

Another work from Zheng and his coworkers [65] was presented in the same period. They synthesized monolayer UL-GO sheets with diameter up to about 100 nm based on a chemical method. TCFs were produced using the UL-GO sheets that were deposited layer by layer on a substrate by the LB assembly technique. The films produced from UL-GO sheets with a closely packed flat structure exhibit exceptionally high electrical conductivity and transparency after thermal reduction. A remarkable sheet resistance of $605 \Omega \text{sq}^{-1}$ at 86% transparency was obtained. Authors claimed that the proposed technique for the production of TCFs is facile, inexpensive, and tunable for mass production.

A novel eutectic-based method for fabrication of high-quality graphene flakes was introduced by Park *et al.* [66] in 2012. They confirmed that the alkali metal (potassium) between graphite interlayers is successfully inserted at the optimized operation condition. The resulting graphene flakes preserve the unique properties of graphene. These high-quality graphene flakes were stably dispersed (>6 months)

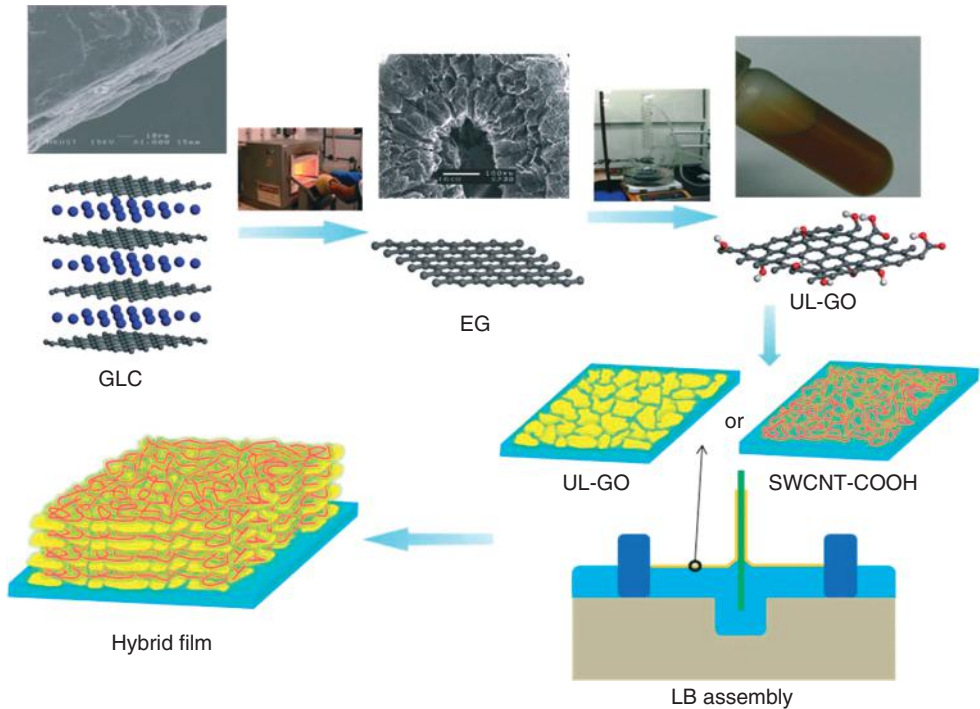


Figure 11.20 Flow chart for the synthesis of UL-GO/SWCNT hybrid films. (Reproduced with permission from Ref. [64].)

in pyridine solution without additional functionalization and surfactant stabilization. Transparent conducting graphene films from well-dispersed graphene flakes with high yield ($\sim 60\%$) were produced by the modified LB assembly [66]. The resulting graphene film exhibits a sheet resistance of $\sim 930 \Omega \text{ sq}^{-1}$ at a transparency of $\sim 75\%$ and a high conductivity ($\sim 91.000 \text{ S m}^{-1}$). The overall results suggest that the eutectic-based method to graphene production is a scalable and low-cost route that brings graphene-based electronics and composite fields closer to practical applications.

Other applications of graphene-based films were reported by Seo *et al.* [67]. The authors fabricated a p–n diode junction of p-type *rGO*/n-doping Si substrate. Electric field-induced (EFI) reduction of GO was performed by conductive atomic force microscopy (C-AFM) in order to create an *rGO* p–n nanopattern diode in a dry and nondestructive single-pot process. Single GO sheets were deposited by the LB method onto semiconducting (n- and p-doping Si) substrates that control charge transfer at the *rGO* interface. EFI nanolithography resulted in locally reduced GO nanopatterns on GO sheets corresponding to the application of a negative bias voltage on an n-doping Si substrate. EFI nanolithography performed as a function of applied voltage, and the *rGO* nanopatterned at -10.0 V

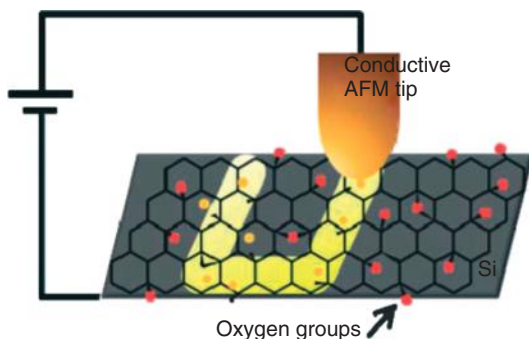


Figure 11.21 EFI reduction nanopatterning for the formation of *rGO* p–n diode junctions. (Reproduced with permission from Ref. [67].)

sub showed high conductivity, comparable with that of the chemically *rGO* [67] (Figure 11.21).

In addition, transport of *rGO* sheets, which were efficiently reduced under a local electric field, showed a uniform conductivity at sheet edges and the basal plane. Current–voltage (I – V) characteristics of *rGO* on n- and p-doping Si substrates indicated that EFI reduction nanolithography produced p-type *rGO* nanopatterns on the Si substrates. This junction is an indispensable electronic component that rectifies charge transport and prevents interference between neighboring electronic components in a high-density integrated crossbar devices.

Li and his coworkers [68] used GO as a novel substrate for dip-pen nanolithography (DPN). After the GO was transferred onto a SiO_2 substrate using the LB technique, CoCl_2 was patterned on both GO and exposed SiO_2 substrates simultaneously by DPN, which was used for growth of different structured CNTs as presented in Figure 11.22. This novel graphene/CNT composite might have potential applications in sensing, solar cells, electrode materials, and so on.

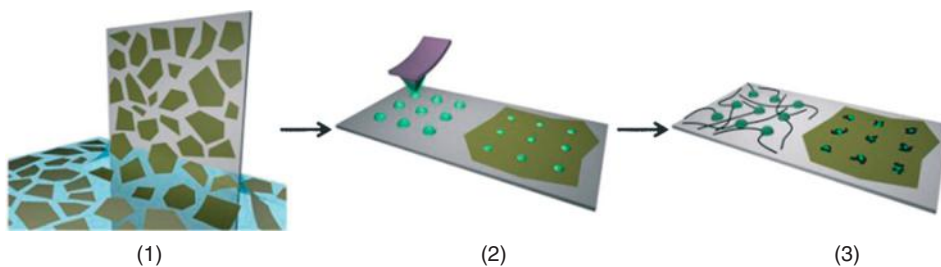


Figure 11.22 Schematic illustration of the experimental procedure. (1) Single-layer GO sheets are transferred onto SiO_2 by using the LB technique. (2) CoCl_2 is

simultaneously patterned on GO and SiO_2 by DPN. (3) CNTs grow on patterned catalyst dots on GO and SiO_2 after CVD. (Reproduced with permission from Ref. [68].)

11.4

Conclusions

LbL assembly has attracted the attention of materials scientific community recently as it is a simple, low-cost, and importantly flexible technique for fabricating multilayered hybrid films. The versatility of this method allows the development of various procedures for the growth of the films by using diverse synthetic or deposition techniques such as sputtering or CVD. Among them, the LB technique is one of the most promising LbL processes as it enables the precise control of the monolayer thickness while allowing homogeneous deposition over large areas and on almost any kind of solid substrate. On the other hand, graphene being a 2D single-layered material exhibits great optoelectronic and mechanical properties, which could be further tailored or enhanced with LbL assembling. In this direction, numerous studies have been reported during the past years concerning the modification of graphene sheets by LbL assembly to produce hybrid films. Owing to their exceptional properties, these multilayered systems are employed in a variety of different application areas from electronics to tribologic fields. However, there are still many challenges in designing and fabricating even better and higher quality graphene-based hybrid films.

References

- Iler, R.K. (1966) *J. Colloid Interface Sci.*, **21**, 569.
- Decher, G. and Hong, J.D. (1991) *Ber. Bunsen. Phys. Chem.*, **95**, 1430.
- Decher, G. and Hong, J.D. (1991) *Makromol. Chem. Macromol. Symp.*, **46**, 321.
- Decher, G., Hong, J.D., and Schmitt, J. (1992) *Thin Solid Films*, **210**, 831.
- Lvov, Y., Decher, G., and Moehwald, H. (1993) *Langmuir*, **9**, 481.
- Ariga, K., Hill, J.P., and Ji, Q. (2007) *Phys. Chem. Chem. Phys.*, **9**, 2319.
- Decher, G. (1997) *Science*, **277**, 1232.
- Zhu, C., Guo, S., Zhai, Y., and Dong, S. (2010) *Langmuir*, **26**, 7614.
- Guo, C.X., Yang, H.B., Sheng, Z.M., Lu, Z.S., Song, Q.L., and Li, C.M. (2010) *Angew. Chem. Int. Ed.*, **49**, 3014.
- Hong, J.Y., Shin, K.Y., Kwon, O.S., Kang, H., and Jang, J. (2011) *Chem. Commun.*, **47**, 7182.
- Shim, B.S., Podsiadlo, P., Lilly, D.G., Agarwal, A., Lee, J., Tang, Z., Ho, S., Ingle, P., Paterson, D., Lu, W., and Kotov, N.A. (2007) *Nano Lett.*, **7**, 3266.
- Gengler, R.Y.N., Veligura, A., Enotiadis, A., Diamanti, E.K., Gournis, D., Jozsa, C., van Wees, B.J., and Rudolf, P. (2010) *Small*, **6**, 35.
- Shen, J., Hu, Y., Li, C., Qin, C., Shi, M., and Ye, M. (2009) *Langmuir*, **25**, 6122.
- Kong, B.S., Geng, J., and Jung, H.T. (2009) *Chem. Commun.*, 2174.
- Seshan, K. (ed.) (2002) *Handbook of Thin-Film Deposition Processes and Techniques: Principles, Methods, Equipment and Applications*, 2nd edn, Noyes Publications, Norwich, NY.
- Wang, Y., Tong, S.W., Xu, X.F., Özyilmaz, B., and Loh, K.P. (2011) *Adv. Mater.*, **23**, 1514.
- Bae, S., Kim, H., Lee, Y., Xu, X., Park, J.S., Zheng, Y., Balakrishnan, J., Lei, T., Ri Kim, H., Song, Y.I., Kim, Y.J., Kim, K.S., Özyilmaz, B., Ahn, J.H., Hong, B.H., and Iijima, S. (2010) *Nat. Nano.*, **5**, 574.
- Li, H., Pang, S., Wu, S., Feng, X., Müllen, K., and Bubeck, C. (2011) *J. Am. Chem. Soc.*, **133**, 9423.

19. Güneş, F., Shin, H.J., Biswas, C., Han, G.H., Kim, E.S., Chae, S.J., Choi, J.Y., and Lee, Y.H. (2010) *ACS Nano*, **4**, 4595.
20. Li, Z., Wang, J., Liu, X., Liu, S., Ou, J., and Yang, S. (2011) *J. Mater. Chem.*, **21**, 3397.
21. Yu, D. and Dai, L. (2009) *J. Phys. Chem. Lett.*, **1**, 467.
22. Sheng, K., Bai, H., Sun, Y., Li, C., and Shi, G. (2011) *Polymer*, **52**, 5567.
23. Lee, D.W., Hong, T.K., Kang, D., Lee, J., Heo, M., Kim, J.Y., Kim, B.S., and Shin, H.S. (2011) *J. Mater. Chem.*, **21**, 3438.
24. Park, J.S., Cho, S.M., Kim, W.J., Park, J., and Yoo, P.J. (2011) *ACS Appl. Mater. Interfaces*, **3**, 360.
25. Yao, H.-B., Wu, L.H., Cui, C.H., Fang, H.Y., and Yu, S.H. (2010) *J. Mater. Chem.*, **20**, 5190.
26. Rani, A., Oh, K.A., Koo, H., Lee, H.J., and Park, M. (2011) *Appl. Surf. Sci.*, **257**, 4982.
27. Wang, X., Wang, J., Cheng, H., Yu, P., Ye, J., and Mao, L. (2011) *Langmuir*, **27**, 11180.
28. Ishikawa, R.B.M., Wada, H., Kurokawa, Y., Sandhu, A., and Konagai, M. (2012) *Jpn. J. Appl. Phys.*, **51**, 11PF01.
29. Seok, C.K., Fei, L., Seob, C.J., and Seok, S.T. (2010) Nanotechnology (IEEE-NANO), 10th IEEE Conference on, 2010, p. 683.
30. Yoo, J.J., Balakrishnan, K., Huang, J., Meunier, V., Sumpster, B.G., Srivastava, A., Conway, M., Mohana Reddy, A.L., Yu, J., Vajtai, R., and Ajayan, P.M. (2011) *Nano Lett.*, **11**, 1423.
31. Zhang, B. and Cui, T. (2011) *Appl. Phys. Lett.*, **98**, 073116.
32. Ji, Q., Honma, I., Paek, S.M., Akada, M., Hill, J.P., Vinu, A., and Ariga, K. (2010) *Angew. Chem.*, **122**, 9931.
33. Zeng, G., Xing, Y., Gao, J., Wang, Z., and Zhang, X. (2010) *Langmuir*, **26**, 15022.
34. Chang, H., Wang, X., Shiu, K.K., Zhu, Y., Wang, J., Li, Q., Chen, B., and Jiang, H. (2013) *Biosens. Bioelectron.*, **41**, 789.
35. Qin, H., Liu, J., Chen, C., Wang, J., and Wang, E. (2012) *Anal. Chim. Acta*, **712**, 127.
36. Shan, C., Wang, L., Han, D., Li, F., Zhang, Q., Zhang, X., and Niu, L. (2013) *Thin Solid Films*, **534**, 572.
37. Ma, J., Cai, P., Qi, W., Kong, D., and Wang, H. (2013) *Colloids Surf., A: Physicochem. Eng. Aspects*, **426**, 6.
38. Mao, Y., Bao, Y., Wang, W., Li, Z., Li, F., and Niu, L. (2011) *Talanta*, **85**, 2106.
39. Liu, Y., Liu, Y., Feng, H., Wu, Y., Joshi, L., Zeng, X., and Li, J. (2012) *Biosens. Bioelectron.*, **35**, 63.
40. Liu, S., Yan, J., He, G., Zhong, D., Chen, J., Shi, L., Zhou, X., and Jiang, H. (2012) *J. Electroanal. Chem.*, **672**, 40.
41. Zhao, X., Zhang, Q., Hao, Y., Li, Y., Fang, Y., and Chen, D. (2010) *Macromolecules*, **43**, 9411.
42. Liu, S., Ou, J., Li, Z., Yang, S., and Wang, J. (2012) *Appl. Surf. Sci.*, **258**, 2231.
43. Xia, F., Hu, X., Sun, Y., Luo, W., and Huang, Y. (2012) *Nanoscale*, **4**, 4707.
44. Jalili, R., Aboutalebi, S.H., Esrafilzadeh, D., Konstantinov, K., Moulton, S.E., Razal, J.M., and Wallace, G.G. (2013) *ACS Nano*, **7**, 3981.
45. KSV NIMA <http://www.ksvnama.com/technologies/langmuir-blodgett-langmuir-schaefer-technique> (accessed 24 October 2013).
46. Cote, L.J., Kim, J., Tung, V.C., Luo, J.Y., Kim, F., and Huang, J.X. (2011) *Pure Appl. Chem.*, **83**, 95.
47. Cote, L.J., Kim, F., and Huang, J.X. (2009) *J. Am. Chem. Soc.*, **131**, 1043.
48. Ling, X. and Zhang, J. (2010) *Small*, **6**, 2020.
49. Szabo, T., Hornok, V., Schoonheydt, R.A., and Dekany, I. (2010) *Carbon*, **48**, 1676.
50. Wang, X.L., Bai, H., and Shi, G.Q. (2011) *J. Am. Chem. Soc.*, **133**, 6338.
51. Imperiali, L., Liao, K.H., Clasen, C., Franssaer, J., Macosko, C.W., and Vermant, J. (2012) *Langmuir*, **28**, 7990.
52. Sutar, D.S., Narayanam, P.K., Singh, G., Botcha, V.D., Talwar, S.S., Srinivasa, R.S., and Major, S.S. (2012) *Thin Solid Films*, **520**, 5991.
53. Gao, Y., Chen, X.Q., Xu, H., Zou, Y.L., Gu, R.P., Xu, M.S., Jen, A.K.Y., and Chen, H.Z. (2010) *Carbon*, **48**, 4475.
54. Ramesha, G.K., Kumara, A.V., and Sampath, S. (2012) *J. Phys. Chem. C*, **116**, 13997.
55. Narayanam, P.K., Singh, G., Botcha, V.D., Sutar, D.S., Talwar, S.S., Srinivasa,

- R.S., and Major, S.S. (2012) *Nanotechnology*, 23.
56. Li, X.L., Zhang, G.Y., Bai, X.D., Sun, X.M., Wang, X.R., Wang, E., and Dai, H.J. (2008) *Nat. Nanotech.*, 3, 538.
57. Cao, Y., Wei, Z.M., Liu, S., Gan, L., Guo, X.F., Xu, W., Steigerwald, M.L., Liu, Z.F., and Zhu, D.B. (2010) *Angew. Chem. Int. Ed.*, 49, 6319.
58. Kulkarni, D.D., Choi, I., Singamaneni, S., and Tsukruk, V.V. (2010) *ACS Nano*, 4, 4667.
59. Yin, Z.Y., He, Q.Y., Huang, X., Zhang, J., Wu, S.X., Chen, P., Lu, G., Zhang, Q.C., Yan, Q.Y., and Zhang, H. (2012) *Nanoscale*, 4, 293.
60. Sutar, D.S., Singh, G., and Botcha, V.D. (2012) *Appl. Phys. Lett.*, 101.
61. Lake, J.R., Cheng, A., Selverston, S., Tanaka, Z., Koehne, J., Meyyappan, M., and Chen, B. (2012) *J. Vac. Sci. Technol. B*, 30.
62. Petersen, S.R., Glyvradal, M., Boggild, P., Hu, W., Feidenhans'l, R., and Laursen, B.W. (2012) *ACS Nano*, 6, 8022.
63. Zheng, Q.B., Ip, W.H., Lin, X.Y., Yousefi, N., Yeung, K.K., Li, Z.G., and Kim, J.K. (2011) *ACS Nano*, 5, 6039.
64. Zheng, Q.B., Zhang, B., Lin, X.Y., Shen, X., Yousefi, N., Huang, Z.D., Li, Z.G., and Kim, J.K. (2012) *J. Mater. Chem.*, 22, 25072.
65. Zheng, Q.B., Shi, F., and Yang, J.H. (2012) *Trans. Nonferrous Met. Soc. China*, 22, 2504.
66. Park, K.H., Kim, B.H., Song, S.H., Kwon, J., Kong, B.S., Kang, K., and Jeon, S. (2012) *Nano Lett.*, 12, 2871.
67. Seo, S., Jin, C., Jang, Y.R., Lee, J., Kim, S.K., and Lee, H. (2011) *J. Mater. Chem.*, 21, 5805.
68. Li, H., Cao, X.H., Li, B., Zhou, X.Z., Lu, G., Liusman, C., He, Q.Y., Boey, F., Venkatraman, S.S., and Zhang, H. (2011) *Chem. Commun.*, 47, 10070.

Index

a

- adsorption
 - on graphene 201–202
 - via π -stacking 110–111
 - – drugs 111
 - – enzymes, proteins, and macromolecules immobilization 116
 - – non-covalent interactions with nucleic acids and aptamers 113–116
 - – pyrene derivatives 111, 112–113
- affinity immobilization 144
- amidation 62, 69, 70, 87, 89, 98
- 6-amino-4-hydroxy-naphthalenesulfonic (ANS) acid 83, 84
- aminopropyl triethoxysilane (APTS) 83, 84
- antibodies tethering 105–106
- aryl amine terminated triphenylamine based polyazomethine (TPAPAM) 69–70
- aryne addition 36–37
- atomic force microscopy (AFM) 3, 8, 9, 10, 16, 39, 77, 164, 181, 188, 193, 212, 226, 258, 263, 302, 303, 320, 325, 371, 374, 384
- atom transfer radical polymerization method (ATRP) 43, 73, 75
- azobenzene chromophore covalently functionalized on GO (Azo-GO) 67–69
- azomethine ylide 1,3-dipolar cycloaddition 22–24
 - through substituted aldehyde pathway 24–27
 - through substituted α amino acid pathway 27–28

b

- bandgap engineering 173, 184, 185, 186, 190, 193, 195
- Bingel type cycloaddition 37–39
- biocatalysis 155, 156–159

- biofuel cells 159–161
- biomolecules 205–207
- biopolymers covalent linkage 103, 105
- biosensors 145–146
 - cytochrome *c*-based biosensors 152
 - DNA sensors 152, 153–154
 - glucose oxidase-based biosensors 146–150
 - horseradish peroxide-based biosensors 150–151
 - immunosensors and aptasensors 154–155
 - protein/enzyme biosensors 152
 - tyrosinase-based biosensors 151
- boron doping 320–321, 326–329
 - chemical vapor deposition 323–326
 - mechanical exfoliation 321
 - thermal annealing 321, 322–323
- boron nitride (BN) doping 329–333

c

- C₆₀ nanocomposites 255–256
 - covalent bonding on GO 256
 - deposition on graphene 256, 257–262
- camptothecin (CPT) 122
- carbene addition 35–36
- carbodiimide chemistry 142
- carbon nanospheres 274, 275, 276–277
- carbon nanostructures 255
 - graphene–C₆₀ nanocomposites 255–256
 - – covalent bonding on GO 256
 - – deposition on graphene 256, 257–262
 - graphene–carbon nanospheres 274, 275, 276–277
 - graphene–carbon nitride dots hybrid nanocomposite 277, 279
 - graphene–CNT hybrid nanostructures 262, 263–264
 - – graphene–CNT composites by simple mixing 264–272

- carbon nanostructures (*contd.*)
 - – graphene–CNTs hybrid nanostructures 272–274
 - carbon nanotube (CNT) hybrid nanostructures 262, 263–264
 - graphene–CNT composites by simple mixing 264–272
 - graphene–CNTs hybrid nanostructures 272–274
 - carbon nitride dots 277, 279
 - carboxylic acids 61
 - ammonia interaction and epoxides 80, 81
 - enrichment 81, 82
 - epoxides reaction and hydroxyl groups 78, 79–80
 - GO esterification 71–75
 - GO functionalization through heterocyclic ring formation 75–77
 - and hydroxyl groups reaction with isocyanate derivatives 78
 - organic functionalization through amide bond formation 61–71
 - chemical functionalization, for biomedical applications 95–97
 - covalent functionalization of graphene nanomaterials 97–99
 - – antibodies tethering 105–106
 - – biopolymers covalent linkage 103, 105
 - – graphene oxide reduction 99, 100
 - – graphene oxide synthesis 99
 - – nucleic acids attachment 106–108
 - – organic molecules and biomolecules attachment 108, 109–110
 - – PEGylated-GO conjugates 100–103
 - – peptides and enzymes grafting 108
 - GO functionalized with targeting ligands and antibodies
 - – antibody-functionalized GO for radioimaging and biosensing 127–129
 - – folic acid-conjugated GO 125, 127
 - non-covalent functionalization, of graphene 110
 - – adsorption via π -stacking 110–116
 - – electrostatic and hydrophobic interactions 116–121
 - polymer -and biopolymer-grafted graphene nanomaterials as nanocarriers 121, 122
 - – chitosan-functionalized GO 125
 - – polymer-functionalized GO for drug delivery 122–123
 - – polymer-functionalized GO for gene delivery 123–125
 - chemical functionalization route 288–289
 - chemical vapor deposition (CVD) 96, 220, 227, 272, 273, 274, 275, 276, 283, 293–300, 323–326, 329, 331, 332, 352, 363, 364
 - chitosan 63, 65, 105, 125
 - chromophores 64, 65–69
 - circular dichroism (CD) spectroscopy 141
 - click chemistry 87–89, 108
 - counter anion exchange 89–90
 - covalent functionalization of graphene nanomaterials 97–99
 - antibodies tethering 105–106
 - biopolymers covalent linkage 103, 105
 - graphene oxide reduction 99, 100
 - graphene oxide synthesis 99
 - nucleic acids attachment 106–108
 - organic molecules and biomolecules attachment 108, 109–110
 - PEGylated-GO conjugates 100–103
 - peptides and enzymes grafting 108
 - covalent immobilization 142–144
 - cross linking of free amine groups 142, 143
 - cycloaddition reactions
 - aryne addition 36–37
 - azomethine ylide 1,3-dipolar cycloaddition 22–28
 - Bingel type cycloaddition 37–39
 - carbene addition 35–36
 - Diels–Alder cycloaddition 29–30, 31
 - nitrene addition 30, 32–35
 - zwitterionic intermediate cycloaddition 28–29
 - cyclodextrins 71–72
 - cytochrome *c*-based biosensors 152
 - CYTOP® 177
- d**
- D band 11, 12
 - DC arcing 284–287
 - density functional theory (DFT) 188, 194, 296, 335
 - dextran (Dex) polymer 63
 - diazonium salt reaction 39–42
 - Diels–Alder cycloaddition 29–30, 31
 - diffuse reflectance spectroscopy (DRS) 185
 - direct methanol fuel cells (DMFCs) 230,
 - DNA sensors 152, 153–154
 - doping 177, 178, 179, 183, 184, 187, 190, 192, 193, 283, 334–339
 - boron doping 320–321, 326–329
 - – chemical vapor deposition 323–326
 - – mechanical exfoliation 321
 - – thermal annealing 321, 322–323

- boron nitride (BN) doping 329–333
- nitrogen-doped graphene 284, 306–320
 - – chemical functionalization route 288–289
 - – chemical vapor deposition and pyrolysis 293–300
 - – DC arcing 284–287
 - – heating with ammonia, hydrazine and reagents 287–288
 - – pyrolysis methods 300–306
 - – solvothermal synthesis 289–293
 - – properties and applications 339–352
- doxorubicin (DOX) 111, 120, 122, 250
- doxorubicin hydrochloride (DXR) 250
- dye sensitized solar cells (DSSCs) 267

e

- electrochemically active surface area (ECSA) 229, 230
- electrochemical surface plasmon resonance (EC-SPR) spectroscopy 381
- electron energy loss spectroscopy (EELS) 284, 286, 320, 330, 333
- electrophilic addition 46, 47–48
- electrostatic and hydrophobic interactions 116
 - adsorption of quantum dots 121
 - coating with polymers and biopolymers 116–119
 - nanoparticles deposition 119–121
- enzyme-based biofuel cells (EBFCs) 159
- enzymes and biomolecules immobilization 139–140
 - approaches 141–144
 - biocatalysis 155, 156–159
 - biofuel cells 159–161
 - biosensors 145–146
 - – cytochrome *c*-based biosensors 152
 - – DNA sensors 152, 153–154
 - – glucose oxidase-based biosensors 146–150
 - – horseradish peroxidase-based biosensors 150–151
 - – immunosensors and aptasensors 154–155
 - – protein/enzyme biosensors 152
 - – tyrosinase-based biosensors 151
 - drug and gene delivery 161–162
 - interaction with nanomaterials 162–164
- epoxide groups
 - chromophores addition 85, 86
 - nucleophilic addition of amine 83–85
 - polymers addition 86–87

f

- field effect transistors 288, 292, 295, 304, 305, 308, 310, 311, 312, 328, 329, 339, 340, 352, 363, 390, 392, 393
- field emission scanning electron microscope (FESEM) 276
- fluorographene 179–183
 - graphene fluorination 175
 - mechanical and chemical exfoliation 175
- 5-fluorouracil (5-FU) 250
- folic acid-conjugated GO 125, 127
- Fourier transform infrared (FTIR) 33, 37, 60, 71, 84, 85, 156, 182, 183, 256, 257, 389
- free radicals addition
 - diazonium salt reaction 39–42
 - radical additions 42, 43–46
- Friedel Crafts acylation 81
- functionalized graphene (*f*-graphene) 220
 - anchoring of NPs 223–227
 - POM 238

g

- G' band 11
- gallium-phthalocyanine (Ga-Pc) addition to GO through Ga–O covalent bond 82–83
- G band 11
- glucose oxidase-based biosensors 146–150
 - grafted from procedure 61
 - grafted to procedure 61
- graphene-enhanced Raman scattering (GERS) 387
- graphene quantum dots (GQDs) 16, 17, 150
- graphite intercalation compounds (GICs) 1

h

- halogenated graphenes 173–174, 190–193
 - characterization 179
 - – fluorographene 179–183
 - – partially fluorinated and halogenated graphenes 183–184
 - chemistry, properties, and applications 184–190
 - chlorinated and brominated graphenes chemistry and properties 190
 - and graphene heterostructures and patterned halogenation 193–195
 - synthesis 174–175, 178–179
 - – fluorographene 175
 - – nonstoichiometric fluorinated graphene and fluorinated graphene oxide 175, 176–178
- heparin 119, 206
- hexamethylenetetramine (HMT) 292

- high-resolution scanning transmission microscopy (HR-SEM) 226, 227
- high-resolution transmission electron microscopy (HRTEM) 234, 256, 257, 273, 297, 304, 318, 330
- history 1–2
- graphene and graphene oxide 2–3
- GO large scale production by
 - Langmuir-Blodgett methods 6
 - graphene production methods 6, 7–8
 - isolation of graphene monolayers 5–6
 - preparation from graphene oxide 3
- graphene characterization 9
- microscopic observation 9–10
- optical properties 13–17
- Raman spectroscopy 11–12
- thermogravimetric analysis (TGA) 12–13
- X-ray diffraction 17–18
- horseradish peroxide-based biosensors 150–151
- HREELS 182, 183
- hyaluronic acid-chlorin e6 conjugate (HA-Ce6) 119
- hydrophilic–biocompatible derivatives 62–64
- hydroxyl groups 77, 78, 79–80
- hydroxyl substituted polymers 73

- i**
- immunosensors and aptasensors 154–155
- in-plane geometry 373, 374
- π -interaction of benzene 200–201
- ionic liquid (IL) 148–149
- Iressa 122

- j**
- Jackson–Meisenheimer (JM) complex 270–271

- l**
- Langmuir–Blodgett approach 6, 359, 385, 386
- GO single layers (GOSLs) 385, 387–389
- nanocomposite films 389–390
- Langmuir–Schaefer method 6
- layer-by-layer assembly (LbL) 359–360
- applications and properties of thin films 390–396
- graphene-based hybrid films 360, 383–385
 - electronics 360–374
 - as sensors 375–382
- Langmuir–Blodgett approach 385, 386
- GO single layers (GOSLs) 385, 387–389
 - nanocomposite films 389–390
- ligands and antibodies and GO functionalization
- antibody-functionalized GO for radioimaging and biosensing 127–129
- folic acid-conjugated GO 125, 127
- lipophilic derivatives 61–62
- liquid–liquid interfacial precipitation (LLIP) 260
- lithium batteries 233–236
- low-pressure chemical vapor deposition (LPCVD) 259

- m**
- magnetic NPs 242
 - biomedical applications 248, 249–252
 - magnetic properties 243–246
 - magnetic separation of metals and pollutants with GO-Mag NPs 247–248
- magnetic resonance imaging 250–252
- mechanical exfoliation 321
- metal and metal oxide nanoparticles
 - immobilization 219
 - graphene production 219–220
 - functionalized graphene (*f*-graphene) 220
 - graphene growth on metal surfaces 220
 - graphene oxide (GO) 220
 - graphite micromechanical cleavage 221
 - magnetic NPs 242
 - biomedical applications 248, 249–252
 - magnetic properties 243–246
 - magnetic separation of metals and pollutants with GO-Mag NPs 247–248
- metal nanoparticles 221
 - anchoring of NPs on *f*-graphene 223–227
 - applications 227–233
 - GO-reducing approach 221–223
 - metal oxide nanoparticles 233
 - lithium batteries 233–236
 - optical properties 236–238
 - photocatalytic reduction of GO 238, 239–242
- metal nanoparticles 221
 - anchoring of NPs on *f*-graphene 223–226
 - controlling size of NPs 226–227
 - applications
 - in biology 232–233
 - in catalysis 229–232
 - optoelectronic devices 227–228
 - GO-reducing approach 221–222
 - reduction assisted by sonication 222–223

- metal oxide nanoparticles 233
 - lithium batteries 233–236
 - optical properties 236–238
 - photocatalytic reduction of GO 238, 239–242
- micromechanical cleavage, of graphite 221
- multi-walled nanotube (MWNT) 265, 266, 267–270, 369

- n**
- Nafion® 208
- nanoparticles deposition 119–121
- nanoribbons (graphene) 7–8, 39, 193, 194
- near-edge X-ray absorption fine structure (NEXAFS) spectroscopy 185, 186
- nitrene addition 30, 32–35
- nitrogen-doped graphene 284, 306–320
 - chemical functionalization route 288–289
 - chemical vapor deposition and pyrolysis 293–300
 - DC arcing 284–287
 - heating with ammonia, hydrazine and reagents 287–288
 - pyrolysis methods 300–306
 - solvothermal synthesis 289–293
- non-covalent functionalization, of graphene 110
 - adsorption via π -stacking 110–116
 - electrostatic and hydrophobic interactions 116–121
- noncovalent functionalization
 - graphene–ligand noncovalent interactions and experiment 210–213
 - – biomolecules 205–207
 - – polycyclic molecules 202–205
 - – polymers 207–210
 - theoretical background 199
 - – adsorption on graphene 201–202
 - – π -interaction of benzene 200–201
- nucleic acids attachment 106–108
- nucleophilic addition 46
 - – cycloaddition by zwitterionic intermediate 28–29
 - – Diels–Alder cycloaddition 29–30, 31
 - – nitrene addition 30, 32–35
 - electrophilic addition 46, 47–48
 - free radicals addition
 - – diazonium salt reaction 39–42
 - – radical additions 42, 43–46
 - nucleophilic addition 46
 - organometallic chemistry 48–49
 - post functionalization reactions 50–55
- organic groups addition, through reactions with oxygen species of GO 59–60
 - ammonia interaction with carboxylic acids and epoxides 80, 81
 - carboxylic acid and hydroxyl groups reaction with isocyanate derivatives 78
 - carboxylic acids 61
 - – GO esterification 71–75
 - – GO functionalization through heterocyclic ring formation 75–77
 - – organic functionalization through amide bond formation 61–71
 - enrichment in carboxylic acids 81, 82
 - epoxide groups
 - – chromophores addition 85, 86
 - – nucleophilic addition of amine to epoxides 83–85
 - – polymers addition 86–87
 - epoxides reaction with carboxylic acids and hydroxyl groups 78, 79–80
 - gallium-phthalocyanine (Ga-Pc) addition to GO through Ga–O covalent bond 82–83
 - graphene/polymer nanocomposites 60–61
 - hydroxyl groups 77
 - post functionalization 87
 - – counter anion exchange 89–90
 - – of organically modified GO via click chemistry 87–89
- organic molecules and biomolecules attachment 108, 109–110
- organometallic chemistry 48–49

- o**
- oligo(phenylenevinylene) (OPV) 65, 66–67
- optical microscopy 9
- organic functional groups covalent attachment 21–22
 - cycloaddition reactions
 - – aryne addition 36–37
 - – azomethine ylide 1,3-dipolar cycloaddition 22–28
 - – Bingel type cycloaddition 37–39
 - – carbene addition 35–36

- p**
- PEGylated-GO conjugates 100–103
- peptides and enzymes grafting 108
- phospholipid monolayer 205, 206
- photocatalytic reduction of GO 238, 239–242
- phthalocyanines 64
- physical adsorption 141, 144
- polycyclic molecules 202–205
- poly(3,4-ethylenedioxythiophene (PEDOT) 366, 373–374
- polyethylenimine (PEI) 109, 117, 119,

- polyhedral oligomeric silsesquioxane (POSS) 70–71
- polymer -and biopolymer-grafted graphene nanomaterials as nanocarriers 121, 122
- chitosan-functionalized GO 125
 - polymer-functionalized GO for drug delivery 122–123
 - polymer-functionalized GO for gene delivery 123–125
- polymer graphene composites 69–71
- poly(*N*-isopropylacrylamide) (PNIPAM) 87
- porphyrins 64
- post functionalization 87
- counter anion exchange 89–90
 - of organically modified GO via click chemistry 87–89
- post functionalization reactions 50–55
- protein/enzyme biosensors 152
- proton exchange membrane (PEMs) fuel cells 229
- pulse voltammetry 379
- pyrene derivatives adsorption 111, 112–113
- pyrolysis
- and chemical vapor deposition and pyrolysis 293–300
 - methods 300–306
- q**
- quantum dots adsorption 121
- r**
- radioimaging and biosensing and antibody-functionalized GO 127–129
- Raman spectroscopy 9, 11–12, 60, 182, 184, 187, 206, 232, 233, 256, 257, 259, 284, 285, 286, 295, 298, 305, 314, 326, 327
- Rashba splitting 202
- reduced graphene-oxide (rGO) 4, 5, 13, 15, 17, 26, 30, 42, 45, 46, 48, 52, 59, 60, 62, 63, 70, 71, 72, 76, 77, 78, 81, 83, 84, 95, 97, 99, 100, 106, 110, 116, 117, 119, 120, 121, 122, 141, 148, 149, 150, 151, 154, 157, 164, 186, 190, 202, 205, 207, 208, 210, 221, 223, 229, 230, 235, 237, 240, 242, 245, 246, 251. *See also carbon nanostructures; doping; layer-by-layer assembly*
- reversible addition-fragmentation chain transfer (RAFT) 43
- s**
- scanning electron microscope (SEM) 7, 71, 230, 261, 263, 273, 295, 314, 315, 319, 325, 332, 338, 371
- scanning tunneling microscopy (STM) 284, 285, 290, 294, 296, 298, 299, 320, 321
- scanning tunneling spectroscopy (STS) 298
- selected area electron diffraction (SAED) 179, 180
- single-walled nanotube (SWNT) 262, 263, 266, 270, 272, 273, 274, 275
- solvothermal synthesis 289–293
- sonication methods 5, 6
- spectromicroscopy 9
- surface-enhanced Raman spectroscopy (SERS) 186, 232, 233, 388
- symmetry-adapted perturbation theory (SAPT) 200
- t**
- tetraphenyl ethylene (TPE) 33–34
- thermal annealing 321, 322–323
- thermogravimetric analysis (TGA) diagrams 9, 12–13, 25, 26, 38, 62, 256, 274, 275
- TorayTM 230
- transmission electron microscope (TEM) 9, 10, 16, 32, 35, 36, 39, 67, 179, 180, 207, 223, 258, 261, 263, 265, 273, 276, 278, 284, 285, 302, 303, 314, 315, 320, 321, 331, 333, 338, 389
- trinitrotoluene (TNT) 270, 271
- Tyndall effect 14,
- tyrosinase-based biosensors 151
- u**
- ultrasonication 44–45, 148
- UV photoemission spectroscopy 295
- UV–vis spectrum 60, 65, 66, 69, 72, 82, 164, 181, 182, 260, 271, 371
- v**
- voltammetric technique 268, 270
- w**
- water splitting 237–238
- Wurtz-type reductive coupling (WRC) 326
- x**
- X-ray diffraction (XRD) 9, 17–18, 67, 68, 75–76, 84, 85, 320
- X-ray photoelectron spectroscopy (XPS) 60, 67, 81, 82, 84, 85, 181, 182, 184, 187, 258, 284, 286, 287, 292, 294, 298, 301, 302, 305, 320, 327, 329, 333, 336, 389
- z**
- zinc phthalocyanine (Zn-PC) 85, 86
- zwitterionic intermediate cycloaddition 28–29